Atlas *of* Fetal MRI

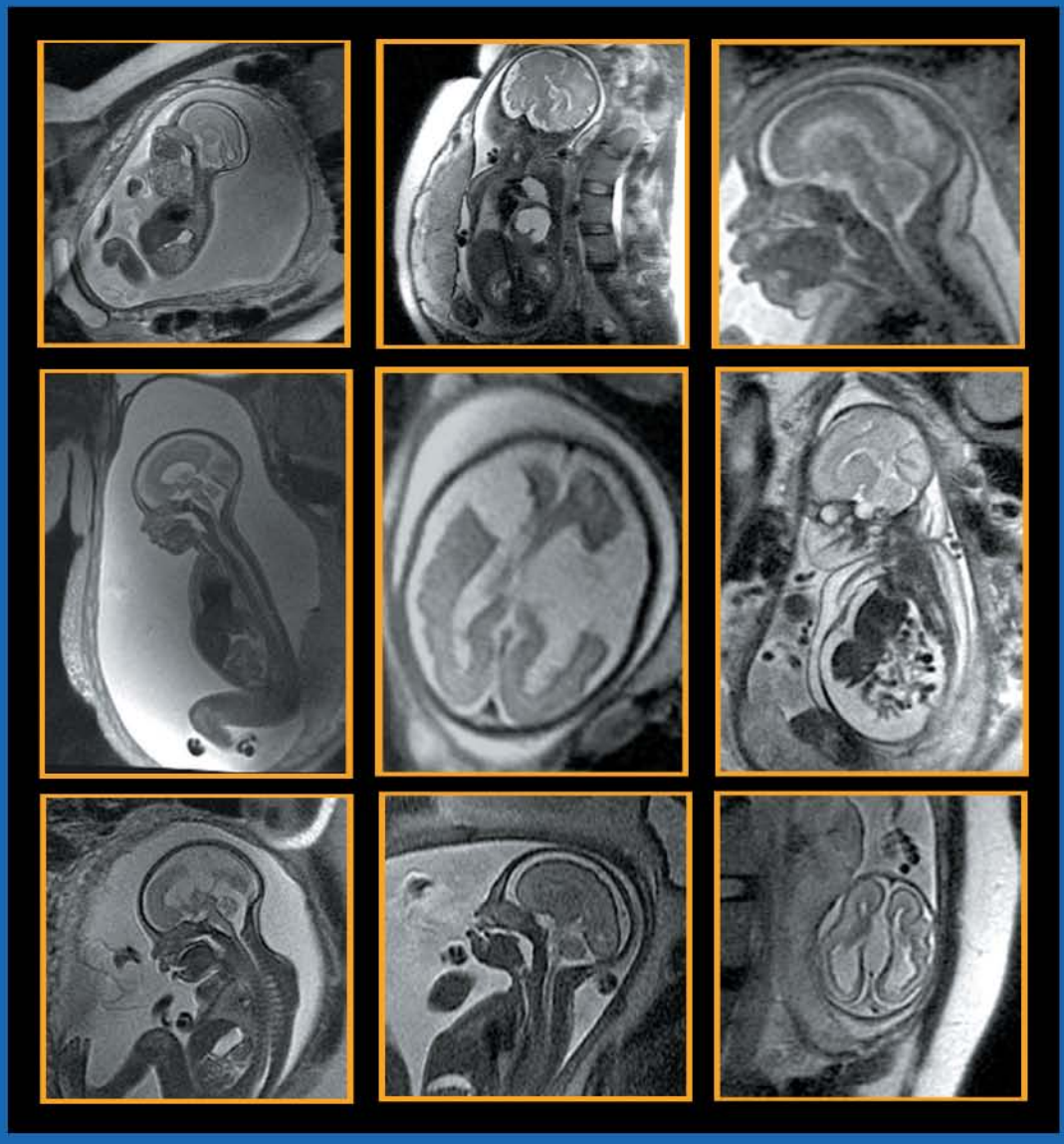

Edited by Deborah Levine

Atlas *of* Fetal MRI

Atlas *of* Fetal MRI

Edited by

Deborah Levine

Beth Israel Deaconess Medical Center
Harvard Medical School
Boston, Massachusetts, U.S.A.

Taylor & Francis
Taylor & Francis Group

Boca Raton London New York Singapore

Published in 2005 by
Taylor & Francis Group
6000 Broken Sound Parkway NW, Suite 300
Boca Raton, FL 33487-2742

Printed in the United States of America on acid-free paper
10 9 8 7 6 5 4 3 2 1

International Standard Book Number-10: 0-8247-2548-4 (Hardcover)
International Standard Book Number-13: 978-0-8247-2548-8 (Hardcover)

Library of Congress Cataloging-in-Publication Data

Catalog record is available from the Library of Congress

T&F informa

Taylor & Francis Group is the Academic Division of T&F Informa plc.

Visit the Taylor & Francis Web site at
http://www.taylorandfrancis.com

This book is dedicated to Alexander, Rebecca, and Julia Jesurum

Preface

Fetal magnetic resonance (MR) imaging has undergone a remarkable growth in the past decade. Fast imaging techniques allow for images to be obtained in a fraction of a second. With this ability, we have begun to view the fetus in a manner not previously possible. Although the appearance of fetal anatomy on sonography has been well-established, there are few resources available that illustrate the MR appearance of normal and abnormal fetal anatomy.

Although ultrasound is the standard imaging technique utilized in pregnancy, there are many cases where sonographic diagnosis is unclear. In these cases, MR imaging can help clarify diagnosis and thus aid in patient counseling and management. This is especially important in evaluation of the fetal central nervous system.

Knowledge of brain anatomy used for pediatric or adult imaging may not be sufficient for evaluation of the fetus, where, for the brain in particular, changes in appearance occur over time. Abnormalities with a particular differential diagnosis in pediatric patients can have a different differential diagnosis in the fetus. As interpretation of MR examinations may be performed by radiologists, obstetricians, and pediatric subspecialists, it is important to have a text that incorporates fetus-specific information needed by all of these subspecialties.

The illustrations in this text were taken from patients undergoing MR examinations for maternal and fetal indications. Many of the studies were obtained under research protocols investigating the utility of fetal MR imaging.

There are many excellent textbooks of fetal anomalies. This book is not intended to replace them, rather, it is a resource to illustrate the changing appearance of fetal anatomy over time and the types of anomalies that can be seen with fetal MR imaging.

In addition to chapters that deal with normal anatomy and pathology, there are chapters with background information on safety of MR in pregnancy, techniques of fast imaging, and artifacts.

I hope that this book will give prenatal diagnosticians an improved ability to counsel patients.

Deborah Levine

Acknowledgments

Many of the images of the fetal brain were obtained under NIH grant NS37945 and NIBIB EB001998. I am very grateful to Dr. Herbert Kressel who encouraged my pursuit of fetal magnetic resonance imaging.

This work on fetal imaging would not have been possible without the training I received in Ultrasound. I feel very lucky to have had as mentors: Barbara Gosink, Dolores Pretorius, George Leopold, Nancy Budorick, Roy Filly, Peter Callen, Ruth Goldstein, and Vickie Feldstein.

The fetal research program at BIDMC would not have been possible without the support of the MR section chiefs, Robert Edelman and Neil Rofsky who allowed use of the research magnet and shared their ideas on fast imaging sequences.

Special thanks go to the physicists who aided in sequence optimization, Qun Chen and Charles McKenzie. I am also very grateful to the many technologists who helped scan patients, in particular Wei Li, Steven Wolff, and Norman Farrar. I would like to thank Ronald Kukla for his administrative support.

I especially would like to thank the many proof-readers of the book chapters, including Alex Jesurum, Daniel Levine, Dolores Pretorius, Philip Boiselle, and Donna Wolfe.

Contents

Contributors

Patrick Barnes, MD *Department of Radiology, Lucille Salter Packard Children's Hospital, Stanford University, Palo Alto, California, USA*

Fergus V. Coakley, MD *Department of Radiology, University of California, San Francisco, California, USA*

Vandana Dialani, MD *Department of Radiology, Beth Israel Deaconess Medical Center, Harvard Medical School, Boston, Massachusetts, USA*

Bonnie N. Joe, MD *Department of Radiology, University of California, San Francisco, California, USA*

Deborah Levine, MD *Department of Radiology, Beth Israel Deaconess Medical Center, Harvard Medical School, Boston, Massachusetts, USA*

Charles A. McKenzie, PhD *Department of Radiology, Beth Israel Deaconess Medical Center, Harvard Medical School, Boston, Massachusetts, USA*

Tejas Mehta, MD *Department of Radiology, Beth Israel Deaconess Medical Center, Harvard Medical School, Boston, Massachusetts, USA*

Ivan Pedrosa, MD *Department of Radiology, Beth Israel Deaconess Medical Center, Harvard Medical School, Boston, Massachusetts, USA*

Caroline Robson, MB, ChB *Department of Radiology, Childrens Hospital, Harvard Medical School, Boston, Massachusetts, USA*

Annemarie Stroustrup Smith, MD *Harvard-MIT Division of Health Science and Technology and Harvard Medical School, Boston, Massachusetts, USA*

1

Safety of MR Imaging in Pregnancy

DEBORAH LEVINE

INTRODUCTION

The risks and benefits of all imaging studies that are carried out during pregnancy need to be discussed with the patient. In the case of magnetic resonance (MR) imaging there are theoretical risks of teratogenicity, but no proven effects in humans. This chapter reviews safety concerns pertaining to MR examinations during pregnancy and illustrates embryonic and fetal anatomy in the first trimester in examinations performed for maternal indications.

LITERATURE REGARDING POTENTIAL TERATOGENIC EFFECTS

There is no consistent or convincing evidence to suggest that short-term exposure to electromagnetic fields, such as that which occurs during MR imaging, harms the developing fetus (1–5). A few studies have linked prolonged or high-level electromagnetic field exposure to deleterious effects on embryogenesis, chromosomal structure, or fetal development (1,6–10). However, in humans who have been exposed to diagnostic MR imaging, no delayed sequelae have been encountered, and it is expected that the potential risk for any delayed sequelae is extremely small or nonexistent. In a study by Myers et al. (11), no increased incidence of growth retardation was observed in follow-up of 74 pregnancies that had been exposed to *in utero* MR echoplanar imaging.

TEMPERATURE INCREASES DURING MR IMAGING

Exposure of patients to MR imaging can produce heat related to the radiofrequency pulses. Fluids, such as in the lens of the eye, are known to be relatively poor in dissipating deposited heat (12). As the fetus essentially lies in a water bath, and because tissues dissipate heat by blood flow, it is possible that heat accumulates in the gravid uterus during medical imaging. The reason why this is of particular concern in pregnant patients is that the specific absorption rate (SAR) monitor, that documents the amount of energy deposited over time, is set for the weight of the patient. However, when performing fetal MR imaging we are actually studying a much smaller patient (the fetus) in a highly conductive "salt-water" bath (amniotic fluid). In addition, the gravid uterus in the third trimester often fills the magnet bore: this limits the amount of air-flow through the bore and around the patient, thus potentially decreasing the ability of the patient to radiate deposited heat to the environment. Although body temperature has been shown to rise during MR imaging at high whole-body SARs (13), in a study using 4.0 W/kg on pregnant patients at 33–39 weeks gestational age, no maternal temperature changes were identified (14). In a study of measuring temperature of amniotic fluid, fetal brain, and fetal abdomen in pregnant pigs, no temperature changes were noted using fast MR imaging techniques (specifically half Fourier single shot turbo spin-echo sequences) (15).

NOISE DURING MR IMAGING

The amount of noise generated during fetal MR imaging is also of potential concern. A model of sound wave transmission of a plane-wave sound across an air–water interface predicts a reduction in sound intensity of almost 30 dB in water (16). Using a fluid-filled stomach as a model for the gravid uterus, Glover et al. (16) demonstrated that the attenuation of the sound intensity is >30 dB at the frequencies generated during echoplanar imaging. Much higher peak pressures could be obtained by tapping the abdomen with the fingers. In a study of 25 children aged 2–4 years born after having been scanned by echoplanar imaging during pregnancy, there were no reported cases of hearing damage or abnormalities (17).

FETAL HEART RATE DURING MR IMAGING

A few in studies have assessed the potential effect of MR procedures on fetal heart rate and motion (18,19). In a study of fetal cardiotopography during MR imaging, maternal temperature, heart rate, and blood pressure, as well as fetal heart rate and motion, were measured in eight women at 33–39 weeks gestational age before, during, and after MR imaging at 1.5 T. No short-term effects were detected (14).

CONTRAINDICATIONS TO MR IMAGING AND PATIENT COMFORT

As for all patients, there are absolute contraindications to MR imaging in pregnant patients (e.g., a ferromagnetic cerebral aneurysm clip, cardiac pacemaker), and some patients are too claustrophobic to undergo the examination. Use of short bore magnets makes claustrophobia less of a concern. However, in patients who have a history of claustrophobia, we have found it helpful to premedicate with sublingual Xanax 0.5–3 mg given 1 hour prior to the examination. In addition, for patients who are claustrophobic but do not want to be medicated, we have found it helpful to cover the eyes before the patient enters the magnet bore. An additional problem in scanning pregnant patients is that they may have difficulty lying on their backs, especially in the third trimester. In these cases, patients can be imaged in the lateral decubitus position.

INTRAVENOUS CONTRAST

Use of intravenous contrast for MR imaging is relatively contraindicated in pregnancy. Gadolinium is a pregnancy Category C drug, meaning that there are insufficient studies to determine potential harmful effects in pregnant women. The drug should be used only if the benefit justifies the potential risk to the fetus. The product insert for Magnevist (gadopentetate dimeglumine) states that gadopentetate dimeglumine slightly retarded fetal development when given intravenously for 10 consecutive days to pregnant rats at daily doses of 2.5 times the human dose and when given intravenously for 13 consecutive days to pregnant rabbits at daily doses of 7.5 times the human dose (20). The Omniscan (Gadodiamide) insert states that Omniscan has been shown to have an adverse effect on embryofetal development in rabbits that is observed as an increased incidence of flexed appendages and skeletal malformations at dosages as low as 0.5 mmol/kg per day for 13 days during gestation (approximately two times the maximum human cumulative dose of 0.3 mmol/kg) (21). Therefore, at the current time, for fetal imaging there are no accepted indications for use of intravenous contrast. For assessment of maternal anatomy, the risk-benefit ratio must be assessed on an individual basis.

IMAGING IN THE FIRST TRIMESTER

Because the greatest theoretic risk is at the time of organogenesis, and the small size of the developing fetus/embryo is difficult to evaluate early in pregnancy, we avoid MR imaging in the first trimester whenever feasible. With currently available techniques, it is not useful to perform MR examinations for fetal diagnosis in the first trimester. Figures 1.1–1.4 demonstrate first trimester pregnancies scanned for maternal indications. As shown in these figures, prior to 13 weeks the developing embryo/fetus is small and difficult to adequately visualize. Anomalies are better detected with ultrasound than with MR imaging during this time period. However, MR imaging can be useful when more information about the location of a presumed abnormal gestational sac is needed (Fig. 1.5). If MR imaging is needed for maternal diagnosis in the first trimester, then imaging should be performed. In a recent article by Shellock and Crues (22), it is stated that "... in cases where the referring physician and the attending radiologist can defend that the findings of the MR procedure have the potential to affect the care of the mother or fetus ... the MR procedure may be performed with oral and written informed consent, regardless of the trimester."

SUMMARY OF RECOMMENDATIONS

According to the Safety Committee of the Society for Imaging (23), MR procedures are indicated for use in pregnant women if other nonionizing forms of diagnostic imaging are inadequate or if the examination provides important information that would otherwise require exposure to ionizing radiation (i.e., X-ray, CT, etc.). It is required that pregnant patients be informed that, to

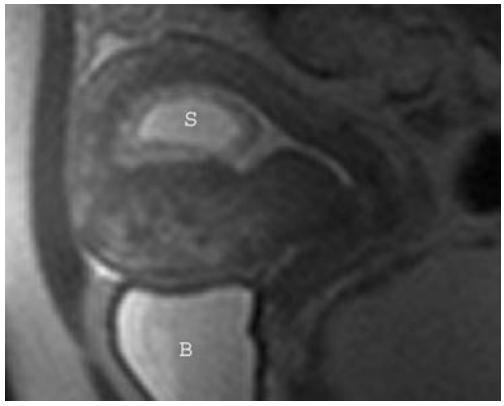

Figure 1.1 Uterus at 7 weeks gestational age. This representative sagittal T_2-weighted image shows fluid in the intrauterine gestational sac (S). The embryonic pole is not visualized on this or other images obtained during the study owing to partial volume averaging. B, bladder.

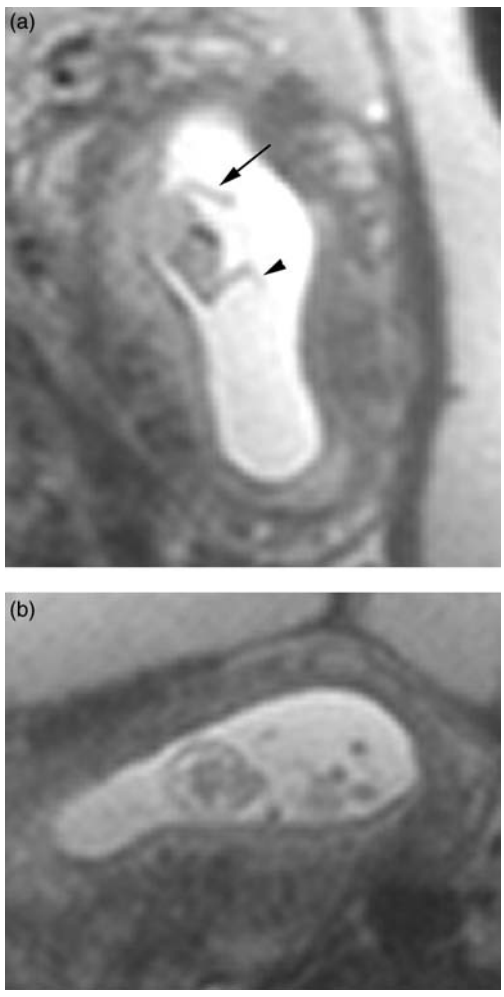

Figure 1.3 Fetus at 11 weeks gestational age. (a) Oblique sagittal view of fetal torso, arm (arrow), and leg (arrowhead). (b) Axial view of fetal head. The intracranial anatomy is poorly visualized secondary to partial volume averaging and early gestational age.

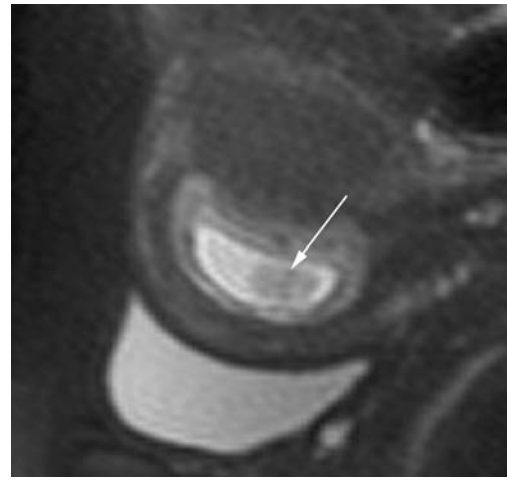

Figure 1.2 Embryo at 9 weeks gestational age. Sagittal T_2-weighted image of the uterus showing a coronal image of embryonic torso. Owing to the small size of the embryo (arrow), it is difficult to visualize anatomic structures.

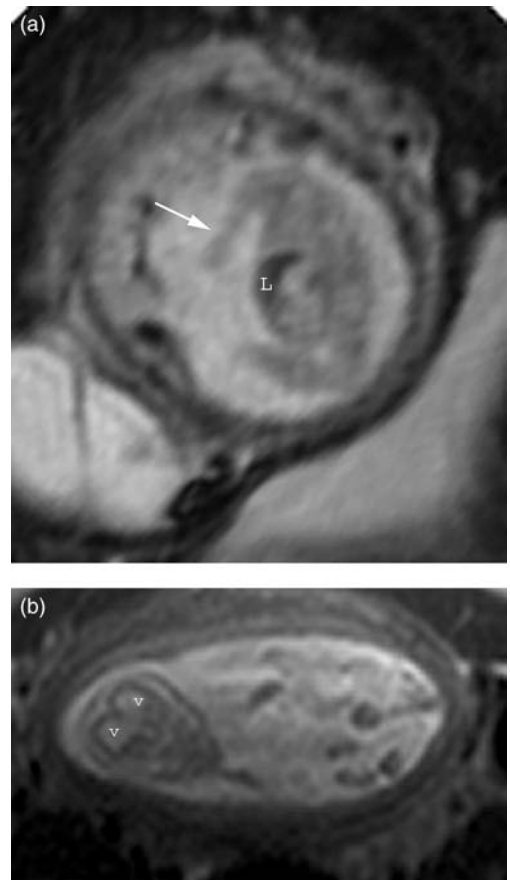

Figure 1.4 Fetus at 13 weeks gestational age. (a) Oblique coronal T_2-weighted image of fetal torso shows the liver (L) and the arm (arrow). (b) Oblique coronal view of fetal head shows the cerebral ventricles (v). Note the improvement in visualization of intracranial anatomy compared with Fig. 1.3.

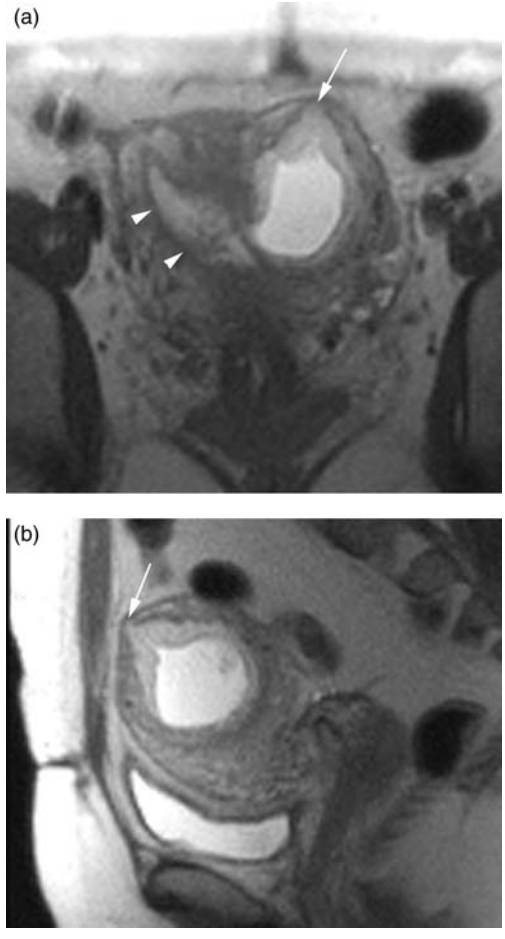

Figure 1.5 Pregnancy in myomectomy scar at 8 weeks gestational age. (a) Coronal and (b) sagittal T_2-weighted images show the gestational sac high in the left fundus, separate from the endometrial cavity (arrowheads). The placenta is seen extending into the myometrium to the uterine serosa (arrow). This is the region of the patient's prior myomectomy. The patient was treated with methotrexate.

date, although there is no indication that the use of clinical MR procedures during pregnancy produces deleterious effects, according to the FDA, the safety of MR procedures during pregnancy has not been definitively proven (24). According to the American College of Radiology White Paper on MR Safety, "Pregnant patients can be accepted to undergo MR scans at any stage of pregnancy if, in the determination of a . . . designated attending radiologist, the risk–benefit ratio to the patient warrants that the study be performed" (25). The White Paper further states that "it is recommended that pregnant patients undergoing an MR examination provide written informed consent to document that they understand the risk/benefits of the MR procedure to be performed, the alternative diagnostic options available to them (if any), and that they wish to proceed" (25).

REFERENCES

1. Elster AD. Does MR imaging have any known effects on the developing fetus? Am J Roentgenol 1994; 162:1493.
2. Geard CR, Osmak RS, Hall EJ et al. Magnetic resonance and ionizing radiation: a comparative evaluation *in vitro* of oncogenic and genotoxic potential. Radiology 1984; 152:199–202.
3. Kay HH, Herfkens RJ, Kay BK. Effect of magnetic resonance imaging on *Xenopus laevis* embryogenesis. Magn Reson Imaging 1988; 6:501–506.
4. Peeling J, Lewis JS, Samoiloff M et al. Biological effects of magnetic fields: chronic exposure of the nematode *Panagrellus redivivus*. Magn Reson Imaging 1988; 6:655–660.
5. Prasad N, Wright DA, Ford JJ et al. Safety of 4-T MR imaging: study of effects on developing frog embryos. Radiology 1990; 174:251–253.
6. Beers GJ. Biological effects of weak electromagnetic fields from 0 Hz to 200 MHz: a survey of the literature with special emphasis on possible magnetic resonance effects. Magn Reson Imaging 1989; 7:309–331.
7. Carnes KI, Magin RL. Effects of *in utero* exposure to 4.7 T MR imaging conditions on fetal growth and testicular development in the mouse. Magn Reson Imaging 1996; 14:263–274.
8. Heinrichs WL, Fong P, Flannery M et al. Midgestational exposure of pregnant BALB/c mice to magnetic resonance imaging conditions. Magn Reson Imaging 1988; 6:305–313.
9. Tyndall DA, Sulik KK. Effects of magnetic resonance imaging on eye development in the C57BL/6J mouse. Teratology 1991; 43:263–275.
10. Yip YP, Capriotti C, Talagala SL et al. Effects of MR exposure at 1.5 T on early embryonic development of the chick. J Magn Reson Imaging 1994; 4:742–748.
11. Myers C, Duncan KR, Gowland PA et al. Failure to detect intrauterine growth restriction following *in utero* exposure to MRI. Br J Radiol 1998; 71:549–551.
12. Shellock FG, Crues JV. Corneal temperature changes induced by high-field-strength MR imaging with a head coil. Radiology 1988; 167:809–811.
13. Shellock FG, Schaefer DJ, Kanal E. Physiologic responses to an MR imaging procedure performed at a specific absorption rate of 6.0 W/kg. Radiology 1994; 192:865–868.
14. Michel SC, Rake A, Keller TM et al. Fetal cardiographic monitoring during 1.5-T MR imaging. Am J Roentgenol 2003; 180:1159–1164.
15. Levine D, Zuo C, Faro CB et al. Potential heating effect in the gravid uterus during MR HASTE imaging. J Magn Reson Imaging 2001; 13:856–861.
16. Glover P, Hykin J, Gowland P et al. An assessment of the intrauterine sound intensity level during obstetric echo-planar magnetic resonance imaging. Br J Radiol 1995; 68:1090–1094.
17. Baker PN, Johnson IR, Harvey PR et al. A three-year follow-up of children imaged *in utero* with echo-planar magnetic resonance. Am J Obstet Gynecol 1994; 170:32–33.

18. Poutamo J, Partanen K, Vanninen R et al. MRI does not change fetal cardiotocographic parameters. Prenat Diagn 1998; 18:1149–1154.
19. Vadeyar SH, Moore RJ, Strachan BK et al. Effect of fetal magnetic resonance imaging on fetal heart rate patterns. Am J Obstet Gynecol 2000; 182:666–669.
20. Product Information, Magnevist, Berlex Laboratories, 2000.
21. Product Information, Omniscan, Amersham Health, 2000.
22. Shellock FG, Crues JV. MR procedures: biologic effects, safety, and patient care. Radiology 2004; 232:635–652.
23. Shellock FG, Kanal E. Policies, guidelines, and recommendations for MR imaging safety and patient management. SMRI Safety Committee. J Magn Reson Imaging 1991; 1:97–101.
24. US Food and Drug Administration. Guidance for content and review of a magnetic resonance diagnostic device 510 (k) application. Washington DC, Aug 2, 1988.
25. Kanal E, Borgstede JP, Barkovich AJ et al. American College of Radiology White Paper on MR Safety. Am J Roentgenol 2000; 178:1335–1347.

2

MR Imaging of Normal Brain in the Second and Third Trimesters

DEBORAH LEVINE, CAROLINE ROBSON

INTRODUCTION

One of the best-accepted applications of fetal magnetic resonance (MR) imaging is assessment of the central nervous system (CNS) (1–5). The anatomic detail provided by MR imaging allows for direct visualization of the brain parenchyma, which can aid in the diagnosis of CNS abnormalities. The changing appearance of the brain throughout gestation can make assessment of abnormalities challenging; thus, it is helpful to have a frame of reference for the normal appearance of anatomy over time. In particular, knowledge of the normal appearance and maturation of the developing sulci and gyri is helpful in the appropriate diagnosis and counseling of anomalous fetuses in whom cortical development may be delayed or altered. There are no accepted indications for fetal MR imaging in the first trimester; therefore this chapter details the developmental changes that are observable from 14 weeks gestational age and beyond.

CORTICAL DEVELOPMENT—AN OVERVIEW

Cortical maturation, as manifested by the progressive appearance, deepening, and increasing complexity of cerebral sulci, is clearly demonstrated by fetal MR imaging. However, normal maturation as visualized on MR examinations follows a predictable course that lags behind the time sequence for maturation described in neuroanatomic specimens (6,7). Table 2.1 reviews the appearance of sulci in normal fetuses with respect to gestational age in neuroanatomic (8) and MR studies (6,7). The neuroanatomic guidelines provided by Chi et al. (8) describe gestational ages at which 25–50% of brain specimens demonstrate particular cortical landmarks, with an interval of ~2 weeks between the earliest appearance of a particular landmark and its occurrence in 75–100% of the brains (8). Magnetic resonance maturation appears slightly delayed relative to neuroanatomic studies due to various factors: (1) neuroanatomic studies being performed on thin slices being directly visualized; (2) MR slice thickness (3–5 mm) being much greater than that used in the anatomic studies (15–30 μm); (3) image quality issues such as suboptimal signal-to-noise; and (4) limited spatial resolution compared with neuroanatomic studies.

Normal cortical development in the second and third trimesters is illustrated in Figs. 2.1–2.14, which are presented in order of gestational age. In general, fetuses with mild ventriculomegaly and other CNS anomalies have delayed cortical development as compared with normal fetuses (Table 2.2) (6).

Second Trimester

At 14 weeks, the cerebral convexities are smooth. The ventricles occupy most of the cerebral hemispheres. The choroid plexus, which is well visualized sonographically as an echogenic structure filling the cerebral ventricles, is not well visualized on MR imaging (Fig. 2.1). A thin rim of smooth parenchyma is present. The interhemispheric fissure separating the cerebral hemispheres is well-developed.

Table 2.1 Reported Appearance of Sulci with Respect to Gestational Age

	Neuropathologic appearance in 25–50% of brains (8)[a] (weeks)	Detectable in 25–75% of brains in study by Levine (6) (weeks)	Detectable in >75% of brains in study by Levine (6) (weeks)	Detectable in 25–75% of brains in study by Garel et al. (7) (weeks)	Detectable in >75% of brains in study by Garel et al. (7) (weeks)
Sulci/fissures of the medial cerebral surface					
Interhemispheric	10	—	10[b]	—	—
Parietoocipital	16	—	18–19	—	—
Cingulate	18	24–25	26–27	22–23[c]	24–25
Secondary cingular	32	—	—	31	33
Calcarine	16	—	18–19	22–23[c]	24–25
Secondary occipital	34			32	34
Sulci of the ventral surface					
Collateral	23	—	—	24–25	27
Occipitotemporal	30	—	—	29	33
Sulci of the lateral surface					
Sylvian	14	—	16–17	—	—
Parietooccipital	16	—	18–19	—	—
Circular	18	—	18–19	—	—
Superior frontal	25	—	—	24–25	29
Inferior frontal	28	30–31	34–35	26	29
Superior temporal	23	26–27	28–29	26	27
Inferior temporal	30	28–29	32–33	30	33
Interparietal	26	—	—	27	28
Insular	34	30–31	32–33	33	34
Secondary Frontal	32	32–33	34–35	—	—
Secondary Temporal	36	32–33	34–35	—	—
Secondary Parietal	33	—	34–35	—	—
Superior occipital	34	34–35	36–37	—	—
Inferior occipital	34	34–35	—	—	—
Tertiary Frontal	40	38–39	—	—	—
Sulci of the vertex					
Central	20	—	26–27	24–25	27
Precentral	24	—	26–27	26	27
Postcentral	25	26–27	28–29	27	28

[a]This article describes the ~2 week interval between when a sulcus is seen in 25–50% and when it is seen in 75–100% of fetuses.
[b]Unreported data.
[c]The earliest gestational age studied in this study was 22 weeks.

At 16 weeks, the Sylvian fissure is visualized as a shallow concavity or groove along the lateral convexity. The Sylvian fissure deepens over time, becoming more angular as the frontal and temporal opercula form (Fig. 2.6). The parietooccipital and calcarine fissures, on anatomic specimens, are seen at ~16 weeks gestational age. They are generally observed on MR examinations by 20–22 weeks (Fig. 2.4).

The callosal sulcus separates the corpus callosum and overlying cingulate gyrus, which is seen at ~18 weeks (Fig. 2.2). The central sulcus appears on the superior parasagittal aspect of the cortex at 20 weeks gestation in anatomic specimens. Although the central sulcus has been observed on MR images as early as 22 weeks, it is not reliably seen until 24–25 weeks gestation (Fig. 2.5).

At 22 weeks, the lateral hemispheres are smooth and the insulae are wide open (Fig. 2.4). The temporal lobe remains smooth until ~23 weeks. The precentral and postcentral gyri appear at ~26 weeks (Fig. 2.6), first as shallow grooves that deepen as gestational age progresses.

On T_2-weighted imaging, three distinct layers are seen comprising cerebral parenchyma (Fig. 2.2) (9). The innermost layer is of low signal intensity and corresponds to the germinal matrix. The middle region is of intermediate signal intensity and corresponds to a less cellular region of developing white matter; and the outermost hypointense layer corresponds to the developing cortex.

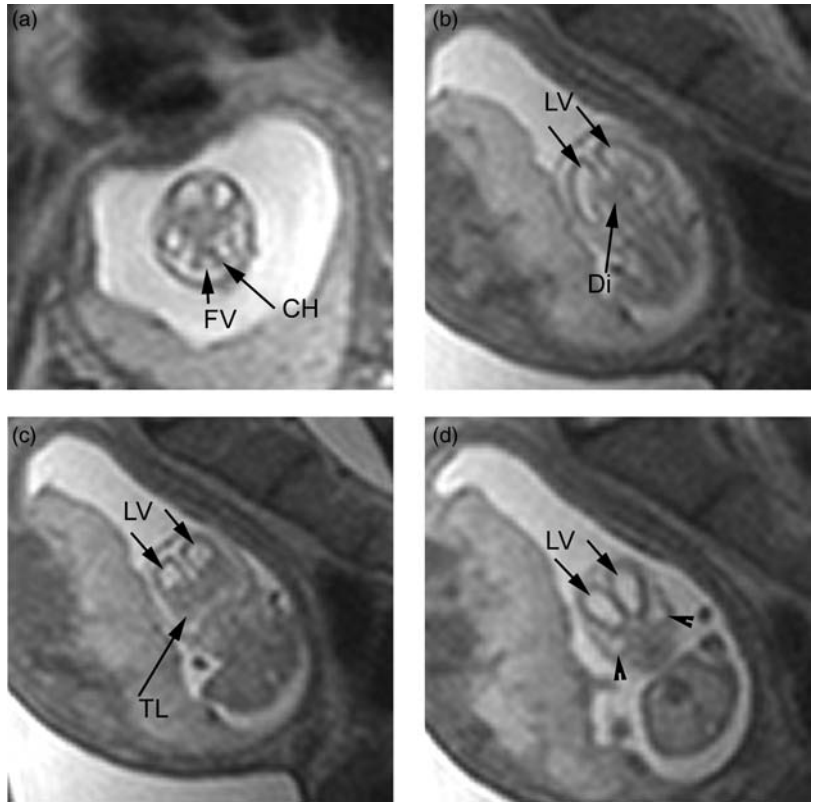

Figure 2.1 Normal anatomy on T_2-weighted images at 14 weeks gestational age. Axial image (a) shows the posterior fossa containing the developing cerebellar hemispheres (CH) and fourth ventricle (FV) with communication between the fourth ventricle and the cisterna magna. Sequential coronal images (b–d) show the smooth cerebral hemispheres. The lateral ventricles (LV) are relatively prominent compared with the brain parenchyma. In (b) the lateral ventricles occupy most of the parietal lobes. The diencephalon (Di) connects the cerebral hemispheres with the brainstem. Image through the frontoparietal region (c) shows the interhemispheric fissure between the lateral ventricles. The developing temporal lobe (TL) is visible on each side. The Sylvian fissure has not yet developed sufficiently for visualization on MR imaging. Coronal image through the frontal lobes (d) reveals the frontal horns of the lateral ventricles. Inferolaterally, the developing globes are visible (arrowheads).

Third Trimester

By 28–30 weeks, numerous new sulci and gyri develop (Figs. 2.9 and 2.10). The insular cortex forms the base of the Sylvian fissure and this region ultimately becomes covered as the opercula develop and mature. As a result, the Sylvian fissure narrows on parasagittal and coronal images (Figs. 2.7–2.13). On the parasagittal images, the Sylvian fissure slopes slightly upwards from front to back (Figs. 2.11–2.13). The germinal matrix is much less prominent, and the cortex is observed as having two layers: the inner layer, which is of relatively high signal intensity, and the outer layer with slightly lower signal intensity (9).

By 32–35 weeks, secondary sulci appear throughout the cortex (Figs. 2.11 and 2.12). By term, tertiary sulci have formed but are often poorly seen because of a relative decrease in the contrast between white matter and the overlying cortex, and a relative decrease in the amount of extra-axial cerebrospinal fluid (Fig. 2.14).

T_1-WEIGHTED IMAGING

T_1-weighted imaging in fetal MR examinations is typically performed to assess blood products or fatty lesions. Fetal motion frequently limits anatomic information due to relatively long scan times. At 13–14 weeks, the germinal matrix appears as a band of increased signal intensity along the lateral ventricular wall (10). It has been reported that at 16–18 weeks there are five distinct layers of signal intensity that represent the innermost hyperintense germinal matrix; a hypointense band of developing white matter; a hyperintense layer of migrating neuroblasts; another hypointense layer of developing white matter; and the outermost hyperintense cerebral cortex (10).

(*text continued on page 20*)

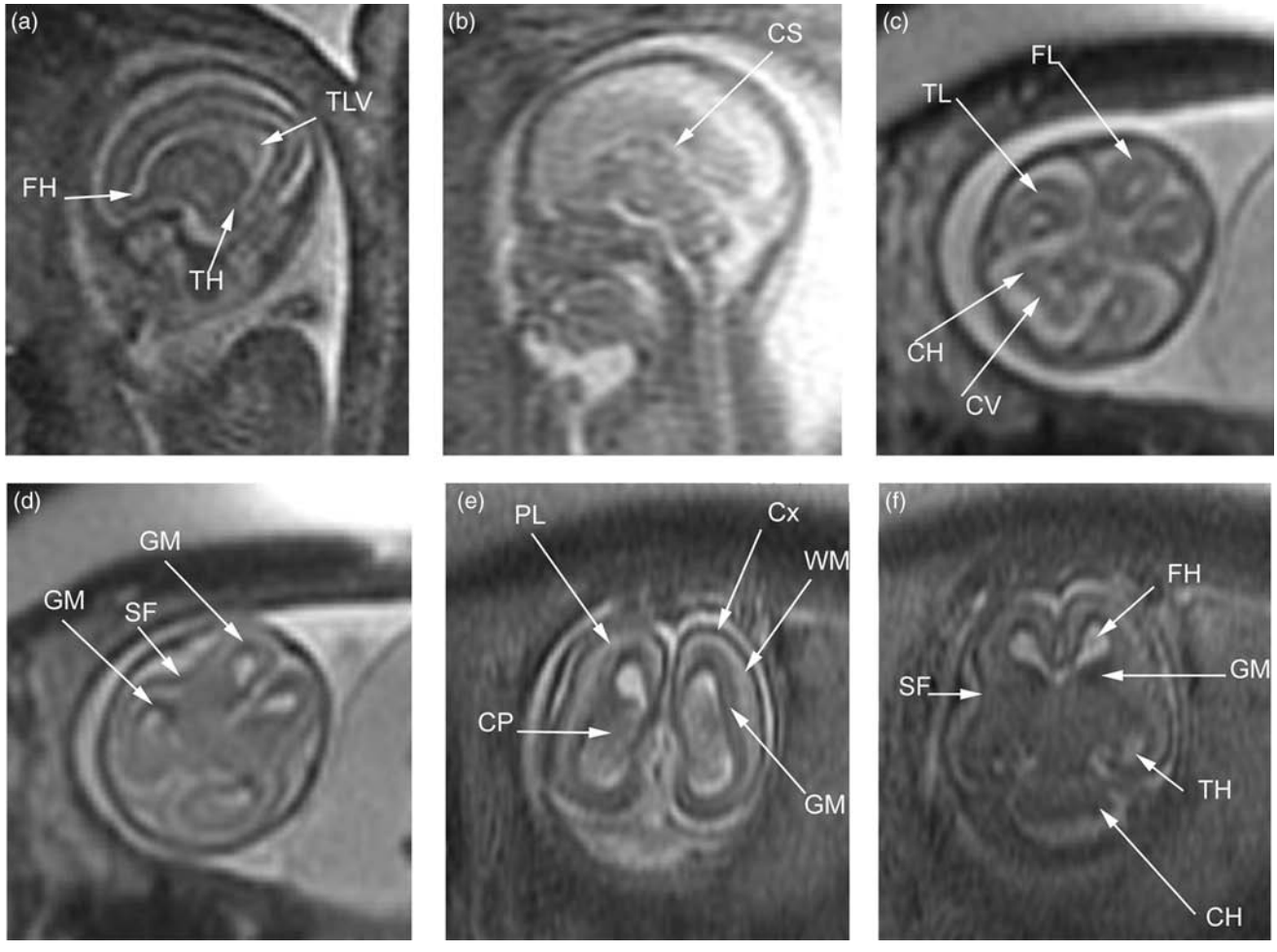

Figure 2.2 Normal anatomy on T_2-weighted images at 18 weeks gestational age. Parasagittal image (a) demonstrates the developing frontal and temporal lobes containing the frontal horn (FH) and temporal horn (TH) of the lateral ventricle. Primitive fetal ventricular morphology is seen. Notice the relatively prominent trigone of the lateral ventricle (TLV). Midline sagittal image (b) reveals the callosal sulcus (CS) separating the corpus callosum below from the cingulate gyrus above. Axial image (c) through the posterior fossa reveals the frontal (FL) and temporal lobes (TL) separated by the developing hypointense sphenoid ridge that separates the anterior cranial fossa from each middle cranial fossa. Within the posterior fossa the developing cerebellum is well seen and the cerebellar hemisphere (CH) and cerebellar vermis (CV) are indicated. The cisterna magna and cisterns around the cerebellum are relatively prominent at this stage of development. A more cephalad axial image (d) reveals early development of the circular or Sylvian fissure (SF) separating the frontal and temporal lobes. The hypointense germinal matrix (GM) is visible along the lateral aspect of the lateral ventricles. Coronal images through the parietal lobes (e) and frontal lobes (f) reveal the hypointense cerebral cortex (Cx), relatively hyperintense white matter (WM), and intermediate intensity germinal matrix (GM). Within the parietal lobe (PL) the trigone of the lateral ventricles is observed and contains choroid plexus (CP).

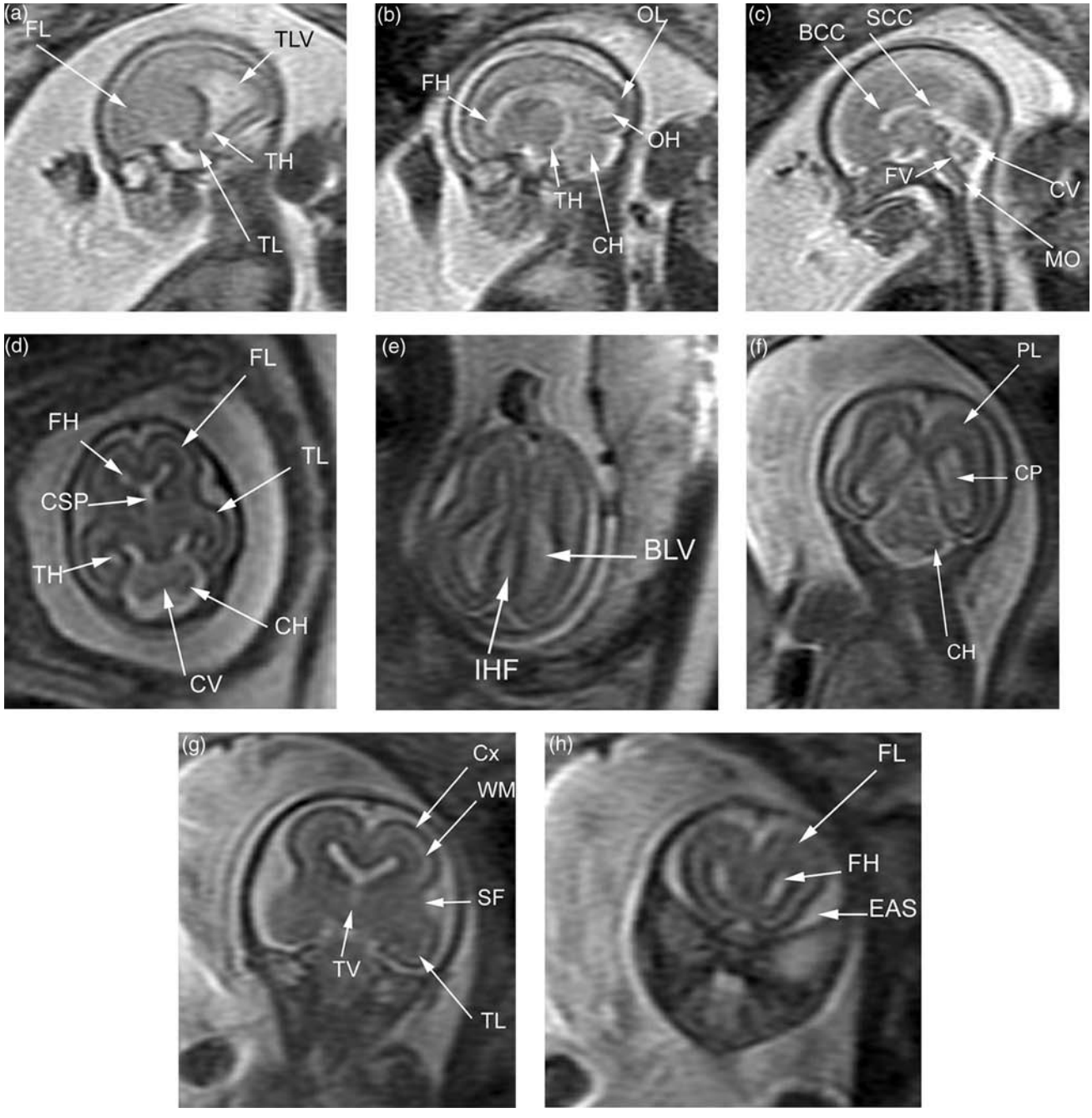

Figure 2.3 Normal anatomy on T_2-weighted images at 20 weeks gestational age. Parasagittal images (a and b) reveal the developing frontal (FL), and temporal lobes (TL). The cortical surface remains smooth prior to sulcal and gyral development. The trigone (TLV) and temporal horn (TH) of the lateral ventricle remain relatively prominent. Notice the relative prominence of the occipital horn (OH) compared with the frontal horn (FH). Midline sagittal image (c) reveals the developing body (BCC) and splenium (SCC) of the corpus callosum. Within the posterior fossa are the developing cerebellar vermis (CV) and fourth ventricle (FV). The medulla oblongata (MO) of the brainstem is also visualized. Axial images (d and e) show the bodies of the lateral ventricles (BLV) and interhemispheric fissure (IHF). Coronal images (f–h) demonstrate features similar to those seen at 18 weeks gestation; however, there has been further interval development of the Sylvian fissures (SF). The cavum of the septum pellucidum (CSP) lies between the frontal horns of the lateral ventricles and above the third ventricle (TV). The extra-axial cerebrospinal fluid spaces (EAS) surrounding the cerebral hemispheres and interhemispheric fissure are relatively prominent at this stage. (OL, occipital lobe; CH, cerebellar hemisphere; PL, parietal lobe; CP, choroid plexus; WM, white matter; Cx, cortex.)

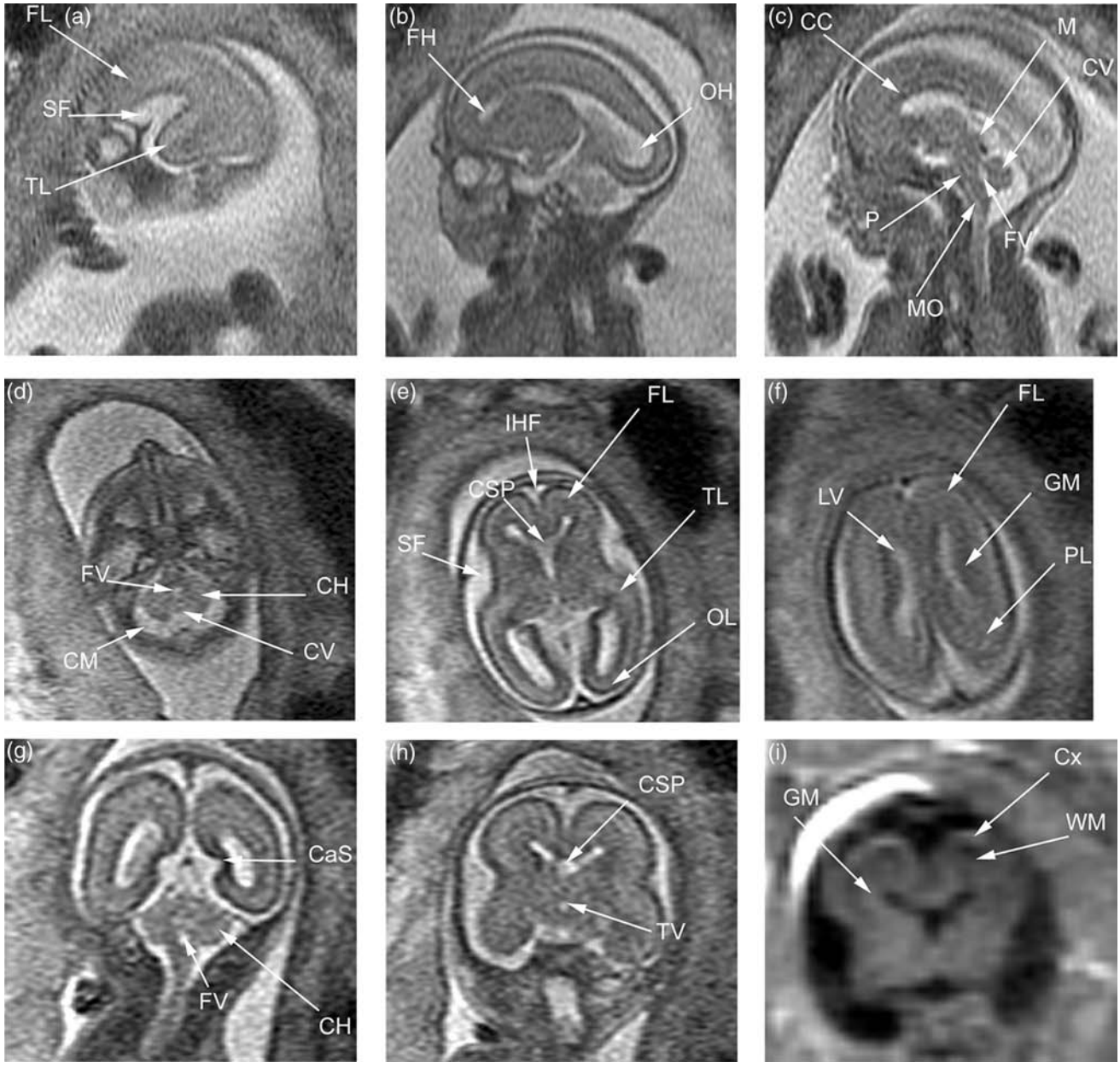

Figure 2.4 Normal anatomy at 22 weeks gestational age. Sagittal T_2-weighted images from lateral to midline (a–c) demonstrate interval deepening of the Sylvian fissure (SF) between the frontal (FL) and temporal lobes (TL). Note the normal prominence of the occipital horn (OH) relative to the frontal horn (FH) of the lateral ventricles. On the midline image (c), the hypointense corpus callosum (CC) is more readily seen. The midbrain (M), pons (P), and medulla oblongata (MO) that comprise the brainstem are all well seen. Axial T_2-weighted image through the posterior fossa (d) reveals that there has been interval growth of the cerebellar hemispheres (CH) and vermis (CV), but the cisterna magna (CM) remains conspicuous. The fourth ventricle (FV) is dorsal to the pons. More cephalad axial images (e and f) and coronal images from posterior to anterior (g–h) reveal further maturation of the frontal (FL), temporal (TL), occipital lobe (OL), parietal lobe (PL), and germinal matrix (GM). The cavum of the septum pellucidum (CSP) is apparent between the frontal horns of the lateral ventricles (LV) and lies cephalad to the third ventricle (TV). Notice the calcarine sulcus (CaS) that indents the posteromedial surface of the cerebral hemisphere. Coronal T_1-weighted image (i) clearly demonstrates the slightly hyperintense cortex (Cx), deep to which is hypointense white matter (WM). The germinal matrix (GM) lies between the white matter and the ventricles. (IHF, interhemispheric fissure.)

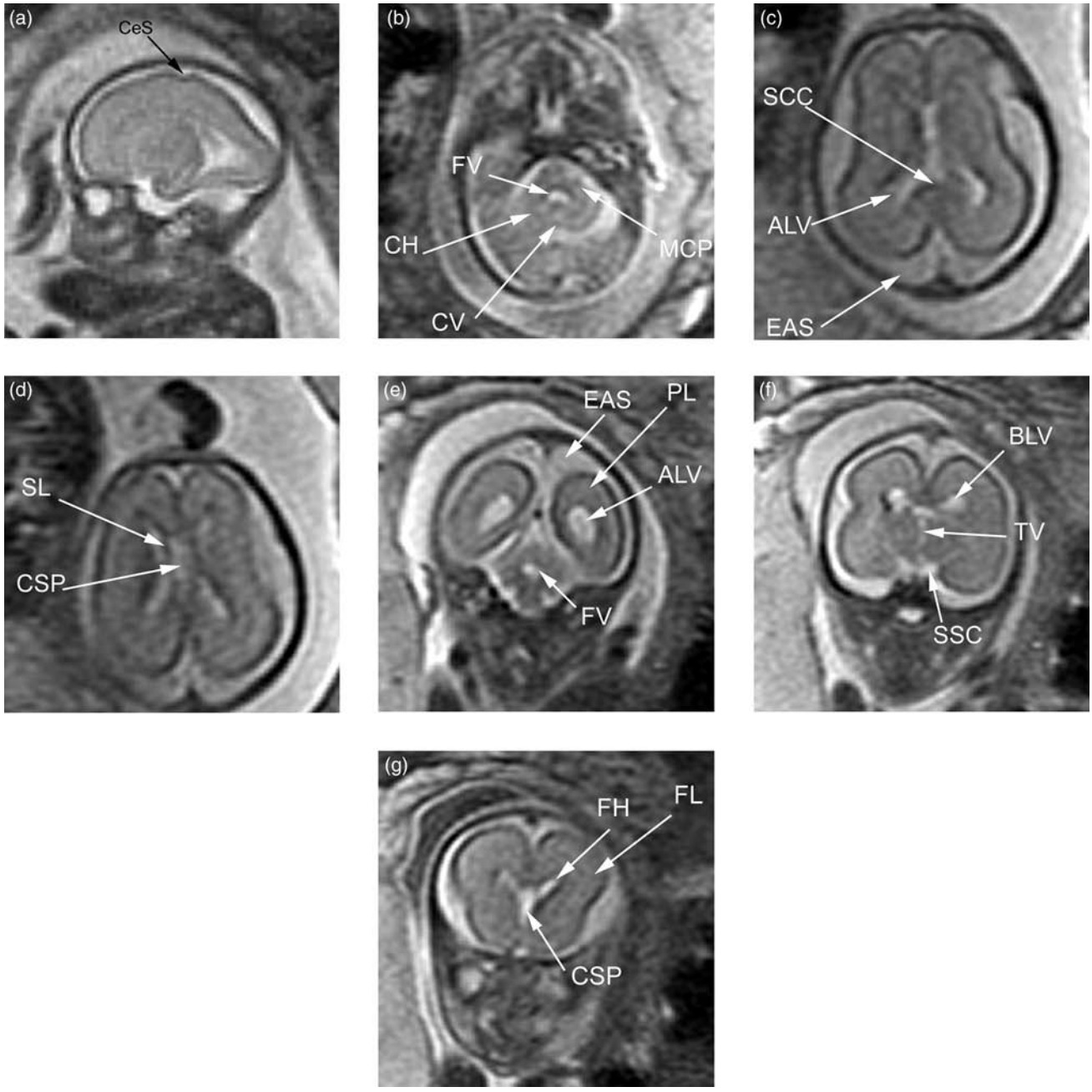

Figure 2.5 Normal anatomy on T_2-weighted images at 25 weeks gestational age. Parasagittal image (a) reveals an indentation in the cortex corresponding to the central sulcus (CeS) between the frontal and parietal lobes. Axial image through the posterior fossa (b) reveals further interval growth of the cerebellar hemispheres (CH) and cerebellar vermis (CV). The fourth ventricle (FV) is bounded laterally by the middle cerebellar peduncles (MCP). More cephalad axial images (c and d), and coronal images from posterior to anterior (e–g) reveal the trigone or atrium of the lateral ventricle (ALV) bounded posteromedially by the hypointense fibers of the splenium of the corpus callosum (SCC). The frontal horns (FH) and bodies of the lateral ventricles (BLV) are separated by the septal leaflets (SL) from the cavum of the septum pellucidum (CSP) which extends posteriorly into the cavum vergae. The extraaxial spaces (EAS) remain relatively prominent. The suprasellar cistern (SSC) is visible medial to the temporal lobes above the sphenoid bone that forms the central skull base. (PL, parietal lobe, TV, third ventricle.)

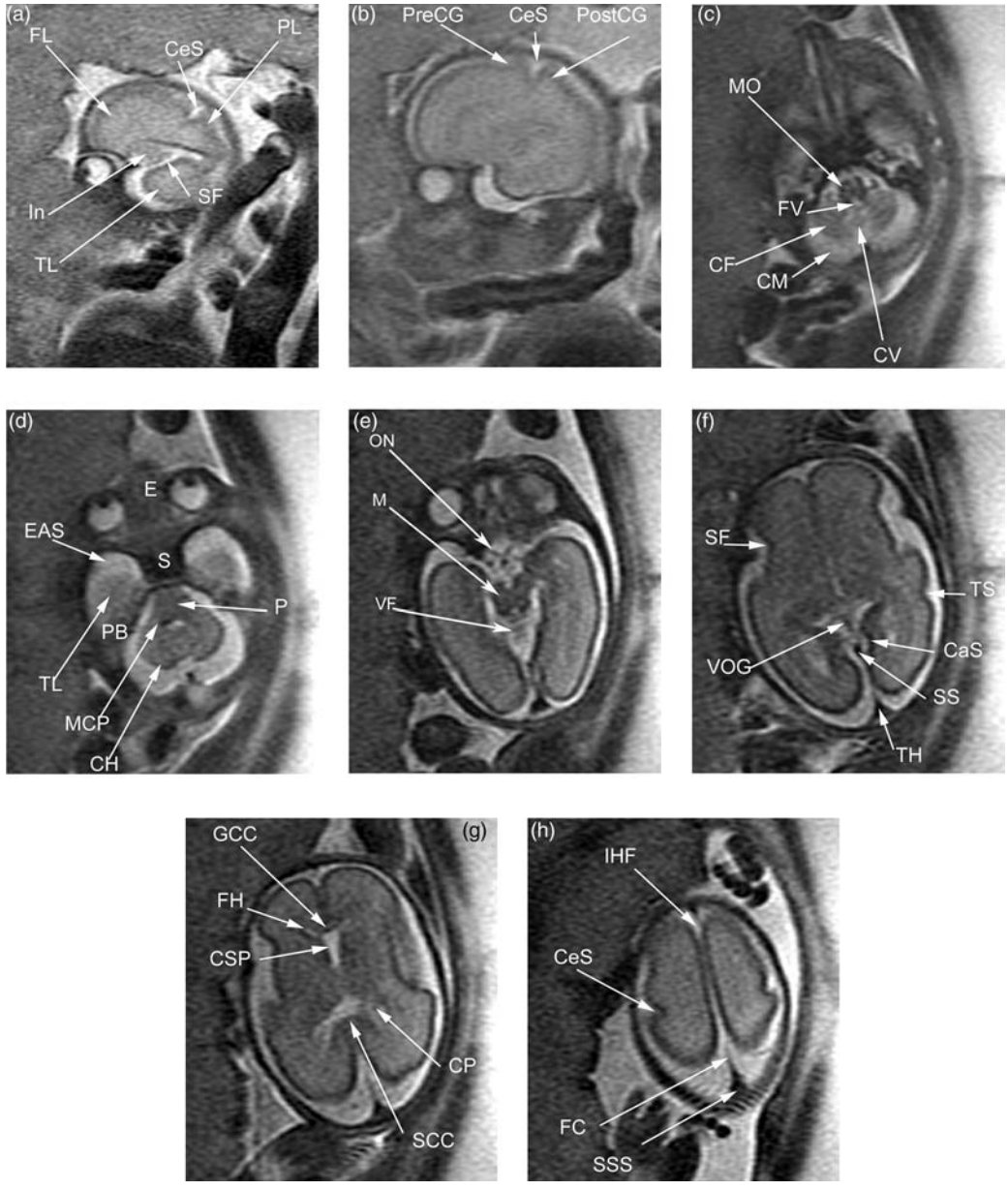

Figure 2.6 Normal anatomy on T_2-weighted images at 26 weeks gestational age. Parasagittal images (a and b) show the insula (In) at the base of the Sylvian fissure (SF) between the developing frontal (FL) and temporal lobes (TL). The central sulcus (CeS) demarcates the anterior border of the parietal lobe (PL), and is bounded posteriorly by the postcentral gyrus (PostCG) and anteriorly by the precentral gyrus (PreCG). Axial images of the posterior fossa (c and d) show greater definition of the medulla oblongata (MO), and pons (P) anteriorly, the middle cerebellar peduncles (MCP) and fourth ventricle (FV). The cerebellar hemispheres (CH) and cerebellar vermis (CV) now have a striated appearance due to hyperintense cerebrospinal fluid that can be distinguished between the cerebellar folia (CF). The cisterna magna (CM) and extraaxial cerebrospinal fluid spaces (EAS) ventral to the temporal lobes (TL) remain conspicuous. The hypointense ethmoid bone (E) between the developing globes, sphenoid (S) and petrous bones (PB) can be distinguished. A more cephalad axial image (e) at the level of the midbrain demonstrates the optic nerves (ON) within the suprasellar cistern, ventral to the midbrain (M) and interpeduncular cistern. Vermian fissures (VF) are also seen at this level. At the level of the third ventricle (f) the linear hypointense vein of Galen (VOG) can be faintly distinguished coursing posteriorly to the straight sinus (SS) which drains into the torcula herophili (TH). The calcarine sulcus (CaS) and one of the temporal sulic (TS) are also seen. Axial image (g) at the level of the cavum of the septum pellucidum (CSP) shows the crossing fibers of the genu of the corpus callosum (GCC) separating the interhemispheric fissure from the cavum. Posteriorly the splenium of the corpus callosum (SCC) is also seen. Intermediate signal intensity choroid plexus (CP) can be discerned within the atrium of the lateral ventricle. Axial image close to the vertex (h) demonstrates the central sulcus (CeS), interhemispheric fissure (IHF), falx cerebri (FC) and superior sagittal sinus (SSS). (FH, frontal horn.)

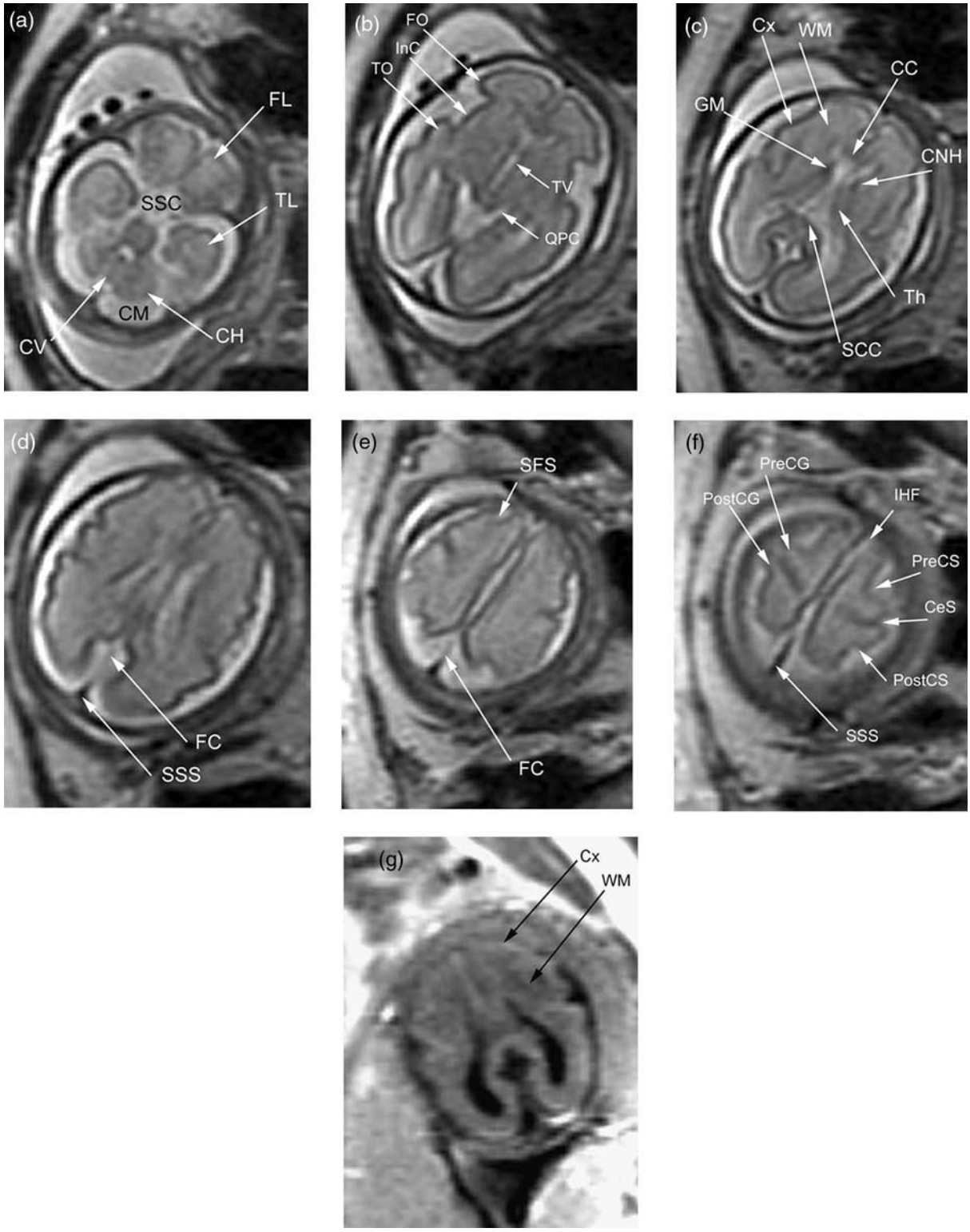

Figure 2.7 Normal axial anatomy at 27 weeks gestational age. Axial image through the posterior fossa (a) reveals the frontal (FL) and temporal lobes (TL), cerebellar hemispheres and vermis as well as the cisterna magna (CM) and suprasellar cistern (SSC). Axial image (b) at the level of the third ventricle (TV) demonstrates formation of the frontal (FO) and temporal opercula (TO) that will ultimately cover the insular cortex (InC). The ambient and quadrigeminal plate cistern (QPC) lies between the tectum and the occipital lobes. More cephalad axial images (c–f) and an axial T_1-weighted image (g) reveal cortex (Cx), white matter (WM) and germinal matrix (GM). Note the prominent cavum vergae. Deep gray matter structures such as the caudate nucleus head (CNH) and thalamus (Th) can now be distinguished. The corpus callosum (CC) is well seen on axial images. The superior frontal sulcus (SFS), pre (PreCS) and post (PostCS) central sulci and gyri (PreCG, PostCG) are all visible. The hypointense linear falx cerebri (FC) extends into the interhemispheric fissure. The triangular signal void of the superior sagittal sinus (SSS) runs along the dorsal aspect of the falx.

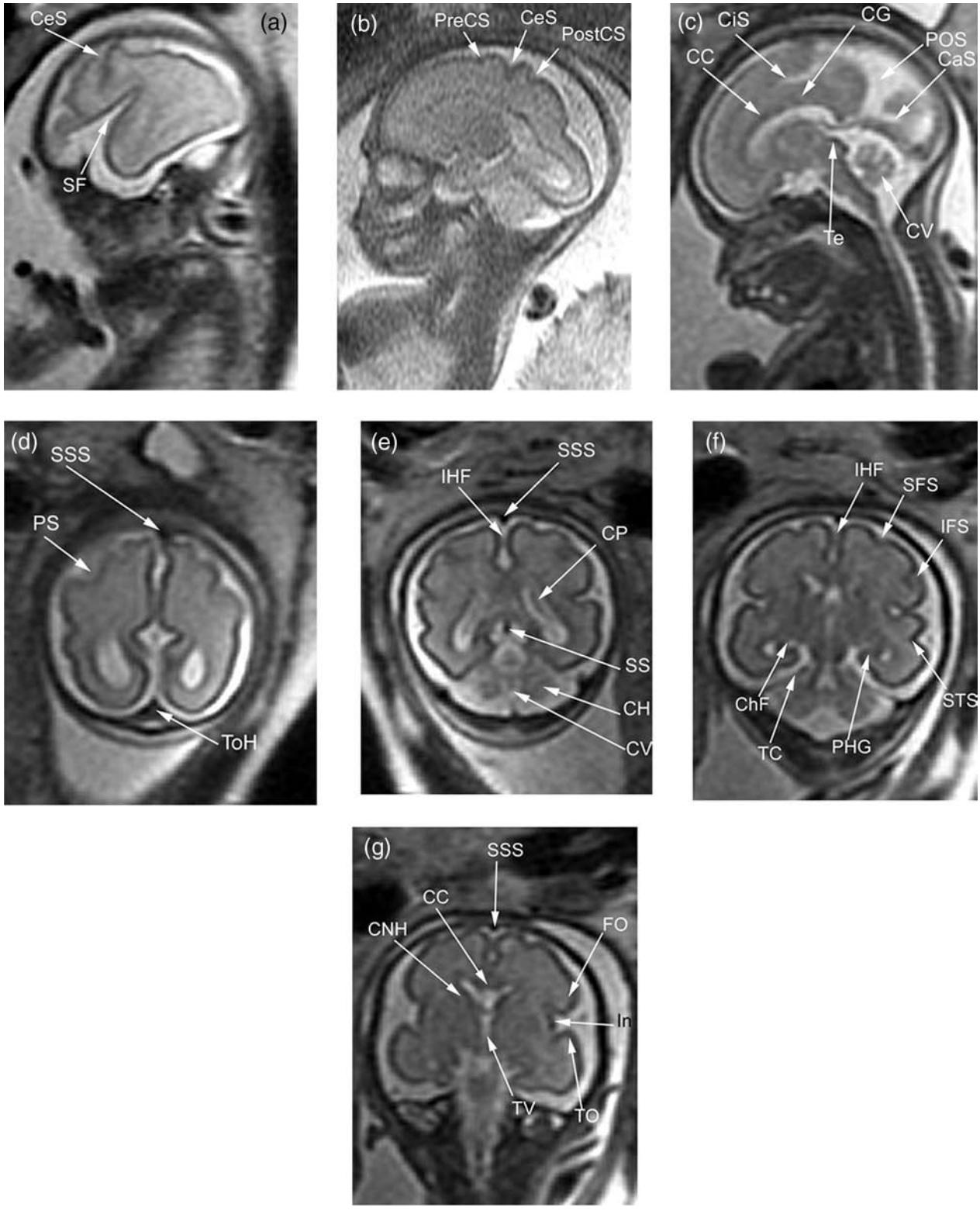

Figure 2.8 Parasagittal T_2-weighted image (a) reveals deepening of the central sulcus (CeS) and narrowing of the Sylvian fissure (SF). On a more medial image (b), the precentral (PreCS) and postcentral (PostCS) sulci can now be observed. Midline sagittal image (c) shows the cingulate gyrus (CG) and sulcus (CiS) above the corpus callosum (CC). The parietooccipital (POS) and calcarine sulcus (CaS) are also visible. The colliculi of the tectum of the midbrain (Te) and fissures of the cerebellar vermis (CV) are demonstrated. Coronal T_2-weighted images from posterior to anterior (d–g) demonstrate additional features such as parietal sulci (PS), the superior (SFS) and inferior frontal sulci (IFS), the superior temporal sulcus (STS), the tentorium cerebelli (TC), the torcula herophili (ToH), and the straight sinus (SS). The choroidal fissure (ChF) is seen medial to the temporal horns and above the parahippocampal gyrus (PHG).

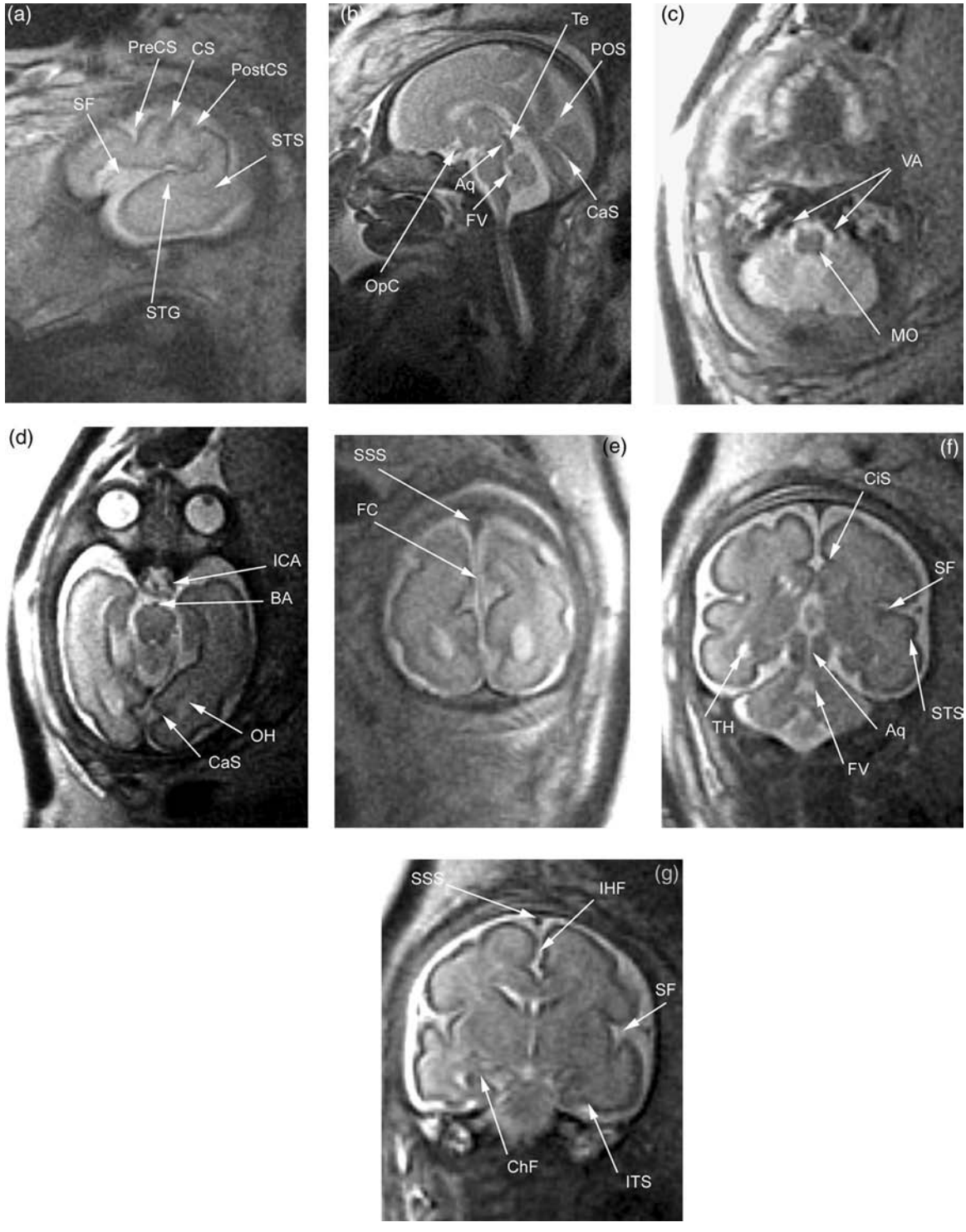

Figure 2.9 Normal anatomy on T_2-weighted images at 28 weeks gestational age. Parasagittal image (a) demonstrates increased undulation of the margins of the Sylvian fissure (SF), precentral (PreCS), central (CeS), and postcentral (PostCS) sulci. The superior temporal gyrus (STG) is visible between the Sylvian fissure and the superior temporal sulcus (STS). Midline sagittal image (b) clearly reveals the aqueduct of Sylvius (Aq) above the fourth ventricle (FV). The parietooccipital (POS) and calcarine (CaS) sulci are again seen. The optic chiasm (OpC) is visible in the suprasellar cistern. Axial images (c and d) reveal signal voids of the vertebral arteries (VA) ventrolateral to the medulla oblongata (MO), and the basilar artery (BA) ventral to the pons. The left internal carotid artery (ICA) lies adjacent to the anterior clinoid process. The occipital horn (OH) of the lateral ventricle and the CaS are also shown. Coronal images from posterior to anterior (e–g) demonstrate the superior sagittal sinus (SSS), interhemispheric fissure (IHF) and falx cerebri (FC), fourth ventricle, aqueduct of Sylvius, and temporal horn of the lateral ventricle (TH). The extra-axial spaces have become less prominent and there has been progressive deepening of sulci such as the Sylvian fissure (SF), cingulate sulcus (CiS) superior (STS) and inferior temporal (ITS) sulci. The choroidal fissure (ChF) is less well visualized due to interval maturational narrowing.

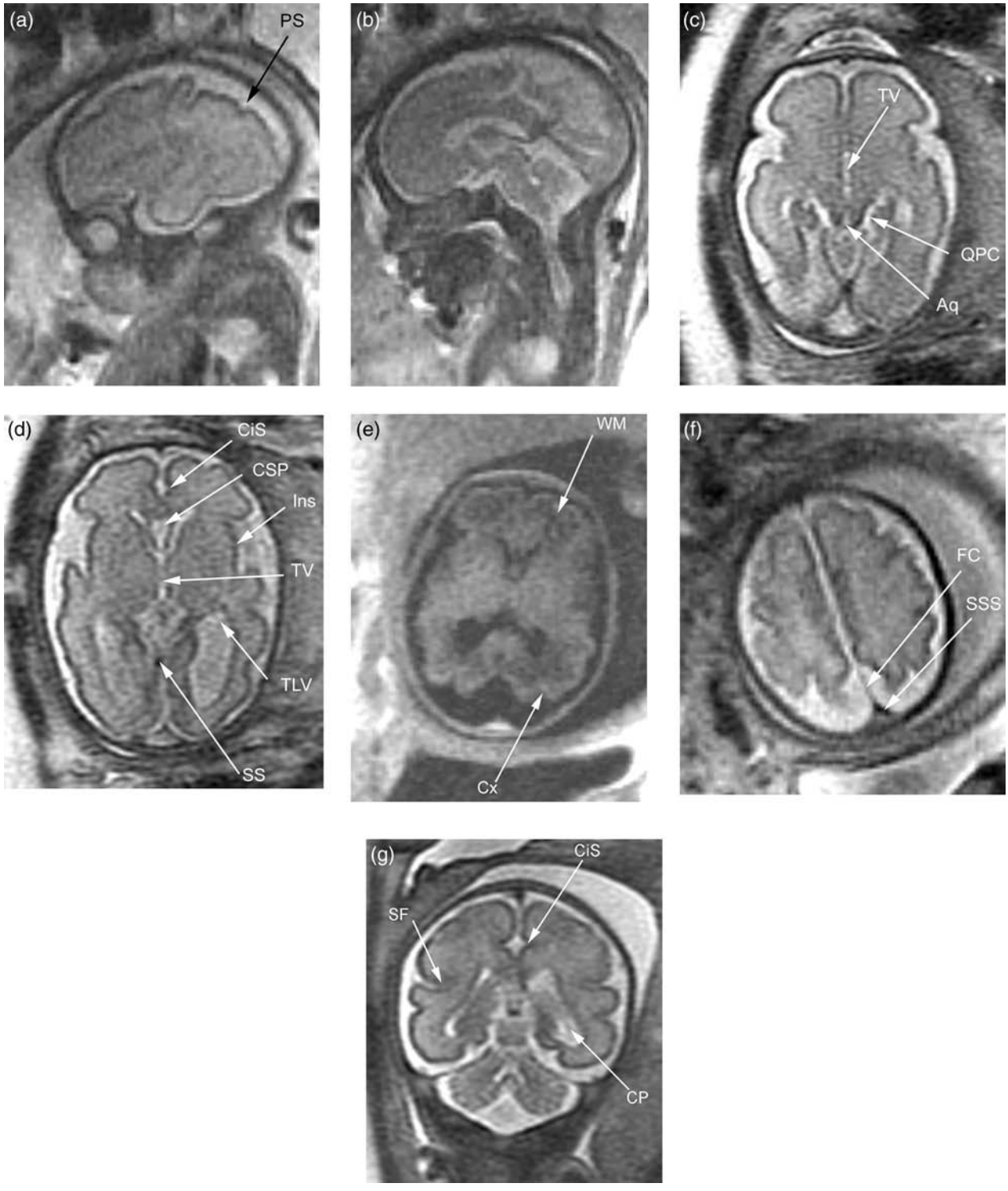

Figure 2.10 Normal anatomy at 30 weeks gestational age. Sagittal T_2-weighted images (a and b) reveal further convolutional maturation. Parietal sulci (PS) are now observable. Axial T_2-weighted images (c, d and f) clearly demonstrate the colliculi of the midbrain and aqueduct of Sylvius (Aq) ventral and medial to the quadrigeminal plate cistern (QPC). Also shown are the cingulate sulcus (CiS), cavum of the septum pellucidum (CSP) third ventricle (TV), trigone of the lateral ventricle (TLV), insula (Ins), straight sinus (SS), falx cerebri (FC), and superior sagittal sinus (SSS). Axial T_1-weighted image (e) reveals similar findings of the white matter (WM) and cortex (Cx) described in Fig. 2.7. Coronal T_2-weighted image (g) demonstrates the cingulate sulcus (CiS), Sylvian fissure (SF) and choroid plexus (CP) within the lateral ventricle.

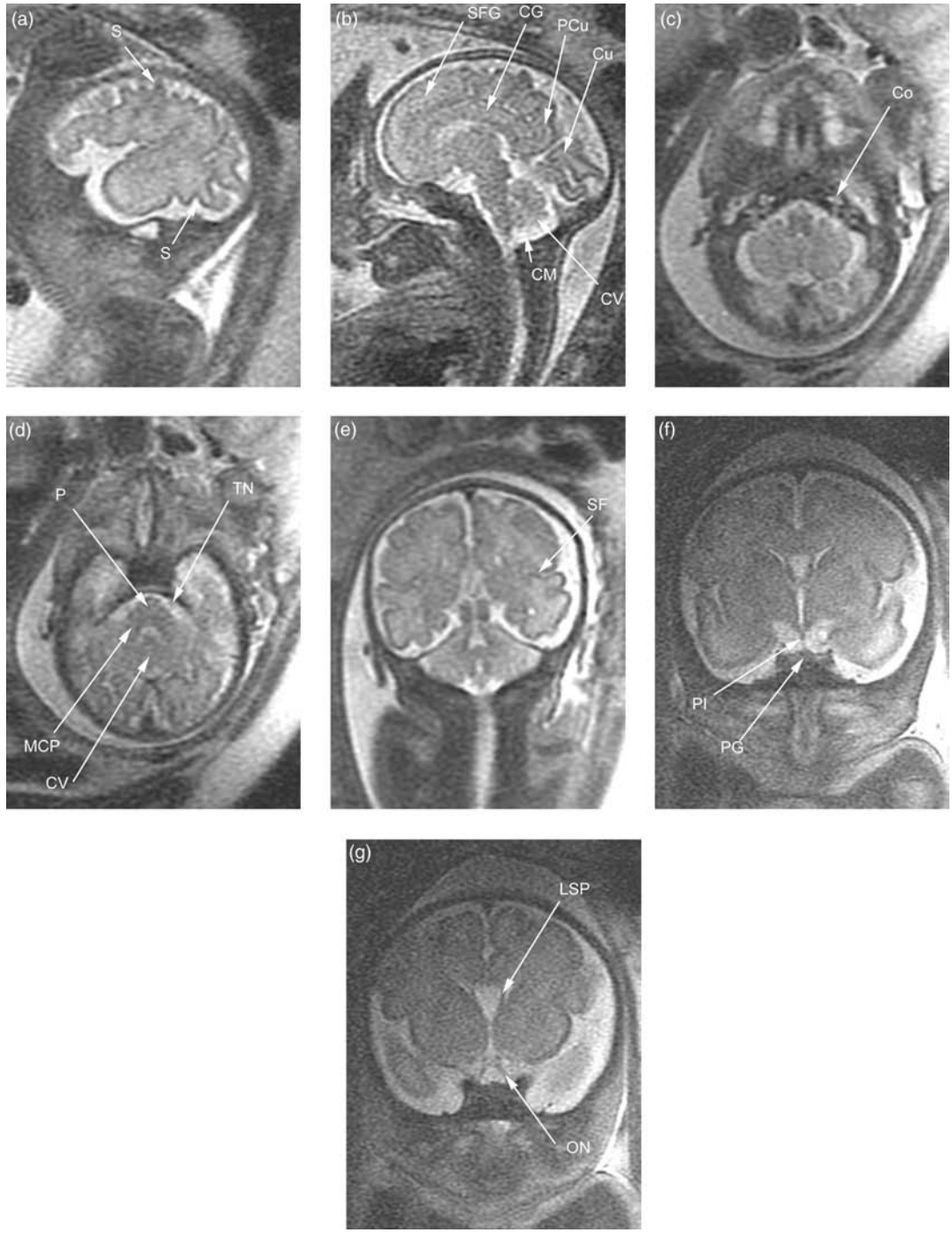

Figure 2.11 Normal anatomy on T_2-weighted images at 32 weeks gestational age. Parasagittal (a) and midline sagittal (b) images demonstrate an increased number of sulci (s) and gyri such as the superior frontal gyrus (SFG), cingulate gyrus (CG), precuneus (PCu), and cuneus (Cu). The cerebellar vermis (CV) has enlarged relative to the cisterna magna (CM). Axial image at the level of the posterior fossa (c) demonstrates the hypointense petrous bones and fluid-containing cochlea (Co). A more cephalad image (d) at the level of the pons (P) and middle cerebellar peduncles (MCP) demonstrates the trigeminal nerves (TN) traversing the cerebellopontine angle cistern. Coronal image (e) reveals that the frontal and temporal opercula are covering the insula with progressive narrowing of the Sylvian fissure (SF). High-resolution coronal images (f and g) through the suprasellar cistern demonstrate the midline pituitary infundibulum (PI) extending inferior to the third ventricle to the pituitary gland (PG) which blends with the hypointense sphenoid bone. Ventral to this are the optic nerves (ON). Notice also the leaflets of the septum pellucidum (LSP) separating the frontal horns of the lateral ventricles from the cavum of the septum pellucidum, which lies cephalad to the third ventricle.

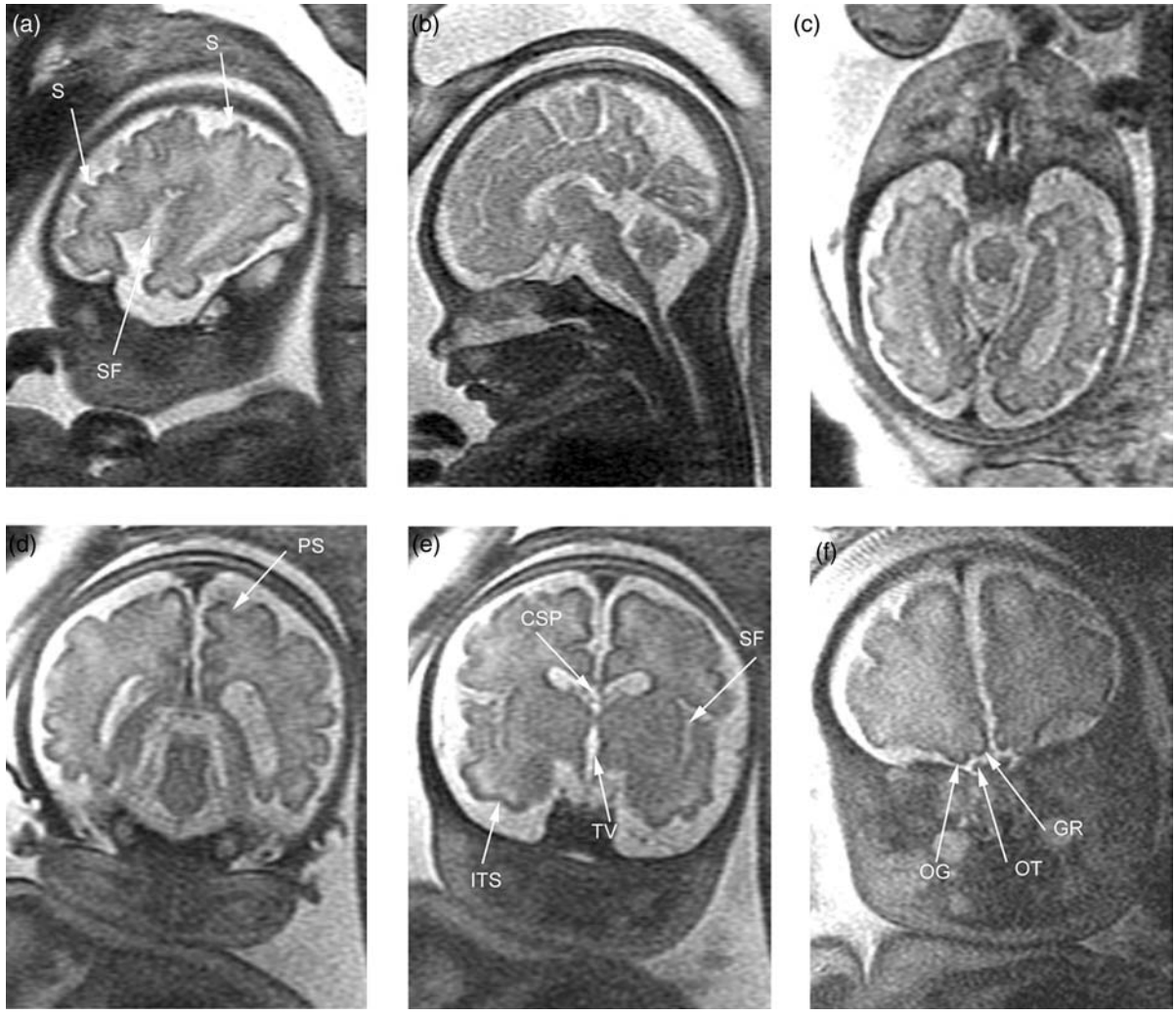

Figure 2.12 Normal anatomy on T_2-weighted images at 34 weeks gestational age. Sagittal (a and b), axial (c), and coronal (d–f) images reveal progressive gyral and sulcal (s) maturation. The parietal sulcus (PS), the inferior temporal sulcus (ITS), and Sylvian fissure (SF) are shown. Notice the relationship between the cavum of the septum pellucidum (CSP) and third ventricle (TV). Note the gyrus rectus (GR), olfactory gyrus (OG), and olfactory tract (OT).

However, in most MR examinations, only three layers (germinal matrix, white matter, and cortex) are readily discerned (Figs. 2.4, 2.7, and 2.10). In the fetal brain in the third trimester, the cortical ribbon is of slightly higher signal than the underlying parenchyma (Figs. 2.7 and 2.10).

NORMAL VENTICULAR SIZE AND CONFIGURATION

Cardoza et al. (11) sonographically evaluated 100 healthy fetuses between the gestational ages of 14 and 38 weeks and found that the normal atrial diameter remained stable through gestation with an average measurement of 7.6 ± 0.6 mm. An upper limit of 10 mm (+4 SD) was set above which ventriculomegaly was defined as being present. There is no reason to believe that atrial diameter measurements would differ when estimated with MR imaging as opposed to sonography. However, one challenge with MR imaging is standardization of the axial view of the head. If an oblique view is obtained, the atria can appear falsely enlarged. In our review of 128 fetuses referred for non-CNS indications between the gestational ages of 15 and 39 weeks, no fetus was found with an atrial diameter >10 mm on MR examination (12). The 10-mm rule, described on a sonographic axial view of the fetal atrium, is therefore the measurement we use as the upper limit of normal on MR imaging. Measurement of the atrial diameter is probably more reliable on sonography where the proscribed plane of measurement can be obtained during

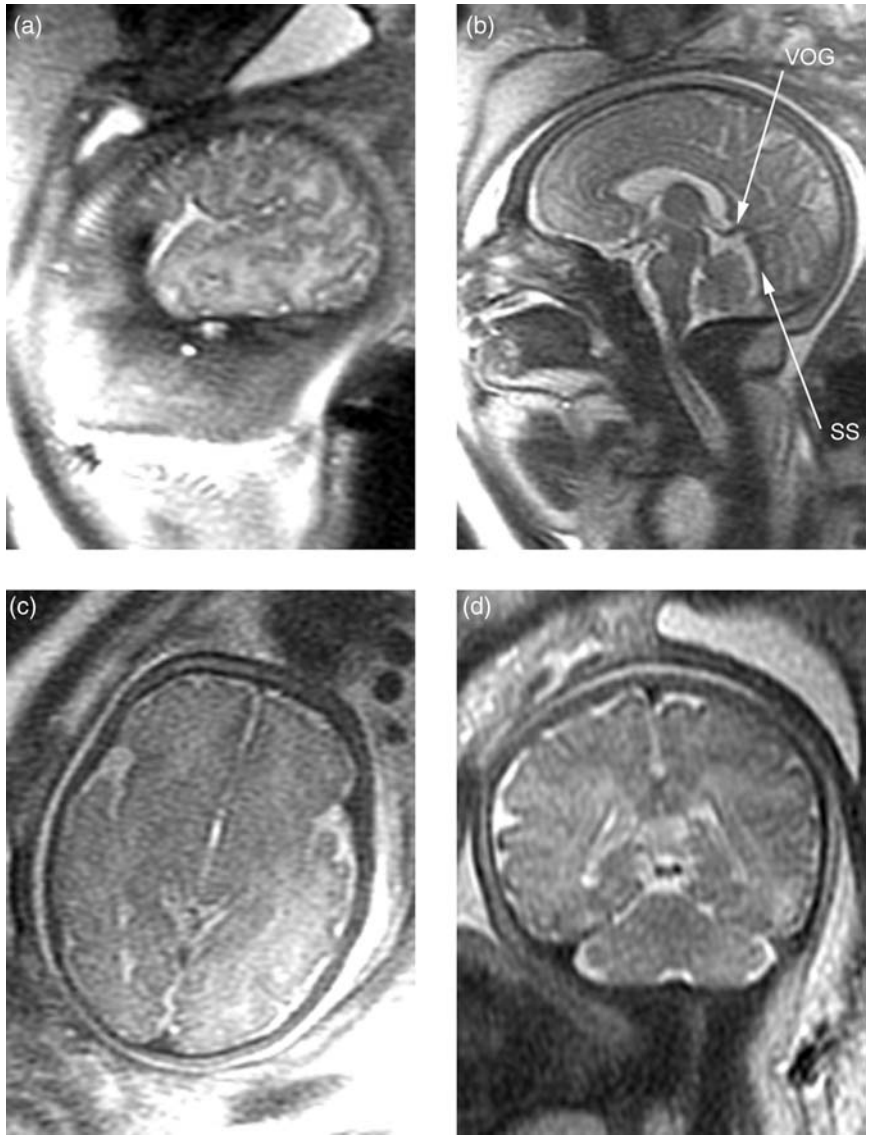

Figure 2.13 Normal anatomy on T_2-weighted images at 36 weeks gestational age. Sagittal (a and b), axial (c), and coronal (d) images reveal decreased conspicuity of the extraaxial cerebrospinal fluid spaces and increased tortuosity of sulci. The midline sagittal image (b) reveals the vein of Galen (VOG) coursing into the straight sinus (SS). As the white matter undergoes myelination, there is less T_2 prolongation (hyperintensity) and the contrast in signal between the white matter and gray matter is reduced.

real-time scanning. However, shadowing artifacts often make it impossible to get an accurate sonographic measurement of the ventricle on the side of the brain closest to the maternal anterior abdominal wall. For these "upside" ventricles, MR measurements are likely more accurate than sonographic measurements. In a study comparing ventricular measurements on ultrasound and MR imaging, there were no significant differences in these measurements in fetuses with ventriculomegaly (3).

In fetuses, the atria and occipital horns of the lateral ventricle appear prominent with respect to the frontal horns (13). This should not be considered as an abnormal finding, as long as the overall contour and size of the ventricles appears normal, especially during the first two trimesters (Fig. 2.4).

CAVUM OF THE SEPTUM PELLUCIDUM AND CAVUM VERGAE

The cavum of the septum pellucidum should always be observed after 20 weeks (Figs. 2.4–2.6). On T_2-weighted images, the septal leaflets should be visible as linear hypointense structures between the frontal horns of the

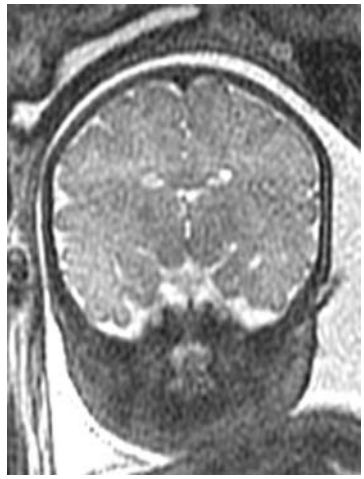

Figure 2.14 Normal anatomy on coronal T_2-weighted image at 38 weeks gestational age. With maturation there has been further reduction in contrast between the gray and white matter and the cerebrospinal fluid spaces are less conspicuous. These factors make analysis of the sulcal gyral morphology more complex as the fetus approaches term.

lateral ventricles (Figs. 2.10 and 2.11). The cavum vergae can be prominent as a normal variant (Fig. 2.7).

GERMINAL MATRIX

The germinal matrix appears as a smooth dark region on T_2-weighted imaging (Fig. 2.2). This will look abnormally thick and dark in cases of germinal matrix hemorrhage (Chapter 3, Fig. 3.62). A nodular appearance will be seen in cases of subependymal tubers (Chapter 3, Figs. 3.40 and 3.41).

POSTERIOR FOSSA AND MIDBRAIN

The cerebellum and brainstem at 14–15 weeks gestation are of homogenous intermediate signal intensity (Fig. 2.1). Folia are not visible. Care should be taken not to overcall vermian defects early in the second trimester, since the inferior vermis is incompletely formed at that time. At 16–18 weeks, the vermis is best appreciated on sagittal and axial images (Fig. 2.2). By 20 weeks, the peripheral cerebellar cortex demonstrates low signal intensity (Fig. 2.3). By 20–23 weeks, the brainstem has posterior low signal in the dorsal pons and medulla (Fig. 2.4). The tectum has low signal intensity (Fig. 2.8). This low signal intensity reaches the midbrain by 32 weeks gestation corresponding to the region of the medial longitudinal fasciculus (14). The cerebellar hemispheres develop a striated appearance due to intervening hyperintense cerebrospinal fluid in the cerebellar fissures and hypointense cerebellar folia (Fig. 2.6). By 32 weeks, prominent cerebellar folia are identified that increase in number as the fetus approaches term (Fig. 2.11) (14).

Table 2.2 Time Lag Between Sulcal Appearance in MR and Neuroanatomic Studies

Group	Mean time lag[a] ± SD (weeks)	Range (weeks)	*p*
Normal	1.9 ± 2.2	0–8	—
Mild ventriculomegaly	4.4 ± 3.2	0–8	<0.01
Other CNS anomaly	4.3 ± 5.6	0–21	<0.01

[a]Time lag refers to the difference between sulcal appearance in neuroanatomic and MRI studies.
Source: From Levine and Barnes (6).

CORPUS CALLOSUM

The corpus callosum is the largest of the commisures that connect the two cerebral hemispheres. It is visible on axial view of the brain as a narrow band of tissue in the shape of a capital "I" running between the lateral ventricles (Figs. 2.5 and 2.6). On coronal and sagittal imaging, the corpus callosum appears as the curved structure separating the cingulum superiorly from the lateral ventricles inferiorly (Figs. 2.3, 2.4 and 2.7). The rostral end of the corpus callosum first appears by the 12th week of gestation (15) in the region that will later be the anterior body of the corpus callosum (16). Development progresses both caudally to form the body and splenium, and rostrally to form the genu and rostum. The entire corpus callosum should be formed (although it will continue to grow) by the 20th week of gestation.

SUBARACHNOID SPACE

The subarachnoid space can appear quite prominent (Fig. 2.3). The subarachnoid space gradually becomes less conspicuous during the latter half of the third trimester (Figs. 2.13 and 2.14). The clinical significance of a prominent subarachnoid space with underlying normal appearance of the cortex is unknown.

CONCLUSION

Knowledge of the normal progression of cortical maturation and normal appearance of neuroanatomy over time will aid in the diagnosis of fetal CNS abnormalities. Examples of CNS pathology are illustrated in Chapter 3.

REFERENCES

1. Dinh DH, Wright RM, Hanigan WC. The use of magnetic resonance imaging for the diagnosis of fetal intracranial anomalies. Childs Nerv Syst 1990; 6:212–215.
2. Levine D. MR imaging of fetal central nervous system abnormalities. Brain Cogn 2002; 50:432–448.
3. Levine D, Barnes PD, Robertson RR et al. Fast MR imaging of fetal central nervous system abnormalities. Radiology 2003; 229:51–61.
4. Levine D, Barnes PD, Madsen JR et al. Fetal central nervous system anomalies: MR imaging augments sonographic diagnosis. Radiology 1997; 204:635–642.
5. Simon EM, Goldstein RB, Coakley FV et al. Fast MR imaging of fetal CNS anomalies in utero. Am J Neuroradiol 2000; 21:1688–1698.
6. Levine D, Barnes PD. Cortical maturation in normal and abnormal fetuses as assessed with prenatal MR imaging. Radiology 1999; 210:751–758.
7. Garel C, Chantrel E, Brisse H et al. Fetal cerebral cortex: normal gestational landmarks identified using prenatal MR imaging. AJNR Am J Neuroradiol 2001; 22:184–189.
8. Chi JG, Dooling EC, Gilles FH. Gyral development of the human brain. Ann Neurol 1977; 1:86–93.
9. Lan LM, Yamashita Y, Tang Y et al. Normal fetal brain development: MR imaging with a half-Fourier rapid acquisition with relaxation enhancement sequence. Radiology 2000; 215:205–210.
10. Chong BW, Babcook CJ, Salamat MS et al. A magnetic resonance template for normal neuronal migration in the fetus. Neurosurgery 1996; 39:110–116.
11. Cardoza JD, Goldstein RB, Filly RA. Exclusion of fetal ventriculomegaly with a single measurement: the width of the lateral ventricular atrium. Radiology 1988; 169:711–714.
12. Trop I, Levine D. Normal fetal anatomy as visualized with fast magnetic resonance imaging. Top Magn Reson Imaging 2001; 12:3–17.
13. Levine D, Trop I, Mehta TS et al. MR imaging appearance of fetal cerebral ventricular morphology. Radiology 2002; 223:652–660.
14. Stazzone MM, Hubbard AM, Bilaniuk LT et al. Ultrafast MR imaging of the normal posterior fossa in fetuses. AJR Am J Roentgenol 2000; 175:835–839.
15. Rakic P, Yakovlev PI. Development of the corpus callosum and cavum septi in man. J Comp Neurol 1968; 132:45–72.
16. Kier EL, Truwit CL. The normal and abnormal genu of the corpus callosum: an evolutionary, embryologic, anatomic, and MR analysis. Am J Neuroradiol 1996; 17:1631–1641.

3

MR Imaging of Fetal CNS Abnormalities

DEBORAH LEVINE, PATRICK BARNES

INTRODUCTION

Numerous reports document the ability of magnetic resonance (MR) imaging to provide superior characterization of fetal central nervous system (CNS) abnormalities when compared with ultrasound (1–14). It is beyond the scope of this atlas to detail the embryology, neuropathology, and clinical aspects of all the potential CNS anomalies. This information is available in a number of well-known texts and publications (15–17). In this atlas we attempt to present and illustrate information that is most pertinent to performing and interpreting MR imaging of fetal abnormalities. In this chapter, we first address ventriculomegaly, and then use a modification of the van der Knaap and Valk classification (18) to present some of the most common and important congenital and developmental abnormalities of the CNS. This classification is based on the gestational timing of insults that give rise to such abnormalities. During the major "formational" period (i.e., up to 5–7 weeks gestational age), insults result in "primary" malformations of the CNS. These include disorders of dorsal and ventral neural tube formation; disorders of neuronal, glial, and mesenchymal proliferation, differentiation, and histogenesis; and disorders of migration and cortical organization. Insults that occur during the "postformational" or maturational period (i.e., after 5–7 weeks gestational age) are encephaloclastic and result in "secondary" injury of formed structures. Such injury may include hydranencephaly, porencephaly, multicystic encephalopathy, encephalomalacia, leukomalacia, hemiatrophy, hydrocephalus, hemorrhage, infarction, and metabolic/degenerative diseases. In some cases, there may be combined malformative and encephaloclastic abnormalities.

VENTRICULOMEGALY

Ventriculomegaly refers to enlargement of the cerebral ventricles without specifying a cause. It is diagnosed on prenatal sonograms when the lateral ventricles measure 10 mm or greater on a transverse image at the level of the glomus of the choroid plexus (19). This measurement can be obtained on MR images in a manner similar to that with ultrasound. Ventriculomegaly can be graded into mild (10–15 mm), moderate ($>$15 mm with $>$3 mm of adjacent cortical thickness), and severe (ventriculomegaly with $<$2 mm of adjacent cortical thickness) categories (4). Ventricular measurements with fetal MR imaging correlate well with those obtained sonographically (4). Hydrocephalus is the term that indicates increased ventricular or subarachnoid space volume due to abnormal cerebrospinal fluid (CSF) dynamics (i.e., CSF overproduction, CSF underabsorption, or CSF pathway obstruction). This term is not ordinarily used unless a causal abnormality is specifically identified.

The cause of fetal ventraculomegaly is often not easy to define. If mild, it may be a transient and possibly normal finding (Figs. 3.1 and 3.2). Ventriculomegaly may be related to cerebral dysgenesis (e.g., in association with

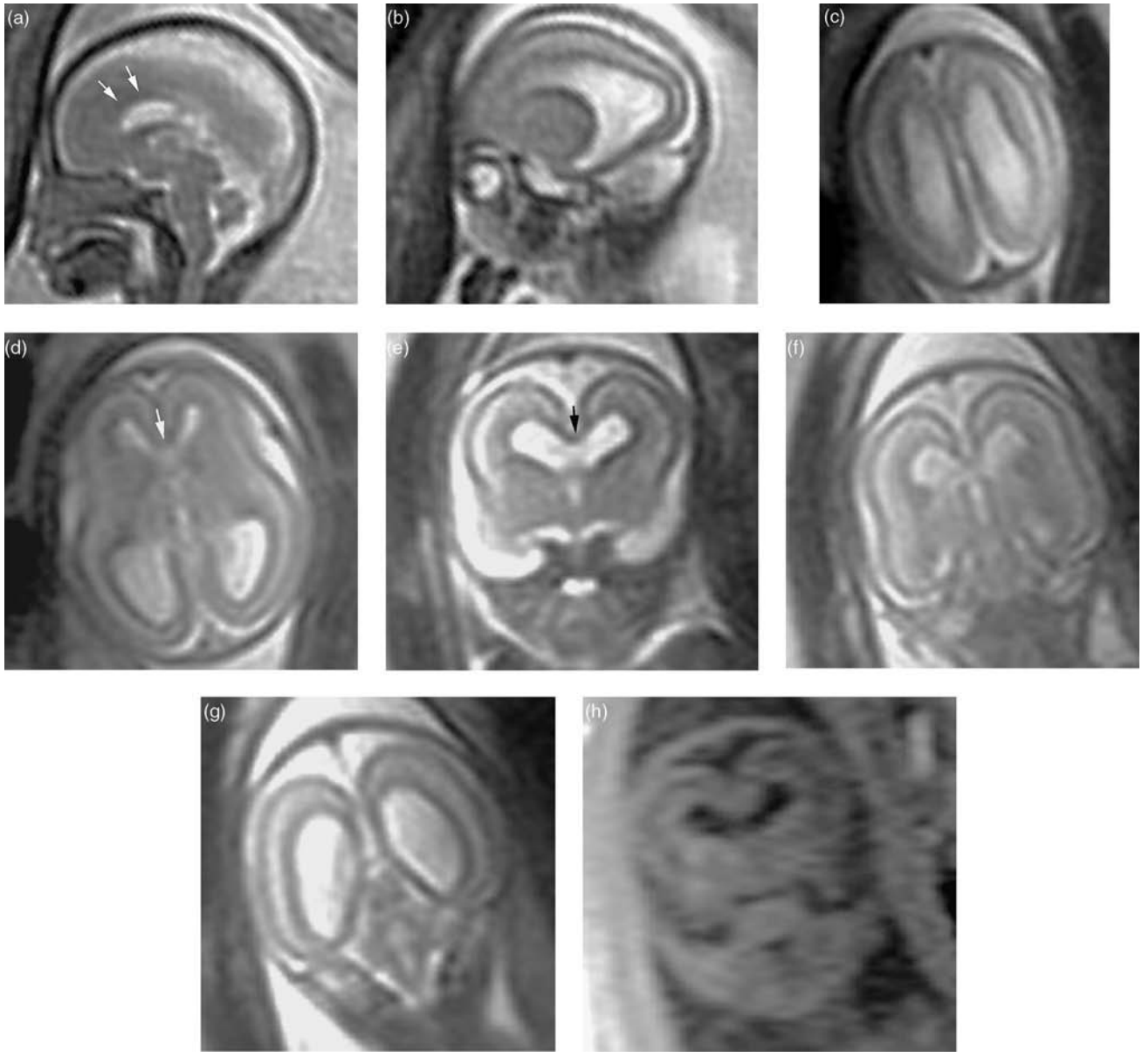

Figure 3.1 Mild isolated ventriculomegaly at 19 weeks. Sagittal (a and b), axial (c and d), and coronal (e–g) T_2-weighted images and coronal T_1-weighted image (h) show mildly dilated ventricles without other abnormalities. Only the anterior portion of the corpus callosum (arrows) is visualized, which is a normal finding on MR at this gestational age. Note the normal orbit, cerebellum, and mantle thickness.

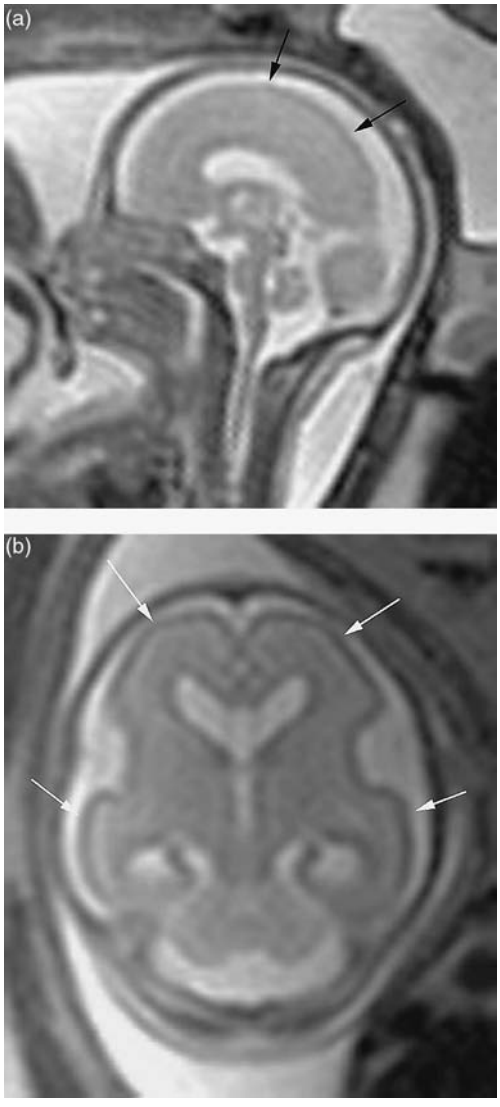

Figure 3.2 Mild ventriculomegaly at 26 weeks gestational age. Sagittal (a) and oblique axial (b) T_2-weighted images. Note smooth hypointense cortical band (arrows), which is a normal finding at this gestational age.

aneuploidy, Figs. 3.3 and 3.4), corpus callosal hypogenesis (Fig. 3.5), or lissencephaly. Ventriculomegaly may be an *ex vacuo* phenomenon (e.g., atrophy secondary to infection or infarction, Fig. 3.6). Finally, ventriculomegaly may represent hydrocephalus (Fig. 3.7) associated with a wide range of developmental or acquired etiologies.

The outcome of ventriculomegaly depends on the cause and degree of ventricular enlargement, any associated

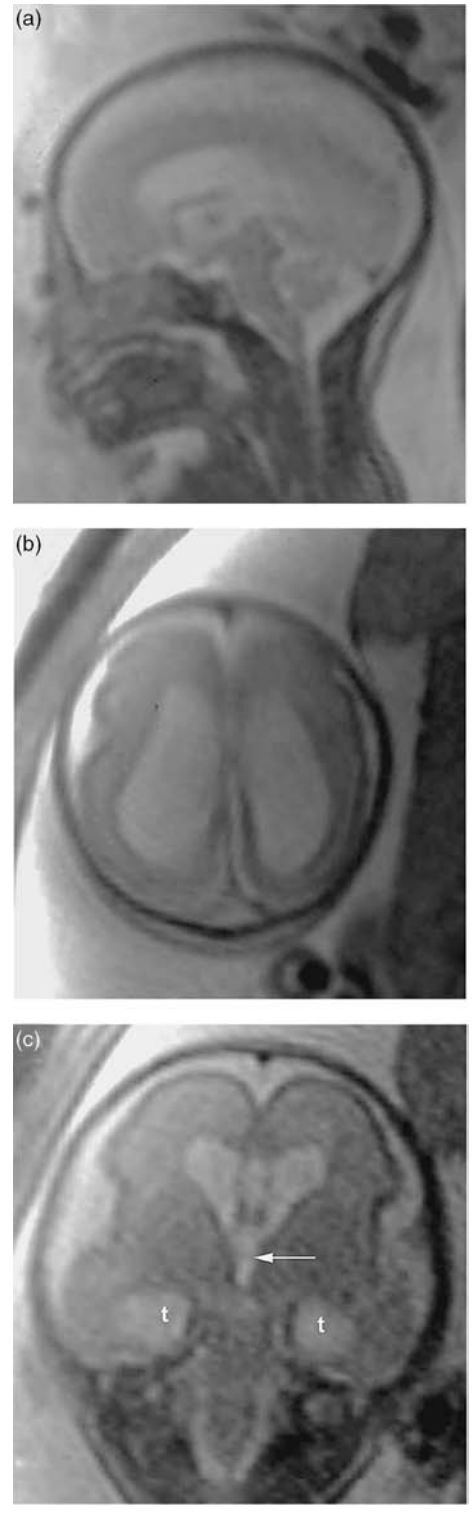

Figure 3.3 Mild ventriculomegaly at 26 weeks gestational age in fetus with trisomy 21. Sagittal (a), axial (b), and coronal (c) T_2-weighted images show mildly large third (arrow) and lateral ventricles including temporal horns (t).

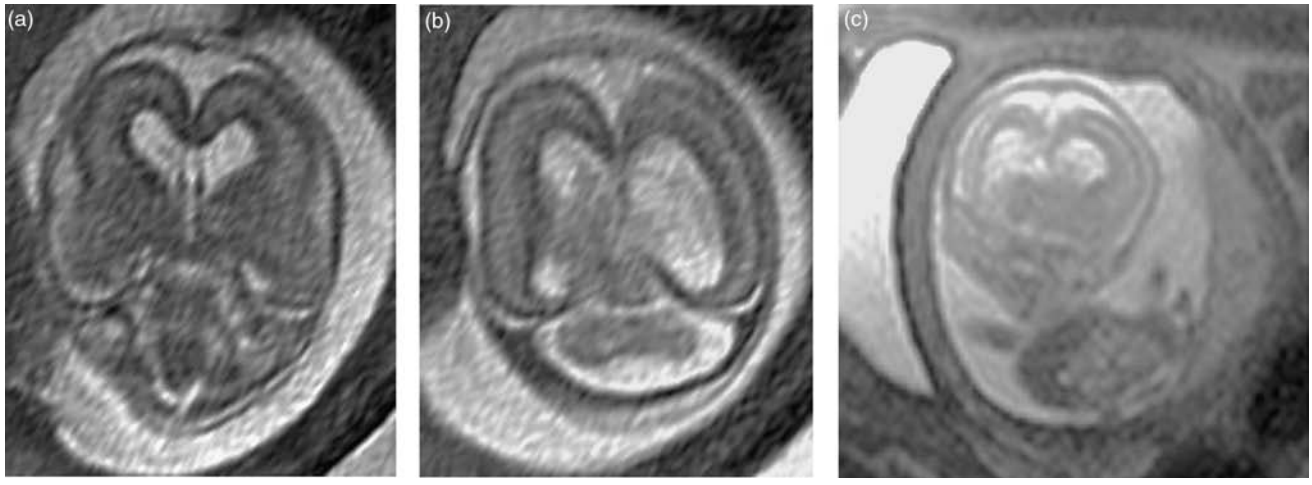

Figure 3.4 Mild ventriculomegaly with triploidy at 19 weeks gestational age. Sonographic biometry showed head measurements 2 weeks less than expected for gestational age and abdominal circumference 4 weeks less than expected. Coronal T_2-weighted images of head (a and b) show mild ventriculomegaly. Coronal view of head and torso (c) shows the relatively small size of the body as compared to the head, consistent with severe intrauterine growth restriction.

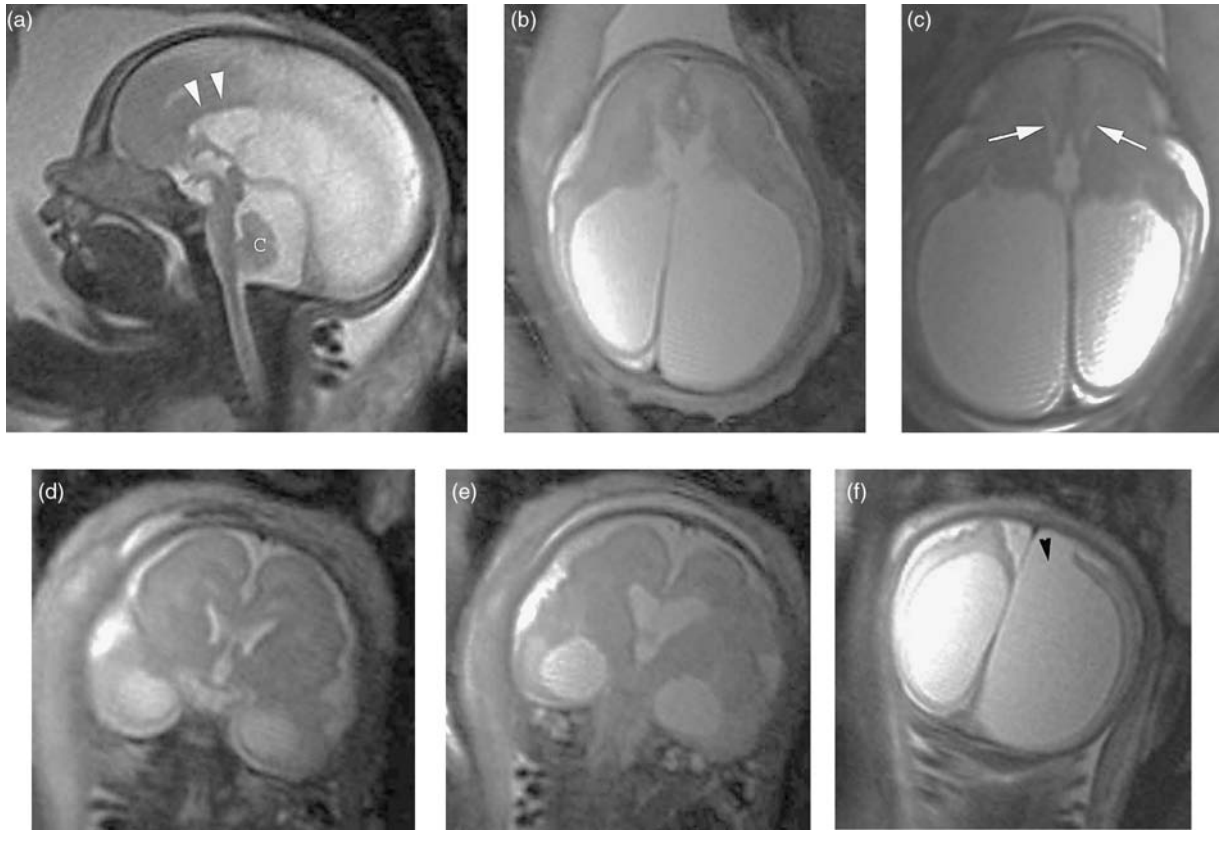

Figure 3.5 Severe ventriculomegaly associated with Walker–Warburg syndrome at 33 weeks gestational age. Sagittal T_2-weighted image (a) shows hypogenesis of the corpus callosum with a thin genu and anterior body (white arrowheads) and a relatively small cerebellum (c) within a large posterior fossa. Axial (b and c) and coronal (d–f) T_2-weighted images show colpocephaly with slit-like frontal horns (arrows) and massively dilated occipital horns. The frontal horns diverge normally. This combination of findings suggests dysgenesis of the corpus callosum. The gyral pattern is abnormally smooth for this gestational age, suggesting abnormal cortical development. Black arrowhead denotes region of porencephaly in (f). The autopsy at birth confirmed muscular dystrophy, subcapsular cataracts, cerebellar hypoplasia, an interhemispheric cyst, hypogenesis of the corpus callosum, and an abnormal gyral pattern with regions of lissencephaly and polymicrogyria.

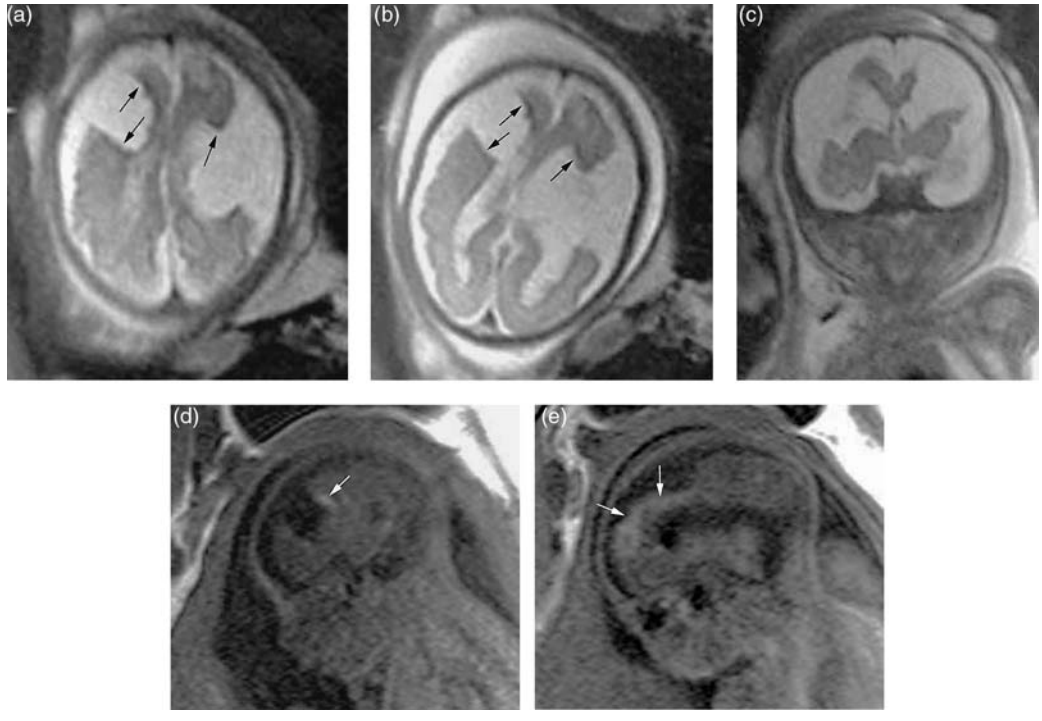

Figure 3.6 Ventriculomegaly and cerebral clefts at 30 weeks gestational age. Axial (a and b) and coronal (c) T_2-weighted images and sagittal T_1-weighted images (d and e) show moderate ventriculomegaly, with bilateral transmantle defects, or clefts. These may represent either porencephaly or schizencephaly. The T_2 low intensities and T_1 high intensities along the margins of the defects suggest hemorrhage or mineralization (arrows). This and the presence of ependymal and cortical septations suggest an encephaloclastic origin occurring beyond 22–23 weeks gestational age (i.e., porencephaly) rather than an earlier migrational disorder (i.e., schizencephaly).

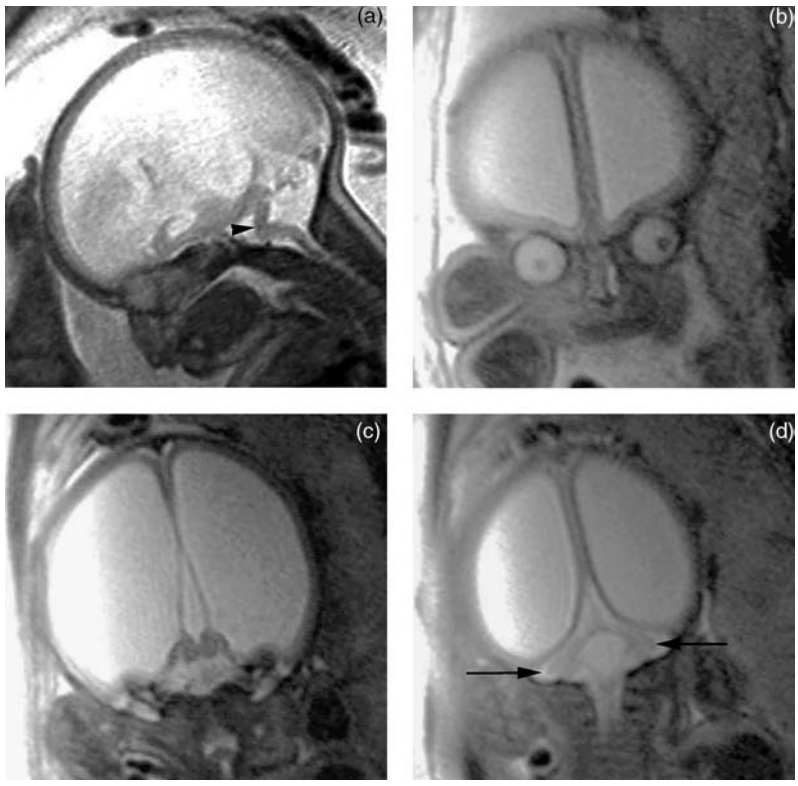

Figure 3.7 Severe ventriculomegaly at 32 weeks gestational age. Sagittal (a) and coronal (b–d) T_2-weighted images. The head size is enlarged. There is a thin smooth mantle. The lack of extra-axial CSF space suggests that the ventriculomegaly represents hydrocephalus rather than a purely dysgenetic process. However, there are dysgenetic features including cerebellar vermian and hemispheric hypogenesis (arrows), a kinked brainstem (arrowhead), a large fourth ventricle, and a small posterior fossa. [(a) From Levine et al. (23)]

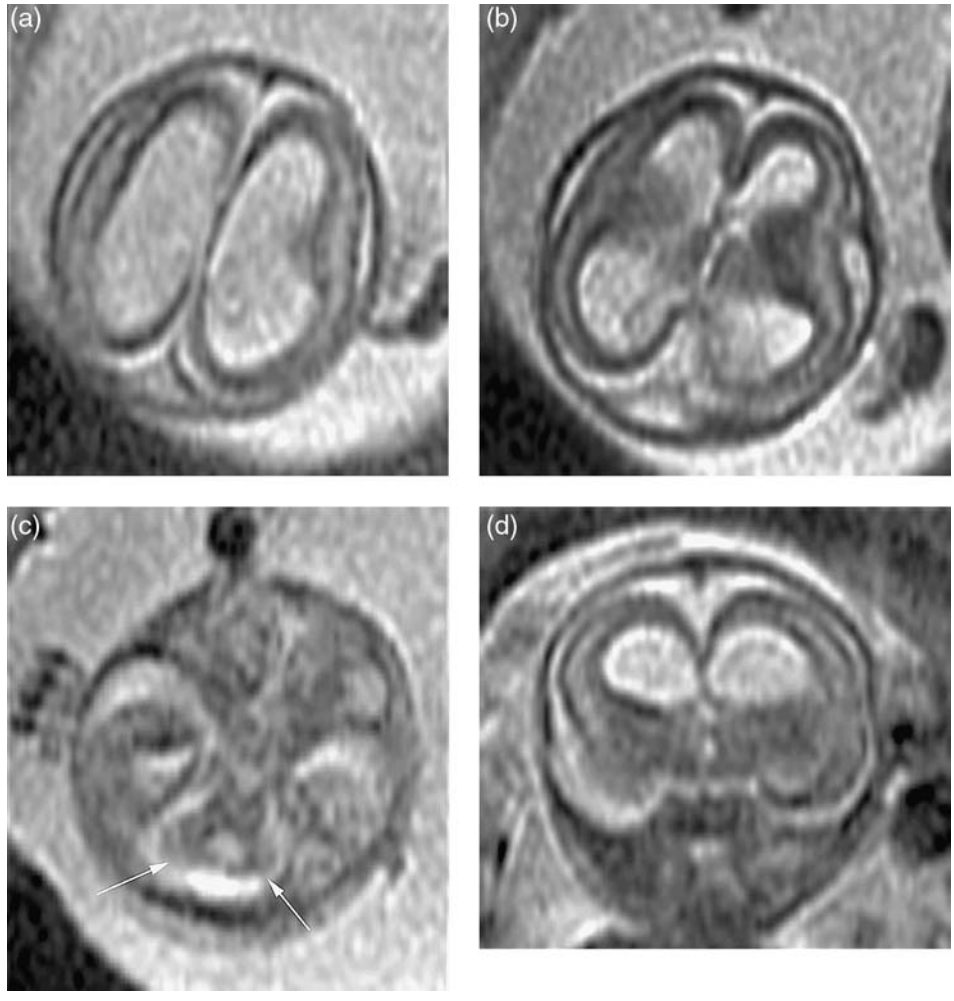

Figure 3.8 Mild ventriculomegaly at 18 weeks gestational age. Axial (a–c) and coronal (d) views demonstrate mild ventriculomegaly. Although the lateral ventricles only measure 11 mm, there is a thin surrounding mantle. The cerebellum (arrows) is hypoplastic.

abnormalities (Figs. 3.8 and 3.9), the gestational age at which it develops, and its progression (Fig. 3.10) (20). Fetal MR imaging is particularly helpful in showing associated anomalies that may be missed by ultrasound (4,8,21–23). However, at times, the etiology of ventriculomegaly cannot be determined by prenatal imaging (Fig. 3.11). When isolated, mild ventriculomegaly (10–12 mm) is not associated with adverse postnatal outcomes in the majority of cases. However, in other cases, it may be associated with developmental delay. Measurements of cortical thickness, cortical volume, and ventricular volumes, along with more quantitative assessments of maturation, may prove to be predictive of postnatal outcome.

The symmetry, proportion, and contour of the ventriculomegaly are important factors. The significance of isolated asymmetric ventriculomegaly is often indeterminate (Fig. 3.12). An angular lateral ventricular contour is a feature of neural tube defects (24). A box-like appearance of the frontal horns is often associated with absence of the septum pellucidum (24). Colpocephaly (i.e., disproportionate dilatation of the atria and occipital horns with small frontal horns) is often present with hypogenesis of the corpus callosum. However, a similar contour may be seen as a normal developmental phase, especially when there is only mild relative disproportion. Therefore, it is important to examine the ventricles in multiple planes (Fig. 3.13).

When the extracerebral CSF spaces are effaced and the head size is enlarged in association with ventriculomegaly, an obstructive component to the ventriculomegaly can be surmised. When the extracerebral CSF spaces are prominent and the head size is small in association with ventriculomegaly, hypogenesis is likely. In some cases, both hypogenesis and hydrocephalus can coexist, or the hydrocephalus develops subsequently.

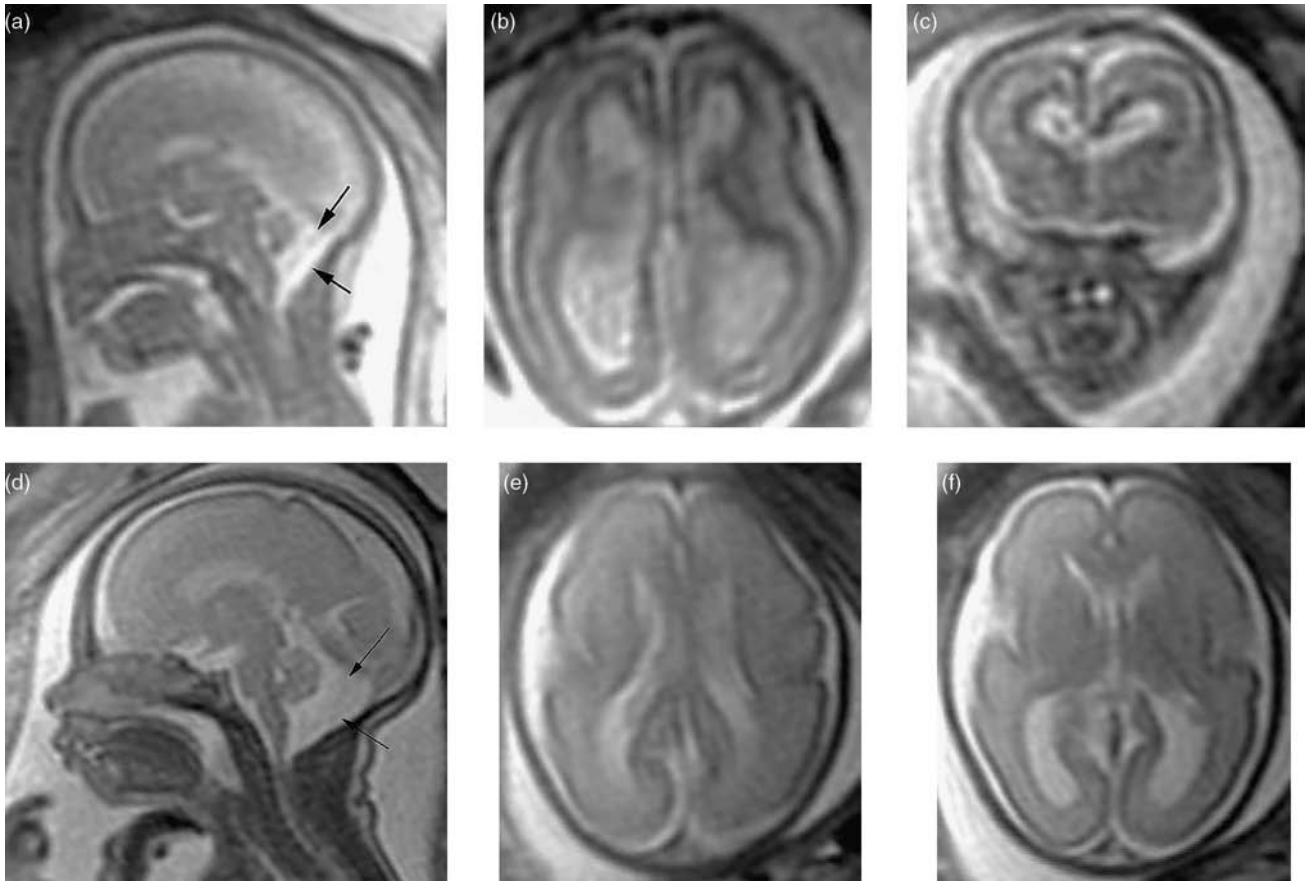

Figure 3.9 Mild ventriculomegaly with enlarged cisterna magna and normal cerebellum at 20 weeks gestational age. Sagittal (a), axial (b), and coronal (c) T_2-weighted images show mild ventriculomegaly, which is stable at 29 weeks gestational age on sagittal (d) and axial views (e and f). The cisterna magna is enlarged (arrows); however, the cerebellum appears normal. Note the normal cortical development at 29 weeks.

DISORDERS OF DORSAL NEURAL TUBE DEVELOPMENT

The CNS develops from the embryonic ectoderm termed the neural plate. The neural plate forms the neural tube (i.e., neurulation), which gives rise to the spinal cord and brain. Primary neurulation refers to the formation of the neural tube along the notochord from the cranial end of the embryo to approximately the L1-2 level caudally. These events occur during the initial 3–4 weeks of gestation. Some of the anomalies associated with the defects of primary neurulation include anencephaly, cephaloceles, myelomeningocele, and Chiari II malformation.

Secondary neurulation refers to the formation of the caudal neural tube below the notochord by canalization and retrogressive differentiation. The lower lumbar, sacral, and coccygeal segments are thus formed. This canalization occurs at 4–7 weeks gestational age. Some of the abnormalities of secondary neurulation include diastematomyelia, meningocele, lipomeningocele, tethered cord, and caudal regression syndrome. These are dealt with in more detail in Chapter 7.

Anencephaly

Anencephaly is characterized by the absence of the cranial vault and telencephalon. There may be a vascular stroma present above the orbits. There is little role for prenatal MR imaging in the diagnosis of anencephaly as it is well characterized by ultrasound. However, MR imaging may be used to examine the co-twin of an anencephalic (Fig. 3.14).

Cephaloceles

Cephaloceles are protrusions of intracranial contents through a bony defect of the skull. The most common locations, in order, are occipital, frontal, parietal, and basal. When the protrusion is comprised only of meninges,

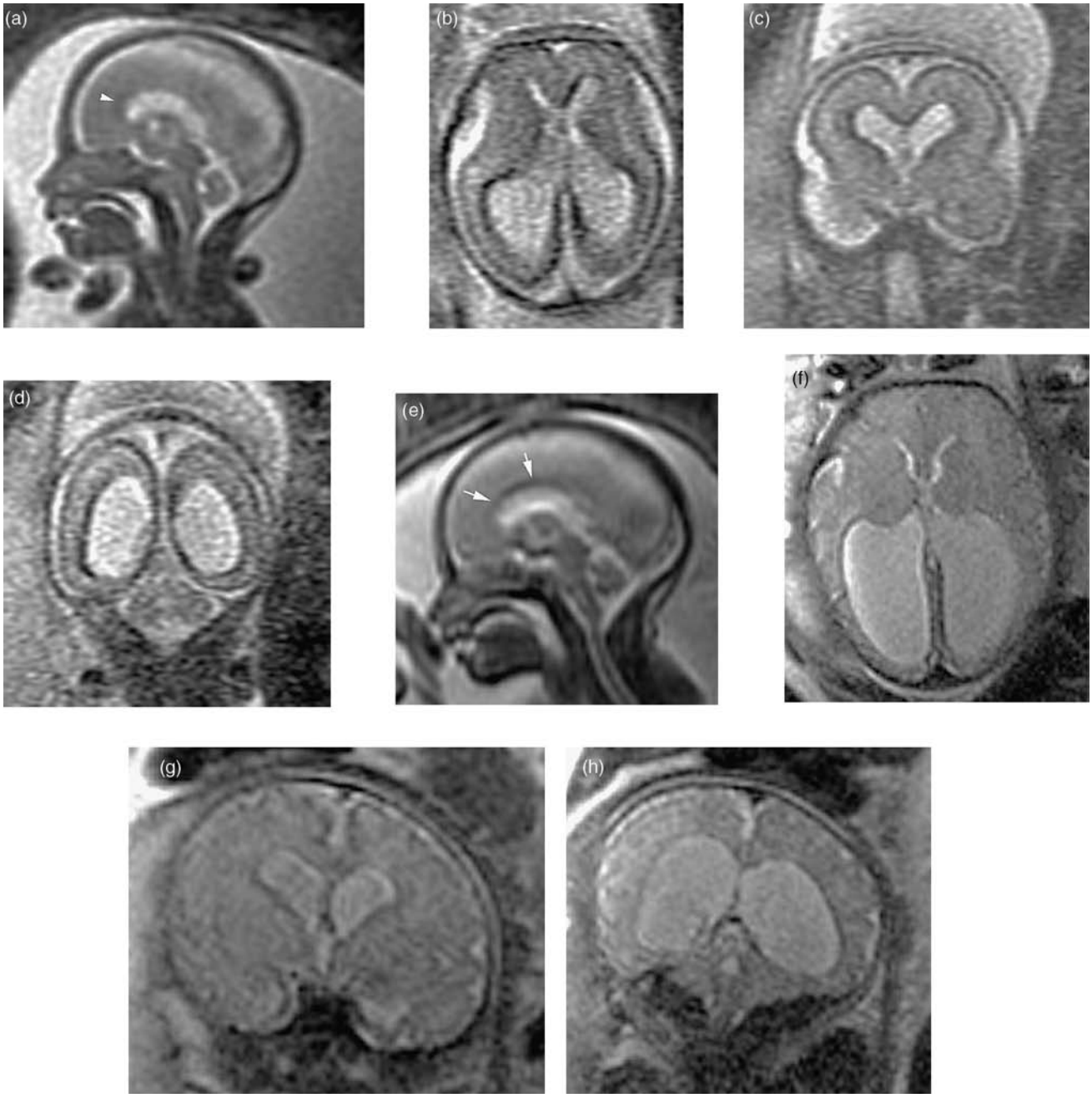

Figure 3.10 Mild ventriculomegaly at 21, 23, and 34 weeks gestational age. Sagittal (a), axial (b), and coronal (c and d), T_2-weighted images at 21 weeks gestational age show mild ventriculomegaly with mild disproportionate enlargement of the posterior portions of the lateral ventricles as compared to the frontal horns. However, the frontal horns have the normal appearance (diverging from the midline). On the sagittal views, the corpus callosum is only faintly visualized (arrowheads). Although the corpus callosum is not visualized in its entirety, its presence, at least partially, is inferred from the normal frontal horn configuration. Midsagittal T_2-weighted image (e) at 23 weeks gestational age clearly demonstrates the corpus callosum (arrows). At 34 weeks gestational age, axial (f) and coronal (g and h) T_2-weighted images show marked progression of the ventriculomegaly, with the atria measuring 30 mm. The third ventricle is mildly dilated and the fourth ventricle is normal. This pattern of ventriculomegaly is suggestive of aqueductal stenosis, which was confirmed postnatally.

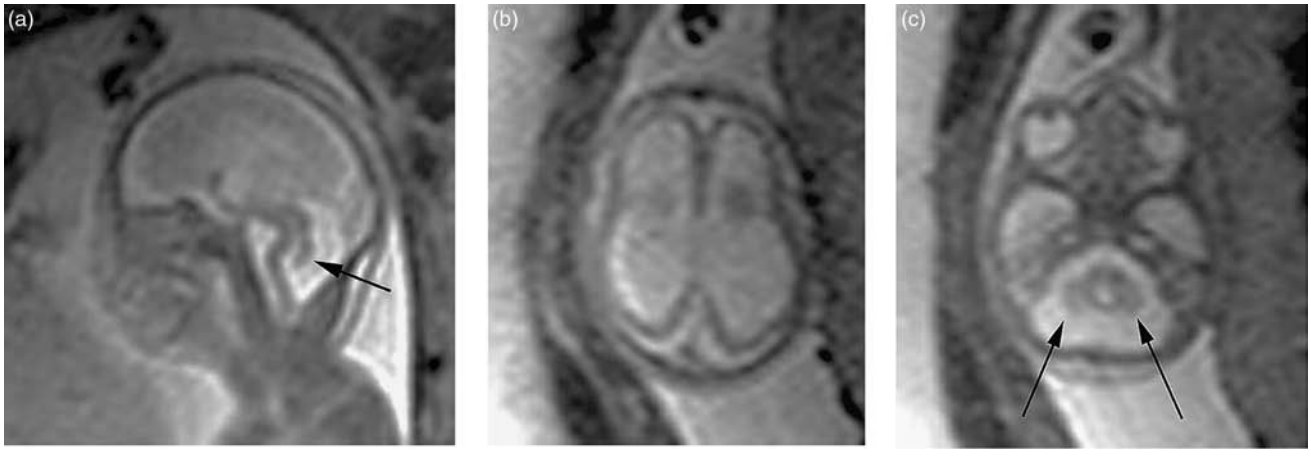

Figure 3.11 Ventriculomegaly and unspecified cerebrocerebellar hypogenesis at 19 weeks gestational age. Sagittal (a) and axial (b and c) T_2-weighted images demonstrate ventriculomegaly with a thin cerebral mantle and prominent extracerebral CSF spaces suggesting hypogenesis rather than hydrocephalus. The cerebellum (arrows) and brainstem are markedly hypogenetic and there is reversal of the normal flexure of the brainstem.

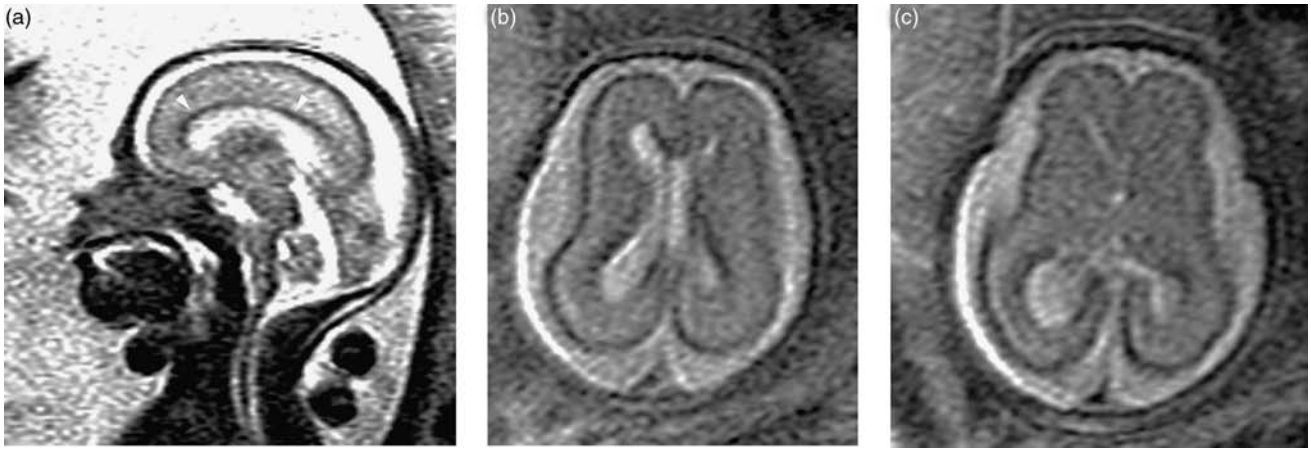

Figure 3.12 Mild unilateral ventriculomegaly at 23 weeks gestational age. Sagittal (a) and axial T_2-weighted images (b and c) demonstrate mild unilateral ventriculomegaly with the lateral ventricles measuring 11 and 6 mm. Note the normal mantle thickness and smooth cortical contour. The corpus callosum (arrowheads) is well delineated at this gestational age.

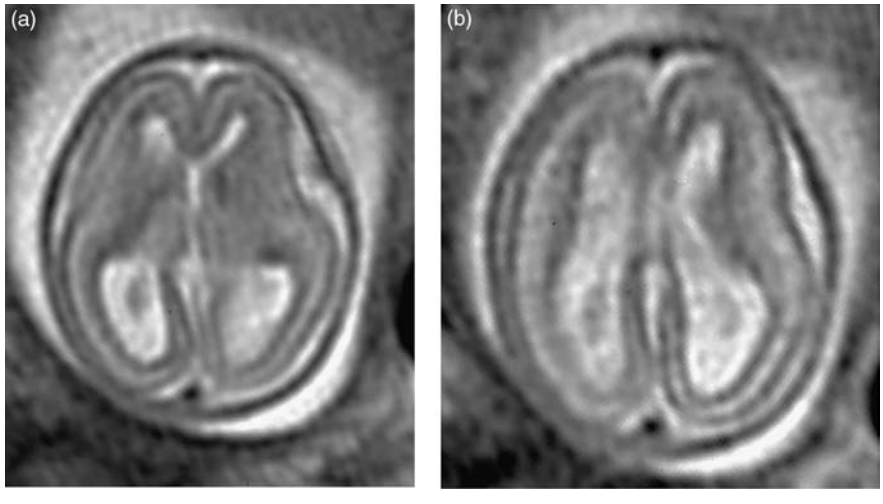

Figure 3.13 Ventriculomegaly with "pseudocolpocephaly" at 17 weeks gestational age. Axial T_2-weighted images show mild ventriculomegaly. The lower axial image (a) gives the appearance of colpocephaly; however, the higher axial image (b) shows a normal configuration.

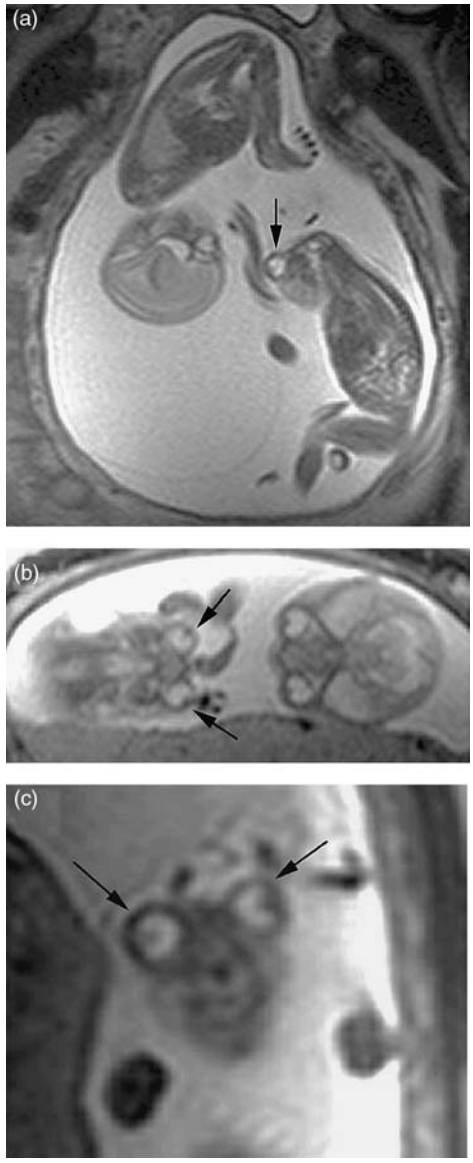

Figure 3.14 Anencephaly of one twin of a monochorionic pair at 20 weeks gestational age. Sagittal (a), axial (b), and coronal (c) T_2-weighted images show lack of brain tissue above the orbits and globes (arrows) in the affected twin as compared to the normal twin. [From Levine (115)]

it is termed a meningocele. Fetal MR imaging can aid in distinguishing a meningocele from other cystic lesions of the head and neck region (e.g., cystic hygroma, teratoma, or hemangioma; Chapter 4, Fig. 4.14). Encephaloceles contain meninges and neural tissue, and are often associated with ventriculomegaly, other malformations, and syndromes. Fetal MR imaging is often important in defining the contents of the encephalocele and in delineating abnormalities of the underlying brain (Figs. 3.15–3.19) (4).

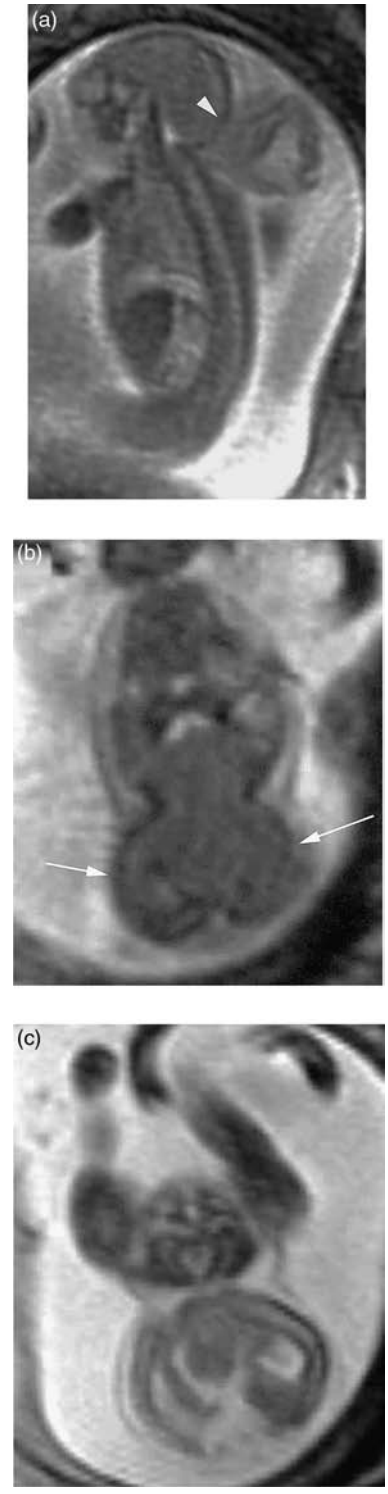

Figure 3.15 Occipital encephalocele and cerebral hypogenesis in fetus with trisomy 18 at 20 weeks gestational age. Sagittal (a) and axial (b and c) T_2-weighted images show the large calvarial defect (arrowhead) and extracranial cerebral tissue with partially formed hemispheres (arrows). There is microcephaly with a small forebrain as shown by the sloping appearance to the forehead on the sagittal image.

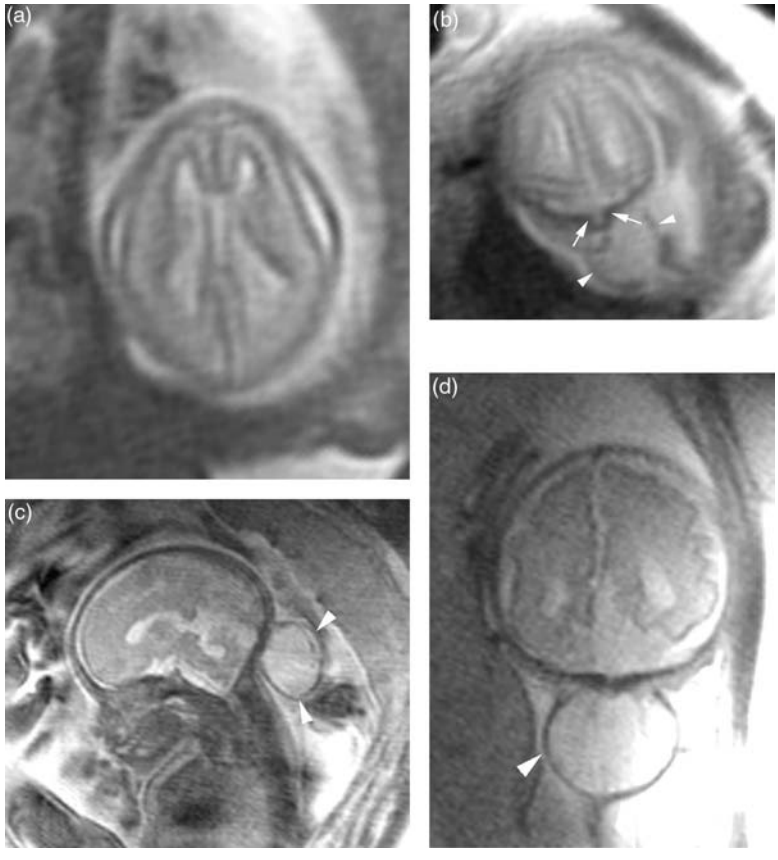

Figure 3.16 Occipital meningoencephalocele with normal brain. At 20 weeks, oblique axial (a) and coronal (b) T_2-weighted images show a small posterior cranial defect (arrows) with a mostly fluid-filled extracranial collection (arrowheads) and a normal brain with an angular ventricular configuration to the ventricles. At 30 weeks, sagittal (c) and axial (d) T_2-weighted images show the meningoencephalocele (arrowheads) with otherwise normal brain morphology. Only a small amount of brain tissue was present in the sac at surgery. This type of cephalocele has a very good outcome.

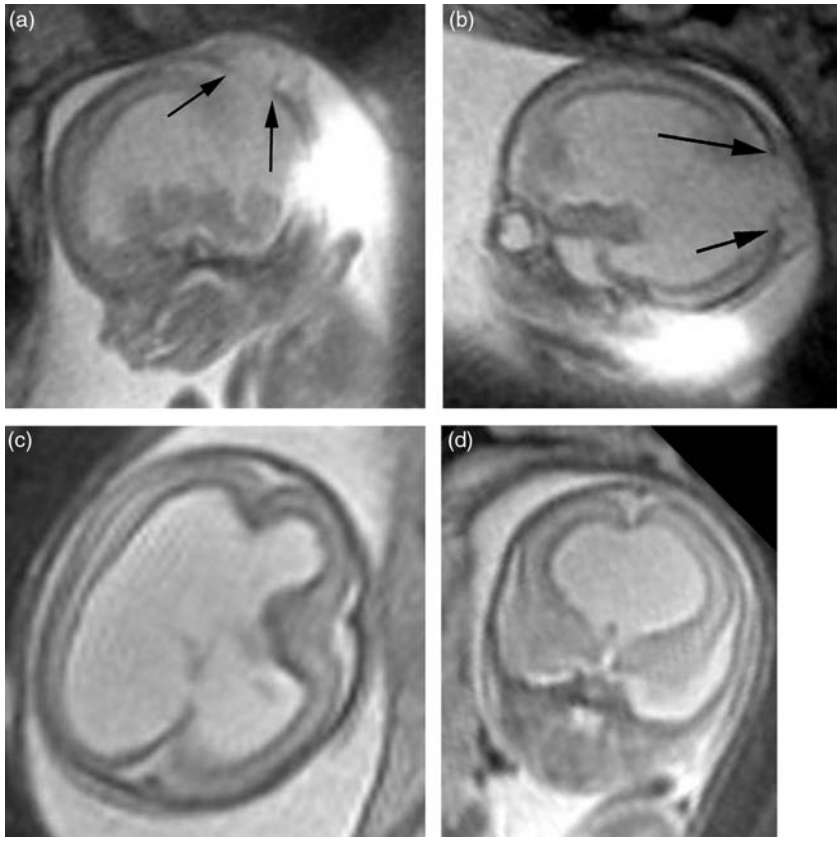

Figure 3.17 Parietal encephalocele at 23 weeks gestational age. Sagittal (a and b), axial (c), and coronal (d) T_2-weighted images show a high parietal bony defect (arrows) with a portion of the lateral ventricle and cerebral tissue extending into the sac. There is ventriculomegaly and deficiency of the septal leaflets (partial absence of the cavum of the septum pellucidum).

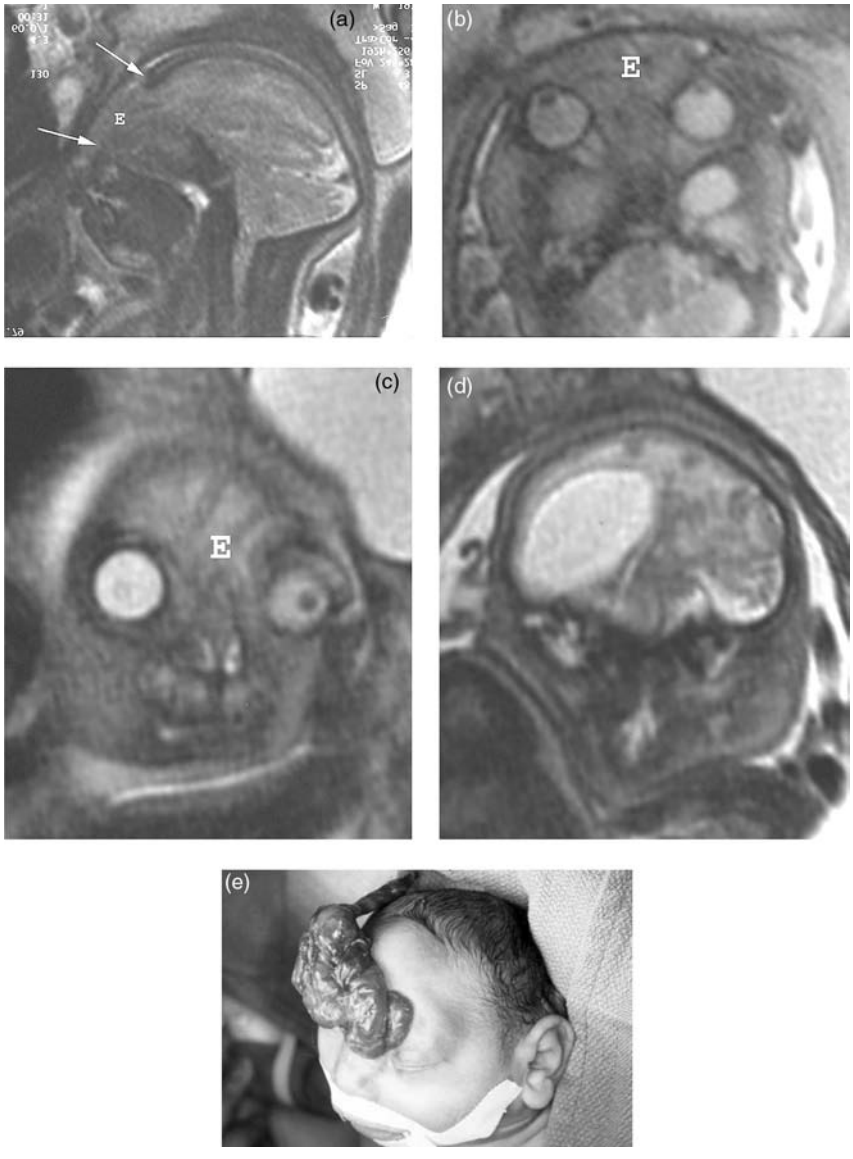

Figure 3.18 Frontal encephalocele and cerebral hypogenesis at 35 weeks gestational age. Sagittal (a), axial (b), and coronal (c and d) T_2-weighted images show a large frontal calvarial defect (arrows) containing cerebral tissue (E). The brain is dysmorphic with a primitive, nonsegmented brainstem and marked hypogenesis to the cerebral hemispheres, especially the frontal lobes (sloping appearance of the forehead representing forebrain underdevelopment). The axial and coronal images (b–d) show the orbital hypertelorism and encephalocele (E). Postnatal preoperative photograph (e) shows the frontal encephalocele above the nose and eyes. [(c and e) From Levine et al. (54)]

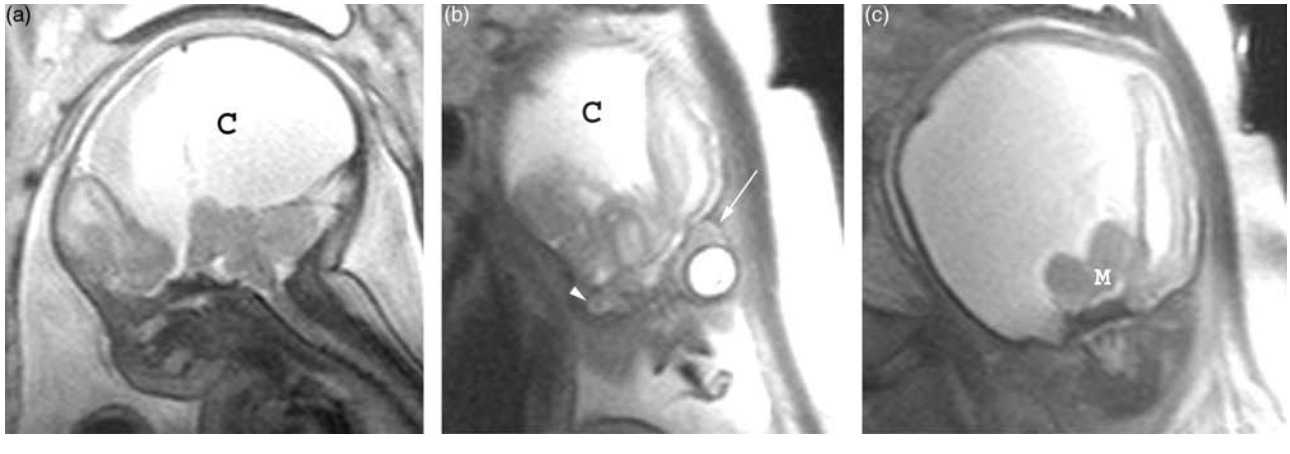

Figure 3.19 Orbital encephalocele with contralateral microtia and cerebral hypogenesis at 35 weeks gestational age. Sagittal (a) and coronal (b and c) T_2-weighted images demonstrate the orbital encephalocele (arrow), contralateral microtia (arrowhead), and large paramedian cerebral cleft (C). The midbrain (M) has an abnormally deep cleavage plane.

Spina Bifida

The spinal findings of neural tube defects are discussed in Chapter 7. Open neural tube defects (e.g., myelocele and myelomeningocele) are almost always associated with the Chiari II (Arnold Chiari) malformation, which includes downward herniation of the cerebellum through the foramen magnum into the upper cervical spinal canal (Figs. 3.20–3.22). The anomaly is best shown by MR imaging (25). Ventriculomegaly or hydrocephalus may be present. The shape of the ventricles commonly is abnormal with an acute angled configuration (Fig. 3.20) (24).

Fetal MR imaging is helpful in triaging patients with fetuses with myelomeningocele, who are potential candidates for *in utero* surgery and to detect concurrent abnormalities such as agenesis of the corpus callosum, cerebellar dysplasia, and migrational disorders (26,27). It can also be utilized to assess the degree of hindbrain herniation after fetal surgery (28).

DISORDERS OF VENTRAL NEURAL TUBE DEVELOPMENT

Ventral neurulation refers to the inductive events occurring in the rostral end of the embryo, resulting in the formation of the face and brain at 5–10 weeks gestational age. The prosencephalon divides into the telencephalon and diencephalon. The rhombencephalon divides into the metencephalon and myelencephalon. These give rise to the cerebrum, brainstem, and cerebellum. Abnormalities of ventral induction include the holoprosencephalies, septo-optic dysplasia, cerebral and cerebellar hypoplasia, and the Dandy–Walker spectrum.

Holoprosencephaly

Holoprosencephaly (Fig. 3.23) is a spectrum of malformations of the prosencephalon, with a failure of normal midline cleavage and incomplete midfacial development. Facial anomalies associated with holoprosencephaly include cyclopia, hypotelorism (Fig. 3.23; Chapter 4, Fig. 4.14) anophthalmia, arhinia (Fig. 3.23), proboscis, and median cleft lip and palate (Chapter 4, Fig. 4.26).

In the alobar form, the interhemispheric fissure and the falx cerebri are totally absent. There is a large monoventricle and dorsal cyst. The thalami are fused. The head is commonly small, which on a sagittal view is visualized as a sloping forehead with protuberant orbits. In the semilobar form, the cerebral hemispheres are partially separated posteriorly but there is a single ventricular cavity. In the lobar form, there are two distinct hemispheres but there is fusion at the level of the cingulate gyrus and frontal horns of the lateral ventricles. The septum

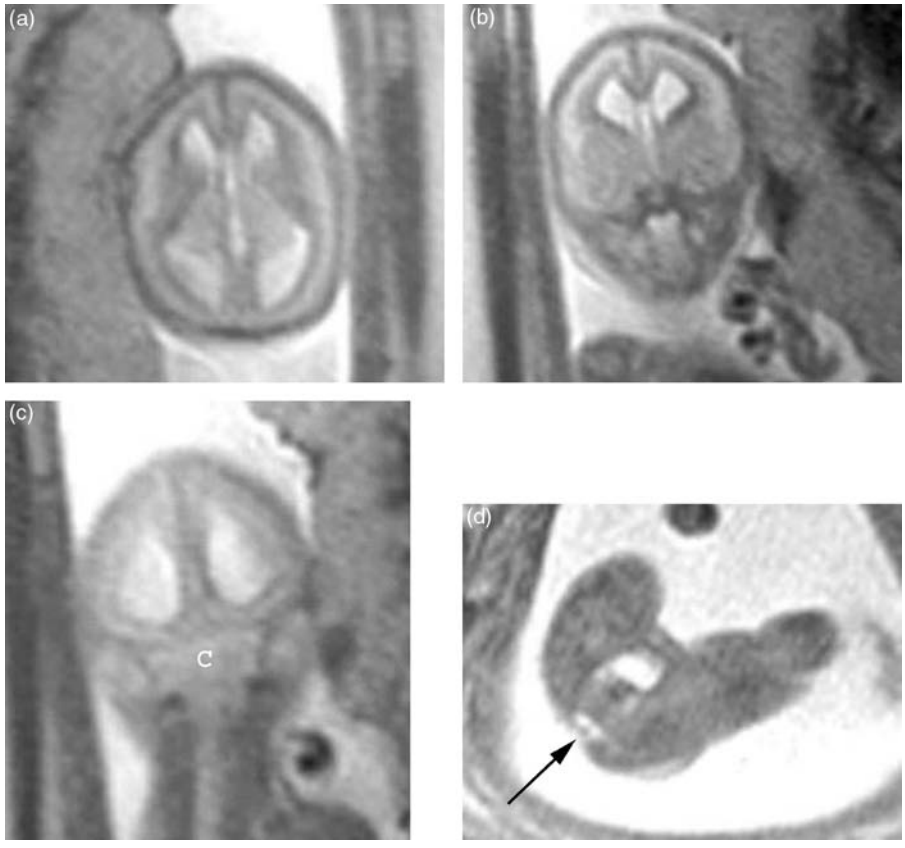

Figure 3.20 Neural tube defect at 21 weeks gestational age. Axial (a) and coronal (b and c) T_2-weighted images of the brain demonstrate the caudal displacement of the cerebellum (Chiari II malformation, C) and angular appearance to the ventricles. As the spinal findings in neural tube defects can be subtle, this angular appearance to the ventricles and Chiari II malformation are key to paying particular attention to the spinal canal. Axial T_2-weighted image at the level of the pelvis (d) shows the dorsal spinal canal defect and low-placed spinal cord (myelomeningocele, arrow).

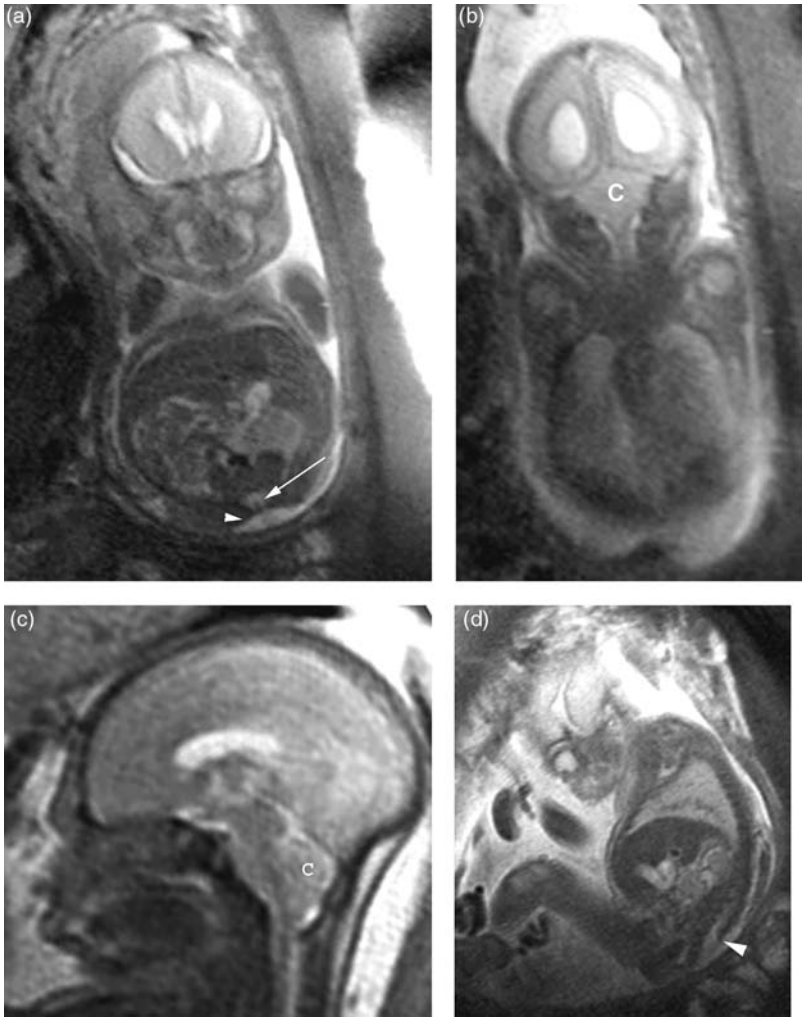

Figure 3.21 Neural tube defect at 26 weeks gestational age. Coronal (a and b) and sagittal (c and d) T_2-weighted images show the slightly enlarged ventricles with slightly effaced extra-axial spaces and the caudal displacement of the cerebellum ("c" indicated in the figure b and c), consistent with the Chiari II malformation. The views including the lower spine (a and d) show the dorsal soft tissue defect (arrowhead) and low spinal cord placement below the level of the kidneys (arrow).

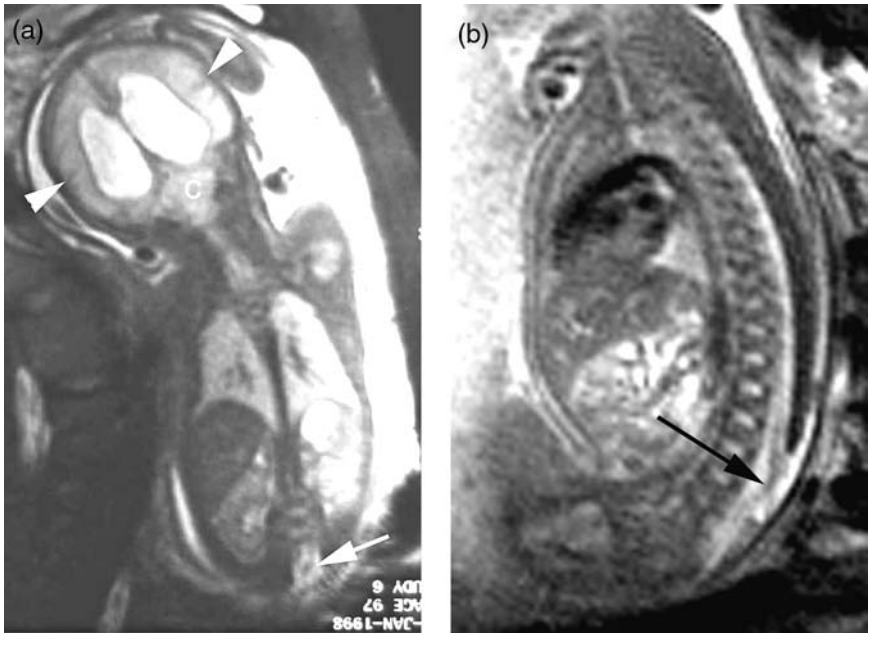

Figure 3.22 Neural tube defect at 29 weeks gestational age. Coronal head and torso (a) and sagittal torso (b) T_2-weighted images show ventriculomegaly with effaced sulci and extracerebral spaces (arrowheads), the Chiari II malformation (C), and the caudal spinal canal defect with low spinal cord placement (myelomeningocele, arrows).

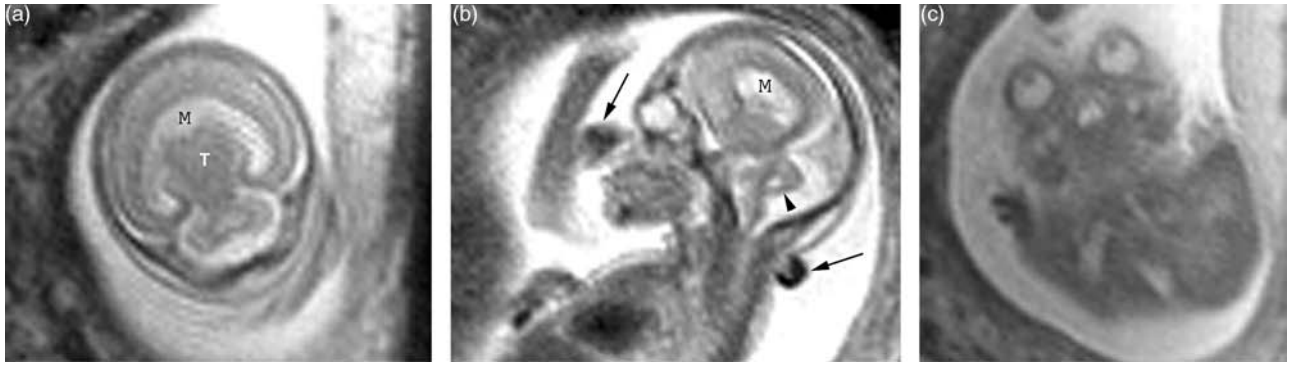

Figure 3.23 Alobar holoprosencephaly at 20 weeks gestational age. Oblique coronal (a), sagittal (b), and oblique axial (c) T_2-weighted images show monoventricle (M), fused thalami (T), flat midface with absent nose, and hypotelorism. Note the loop of umbilical cord anterior to the face and behind the neck (arrows). The cerebellum (arrowhead) is hypoplastic. [(a) From Levine (115).]

pellucidum is absent. It may be difficult to distinguish between lobar holoprosencephaly and septo-optic dysplasia. Rarer forms include the middle interhemispheric variant and vertex cephalocele.

The varied types of holoprosencephaly are usually diagnosed by ultrasound. When the sonographic diagnosis is uncertain (e.g., when fetal size or position, or maternal body habitus, make it difficult to visualize the falx and other midline structures), MR imaging can be helpful. Fetal MR imaging is particularly helpful in distinguishing holoprosencephaly from agenesis of the corpus callosum with large midline clefts or cysts (3,8).

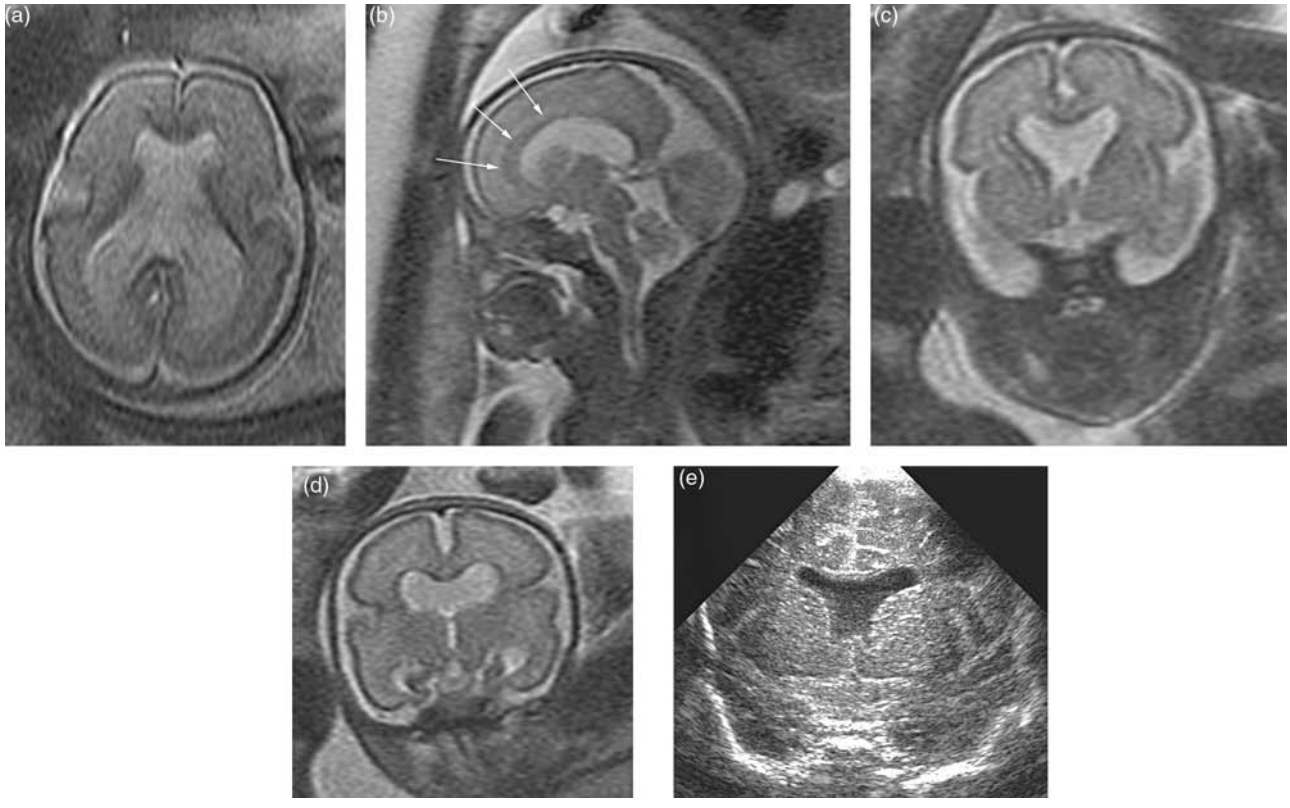

Figure 3.24 Absent cavum of the septum pellucidum at 28 weeks gestational age. Axial (a), sagittal (b), and coronal (c and d) T_2-weighted images show absent septal leaflets and moderately enlarged frontal horns with inferior beaking. Note the normal appearance to the corpus callosum (arrows). Compare this appearance to Fig. 3.1, where the normal cavum of the septum pellucidum is present. Postnatal sonogram (e) confirms the diagnosis.

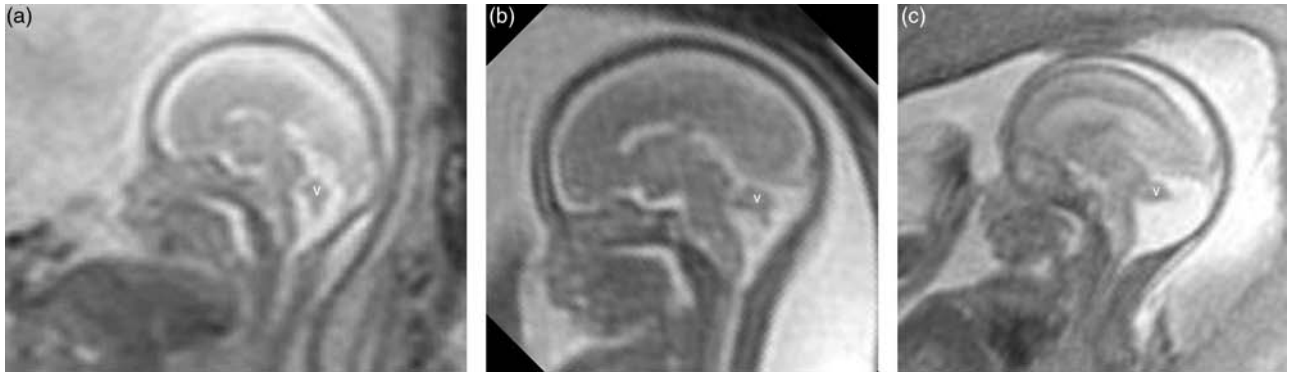

Figure 3.25 The Dandy–Walker spectrum in three fetuses at 19 weeks gestational age (sagittal T_2-weighted images). In the first fetus (a), the vermis (v) is slightly tilted upward and is possibly slightly small. There is a mildly prominent fourth ventricle, vallecula, and retrocerebellar space. In the second fetus (b), the inferior vermis is small and mildly elevated. The vallecula is wider with a higher torcular Herophili. In the third fetus (c), the inferior vermis is absent (or very small) and there is upward tilting of the superior vermian remnant with markedly widened vallecula and wide continuity of the fourth ventricle with a large retrocerebellar space and a high torcula. Although the findings in the first two fetuses (a and b) may be more consistent with the Dandy–Walker variant (arachnoid cyst is also a possibility), the findings in the third fetus (c) is more consistent with the Dandy–Walker malformation.

Absence of the Cavum of the Septum Pellucidum and Septo-Optic Dysplasia

The cavum of the septum pellucidum may be absent with or without other abnormalities (Fig. 3.24). There is likely a spectrum of abnormalities ranging from isolated partial absence of the septal leaflets to complete absence of the septal leaflets. In septo-optic dysplasia (De Morsier syndrome), there is associated optic tract hypoplasia, endocrine abnormalities, and visual impairment. The prognosis depends on these associated abnormalities. The frontal horns are fused in the midline and have a squared appearance. The corpus callosum is usually present (29). Though it may be difficult to distinguish septo-optic dysplasia from lobar holoprosencephaly, the presence of fused fornices within the ventricular cavity favors the latter.

Dandy–Walker Spectrum

In general, posterior fossa and hindbrain anomalies are suspected by ultrasound when the cisterna magna is too small (e.g., in the Chiari II malformation) or when it is too large (e.g., Dandy–Walker spectrum, cerebellar hypogenesis). A "large" cisterna magna is diagnosed on ultrasound on an image through the suboccipital bregmatic plane when the cisterna magna measures ≥ 1 cm. The Dandy–Walker spectrum (Figs. 3.25–3.31) is commonly

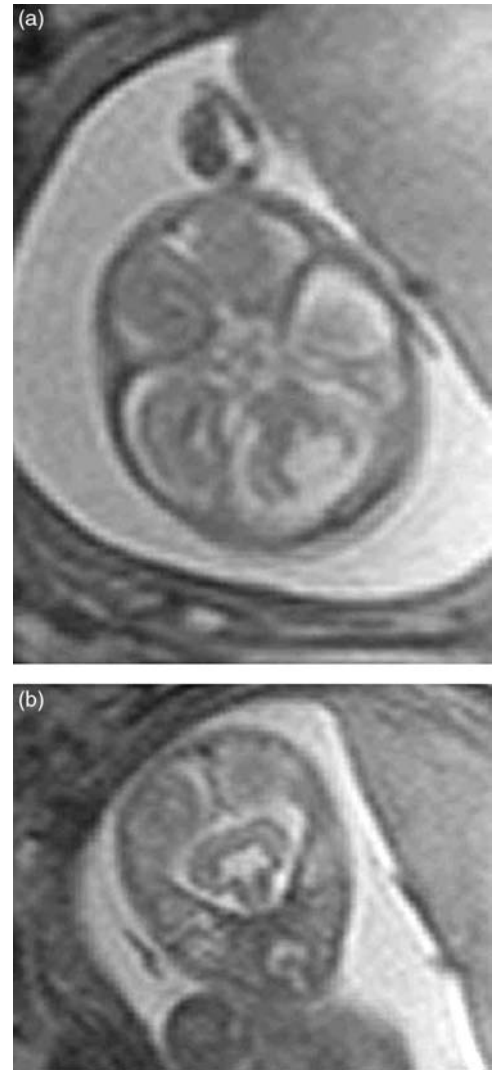

Figure 3.26 Dandy–Walker variant at 19 weeks gestational age. Axial (a) and coronal (b) T_2-weighted images [same fetus as Fig. 3.25(b)] show prominent fourth ventricle and vallecula separating the cerebellar hemispheres. Although this could potentially represent a midline posterior fossa arachnoid cyst, the appearance is most suggestive of Dandy–Walker variant. This was confirmed on postnatal imaging.

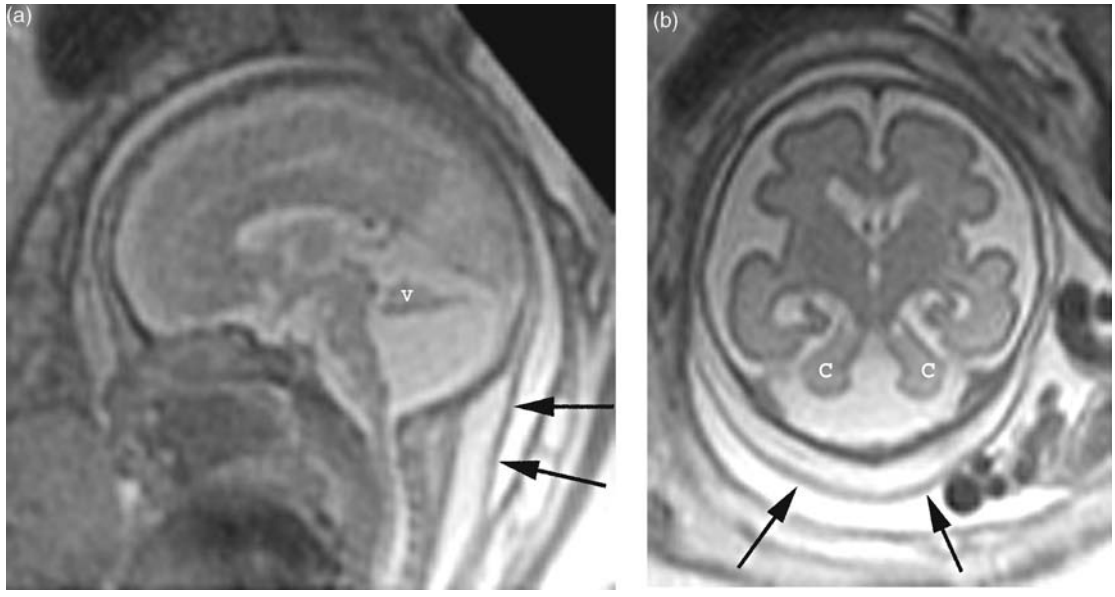

Figure 3.27 Dandy–Walker malformation at 29 weeks gestational age. Sagittal (a) and axial (b) T_2-weighted images show marked hypogenesis of the vermis with a small remnant (v) elevated above the large fourth ventricle which is in continuity with a large posterior fossa cyst (note the elevated torcular Herophili). The small cerebellar hemispheres (c) are separated by the prominent fourth ventricle. The corpus callosum is normally formed. Nuchal thickening is present (arrows).

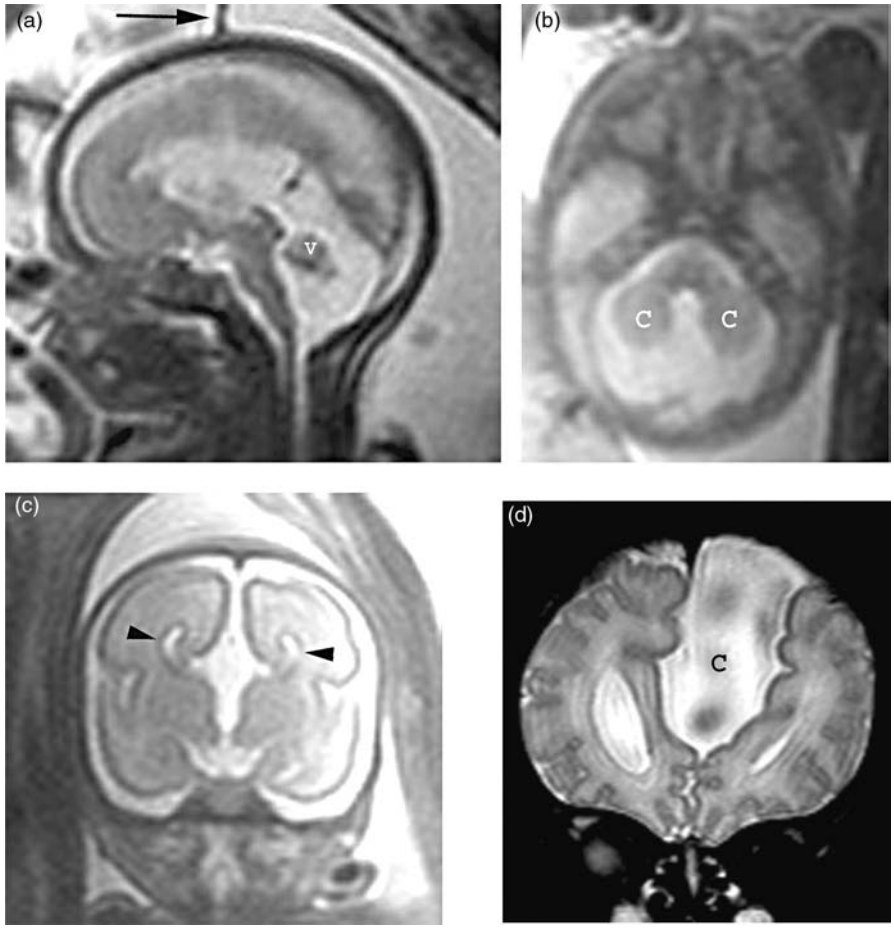

Figure 3.28 Dandy–Walker malformation and agenesis of the corpus callosum at 26 weeks gestational age. Sagittal (a), axial (b), and coronal (c) views demonstrate an elevated vermian remnant (v), small cerebellar hemispheres (white c indicated in the figure b), and wide continuity of the fourth ventricle with the large retrocerebellar space. Note the vertical orientation of the frontal horns (arrowheads) and absent corpus callosum. (d) Postnatally, a large interhemispheric cyst (black c indicated in the figure d) was visualized, which had not been noted prenatally on either ultrasound or MR imaging. At the time the cyst was present, the ventricles also were larger, suggesting that the cyst was at least partially formed secondary to increased intraventricular pressure. [(c) From Stroustrup Smith and Levine (33)]

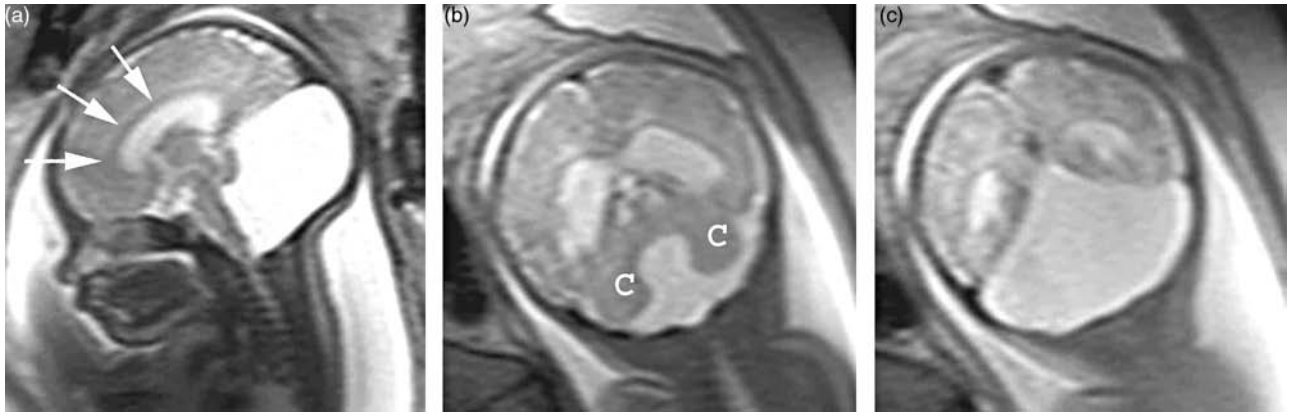

Figure 3.29 Dandy–Walker malformation at 36 weeks gestational age. Sagittal (a) and coronal (b and c) T_2-weighted images demonstrate near-absence of the vermis, widely separated cerebellar hemispheres ("c" indicated in the figure b), a large posterior fossa cyst continuous with the fourth ventricle, and a high torcular Herophili. The corpus callosum is normally formed (arrows).

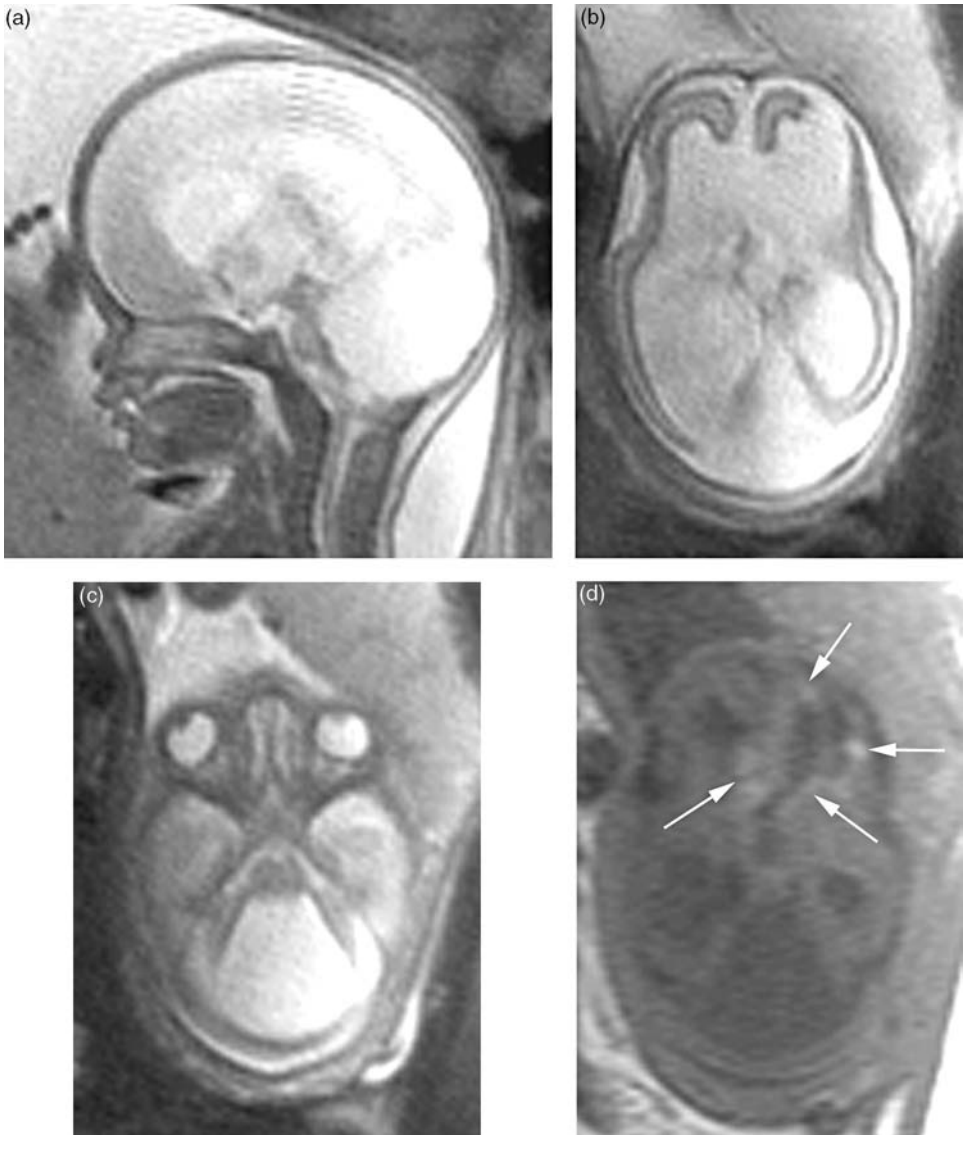

Figure 3.30 Dandy–Walker malformation, agenesis of the corpus callosum, and hydrocephalus at 25 weeks gestational age. Sagittal (a) and axial (b and c) T_2-weighted images show absence of the vermis and corpus callosum with a huge posterior fossa cyst and massive ventriculomegaly. The enlarged head size (note bulging forehead on the sagittal image) shows that there is an obstructive process as the etiology of the ventriculomegaly. Transmantle clefts are present which may represent areas of schizencephaly or porencephaly. Axial T_1-weighted image (d) shows areas of increased intensity probably representing prior hemorrhage or mineralization (arrows), which suggests that at least some of the cleft are porencephalic. Postnatal diagnosis revealed acrocallosal syndrome.

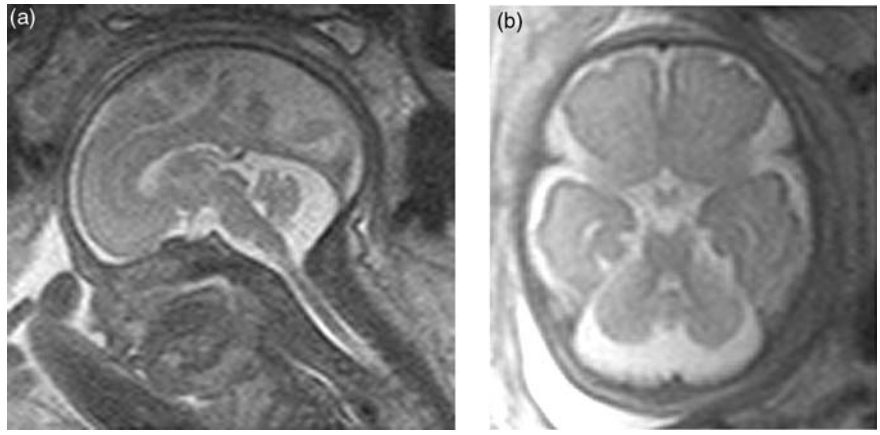

Figure 3.31 Megacisterna magna at 29 weeks gestational age. Sagittal (a) and axial (b) T_2-weighted images show an enlarged cisterna magna, measuring 13 mm (in the axial plane). The vermis is completely formed with a normal fourth ventricle and normal cerebellar hemispheres. No other abnormalities are present.

the cause of an "enlarged" cisterna magna. This spectrum variably includes the Dandy–Walker malformation, the Dandy–Walker variant, mega cisterna magna, Blake's pouch cyst, and the retrocerebellar arachnoid cyst (30–32). The midline sagittal view is very helpful in visualizing the cerebellar vermis, the cystic component, and the size of the posterior fossa (Fig. 3.25).

The Dandy–Walker malformation (Figs. 3.28–3.30) consists of a large cisterna magna that communicates with the fourth ventricle because of complete or partial agenesis of the cerebellar vermis. The volume of the posterior fossa is increased with cystic dilatation of the combined fourth ventricle and cisterna magna, along with upward displacement of the tentorium, lateral venous sinuses, and torcula. Hydrocephalus is commonly present or develops later. The vermis remnant is often rotated anterosuperiorly. There may be bulging and erosive scalloping of the occipital portion of the skull. The cerebellar hemispheres may be hypoplastic and in extreme cases are compressed laterally to the wall of the posterior fossa. Dandy–Walker malformation is often associated with other CNS or systemic anomalies, including chromosomal anomalies, hypogenesis of the corpus callosum (33), holoprosencephaly, and disorders of cortical migration and organization (e.g., Walker–Warburg syndrome).

The Dandy–Walker variant represents a lesser degree of cerebellar vermis hypogenesis with less dilatation of the fourth ventricle, more separation from the prominent cisterna magna, and less enlargement of the posterior fossa (Fig. 3.26). Fetal MR imaging is helpful in the diagnosis of the Dandy–Walker variant (4,6) as it provides a midsagittal view of the posterior fossa to demonstrate the continuity of the cisterna magna with the fourth ventricle, the amount of inferior vermian tissue, and the size of the posterior fossa. At times, it may be difficult to distinguish Dandy–Walker variant from Blake's pouch cyst or retrocerebellar arachnoid cyst.

Mega cisterna magna (Figs. 3.9 and 3.31) is considered to be the mildest form of this spectrum by some observers and to be a normal variant by others. The vermis is completely formed with a separate fourth ventricle, but there is a large cisterna magna and a large posterior fossa. Blake's pouch cyst represents persistent continuity of the fourth ventricle with a prominent cisterna magna and mild hypoplasia of the inferior vermis. Retrocerebellar arachnoid cyst is associated with a completely formed vermis and separate fourth ventricle, both of which are deformed by the large cyst. Hydrocephalus is common. When compared with Dandy–Walker malformation, the Dandy–Walker variant, mega cisterna magna, and Blake's pouch cyst, the retrocerebellar arachnoid cyst is less likely to be associated with other CNS or systemic anomalies.

Cerebellar Hypogenesis

Cerebellar aplasia occurs when there is nonformation of one or both cerebellar hemispheres (Fig. 3.32). In cerebellar hypoplasia (Figs. 3.33 and 3.34), the cerebellum is completely formed but smaller in size than normal. In other cases, there is vermian hypogenesis with or without cerebellar hypogenesis. Because cerebellar hypogenesis is a common finding with fetal ventriculomegaly, it is important to always measure the cerebellar diameter. This measurement is taken transversely across the widest portion of the cerebellar hemispheres either in the

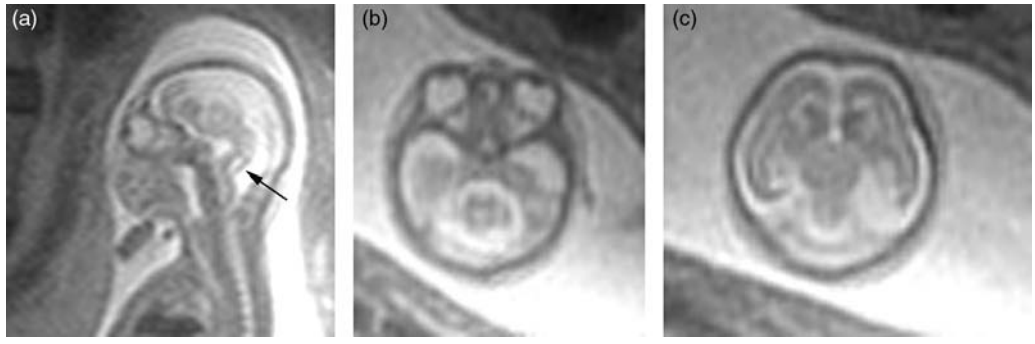

Figure 3.32 Cerebrocerebellar hypogenesis with microcephaly at 19 weeks gestational age. Sagittal (a) and axial (b and c) T_2-weighted images show marked hypogenesis of the cerebellar vermis, hemispheres, and pons, resulting in a kinked brainstem configuration with a small fourth ventricle (arrow). Also, there is microcephaly with sloping forehead. The lateral ventricles are dysmorphic and there are bilateral parietooccipital clefts. At this stage, it is not certain whether this maldevelopment may be part of either the pontocerebellar or pontoneocerebellar hypoplasias, the microlissencephalies, or other cerebrocerebellar hypogenetic conditions (e.g., Walker–Warburg, Joubert).

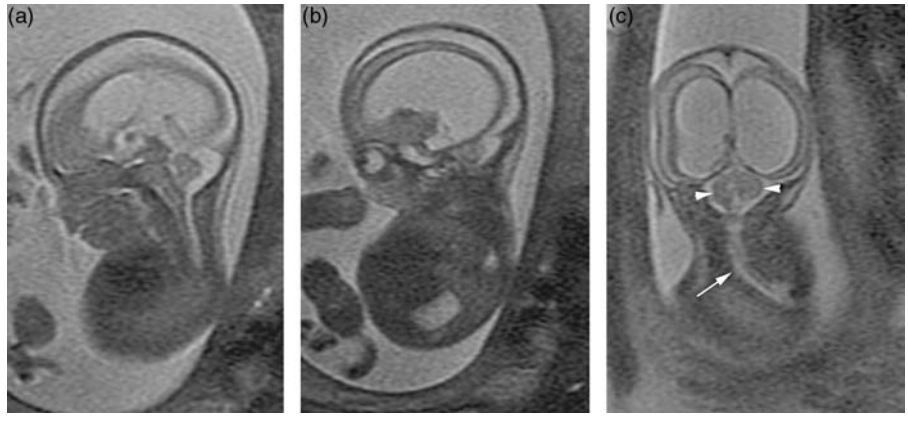

Figure 3.33 Cerebellar hypogenesis, marked ventriculomegaly, and scoliosis at 21 weeks gestational age. Sagittal (a and b) and coronal (c) T_2-weighted images demonstrate a small cerebellum (measuring 17 mm, less than 5th percentile for age) including the vermis, hemispheres, and the small fourth ventricle (arrowheads). The lateral ventricles are enlarged (atria measuring 19 mm) along with a large third ventricle. There is scoliosis, which is apparent by the abnormal curvature of the spinal canal (arrow) and abnormal position of the head with respect to the torso.

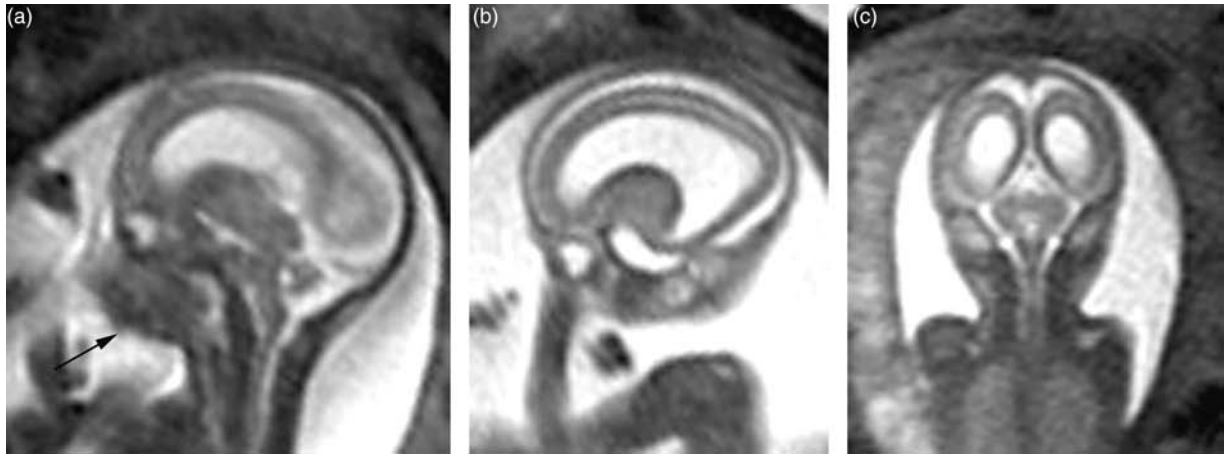

Figure 3.34 Cerebellar hypogenesis, ventriculomegaly, and micrognathia at 19 weeks gestational age. Sagittal (a and b) and coronal (c) T_2-weighted images demonstrate a small cerebellum (16 mm, less than 10th percentile for age). There is lateral ventricular enlargement. Cerebellar hypoplasia is commonly associated with ventriculomegaly. Note also micrognathia (arrow).

coronal or in the axial plane. Included in this category are Joubert syndrome, pontocerebellar hypoplasia, pontoneocerebellar hypoplasia, and cytomegaloviral infection. In cerebellar dysplasia, there are abnormalities of the cerebellar folia. Included in this latter category are rhombencephalosynapsis and Lhermitte–Duclos.

DISORDERS OF NEURONAL, GLIAL, AND MESENCHYMAL PROLIFERATION, DIFFERENTIATION, AND HISTOGENESIS

These disorders occur at 2–5 weeks gestational age or later and include microcephaly, megalencephaly, neurocutaneous disorders, congenital tumors and vascular malformations, aqueductal stenosis, and some forms of porencephaly and hydranencephaly.

Microcephaly

Microcephaly (Figs. 3.32, 3.35–3.37) may result from failure of formation or from widespread necrosis *in utero.* It may be environmental (secondary to infection, anoxia, or radiation) or genetic (34). By ultrasound, the head circumference is 2–3 standard deviations below the mean. The brain is visibly small and the forehead is sloping. The cerebral hemispheres are affected to a greater extent than the other structures (35). Abnormal gyral patterns, porencephaly, and holoprosencephaly are commonly accompanied by microcephaly (35).

Hemimegalencephaly

Hemimegalencephaly represents overgrowth of one lobe or an entire hemisphere (Fig. 3.38). It may occur in

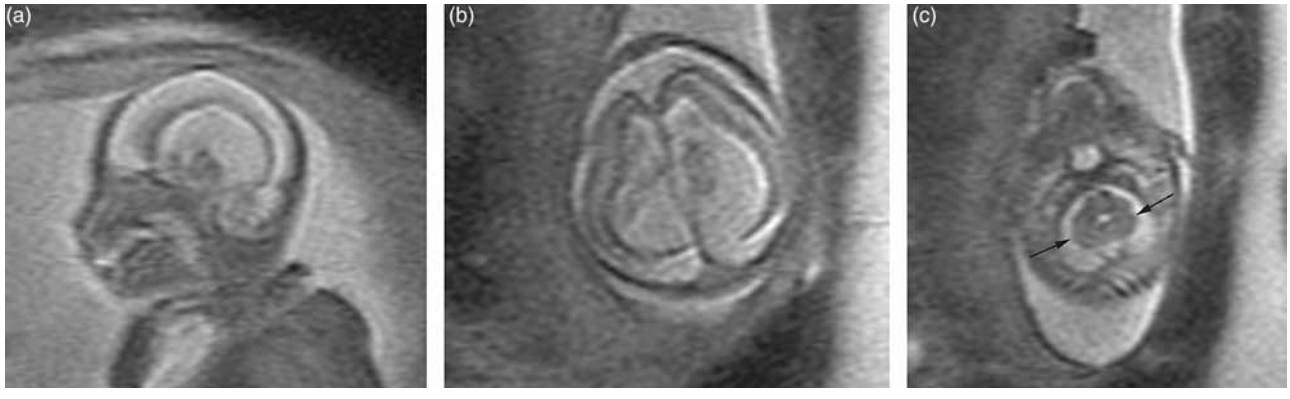

Figure 3.35 Microcephaly with cerebrocerebellar hypogenesis at 18 weeks gestational age. Sagittal (a) and axial (b and c) T_2-weighted images show a sloping forehead (consistent with microcephaly), thin cerebral mantle, absent parietooccipital mantle, and increased pericerebral and pericerebellar CSF spaces. The cerebellum (arrows) measures 14 mm transversely (i.e., cerebellar hypogenesis). A falx is present. The findings most likely represent dysgenesis (i.e., maldevelopment) rather than encephaloclasia (i.e., encephalomalacia) or hydrocephalus.

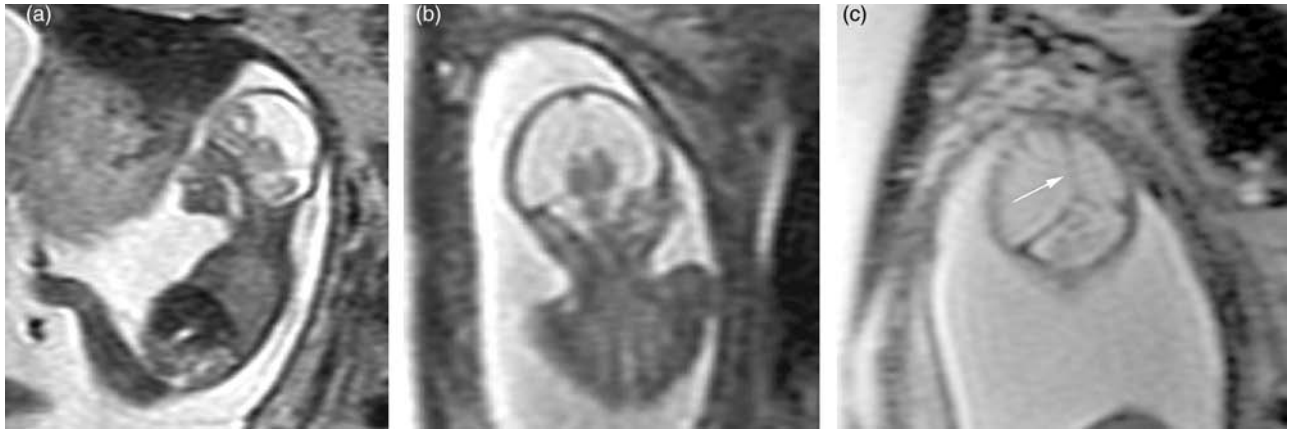

Figure 3.36 Microcephaly with cerebral hypogenesis at 19 weeks gestational age. Sagittal (a) and coronal (b and c) T_2-weighted images show a sloping forehead, commonly seen with microcephaly. Malformed cerebral tissue is seen anteriorly with possible monoventricle. There is absence of cerebral tissue more posteriorly, although a falx is present (arrow). The thalami appear fused. The findings may be more consistent with a form of holoprosencephaly than with hydranencephaly, but the finding of a falx is against this diagnosis.

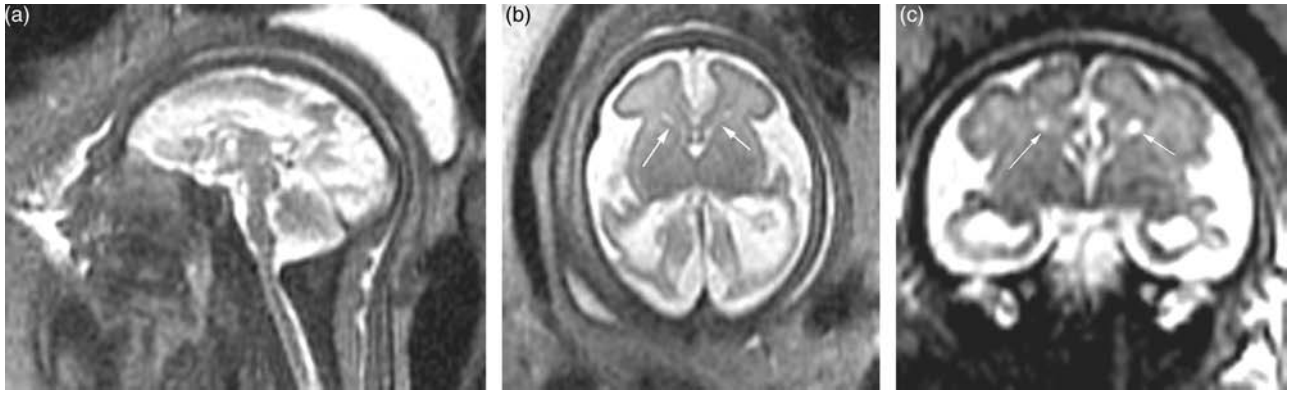

Figure 3.37 Microcephaly, dysgenesis of the corpus callosum, and primitive sulcal development at 37 weeks gestational age. Sagittal (a), axial (b), and coronal (c) images show sloping forehead and small head consistent with microcephaly. The corpus callosum is not visualized and there is colpocephaly with irregular ventricular margins posteriorly; however, the frontal horns are smooth and diverge normally (arrows). The cerebral mantle anteriorly is smooth and there are widened sylvian fissures, whereas posteriorly the mantle is irregularly thinned. Anteriorly, the findings have the appearance of lissencephaly. Posteriorly, the findings have the appearance of encephalomalacia. This combination may indicate transgestational brain injury, with both formational and postformational components. Such manifestations may be seen with infections such as cytomegalovirus. In this case, the viral cultures were negative after birth, and the etiology is unknown.

association with hemigigantism of the body. Abnormal gyral patterns are common with thickened cortex and disorganized cortical layers (36). Imaging findings include enlargement of one cerebral hemisphere in the absence of mass effect and ipsilateral ventriculomegaly (37,38). Fetal MR imaging has been shown to aid in the diagnosis (39).

Hydranencephaly

Hydranencephaly (Fig. 3.39) is considered to result from an ischemic event in the distribution of the internal carotid arteries sometime after the basic structure of the brain has been established. Therefore, large portions of the cerebral hemispheres are replaced with fluid-filled

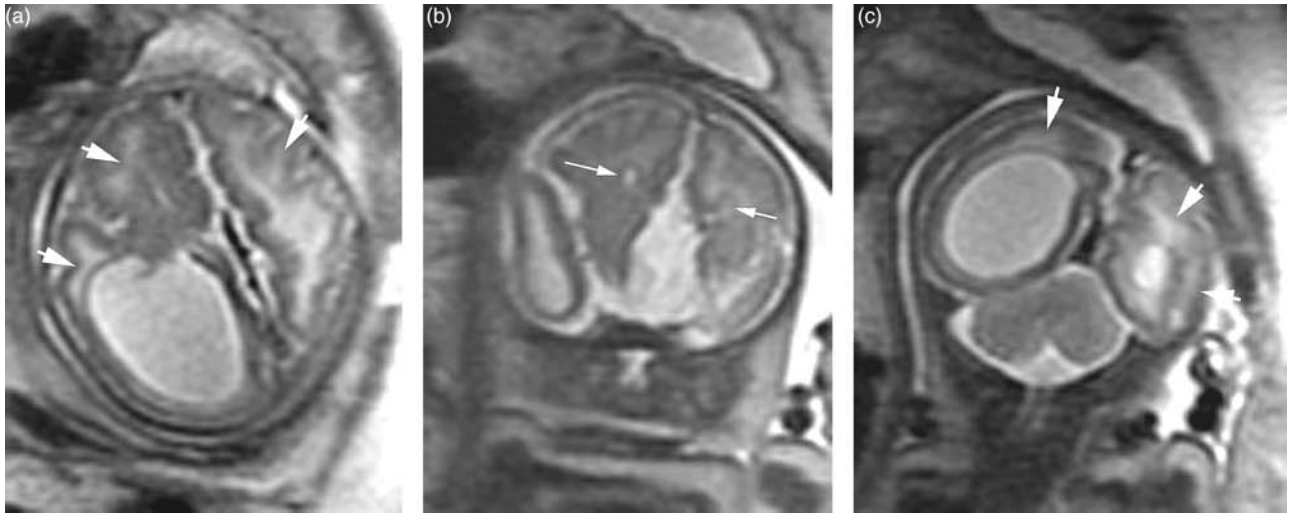

Figure 3.38 Hemimegalencephaly with bilateral cerebral dysgenesis at 35 weeks gestational age. Axial (a) and coronal (b and c) T_2-weighted images demonstrate larger right cerebral hemisphere and lateral ventricle plus abnormal cortical gray matter and subcortical white matter intensities (short arrows). Additional findings include agenesis of the corpus callosum (long arrows indicate vertical orientation of the frontal horns) and right anophthalmia (shown in Chapter 4, Fig. 4.18).

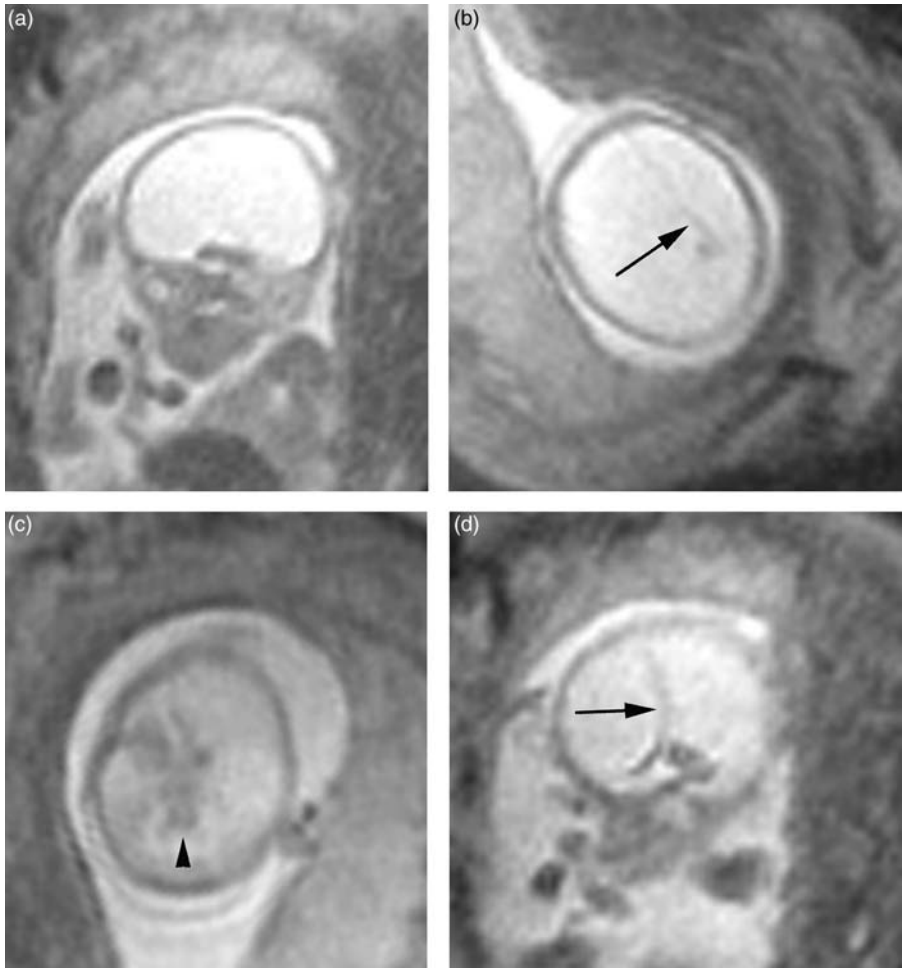

Figure 3.39 Hydranencephaly at 16 weeks gestational age. Sagittal (a), axial (b and c), and coronal (d) T_2-weighted images show large supratentorial CSF-high signal intensity spaces with no demonstrable lateral ventricles and marked deficiency of the cerebral hemispheres. Only a small portion of the frontal and temporal lobes are present near the skull base along with a small brainstem and cerebellum (arrowhead). The falx (long arrows) and tentorium are present, but asymmetric. This anomaly may result from an early vascular occlusive insult with destruction of cerebral tissue in the anterior, middle, and posterior carotid artery distributions. [(c and d) From Levine (115)]

cavities. The presence of an intact falx distinguishes hydranencephaly from alobar holoprosencephaly. When occurring earlier in gestation and with more arterial territory involvement, the degree of tissue loss may be quite extensive (Fig. 3.39).

Neurocutaneous Disorders

The most common neurocutaneous disorder identified *in utero* is tuberous sclerosis (Figs. 3.40 and 3.41). Tuberous sclerosis complex (TSC) is an autosomal dominant multisystem disorder comprised of angiomyolipomas, cardiac rhabdomyomas, epilepsy, and mental retardation. The estimated prevalence is approximately 1/6000–1/10,000. Genetic testing is not widely available for prenatal diagnosis because of the genetic heterogeneity of TSC and the wide variety of mutations, many of which are not amenable to the commonly used mutation detection systems (40).

Antenatal diagnosis has previously been based on the ultrasound detection of cardiac rhabdomyomas. These can be seen in the mid-second trimester (41). However, only about half of the cases of TSC have cardiac rhabdomyomas (42), the majority of which are not present at the typical time of prenatal screening of 20 weeks gestational age.

The brain lesions of TSC are subependymal nodules and cortical tubers. Subependymal nodules can be visualized as early as 21 weeks gestational age by MR imaging (43), appearing as focal T_2 hypointensities that project into the high intensity of the lateral ventricular CSF. Subcortical nodules may also be visualized as T_2 hypointense contrasted against the hyperintensity of the subarachnoid CSF. The T_2 hypointensity is probably related to magnetic susceptibility artifact (from calcification) or low-mobile water concentration. On T_1-weighted images, these are of higher intensity than adjacent white matter (7). The subependymal nodules may be distinguished from artifact by their identification on at least two orthogonal sequences and by the associated ventricular wall deformity.

Because cortical tubers are more common than cardiac rhabdomyomas and cardiac rhabdomyomas are not

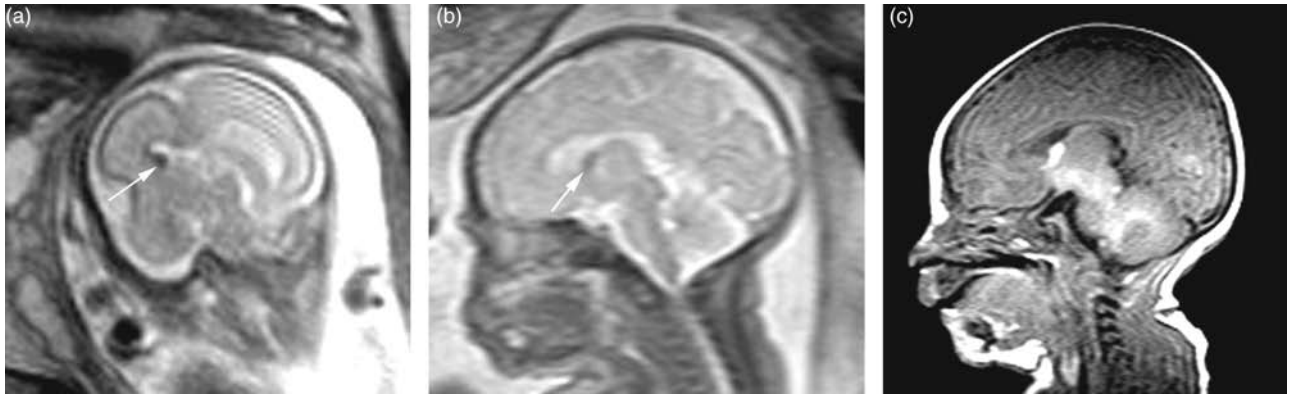

Figure 3.40 Screening for a family history of tuberous sclerosis at 22 and 32 weeks gestational age. Coronal T_2-weighted image (a) at 22 weeks gestational age shows a focal nodular hypointensity projecting into the lateral ventricle (arrow). Sagittal (b) T_2-weighted image at 32 weeks gestational age shows subependymal nodules (arrows). Multiple other subependymal tubers were visualized (not shown). Postnatal sagittal (c) T_1-weighted image confirms the diagnosis of tuberous sclerosis.

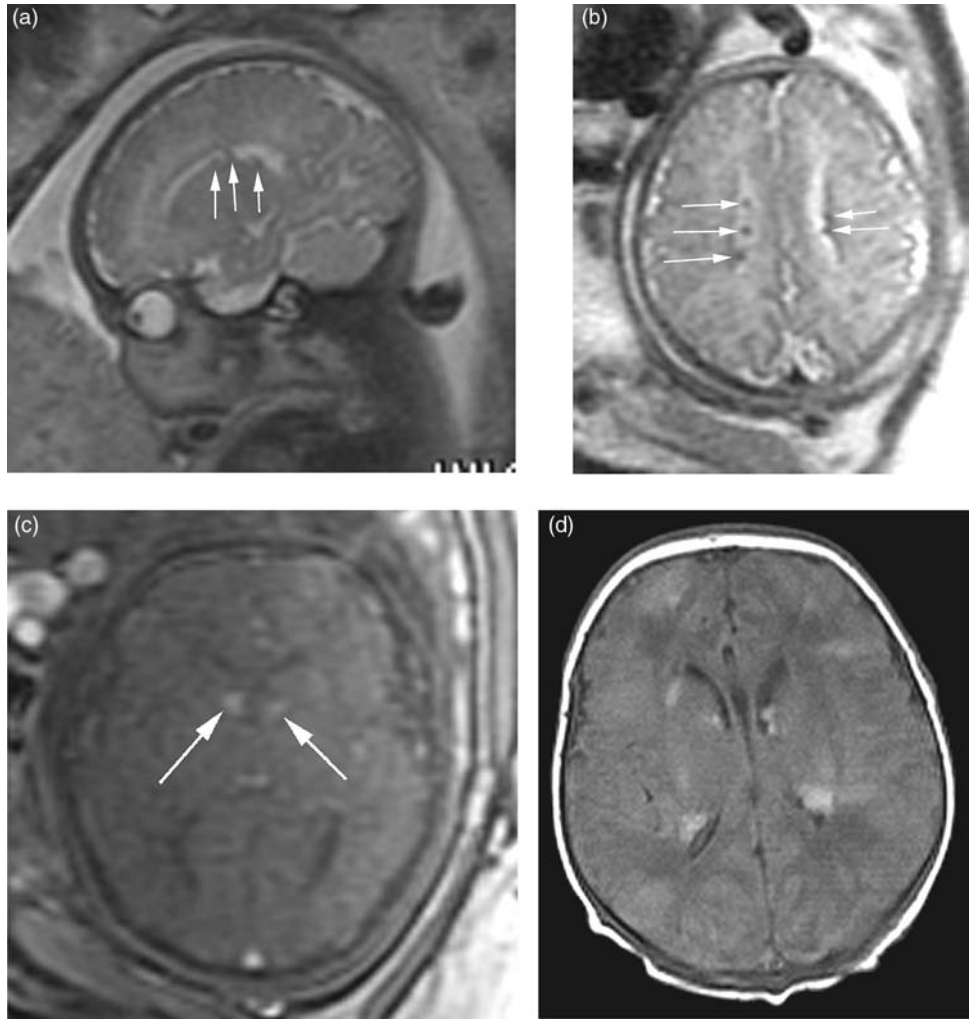

Figure 3.41 Screening for tuberous sclerosis in a fetus with cardiac rhabdomyomas at 34 weeks gestational age. Sagittal (a) and axial (b) T_2-weighted images show low intensity periventricular nodules (arrows). Axial T_1-weighted image (c), although of lower signal-to-noise, shows the nodules to be high intensity. Postnatal axial T_1-weighted image (d) confirms the tubers.

frequently visualized with sonography until the third trimester, it is possible that MR imaging combined with sonography will allow for improved prenatal diagnosis of TSC. Further studies will be needed to determine the sensitivity and specificity of prenatal MR imaging for screening for this complex.

Congenital Tumors

Congenital brain tumors are rare. A 1999 review of fetal brain tumors found 89 reported cases with the majority being teratomas (54%), followed by glioblastomas (15%, Fig. 3.42) (44). Fetal MR imaging helps determine the nature of the mass, its location, and extent of involvement (45–50).

Congenital Vascular Malformations

The vein of Galen malformation (Fig. 3.43) is the most common cerebrovascular malformation diagnosed prenatally. Arterial feeders arise from the circle of Willis and the vertebrobasilar arterial system and anastomose with the vein of Galen (median promesencephalic vein) which becomes aneurysmally dilated (51). Two types of veins of Galen malformation may be seen in the fetus and neonate. In the choroidal type, there are multiple

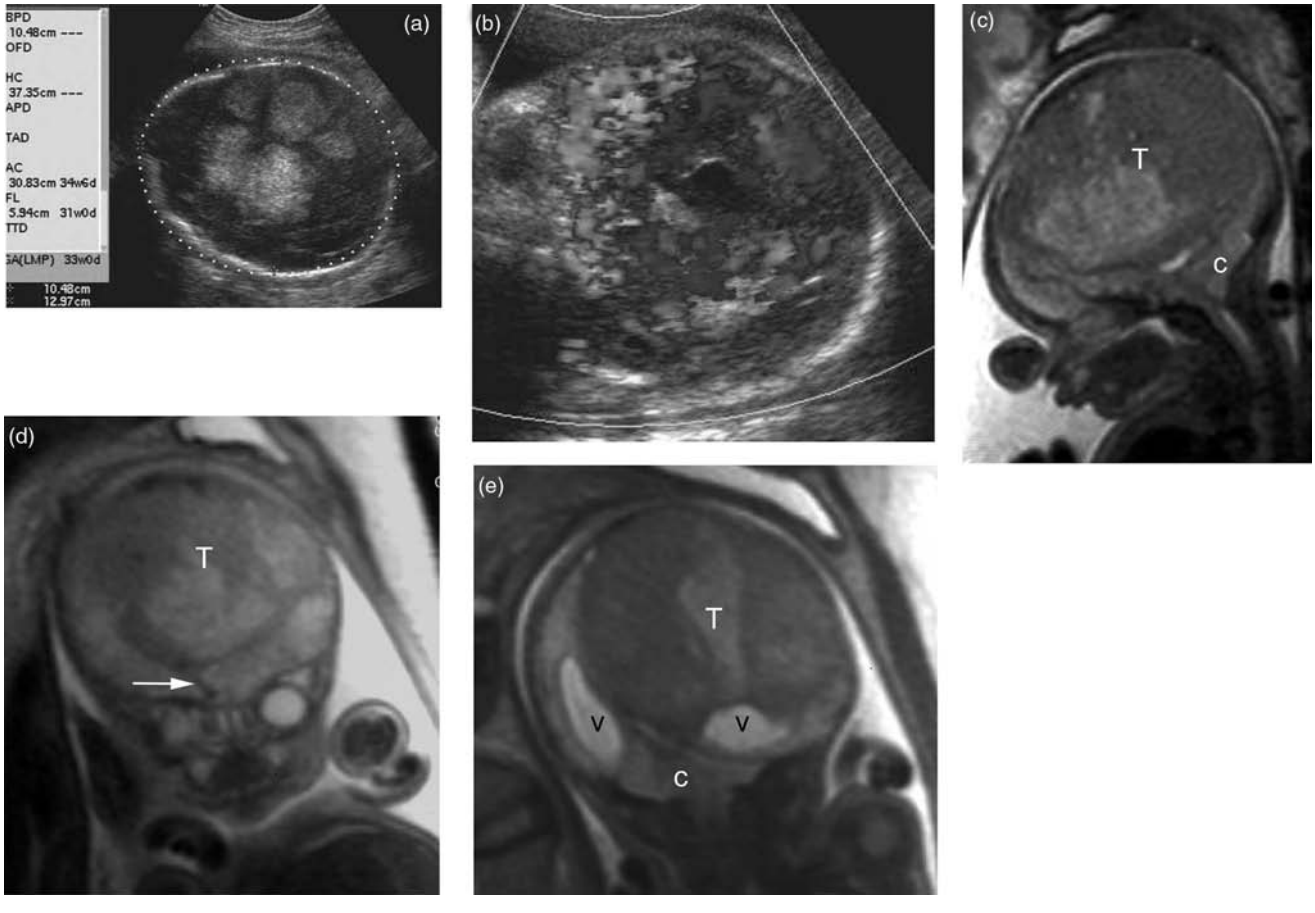

Figure 3.42 Glioblastoma multiforme at 33 weeks gestational age. Gray scale (a) and color Doppler (b) sonograms demonstrate an enlarged head (with head size at least 7 weeks greater than expected for dates) with multifocal echogenic and hypervascular intracranial masses. Sagittal (c) and coronal (d and e) T_2-weighted images show the heterogeneous and hypointense tumor (T) which replaces much of the normal isointense cerebral intensities and displaces the falx (arrow) and lateral ventricles (v). Note the compressed cerebellum ("c" indicated in the figure c and e). The heterogeneity with high and low intensities is more consistent with the hypervascularity of an aggressive neoplasm such as glioblastoma multiforme, rather than a diffuse vascular malformation. Glioblastoma multiforme was confirmed at autopsy. Prenatal imaging in this case allowed for the decision to be made prior to delivery to not admit the baby to the intensive care unit and to not resuscitate the baby at birth. [(b, c, and e) From Morof et al. (50)]

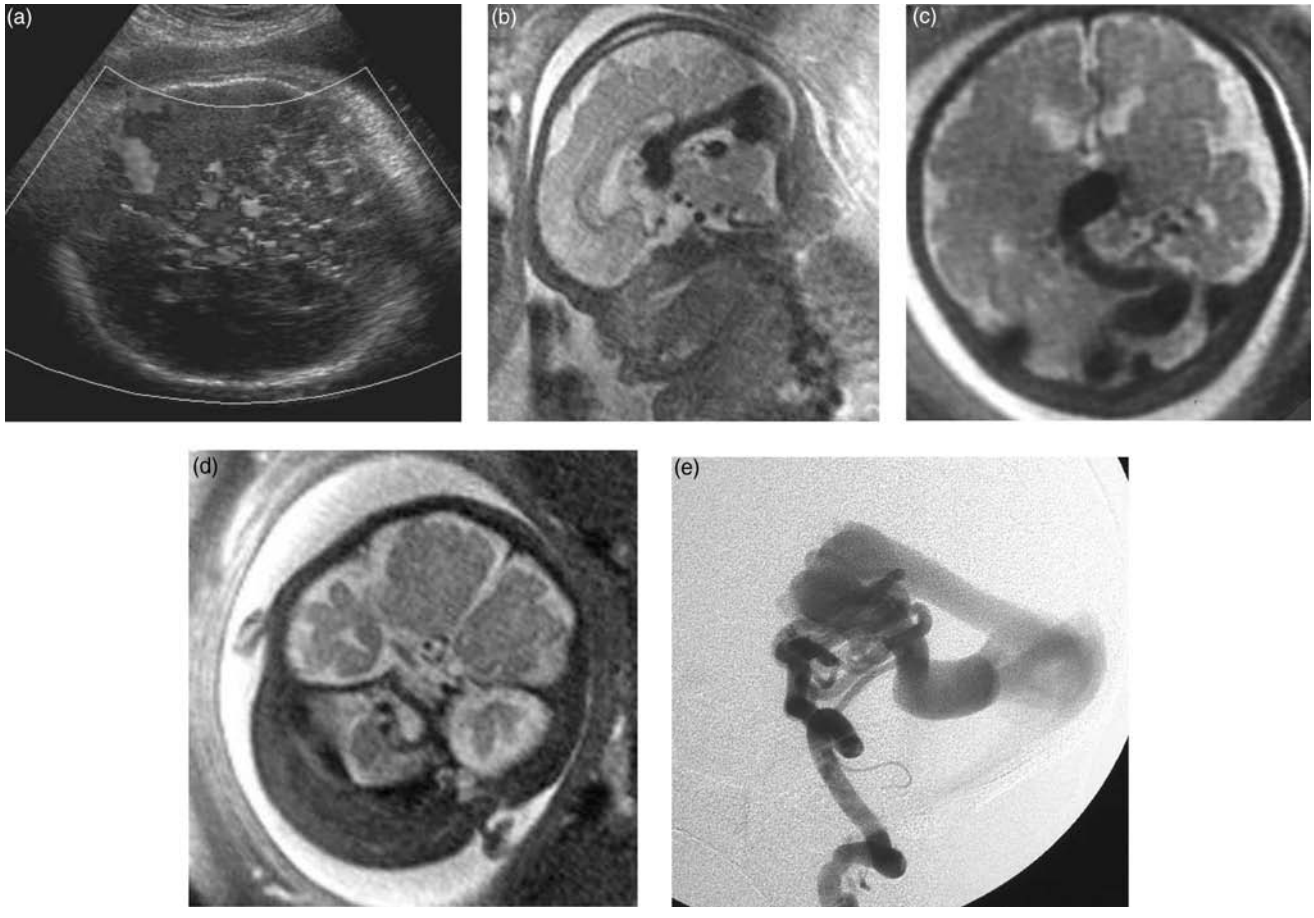

Figure 3.43 Galenic arteriovenous fistula at 38 weeks gestational age. Transverse color Doppler sonogram (a) shows high flow turbulence (arrows) in the pineal region. Sagittal (b) and oblique coronal (c and d) T_2-weighted images show the vascular flow voids of the enlarged vein of Galen varix draining into enlarged transverse sinuses as well as a number of prominent arterial feeder flow voids suggesting the choroidal type of Galenic arteriovenous fistula. As a fetus with this type of vascular malformation is at risk for high output congestive heart failure, a cesarean section was performed. Postnatal lateral digital subtraction angiogram (e) confirms the choroidal type of Galenic arteriovenous fistula. [(a, c, and e) From Levine (115)]

arteriovenous fistulae with dilatation of the median prosencephalic vein. Often there is cardiomegaly and high-output congestive heart failure. Cerebral ischemic changes may be related to steal effects. In the mural type, there is less arteriovenous shunting due to outflow venous obstruction, and hydrocephalus is often present. These are rarely hemorrhagic. On T_2-weighted imaging, large midline vascular flow voids are often present in the region of the vein of Galen and straight sinus. Fetal MR imaging can aid in distinguishing between these types (4). A less common type of vascular malformation is that of a nongalenic dural arteriovenous malformation (Fig. 3.44). In this case, the vascular malformation is located off midline and is usually extra-axial. Small venous malformations may also be detected by prenatal MR imaging (Fig. 3.45). These are often asymptomatic.

Aqueductal Stenosis

Aqueductal stenosis may be hereditary, for example, in association with X-linked hydrocephalus. In the early second trimester, there may be only mild ventriculomegaly (Fig. 3.46). The characteristic enlargement of the lateral and third ventricles with normal fourth ventricle may not be present until the third trimester (Figs. 3.47 and 3.48). Aqueductal stenosis may be associated with other anomalies (e.g., hypogenesis of the corpus callosum,

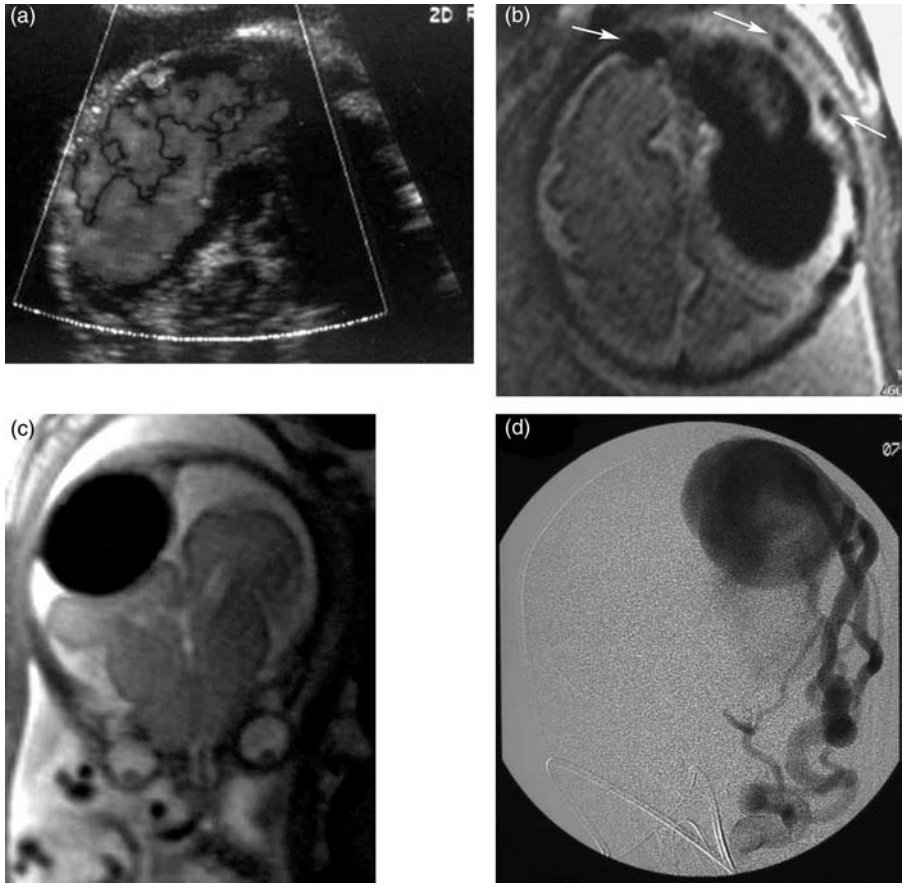

Figure 3.44 Dural arteriovenous fistula at 29 weeks gestational age. Color Doppler sonogram (a) shows an extra-axial mass with high flow turbulence. Axial (b) and coronal (c) T_2-weighted images show the large flow void of the extra-axial varix and the flow voids of the prominent extracerebral feeding arteries suggesting a dural arteriovenous fistula. The fact that the lesion had meningeal feeders was used to direct the postnatal angiogram (d) to the external carotid circulation. The frontal digital subtraction angiogram confirms the arteriovenous fistula with multiple feeders from the external artery. [From Levine et al. (54)]

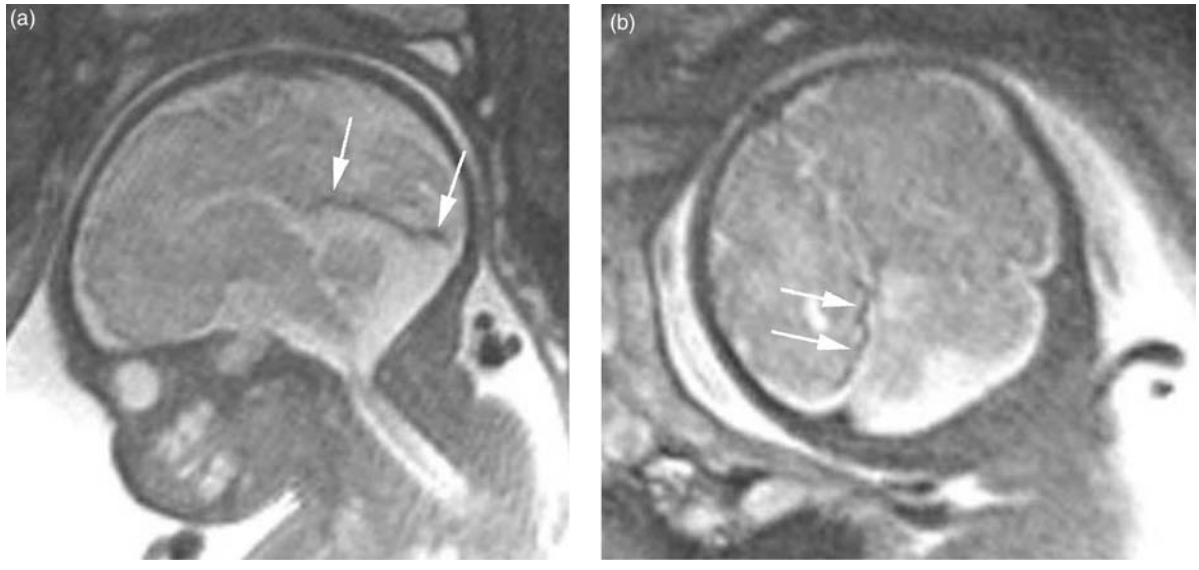

Figure 3.45 Enlarged subtemporal vein at 35 weeks gestational age in a fetus referred for megacisterna magna. The cisterna magna was normal, but incidental note was made of an enlarged subtemporal vein. The clinical significance of this finding is uncertain. This could be a normal variant or in association with a developmental venous anomaly. This illustrates how MR imaging can show unsuspected findings that increase patient anxiety. [(a and b) From Levine (115)]

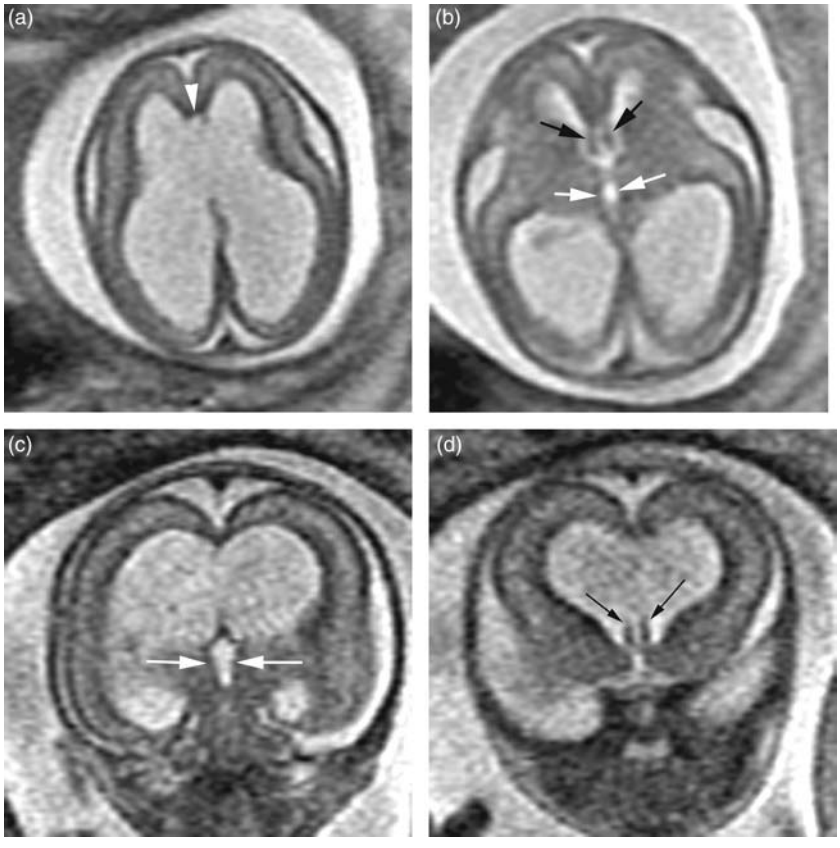

Figure 3.46 Aqueductal stenosis at 21 weeks gestational age. Axial (a and b) and coronal (c and d) T_2-weighted images demonstrate moderately enlarged lateral ventricles, a mildly large third ventricle (white arrows), and a small fourth ventricle (not shown). The corpus callosum is only partially visualized anteriorly (arrowhead) and thinned due to the hydrocephalus. The septum pellucidum is partially absent (leaflet remnants shown with black arrows), also likely due to the hydrocephalus. The diagnosis was confirmed postnatally, including a formed but attenuated corpus callosum, and the infant underwent shunting.

Dandy–Walker malformation) or may be acquired (e.g., following hemorrhage or infection).

Arachnoid and Neuroepithelial Cysts

Arachnoid cysts (Figs. 3.49–3.53) are benign CSF collections that develop within the layers of the arachnoid membrane. They often do not communicate freely with the subarachnoid spaces or the ventricles (52). The location of these cysts may differ in the fetus as compared to the postnatal population. Pierre-Kahn (53) reported that 63% are supratentorial (16% interhemispheric), 22% infratentorial, and 15% incisural. The cysts are well marginated, have a smooth wall, and are

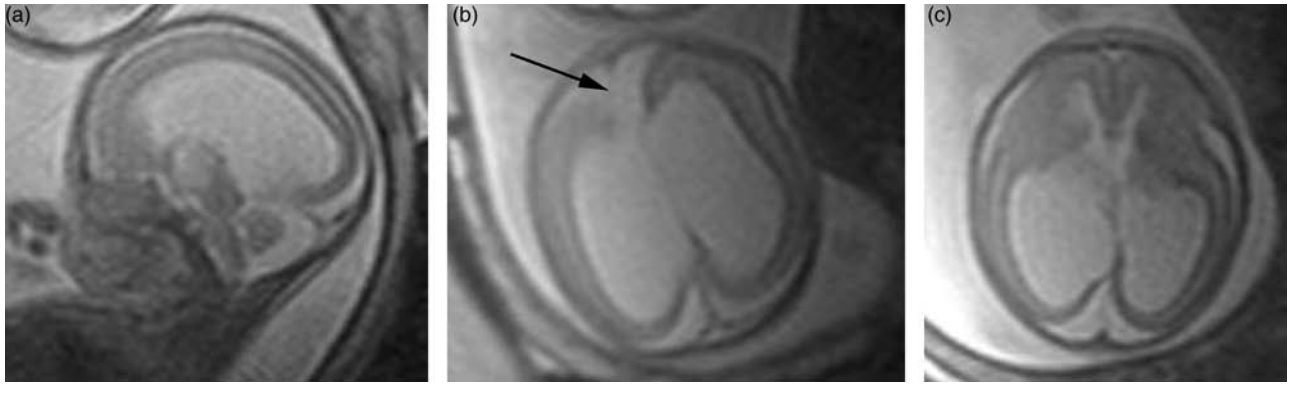

Figure 3.47 Aqueductal stenosis with callosal hypogenesis at 21 weeks gestational age. Sagittal (a) and axial (b and c) T_2-weighted images demonstrate the enlarged lateral and third ventricles. The corpus callosum is not visualized; however, the frontal horns of the lateral ventricles diverge normally. The colpocephaly (i.e., disproportion between the frontal horn and occipital horn sizes) suggests hypogenesis of the corpus callosum. There is a small region of porencephaly superiorly (arrow). At birth, the diagnosis was confirmed, including the corpus callosum hypogenesis.

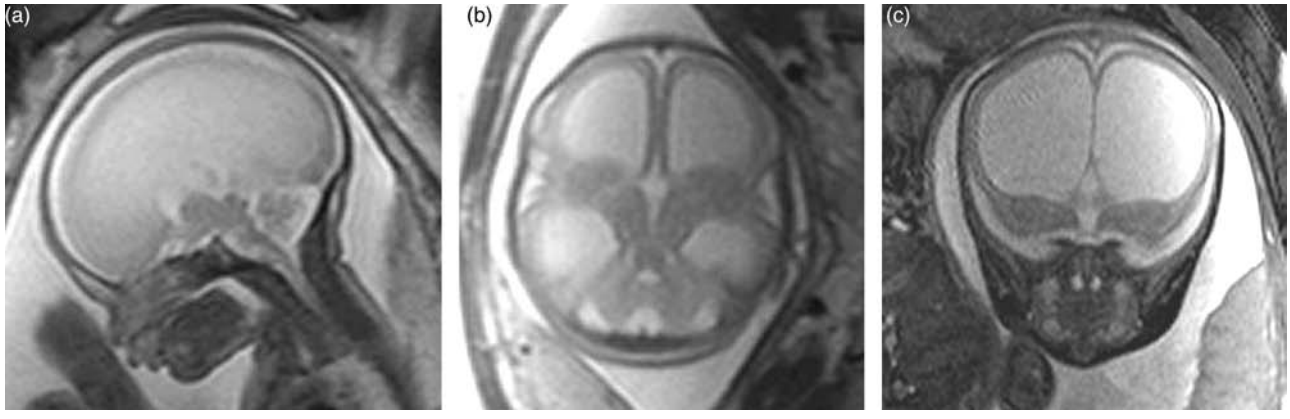

Figure 3.48 Aqueductal stenosis at 31 weeks gestational age with severe ventriculomegaly and macrocephaly. Sagittal (a), axial (b), and coronal (c) T_2-weighted images show large head size with markedly dilated lateral ventricles with thin cortical mantle, dilated third ventricle, and normal sized fourth ventricle.

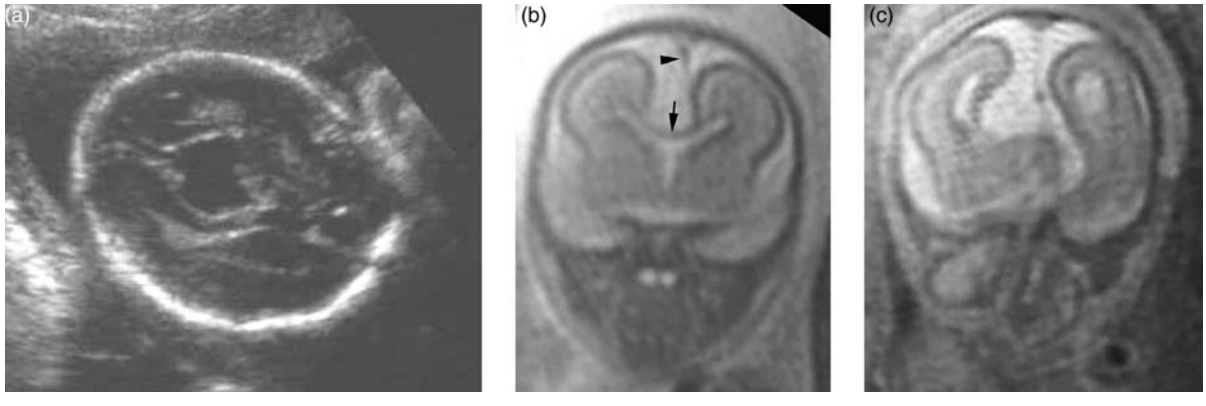

Figure 3.49 Anterior paramedian interhemispheric arachnoid cyst at 20 weeks gestational age. (a) Sonogram shows the cyst. (b and c) Coronal T_2-weighted images do not show the cyst wall, but show mass effect by the cyst upon the falx (arrowhead), cerebral cortex, and corpus callosum (arrow). [(a and b) From Levine et al. (54)]

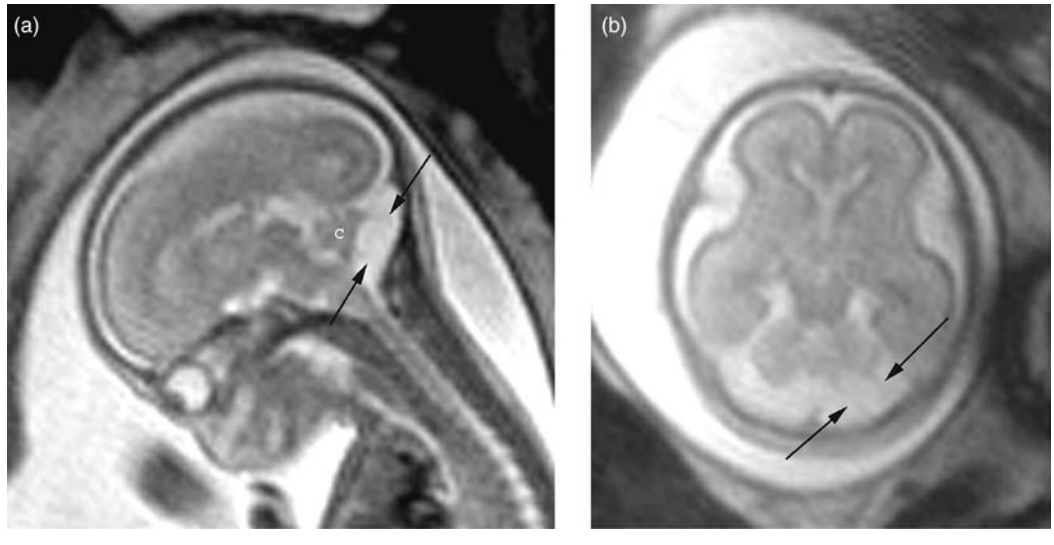

Figure 3.50 Posterior fossa arachnoid cyst at 22 weeks gestational age. Sagittal (a) and axial (b) T_2-weighted images show a small posterior fossa arachnoid cyst deforming the cerebellum ("c" indicated in the figure a). The walls of the cyst are barely visible (arrows).

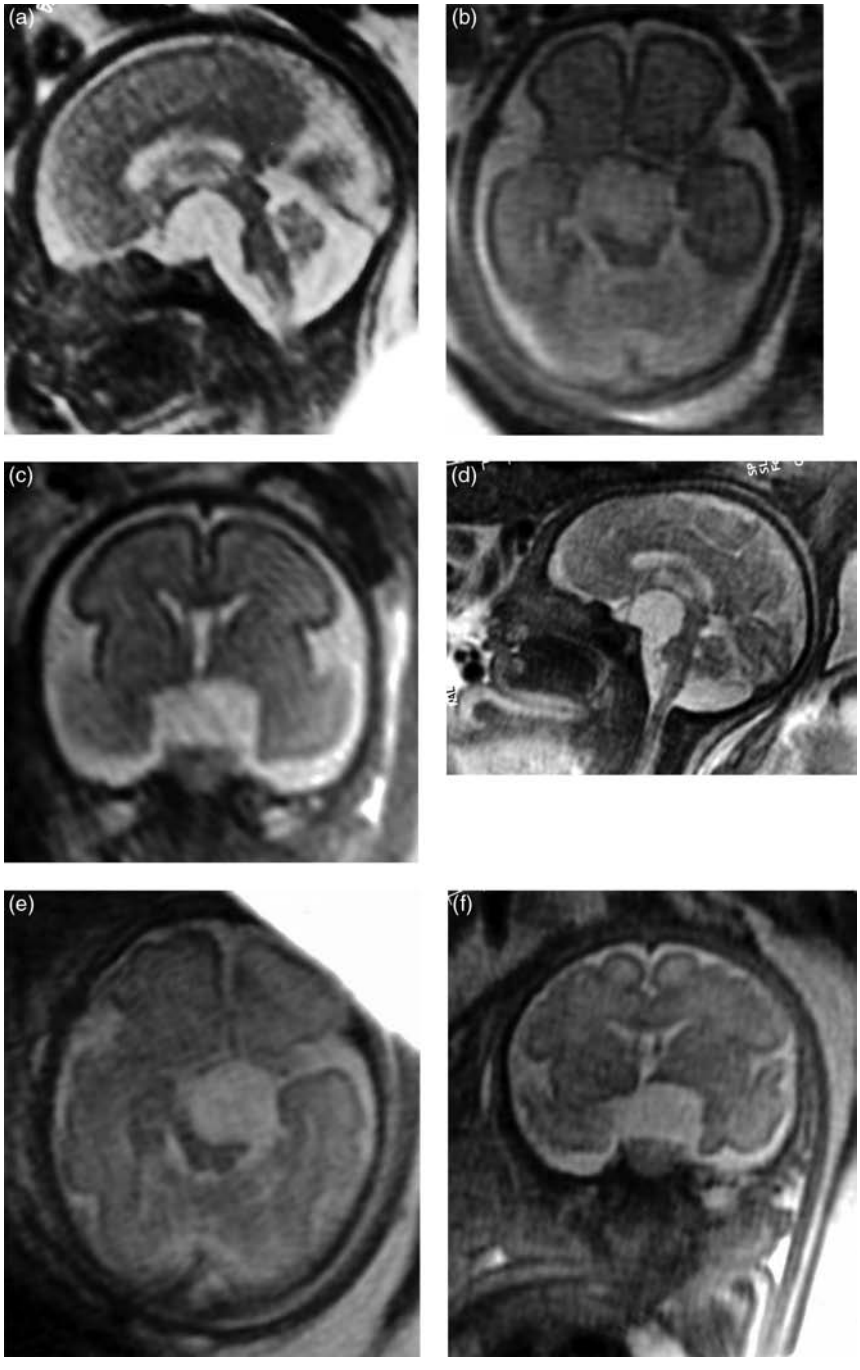

Figure 3.51 Suprasellar arachnoid cyst at 26 and 33 weeks gestational age. Sagittal (a), axial (b), and coronal (c) views at 26 weeks and sagittal (d), axial (e), and coronal (f) views at 33 weeks gestational age show a suprasellar CSF-intensity mass deforming the third ventricle, optic chiasm, midbrain, and pons. The cyst wall is imperceptible. Although the cyst measures larger on the second MR image, the mass effect is similar. [(a and b) From Levine et al. (54)]

nearly always unilocular. On MR imaging, the cyst has fluid intensity similar to CSF. Adjacent brain may be deformed (e.g., compressed due to mass effect), but is often morphologically normal. Fetal MR imaging is helpful in confirming the diagnosis and delineating anatomic detail (53–56). As the fetal brain grows, the cyst may stay the same size or may exhibit decreased size, extent, and deformity of the adjacent brain (Fig. 3.52). Interhemispheric arachnoid cysts are associated with callosal dysgenesis. Posterior fossa arachnoid cysts may be confused with other cyst-like anomalies of the Dandy–Walker spectrum. If the posterior fossa lesion causes mass effect on surrounding structures (including a "formed" cerebellar vermis) and is associated with hydrocephalus, it is probably an arachnoid cyst. In some cases of Dandy–Walker variant, or megacisterna magna,

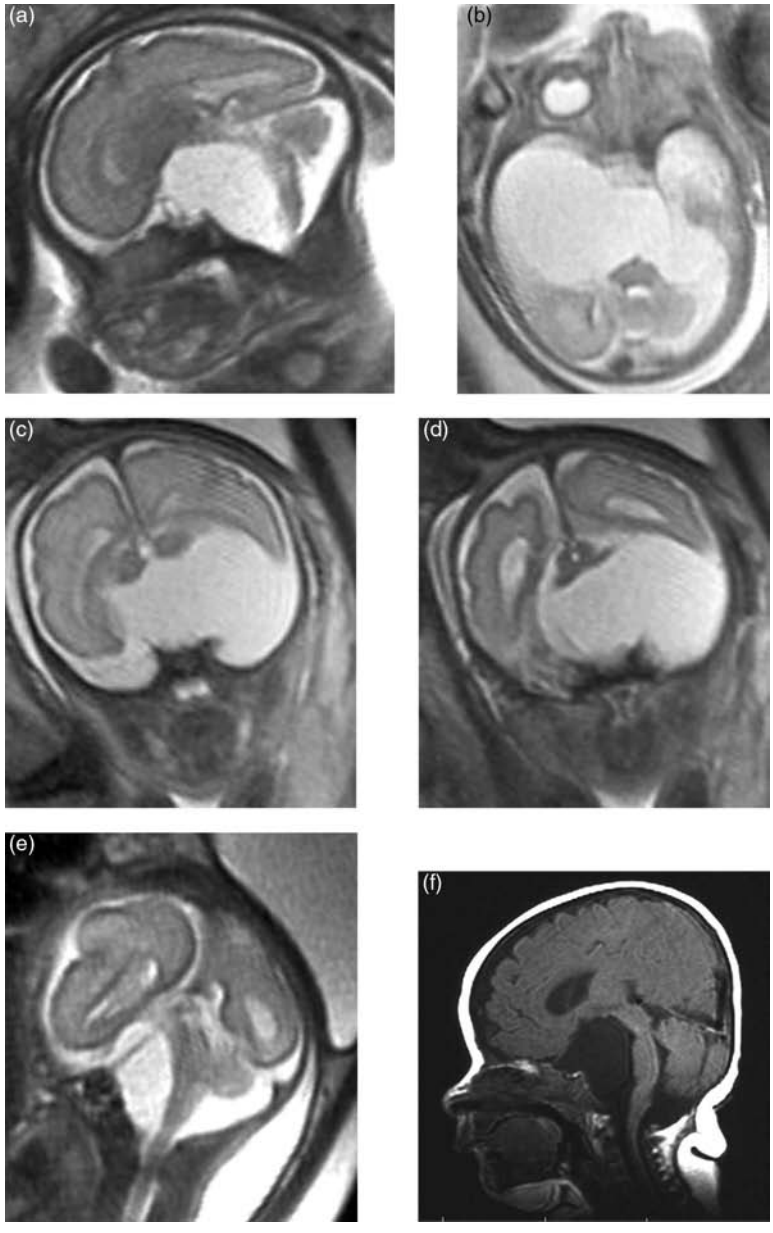

Figure 3.52 Large suprasellar arachnoid cyst at 27 weeks gestational age. Sagittal (a), axial (b), and coronal (c–e) T_2-weighted images show a large suprasellar arachnoid cyst with extension into the middle and posterior cranial fossae. The cyst deforms the pons, midbrain, and medulla. T_1-weighted image after birth (f) showed no increase in size or extent of the cyst, with a relative decrease in mass effect on the pons and midbrain. This figure illustrates potential pitfall in counseling patients with fetal anomalies, as the natural history of many of these processes has not been well established. [(a and f) From Levine (96); (c) from Levine et al. (23); (d) from Levine (56)]

without hydrocephalus, the distinction from arachnoid cyst may be difficult (Fig. 3.26).

Neuroepithelial cysts include choroid, pineal, and colloid cysts. The choroid plexus cyst is the most common neuroepithelial cyst seen in the fetus and neonate. It is a common finding on ultrasound in second trimester fetuses, occurring in ~1% of normal pregnancies (57). These are often visualized in association with trisomy 18. At times, large cysts can cause ventricular dilation. The majority of small choroid plexus cysts are not visualized by MR imaging because they are of similar intensity to ventricular CSF. Large cysts may be seen at slightly higher intensity than the surrounding choroid plexus (Figs. 3.54 and 3.55).

DISORDERS OF MIGRATION AND CORTICAL ORGANIZATION

Migration of neuronal and glial stem cells from their site of origin in the periventricular germinal matrix to the cortical and subcortical areas of the brain occurs primarily from 3–5 months of gestation. Disorders of migration include schizencephaly, lissencephaly, pachygyria, polymicrogyria,

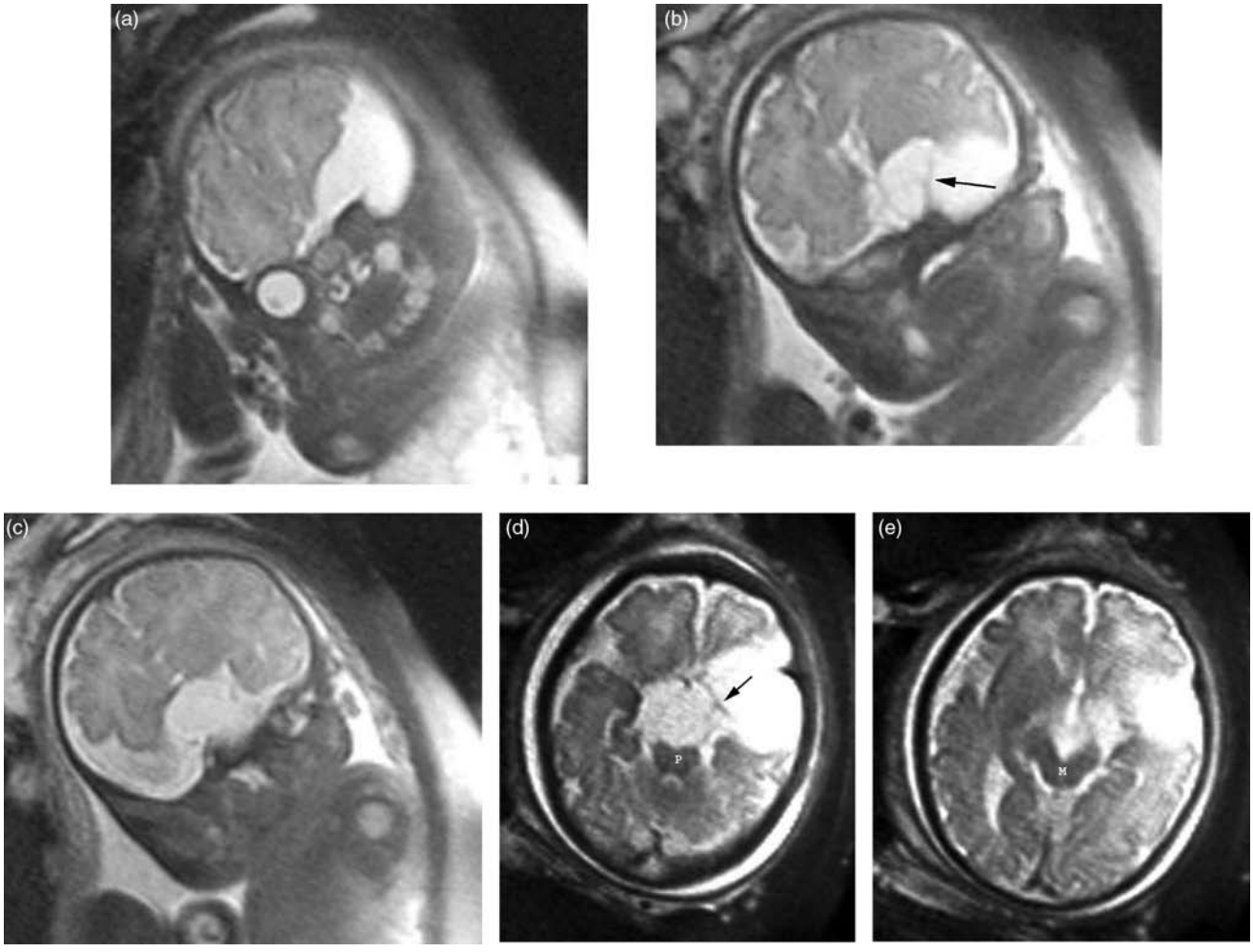

Figure 3.53 Middle cranial fossa, prepontine, and suprasellar arachnoid cyst at 36 weeks gestational age. Coronal (a–c) and axial (d and e) T_2-weighted images show a large cyst (with signal intensity that is similar to CSF) that deforms the internal carotid artery and middle cerebral artery (arrow), the midbrain (M), and pons (P).

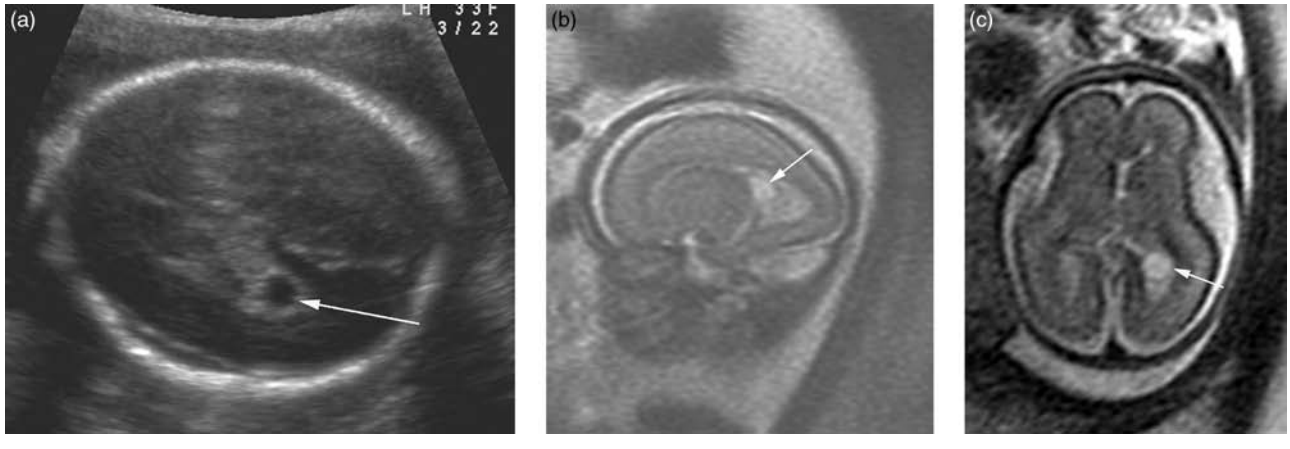

Figure 3.54 Choroid plexus cyst at 20 weeks gestational age. Axial sonogram (a) demonstrates the choroid plexus cyst (arrow). Sagittal (b) and axial (c) T_2-weighted images show the cyst (arrow). The cyst is more difficult to visualize on MR compared with the sonogram, but can be detected as a region of slightly higher signal intensity within the choroid plexus.

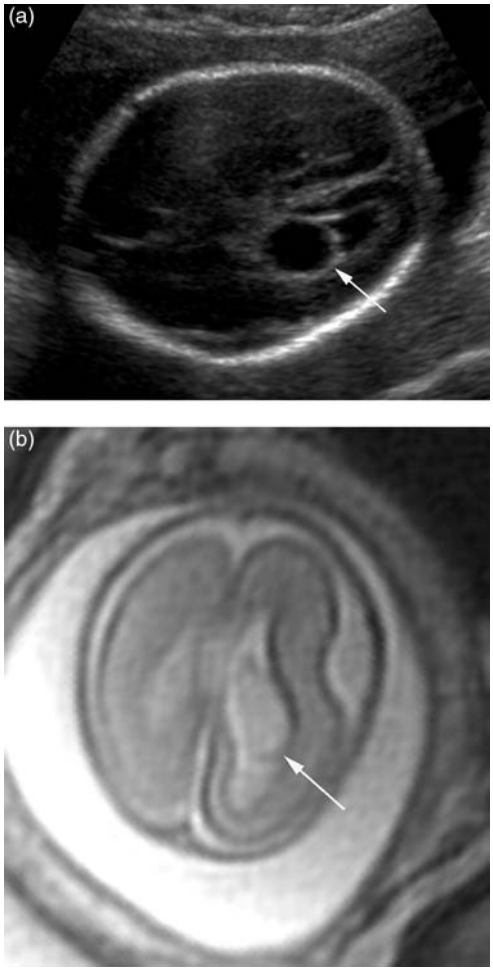

Figure 3.55 Choroid plexus and ventriculomegaly in trisomy 18 at 22 weeks gestational age. Axial sonogram (a) and axial (b) T_2-weighted image demonstrate the choroid plexus cyst (arrow) that is causing enlargement of the lateral ventricle.

heterotopias, and hypogenesis of the corpus callosum. The causes of these disorders include genetic, metabolic, infectious, and ischemic processes. Postnatally, these patients usually present clinically with developmental delay, hypotonia, and seizures. Magnetic resonance imaging is better able to detect migrational abnormalities than is ultrasound (2,4).

Lissencephaly (Agyria–Pachygyria)

The terms lissencephaly and agyria–pachygyria describe brains with absent or poor sulcation and gyration (Fig. 3.56). In type I lissencephaly (e.g., classical lissencephaly), there is a thickened cortex with broad flat gyri and a few shallow sulci, diminished white matter, and shallow vertical sylvian fissures. In severe cases, the corpus callosum is hypogenetic. This may be isolated or syndromic (e.g., Miller–Dieker syndrome). Head size is normal to small prenatally, but progressive microcephaly commonly occurs in the first few years of life. Patients are often hypotonic at birth, but develop progressive spasticity. Seizures are common (58–66).

Type II lissencephaly (e.g., cobblestone lissencephaly) has a thickened and severely disorganized unlayered cortex. The meninges are thickened and densely adherent to the cortex, obliterating the subarachnoid space and resulting in hydrocephalus (e.g., Walker–Warburg syndrome). Subcortical heterotopias may occur. Associated anomalies include microphthalmia, callosal hypogenesis, cerebellar cortical dysplasia, and cerebellar vermian hypoplasia. These patients may have muscular dystrophy, congenital eye malformations, or posterior cephaloceles (58–66). Fetal MR imaging may show characteristic findings in these cases (Fig 3.56) (2,67,68).

Polymicrogyria

Polymicrogyria occurs when there are too many small convolutions in the cortical gyri. Many types of polymicrogyria are likely the result of ischemic injury. Unlayered polymicrogyria results from early second trimester injury, whereas layered polymicrogyria results from mid to late second trimester injury (59). More specific etiologies include cytomegalovirus, toxoplasmosis, syphilis, and maternal shock (69). Patients with diffuse polymicrogyria clinically resemble those with lissencephaly including microcephaly, hypotonia evolving to spasticity, seizures, and severe developmental delay. Patients with bilateral focal polymicrogyria have developmental delay, spastic motor dysfunction, and seizures. On MR imaging, polymicrogyria appears as a slightly thickened and irregular cortex with shallow sulci (66,70,71). Fetal MR imaging shows the features of polymicrogyria better than ultrasound (Fig. 3.57) (2,4,72).

Schizencephaly

Schizencephaly represents one or more polymicrogyria-lined clefts of the cerebral hemispheres. The etiology and clinical presentation are similar to that for polymicrogyria. Schizencephaly has been documented by fetal MR imaging (73,74) as CSF-filled, gray matter-lined clefts that extend from the cortex through the wall of the lateral ventricle (69). Associated malformations include ventriculomegaly, polymicrogyria, heterotopias, callosal hypogenesis, and absence of the septum pellucidum (75).

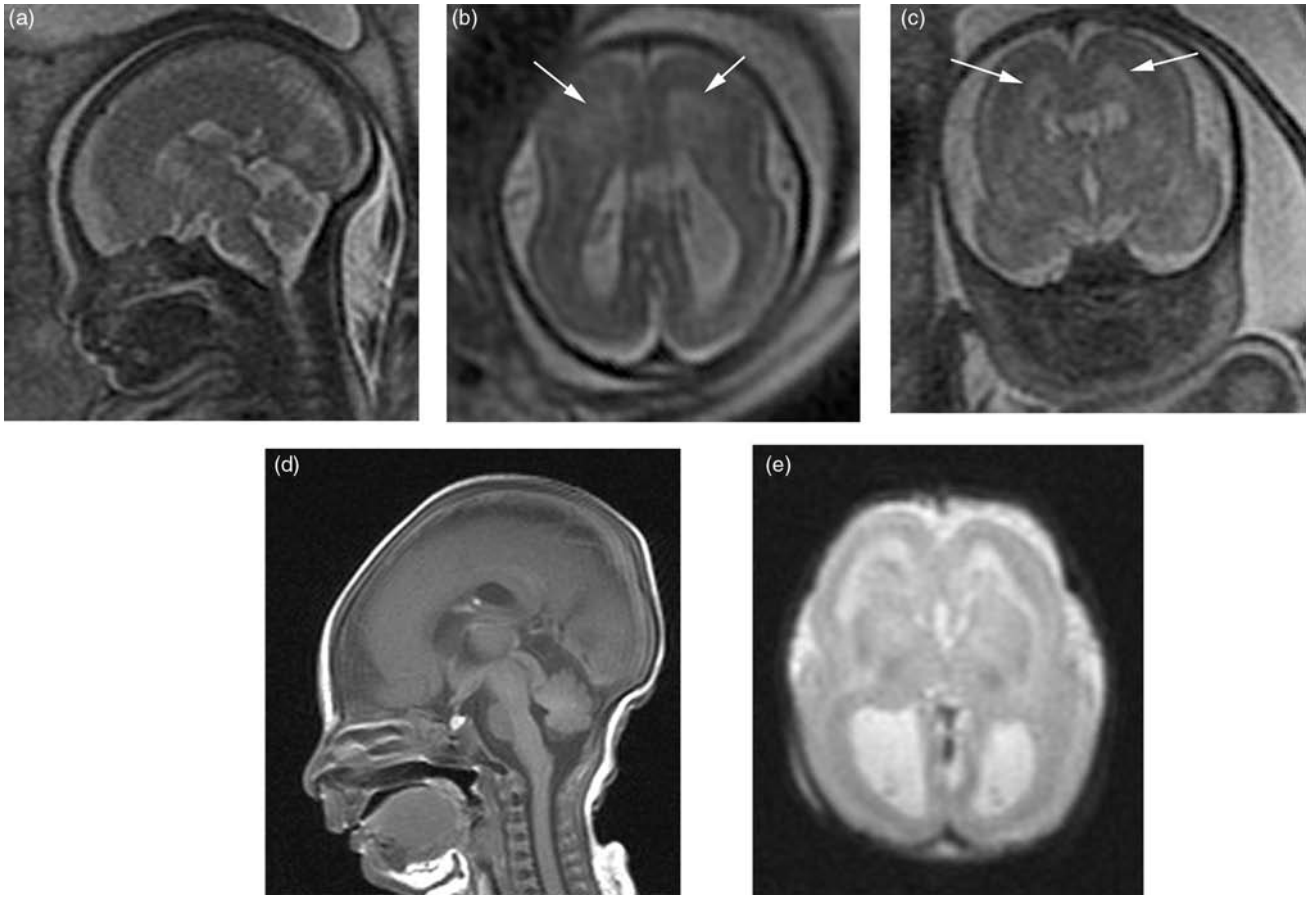

Figure 3.56 Lissencephaly at 35 weeks gestational age. Sagittal (a), axial (b), and coronal (c) T_2-weighted images demonstrate abnormally smooth cortex with lack of gyral and sulcal definition. Abnormal hyperintensity is present within the frontal subcortical white matter (arrows). There is hypogenesis of the corpus callosum and colpocephaly. Postnatal sagittal (d) T_1- and axial (e) T_2-weighted images confirm the findings.

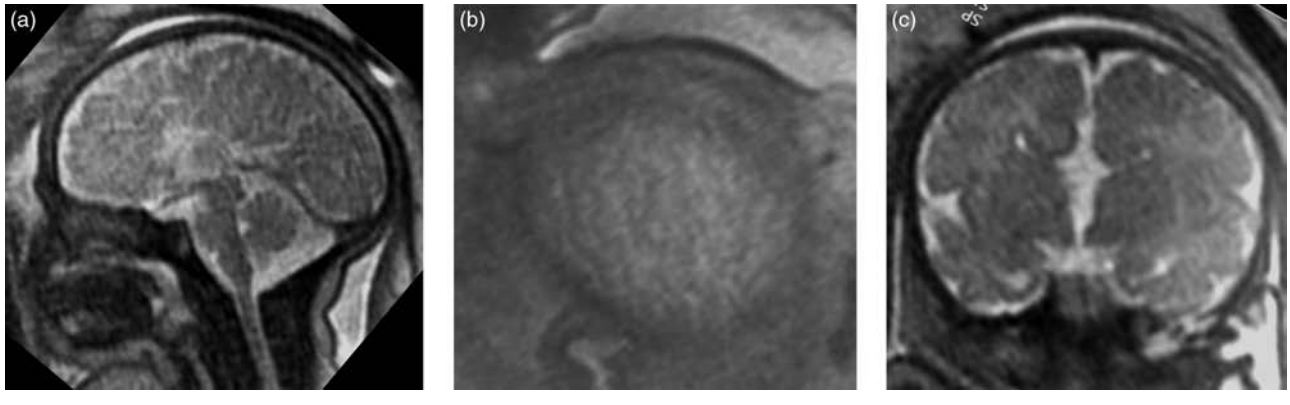

Figure 3.57 Agenesis of the corpus callosum with stenogyria at 35 weeks gestational age. Sagittal midline (a) and far lateral (b) imaging and coronal (c) T_2-weighted images show no corpus callosum plus abnormally irregular sulci and gyri. [(a and c) From Levine et al. (54)]

Neuronal Heterotopia

Neuronal heterotopias (Fig. 3.58) represent gray matter in abnormal locations as the result of arrested migration. Etiologies include genetic, vascular, and environmental causes (e.g., trisomy 13, fetal alcohol syndrome). The heterotopias may be focal or laminar and may occur in subependymal, subcortical, or cortical sites.

Patients with subependymal heterotopias tend to have seizures beginning in the second decade of life. Patients with focal subcortical heterotopias have symptoms and signs in proportion to the quantity and location of the lesions. Patients with laminar, or band, heterotopias often have developmental delay and the early onset of seizures (59,76–78). Fetal MR imaging detects these lesions as nodules of grey matter intensity projecting into the ventricular wall (2,79) and thus distinguishes them from the subependymal tubers of tuberous sclerosis (which are of lower signal intensity on T_2-weighted imaging). However, the distinction may be difficult in some cases.

Hypogenesis of the Corpus Callosum

Hypogenesis of the corpus callosum (Figs. 3.57–3.63) can be complete (i.e., agenesis) or partial and probably results from a vascular or inflammatory insult occurring before 12 weeks of gestation. It frequently is associated with other malformations, chromosomal abnormalities, and genetic syndromes. In hypogenesis of the corpus

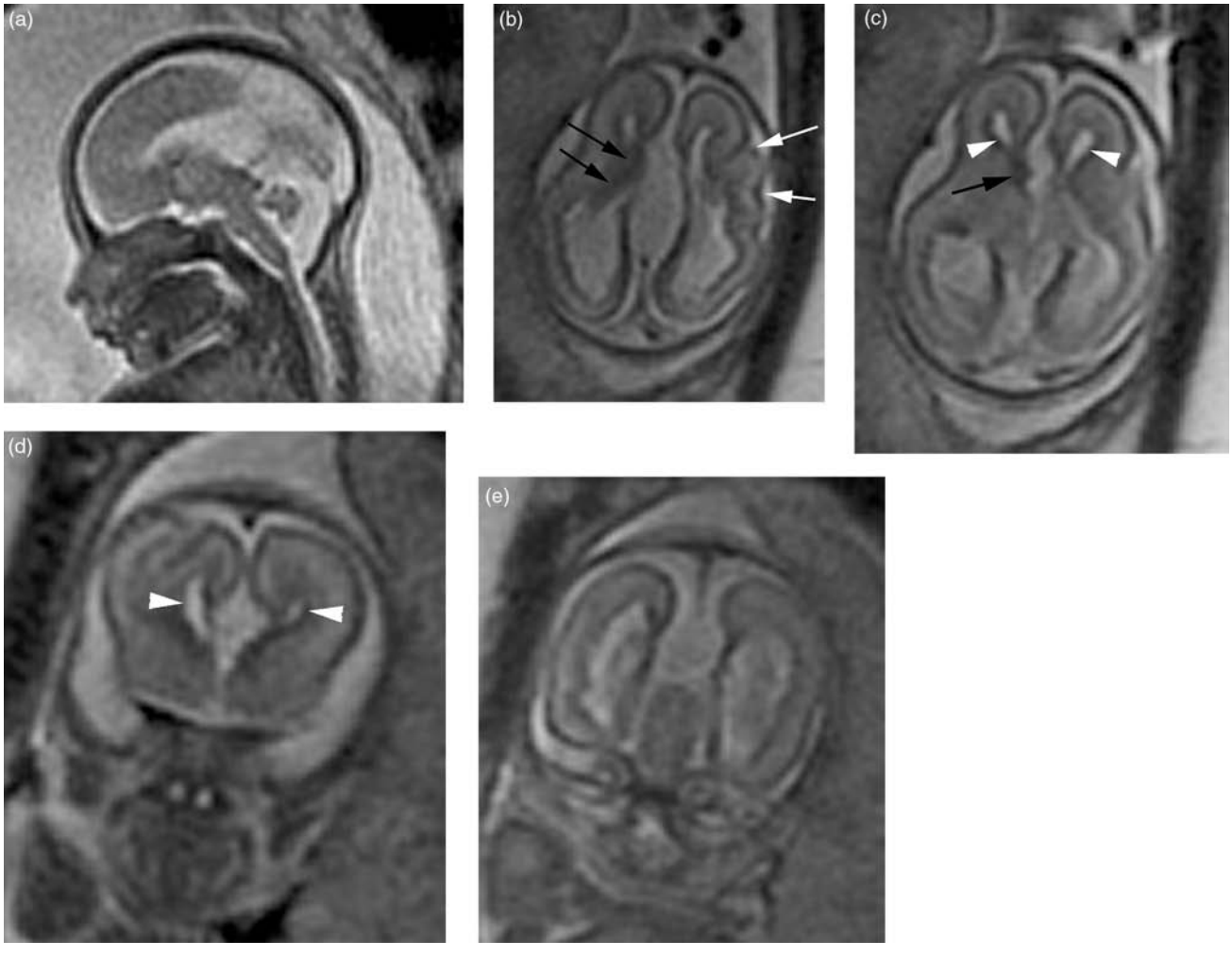

Figure 3.58 Aicardi syndrome with agenesis of the corpus callosum, neuronal heterotopia, and cortical dysgenesis at 21 weeks gestational age. Sagittal (a), axial (b and c), and coronal (d and e) T_2-weighted images demonstrate absence of the corpus callosum (note vertical orientation of the frontal horns (arrowheads) with hypointense periventricular heterotopia (black arrows) and irregular cortical gyral/sulcal pattern (white arrows).

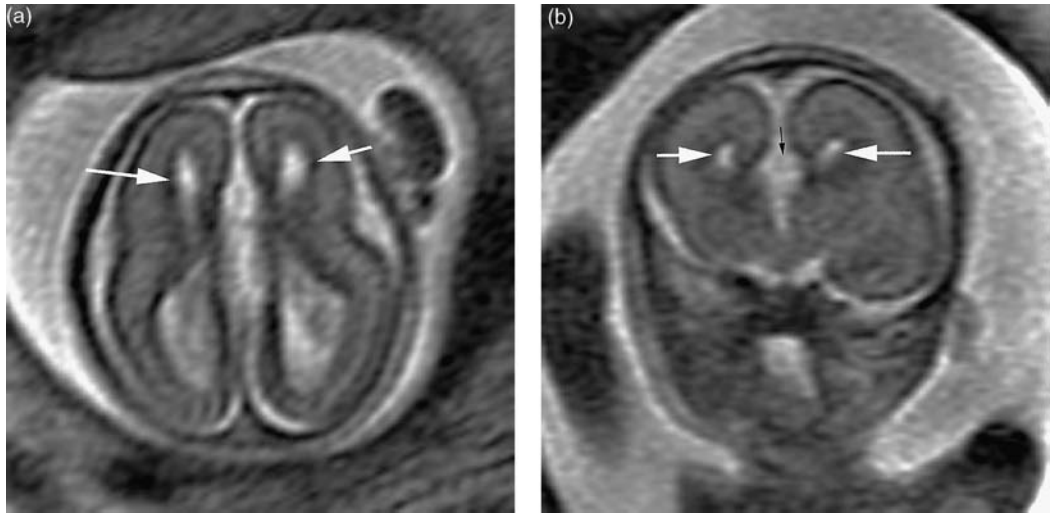

Figure 3.59 Agenesis of the corpus callosum at 20 weeks gestational age. Axial (a) and coronal (b) T_2-weighted images demonstrate the parallel and vertical orientation of the frontal horns (white arrows) and lack of callosal tissue crossing the midline (black arrow). There is disproportionate prominence of the atria and occipital horns of the lateral ventricles (colpocephaly). The fetus also had an abnormal heart on prenatal sonography.

callosum, the interhemispheric cerebral axonal fibers do not migrate across the midline. The residual commissural fibers are distributed longitudinally as Probst bundles, are located along the superomedial margins of the lateral ventricles, and can protrude into the frontal horns. Colpocephaly is often seen and the third ventricle extends superiorly. Hypogenesis of the corpus callosum is associated with a broad functional spectrum ranging from normal to severe cognitive impairment. This impairment is often attributed to additional brain abnormalities (80,81).

The prenatal ultrasound diagnosis of hypogenesis of the corpus callosum is often problematic. In a recent retrospective study, 43% of cases (6 of 14) of confirmed hypogenesis of the corpus callosum were detected by fetal MR imaging but not by ultrasound (82). Also, there are numerous reports of hypogenesis of the corpus callosum

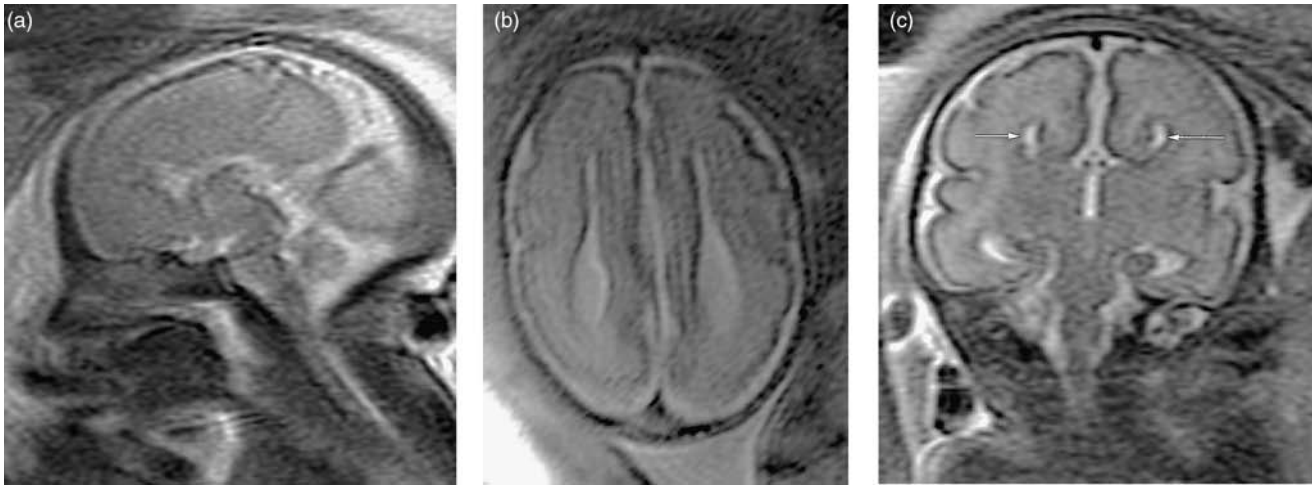

Figure 3.60 Agenesis of the corpus callosum at 27 weeks gestational age. Sagittal (a), axial (b), and coronal (c) T_2-weighted images show deficiency of midline callosal landmarks, parallel orientation of the frontal horns (arrows), and lack of callosal tissue across the midline. Colpocephaly is present along with slightly enlarged, dysmorphic temporal horns. [(b and c) From Levine (115)]

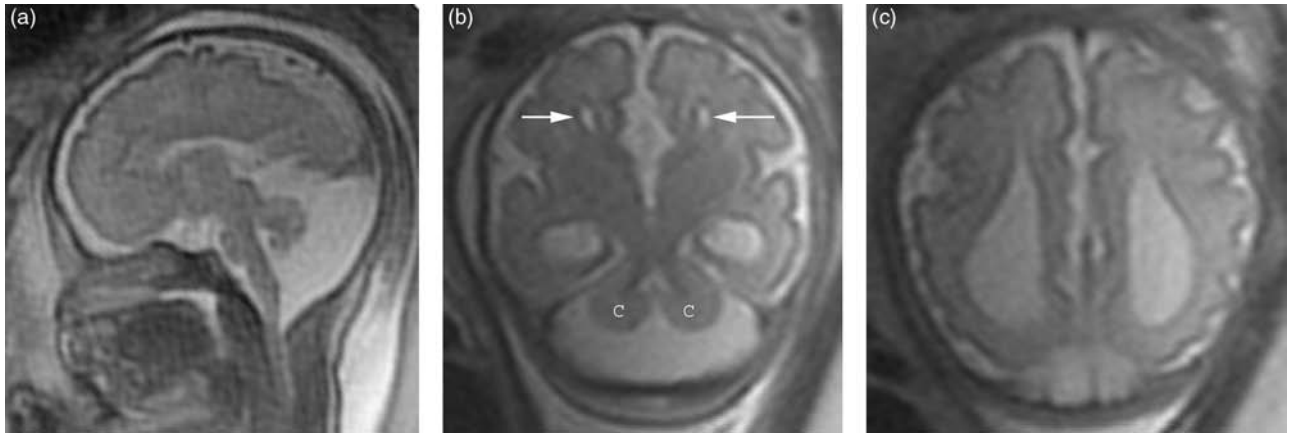

Figure 3.61 Agenesis of the corpus callosum with Dandy–Walker variant at 33 weeks gestational age. Head size measured only 29 weeks. Midsagittal (a) and oblique coronal (b and c) T_2-weighted images show deficiency of midline callosal landmarks and a small inferior cerebellar vermis with a large retrocerebellar space. Note the parallel orientation of the frontal horns (arrows), the lack of callosal tissue across the midline, large and dysmorphic temporal horns, small cerebellar hemispheres (c), separate fourth ventricle, and large cisterna magna with elevated torcular Herophili.

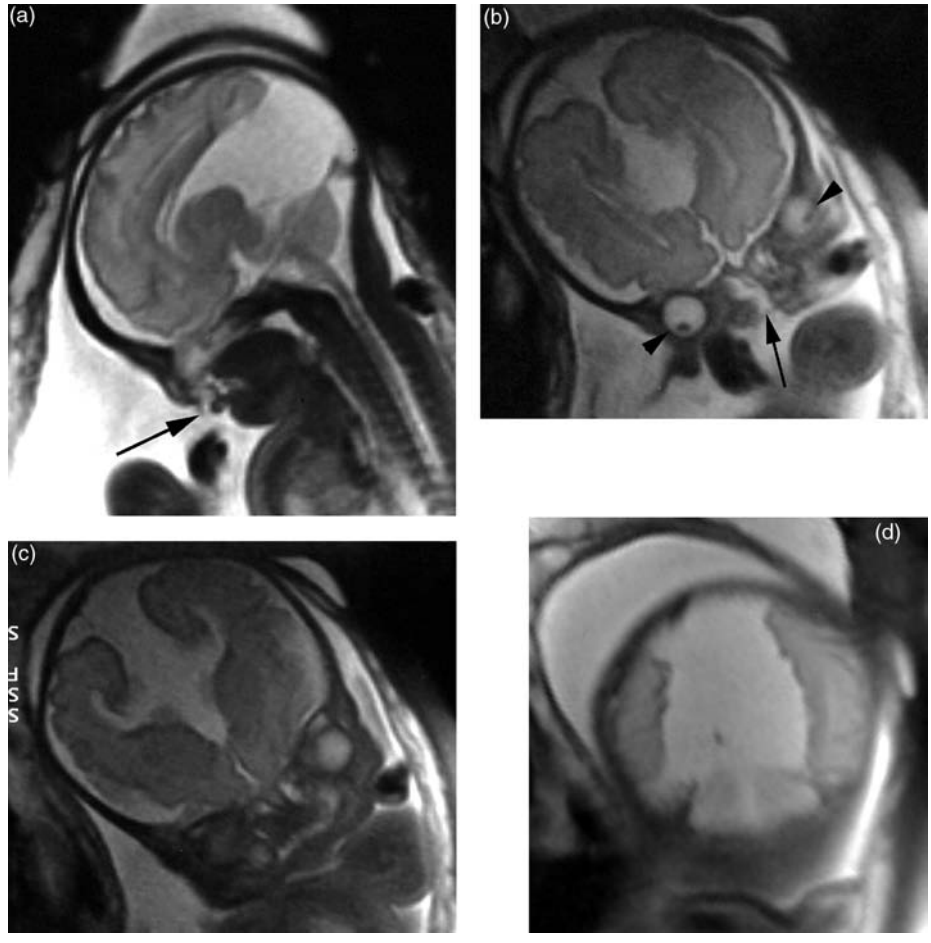

Figure 3.62 Agenesis of the corpus callosum with interhemispheric cyst and cleft lip/palate at 33 weeks gestational age. Sagittal (a) and coronal (b–d) T_2-weighted images demonstrate a wide and cyst-like interhemispheric fissure, widely separated and parallel-oriented frontal horns, and deficiency of the callosal landmarks. There is orbital hypertelorism (arrowheads) and a unilateral cleft lip and palate (arrows). On referral sonogram, this was felt to be holoprosencephaly due to the large midline cleft. [(a) From Levine (8)]

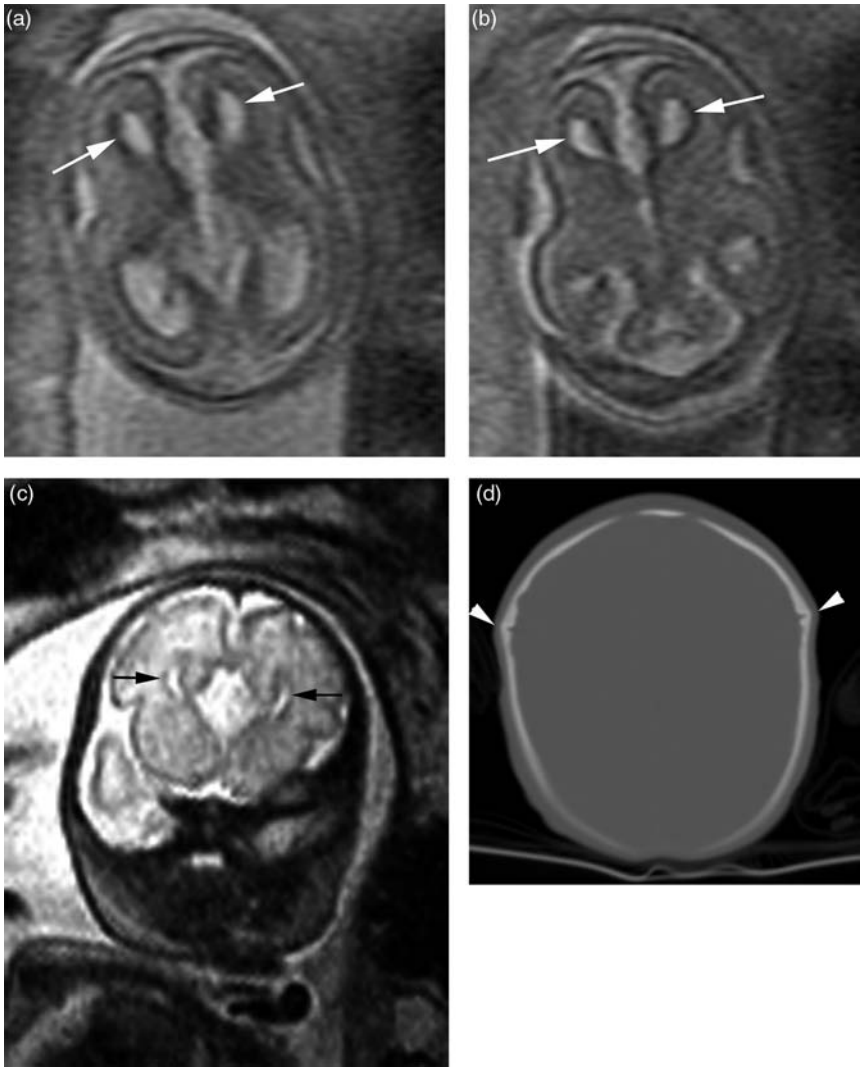

Figure 3.63 Agenesis of the corpus callosum and craniosynostosis in Apert's syndrome. Axial (a) and coronal (b) T_2-weighted images at 18 weeks gestational age show the parallel and vertical orientation of the frontal horns (arrows) and deficiency of callosal tissue across the midline. Coronal T_2-weighted image (c) at 32 weeks gestational age again demonstrates findings of callosal hypogenesis plus abnormal contour of the skull. Postnatal CT (d) shows anterior brachycephaly with fused coronal sutures (arrowheads). This is the same fetus as shown in Chapter 4, Fig. 4.10 and Chapter 7, Fig. 7.26.

suspected by prenatal ultrasound but not confirmed by prenatal MR imaging (3,7,12,14). Associated findings include colpocephaly, ventriculomegaly, parallel orientation of the frontal horns, wide interhemispheric fissure, absence of the septum pellucidum, elevated third ventricle, cerebellar hypoplasia, and small head size. The cingulate sulcus is absent in complete agenesis of the corpus callosum. Dandy–Walker malformation and neural tube defects (e.g., Chiari II) are also frequently associated with hypogenesis of the corpus callosum. The association of interhemispheric clefts and cysts with hypogenesis of the corpus callosum is well recognized (83). These may be extensions of the ventricles or may be separate from the ventricular system (84). When the interhemispheric cyst is large, the anomaly may be mistaken for holoprosencephaly (Fig. 3.62). Fetal MR imaging provides clarification in such cases (3,8).

In contradistinction to complete agenesis of the corpus callosum, which is a developmental malformation, partial hypogenesis of the corpus callosum can result from incomplete formation or from a postformational encephaloclastic process. It may be difficult to diagnose hypogenesis of the corpus callosum in cases of marked to massive ventriculomegaly because the thinned corpus callosum is not completely visualized. In these cases, a normal lateral ventricular contour suggests that the corpus callosum is present but attenuated. If there is severe colpocephaly with normally divergent frontal horns, then partial hypogenesis of the corpus callosum is implied (Figs. 3.37 and 3.47). Fetal MR imaging also can delineate associated findings of pericallosal lipoma, abnormal gyration (e.g., stenogyria), and neuronal heterotopias (Fig. 3.58) (82,85,86).

Table 3.1 Postnatal Progression of Appearance of Intracranial Hemorrhage[a]

Stage	Age	Biochemical form	Site	T_1 SI	T_2 SI
Hyperacute (+edema)	<12 hours	Ferrous oxyHb	Intact RBC	Iso-low	High
Acute (+edema)	1–3 days	Ferrous deoxyHb	Intact RBC	Iso-low	Low
Early subacute (+edema)	3–7 days	Ferrous metHb	Intact RBC	High	Low
Late subacute (−edema)	1–2 weeks	Ferrous metHb	Lysed RBC, extracellular	High	High
Early chronic (−edema)	>2 weeks	Ferric transferring	Extracellular	High	High
Chronic		Ferritin and hemosiderin	Phagocytosis	Iso-low	Low

[a]This does not take into account the effect of fetal hemoglobin (Hb) which may alter the progression of appearances.
Source: Modified from Barnes (93).

ENCEPHALOCLASTIC ABNORMALITIES OF THE DEVELOPING CNS

Abnormalities in this category may overlap with the formational categories and include infarction, hemorrhage, hydranencephaly (previously discussed), porencephaly, multicystic encephalopathy, encephalomalacia, leukomalacia, hemiatrophy, and hydrocephalus (e.g., secondary to aqueductal stenosis).

Infarction

Magnetic resonance imaging is the preferred modality to assess fetal stroke (87). Fetal MR imaging often shows infarction that is either not apparent by ultrasound (88) or has an appearance of another lesion (e.g., arachnoid cyst) (6). Diffusion imaging may be utilized to demonstrate acute/subacute ischemia that is not apparent on T_2-weighted imaging (89).

Hemorrhage

Intracranial hemorrhage (extra-axial, intraventricular, or parenchymal) may result from an underlying vascular malformation, a coagulopathy, trauma, or hypoxic–ischemic injury (90). Hemorrhage that occurs remote to the time of examination may not be specifically visualized except for its residuum (e.g., ventriculomegaly, cysts, cavities, porencephaly, or atrophy). Fetal MR imaging may be utilized to visualize blood products (90–92) and to estimate the age of the bleed, using T_1 and T_2 sequences (Table 3.1) (93). However, the timing criteria for fetal and neonatal hemorrhage (i.e., fetal hemoglobin) have not been precisely established. Although hemorrhage may be visualized by ultrasound but not by MR imaging, there are numerous reports in which MR imaging identifies hemorrhage not seen on ultrasound (Figs. 3.64–3.69) (13,94,95). Clues to the presence of intraventricular hemorrhage include intraventricular T_2 hypointensity outside of the choroid plexus (e.g., frontal horns or temporal horns)

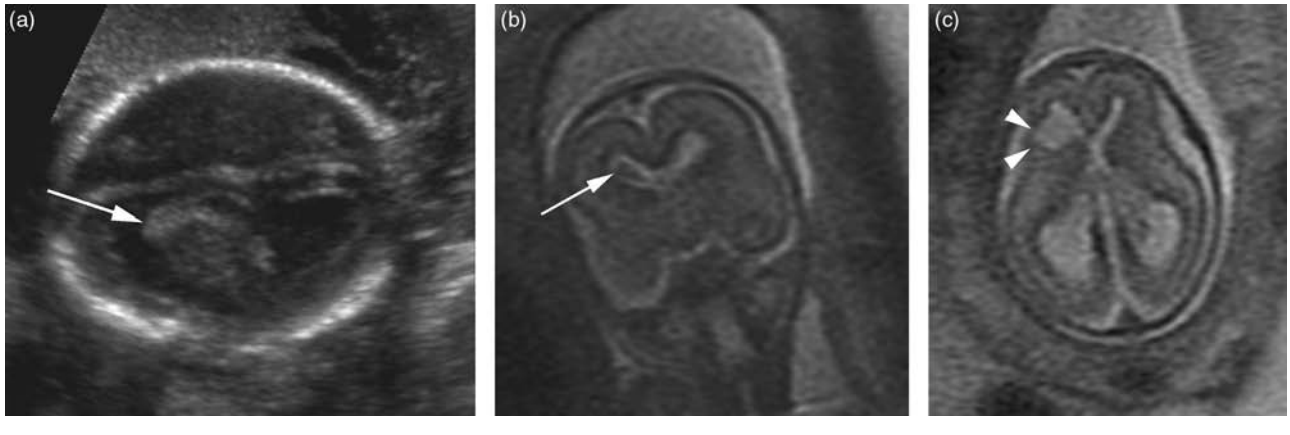

Figure 3.64 Interventricular hemorrhage with cerebral injury in fetus with ventriculomegaly at 20 weeks gestational age. (a) Axial sonogram demonstrates echogenic material in the right frontal horn (arrow) consistent with hemorrhage. Coronal (b) and axial (c) T_2-weighted images demonstrate the hypointense hemorrhage within the frontal horn (arrow) along with porencephaly (arrowheads), which was not identified on sonography. [(b and c) From Levine (96)]

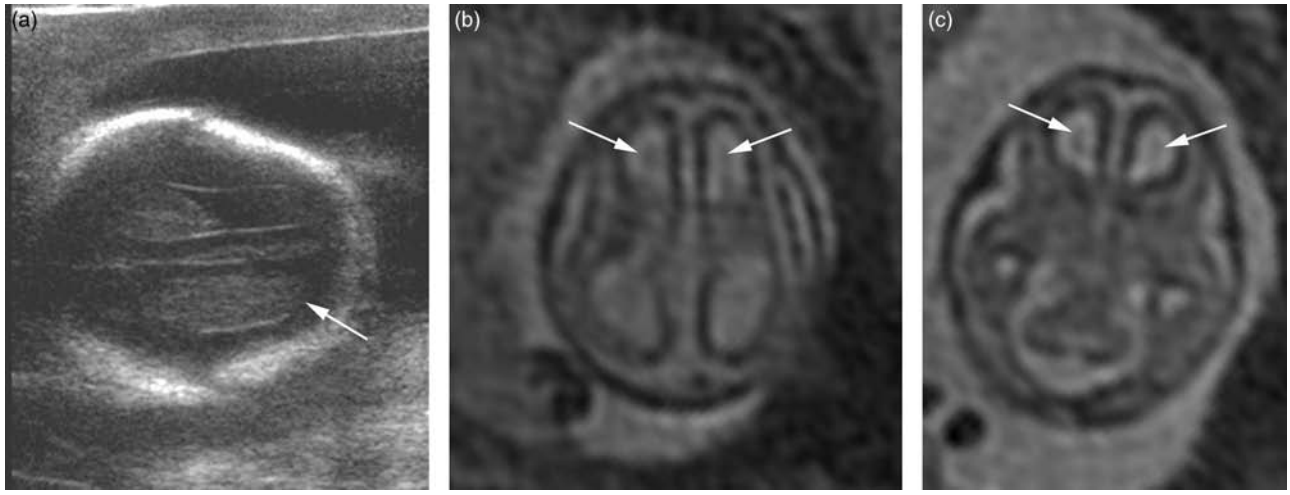

Figure 3.65 Interventricular hemorrhage at 16 and 20 weeks gestational age. Sonogram at 16 weeks (a) shows echogenic material in the left frontal horn (arrow). Axial T_2-weighted image at 16 weeks (b) and 20 weeks (c) gestational age show subtle hypointensities in the frontal horns. The hemorrhage resolved over the course of the pregnancy and no brain injury was demonstrated postnatally. The delivery was by cesarean section.

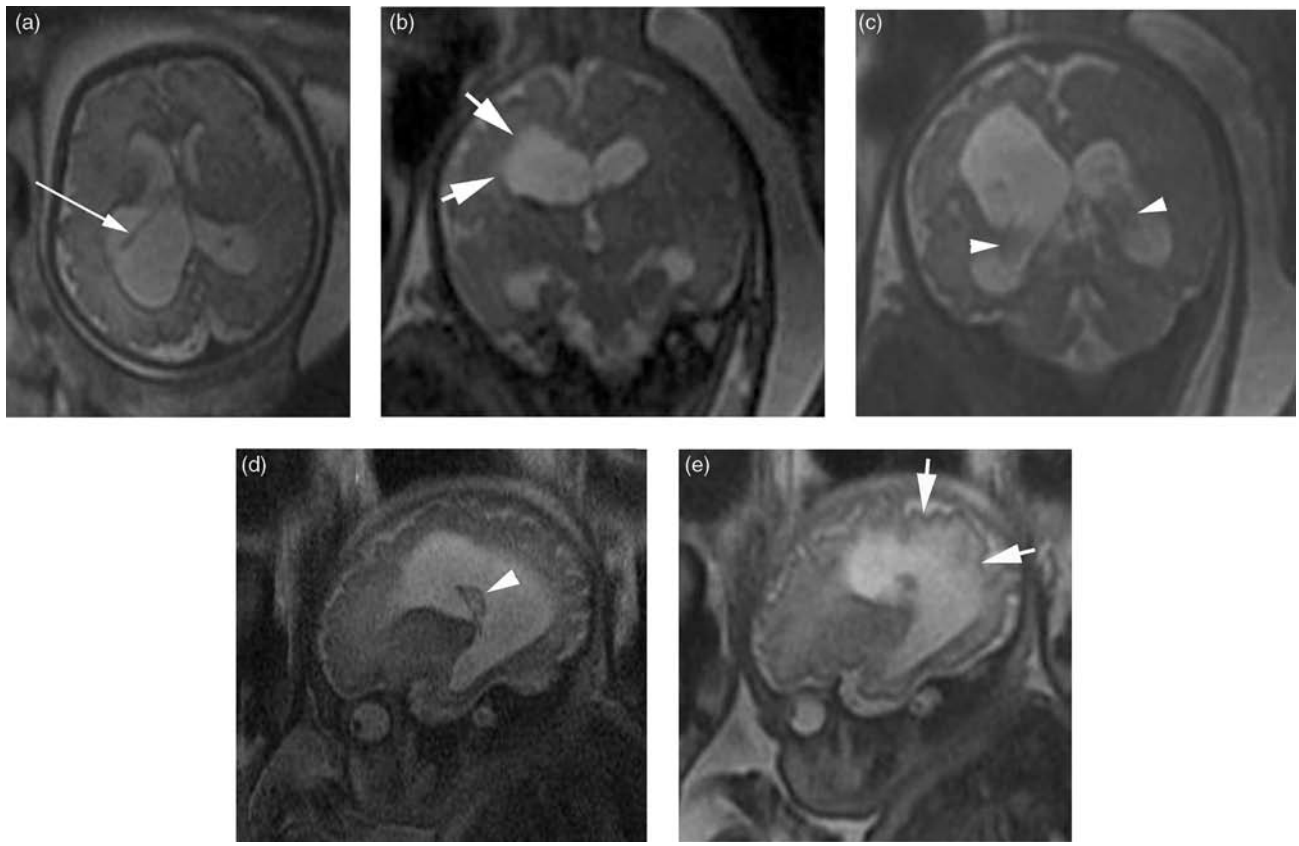

Figure 3.66 Interventricular hemorrhage with porencephaly at 35 weeks gestational age. Axial (a), coronal (b and c), and sagittal (d and e) T_2-weighted images show asymmetric ventriculomegaly with porencephaly (short arrows). The choroid plexus (long thin arrow) is seen as a thin structure dangling due to the ventricular size. There are intraventricular hypointensities (arrowheads) separate from the choroid plexus which is consistent with hemorrhage. Clues to the presence of interventricular hemorrhage include low signal intensity material in the frontal horns and tip of the temporal horn, the choroid plexus having an irregular or unusually dark appearance, and material other than the choroid plexus visualized in the ventricles.

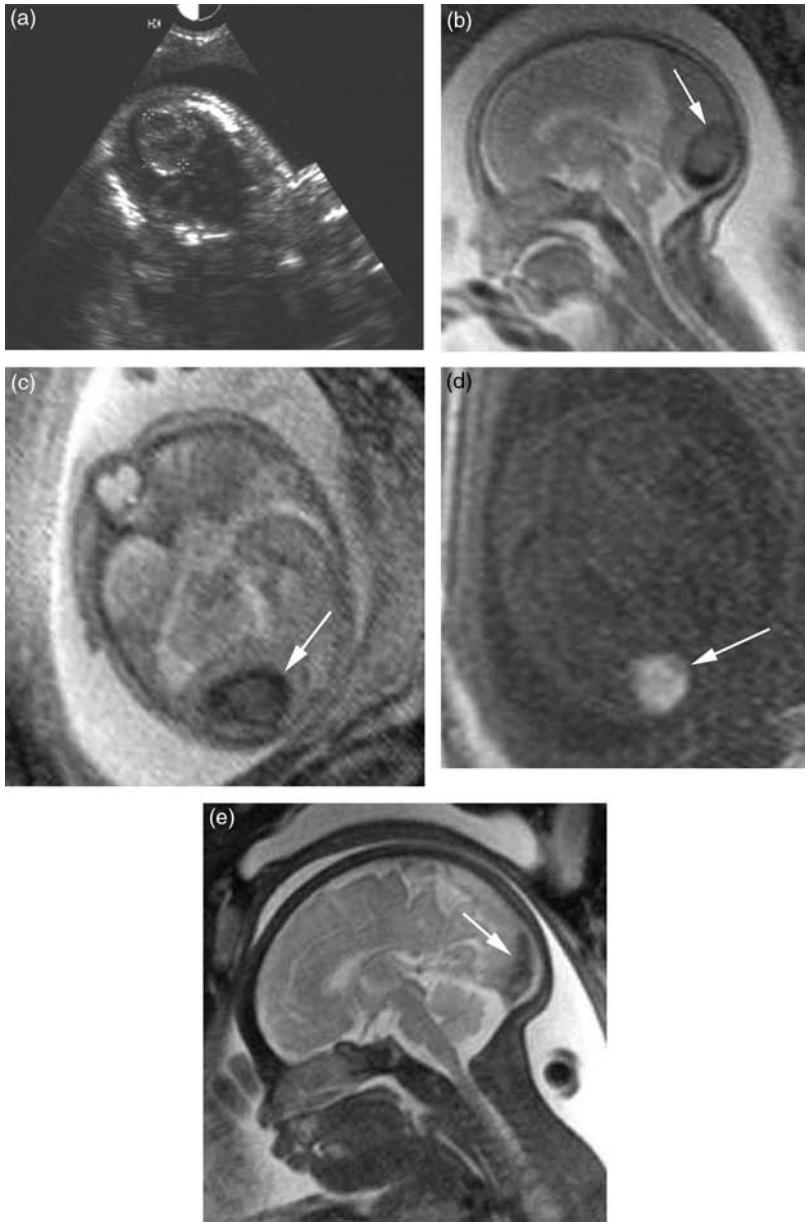

Figure 3.67 Tentorial and falcine hematoma in Von Willebrand's disease. (a) Sonogram at 22 weeks gestational age shows a mixed echogenic collection (calipers) in the posterior fossa consistent with hemorrhage. Sagittal (b) and axial (c) T_2-weighted images and axial T_1-weighted image (d) at 22 weeks gestational age show the collection to be T_2-hypointense and T_1-hyperintense (arrows). (e) Sagittal T_2-weighted image at 34 weeks gestational age shows a decrease in the size of the T_2-hypointense collection (arrow). Owing to the risk of recurrent bleed, the delivery was performed by cesarean section. Neonatal head ultrasound (not shown) showed resolution of this collection but demonstrated a new parietal hemorrhage. [(b) From Levine (96)]

and irregular or unusual T_2 hypointensity of the choroid plexus (96).

Fetal MR imaging adds information over ultrasound by demonstrating the nature of the intraventricular mass when hemorrhage is present (e.g., an underlying vascular malformation) (97) and the extent of parenchymal lesions resulting from hemorrhage (e.g., porencephaly and encephalomalacia) (2,4,91). Fetal MR imaging is also helpful in confirming the extra-axial location of hematomas (98–103). The prognosis is worse for fetal parenchymal and subdural hemorrhage than for isolated intraventricular hemorrhage (104). Cases of fetal peritentorial hemorrhage (Figs. 3.67 and 3.68) or dural venous sinus thrombosis have even better outcomes (100,101). Isolated germinal matrix hemorrhage may be visualized by MR imaging (Fig. 3.69) but not by ultrasound. The clinical significance of isolated fetal germinal matrix hemorrhage is unknown.

Porencephaly and Encephalomalacia

Porencephaly or encephalomalacia may result from necrosis caused by infection, trauma, hemorrhage, or infarction. Fetal MR imaging is helpful in delineating these lesions

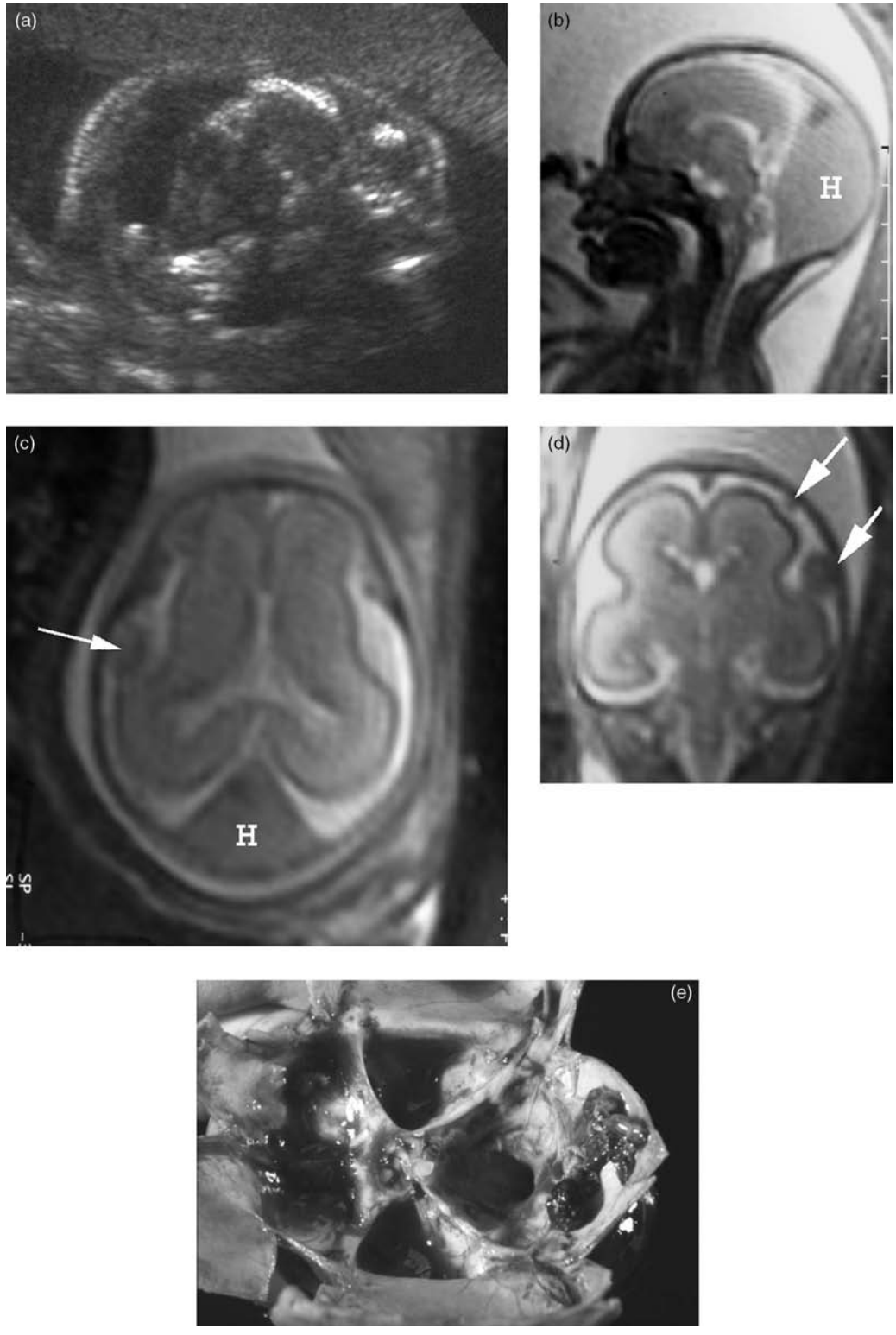

Figure 3.68 Tentorial, falcine, and other extracerebral hemorrhages at 22 weeks gestational age. Axial sonogram (a) shows a posterior fluid collection with an echogenic component. Sagittal (b), axial (c), and coronal (d) T_2-weighted images show a large posterior midline hypointense collection (H) plus small extracerebral hypointense hemorrhages (arrows). These findings were confirmed at autopsy (e). [(a and b) From Folkerth et al. (100); (d) from Trop and Levine (103)]

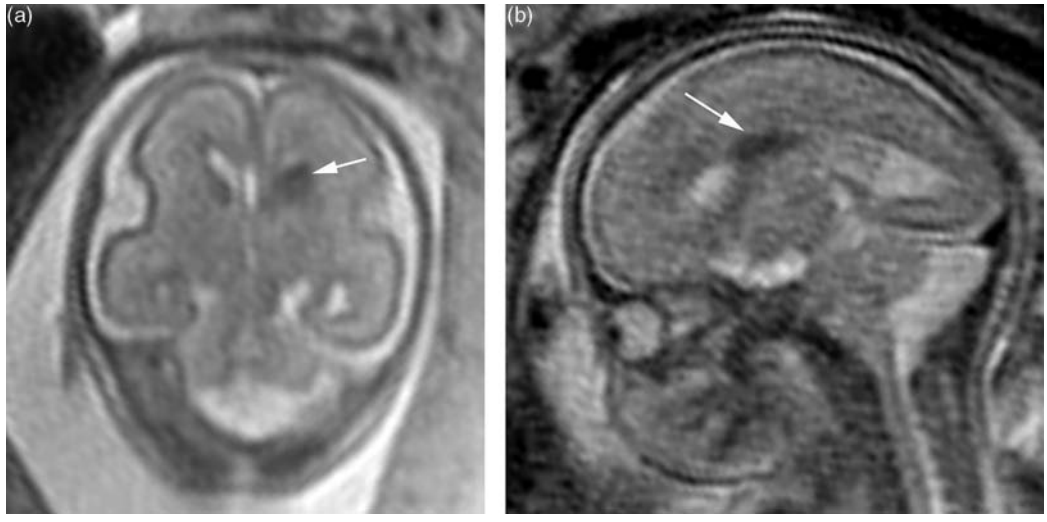

Figure 3.69 Grade I subependymal hemorrhage at 18 weeks gestational age. Coronal (a) and sagittal (b) T_2-weighted images demonstrate a left subependymal hypointensity (arrows). The finding was confirmed on separate sequences or in multiple planes. The presumed hemorrhage resolved *in utero.* Neonatal head ultrasound (not shown) was normal.

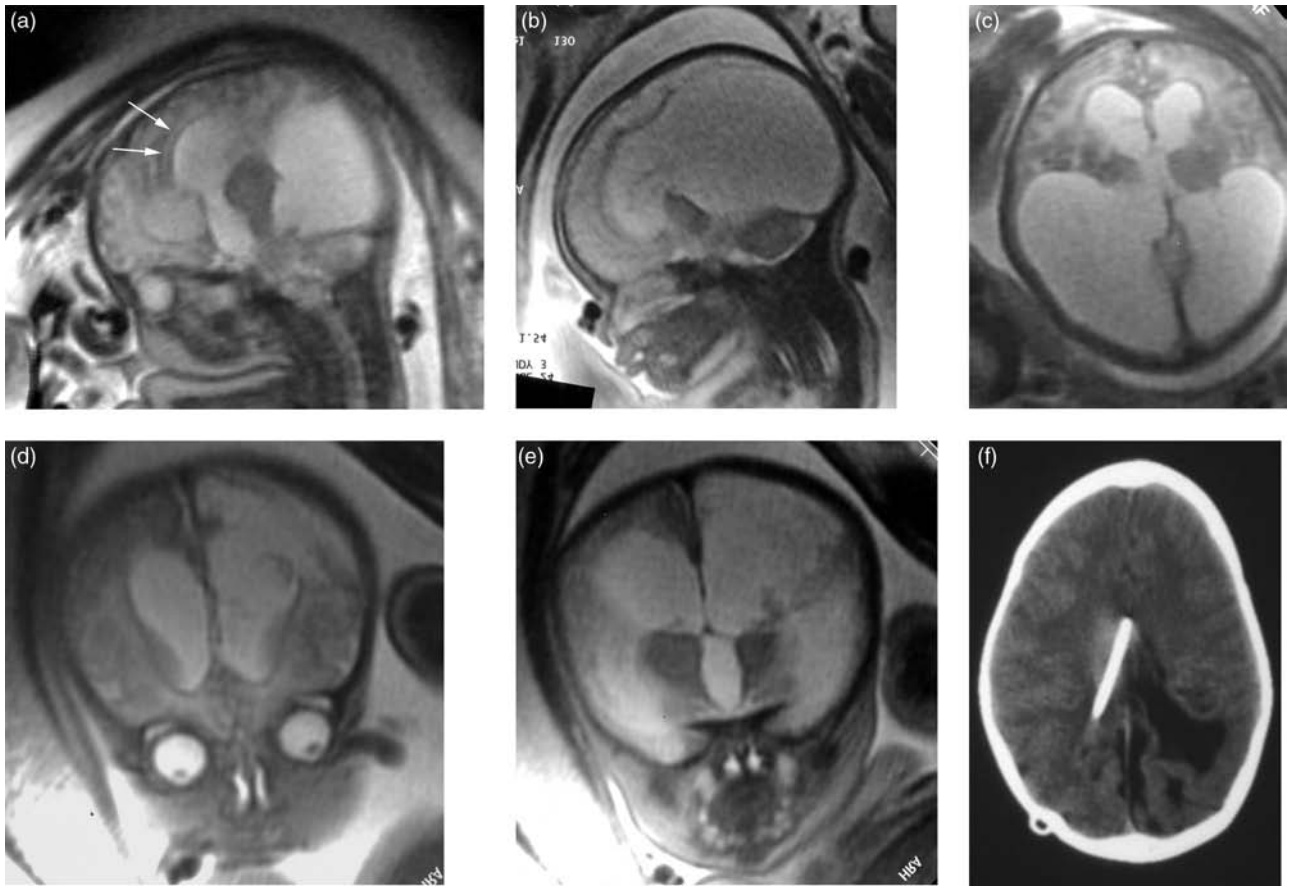

Figure 3.70 Hydrocephalus and porencephaly at 38 weeks gestational age. Sagittal (a and b), axial (c), and coronal (d and e) T_2-weighted images show marked ventriculomegaly and a large frontal cavity continuous with the lateral ventricle. The anterior corpus callosum is present (arrows). The posterior portion of the corpus callosum is absent. Postnatal axial CT (f) after shunting shows the residual porencephalic defect posteriorly and the re-established cerebral mantle elsewhere. [(a) From Levine et al. (8)]

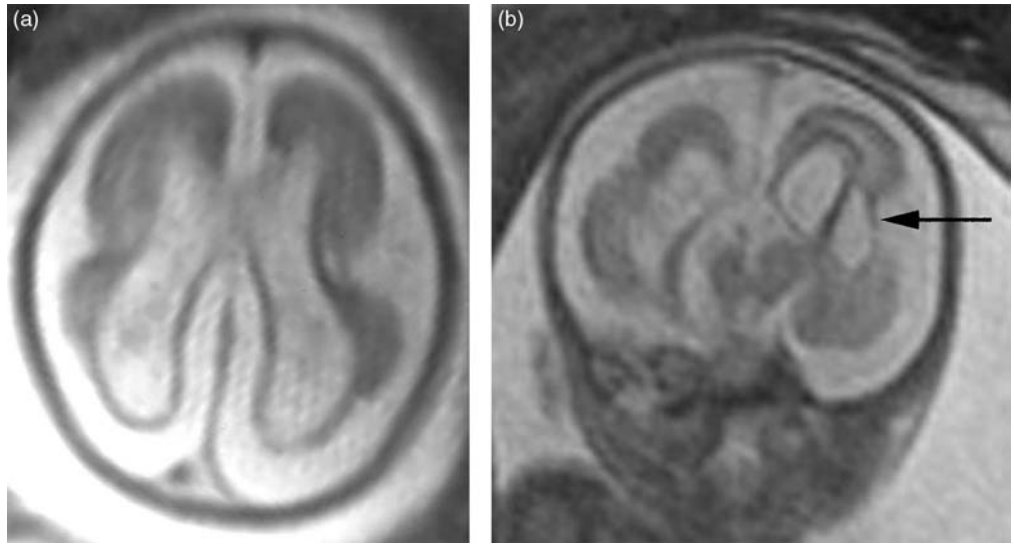

Figure 3.71 Encephalomalacia in surviving twin after demise of monochorionic co-twin. Axial (a) and coronal (b) T_2-weighted images in the surviving twin show marked thinning of the parieto-occipital cerebral mantle with enlargement of the occipital horns, prominent overlying extracerebral spaces, and an area of porencephaly (arrow). [(b) From Levine (114)]

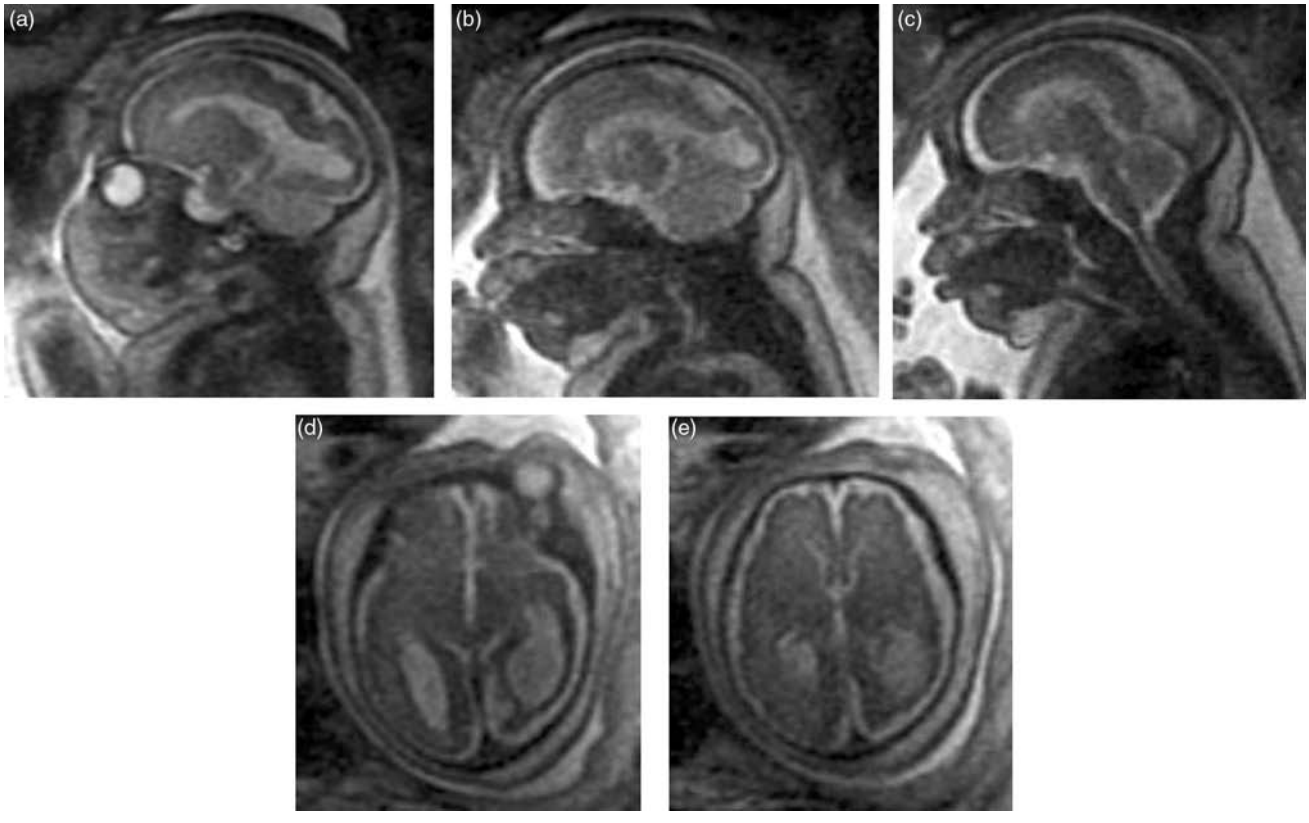

Figure 3.72 Congenital CMV at 30 weeks gestational age. Sagittal (a–c) and axial (d and e) T_2-weighted images show microcephaly and polymicrogyria. Note diffuse skin thickening due to subcutaneous edema. (Images courtesy of I. Trop, Montreal, Canada.)

(Figs. 3.70 and 3.71) (105). Demise of a monochorionic twin in the second or third trimester may be associated with porencephaly or multicystic encephalomalacia of the surviving twin (Fig. 3.71 and Chapter 8, Fig. 8.13). There are two major theories regarding pathogenesis. One theory postulates multiembolic infarction. This is supported by the identification of multifocal infarctions of varying age by from a few days to 8 weeks in one series (106) and from postmortem histologic evidence of both fresh and old thrombi (107). A second theory proposes acute hypoperfusion due to blood loss from the survivor into the placenta (108–111). Abnormalities (e.g., cavitations, atrophy) are usually not apparent by ultrasound until at least 2 weeks after the demise of the co-twin (112). Fetal MR imaging may allow for earlier diagnosis; however, its role has not yet been clearly defined (112–114). The lesions may be too small for early detection using current imaging methods. Once the injury is identified, interventions (such as early delivery of the live twin) are unlikely to improve prognosis. However, the recognition of the severe brain injury is important for counseling for planning the delivery.

COMBINED MALFORMATIVE AND ENCEPHALOCLASTIC ABNORMALITIES

Congenital infection (e.g., cytomegaloviral) may result in microcephaly, migrational disorder, ventriculomegaly, and mineralization (Fig. 3.72). Periventricular calcifications may be apparent on ultrasound but not on MR imaging (5). Fetal MR imaging may show both atrophy and polymicrogyia (72).

CONCLUSION

When a fetus has a CNS abnormality, there is a high likelihood that fetal MR imaging will provide information beyond that available with ultrasound. This information can be utilized in counseling the parents and making decisions about care of the fetus prior to delivery and at the perinatal period.

REFERENCES

1. Resta M, Greco P, D'Addario V et al. Magnetic resonance imaging in pregnancy: study of fetal cerebral malformations. Ultrasound Obstet Gynecol 1994; 4:7–20.
2. Sonigo PC, Rypens FF, Carteret M et al. MR imaging of fetal cerebral anomalies. Pediatr Radiol 1998; 28:212–222.
3. Whitby E, Paley MN, Davies N et al. Ultrafast magnetic resonance imaging of central nervous system abnormalities *in utero* in the second and third trimester of pregnancy: comparison with ultrasound. Br J Obstet Gynecol 2001; 108:519–526.
4. Levine D, Barnes PD, Robertson RR et al. Fast MR imaging of fetal central nervous system abnormalities. Radiology 2003; 229:51–61.
5. d'Ercole C, Girard N, Boubli L et al. Prenatal diagnosis of fetal cerebral abnormalities by ultrasonography and magnetic resonance imaging. Eur J Obstet Gynecol Reprod Biol 1993; 50:177–184.
6. Yuh WT, Nguyen HD, Fisher DJ et al. MR of fetal central nervous system abnormalities. Am J Neuroradiol 1994; 15:459–464.
7. Revel MP, Pons JC, Lelaidier C et al. Magnetic resonance imaging of the fetus: a study of 20 cases performed without curarization. Prenat Diagn 1993; 13:775–799.
8. Levine D, Barnes PD, Madsen JR et al. Fetal central nervous system anomalies: MR imaging augments sonographic diagnosis. Radiology 1997; 204:635–642.
9. Tsuchiya K, Katase S, Seki T et al. Short communication: MR imaging of fetal brain abnormalities using a HASTE sequence. Br J Radiol 1996; 69:668–670.
10. Dinh DH, Wright RM, Hanigan WC. The use of magnetic resonance imaging for the diagnosis of fetal intracranial anomalies. Childs Nerv Syst 1990; 6:212–215.
11. Girard N, Raybaud C, Gambarelli D et al. Fetal brain MR imaging. Magn Reson Imaging Clin N Am 2001; 9:19–56.
12. Wagenvoort AM, Bekker MN, Go AT et al. Ultrafast scan magnetic resonance in prenatal diagnosis. Fetal Diagn Ther 2000; 15:364–372.
13. Girard N, Raybaud C, Dercole C et al. *In vivo* MRI of the fetal brain. Neuroradiology 1993; 35:431–436.
14. Shakudo M, Inoue Y, Mochizuki K et al. Fast MR imaging and ultrafast MR imaging of fetal central nervous system abnormalities. Osaka City Med J 2001; 47:127–135.
15. Barkovich AJ. Pediatric Neuroimaging. Philadelphia: Lippencott-Raven, 2000.
16. Ball WJ. Pediatric Neuroradiology. Philadelphia: Lipponcott-Raven, 1997.
17. Wolpert S, Barnes PD. MRI In Pediatric Neuroradiology. St Louis: Mosby, 1992.
18. van der Knaap MS, Valk J. Classification of congenital abnormalities of the CNS. Am J Neuroradiol 1988; 9:315–326.
19. Cardoza JD, Goldstein RB, Filly RA. Exclusion of fetal ventriculomegaly with a single measurement: the width of the lateral ventricular atrium. Radiology 1988; 169:711–714.
20. Oi S, Honda Y, Hidaka M et al. Intrauterine high-resolution magnetic resonance imaging in fetal hydrocephalus and prenatal estimation of postnatal outcomes with "perspective classification." J Neurosurg 1998; 88:685–694.
21. Hubbard AM, Harty MP, States LJ. A new tool for prenatal diagnosis: ultrafast fetal MRI. Semin Perinatol 1999; 23:437–447.
22. Garel C, Brisse H, Sebag G et al. Magnetic resonance imaging of the fetus. Pediatr Radiol 1998; 28:201–211.
23. Levine D, Barnes PD, Edelman RR. Obstetric MR imaging. Radiology 1999; 211:609–617.

24. Levine D, Trop I, Mehta TS et al. MR imaging appearance of fetal cerebral ventricular morphology. Radiology 2002; 223:652–660.
25. Mangels KJ, Tulipan N, Tsao LY et al. Fetal MRI in the evaluation of intrauterine myelomeningocele. Pediatr Neurosurg 2000; 32:124–131.
26. Aaronson OS, Hernanz-Schulman M, Bruner JP et al. Myelomeningocele: prenatal evaluation—comparison between transabdominal US and MR imaging. Radiology 2003; 227:839–843.
27. Midrio P, Silberstein HJ, Bilaniuk LT et al. Prenatal diagnosis of terminal myelocystocele in the fetal surgery era: case report. Neurosurgery 2002; 50:1152–1154.
28. Sutton LN, Adzick NS, Bilaniuk LT et al. Improvement in hindbrain herniation demonstrated by serial fetal magnetic resonance imaging following fetal surgery for myelomeningocele. JAMA 1999; 282:1826–1831.
29. Pilu G, Sandri F, Cerisoli M et al. Sonographic findings in septo-optic dysplasia in the fetus and newborn infant. Am J Perinatol 1990; 7:337–339.
30. Nelson MD Jr, Maher K, Gilles FH. A different approach to cysts of the posterior fossa. Pediatr Radiol 2004; 34:720–732.
31. Calabro F, Arcuri T, Jinkins JR. Blake's pouch cyst: an entity within the Dandy–Walker continuum. Neuroradiology 2000; 42:290–295.
32. Strand RD, Barnes PD, Poussaint TY et al. Cystic retrocerebellar malformations: unification of the Dandy–Walker complex and the Blake's pouch cyst. Pediatr Radiol 1993; 23:258–260.
33. Stroustrup Smith AS, Levine D. Appearance of an interhemispheric cyst associated with agenesis of the corpus callosum. Am J Neuroradiol 2004; 25:1037–1040.
34. Book JA, Schut JW, Reed SC. A clinical and genetical study of microcephaly. Am J Ment Defic 1953; 57:637–660.
35. Pilu G, Falco P, Perolo A et al. Ultrasound Evaluation of the Fetal Neural Axis. Philadelphia: W.B. Saunders, 2000:277–306.
36. Barkovich AJ, Chuang SH. Unilateral megalencephaly: correlation of MR imaging and pathologic characteristics. Am J Neuroradiol 1990; 11:523–531.
37. Bignami A, Palladini G, Zappella M. Unilateral megalencephaly with nerve cell hypertrophy. An anatomical and quantitative histochemical study. Brain Res 1968; 9:103–114.
38. Sandri F, Pilu G, Dallacasa P et al. Sonography of unilateral megalencephaly in the fetus and newborn infant. Am J Perinatol 1991; 8:18–20.
39. Ramirez M, Wilkins I, Kramer L et al. Prenatal diagnosis of unilateral megalencephaly by real-time ultrasonography. Am J Obstet Gynecol 1994; 170:1384–1385.
40. Au KS, Rodriguez JA, Finch JL et al. Germ-line mutational analysis of the TSC2 gene in 90 tuberous-sclerosis patients. Am J Hum Genet 1998; 62:286–294.
41. Wallace G, Smith HC, Watson GH et al. Tuberous sclerosis presenting with fetal and neonatal cardiac tumours. Arch Dis Child 1990; 65:377–379.
42. Bass JL, Breningstall GN, Swaiman KF. Echocardiographic incidence of cardiac rhabdomyoma in tuberous sclerosis. Am J Cardiol 1985; 55:1379–1382.
43. Levine D, Barnes PB, Korf B et al. Tuberous sclerosis in the fetus: second-trimester diagnosis of subependymal tubers with ultrafast MR imaging. Am J Roentgenol 2000; 175:1067–1069.
44. Rickert CH. Neuropathology and prognosis of foetal brain tumours. Acta Neuropathol (Berl) 1999; 98:567–576.
45. Guibaud L, Champion F, Buenerd A et al. Fetal intraventricular glioblastoma: ultrasonographic, magnetic resonance imaging, and pathologic findings. J Ultrasound Med 1997; 16:285–288.
46. Bailey W, Freidenberg GR, James HE et al. Prenatal diagnosis of a craniopharyngioma using ultrasonography and magnetic resonance imaging. Prenat Diagn 1990; 10:623–629.
47. Kultursay N, Gelal F, Mutluer S et al. Antenatally diagnosed neonatal craniopharyngioma. J Perinatol 1995; 15:426–428.
48. Peng SS, Shih JC, Liu HM et al. Ultrafast fetal MR images of intracranial teratoma. J Comput Assist Tomogr 1999; 23:318–319.
49. Kamitomo M, Sameshima H, Uetsuhara K et al. Fetal glioblastoma: rapid growth during the third trimester. Fetal Diagn Ther 1998; 13:339–342.
50. Morof DF, Levine D, Stringer KF et al. Congenital glioblastoma multiforme: prenatal diagnosis on the basis of sonography and magnetic resonance imaging. J Ultrasound Med 2001; 20:1369–1375.
51. Normal MC, McGillivray BC, Kalousel DK et al. Congenital malformations of the brain: pathological, embryological, clinical, radiological, and genetic aspects. New York: Oxford University Press, 1995.
52. Schachenmayr W, Friede RL. Fine structure of arachnoid cysts. J Neuropathol Exp Neurol 1979; 38:434–446.
53. Pierre-Kahn A, Hanlo P, Sonigo P et al. The contribution of prenatal diagnosis to the understanding of malformative intracranial cysts: state of the art. Childs Nerv Syst 2000; 16:619–626.
54. Levine D, Barnes PD, Madsen JR et al. Fetal CNS anomalies revealed on ultrafast MR imaging. Am J Roentgenol 1999; 172:813–818.
55. Golash A, Mitchell G, Mallucci C et al. Prenatal diagnosis of suprasellar arachnoid cyst and postnatal endoscopic treatment. Childs Nerv Syst 2001; 17:739–742.
56. Levine D. Ultrasound versus magnetic resonance imaging in fetal evaluation. Top Magn Reson Imaging 2001; 12:25–38.
57. Gupta JK, Cave M, Lilford RJ et al. Clinical significance of fetal choroid plexus cysts. Lancet 1995; 346:724–729.
58. Aicardi J. The agyria–pachygyria complex: a spectrum of cortical malformations. Brain Dev 1991; 13:1–8.
59. Barth PG. Disorders of neuronal migration. Can J Neurol Sci 1987; 14:1–16.
60. Barkovich AJ, Chuang SH, Norman D. MR of neuronal migration anomalies. Am J Roentgenol 1988; 150:179–187.

61. Friede RL. Developmental Neuropathology. New York: Springer-Verlag, 1989.
62. Barkovich AJ, Koch TK, Carrol CL. The spectrum of lissencephaly: report of ten patients analyzed by magnetic resonance imaging. Ann Neurol 1991; 30:139–146.
63. Dobyns WB. The neurogenetics of lissencephaly. Neurol Clin 1989; 7:89–105.
64. Gastaut H, Pinsard N, Raybaud C et al. Lissencephaly (agyria–pachygyria): clinical findings and serial EEG studies. Dev Med Child Neurol 1987; 29:167–180.
65. de Rijk-van Andel JF, Arts WF, Barth PG et al. Diagnostic features and clinical signs of 21 patients with lissencephaly type 1. Dev Med Child Neurol 1990; 32:707–717.
66. Barkovich AJ, Norman D. Anomalies of the corpus callosum: correlation with further anomalies of the brain. Am J Roentgenol 1988; 151:171–179.
67. Greco P, Resta M, Vimercati A et al. Antenatal diagnosis of isolated lissencephaly by ultrasound and magnetic resonance imaging. Ultrasound Obstet Gynecol 1998; 12:276–279.
68. Okamura K, Murotsuki J, Sakai T et al. Prenatal diagnosis of lissencephaly by magnetic resonance image. Fetal Diagn Ther 1993; 8:56–59.
69. Barkovich AJ, Kjos BO. Nonlissencephalic cortical dysplasias: correlation of imaging findings with clinical deficits. Am J Neuroradiol 1992; 13:95–103.
70. Richman DP, Stewart RM, Caviness VS Jr. Cerebral microgyria in a 27-week fetus: an architectonic and topographic analysis. J Neuropathol Exp Neurol 1974; 33:374–384.
71. Ferrer I. A Golgi analysis of unlayered polymicrogyria. Acta Neuropathol (Berl) 1984; 65:69–76.
72. Soussotte C, Maugey-Laulom B, Carles D et al. Contribution of transvaginal ultrasonography and fetal cerebral MRI in a case of congenital cytomegalovirus infection. Fetal Diagn Ther 2000; 15:219–223.
73. Denis D, Maugey-Laulom B, Carles D et al. Prenatal diagnosis of schizencephaly by fetal magnetic resonance imaging. Fetal Diagn Ther 2001; 16:354–359.
74. Lituania M, Passamonti U, Cordone MS et al. Schizencephaly: prenatal diagnosis by computed sonography and magnetic resonance imaging. Prenat Diagn 1989; 9:649–655.
75. Komarniski CA, Cyr DR, Mack LA et al. Prenatal diagnosis of schizencephaly. J Ultrasound Med 1990; 9:305–307.
76. Barkovich AJ, Kjos BO. Gray matter heterotopias: MR characteristics and correlation with developmental and neurologic manifestations. Radiology 1992; 182:493–499.
77. Barkovich AJ, Jackson DE Jr, Boyer RS. Band heterotopias: a newly recognized neuronal migration anomaly. Radiology 1989; 171:455–458.
78. Livingston JH, Aicardi J. Unusual MRI appearance of diffuse subcortical heterotopia or "double cortex" in two children. J Neurol Neurosurg Psychiatry 1990; 53:617–620.
79. Bargallo N, Puerto B, De Juan C et al. Hereditary subependymal heterotopia associated with mega cisterna magna: antenatal diagnosis with magnetic resonance imaging. Ultrasound Obstet Gynecol 2002; 20:86–89.
80. Serrien DJ, Nirkko AC, Wiesendanger M. Role of the corpus callosum in bimanual coordination: a comparison of patients with congenital and acquired callosal damage. Eur J Neurosci 2001; 14:1897–1905.
81. Gupta JK, Lilford RJ. Assessment and management of fetal agenesis of the corpus callosum. Prenat Diagn 1995; 15:301–312.
82. d'Ercole C, Girard N, Cravello L et al. Prenatal diagnosis of fetal corpus callosum agenesis by ultrasonography and magnetic resonance imaging. Prenat Diagn 1998; 18:247–253.
83. Probst FP. Congenital defects of the corpus callosum. Morphology and encephalographic appearances. Acta Radiol Suppl 1973; 331:1–152.
84. Barkovich AJ, Simon EM, Walsh CA. Callosal agenesis with cyst: a better understanding and new classification. Neurology 2001; 56:220–227.
85. Rypens F, Sonigo P, Aubry MC et al. Prenatal MR diagnosis of a thick corpus callosum. Am J Neuroradiol 1996; 17:1918–1920.
86. Kim TH, Joh JH, Kim MY et al. Fetal pericallosal lipoma: US and MR findings. Korean J Radiol 2002; 3:140–143.
87. Ozduman K, Pober BR, Barnes P et al. Fetal stroke. Pediatr Neurol 2004; 30:151–162.
88. Huisman TA, Wisser J, Martin E et al. Fetal magnetic resonance imaging of the central nervous system: a pictorial essay. Eur Radiol 2002; 12:1952–1961.
89. Baldoli C, Righini A, Parazzini C et al. Demonstration of acute ischemic lesions in the fetal brain by diffusion magnetic resonance imaging. Ann Neurol 2002; 52:243–246.
90. Fusch C, Ozdoba C, Kuhn P et al. Perinatal ultrasonography and magnetic resonance imaging findings in congenital hydrocephalus associated with fetal intraventricular hemorrhage. Am J Obstet Gynecol 1997; 177:512–518.
91. Kirkinen P, Partanen K, Ryynanen M et al. Fetal intracranial hemorrhage. Imaging by ultrasound and magnetic resonance imaging. J Reprod Med 1997; 42:467–472.
92. Kawabata I, Imai A, Tamaya T. Antenatal subdural hemorrhage causing fetal death before labor. Int J Gynaecol Obstet 1993; 43:57–60.
93. Barnes PD. Neuroimaging and the timing of fetal and neonatal brain injury. J Perinatol 2001; 21:44–60.
94. Canapicchi R, Cioni G, Strigini FA et al. Prenatal diagnosis of periventricular hemorrhage by fetal brain magnetic resonance imaging. Childs Nerv Syst 1998; 14:689–692.
95. Fukui K, Morioka T, Nishio S et al. Fetal germinal matrix and intraventricular haemorrhage diagnosed by MRI. Neuroradiology 2001; 43:68–72.
96. Levine D. Fetal magnetic resonance imaging. J Matern Fetal Neonatal Med 2004; 15:85–94.

97. Hashimoto I, Tada K, Nakatsuka M et al. Fetal hydrocephalus secondary to intraventricular hemorrhage diagnosed by ultrasonography and *in utero* fast magnetic resonance imaging. A case report. Fetal Diagn Ther 1999; 14:248–253.
98. Emamian SA, Bulas DI, Vezina GL et al. Fetal MRI evaluation of an intracranial mass: *in utero* evolution of hemorrhage. Pediatr Radiol 2002; 32:593–597.
99. Lafont M, Lamarque M, Daussac E. Favorable outcome of a subdural hematoma diagnosed *in utero*. Arch Pediatr 1999; 6:962–965.
100. Folkerth RD, McLaughlin ME, Levine D. Organizing posterior fossa hematomas simulating developmental cysts on prenatal imaging: report of 3 cases. J Ultrasound Med 2001; 20:1233–1240.
101. Gicquel JM, Potier A, Sitruk S et al. Normal outcome after prenatal diagnosis of thrombosis of the torcular Herophili. Prenat Diagn 2000; 20:824–827.
102. Poutamo J, Vanninen R, Partanen K et al. Magnetic resonance imaging supplements ultrasonographic imaging of the posterior fossa, pharynx and neck in malformed fetuses. Ultrasound Obstet Gynecol 1999; 13:327–334.
103. Trop I, Levine D. Hemorrhage during pregnancy: sonography and MR imaging. Am J Roentgenol 2001; 176:607–615.
104. Vergani P, Strobelt N, Locatelli A et al. Clinical significance of fetal intracranial hemorrhage. Am J Obstet Gynecol 1996; 175:536–543.
105. Toma P, Lucigrai G, Ravegnani M et al. Hydrocephalus and porencephaly: prenatal diagnosis by ultrasonography and MR imaging. J Comput Assist Tomogr 1990; 14:843–845.
106. Szymonowicz W, Preston H, Yu VY. The surviving monozygotic twin. Arch Dis Child 1986; 61:454–458.
107. Larroche JC, Droulle P, Delezoide AL et al. Brain damage in monozygous twins. Biol Neonate 1990; 57:261–278.
108. Bernischke K. Twin placenta in prenatal mortality. NY State J Med 1961; 61:1499–1508.
109. Fusi L, McParland P, Fisk N et al. Acute twin–twin transfusion: a possible mechanism for brain-damaged survivors after intrauterine death of a monochorionic twin. Obstet Gynecol 1991; 78:517–520.
110. Okamura K, Murotsuki J, Tanigawara S et al. Funipuncture for evaluation of hematologic and coagulation indices in the surviving twin following co-twin's death. Obstet Gynecol 1994; 83:975–978.
111. Nicolini U, Pisoni MP, Cela E et al. Fetal blood sampling immediately before and within 24 hours of death in monochorionic twin pregnancies complicated by single intrauterine death. Am J Obstet Gynecol 1998; 179:800–803.
112. Bejar R, Vigliocco G, Gramajo H et al. Antenatal origin of neurologic damage in newborn infants. II. Multiple gestations. Am J Obstet Gynecol 1990; 162:1230–1236.
113. Levine D, Barnes PD, Madsen JR et al. Central nervous system abnormalities assessed with prenatal magnetic resonance imaging. Obstet Gynecol 1999; 94:1011–1019.
114. Levine D. Case 46: encephalomalacia in surviving twin after death of monochorionic co-twin. Radiology 2002; 223:392–395.
115. Levine D, Stroustrup Smith A, Barbaras L et al. Compendium of Fetal MRI (image). Available online at Beth Israel Deaconess Medical Center Radiology department website, http://bidmc.harvard.edu/fetalatlas/, 2004.

4

MR Imaging of the Fetal Skull, Face, and Neck

ANNEMARIE STROUSTRUP SMITH, DEBORAH LEVINE

INTRODUCTION

Abnormalities of the face, skull, and neck are frequently visualized in association with central nervous system abnormalities, aneuploidy, syndromes, and teratogen exposure. In many of these cases, magnetic resonance (MR) imaging is performed for indications other than the facial, head, or neck abnormality. Exceptions to this include the evaluation of the mass effect of tumors that could cause airway obstruction. In such cases, where fetal intervention is being considered, MR imaging of now routinely performed in many centers. If there is a question of a scalp mass vs. an encephalocele, MR imaging can be helpful in demonstrating a normal (or abnormal) brain. Newer applications of MR imaging of the fetus include evaluation for cleft soft palate, which is difficult to diagnose by sonography. This chapter reviews the normal anatomy of the fetal face, skull, and neck and describes common pathology involving these areas.

NORMAL ANATOMY

As with all fetal MR examinations, visualization of the fetus in planes orthogonal to fetal anatomy is helpful. This is especially important in assessing axial and coronal views of the face where symmetry, or lack of symmetry, can aid in diagnosis.

A true midline sagittal image is very important for assessing the profile and the soft palate (Fig. 4.1). The scalp closely approximates the skull and normally cannot be seen as a separate layer against the cranium early in the second trimester. However, as fetal fat increases, the skin can be observed as a separate layer from the skull. The external ear can be well visualized on axial and sagittal MR images (Fig. 4.2).

Figure 4.3 illustrates views of the normal face. The orbits are best evaluated on coronal and axial MR images of the fetal face (Fig. 4.4). Normal orbits are symmetric in size and shape and positioned with expected interocular and binocular distance based on gestational age [Fig. 4.4(b)]. Normative values have been established with ultrasound (1,2) but can be used for MR imaging. The lens is visualized as a lower signal intensity disc in the anterior portion of the fluid-filled globe. The corneal protrusion and lens indicate the direction of fetal eye position, which may be disconjugate (Figs. 4.3 and 4.4).

The fetal nose is well visualized in profile on midline sagittal view (Fig. 4.1). Images in the coronal plane are also useful, as late in gestation the nasal passages and concha are outlined by amniotic fluid (Fig. 4.3). Fluid motion caused by fetal exhalation can also be observed (Fig. 4.5). Sequential coronal images show the nose, lips, and palate (Fig. 4.3). Axial images in the plane of the maxilla demonstrate toothbuds, which should appear as a smooth continuous arc (Fig. 4.6) with 10 symmetric toothbuds (3). The palate consists of the hard palate and soft palate, which together form the roof of the mouth and the floor of the nose. The primary palate is a triangular area of the anterior hard palate extending from anterior to the incisive foramen to a point just lateral to the lateral incisor teeth. It includes that portion of the alveolar

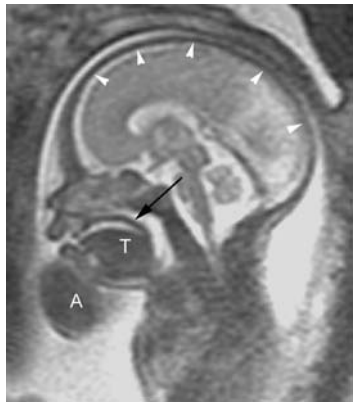

Figure 4.1 Normal profile at 27 weeks gestation. Sagittal midline T_2-weighted image demonstrates the normal appearance of the skull (arrowheads), nose, upper lip, lower lip, tongue (T), and chin at 27 weeks gestation. The secondary palate can be visualized directly on fetal MR imaging and is particularly well seen as a continuous band of soft tissue intensity extending from the primary palate to the posterior oropharynx when surrounded by amniotic fluid (arrow). A portion of an arm (A) is seen anterior to the chin. Note the relatively low signal intensity of the skull, which blends into the subcutaneous tissues (except where subcutaneous fat can be seen), most prominent in this image behind the neck and around the chin.

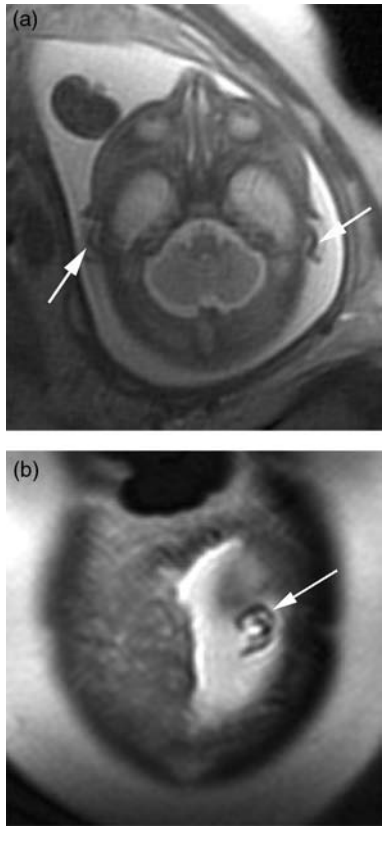

Figure 4.2 Axial (a) and sagittal (b) T_2-weighted images of normal fetal external ears (arrows) at 27 weeks gestation.

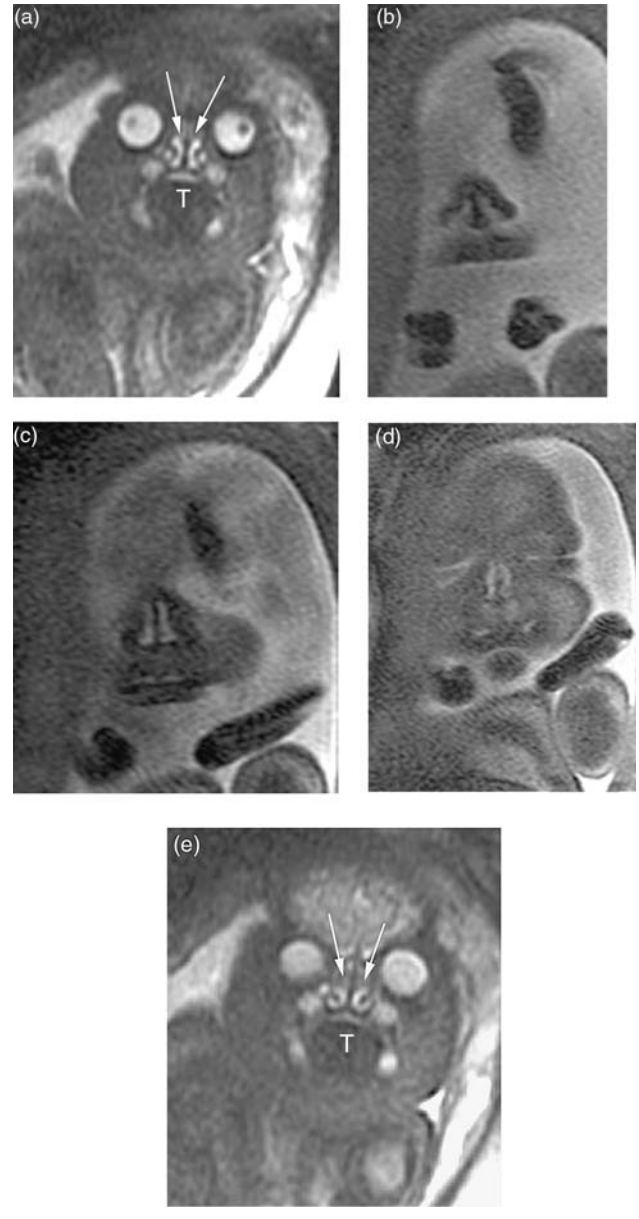

Figure 4.3 Normal fetal face. Coronal T_2-weighted images at 36 weeks gestational age (a–c) illustrate the nose, lips, and eyelids. Coronal T_2-weighted images at 37 weeks gestational age (in a different fetus, d and e) show the orbits, tongue (T), and nasal concha (arrows).

ridge containing the four incisor teeth. The secondary palate consists of the remaining hard palate and all of the soft palate. Although the lips and hard palate can be assessed on sonography, the soft palate is almost impossible to visualize directly because of shadowing by bones. Midline sagittal MR images demonstrate the normal secondary palate as a smooth curve of soft tissue extending posteriorly through the oropharynx [Fig. 4.1(c)].

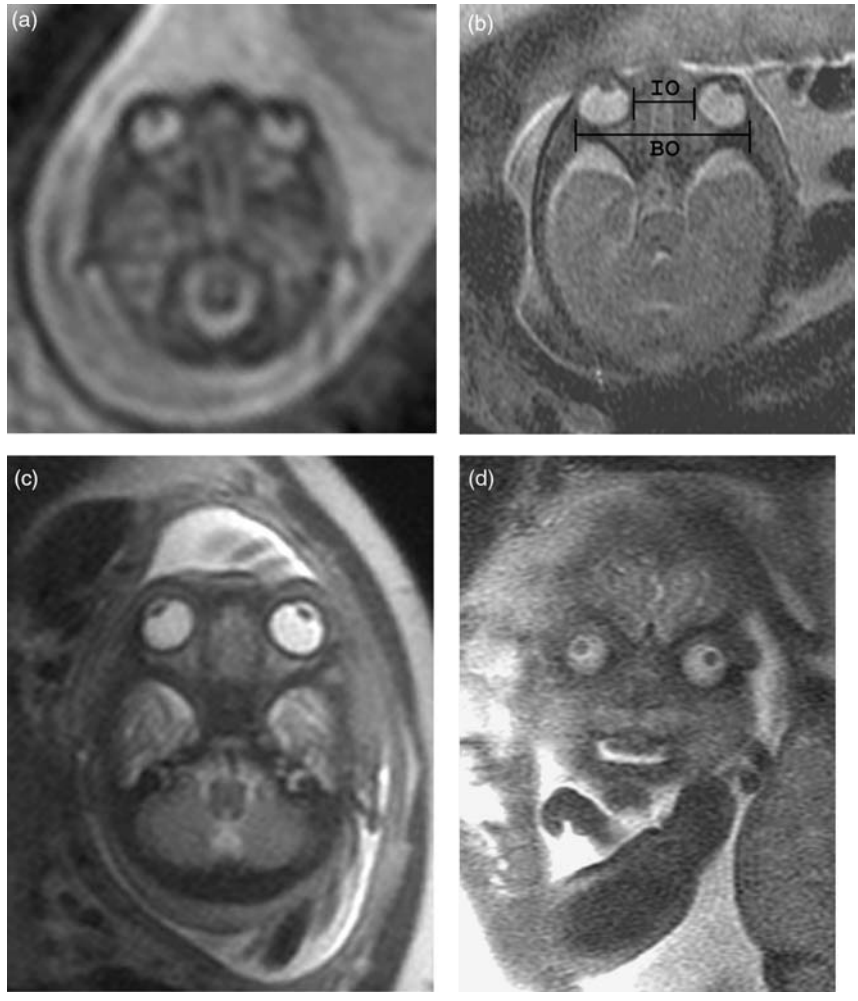

Figure 4.4 Normal orbits. T_2-weighted images of the orbits in axial plane at 18 (a), 27 (b), and 30 weeks gestational age and in coronal plane at 38 weeks gestational age. (b) and (d) were obtained with a higher matrix size than (a) and (c). This gives better resolution but more noise. Measurements of interocular distance (IO) and binocular distance (BO) on MR imaging can be made in a similar manner to that utilized in obstetric US, as shown in (b). Standard sonographic tables can be utilized to assess these measurements. The lens is a dark structure in the fluid-filled globe and may demonstrate disconjugate gaze (c, d), a normal finding in the fetus.

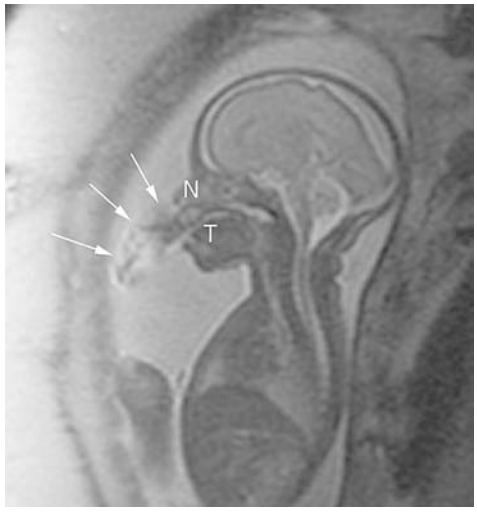

Figure 4.5 Sagittal T_2-weighted image demonstrating fluid motion at 26 weeks gestational age. The fetus was most likely exhaling from the nose (N) during image acquisition causing the fluid immediately anterior to the face (arrows) to lose signal, imitating a mass. T, tongue. [From Levine et al. (22)]

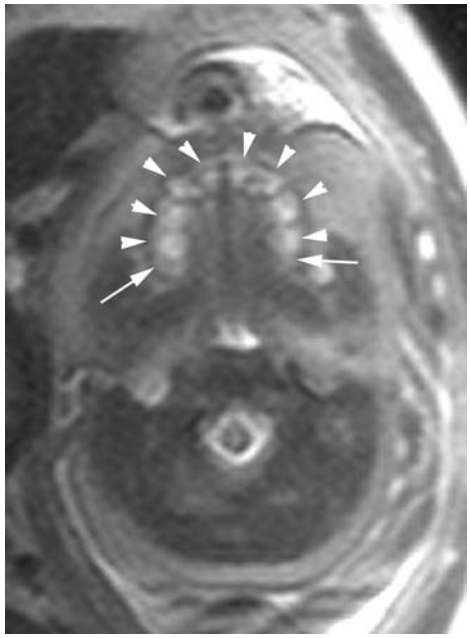

Figure 4.6 Axial T_2-weighted image of the maxilla at 35 weeks gestational age. The normal maxilla has a continuous horseshoe-shaped curve with 10 symmetric toothbuds. In this example, four toothbuds (arrowheads) are clearly seen on each side with the fifth toothbud being partially visualized because of being slightly out of the plane of imaging (arrows). [From Levine (34)]

Sequential midline images obtained at 4 second intervals (time delay to allow for improved signal-to-noise ratio on sequential images) allow for the visualization of fetal swallowing, which allows amniotic fluid to fill the oropharynx and outline the soft palate. This midline sagittal MR image is particularly important in the assessment of the palate, because the soft palate cannot be visualized directly using sonography.

The mandible is best assessed on sagittal midline images (Fig. 4.1) (4). If micrognathia is suspected, axial views can be obtained for mandibular measurements. The pharynx is best visualized during swallowing, when distended by amniotic fluid (Fig. 4.7). The trachea is visualized as a fluid-filled structure anterior to the spine (Fig. 4.7). When distended by fluid, both the esophagus and the trachea can be visualized as parallel tubular structures in the neck (Fig. 4.8) (5).

The neck normally has a thin layer of subcutaneous fat on the dorsal aspect, separating skin from deep structures [Fig. 4.1(e)]. It is common to observe one to two loops of umbilical cord encircling the fetal neck, that is, a nuchal cord (Fig. 4.9). If there are two or fewer loops of cord around the neck, this finding is unlikely to be of clinical concern.

PATHOLOGY

Skull Shape

There are many causes for an abnormal fetal skull shape. Some of the more common abnormalities seen on fetal MR examinations include macrocrania due to hydrocephalus or tumor (Chapter 3, Figs. 3.7 and 3.42), craniosynostosis (premature closure of sutures, Fig. 4.10), frontal bossing (unusually prominent forehead) in association with dwarfism, indentation of the frontal bones in association with neural tube defect (Fig. 4.11), or "strawberry skull" associated with trisomy 18. In addition,

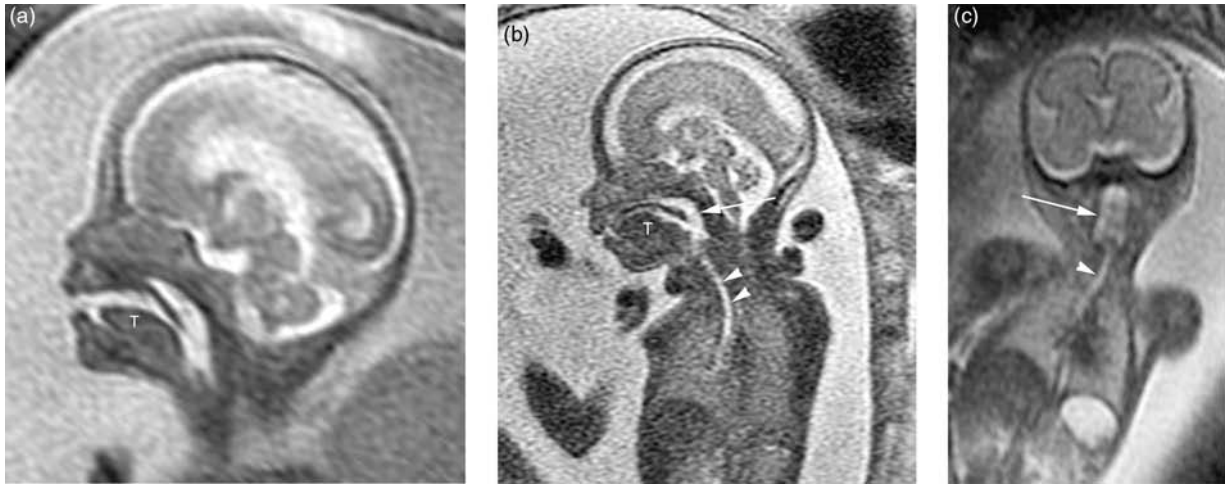

Figure 4.7 Sagittal (a and b) and coronal (c) T_2-weighted images of the normal oropharynx in fetuses at 24–25 weeks gestation. The tongue (T) and soft palate are outlined by amniotic fluid in (a and b). Observe the vallecula (arrow) and trachea (arrowheads) in (b and c).

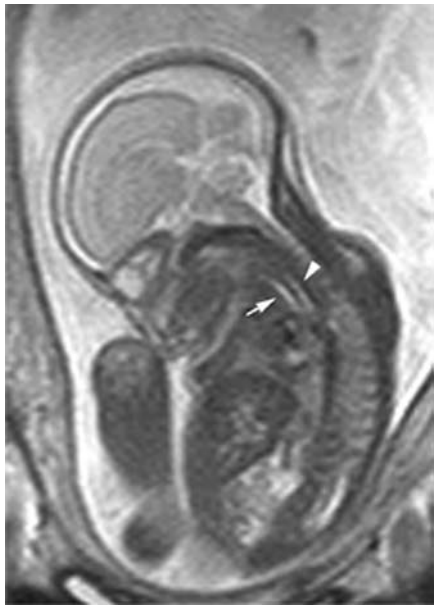

Figure 4.8 Oblique sagittal T_2-weighted image of the esophagus and trachea in a fetus with microgastria at 24 weeks gestational age. The stomach was not visualized on this or other images. Note the parallel, tubular (white) structures representing the fluid-filled esophagus (arrowhead) and trachea (arrow). [From Levine (5)]

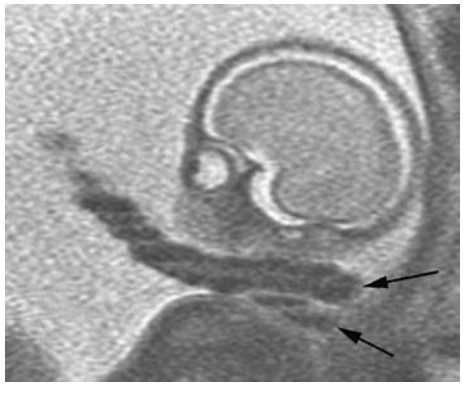

Figure 4.9 Sagittal T_2-weighted image of nuchal cord (arrows) at 25 weeks gestation. One loop of umbilical cord encircling the neck is a common finding of no significance.

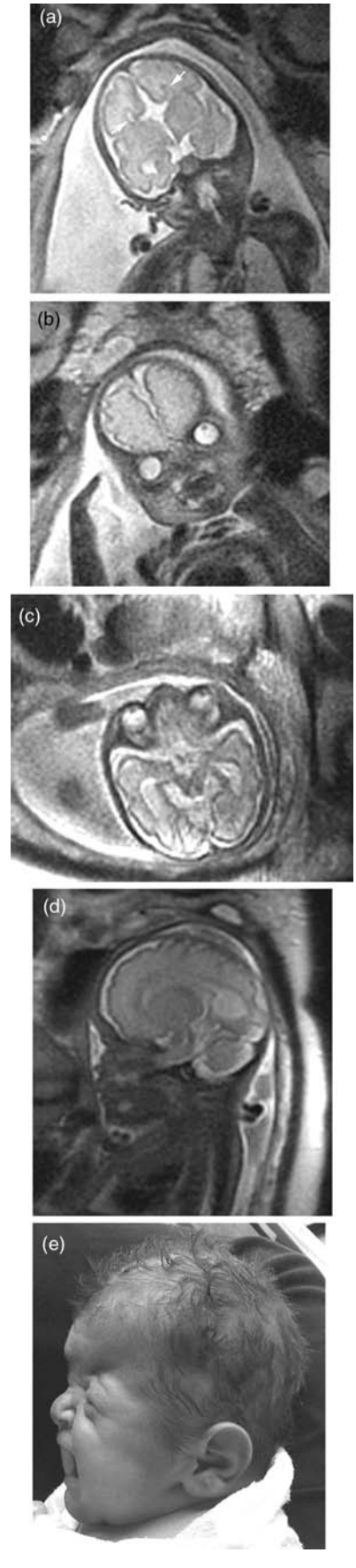

Figure 4.10 Craniosynostosis. Coronal (a and b), oblique axial (c), and sagittal (d) T_2-weighted images at 32 weeks gestational age of a fetus with Aperts syndrome with agenesis of the corpus callosum (note parallel orientation of the frontal horns, arrows, and lack of corpus callosum crossing midline), and mild hypertelorism. The turricephaly (elongation of the skull) and brachycephaly are caused by premature closure of the coronal sutures. The actual fusion of the bones cannot be visualized in these images, but the abnormal skull shape can be identified. The orbits are shallow leading to exorbitism. There is midfacial retrusion. Postnatal photograph (e) illustrates the facial features. This is the same fetus as in Chapter 3, Fig. 3.63 and Chapter 7, Fig. 7.26.

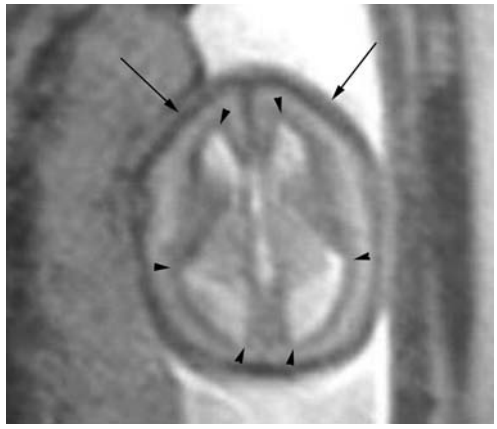

Figure 4.11 Axial T_2-weighted image of fetal head at 21 weeks gestational age with neural tube defect. Note the flattening of frontal bones (lemon sign, arrows) associated with neural tube defect. The cerebral ventricles have an angular appearance (arrowheads), which is also a feature associated with neural tube defect. Further examples of neural tube defects are described in Chapters 3 and 7. [From Levine (34)]

when the brain is abnormally small, there is often a sloped appearance to the forehead (Fig. 4.12), which is associated with hypoplastic or dysplastic frontal lobes.

Scalp Masses

When an extracranial mass is identified on prenatal US examination, encephalocele is of utmost concern (Chapter 3, Figs. 3.15–3.19). If no calvarial defect is identified, other causes include a cystic hygroma, subcutaneous edema, cervical teratoma, mesenchymal sarcoma, hemangioma, or epidermal cyst (6). In cases where sonographic examination cannot fully determine the extent of neuronal involvement in a cephalocele, MR imaging can often demonstrate the presence or absence of brain parenchyma in the cephalocele and can differentiate a cephalocele from a more benign soft tissue lesion of the scalp (Fig. 4.13) (6,7).

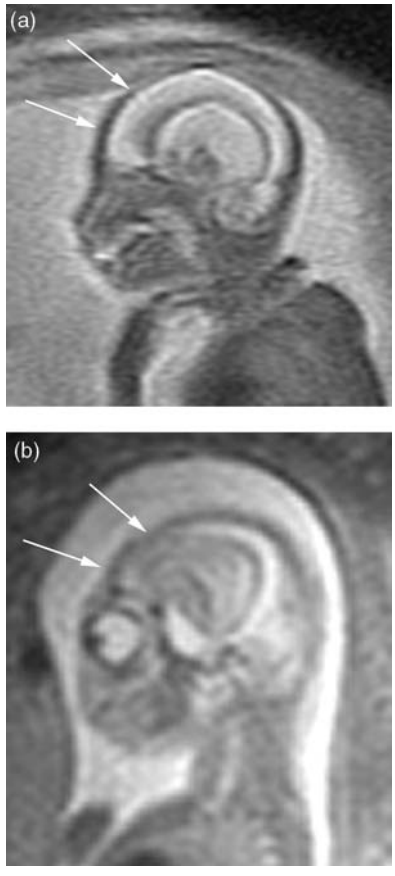

Figure 4.12 Sagittal T_2-weighted images at 18–19 weeks gestational age of two different fetuses, each with a dysgenetic brain and an abnormally sloped forehead (arrows). (a) was obtained with a higher matrix size than was (b). This provides better resolution but more noise.

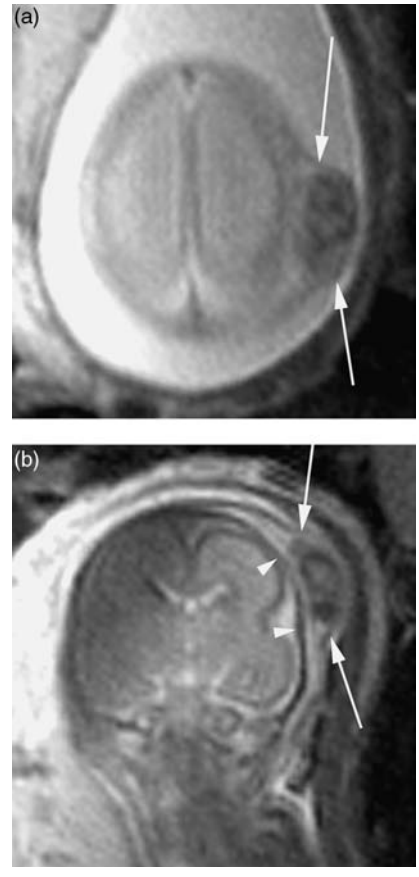

Figure 4.13 Scalp hemangioma at 22 weeks gestational age. Axial (a) and coronal (b) T_2-weighted images show skin thickening with a low signal intensity mass (arrows) protruding from the soft tissues of the scalp external to the skull (arrowheads). The mass does not involve intracranial contents. [From Levine (34)]

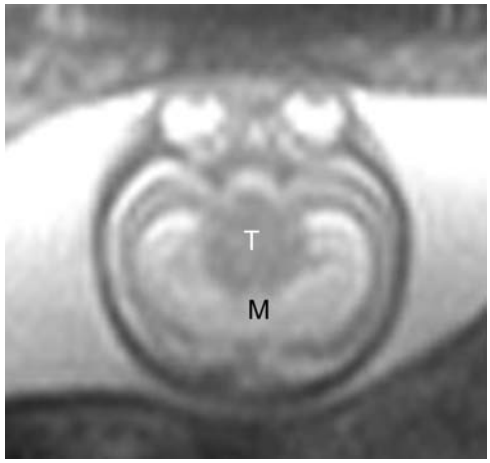

Figure 4.14 Oblique coronal T_2-weighted image at 19 weeks gestation of a fetus with hypotelorism and holoprosencephaly. A single monoventricle (M) is present as well as a fused thalamus (T). The interventricular cerebrospinal fluid has increased signal intensity which is caused by motion artifact. [From Stroustrup Smith et al. (13)]

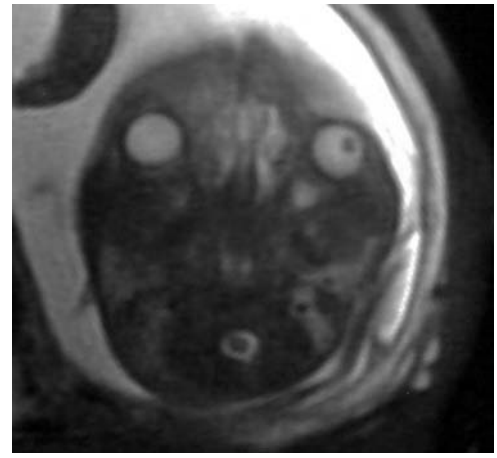

Figure 4.16 Hypertelorism at 33 weeks gestation. Axial T_2-weighted image of a fetus with hypertelorism and complex intracranial malformation. The widely spaced orbits are well visualized on this image. The other findings of intracranial cyst, cleft lip, and palate and agenesis of the corpus callosum are not shown on this image. [From Levine (34)]

Orbit Abnormalities

Hypotelorism

Hypotelorism refers to a decrease in the normal interocular distance, typically below the fifth percentile for gestational age (Figs. 4.14 and 4.15) (1). Hypotelorism is most commonly associated with holoprosencephaly (Fig. 4.14), although it can occur with a variety of other chromosomal abnormalities, syndromes (Fig. 4.15), and anomalies of skull development (8).

Hypertelorism

Hypertelorism, or abnormally wide-set eyes, can result as an isolated abnormality or as one part of numerous syndromes (Fig. 4.16). The most common cause of hypertelorism, however, is mechanical disruption of migration of the orbits from a lateral to a more anterior position because of the presence of an anterior cephalocele (Chapter 3, Fig. 3.18) (9).

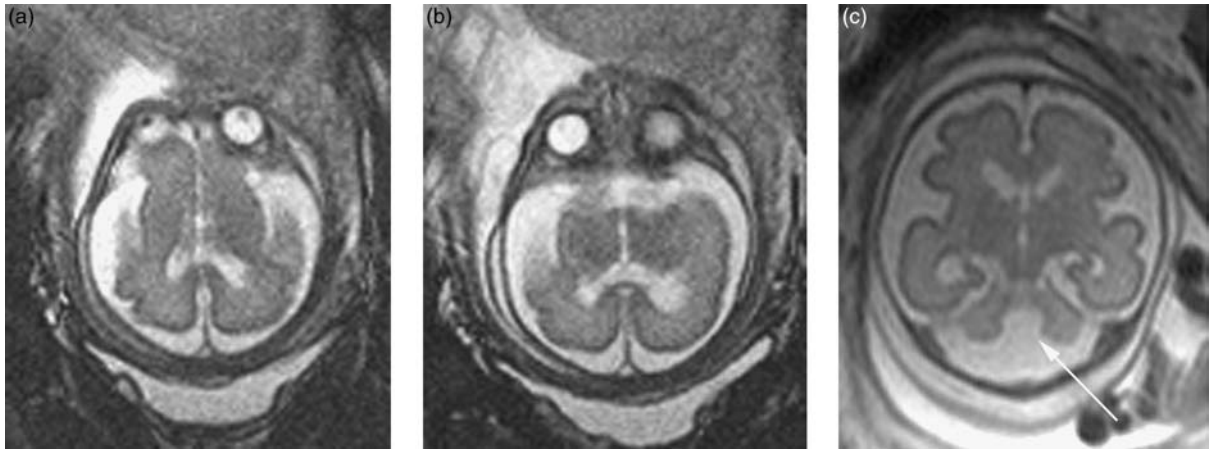

Figure 4.15 Hypotelorism and Dandy-Walker malformation at 29 weeks gestational age. Axial (a and b) and coronal (c) T_2-weighted images demonstrate the close position of the orbits and "keyhole" deformity (arrow) characteristic of cerebellar vermis agenesis.

Microphthalmia and Anophthalmia

Microphthalmia, an orbit measuring below the fifth percentile for gestational age, is rarely detected by prenatal sonography (10). It can be easily detected on fetal MR examinations, however, as either an unilateral (Fig. 4.17) or a bilateral finding. Microphthalmia is associated with karyotype abnormalities, teratogen exposure, and both sporadic and heritable genetic syndromes (8). Anophthalmia (absence of the eye) results from failure of the formation of the optic vesicle. The orbit is also small or absent (Fig. 4.18).

Proptosis

A protruding appearance to the globes can be due to a variety of causes such as an orbital encephalocele (Fig. 4.17) or shallow orbits in association with craniosynostosis (Fig. 4.10).

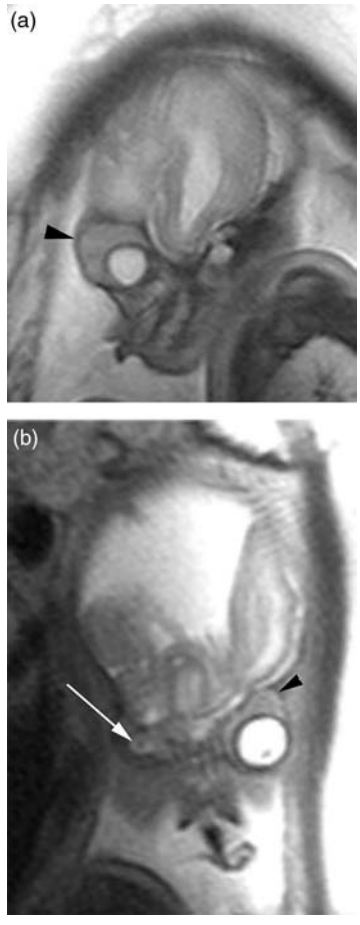

Figure 4.17 Orbital encephalocele, microphthalmia at 33 weeks gestational age. Left parasagittal (a) and coronal (b) T_2-weighted images show an orbital encephalocele on the left (arrowhead) and microphthalmia (arrow) on the right. The fetal brain is severely dysgenetic. There is a loop of cord anterior to the nose on image (b).

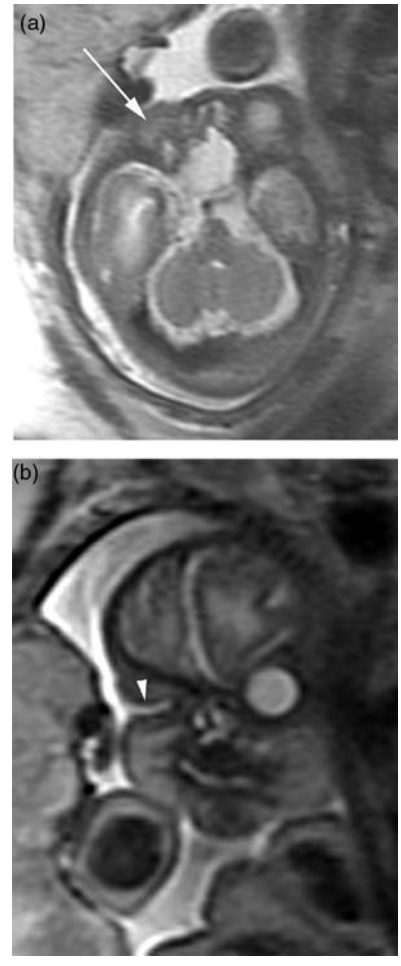

Figure 4.18 Axial (a) and coronal (b) T_2-weighted images of a 35 week gestational age fetus with absent right globe (arrows). (Same fetus as Chapter 3, Fig. 3.38.)

Midface Retrusion and Hypoplasia

Midface retrusion (Fig. 4.10) and hypoplasia (Fig. 4.19) can be present in a variety of syndromes, in association with median facial cleft, and in teratogen exposure (Fig. 4.19). Sagittal views demonstrate the flattened midface and absent or hypoplastic nose.

Cleft Lip and Palate

Cleft Lip With or Without Cleft Palate

Cleft lip with or without cleft palate can occur as a unilateral (Figs. 4.20 and 4.21) or bilateral (Fig. 4.22) defect (11). Cleft lip and/or palate often occurs as part of a syndrome or with a chromosomal abnormality (12). Fetal MR imaging provides information about the palate that can aid in prenatal counseling (13,14). In cases of complete clefts

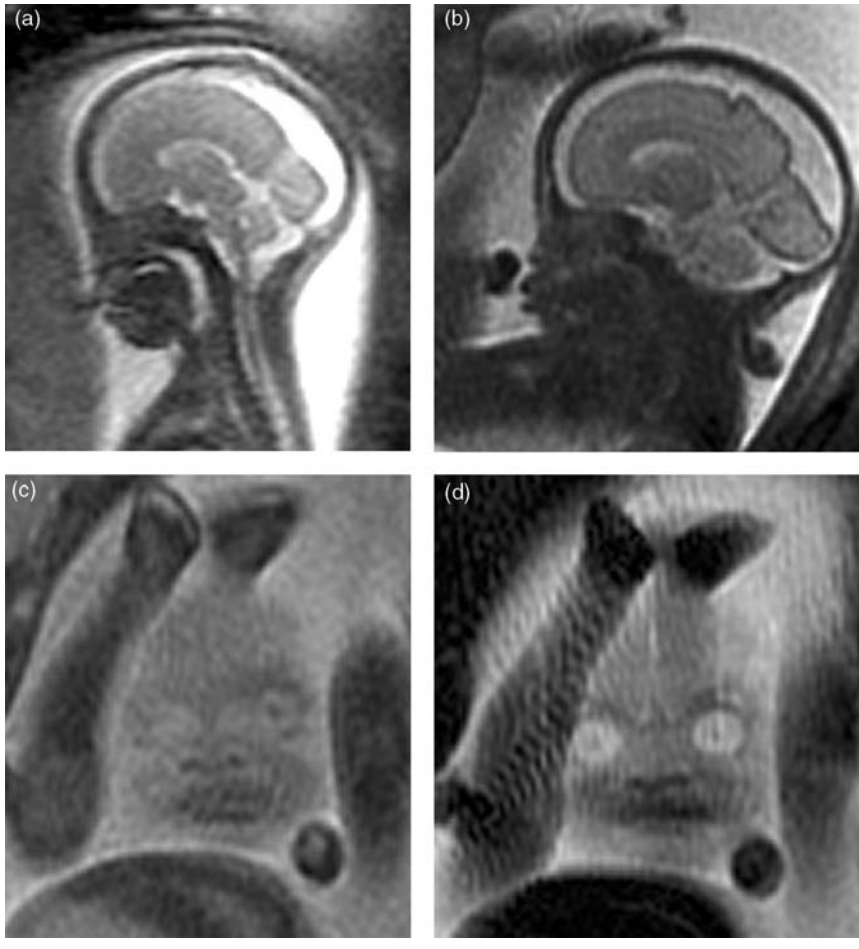

Figure 4.19 Sagittal T_2-weighted images at 25 weeks (a), and sagittal (b) and coronal (c and d) images at 31 weeks gestation of a fetus evaluated for midface hypoplasia and hypoplastic nose after Tegretol exposure early in pregnancy. Note the flattened appearance of the midface. (d) is taken with a 20 mm slice thickness in order to show the midface features in a single image.

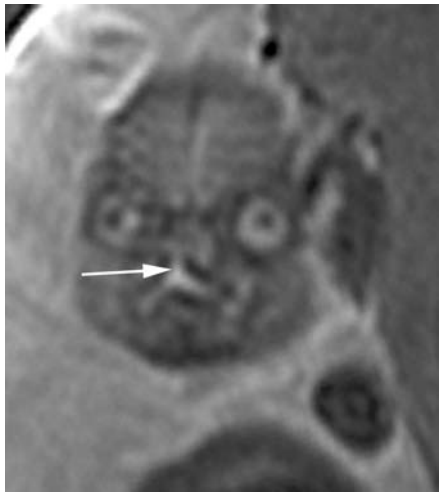

Figure 4.20 Unilateral cleft lip and palate at 20 weeks gestational age. Coronal T_2-weighted image shows a right-sided cleft (arrow) filled with amniotic fluid. The cleft extends through the upper lip to the nose and communicates with the nasal passages. This was confirmed on other images and postnatally. Note hypertelorism.

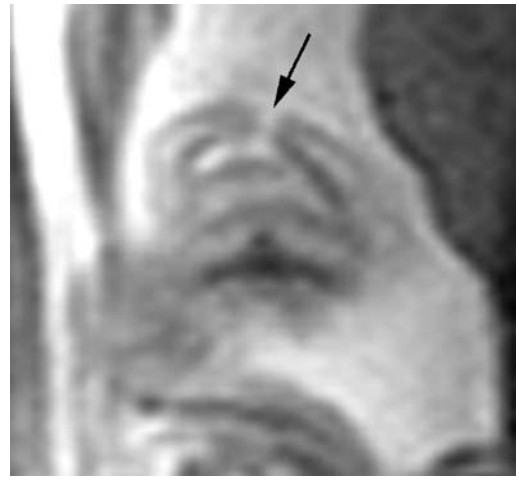

Figure 4.21 Cleft lip without cleft palate at 24 weeks gestational age. Oblique coronal T_2-weighted image shows an unilateral cleft lip (arrow). [From Stroustrup Smith et al. (13)]

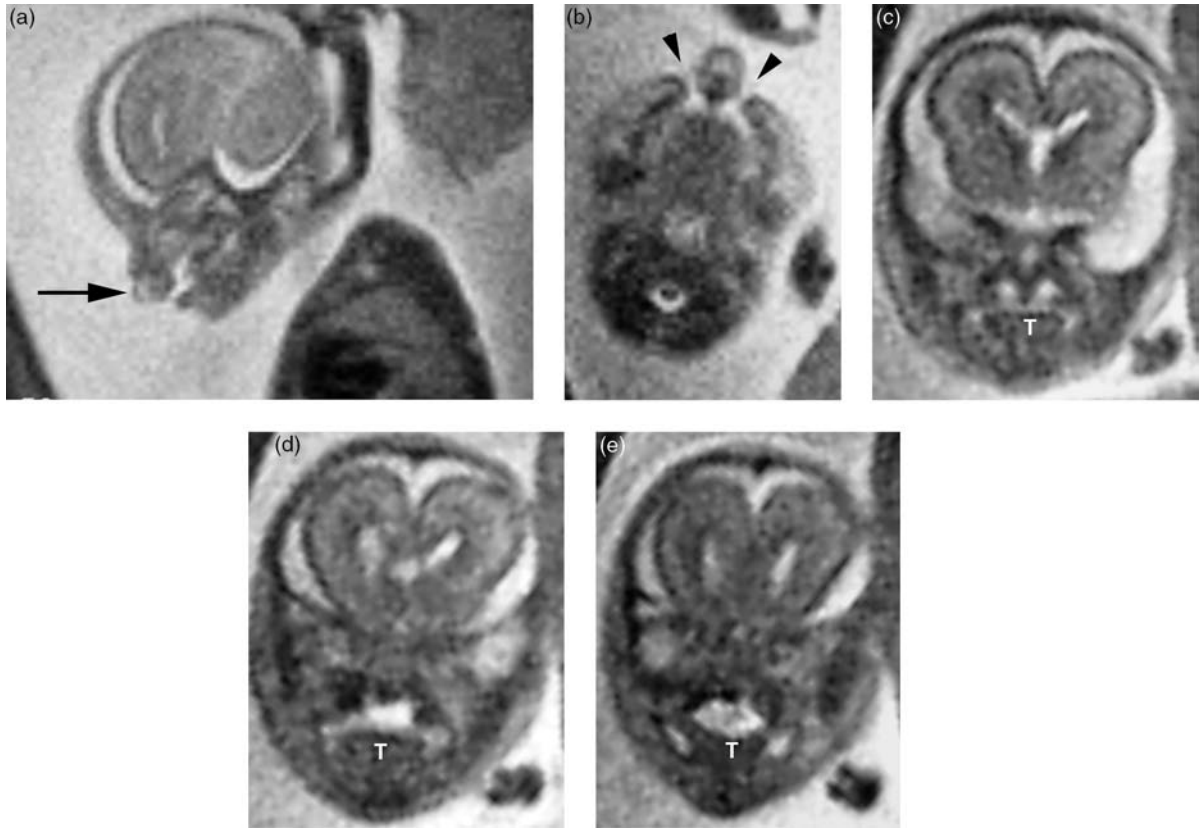

Figure 4.22 Sagittal (a), axial (b), and coronal (c–e) T_2-weighted images at 18 weeks gestation of a fetus with bilateral complete cleft lip and palate. Note the premaxillary protrusion as the median nasal prominence is elevated on the sagittal view (arrow). The bilateral clefts in the primary palate (arrowheads) are well seen on the axial view. The primary and secondary palate defects are observed as amniotic fluid communicates between the oro- and nasopharynx, appearing best on the coronal images as bright signal extending upwards from the tongue (T). (Images courtesy of S. Ulrich, Perth, Australia.)

of the lip and/or palate, the cleft extends through the upper lip to the nose, forming a channel easily observed on fetal MR images as it fills with amniotic fluid (Figs. 4.20 and 4.22). Additional abnormalities such as a flattened nose with short columella in bilateral complete clefts (Fig. 4.22) or the deviation of the nasal septum in unilateral clefts (Fig. 4.23) are also common in fetuses with facial clefts (13). When a cleft is complete and bilateral, the median nasal prominence elevates and forms a characteristic premaxillary protrusion (Fig. 4.22).

Isolated Cleft Palate

Cleft secondary palate in the absence of any anterior defect is etiologically different from, and much less common than, cleft lip with or without cleft palate (15). Isolated cleft palate is rarely diagnosed by sonography, but can be identified on fetal MR examinations when the absence of the secondary palate on midline sagittal view is noted (Figs. 4.24 and 4.25). For this evaluation, real-time imaging is helpful because it allows repeated

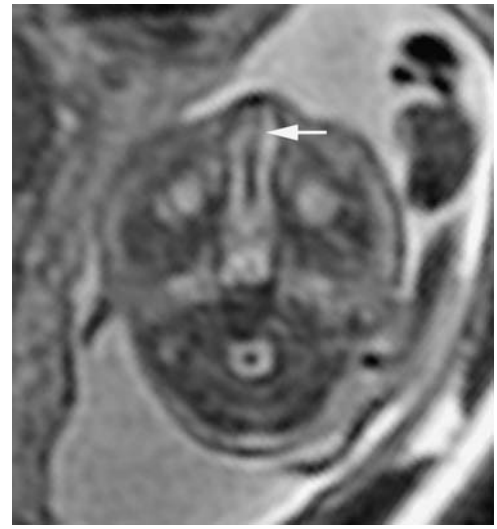

Figure 4.23 Deviated nasal septum in association with facial cleft at 28 weeks gestational age. Axial T_2-weighted image shows the deviated septum (arrow) in a fetus with an unilateral left cleft (cleft not shown on this image).

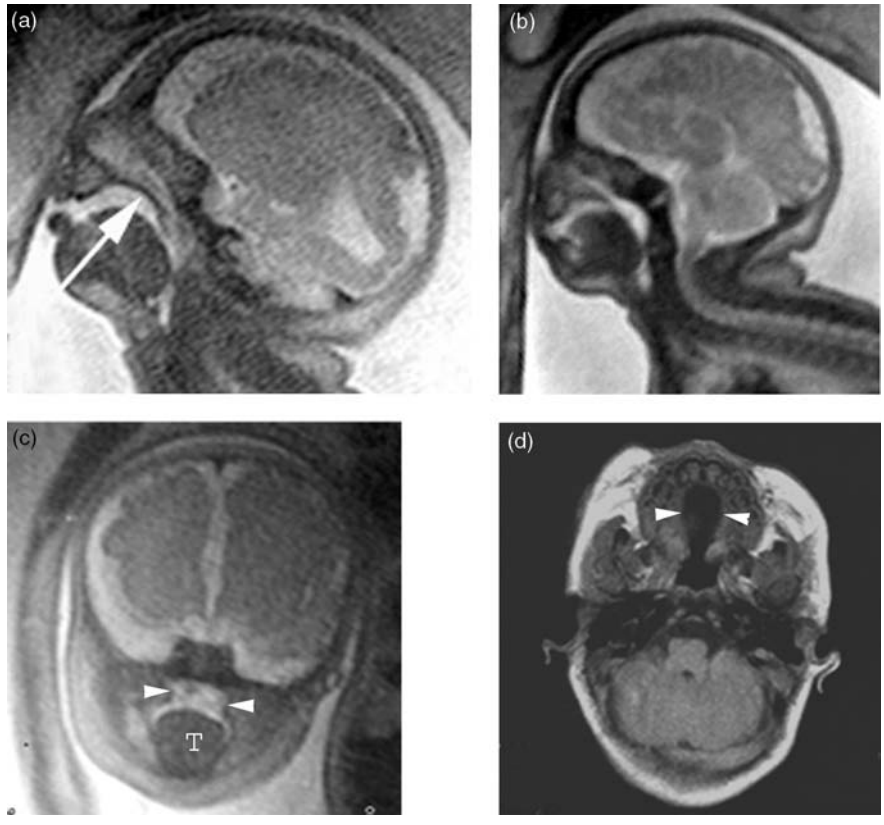

Figure 4.24 Pre- and postnatal imaging of cleft soft palate in fetus with agenesis of the corpus callosum. The cleft secondary palate was not detected prenatally, although in retrospect it can be visualized. Sequential sagittal T_2-weighted images (a and b) at 33 weeks gestation show the secondary palate present off midline (a, arrow) but cleft soft palate centrally (b). Coronal T_2-weighted image (c), also at 33 weeks gestation, demonstrates communication between the oropharynx and nasopharynx in a plane posterior to the primary palate. Note the fluid extending upwards from the tongue (T) due to the soft palate defect (arrowheads). Axial T_1-weighted image acquired after birth (d) demonstrates cleft secondary palate (arrowheads). As shown on this image, tissue of the secondary palate is present laterally, but not in the midline. [From Stroustrup Smith et al. (13)]

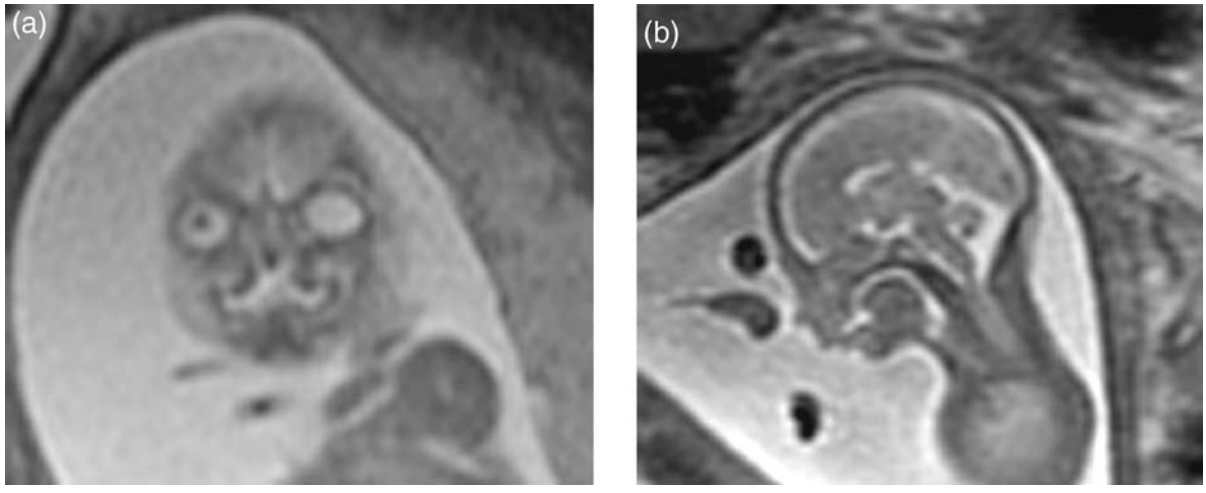

Figure 4.25 Coronal (a) and sagittal (b) T_2-weighted images at 19 weeks gestational age in fetus with micrognathia, retrognathia, and cleft soft palate without cleft lip. Note the high position of the tongue on the sagittal image and the absence of the soft palate. (Compare this to Fig. 4.1 where a normal soft palate is visualized). Note the small receding chin.

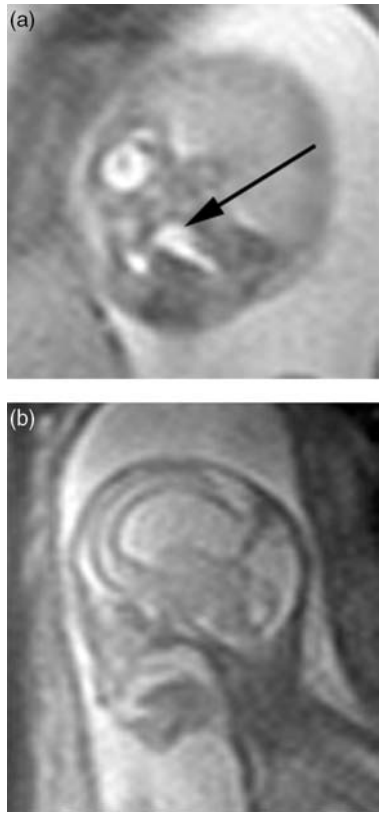

Figure 4.26 Midline cleft and midface hypoplasia with holoprosencephaly at 19 weeks gestation. Oblique coronal T_2-weighted image (a) shows the absence of midline tissue in the upper lip and palate (arrow). The left globe is not visualized secondary to the obliquity of the scan plane. Oblique sagittal T_2-weighted image (b) shows tissue of the soft palate present on paramidline imaging. Visualization of the lateral aspect of the soft palate is an important potential pitfall in the diagnosis of cleft soft palate. This is the same fetus as shown in Fig. 4.14. [From Stroustrup Smith et al. (13)]

images to be obtained in the midline sagittal plane during fetal swallowing. An important pitfall in the diagnosis of cleft soft palate is that soft tissue in normal and cleft soft palates is present laterally and can be mistaken for the midline soft palate (Figs. 4.24 and 4.26).

Median Cleft

A median facial cleft, often associated with midface hypoplasia and holoprosencephaly, is readily apparent on fetal MR imaging (Fig. 4.26). Coronal images demonstrate amniotic fluid in the midface region.

Mandibular Abnormalities

Micrognathia is a term often used to characterize a small and/or receding mandible, however, these are two different (often concurrent) conditions. Retrognathia and micrognathia are more specific descriptions of mandibular abnormalities. Retrognathia has been defined as being present when the angle between (1) the line orthogonal to the vertical part of the forehead at the level of the synostosis of the nasal bones and (2) the line joining the tip of the mentum and the anterior part of the most protruding lip is $<50^{\circ}$ on a sagittal midline view (Fig. 4.25) (16). Micrognathia is judged to be present when the mandible width/maxilla width ratio (obtained at the alveolar level 1 cm behind the anterior osseous border) is <0.8 (16,17). Micrognathia and retrognathia are associated with multiple syndromes and chromosomal abnormalities (Fig. 4.25) (18). Mandibular hypoplasia can displace the tongue superiorly which prevents normal development of the palate, resulting in a cleft soft palate (19). Magnetic resonance imaging can detect the soft palate defect in such cases. This is important in planning for delivery

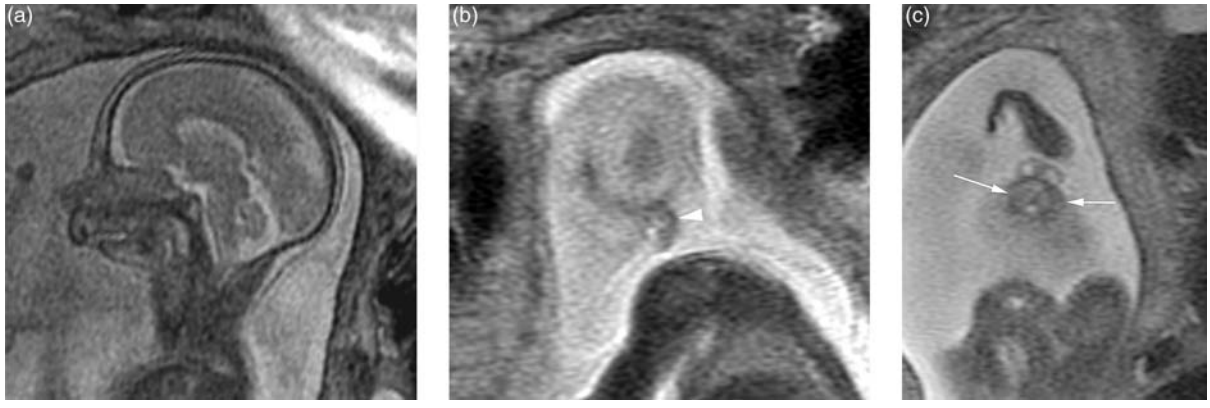

Figure 4.27 Agnathia–microstomia at 21 weeks gestational age. Sagittal midline (a) T_2-weighted image shows the absent mandible. Little, if any, muscular tissue is visualized in the expected region of the tongue. Lateral sagittal (b) image shows low-set ear (arrowhead). Coronal image (c) shows small mouth (arrows).

because cases with clefts are associated with airway obstruction at birth.

Agnathia is very rare and is commonly associated with microstomia (small mouth) and absent tongue (Fig. 4.27). The combination of ultrasound and MR imaging allows precise definition of the facial abnormalities in the syndromes associated with agnathia (10).

Masses of the Face and Neck

Excess soft tissue in the posterior neck area is associated with trisomy 21 and other chromosomal abnormalities and syndromes. On second trimester sonography, >5 mm of tissue and/or edema in the nuchal area is considered abnormal before 24 weeks gestation. Later in gestation, the diagnosis of nuchal thickening should be made with caution due to the normal increase in fetal subcutaneous fat. This nuchal thickening is visualized on MR imaging as an abnormal subcutaneous region of fluid intensity in the posterior neck (Figs. 4.28 and 4.29).

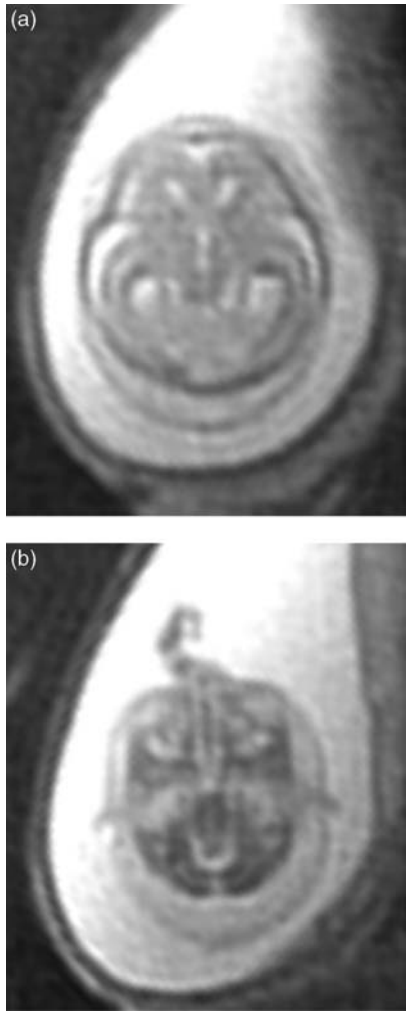

Figure 4.28 Axial T_2-weighted images demonstrate prominent nuchal thickening (measuring up to 11 mm) in a fetus with trisomy 21.

The most common neck mass *in utero* is a cystic hygroma. Cystic hygroma results from a congenital abnormality of the lymphatic system causing characteristic single or multiple cysts that can be visualized on ultrasound and MR imaging (Fig. 4.30) (20,21). Septations detected on sonography may be missed on MR imaging (22). Cystic hygroma has a high association with Turner syndrome, but can also occur in other chromosomal abnormalities and syndromes (23).

Congenital tumors of the face and neck are rare but are important because they may cause airway obstruction at the time of delivery. Lesions that can interfere with breathing include teratomas (Figs. 4.31–4.33), lymphangiomas (Fig. 4.34), hemangiomas; and goiter (24). Fetal MR imaging can demonstrate the size, location, and impact on adjacent structures (25). Especially important is the visualization of the entire airway. If the fluid-filled trachea cannot be visualized after repeated imaging through the region of a neck mass, the trachea can be assumed to be compressed, and the airway thus compromised. In these cases, an *ex utero* intrapartum treatment (EXIT) procedure, where the fetus is partially delivered and the airway is secured prior to cutting the umbilical cord, can be life-saving (25–31).

When assessing neck masses, the location and signal characteristics are helpful in differentiating types of tumors. Teratomas of the neck usually occur in the midline and may arise from the thyroid gland (Fig. 4.32) (32). Calcifications within the lesions are more easily observed with ultrasound than with MR imaging. Teratomas tend to be heterogeneous, well-circumscribed lesions. Fetal thyromegaly typically is assessed with ultrasound but may be visualized with MR imaging. T_1-weighted images are best to depict the thyroid (33). T_2-weighted images are used to visualize the airway. Lymphangiomas (Fig. 4.34) tend to invade tissue planes and surround major neurovascular structures. A key issue in prenatal assessment includes involvement of the tongue, because it can interfere with the infants' ability to swallow secretions. On MR imaging, these tumors appear cystic, sometimes with hemorrhage (25).

CONCLUSION

There are a wide variety of abnormalities of the fetal face, skull, and neck. Knowledge of the normal and abnormal

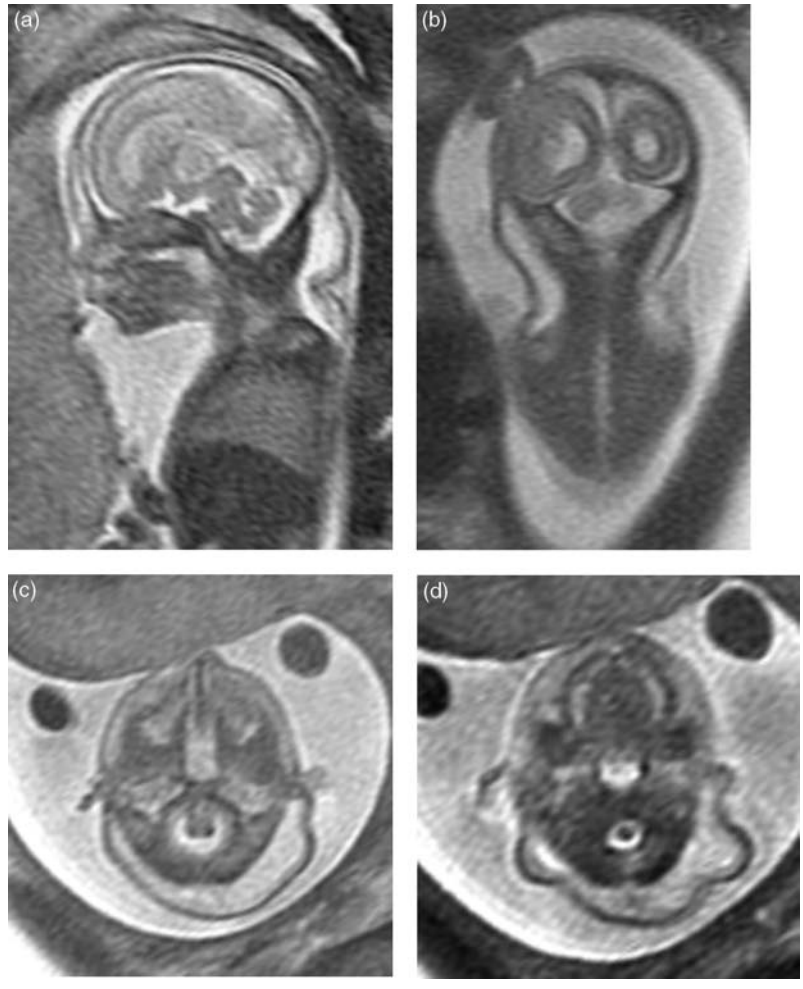

Figure 4.29 Large cystic hygroma in 21 weeks gestational age fetus with Turner syndrome. Sagittal (a), coronal (b), and axial (c and d) T_2-weighted images show a large fluid collection with wavy margins. Septations within the cystic hygroma were visible on the sonogram but not the MR examination.

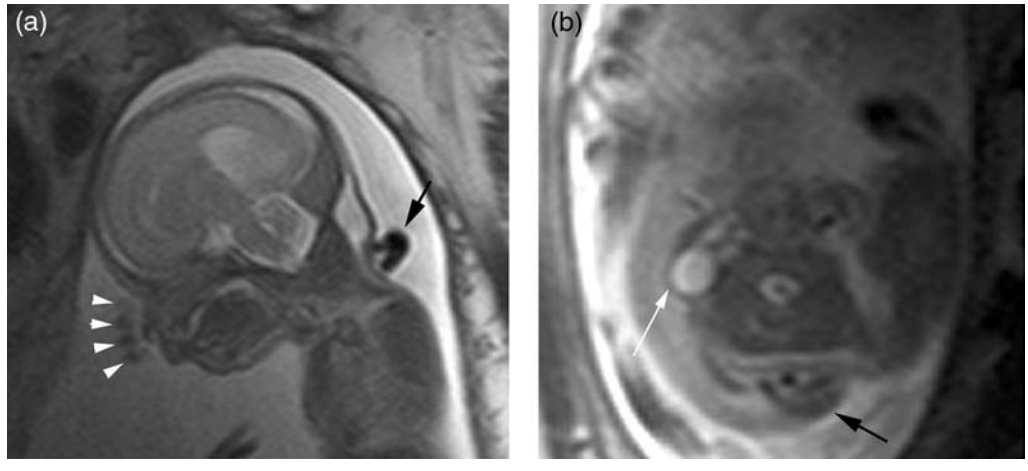

Figure 4.30 Nuchal thickening with focal fluid collections within the neck in 23 weeks gestational age fetus with Perlman syndrome. Sagittal (a) and axial (b) T_2-weighted images demonstrate nuchal thickening. A focal fluid collection is visualized in the right neck (arrow). A similar finding was seen in the left neck (not shown).

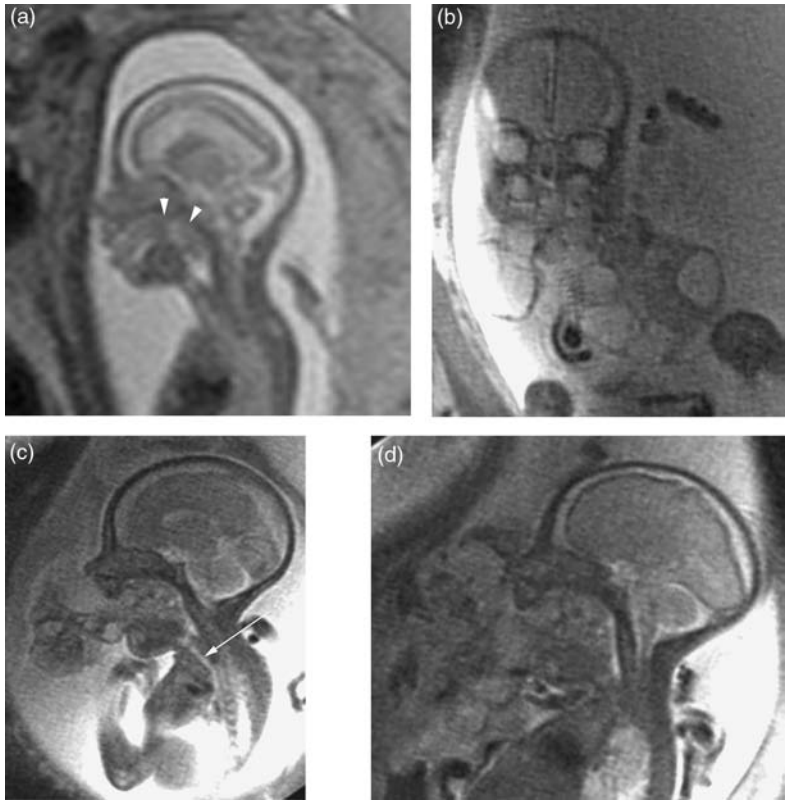

Figure 4.31 Oropharyngeal teratoma. Sagittal (a) T_2-weighted image at 16 weeks gestational age shows a soft tissue mass (arrowheads) filling the oropharynx. Coronal (b) and sagittal (c–d) T_2-weighted images at 28 weeks gestational age show a lobulated mass with both cystic and solid components that distends the mouth. A patent trachea in the mid and lower neck was demonstrated (c, arrow). This information (and information about a nuchal cord that also went around the fetal shoulder, not shown) was important for planning delivery by EXIT procedure in which the fetus is partially delivered by Cesarean section, a fetal airway is established—in this case by tracheotomy—while the umbilical cord is still intact, and only then is the delivery completed. The mass was surgically removed on day 1 of life, and reconstruction of the mandible was successful. [(a) from Morof et al. (26)]

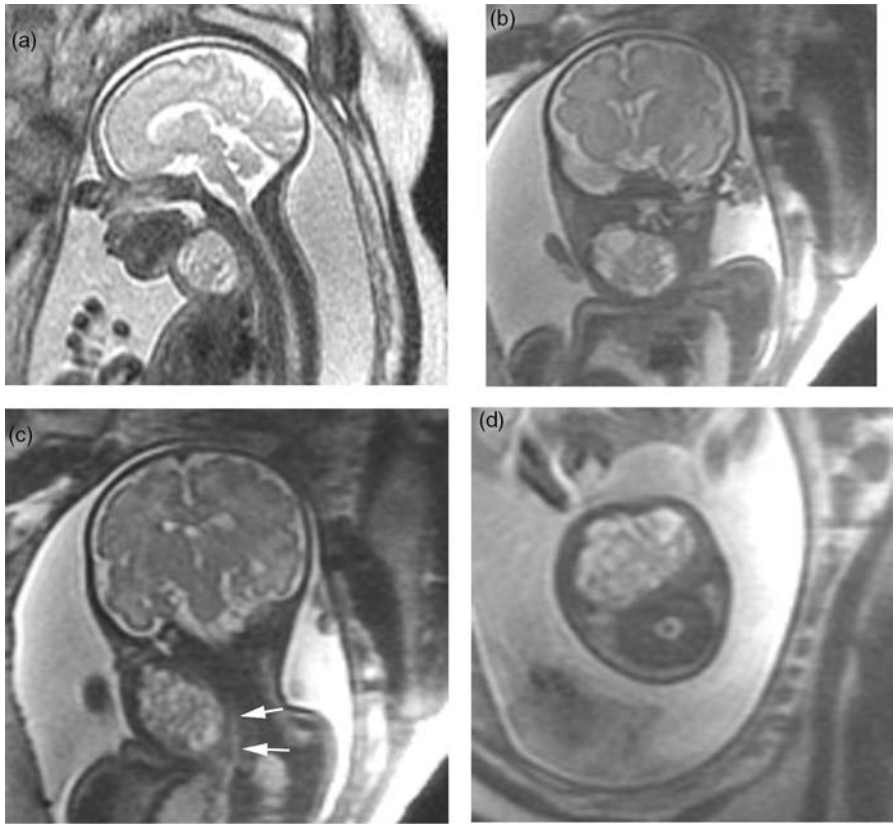

Figure 4.32 Thyroid teratoma at 33 weeks gestational age. Sagittal (a), coronal (b and c), and axial (d) T_2-weighted images show a heterogenous mass in the right neck. The mass displaces the trachea (arrows in c) but the trachea is patent throughout its course.

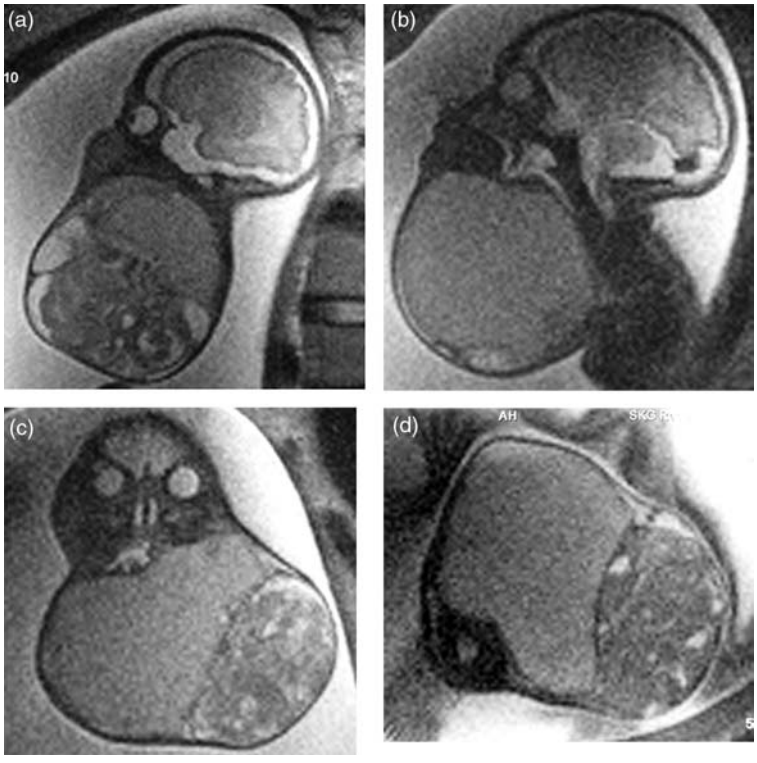

Figure 4.33 Cervical teratoma at 30 weeks gestational age. Sagittal (a and b), coronal (c), and axial (d) T_2-weighted images show a large heterogenous mass with components of differing signal intensities, suggestive of a teratoma. The mass extends into the neck and compresses the trachea. The fetus was delivered by EXIT procedure. (Images courtesy of S. Ulrich, Perth, Australia.)

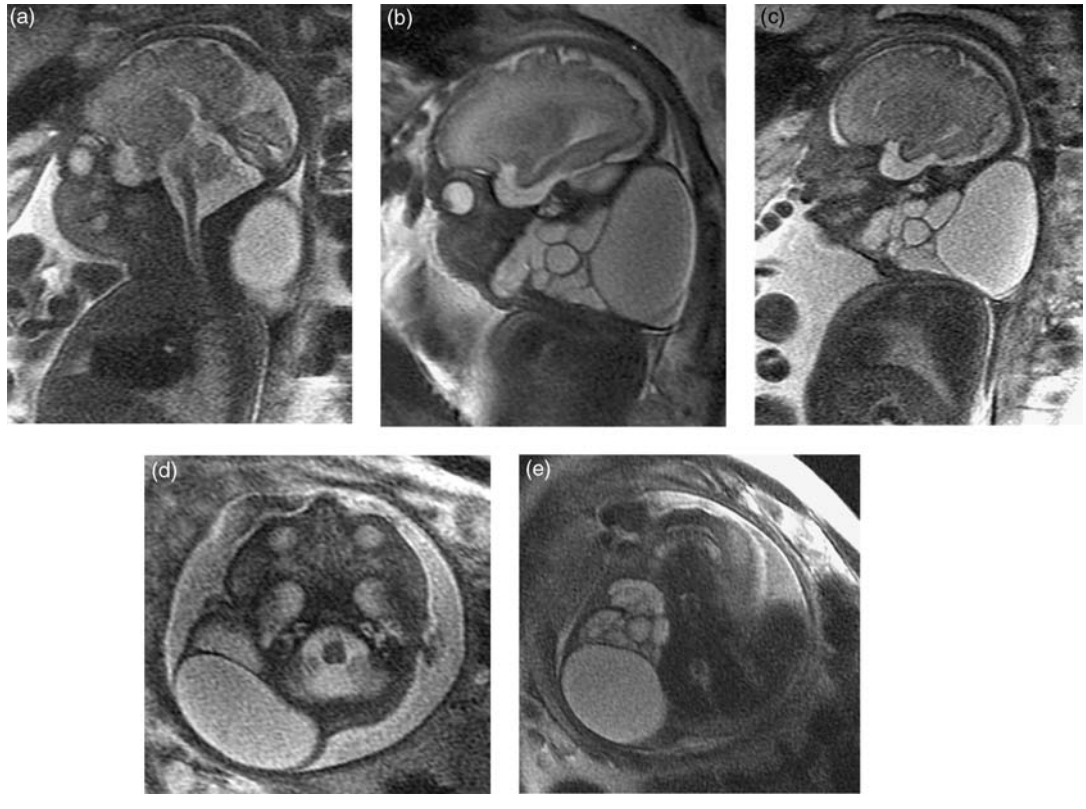

Figure 4.34 Lymphatic malformation at 33 weeks gestational age. Sagittal (a–c) and axial (d and e) T_2-weighted images show a lobulated cystic mass protruding from the neck.

appearance of these regions on MR imaging aids in diagnosis, helps guide *in utero* therapy, and can direct the mode of delivery in cases of potential airway obstruction.

REFERENCES

1. Trout T, Budorick NE, Pretorius DH et al. Significance of orbital measurements in the fetus. J Ultrasound Med 1994; 13:937–943.
2. Mayden KL, Tortora M, Berkowitz RL et al. Orbital diameters: a new parameter for prenatal diagnosis and dating. Am J Obstet Gynecol 1982; 144:289–297.
3. Ulm MR, Kratochwil A, Ulm B et al. Three-dimensional ultrasound evaluation of fetal tooth germs. Ultrasound Obstet Gynecol 1998; 12:240–243.
4. Turner GM, Twining P. The facial profile in the diagnosis of fetal abnormalities. Clin Radiol 1993; 47:389–395.
5. Levine D, Barnewolt CE, Mehta TS et al. Fetal thoracic abnormalities: MR imaging. Radiology 2003; 228:379–388.
6. Okaro E, Broussin B, Ville Y. Prenatal diagnosis of atypical cystic lesions of the fetal scalp. Ultrasound Obstet Gynecol 1998; 12:442–444.
7. Lau TK, Leung TN, Leung TY et al. Fetal scalp cysts: challenge in diagnosis and counseling. J Ultrasound Med 2001; 20:175–177.
8. Babcook CJ. The Fetal Face and Neck. Philadelphia, PA: W.B. Saunders, 2000:307–330.
9. Cohen MM Jr, Richieri-Costa A, Guion-Almeida ML et al. Hypertelorism: interorbital growth, measurements, and pathogenetic considerations. Int J Oral Maxillofac Surg 1995; 24:387–395.
10. Chen CP, Wang KG, Huang JK et al. Prenatal diagnosis of otocephaly with microphthalmia/anophthalmia using ultrasound and magnetic resonance imaging. Ultrasound Obstet Gynecol 2003; 22:214–215.
11. Hafner E, Sterniste W, Scholler J et al. Prenatal diagnosis of facial malformations. Prenat Diagn 1997; 17:51–58.
12. Benacerraf BR, Mulliken JB. Fetal cleft lip and palate: sonographic diagnosis and postnatal outcome. Plast Reconstr Surg 1993; 92:1045–1051.
13. Stroustrup Smith A, Estroff J, Barnewolt C et al. Prenatal diagnosis of cleft lip and cleft palate using MRI. Am J Roentgenol 2004; 183:229–235.
14. Ghi T, Tani G, Savelli L et al. Prenatal imaging of facial clefts by magnetic resonance imaging with emphasis on the posterior palate. Prenat Diagn 2003; 23:970–975.
15. Cash C, Set P, Coleman N. The accuracy of antenatal ultrasound in the detection of facial clefts in a low-risk screening population. Ultrasound Obstet Gynecol 2001; 18:432–436.
16. Rotten D, Levaillant JM, Martinez H et al. The fetal mandible: a 2D and 3D sonographic approach to the diagnosis of retrognathia and micrognathia. Ultrasound Obstet Gynecol 2002; 19:122–130.
17. Chitty LS, Campbell S, Altman DG. Measurement of the fetal mandible—feasibility and construction of a centile chart. Prenat Diagn 1993; 13:749–756.
18. Bromley B, Benacerraf BR. Fetal micrognathia: associated anomalies and outcome. J Ultrasound Med 1994; 13:529–533.
19. Hanson JW, Smith DW. U-shaped palatal defect in the Robin anomalad: developmental and clinical relevance. J Pediatr 1975; 87:30–33.
20. Kang L, Chang CH, Yu CH et al. Prenatal depiction of cystic hygroma using three-dimensional ultrasound. Ultrasound Med Biol 2002; 28:719–723.
21. Shinmoto H, Kashima K, Yuasa Y et al. MR imaging of non-CNS fetal abnormalities: a pictorial essay. Radiographics 2000; 20:1227–1243.
22. Levine D, Smith AS, McKenzie C. Tips and tricks of fetal MR imaging. Radiol Clin North Am 2003; 41:729–745.
23. Taipale P, Hiilesmaa V, Salonen R et al. Increased nuchal translucency as a marker for fetal chromosomal defects. N Engl J Med 1997; 337:1654–1658.
24. Shiraishi H, Nakamura M, Ichihashi K et al. Prenatal MRI in a fetus with a giant neck hemangioma: a case report. Prenat Diagn 2000; 20:1004–1007.
25. Hubbard AM, Crombleholme TM, Adzick NS. Prenatal MRI evaluation of giant neck masses in preparation for the fetal exit procedure. Am J Perinatol 1998; 15:253–257.
26. Morof D, Levine D, Grable I et al. Oropharyngeal teratoma: prenatal diagnosis and assessment using sonography, MRI, and CT with management by *ex utero* intrapartum treatment procedure. Am J Roentgenol 2004; 183:493–496.
27. Liechty KW, Crombleholme TM, Weiner S et al. The *ex utero* intrapartum treatment procedure for a large fetal neck mass in a twin gestation. Obstet Gynecol 1999; 93:824–825.
28. Kathary N, Bulas DI, Newman KD et al. MRI imaging of fetal neck masses with airway compromise: utility in delivery planning. Pediatr Radiol 2001; 31:727–731.
29. Stevens GH, Schoot BC, Smets MJ et al. The *ex utero* intrapartum treatment (EXIT) procedure in fetal neck masses: a case report and review of the literature. Eur J Obstet Gynecol Reprod Biol 2002; 100:246–250.
30. Rohrer SE, Nugent CE, Mukherji SK. Fetal MR imaging of lymphatic malformation in a twin gestation. Am J Roentgenol 2003; 181:286–287.
31. Hubbard AM, Harty MP. MRI for the assessment of the malformed fetus. Baillieres Best Pract Res Clin Obstet Gynaecol 2000; 14:629–650.
32. Azizkhan RG, Haase GM, Applebaum H et al. Diagnosis, management, and outcome of cervicofacial teratomas in neonates: a Childrens Cancer Group study. J Pediatr Surg 1995; 30:312–316.
33. Karabulut N, Martin DR, Yang M et al. MR imaging findings in fetal goiter caused by maternal graves disease. J Comput Assist Tomogr 2002; 26:538–540.
34. Levine D, Stroustrup Smith A, Barbaras L et al. Compendium of Fetal MRI [image]. In: Beth Israel Deaconess Medical Center Radiology department website. http://bidmc.harvard.edu/fetalatlas/, 2004.

5

MR Imaging of Fetal Thoracic Abnormalities

DEBORAH LEVINE

INTRODUCTION

A number of publications have described the benefit of magnetic resonance (MR) imaging in the evaluation of fetuses with thoracic abnormalities (1–10). In a study by Levine et al. (9), of 74 fetuses with thoracic abnormalities, MR imaging provided additional information over sonography in 28 (37.8%) patients. However, MR information regarding the thorax impacted care in only 6/74 (8.1%) fetuses. Prenatal thoracic MR is most likely to impact care in the fetal surgery patient and in the cases where the diagnosis is unclear by sonography.

NORMAL ANATOMY

Lung Signal Intensity

T_2 lung signal intensity in normal lungs is higher in older gestational age fetuses compared with younger gestational age fetuses (Figs. 5.1–5.3) (9,11). T_1 signal intensity similarly decreases with increasing gestational age (12). Normal lung volumes have been documented by MRI studies (11). There is growth of the lungs with increasing gestational age. This growth is proportionate to fetal body size.

Thoracic Vascularity

The main pulmonary arteries with first-order branches can be seen as flow voids in the central lungs (Fig. 5.2) (9). These are best visualized in the late second trimester and throughout the third trimester when the lungs display higher signal intensity and larger size than in the early second trimester (9). The aorta, superior vena cava, inferior vena cava, and ductal arch all can be viewed when the image is in the appropriate plane (Figs. 5.4–5.6) (44). The individual chambers of the heart are rarely visualized secondary to constant cardiac motion, but at times, the image is obtained either at just the right time for a single-shot image or at the correct phase of the cardiac cycle such that cardiac gating has occurred for images obtained during a breathhold (Fig. 5.7).

The Airway and Esophagus

The trachea, carina, and mainstem bronchi can be seen in many examinations of the chest (Fig. 5.8). Small portions of the esophagus are commonly visualized (9). The esophagus appears as a tubular structure in the posterior mediastinum. It is best visualized when the image acquisition coincides with the fetus swallowing a bolus of amniotic fluid or reflux occurs. The esophagus is then visualized as it is distended and filled with amniotic fluid (Fig. 5.9).

The Diaphragm

The diaphragm is visible as a thin dome-shaped band separating the abdomen from the thorax. It has low signal intensity on T_2-weighted images and is of a signal intensity slightly lower than that of the liver (14). It is most clearly seen on the coronal and sagittal images

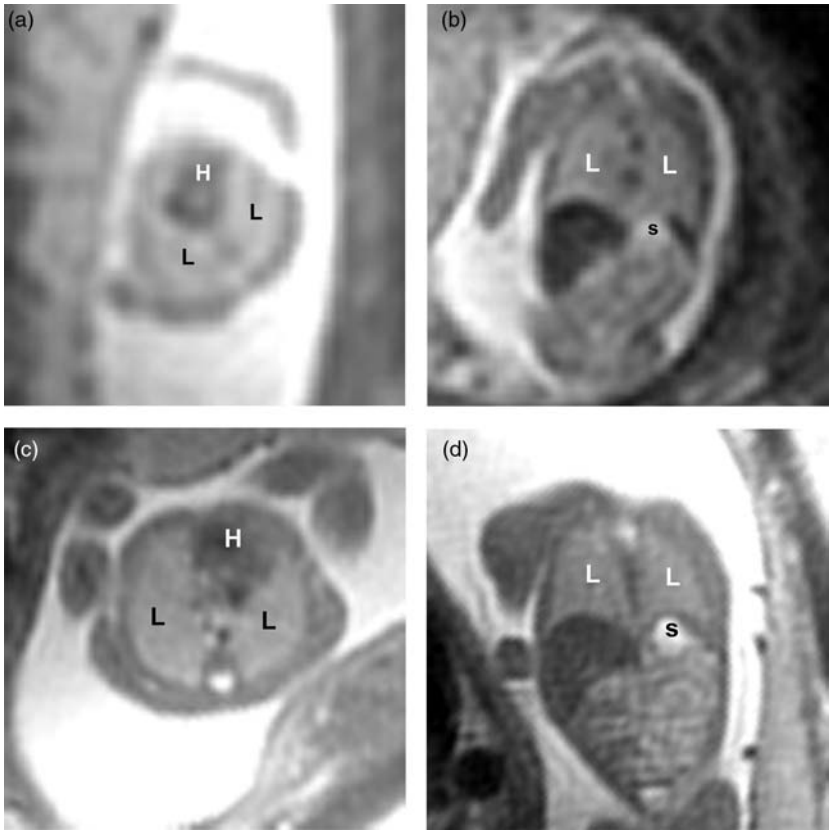

Figure 5.1 Normal lungs in early- to mid-second trimester. Axial and coronal T_2-weighted images at 14 (a and b) and 18 (c and d) weeks gestational age show the lungs (L) and the heart (H). The pulmonary vasculature is difficult to assess at these early gestational ages. s, stomach.

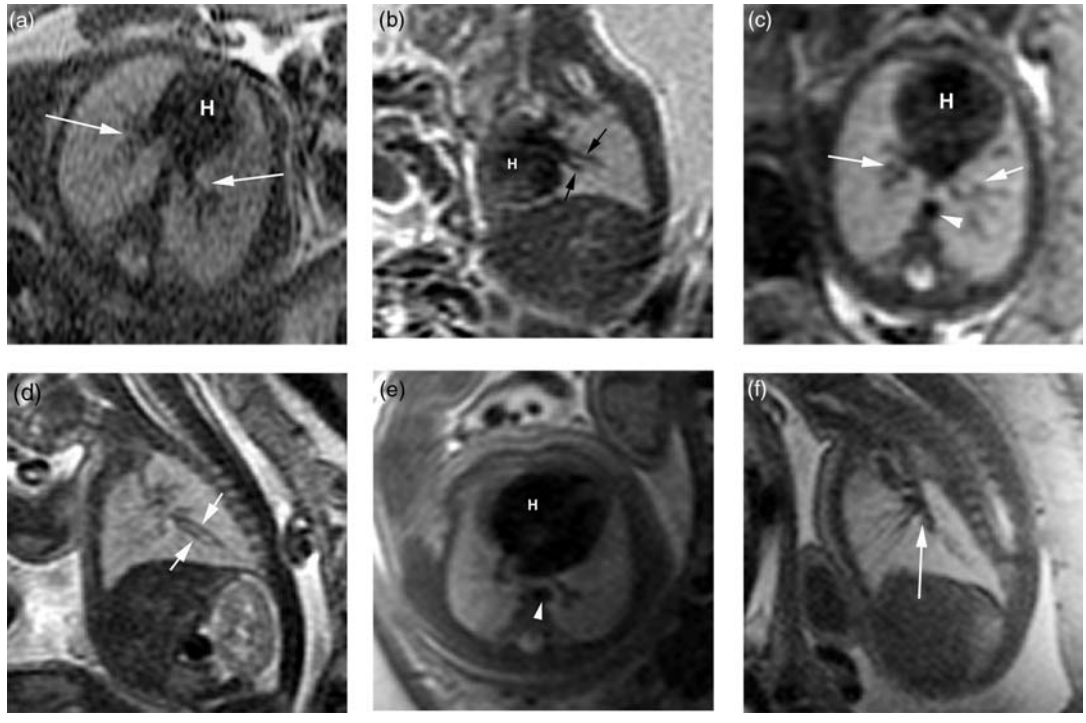

Figure 5.2 Normal lungs late second to third trimesters. Axial and sagittal T_2-weighted images at 24 (a and b), 28 (c and d), and 32 (e and f) weeks gestational age. The lung signal intensity is now increased in comparison with the lungs in Fig. 5.1, and the pulmonary vessels appear as prominent flow voids branching (arrows) from the hila. Note the descending aorta (arrowhead) anterior to the spine. H, heart.

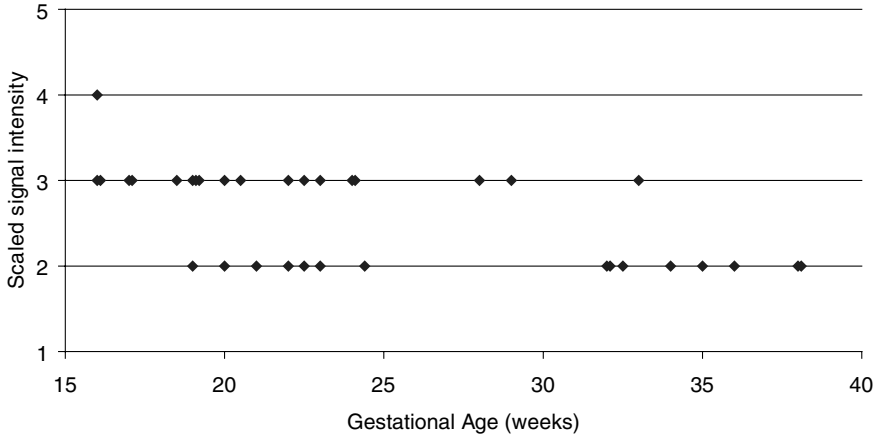

Figure 5.3 Chart of lung signal intensity compared to gestational age in normal lungs. Lung signal intensity on T_2-weighted images was graded on a five-point scale as follows: 1, as bright as fluid (using either amniotic fluid or cerebrospinal fluid at a similar distance from the coil as comparison); 2, slightly less than fluid; 3, intermediate between fluid and muscle; 4, slightly greater than muscle; or 5, similar to muscle. [From Levine et al. (9)]

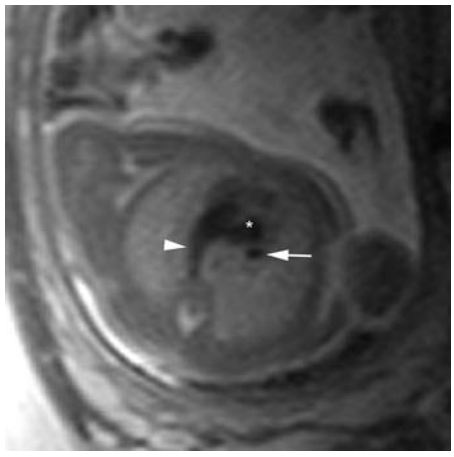

Figure 5.4 Great vessels in axial plane in fetus at 23 weeks gestational age. Axial T_2-weighted image shows the pulmonary outflow tract (arrowhead), aortic outflow tract (∗), and superior vena cava (arrow).

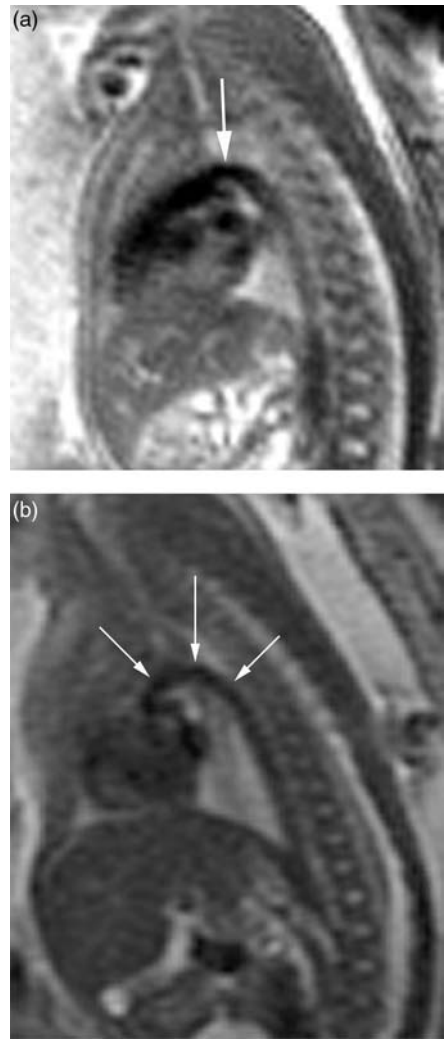

Figure 5.5 Ductal arch and aortic arch. Oblique sagittal T_2-weighted images in two different fetuses show the ductal arch (arrow in a) arising from the anteriorly located pulmonary outflow tract and aortic arch (arrows in b) arising from the more medially located aortic outflow tract. The ductal and aortic arch supply the descending aorta, located anterior to the spine.

(Fig. 5.10). At least portions of the diaphragm can be observed on most studies (15).

The Thymus

The thymus is best visualized in the third trimester when it appears as an intermediate to low signal intensity structure in the anterior mediastinum (Fig. 5.11). The normal size of the thymus in the fetus has not yet been established.

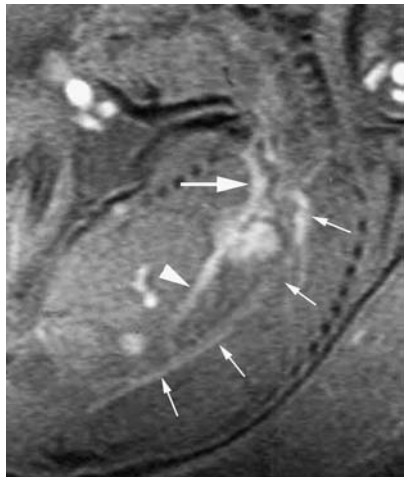

Figure 5.6 Normal vascularity. Oblique coronal spectral spatial water excitation sequence shows flowing blood as high signal intensity. The inferior vena cava (arrowhead), aorta (thin arrows), and superior vena cava (large arrow) are all well-visualized. [From Levine et al. (13)]

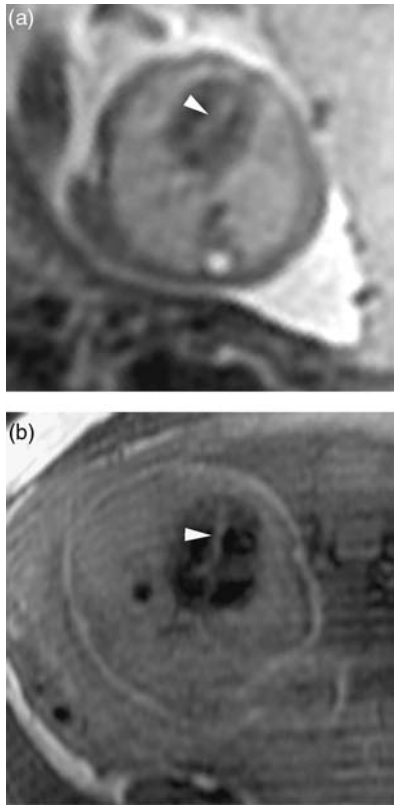

Figure 5.7 Normal heart. Axial T_2-weighted image at 19 weeks gestational age (a) and T_1-weighted image at 26 weeks gestational age (b) illustrate the heart and the interventricular septum (arrowhead). Normally images are not cardiac gated, and thus the chambers of the heart are not well-visualized. At times, imaging serendipitously shows the cardiac chambers.

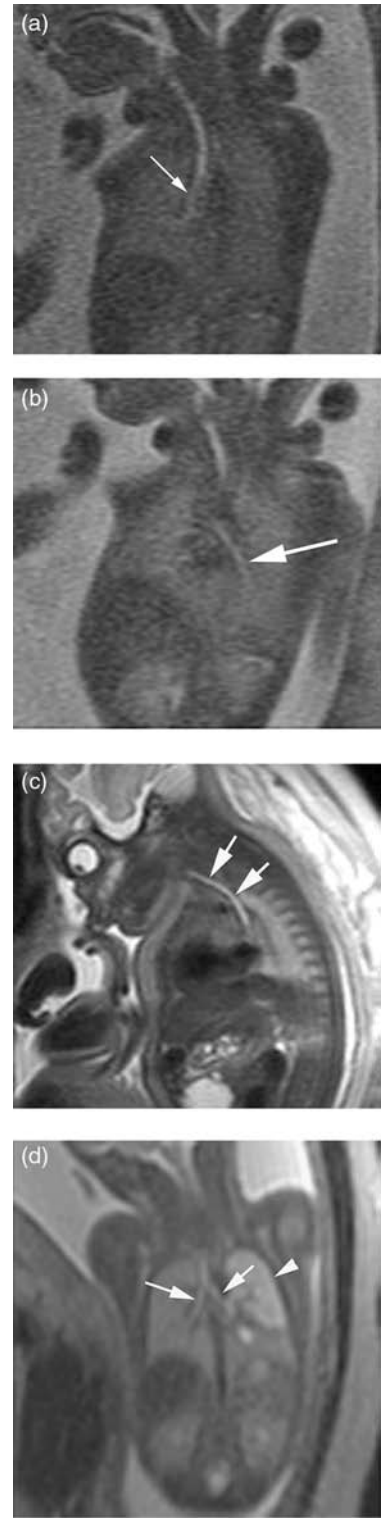

Figure 5.8 Normal airway. (a and b) Oblique coronal T_2-weighted images at 23 weeks gestational age show the right and left mainstem bronchi (arrows). (c) Sagittal T_2-weighted image in a different fetus at 34 weeks gestational age shows the trachea. (d) Coronal T_2-weighted image in a fetus with a CCAM (arrowhead) shows the carina and mainstem bronchi (arrows).

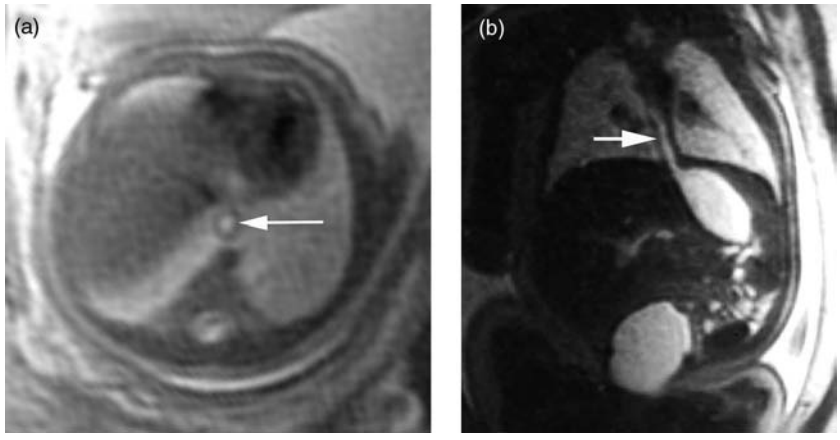

Figure 5.9 Normal distal esophagus. Axial (a) and coronal (b) T_2-weighted images in two different fetuses with fluid in the distal esophagus. Fluid can be detected in the esophagus (arrow) resulting from either swallowing or refluxing.

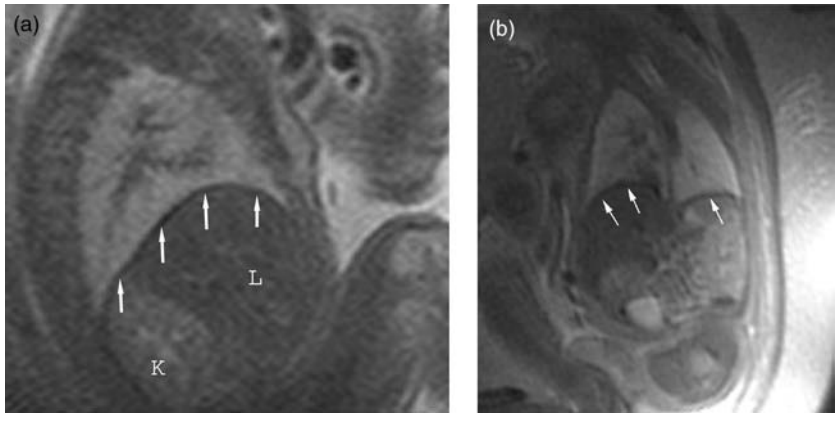

Figure 5.10 Normal diaphragm. Sagittal (a) and coronal (b) T_2-weighted images at 31–32 weeks gestational age show the diaphragm (arrows) as a low intensity dome-shaped structure separating the thorax from the abdomen. L, liver; K, kidney.

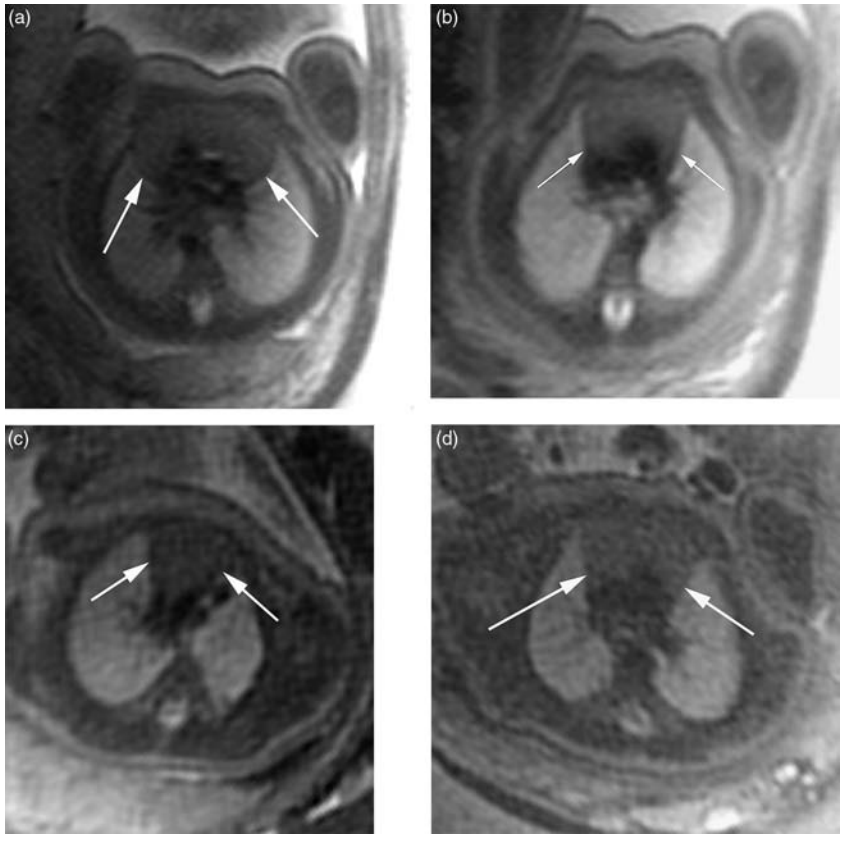

Figure 5.11 Normal thymus. Axial T_2-weighted images of the thymus (arrows) in different fetuses at 33 (a and b), 34 (c), and 37 (d) weeks gestational age.

THORACIC ABNORMALITIES

Lung Masses

On sonography, the classic differential diagnosis for an echogenic lung mass is congenital cystic adenomatoid malformation (CCAM), sequestration, or congenital diaphragmatic hernia (CDH). Each of these may cause mediastinal shift. When the stomach is in the chest, the obvious diagnosis is CDH. When the lesion has macrocysts, it is assumed to be a CCAM. When systemic blood supply is visualized, it is assumed to be a sequestration. Fetal MR imaging can be helpful when the diagnosis is unclear, but in most cases, it is only the potential fetal surgery patients who will need an MR to assess prognostic factors in association with CDH such as presence of liver in the chest and measured lung volume.

The CCAM to Sequestration Spectrum

Congenital cystic adenomatoid malformations are classically described as pulmonary lesions with abnormal proliferation of bronchiolar structures that connect to the normal bronchial tree. The vascular supply of a classic CCAM is from the pulmonary artery with drainage into the pulmonary veins. Sequestrations are pulmonary tissues with vascular supply from the systemic circulation, and lack of connection to the bronchopulmonary tree. However, there is a wide spectrum of these anomalies with much overlap (16,17). Both CCAMs and sequestrations appear as echogenic lung lesions on ultrasound. On MR imaging, they typically have higher signal intensity than normal adjacent lung tissue on T_2-weighted imaging, (3–5, 14) and lower signal intensity than normal lung on T_1-weighted imaging. If large, they can cause mediastinal shift. Congenital cystic adenomatoid malformations may have macrocysts that will be discretely visible (Figs. 5.12 and 5.13), although these tend to be better visualized sonographically (Fig. 5.14).

When adjacent normal lung is compressed by a pulmonary mass, such as a CCAM or sequestration, it can be visualized on MR as of slightly lower signal intensity than adjacent normal lung (Fig. 5.15) (15).

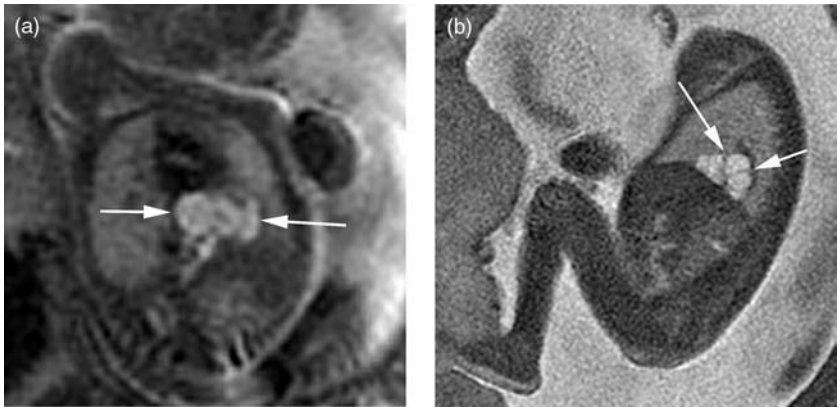

Figure 5.12 Cystic appearing CCAM at 24 weeks gestational age. Oblique axial (a) and sagittal (b) T_2-weighted images show a high signal intensity cystic appearing mass (arrows) in the left lower lobe consistent with a CCAM.

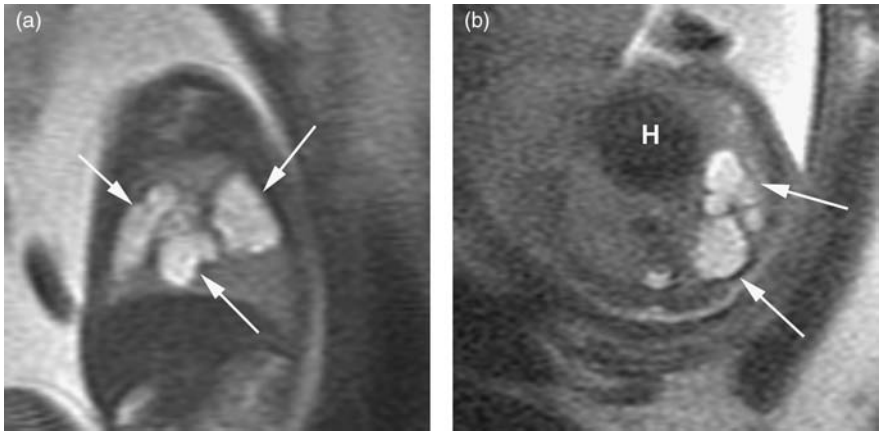

Figure 5.13 Lobular appearing CCAM at 20 weeks gestational age. Axial (a) and sagittal (b) T_2-weighted images show a high signal intensity lobular mass (arrows) in the left lung, with mediastinal shift to the right. Note the relatively low signal intensity of the adjacent and contralateral lung. The lesion is not large enough to be causing atelectasis of the contralateral lung. The relatively low signal intensity is due to early gestational age. H, heart.

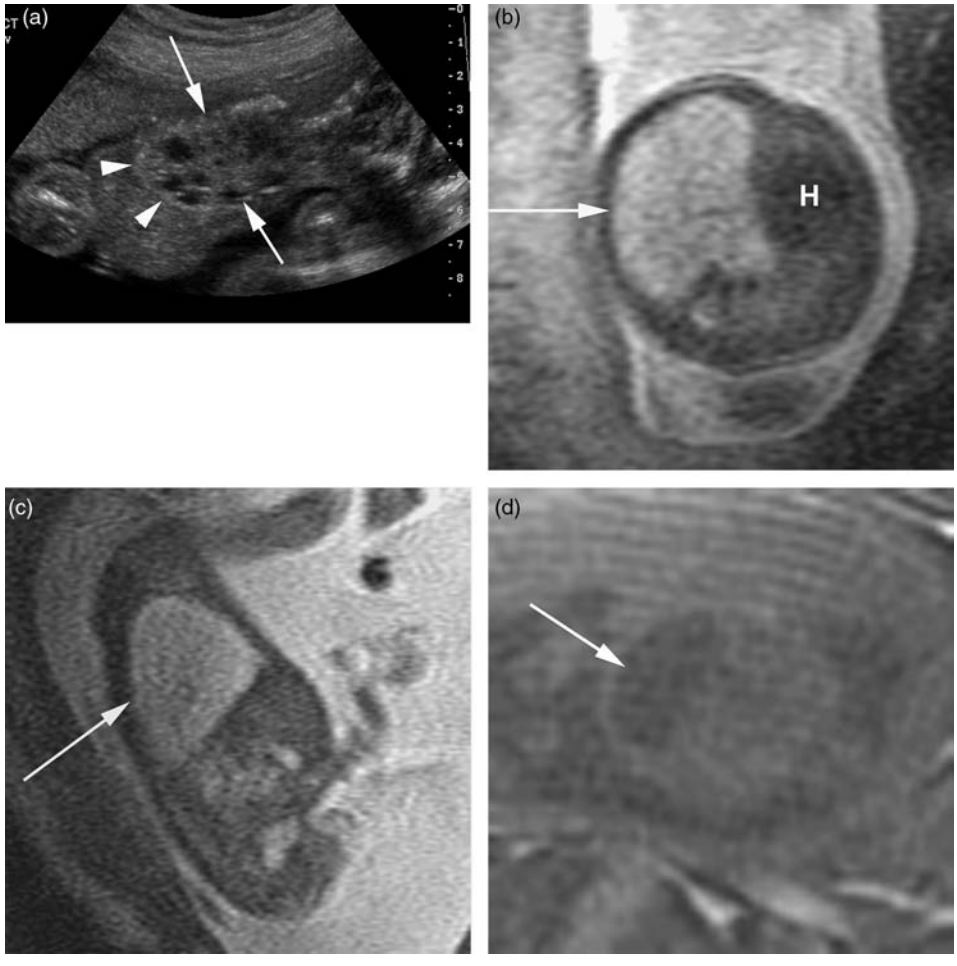

Figure 5.14 Congenital cystic adenomatoid malformation at 19 weeks gestational age, comparison of ultrasound and MR imaging. (a) Sagittal sonogram reveals a cystic lung mass (arrows) with eversion of the hemidiaphragm (arrowheads). Axial (b) and sagittal (c) T_2-weighted images show a high signal intensity mass (arrows). Individual cysts are not as well appreciated as they are on the sonogram. (d) Axial T_1-weighted image shows the lesion to be of relatively low signal intensity. H, heart.

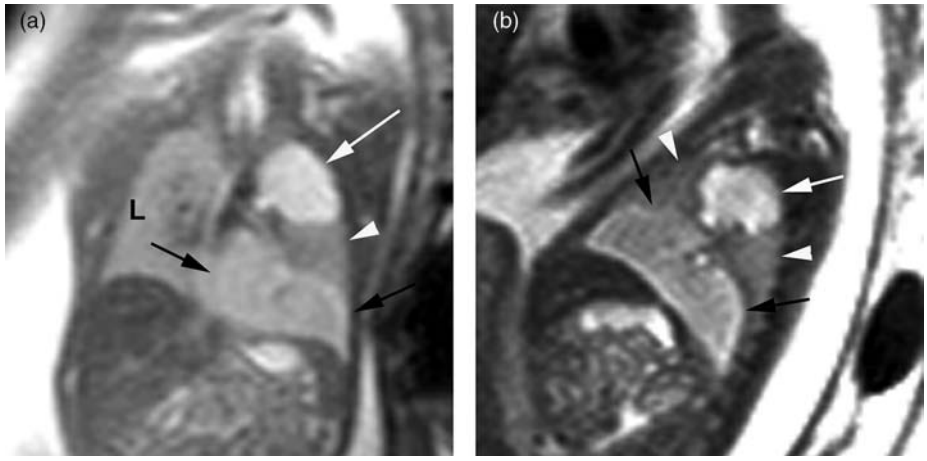

Figure 5.15 Two CCAMs compressing normal intervening lung in fetus at 24 weeks gestational age. Coronal (a) and sagittal (b) T_2-weighted images show a high signal intensity upper lobe mass (white arrow) and slightly high signal intensity lower lobe mass (black arrows). Note the relatively low signal intensity of the atelectatic lung between the two lesions (arrowheads) and the intermediate signal intensity of the normal lung (L) on the right side of the chest. [From Levine et al. (46)]

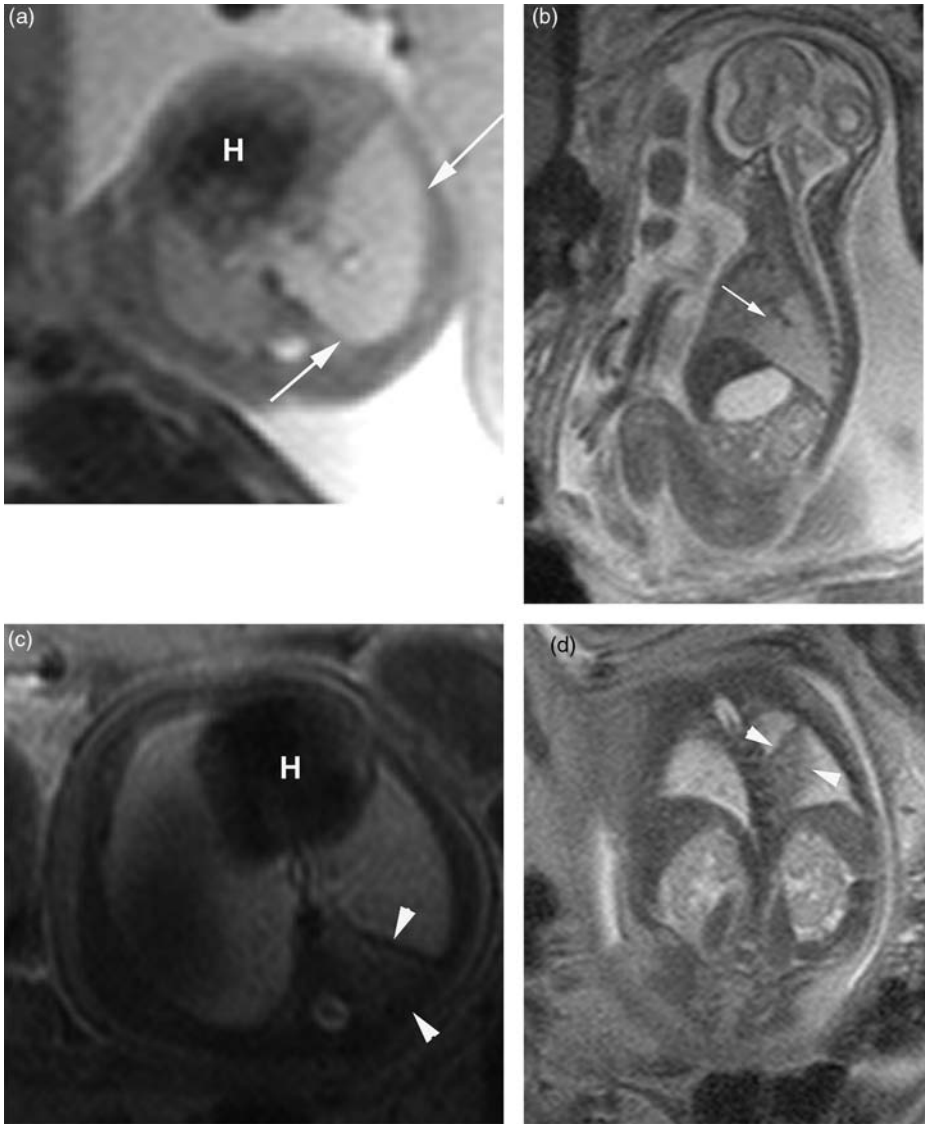

Figure 5.16 Changing appearance of CCAM. Axial (a) and sagittal (b) T_2-weighted images at 21 weeks show a high signal intensity left-sided lung lesion (arrows), with moderate mediastinal shift to the right. Axial (c) and sagittal (d) T_2-weighted images at 37 weeks show a small residual mass (arrowheads). The mediastinal shift has resolved. At this time, the mass was no longer visible sonographically.

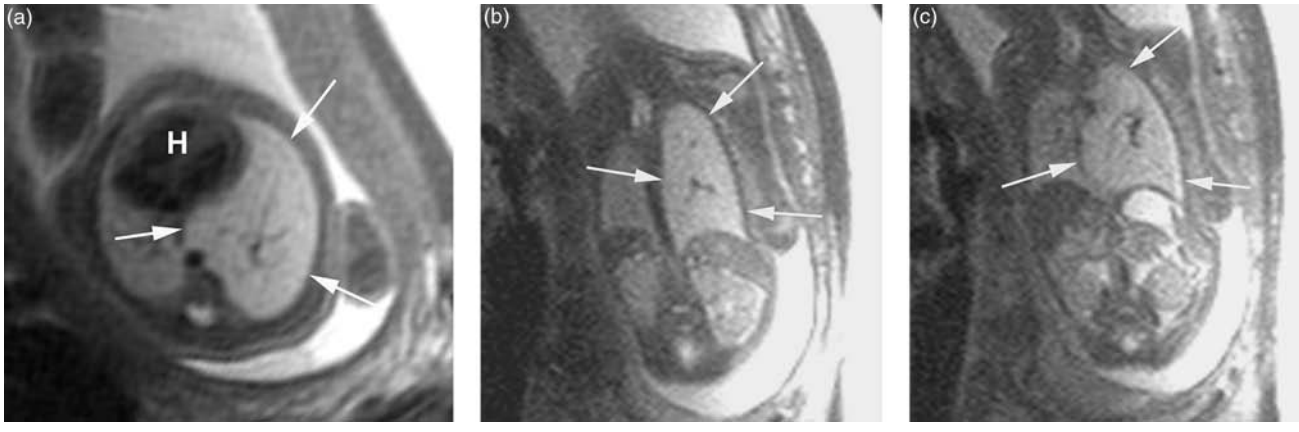

Figure 5.17 Sequestration at 27 weeks gestational age. Axial (a) and coronal (b and c) T_2-weighted images show a mass (arrows) filling the left hemithorax, with mediastinal shift to the right. The tissue in the left hemithorax is of slightly higher signal intensity than the normal lung on the right. Systemic vascular supply was not visible on ultrasound or MR images, however, this was found to be a sequestration at the time of postnatal surgery. H, heart.

The normal and abnormal vasculature supplying CCAMs and sequestrations can be visualized on MR images. If a vessel arises from the aorta, the lesion is presumed to be a sequestration. The branching pattern of the vessels supplying a CCAM can either have a normal branching pattern or appear stretched (9). As these lesions regress their signal intensity decreases (9). A pleural effusion may be visualized transiently as the lesion decreases in size. The lesion may become inapparent on sonography, but still be visible on MR imaging (Fig. 5.16) (4,9).

Sequestrations classically are in the lower lobes (Fig. 5.17). However, they may occur in the upper lobes (Fig. 5.18). They may be infradiaphragmatic and masquerade as an adrenal mass (see Chapter 6, Fig. 6.30), or within the leaves of the diaphragm (see Chapter 6, Fig. 6.30). Occasionally, they span the diaphragm. The distinction between CCAM and sequestration can be made in a homogenously high signal intensity lung lesion when systemic vasculature (i.e., off the aorta) is visualized feeding the lesion (Fig. 5.19).

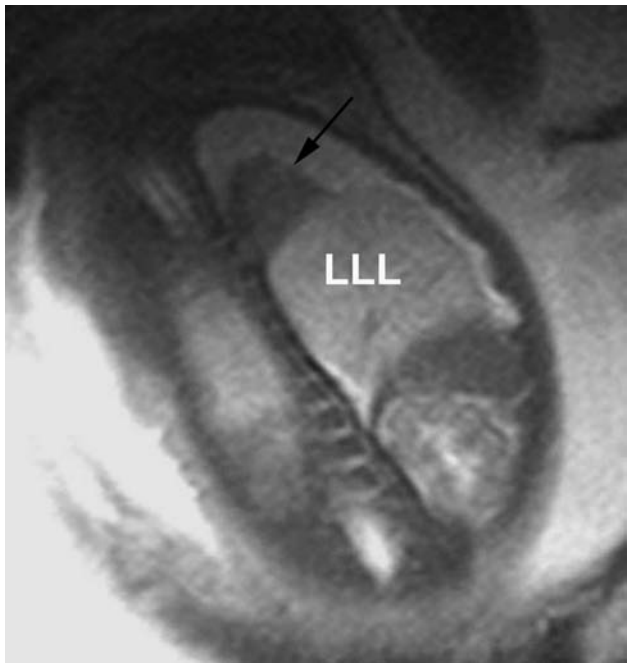

Figure 5.18 Atelectatic sequestration at 32 weeks gestational age. Coronal T_2-weighted image shows a low signal intensity lesion above the more normal appearing left lower lobe (LLL). A pleural effusion is present. Systemic vascular supply was not visible on ultrasound or MR images, however, this was found to be a sequestration at the time of postnatal surgery. In our experience, pleural effusions are often present as lung lesions begin to resolve.

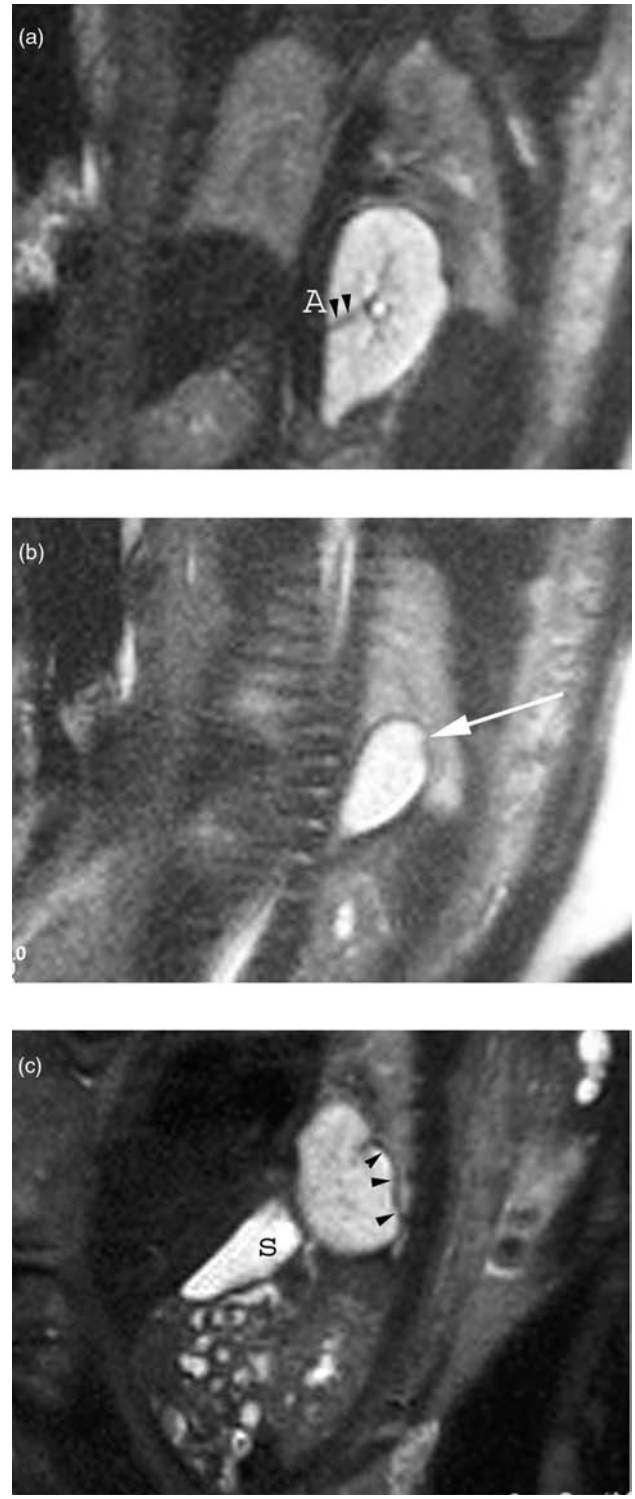

Figure 5.19 Sequestration at 35 weeks gestational age. Coronal (a and b) and oblique sagittal (c) T_2-weighted images show a left-sided high signal intensity mass (arrow) spanning the diaphragm. A vessel feeding the mass (arrowheads) originates from the aorta (A). S, stomach. (Courtesy of S. Ulrich, Perth, Australia.)

Congenital Diaphragmatic Hernia

Congenital diaphragmatic hernia (CDH) is a developmental defect of the diaphragm with herniation of the abdominal viscera into the thorax. Although this typically occurs in the posterolateral left hemidiaphragm (Figs. 5.20–5.23), right-sided, bilateral (Fig. 5.24), paraesophageal, and pericardial hernias can also occur.

The high morbidity associated with CDH is due to pulmonary hypoplasia resulting from the compression of the developing lungs by the herniated viscera. Because *in utero* surgery is now available to treat CDH, it is important to accurately characterize the lesion in order to appropriately triage those patients who will benefit from surgery (3,19). This is discussed in more detail in Chapter 10.

Fetal MR imaging permits the calculation of lung volumes (12,20–24). For these calculations, consecutive images are utilized to measure cross-sectional areas of the lungs with area on each slice being multiplied by the thickness of the section. In fetuses with suspected pulmonary hypoplasia on ultrasound, lung volumes as calculated on MR are lower than those of normal fetuses (20). In infants with poor respiratory outcome, lung volumes are smaller than those with normal respiratory outcomes (25). However, volume measurements alone have been shown to be inaccurate for the prediction of outcome in fetuses with left-sided CDH (26). Instead, relative lung volume (measured lung volume divided by volume predicted for gestational age) has been suggested as an accurate manner to assess for pulmonary hypoplasia (20,27) and has been demonstrated to be predictive of outcome in fetuses with CDH (20).

Herniation of liver into the chest is associated with a worse prognosis than when the liver is completely

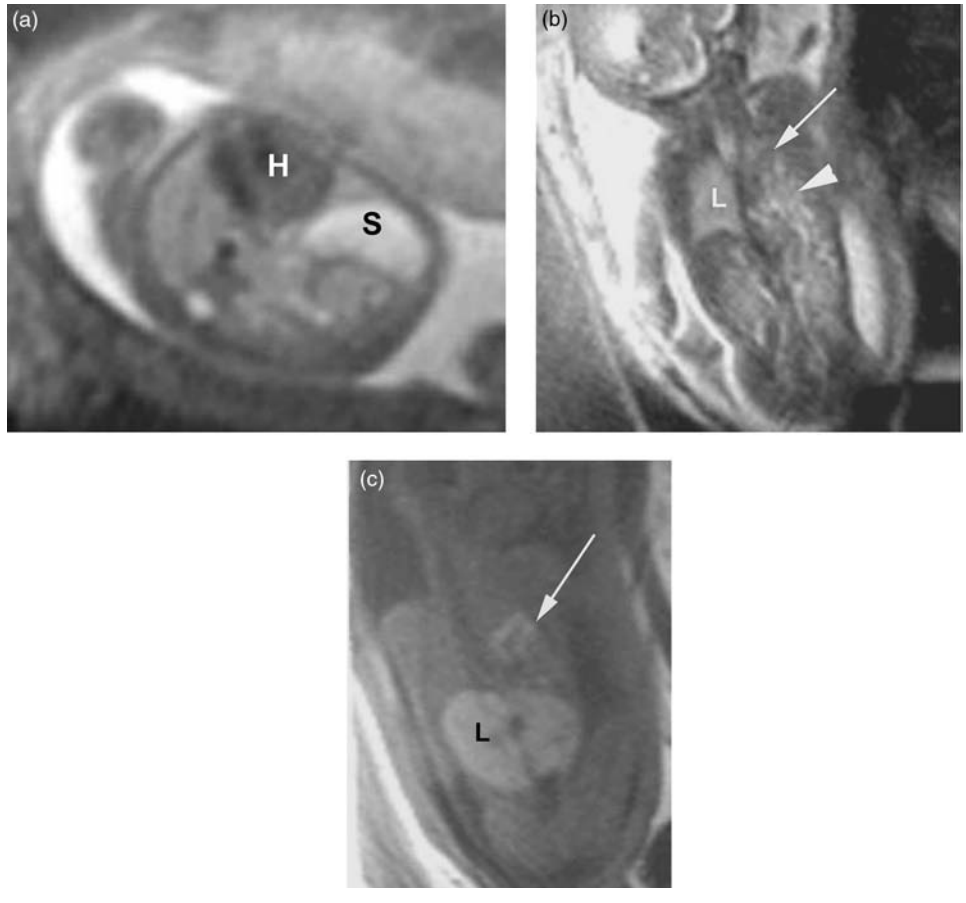

Figure 5.20 Left-sided CDH with liver in the abdomen at 22 weeks gestational age. Axial (a) and coronal (b) T_2-weighted images show the stomach (S) in the chest. There is mediastinal shift to the right with the heart (H) on the right side of the chest. There are small bowel loops in chest (arrowhead) and a slightly darker loop that likely represents colon (arrow). (c) Coronal T_1-weighted image shows the liver (L) in the abdomen. A bright loop of bowel in the chest most likely represents meconium in colon (arrow). [From Levine et al. (46)]

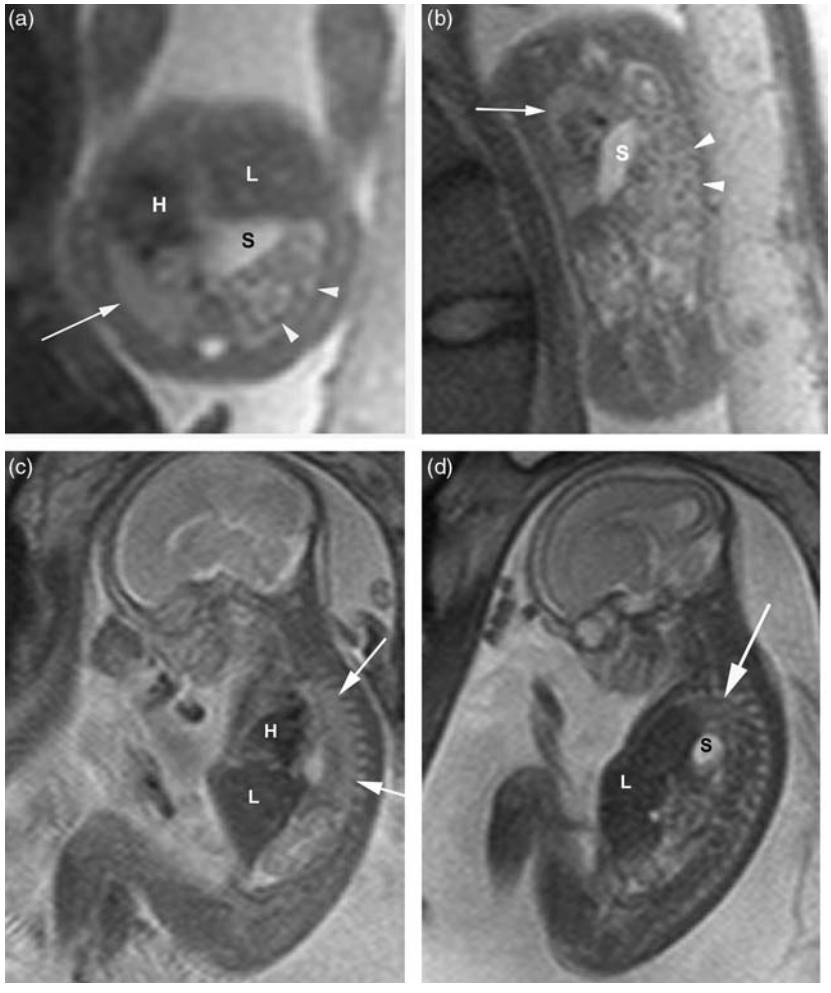

Figure 5.21 Left-sided CDH with liver in the chest at 21 weeks gestational age. Axial (a), coronal (b), and sagittal (c and d) T_2-weighted images demonstrate the stomach (S) in the chest. There is mediastinal shift to the right with the heart (H) on the right side of the chest. A large portion of the liver (L) is in the chest. The lung (arrows) can be visualized posterior and superior to the herniated structures on the left and the right chest. Arrowheads indicate small bowel in the chest.

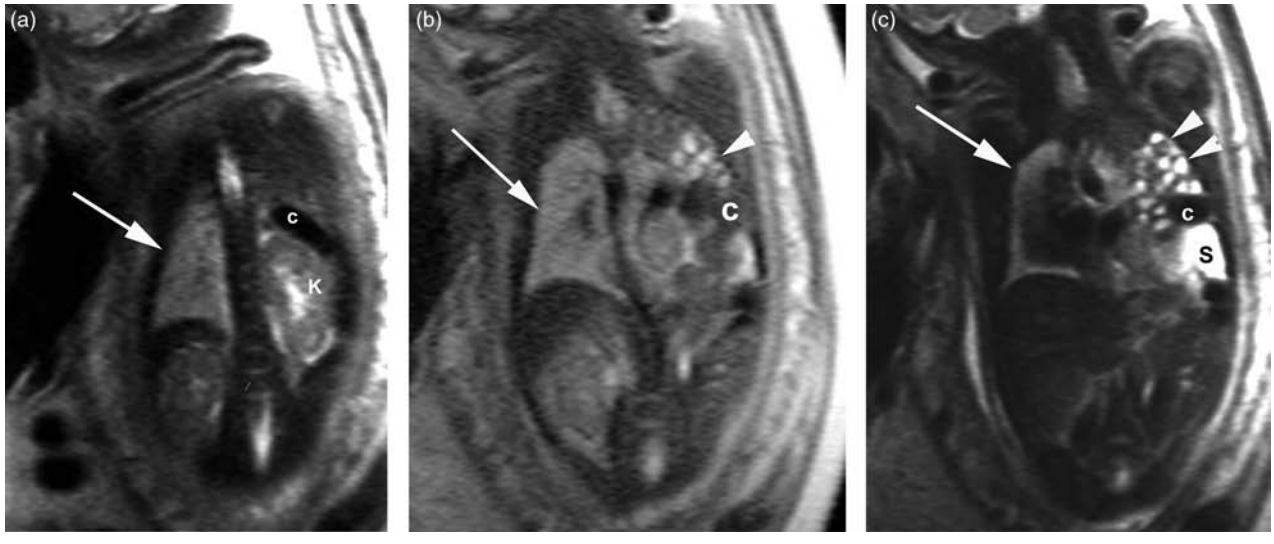

Figure 5.22 Left-sided CDH at 31 weeks gestational age. Coronal T_2-weighted images show the stomach (S), small bowel (arrowheads), colon ("c" indicated in the figure), and kidney (K) in the chest. The liver is in the abdomen. [(a) and (c) from Levine (31)]

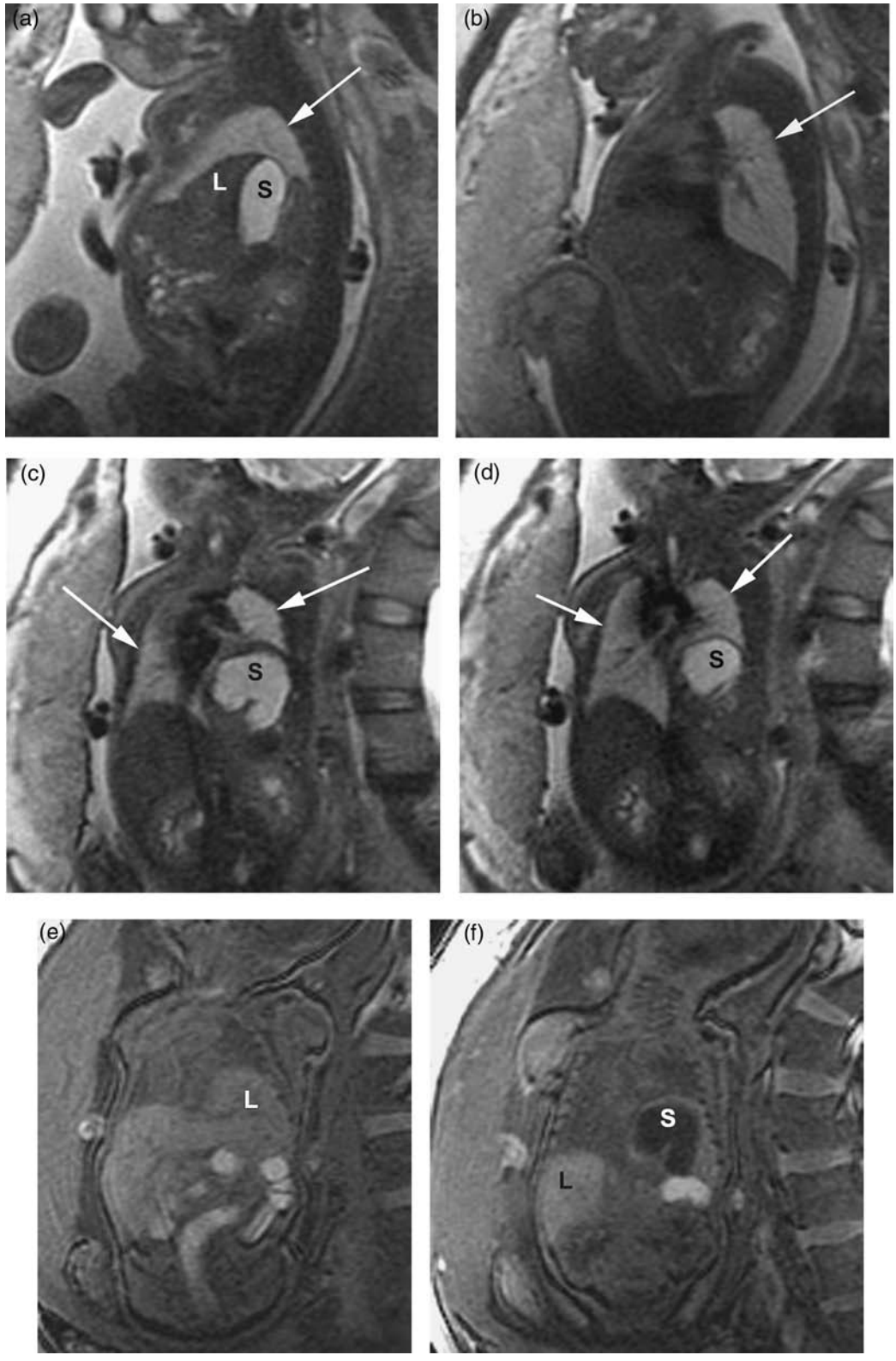

Figure 5.23 Left-sided CDH with organoaxial rotation of the stomach at 36 weeks gestational age. Sagittal left (a), sagittal right (b), and coronal (c and d) T_2-weighted images and coronal (e and f) T_1-weighted images show a well-contained left-sided CDH. The stomach (S) and a portion of the liver (L) are in the chest, but a large amount of normal appearing lung (arrows) is present. The axis of the stomach is flipped with the greater curvature more superiorly located than the lesser curvature.

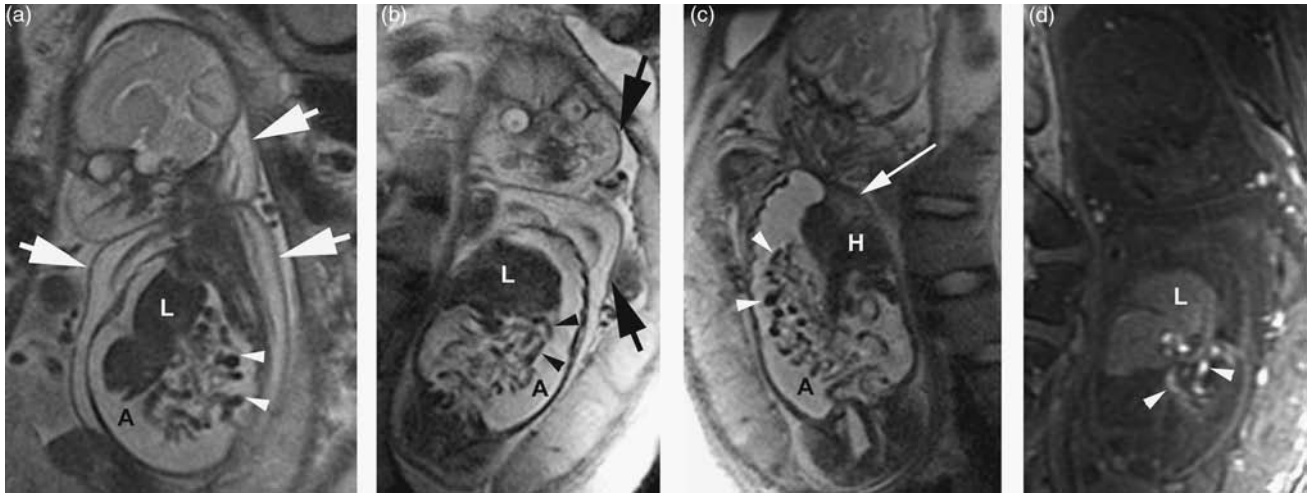

Figure 5.24 Right-sided CDH (with probable left-sided component) with massive ascites and skin thickening at 30 weeks gestational age. Sagittal (a) and coronal (b and c) T_2-weighted images and coronal (d) T_1-weighted image show a large right-sided CDH. Note the abnormal signal intensity of the small bowel (arrowheads) being of low signal intensity on the T_2-weighted images and high signal intensity on the T_1-weighted image. The ascites is in contiguity with the fluid in the chest. The probable cause of the ascites and hydrops is the abnormal liver position, leading to the obstruction of venous return. Thin arrow indicates compressed lung tissue. Large arrow indicates skin thickening.

intra-abdominal (28–30). With ultrasound, the liver can be difficult to visualize and liver position in the chest is inferred from the visualization of abnormal position of the hepatic vasculature. The liver can be observed on MR imaging as a slightly low signal intensity structure on T_2-weighted imaging that is of higher signal intensity on T_1-weighted imaging. In studies by Hubbard et al. (3,31,32), MR imaging was determined to be better than ultrasound at assessing the location of the liver in the chest. However, in a study by Levine et al. (9), there was 100% concordance between sonographic and MR determinations of liver position, with 100% accuracy based on postnatal surgical findings. This high concordance rate is likely to be secondary to the use of confirmatory sonography prior to MR imaging, performed with the specific question of liver location in any fetus with CDH.

The contents of CDH are clearly characterized by MR imaging (8,29,32,33). The stomach tends to be more anteriorly located when the liver is in the abdomen and becomes posteriorly displaced when the liver herniated into the chest (29). Organoaxial volvulus of the herniated stomach can occur and is diagnosed when the greater curvature is located superior to the lesser curvature (Fig. 5.23) (29,34). Colon, with high signal intensity on T_1-weighted imaging and low signal intensity on T_2-weighted imaging, small bowel with fluid-filled loops, stomach, kidney, and spleen, all can be well-visualized in hernias (Figs. 5.20–5.24).

In right-sided CDH, hepatic venous obstruction can lead to ascites, hydrothorax, and skin edema (Fig. 5.24) (35).

Pleural Effusion

A pleural effusion can occur as an isolated finding in the fetus or in association with hydrops or other syndromes (Fig. 5.25). Pleural effusions have the appearance of fluid on MR imaging, being a high signal intensity collection surrounding the lungs on T_2-weighted imaging.

Pericardial Effusion and Mediastinal Masses

Pericardial effusions can be caused by infection, hydrops, or pericardial tumor. Pericardial effusions surround the heart, and when large will appear as anterior collections that deviate the lungs posteriorly (Fig. 5.26). The most likely etiology of a pericardial tumor is a teratoma. A pericardial teratoma appears as a heterogenous middle mediastinal mass (Fig. 5.27). Anterior mediastinal masses in the fetus can be due to teratomas or lymphangiomas (Fig. 5.28).

Lymphangiomas are benign tumors of the lymphatic system and appear as cystic or septated cystic masses. Although they typically occur in the neck or axilla, they can grow quite large. Prognosis depends on the size and location of the lesion as well as development of hydrops

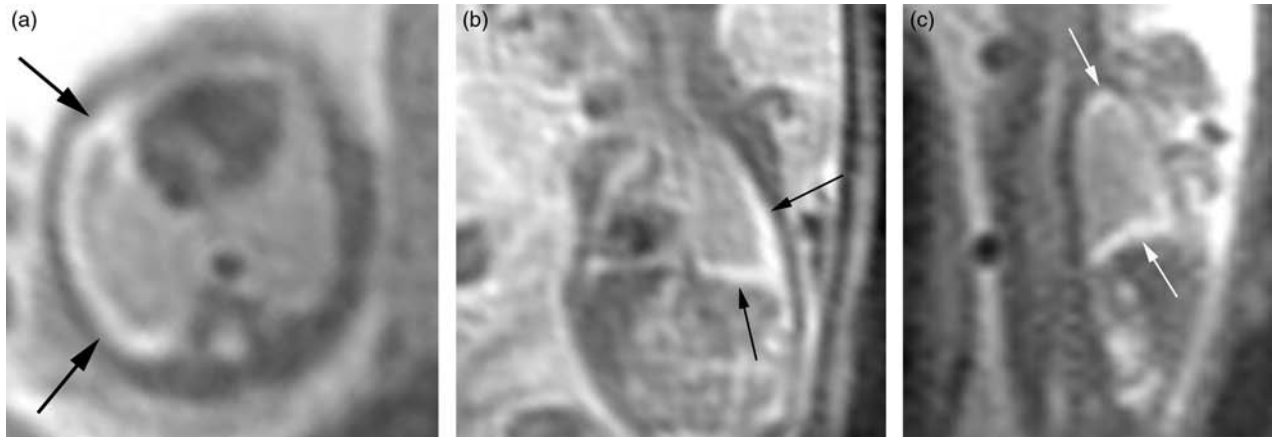

Figure 5.25 Pleural effusion at 19 weeks gestational age in fetus with trisomy 21. Axial (a), oblique coronal (b), and oblique sagittal (c) T_2-weighted images show a fluid collection (arrows) surrounding the lungs. Note how this pleural effusion appears different from a pericardial effusion in Fig. 5.26.

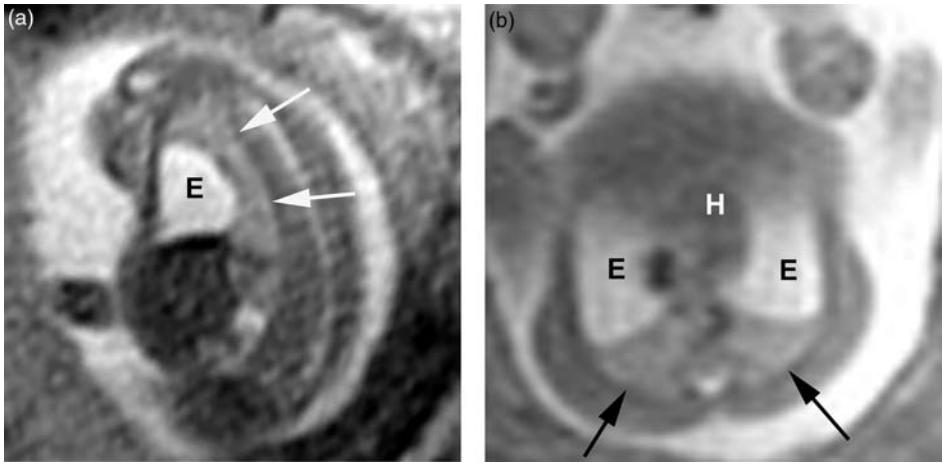

Figure 5.26 Large pericardial effusion at 18 weeks gestational age. Sagittal (a) and axial (b) T_2-weighted images show a large fluid collection (E) surrounding the heart (H). The effusion compresses the lungs (arrows) posteriorly. Note how this effusion is different from the more common pleural effusions (Fig. 5.25) that surround the lungs.

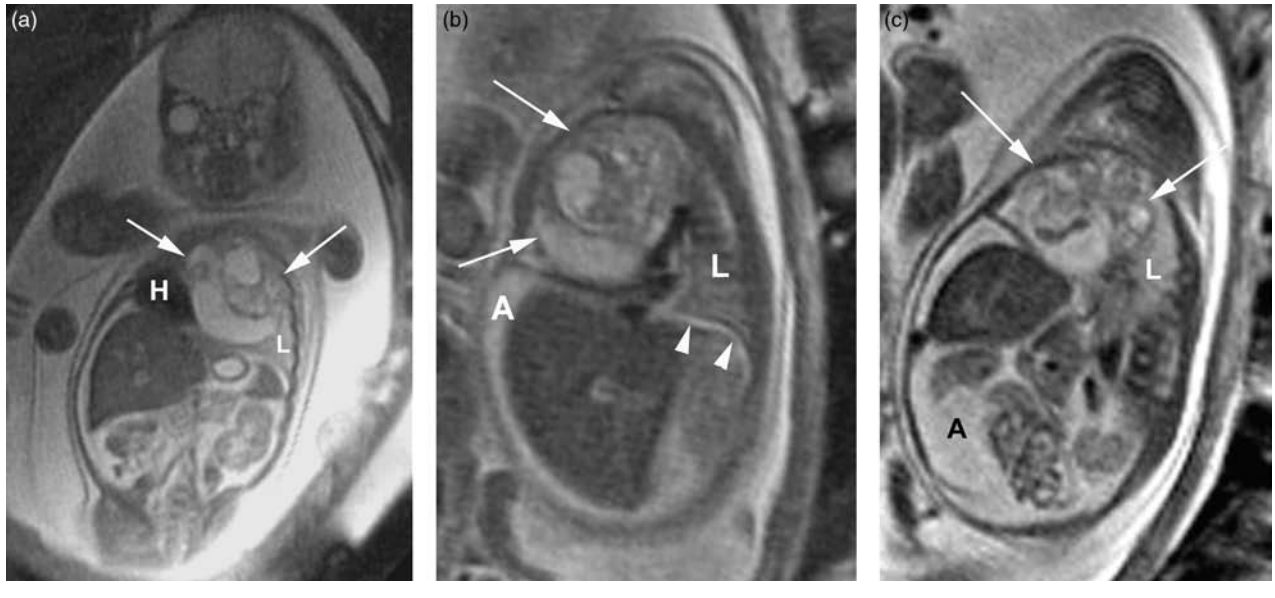

Figure 5.27 Mediastinal teratoma at 29 weeks gestational age. Coronal (a) and sagittal (b and c) T_2-weighted images show a large heterogenous mediastinal mass (arrows) that deviates the heart (H) inferiorly and to the right. Some normal appearing lung (L) is visualized posteriorly. Note ascites in the abdomen (A) and small pleural effusion (arrowheads).

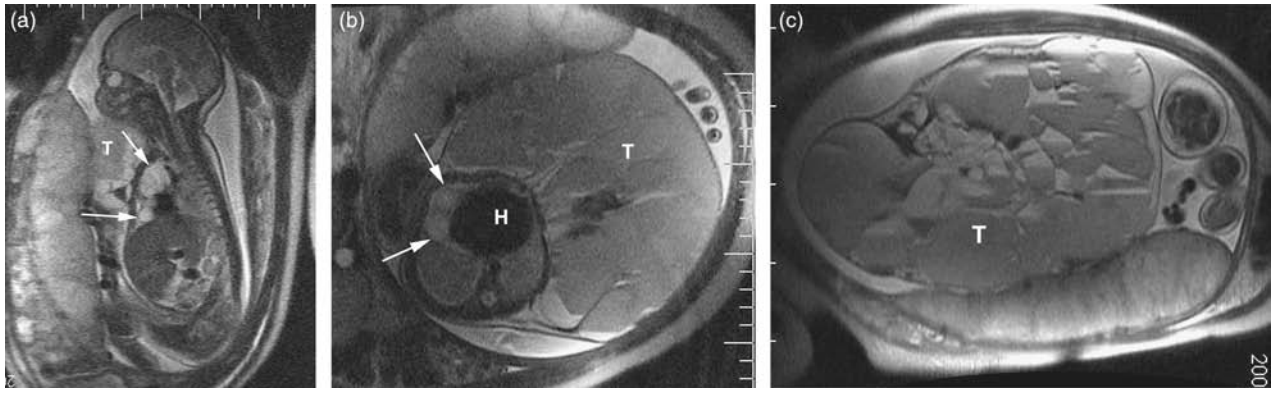

Figure 5.28 Large lymphangioma in fetus at 31 weeks gestational age. Sagittal (a) and axial (b) T_2-weighted images of the chest show the large tumor (T) with intrathoracic extent (arrows) seen as regions of high signal intensity in the anterior mediastinum. (c) Transverse T_2-weighted image orientated to maternal anatomy shows the multiple fluid levels within loculations of the tumor. MR volumetry showed that the volume of the tumor was 1.5 times that of the fetus. (Courtesy of J. Kazan, Sao Paulo, Brazil.)

(36). Prenatal MR can be utilized to evaluate the extent of the lesion and associated organ involvement (Fig. 5.28) (37,38).

Bronchogenic Cyst

Foregut cysts represent 11–18% of mediastinal masses in infants and children (39). Most of these cysts are in the perihilar region (39). They are lined with ciliated columnar epithelium, and cause symptoms of airway obstruction when they are adherent to the wall, or impinge upon the lumen of the trachea or a major bronchus. A foregut cyst on MR imaging is seen as a fluid-filled cyst of high signal intensity (Fig. 5.29) (40). The cyst may be large and there may be an associated vertebral body abnormality.

MR has been shown to be helpful in the diagnosis of a mediastinal bronchogenic cyst that caused obstruction, by characterizing the cyst and defining the hyperexpanded lungs (Fig. 5.30) (10).

Dark Lungs: Atelectasis, Compression, and Pulmonary Hypoplasia

When a lung mass or large effusion is present, the adjacent lung may be compressed. On T_2-weighted imaging, this lung has lower signal intensity than that of the noncompressed lung (Figs. 5.15 and 5.31) (3,9).

As discussed previously, MR imaging has been suggested as a modality to assess the volume of the lungs to predict pulmonary hypoplasia. The signal intensity of the lungs has also been suggested as being

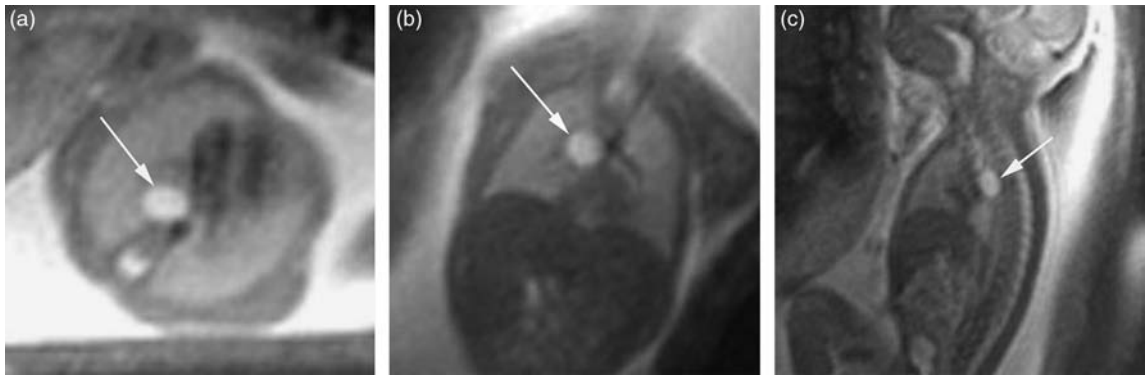

Figure 5.29 Esophageal atresia and bronchogenic cyst at 20 weeks gestational age. Axial (a), coronal (b), and sagittal (c) T_2-weighted images show an absent stomach. There is a cyst (arrow) in the chest posterior to the heart, however, there is no mediastinal shift to suggest a diaphragmatic hernia. This is most consistent with combined esophageal atresia and bronchogenic cyst, which is what was found postnatally. [(b and c) From Levine et al. (46)]

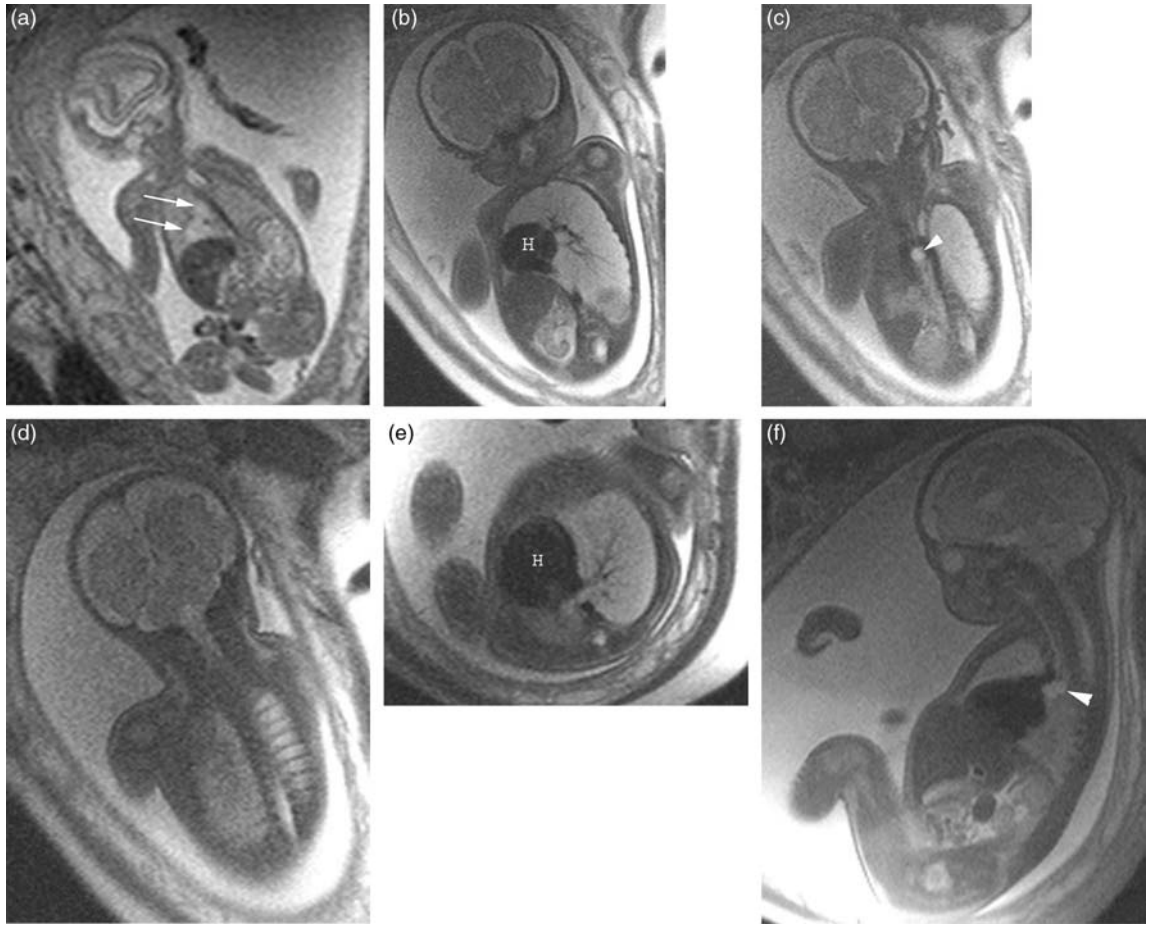

Figure 5.30 Obstructing bronchogenic cyst. (a) Coronal T_2-weighted image at 19 weeks gestational age shows a slightly high signal intensity bi-lobed right-sided mass (arrows). Coronal (b–d), axial (e), and sagittal (f) T_2-weighted images at 31 weeks show an enlarged left lung herniating across midline. The left lung appears hyperinflated with stretched vessels. Lung parenchyma protrudes between ribs. There is a high signal intensity mediastinal mass (arrowhead) just below aortic arch, at inferior margin of trachea. The right lung is compressed of lower signal intensity than the lung on the left. On follow-up both lungs appeared obstructed. The baby was delivered by *ex utero* intrapartum treatment (EXIT) procedure and was placed on extracorporeal membrane oxygenation prior to clamping the umbilical cord. The obstructing bronchogenic cyst was then surgically removed. H, heart. [(a, e, and f) from Levine et al. (10); (c) from Levine (31)]

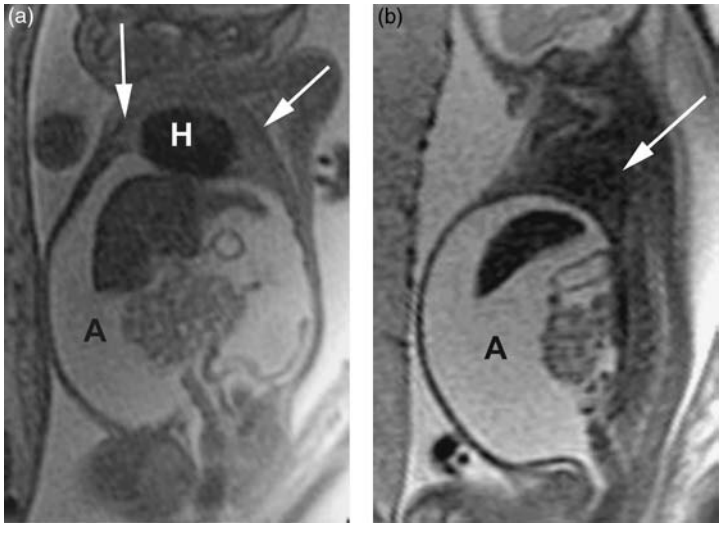

Figure 5.31 Compressed lungs in fetus with massive ascites at 27 weeks gestational age resulting from lymphatic leak. Coronal (a) and sagittal (b) T_2-weighted images show massive ascites (A) elevating the hemidiaphragms. Note the small lungs (arrows) of relatively low signal intensity. The fetus was treated with large volume paracentesis. At surgery, a lymphatic leak was documented. H, heart.

prognostic for lung maturity (11) and for pulmonary hypoplasia. Low signal intensity of the lungs on T_2-weighted imaging has been described as consistent with pulmonary hypoplasia (Fig. 5.32) (2,25). However, in the second trimester, this finding may not yet be apparent even in fetuses with anomalies known to occur in conjunction with pulmonary hypoplasia such as bilateral renal agenesis (9). Lung volume or a combination of lung volume with lung signal intensity (25) will likely be a better indicator of pulmonary hypoplasia than subjective assessment of signal intensity alone.

Cardiac Abnormalities

Fetal MR imaging is less sensitive than ultrasound in the diagnosis of cardiac abnormalities. As fetal MR scans are not gated for fetal cardiac motion, cardiac chambers are not adequately assessed (41). The small outflow tracts also cannot be adequately evaluated with current technology. However, attention should be paid to the size of the heart (Fig. 5.33) and its position in the chest with respect to fetal situs and abdominal situs (Figs. 5.34 and 5.35). Magnetic resonance imaging is helpful in better characterizing associated findings in the cases of heterotaxy syndrome, for example visualization of polysplenia and azygous continuation of the inferior vena cava (Fig. 5.35). Magnetic resonance has been helpful and beneficial in supplementing sonography by displaying features of congenital heart disease in the cases of hypoplastic left heart syndrome (42), poststenotic dilatation in a case of aortic stenosis (43), truncus arteriosus (44), single ventricle (Fig. 5.36), and coarctation of the aorta (Fig. 5.37).

Although cardiac rhabdomyomas may be visualized (Fig. 5.38) (45,46), in the cases of tuberous sclerosis, the benefit of MR is the evaluation of the brain for intracranial tubers.

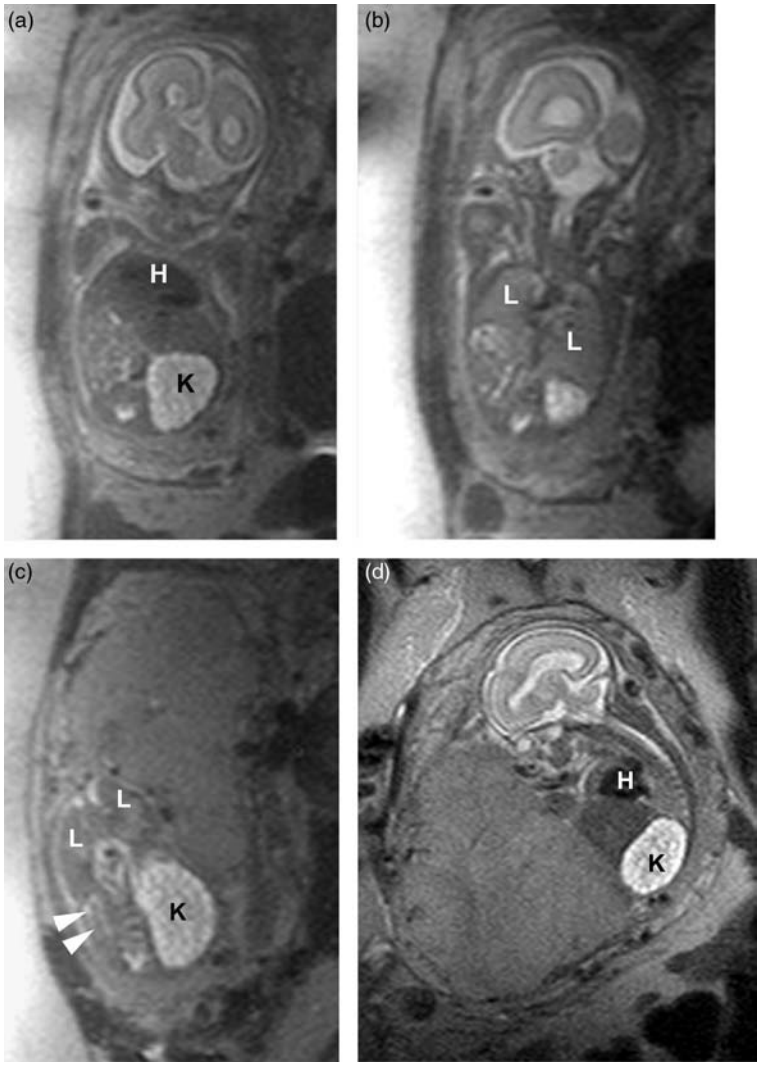

Figure 5.32 Pulmonary hypoplasia at 22 weeks gestational age in fetus with right-sided renal agenesis and left-sided multicystic dysplastic kidney. Coronal (a–c) and sagittal (d) T_2-weighted images show the enlarged left kidney (K) with multiple cysts. The empty right renal fossa is shown by the lying down adrenal sign (arrowheads). There is severe oligohydramnios. The lungs (L) are small and are of relatively low signal intensity. H, heart. [From Levine et al. (46)]

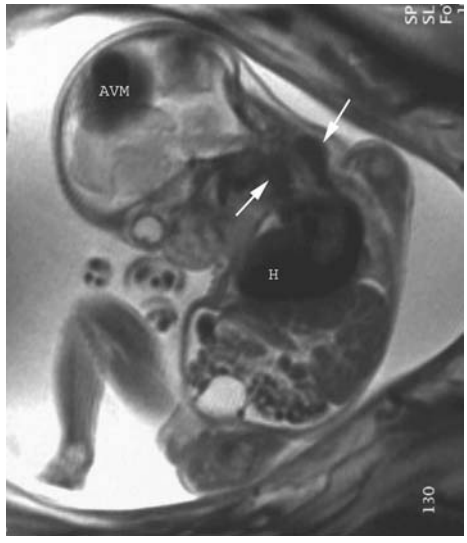

Figure 5.33 Cardiomegaly in association with intracranial vascular malformation at 28 weeks gestational age. Coronal T_2-weighted images show an enlarged heart (H) spanning the majority of the diameter of the chest. Large vessels (arrows) in the neck extend up the dural arteriovenous malformation (AVM).

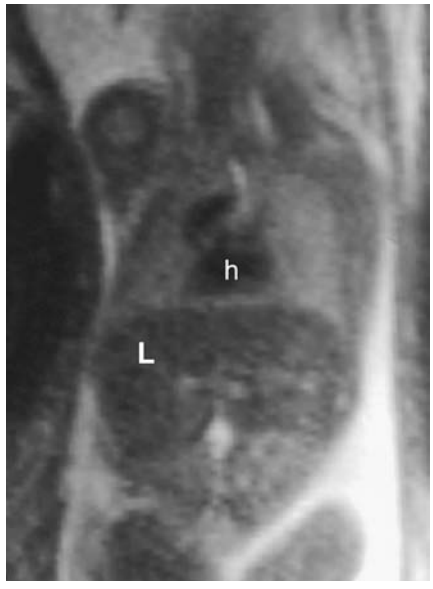

Figure 5.34 Dextrocardia. Coronal T_2-weighted image shows the heart (h) on the right side of the fetus consistent with dextrocardia. L, liver.

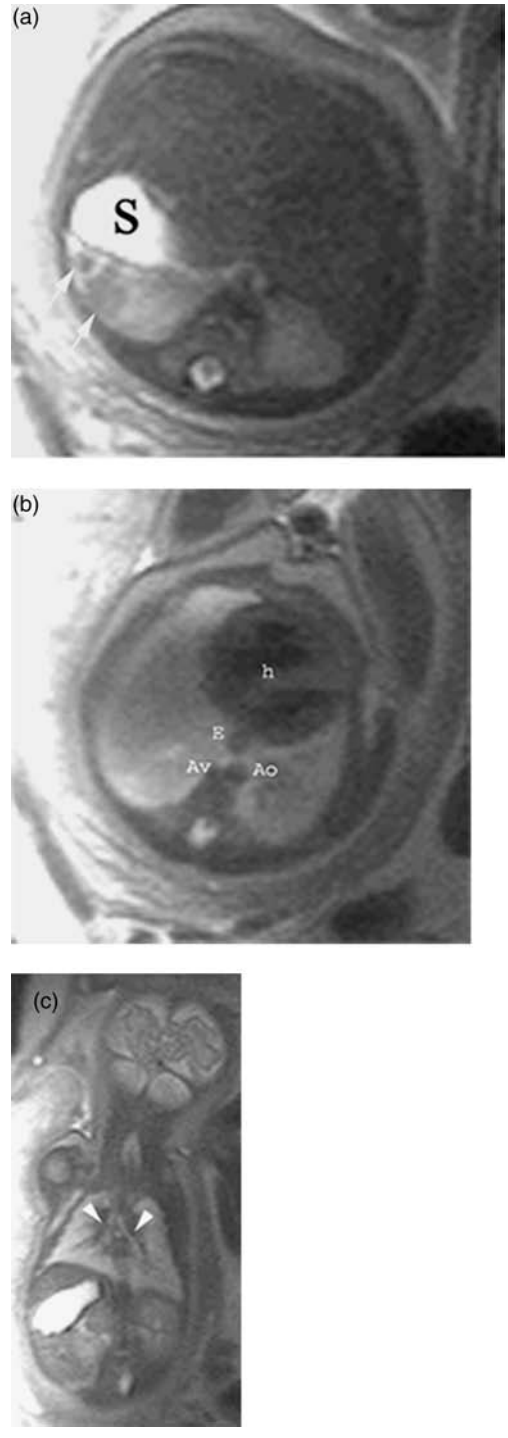

Figure 5.35 Heterotaxy syndrome at 34 weeks gestational age. Axial (a and b) and coronal (c) T_2-weighted image of fetus show right-sided stomach (S) and left-sided heart (h). MR shows polysplenia (arrow) and two vessels are seen anterior to the spine, the aorta (Ao), and the azygous vein (Av), consistent with azygous continuation of the inferior vena cava. The esophagus (E) is also visualized. Coronal view (c) shows bilateral high signal intensity hyparterial bronchi (arrowheads). [From Levine et al. (9)]

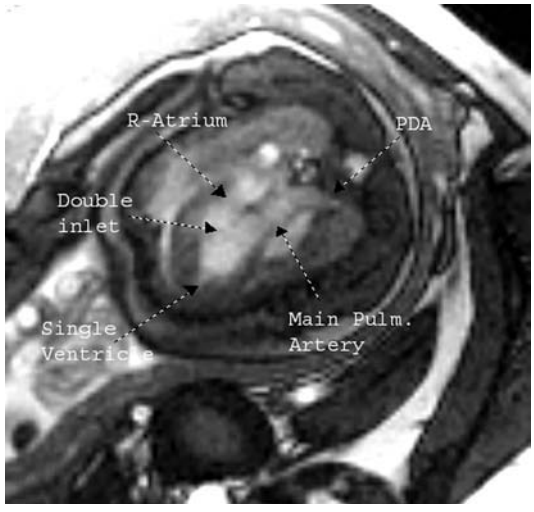

Figure 5.36 Single ventricle. Axial view of the heart showing a single ventricle. R, right; PDA, patent ductus arteriosus; Pulm, pulmonary. (Courtesy of K. Siddiqui, Danville, PA.)

Pulmonary Agenesis

It has been suggested that nonvisualization of the mainstem bronchus in a fetus with mediastinal shift without mass lesion was sufficient for the diagnosis of unilateral pulmonary agenesis (6). Although these findings should be absent in pulmonary agenesis, it is common to have poor visualization of the airways and central pulmonary vasculature on MR in the cases of unexplained mediastinal shift (9).

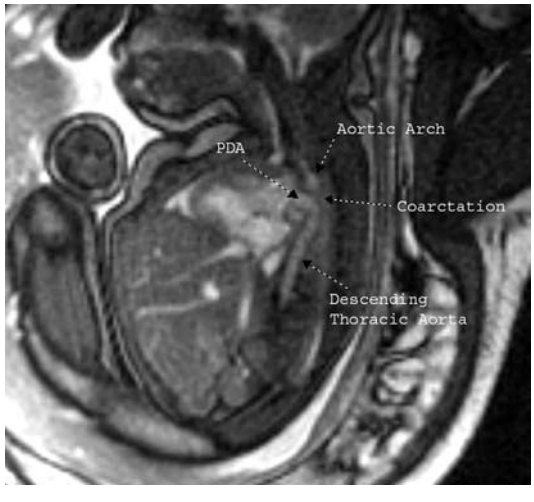

Figure 5.37 Coarctation of the aorta. Oblique sagittal view of the chest showing coarctation of the aorta. PDA, patent ductus arteriosus. (Courtesy of K. Siddiqui, Danville, PA.)

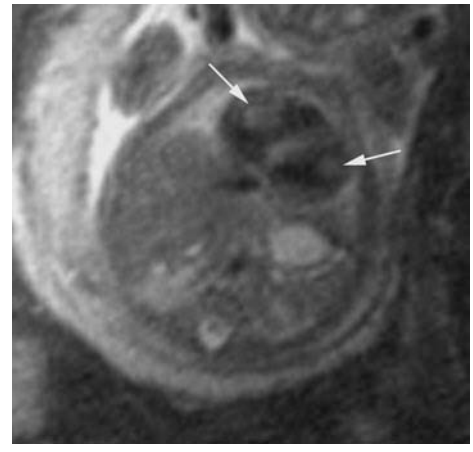

Figure 5.38 Cardiac rhabdomyomas in fetus with tuberous sclerosis at 24 weeks gestational age. Oblique axial T_2-weighted image of the heart shows two masses (arrows) with signal intensity similar to myocardium. Multiple other masses were also present in the heart and in the subependymal regions of the brain, consistent with tuberous sclerosis.

Esophageal Atresia

After 19 weeks gestation, esophageal atresia should be one of the first diagnoses considered with persistent nonvisualization of the stomach (Fig. 5.39). The increased incidence of karyotypic abnormalities with esophageal atresia suggests that fetal karyotyping should be

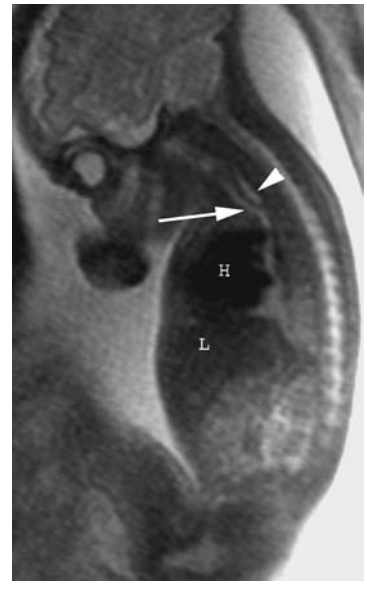

Figure 5.39 Esophageal atresia in a fetus with an absent stomach. Oblique sagittal T_2-weighted image shows the fluid–fluid proximal esophagus (arrowhead) posterior to the fluid-filled trachea (arrow). H, heart; L, liver.

considered whenever the stomach is not visualized on serial ultrasounds. Magnetic resonance imaging appears to be accurate for establishing or ruling out a prenatal diagnosis of esophageal atresia and should be considered in fetuses that are at high risk based on ultrasound findings.

Prenatal MR visualization of a distended esophagus in fetuses with an absent stomach has been reported to be 100% sensitive and specific for esophageal atresia (7). However, in another report, of three fetuses with esophageal atresia, the esophagus was visualized at the thoracic inlet in 1/3 (33.3%) and not visualized at all in 2/3 (66.7%) fetuses (9). Associated polyhydramnios may be present, especially in the third trimester.

Obstructed Hyperexpanded Lungs

Obstructed portions of lung can become hyperexpanded, and if so, will be visualized as of higher signal than normal non-obstructed lung (Fig. 5.30). Laryngeal or tracheal atresias can cause enlargement of both lungs. On MR imaging, these are seen as bilateral enlarged lungs of relatively increased signal intensity (Chapter 10, Fig. 10.4). The dilated trachea and bronchi are visualized as filled with fluid and there is eversion of the diaphragms (3).

CONCLUSION

Fetal MR imaging is helpful in complex chest anomalies where the sonographic diagnosis is unclear. Quantitative data available with MR lung volumetry is helpful in predicting outcome in fetuses with risk of pulmonary hypoplasia. Prenatal MR is particularly helpful in assessing organ involvement and predicting outcome in fetuses with CDH.

REFERENCES

1. Coakley FV, Hricak H, Filly RA et al. Complex fetal disorders: effect of MR imaging on management—preliminary clinical experience. Radiology 1999; 213:691–696.
2. Ikeda K, Hokuto I, Mori K et al. Intrauterine MRI with single-shot fast-spin echo imaging showed different signal intensities in hypoplastic lungs. J Perinat Med 2000; 28:151–154.
3. Hubbard AM, Adzick NS, Crombleholme TM et al. Congenital chest lesions: diagnosis and characterization with prenatal MR imaging. Radiology 1999; 212:43–48.
4. Quinn TM, Hubbard AM, Adzick NS. Prenatal magnetic resonance imaging enhances fetal diagnosis. J Pediatr Surg 1998; 33:553–558.
5. Ohgiya Y, Gokan T, Hamamizu K et al. Fast MRI in obstetric diagnoses. J Comput Assist Tomogr 2001; 25:190–200.
6. Kalache KD, Chaoui R, Paris S et al. Prenatal diagnosis of right lung agenesis using color Doppler and magnetic resonance imaging. Fetal Diagn Ther 1997; 12:360–362.
7. Langer JC, Hussain H, Khan A et al. Prenatal diagnosis of esophageal atresia using sonography and magnetic resonance imaging. J Pediatr Surg 2001; 36:804–807.
8. Liu X, Ashtari M, Leonidas JC et al. Magnetic resonance imaging of the fetus in congenital intrathoracic disorders: preliminary observations. Pediatr Radiol 2001; 31:435–439.
9. Levine D, Barnewolt CE, Mehta TS et al. Fetal thoracic abnormalities: MR imaging. Radiology 2003; 228:379–388.
10. Levine D, Jennings R, Barnewolt C et al. Progressive fetal bronchial obstruction caused by a bronchogenic cyst diagnosed using prenatal MR imaging. Am J Roentgenol 2001; 176:49–52.
11. Duncan KR, Gowland PA, Moore RJ et al. Assessment of fetal lung growth *in utero* with echo-planar MR imaging. Radiology 1999; 210:197–200.
12. Duncan KR, Gowland PA, Freeman A et al. The changes in magnetic resonance properties of the fetal lungs: a first result and a potential tool for the non-invasive *in utero* demonstration of fetal lung maturation. Br J Obstet Gynaecol 1999; 106:122–125.
13. Conran RM, Stocker JT. Extralobar sequestration with frequently associated congenital cystic adenomatoid malformation, type 2: report of 50 cases. Pediatr Dev Pathol 1999; 2:454–463.
14. Cass DL, Crombleholme TM, Howell LJ et al. Cystic lung lesions with systemic arterial blood supply: a hybrid of congenital cystic adenomatoid malformation and bronchopulmonary sequestration. J Pediatr Surg 1997; 32:986–990.
15. Shinmoto H, Kashima K, Yuasa Y et al. MR imaging of non-CNS fetal abnormalities: a pictorial essay. Radiographics 2000; 20:1227–1243.
16. Hubbard AM, States LJ. Fetal magnetic resonance imaging. Top Magn Reson Imaging 2001; 12:93–103.
17. Vimercati A, Greco P, Vera L et al. The diagnostic role of "*in utero*" magnetic resonance imaging. J Perinat Med 1999; 27:303–308.
18. Coakley FV, Lopoo JB, Lu Y et al. Normal and hypoplastic fetal lungs: volumetric assessment with prenatal single-shot rapid acquisition with relaxation enhancement MR imaging. Radiology 2000; 216:107–111.
19. Rypens F, Metens T, Rocourt N et al. Fetal lung volume: estimation at MR imaging-initial results. Radiology 2001; 219:236–241.
20. Paek BW, Coakley FV, Lu Y et al. Congenital diaphragmatic hernia: prenatal evaluation with MR lung volumetry—preliminary experience. Radiology 2001; 220:63–67.
21. Mahieu-Caputo D, Sonigo P, Dommergues M et al. Fetal lung volume measurement by magnetic resonance imaging in congenital diaphragmatic hernia. Bjog 2001; 108:863–868.
22. Tanigaki S, Miyakoshi K, Tanaka M et al. Pulmonary hypoplasia: prediction with use of ratio of MR imaging-measured fetal lung volume to US-estimated fetal body weight. Radiology 2004; 232:767–772.
23. Osada H, Kaku K, Masuda K et al. Quantitative and qualitative evaluations of fetal lung with MR imaging. Radiology 2004; 231:887–892.

24. Walsh DS, Hubbard AM, Olutoye OO et al. Assessment of fetal lung volumes and liver herniation with magnetic resonance imaging in congenital diaphragmatic hernia. Am J Obstet Gynecol 2000; 183:1067–1069.
25. Williams G, Coakley FV, Qayyum A et al. Fetal relative lung volume: quantification by using prenatal MR imaging lung volumetry. Radiology 2004; 233:457–462.
26. Metkus AP, Filly RA, Stringer MD et al. Sonographic predictors of survival in fetal diaphragmatic hernia. J Pediatr Surg 1996; 31:148–151.
27. Leung JW, Coakley FV, Hricak H et al. Prenatal MR imaging of congenital diaphragmatic hernia. Am J Roentgenol 2000; 174:1607–1612.
28. Adzick NS, Harrison MR, Glick PL et al. Diaphragmatic hernia in the fetus: prenatal diagnosis and outcome in 94 cases. J Pediatr Surg 1985; 20:357–361.
29. Pumberger W, Patzak B, Prayer D et al. Fetal liver magnetic resonance imaging in anterior body wall defects: a study of specimens from the museum of pathology. J Pediatr Surg 2003; 38:1147–1151.
30. Hubbard AM, Adzick NS, Crombleholme TM et al. Left-sided congenital diaphragmatic hernia: value of prenatal MR imaging in preparation for fetal surgery. Radiology 1997; 203:636–640.
31. Levine D. Ultrasound versus magnetic resonance imaging in fetal evaluation. Top Magn Reson Imaging 2001; 12:25–38.
32. Beckmann KR, Nozicka CA. Congenital diaphragmatic hernia with gastric volvulus presenting as an acute tension gastrothorax. Am J Emerg Med 1999; 17:35–37.
33. Gilsanz V, Emons D, Hansmann M et al. Hydrothorax, ascites, and right diaphragmatic hernia. Radiology 1986; 158:243–246.
34. Suzuki N, Tsuchida Y, Takahashi A et al. Prenatally diagnosed cystic lymphangioma in infants. J Pediatr Surg 1998; 33:1599–1604.
35. Ruano R, Aubry JP, Simon I et al. Prenatal diagnosis of a large axillary cystic lymphangioma by three-dimensional ultrasonography and magnetic resonance imaging. J Ultrasound Med 2003; 22:419–423.
36. Kaminopetros P, Jauniaux E, Kane P et al. Prenatal diagnosis of an extensive fetal lymphangioma using ultrasonography, magnetic resonance imaging and cytology. Br J Radiol 1997; 70:750–753.
37. Snyder ME, Luck SR, Hernandez R et al. Diagnostic dilemmas of mediastinal cysts. J Pediatr Surg 1985; 20:810–815.
38. Gulrajani M, David K, Sy W et al. Prenatal diagnosis of a neurenteric cyst by magnetic resonance imaging. Am J Perinatol 1993; 10:304–306.
39. Levine D, Barnes PD, Sher S et al. Fetal fast MR imaging: reproducibility, technical quality, and conspicuity of anatomy. Radiology 1998; 206:549–554.
40. Hata K, Hata T, Manabe A et al. Hypoplastic left heart syndrome: color Doppler sonographic and magnetic resonance imaging features *in utero*. Gynecol Obstet Invest 1995; 39:70–72.
41. Hata T, Makihara K, Aoki S et al. Prenatal diagnosis of valvar aortic stenosis by Doppler echocardiography and magnetic resonance imaging. Am J Obstet Gynecol 1990; 162:1068–1070.
42. Muhler MR, Rake A, Schwabe M et al. Truncus arteriosus communis in a midtrimester fetus: comparison of prenatal ultrasound and MRI with postmortem MRI and autopsy. Eur Radiol 2004; 14:2120–2124.
43. Kivelitz DE, Muhler M, Rake A et al. MRI of cardiac rhabdomyoma in the fetus. Eur Radiol 2004; 14:1513–1516.
44. Levine D, Barnes PB, Korf B et al. Tuberous sclerosis in the fetus: second-trimester diagnosis of subependymal tubers with ultrafast MR imaging. Am J Roentgenol 2000; 175:1067–1069.
45. Levine D, Hatabu H, Gaa J et al. Fetal anatomy revealed with fast MR sequences. Am J Roentgenol 1996; 167:905–908.
46. Levine D, Stroustrup Smith A, Barbaras L et al. Compendium of Fetal MRI [image]. Available online of Beth Israel Deaconess Medical Center Radiology department website, http://bidmc.harvard.edu/fetalatlas/, 2004.

6

MR Imaging of the Fetal Abdomen and Pelvis

VANDANA DIALANI, TEJAS MEHTA, DEBORAH LEVINE

INTRODUCTION

The indications for magnetic resonance (MR) imaging of the fetal abdomen and pelvis are less well established than those of the fetal central nervous system and chest. It has been demonstrated that in cases where the sonographic diagnosis is unclear, MR examinations can provide important anatomic information that aids in diagnosis, parental counseling, planning delivery, and perinatal surgical procedures (1–11).

NORMAL ANATOMY

Gastrointestinal Tract

The stomach is seen as a fluid-filled structure in the left upper quadrant and is hyperintense on T_2-weighted images (Fig. 6.1) and hypointense on T_1-weighted images. It is well visualized by 14–15 weeks of gestation. It may transiently not be visualized owing to emptying but should be apparent at some point during a 20 min MR examination of the fetal torso.

The normal small bowel is fluid-filled. The small bowel wall is of intermediate signal intensity and the internal fluid is of high signal centrally on T_2-weighted images (Fig. 6.2) and lower signal intensity on T_1-weighted images. The colon and rectum contain meconium which, by the late second trimester, has low signal intensity on T_2-weighted images (Fig. 6.2) and high signal intensity on T_1-weighted images (Fig. 6.3) (12,13). The haustral pattern of the large bowel is recognized after 25 weeks of gestation (Figs. 6.2 and 6.3) (13).

Genitourinary System

The renal parenchyma is of intermediate signal intensity on T_2-weighted images, with high signal intensity in the collecting system (Fig. 6.4) (12). A thick slice (20 mm) heavily T_2-weighted sequence can be helpful for visualizing the entire collecting system (Fig. 6.5) (14). The adrenal gland is of relatively low signal intensity on T_2-weighted images (Fig. 6.4) and can be observed in the suprarenal position. As fat is of high signal intensity on T_2-weighted sequences used for fetal imaging, the perinephric fat also appears to be of high signal, and should not be mistaken for ascites (Fig. 6.4).

The urinary bladder is visualized as a high signal intensity structure on T_2-weighted images of the pelvis (Fig. 6.6). Urinary jets can cause focal loss of signal in the bladder (Chapter 10, Fig. 10.16).

The genitalia are typically well visualized on axial or sagittal views (Figs. 6.7 and 6.8). The testicles descend into the scrotum between 28 and 35 weeks and are intermediate signal intensity structures within the scrotum.

Liver

The liver is of homogenous, low to intermediate signal intensity on T_2-weighted images, and slightly high signal intensity on T_1-weighted images (Fig. 6.9). The two lobes of the liver are generally equal in size because of the distribution of the fetal circulation. The ductus venosus is visualized in the late third trimester (10). T_1-weighted images are typically utilized to assess for herniated liver in fetuses with congenital diaphragmatic hernia (15).

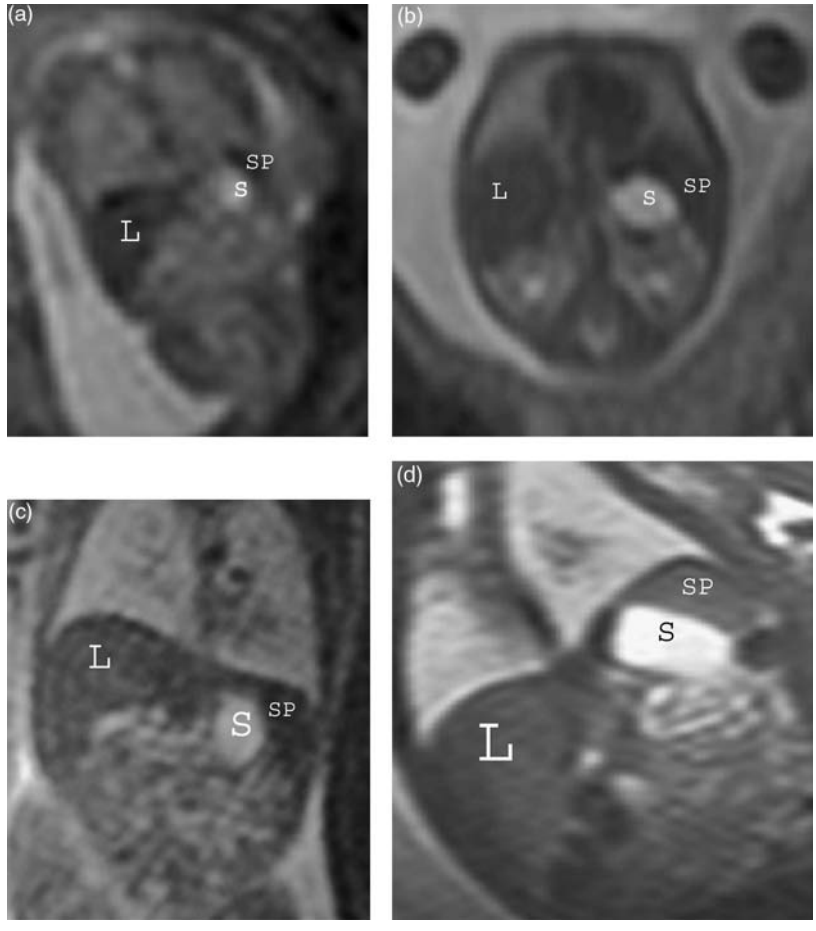

Figure 6.1 Normal stomach and spleen. Coronal T_2-weighted images at 14 (a), 18 (b), 21 (c), and 34 (d) weeks gestational age. The stomach (S) is of high signal intensity because of fluid content. The spleen (SP) is of homogenous low to intermediate signal intensity, just lateral to the stomach. L, liver.

Gallbladder

The gallbladder is visualized as a fluid-filled structure in the right abdomen and has high signal intensity on T_2-weighted images (Fig. 6.9) and low signal intensity on T_1-weighted images (10).

Spleen

The spleen is of similar signal intensity to the liver and is visualized as a solid organ lateral to the stomach (10). It has a homogenous, low to intermediate signal on T_2-weighted images (Fig. 6.1).

Umbilical Cord

The normal umbilical cord consists of two umbilical arteries and one umbilical vein. The umbilical arteries proceed from their origin at the iliac arteries along the lateral margins of the urinary bladder (Fig. 6.6) and then to the umbilicus. The cord insertion site into the abdominal wall is well visualized on sagittal and axial images (Fig. 6.10). The three vessels of the umbilical cord can also be seen in cross-section on T_2-weighted images, because of the flow void in the vessels surrounded by the high signal intensity of the amniotic fluid.

Abdominal Vasculature

The flowing vessels in the abdomen and pelvis are of low signal intensity on T_2-weighted images as a result of flow void (Fig. 6.11) (7). On flow sensitive sequences such as gradient echo, vascularity can appear hyperintense (Chapter 5, Fig. 5.6) (10).

(*text continued on page 121*)

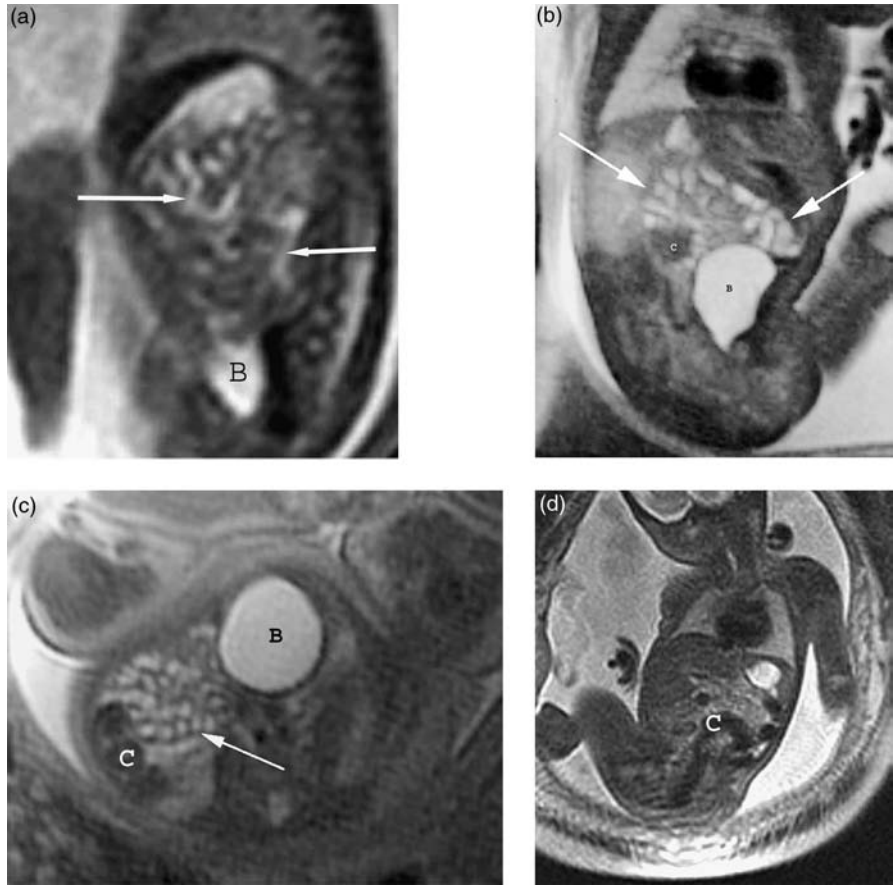

Figure 6.2 Normal small and large bowel. T_2-weighted images at 25 (a), 30 (b), 33 (c), and 37 (d) weeks gestational age. The small bowel (arrows) appears of high signal intensity and the colon ("c" indicated in the figure) of low signal intensity. B, bladder.

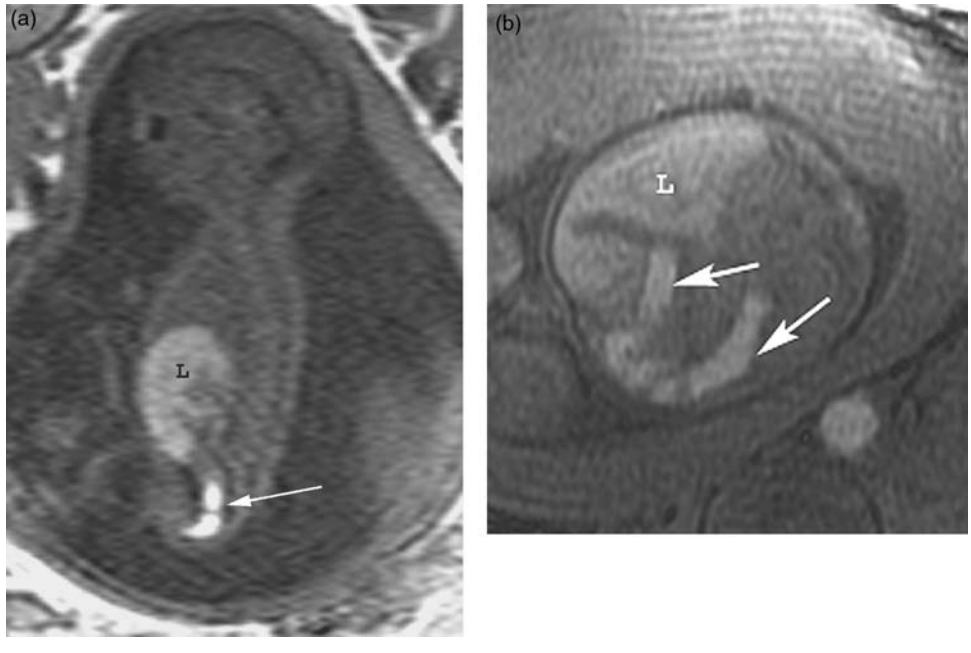

Figure 6.3 Normal colon. T_1-weighted images at 24 (a) and 31 (b) weeks show the relatively high signal intensity of the colon (arrow) and the liver (L).

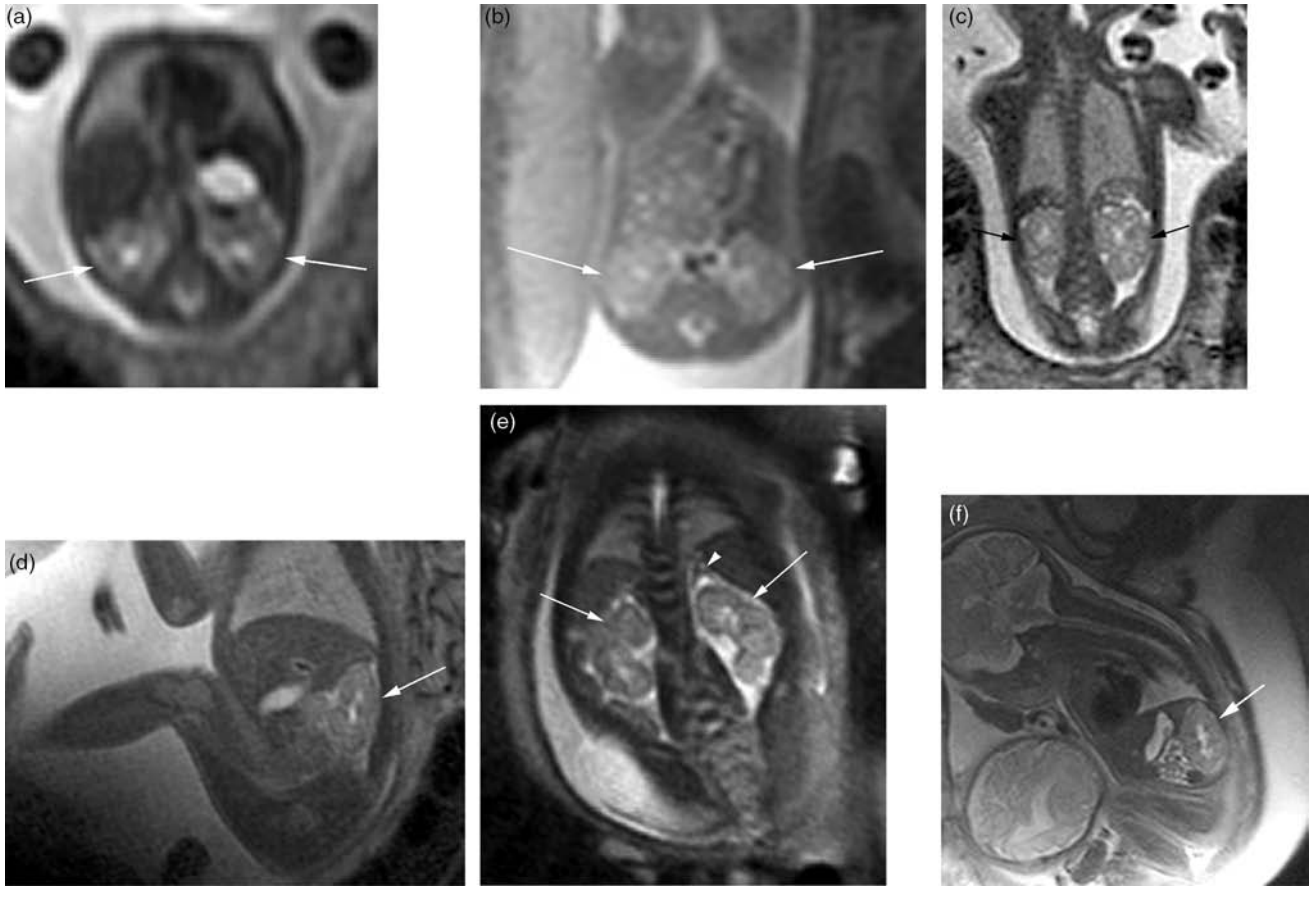

Figure 6.4 Normal kidneys. T_2-weighted images at 18 (a), 21 (b), 24 (c), 29 (d), 32 (e), 35 (f) weeks gestational age. The renal parenchyma (arrows) shows low to intermediate signal intensity and the renal collecting system shows high signal intensity. Note that as fat appears bright on the sequences typically used for fetal imaging, perinephric fat will appear of high signal intensity, and should not be mistaken for ascites. The adrenal gland (arrowhead in e) is visualized as a low signal intensity cap over the kidney.

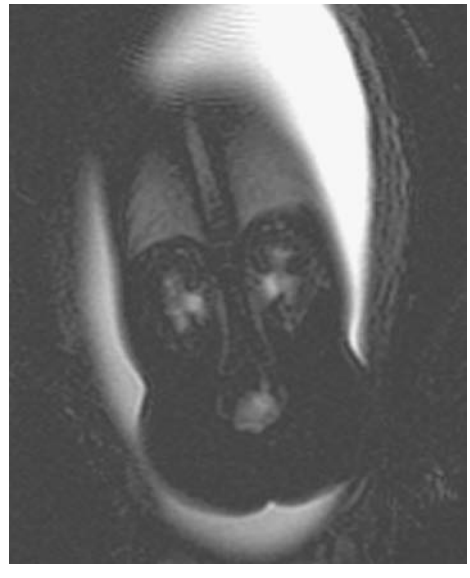

Figure 6.5 MR urogram. Coronal heavily T_2-weighted thick slice (20 mm) showing the entire collecting system at 30 weeks gestation.

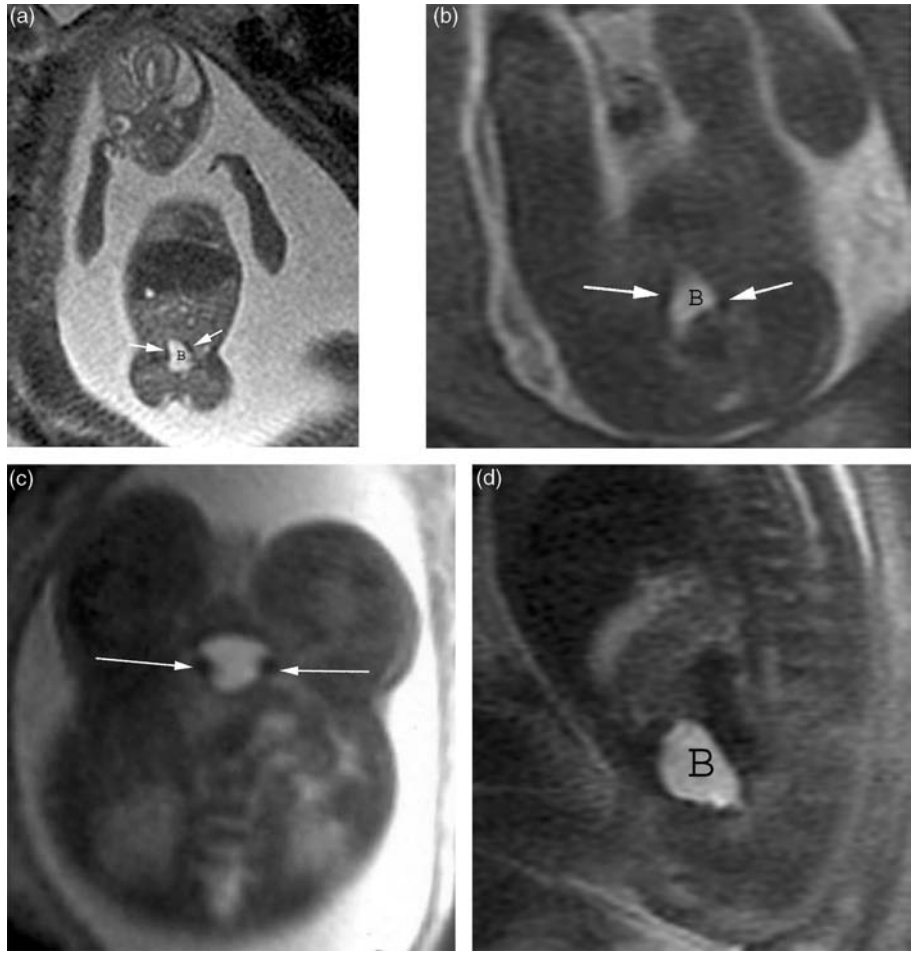

Figure 6.6 Normal urinary bladder. T_2-weighted images at 18 (a), 21 (b), and 26 (c, d) weeks gestational age. The bladder is the hyperintense structure seen in the pelvis. The umbilical arteries (arrows) are recognized as flow voids on either side of the bladder.

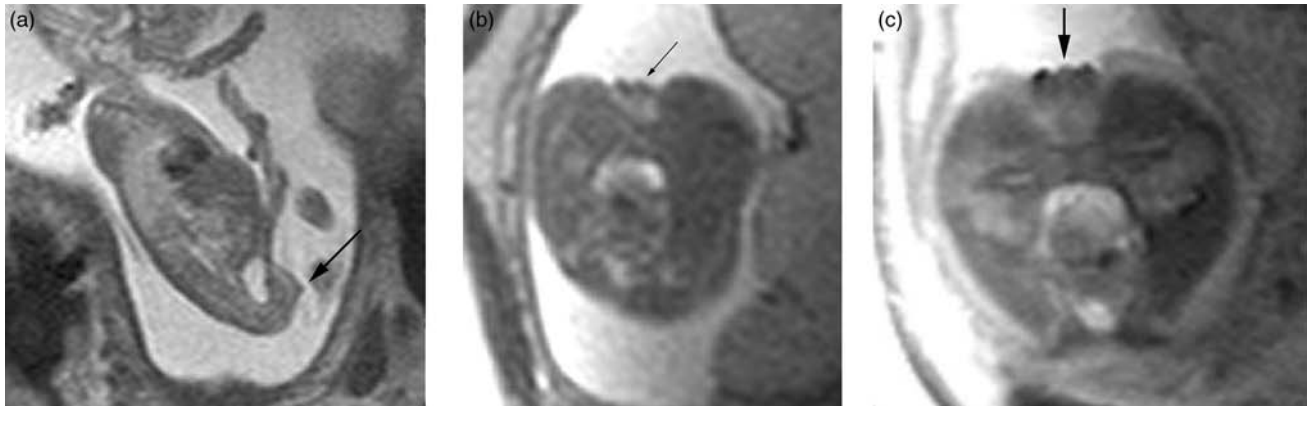

Figure 6.7 Normal female genitalia. T_2-weighted images at 18 (a), 24 (b), and 31 (c) weeks gestational age. In the sagittal view (a) the female genitalia (arrow) has a downward orientation.

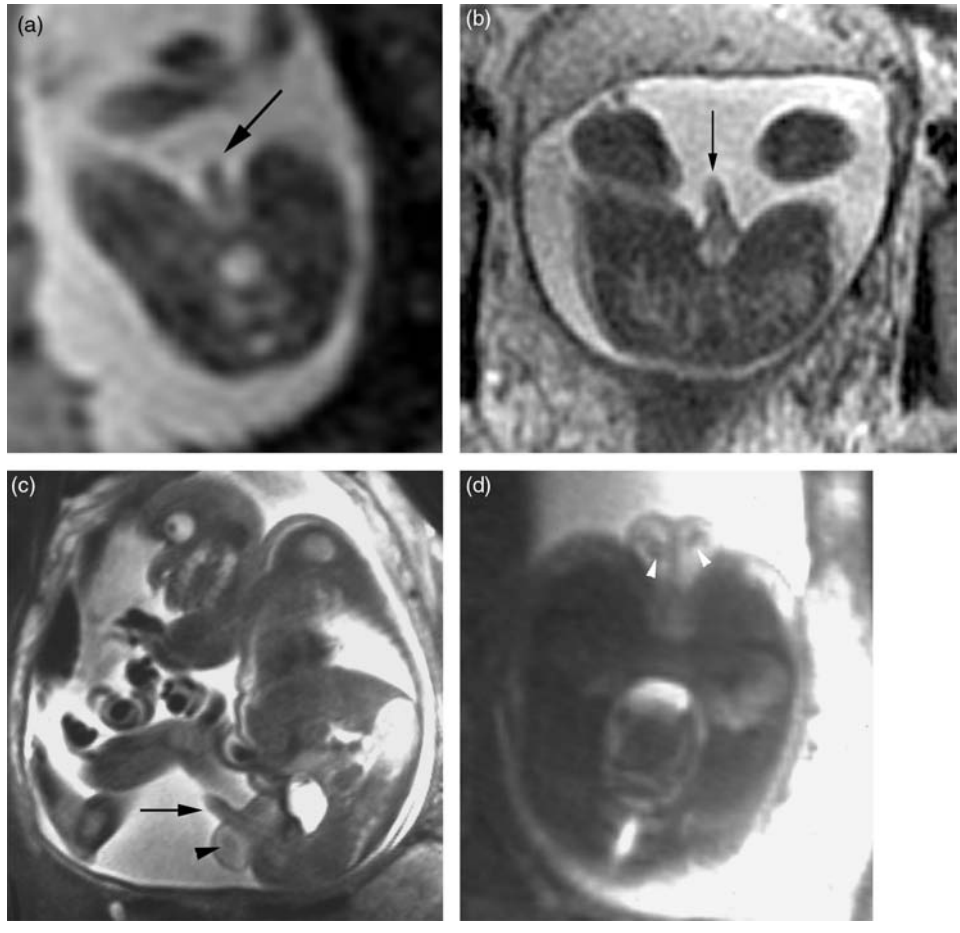

Figure 6.8 Normal male genitalia. T_2-weighted images at 16 (a), 24 (b), and 31 (c, d) weeks gestational age. Note the phallus (arrow). The testicles (arrowheads) descend into the scrotum between 28 and 35 weeks, and are intermediate signal intensity structures within the scrotum.

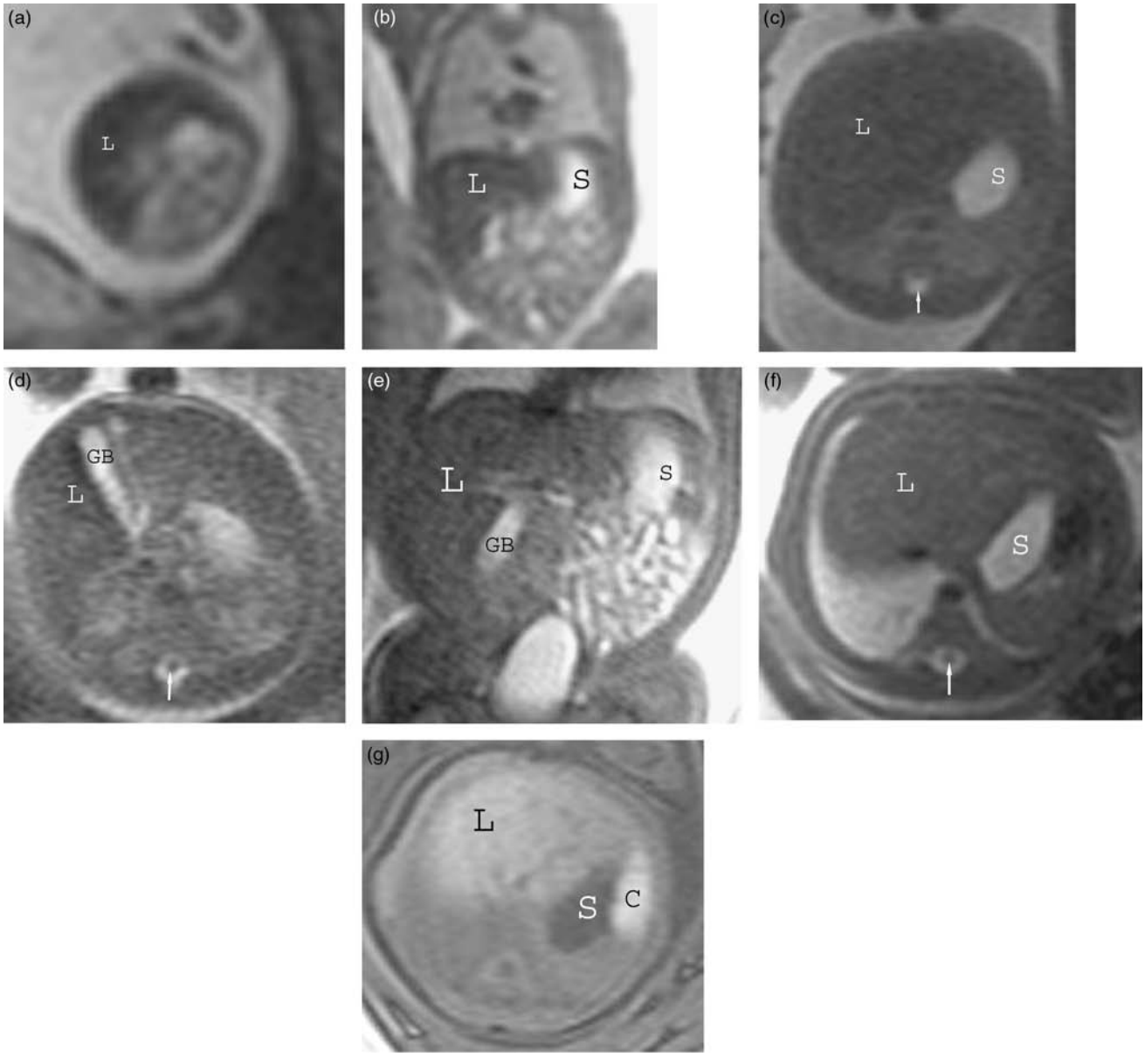

Figure 6.9 Normal liver. T_2-weighted images at 14 (a), 18 (b), 22 (c), 26 (d) 31 (e), and 32 (f) weeks gestational age and T_1-weighted image at 32 weeks (g). The liver (L) is of low to intermediate signal intensity on T_2-weighted images and is of slightly high signal intensity on T_1-weighted image. S, stomach; GB, gall bladder; C, colon; arrow indicates the spinal cord.

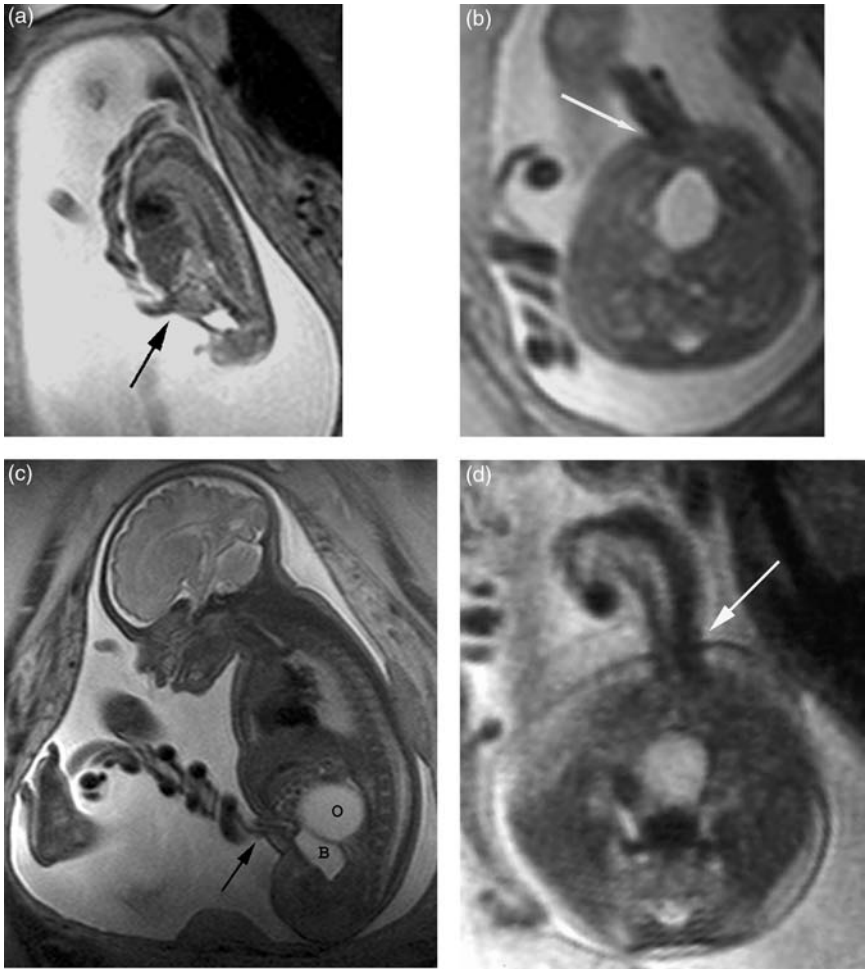

Figure 6.10 Normal umbilical cord. T_2-weighted images at 19 (a), 25 (b), and 33 (c, d) weeks gestational age. The cord inserts into the mid-anterior abdominal wall (arrow). The three vessels (two arteries and one vein) are individually identified as flow voids within the cord, with the vein being slightly larger than the arteries. (c) has an ovarian cyst (O) above the bladder (B).

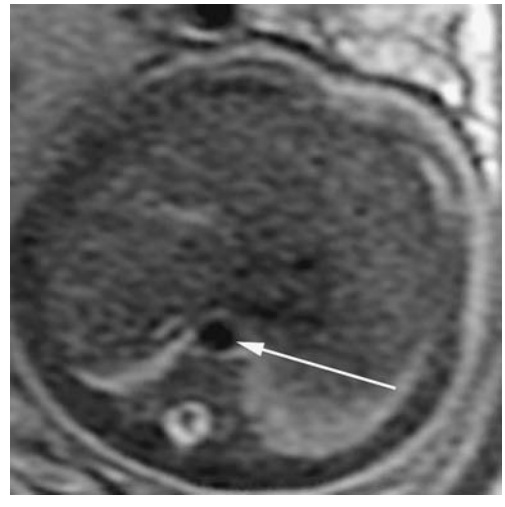

Figure 6.11 Normal abdominal aorta. Axial T_2-weighted image at 20 weeks gestational age shows low signal intensity in the aorta (arrow).

ANOMALIES

Fetal Gastrointestinal Tract Anomalies

The fetal gastrointestinal tract is a common site for congenital anomalies. Most of these are well assessed by sonography. The MR appearance of most of these anomalies follows that expected by ultrasound.

Absent or Malpositioned Stomach

The stomach should be normally seen in the left upper abdomen at some point during a 20 minute ultrasound or MR examination. Persistent nonvisualization of the fetal stomach can be because of esophageal atresia (Chapter 5, Fig. 5.39), anhydramnios, chromosomal anomalies, or a swallowing disorder. When a stomach is not seen in the left upper abdomen, an attempt should be made to identify a stomach-like structure elsewhere in the fetal body. In most cases of congenital diaphragmatic hernia, the stomach is seen in the fetal thorax (Chapter 5, Figs. 5.20–5.24). Congenital diaphragmatic hernia is discussed in more detail in Chapter 5.

It is also important to assess abdominal situs. Both stomach and heart should be on the left side of the fetus. However, in certain cases of situs inversus, the stomach can be located on the opposite side of the heart and be in the right upper abdomen (Fig. 6.12 and Chapter 5, Fig. 5.35).

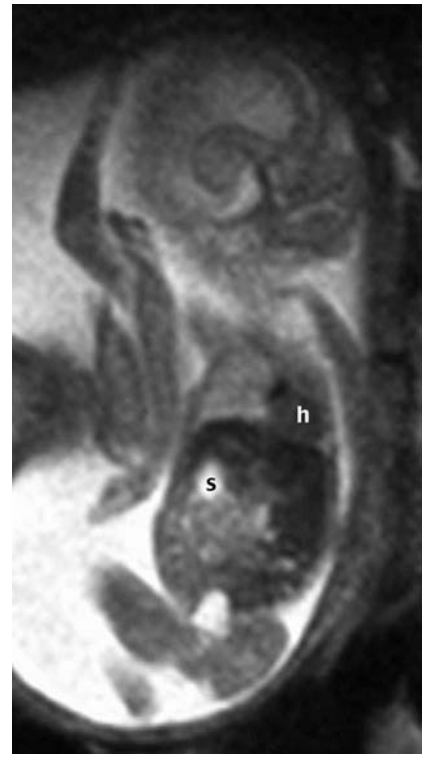

Figure 6.12 Situs inversus at 18 weeks gestational age. Coronal T_2-weighted image shows a left-sided heart (h) and right-sided stomach (s).

Duodenal Stenosis and Atresia

Duodenal stenosis and atresia are diagnosed characteristically by the double bubble sign on ultrasound and MR imaging (Fig. 6.13). The dilated stomach and the proximal portion of the duodenum produce the characteristic appearance. These are very well visualized on the T_2-weighted coronal and axial images. There is a high association of duodenal atresia with trisomy 21 (16,17).

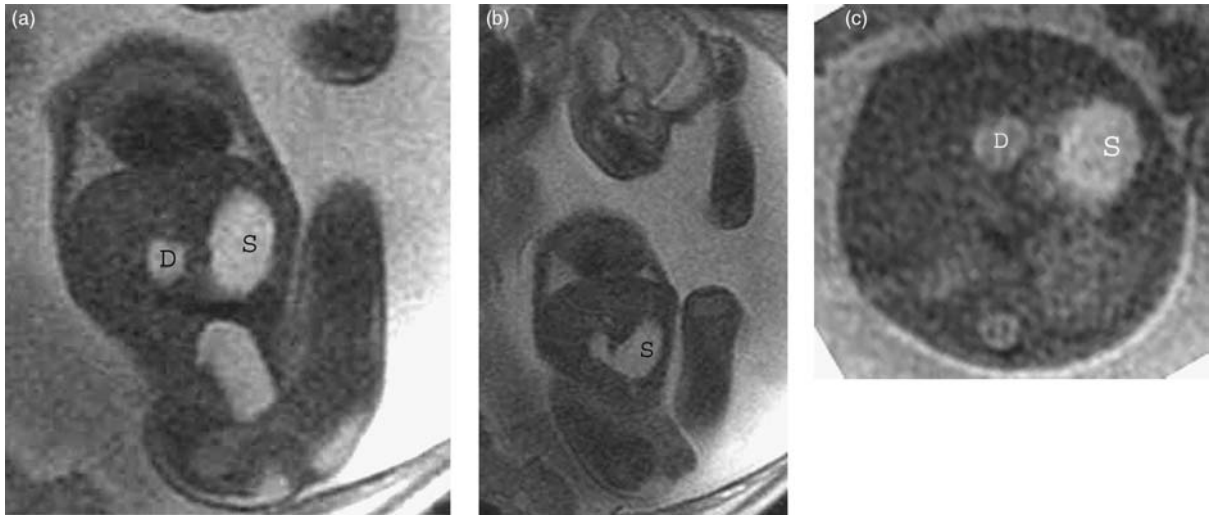

Figure 6.13 Duodenal atresia in association with trisomy 21 at 35 weeks gestational age. Coronal (a, b) and axial (c) views show the distended stomach (S) and proximal duodenum (D) giving the "double bubble appearance." Note the associated polyhydramnios.

Small Bowel Atresia

In cases of small bowel atresia, MR imaging can provide additional information beyond that provided by ultrasound regarding the obstruction. In proximal small bowel obstruction, the dilated proximal intestine appears hyperintense on T_2-weighted images and hypointense on T_1-weighted images, whereas in distal bowel obstruction the dilated meconium-filled distal intestine appears hypointense on T_2-weighted images and hyperintense on T_1-weighted images (13).

Meconium Peritonitis

In utero bowel perforation results in a sterile chemical peritonitis. Punctate calcifications may result, scattered throughout the abdomen. The perforated loops may seal off and a meconium pseudocyst may develop. Sonographic features suggestive of severe meconium peritonitis are distended fetal bowel loops, large cystic masses, ascites, and polyhydramnios (18,19). The calcifications associated with meconium peritonitis are better visualized on ultrasound than on MR imaging (Fig. 6.14) (21).

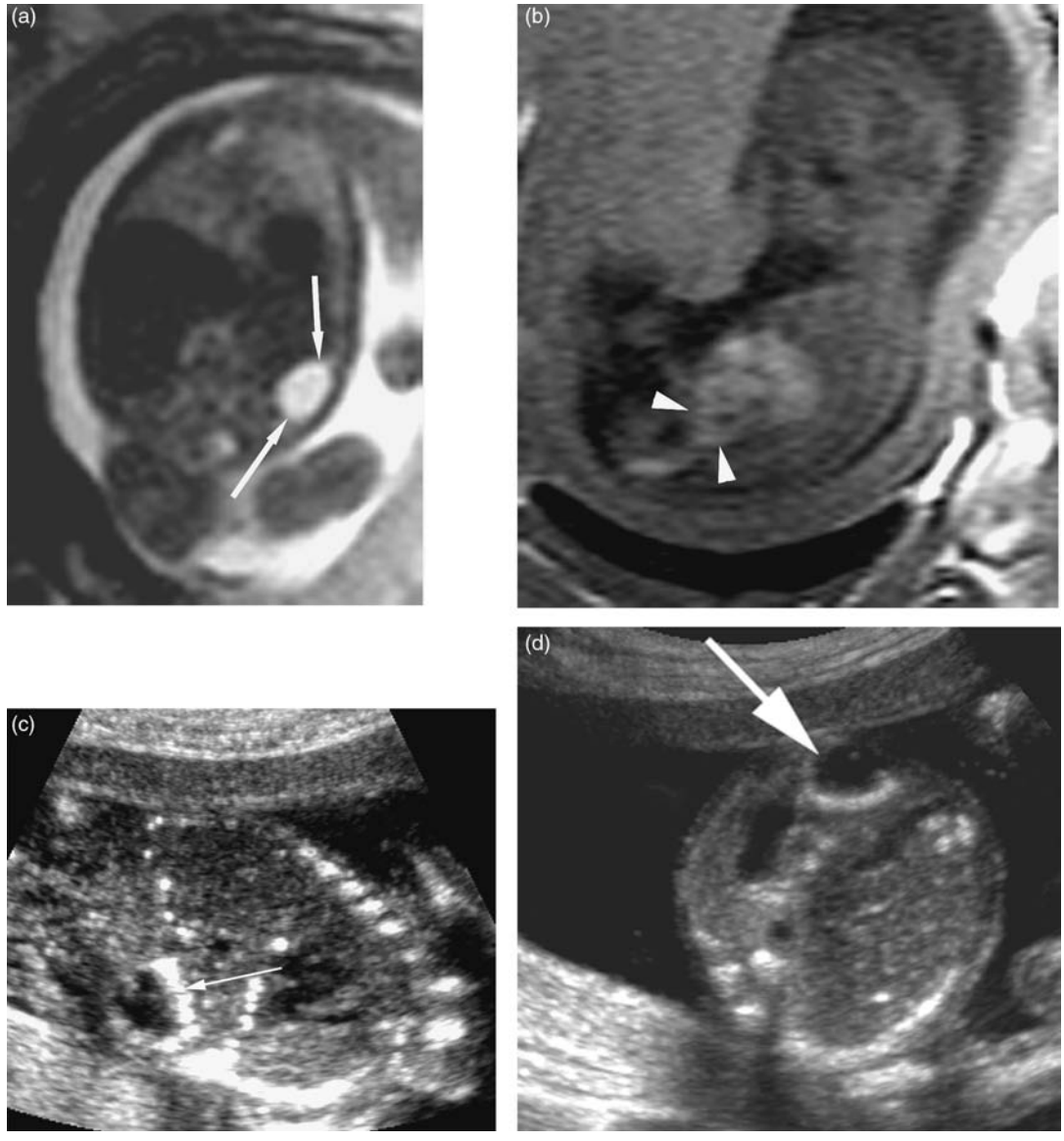

Figure 6.14 Meconium pseudocyst at 19 weeks gestational age. Coronal T_2-weighted image (a) and sagittal T_1-weighted image (b) show a cyst in the left upper quadrant (arrows). Note the abnormal signal intensity of the small bowel loops, which are of low signal intensity on the T_2-weighted image, and of slightly high signal intensity on the T_1-weighted image (arrowheads). Sonogram (c, d) shows calcifications around the pseudocyst and calcifications around the liver and within the abdomen that are not seen on the MR images. [From Levine et al. (20)]

Fetal Genitourinary Tract

Renal anomalies are typically best assessed with ultrasound. However, MR imaging can play an important role in diagnosis when visualization of the fetal anatomy is limited by anhydramnios (or severe oligohydramnios) or maternal body habitus (6,22,23).

Hydronephrosis and Pelvicaliectasis

Pelviectasis is defined as dilatation of the central renal pelvis, and may be seen as a normal variant. If the pelviectasis is <4 mm (measured in the anteroposterior dimension in the axial plane) at or before 22 weeks gestational age, or <7 mm after 22 weeks, it is unlikely to be of clinical significance (Fig. 6.15) (24,25). If there is associated caliectasis then this is termed hydronephrosis. The dilated renal collecting system is easily observed on MR examinations because of the high signal intensity of urine on T_2-weighted images (Fig. 6.16). It is detected best in coronal or axial plane (26). Fetal MR urography is performed with thick slice (20 mm) heavily T_2-weighted images in the coronal plane to demonstrate the entire course of the ureters (Fig. 6.5) (14).

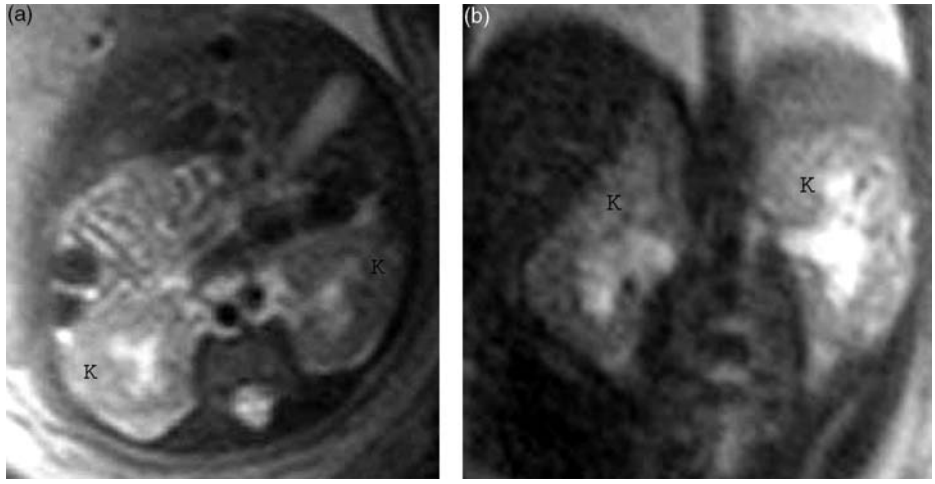

Figure 6.15 Central renal dilatation and mild hydronephrosis. T_2-weighted axial (a) and coronal (b) images at 26 weeks gestational age and coronal image at 30 weeks gestational age show central renal dilatation of 5–6 mm. Since the fluid slightly distends the calices on the coronal view this is mild hydronephrosis. K, kidneys. [From Levine et al. (20)]

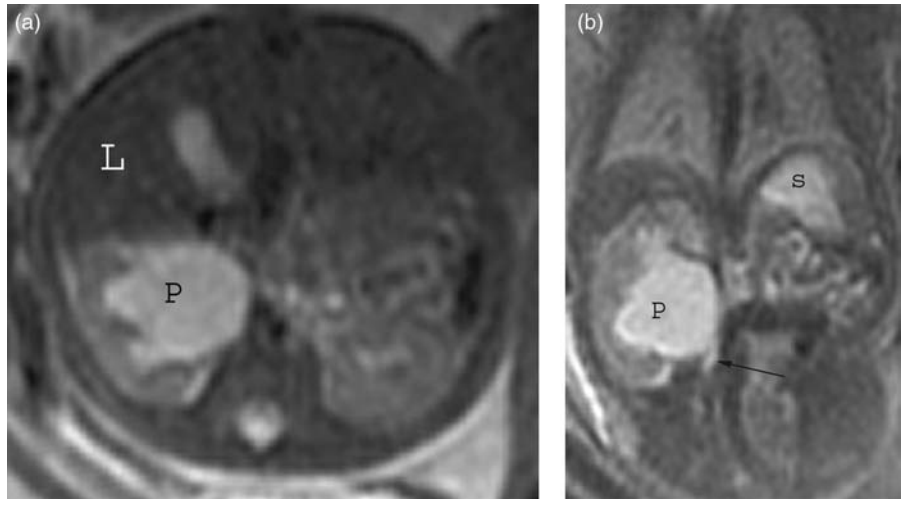

Figure 6.16 Ureteropelvic obstruction at 19 weeks gestational age. Axial (a) and coronal (b) T_2-weighted images reveal that the renal pelvis (P) is dilated out of proportion to the calices and proximal ureter (arrow). L, liver; S, stomach. [From Levine et al. (20)]

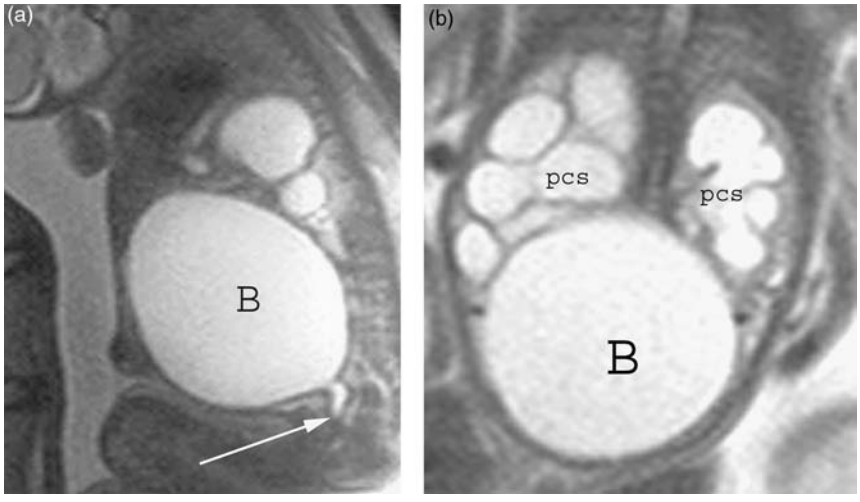

Figure 6.17 Posterior urethral valves at 27 weeks gestational age. Sagittal (a) and coronal (b) T_2-weighted images show a dilated bladder (B), severe hydronephrosis with dilatation of the entire pelvicalyceal system (pcs) and dilated posterior urethra (arrow). [From Levine et al. (20)]

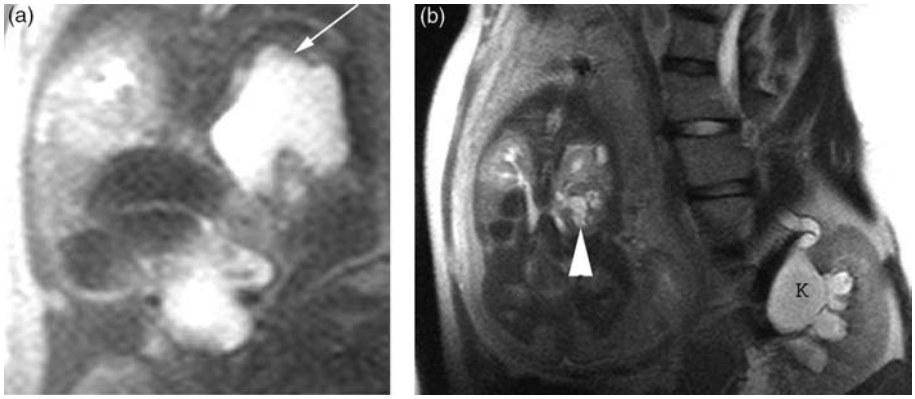

Figure 6.18 Obstructed upper pole moiety of duplex kidney at 37 weeks gestational age. Coronal T_2-weighted images show a severely hydronephrotic upper pole moiety (arrow) and distended lower pole moiety as well (arrowhead). Note the hydronephrotic maternal kidney (K, note that the image is oriented with respect to fetal anatomy).

Ureteropelvic junction obstruction is the most common cause of hydronephrosis detected prenatally (27). In this condition, the ureter is not dilated and the renal pelvis is dilated out of proportion to the degree of calyceal dilatation (Fig. 6.16). With progressive obstruction, there is progressive dilatation of the renal tubules, resulting in renal dysplastic changes that manifest as cysts in the cortex and medulla (27). These post-obstructive cysts tend to be small, of similar size, and primarily peripherally located, although in more severe cases can extend centrally.

Posterior urethral valves are typically diagnosed by ultrasound with findings of a distended bladder with keyhole deformity and hydroureteronephrosis in a male fetus. Similar findings can be documented with MR imaging (Fig. 6.17).

Duplex kidneys can have a distended collecting system from either reflux (typically in the lower pole moiety) or obstruction (typically in the upper pole moiety). Fetal MR examinations can show the duplicated collecting system (Fig. 6.18) and can demonstrate an associated ureterocele (28).

Horseshoe kidney may be visualized on MR imaging with renal tissue extending across the spine on axial T_2-weighted images (Fig. 6.19).

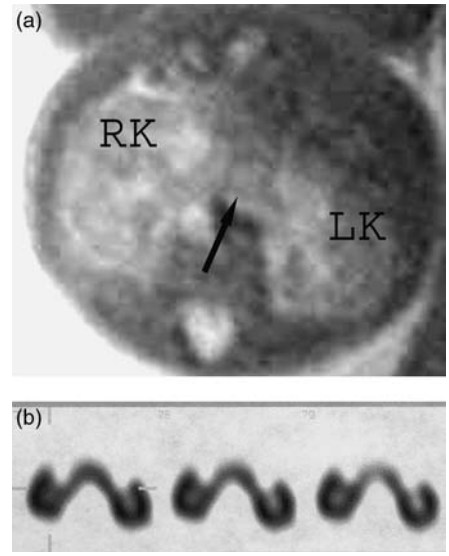

Figure 6.19 Horseshoe kidney at 27 weeks gestational age. (a) Axial T_2-weighted image shows the kidneys (RK, LK) with renal tissue extending across the spine (arrow). (b) Postnatal technetium-99m DMSA (dimercaptosuccinic acid) scan confirms the horseshoe kidney.

Renal Agenesis and Ectopic Kidneys

At times, the anhydramnios associated with bilateral renal agenesis makes definitive sonographic diagnosis of this abnormality difficult. In these cases fetal MR imaging can be helpful (Fig. 6.20) (29). Absence of the kidney in the renal fossa is indicated by the detection of a flattened ("lying down") adrenal gland (Figs. 6.20 and 6.21) (30). In bilateral renal agenesis the bladder will not be visualized and there will be severe oligohydramnios or anhydramnios. Although bilateral renal agenesis is a fatal condition, unilateral renal agenesis is most often an isolated finding and associated with normal life expectancy. It may, however, be associated with VACTERL complex (vertebral, anal, cardiac, tracheoesophageal, renal, and limb anomalies); thus, the entire fetus needs to be well assessed when one kidney is not visualized. When a kidney is not visualized in the renal fossa, MR imaging can be utilized to identify the ectopic location (Fig. 6.21).

Renal Cystic Diseases

As mentioned earlier, cysts may occur in the kidney as sequelae of obstruction. These cysts are generally small, uniform, and primarily peripherally located. Multicystic dysplastic kidney (MCDK) manifests as an enlarged kidney with multiple, randomly scattered cysts of varying sizes (Fig. 6.22) (31,32). The cysts are of high signal intensity on T_2-weighted images and are seen separate from the pelvicalyceal system. The renal parenchyma is seen in small islands in-between the cysts. The normal reniform contour of the kidney is lost as a result of bulging cysts (Fig. 6.22) (31,33). Fetal MR imaging can be helpful in rare cases where the abnormality is not well established sonographically (34). Bilateral MCDK is uniformly fatal.

Autosomal recessive polycystic kidney disease (ARPKD) is an inherited disorder involving cystic dilatation of the renal collecting tubules. The innumerable tiny cysts are too small to resolve on ultrasound, where the appearance is that of bilaterally enlarged echogenic kidneys (32). Case reports have illustrated the MR appearance of ARPKD as low signal intensity on T_1-weighted images and high signal intensity on T_2-weighted images (Fig. 6.23). Corticomedullary differentiation and pelvicalyceal system are not identified (29,35–38).

Isolated renal cysts, although commonly seen in adulthood, are acquired lesions and are rare in fetal imaging.

Cloacal Malformation and Bladder and Cloacal Exstrophy

Cloacal malformation is a rare cause of fetal obstructive uropathy. It is the result of failure of division of the primitive cloaca with direct communication between the gastrointestinal, urinary, and genital structures, resulting in a single perineal opening. This anomaly occurs mostly in females, although males may be affected rarely. It should be considered in any female fetus presenting with bilateral hydronephrosis, a poorly visualized bladder, and a cystic lesion arising from the pelvis (Figs. 6.24 and 6.25) (39). Calcified meconium in the colon and urinary tract provides an important clue to diagnosis (40). These calcifications are better visualized with ultrasound than with MR imaging (Fig. 6.25).

Bladder exstrophy is a rare congenital malformation in which the anterior wall of the bladder is absent and the posterior wall is exposed externally. A solid mass extrudes from an infraumbilical position (Fig. 6.26). The relationship between umbilical arteries and bladder exstrophy is

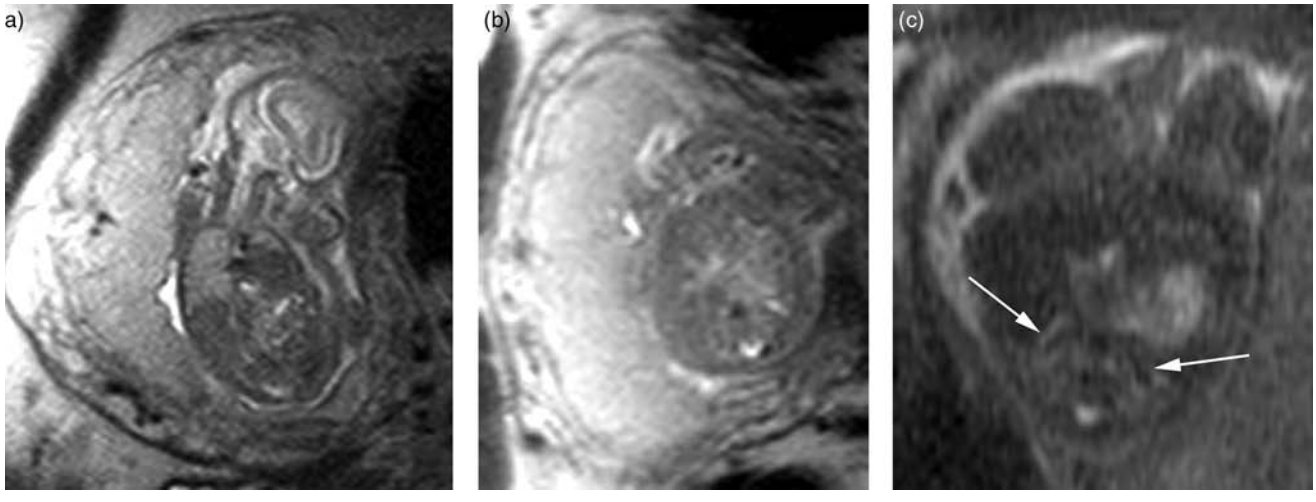

Figure 6.20 Bilateral renal agenesis at 17 weeks gestation. Coronal (a) and axial (b, c) T_2-weighted images show severe oligohydramnios and absent kidneys. Note the lying down adrenal sign (arrows in c). [From Levine et al. (20)]

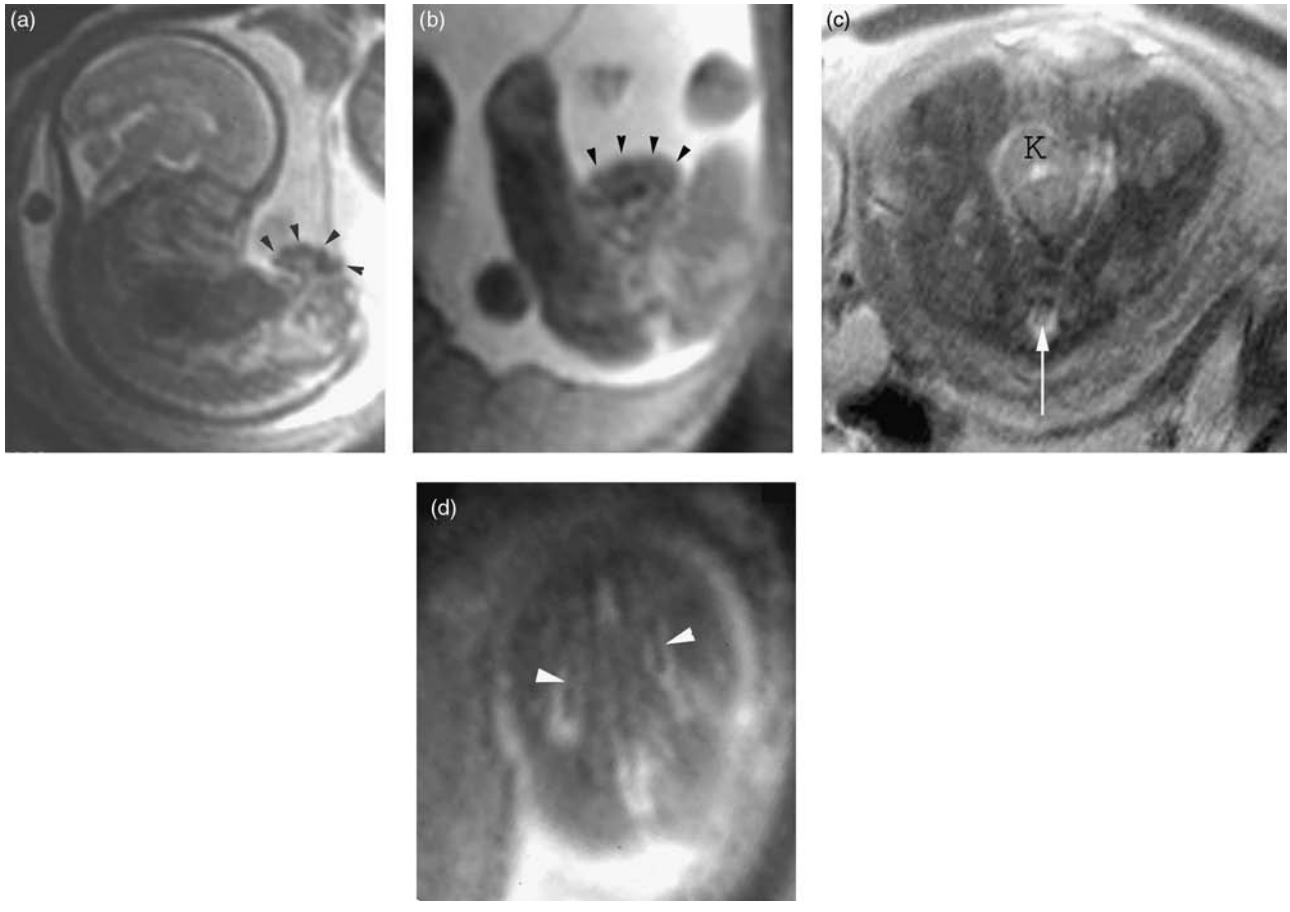

Figure 6.21 Cloacal exstrophy with pelvic kidney. Sagittal (a) and axial (b) T_2-weighted images at 18 weeks gestational age show a low anterior abdominal wall defect (black arrowheads). Axial T_2-weighted image at 32 weeks gestational age (c) shows a pelvic kidney (K), a tethered cord (arrow), and oligohydramnios. Coronal T_2-weighted image (d) shows the linear appearance of the adrenals caused by lack of kidneys in the renal fossa (white arrowheads), the "lying down adrenal sign." The lying down adrenal, pelvic kidney, and tethered cord were all findings that were not visualized sonographically. [(a, b, and d) from Levine et al. (20); (c) from Levine (34)]

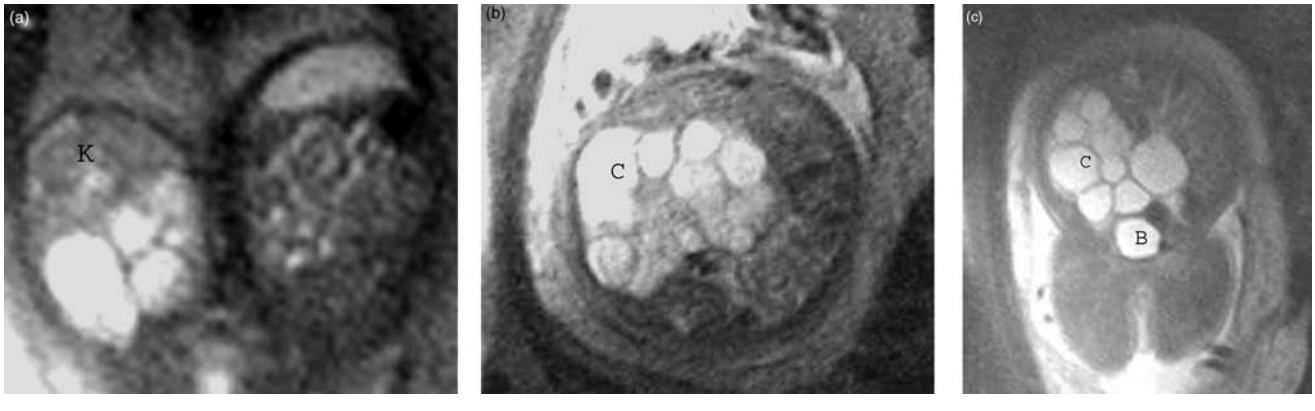

Figure 6.22 Cross-fused ectopia with cystic dysplastic lower moiety, at 28 weeks gestational age. Coronal (a) and axial (b, c) images show no left kidney and a dysplastic lower pole moiety (C) of the right kidney. The bladder (B) and amniotic fluid volume are normal. Note the normal appearance of the upper pole moiety (K). [(a) from Levine (33); (b, c) from Levine et al. (20)]

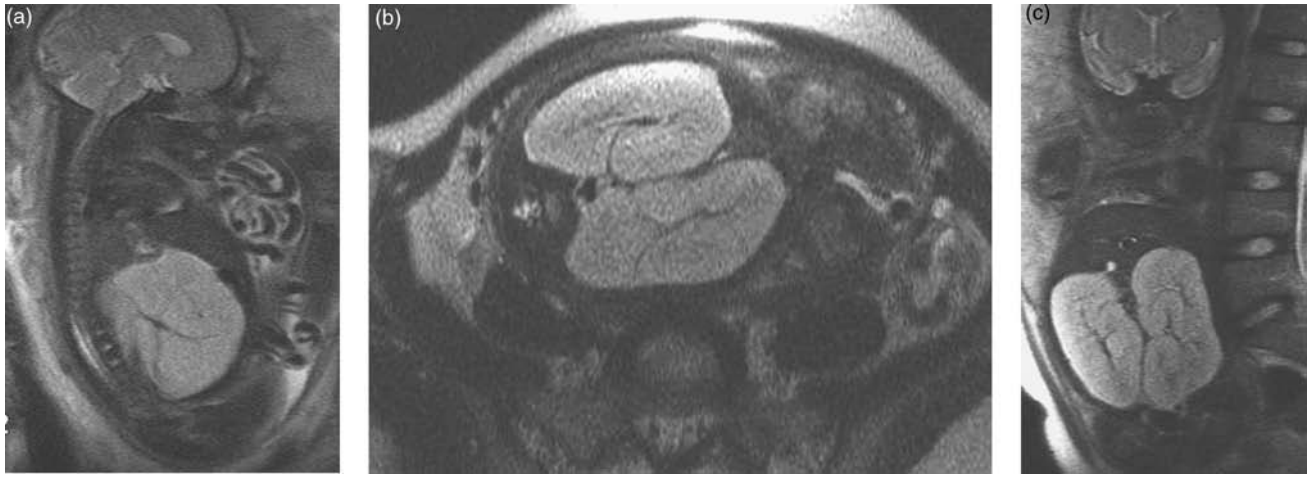

Figure 6.23 ARPKD at 32 weeks gestational age. Sagittal (a), axial (b) and coronal (c) T_2-weighted images show bilaterally enlarged, hyperintense kidneys. Note the associated oligohydramnios.

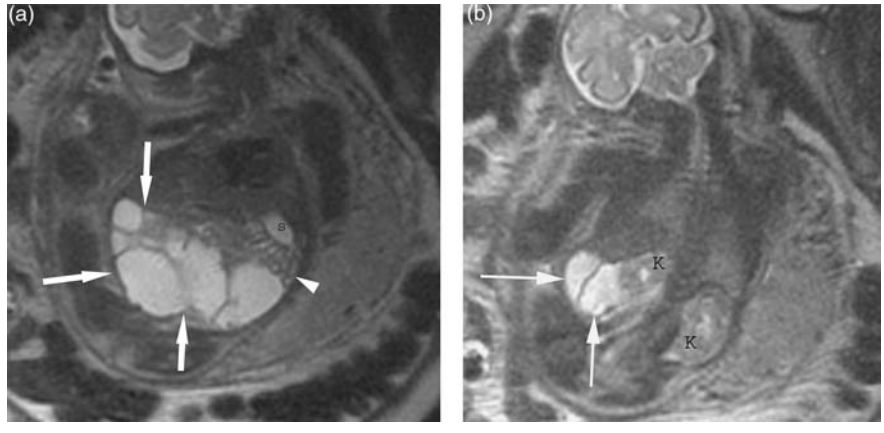

Figure 6.24 Cloacal malformation at 29 weeks gestational age. Coronal T_2-weighted images depict multiple dilated bowel loops (arrows) in the abdomen and pelvis. The bladder is not visualized separately. The kidneys (K) demonstrate central renal dilatation but no frank hydronephrosis. The stomach (s) and proximal small bowel (arrowheads) appear normal. Note the severe oligohydramnios.

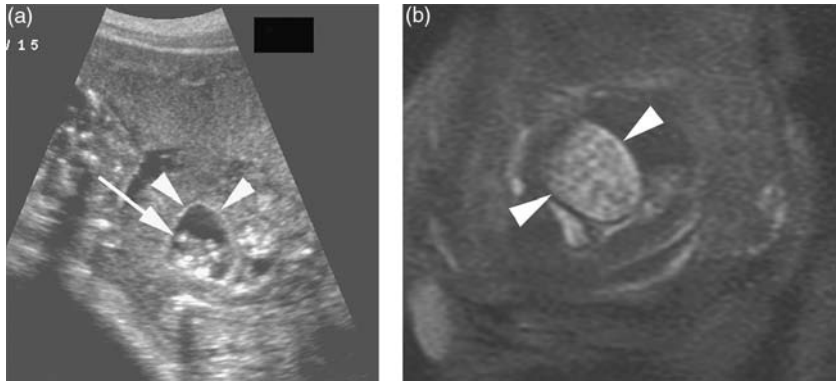

Figure 6.25 Cloacal malformation at 20 weeks gestational age. Sonogram (a) and oblique sagittal T_2-weighted MR image (b) show severe oligohydramnios and a cystic collection (arrowheads) in the fetal abdomen–pelvis. The calcifications (arrow) in the cloacal malformation are better visualized on the sonogram compared with the MR image.

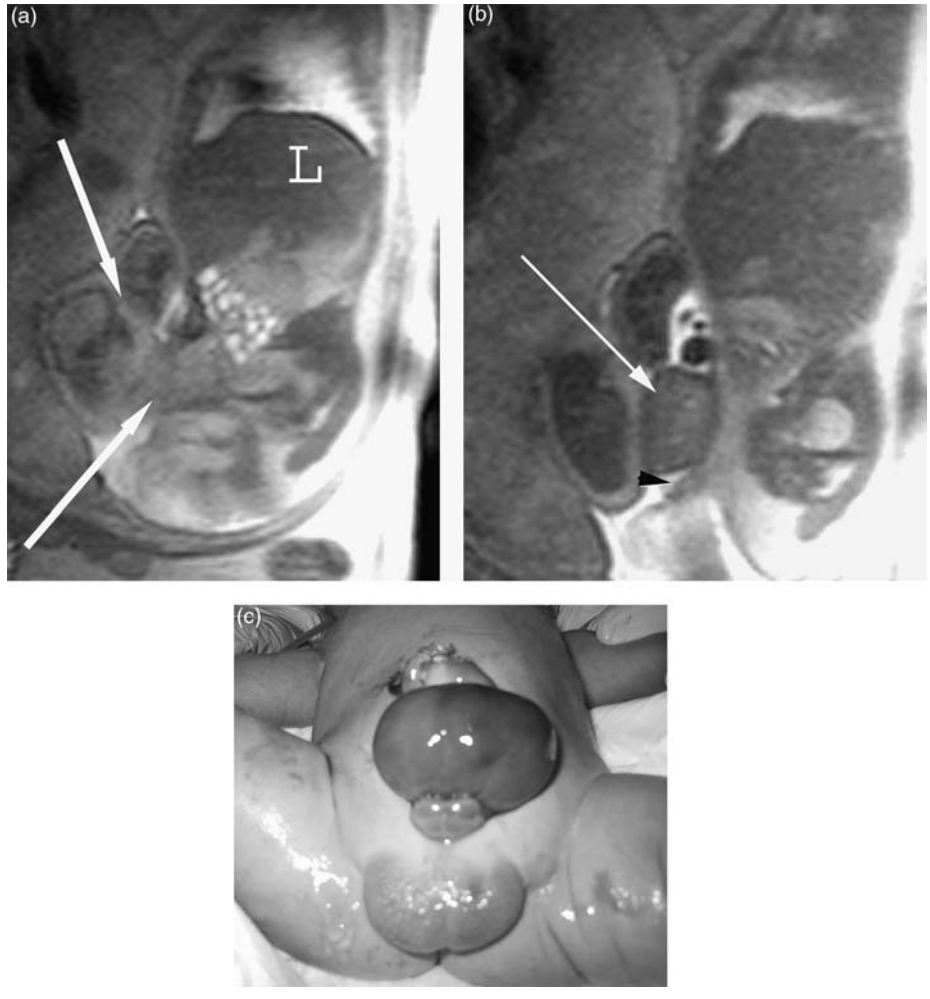

Figure 6.26 Bladder extrophy at 36 weeks gestational age. (a, b) Sagittal T_2-weighted images show a solid appearing mass (arrows) extending out of an anterior abdominal wall defect below the cord insertion site just above the phallus (arrowhead). (c) Postnatal photograph shows the bladder exstrophy. [From Levine et al. (20)]

a finding which may be helpful in the prenatal diagnosis of this condition (41).

Cloacal exstrophy has a more heterogeneous appearance of the infra-abdominal mass. Cloacal exstrophy results from persistence and subsequent rupture of the infraumbilical cloacal membrane during the fifth embryonic week (42). In this condition there is a heterogeneous soft tissue mass projecting from an infraumbilical position (Fig. 6.21). The bladder is absent, the external genitalia are malformed, but normal kidneys are typically present (43). A tethered spinal cord is commonly present in this condition, and may be better assessed with MR imaging than with ultrasound (Fig. 6.21) (44).

Retroperitoneal Masses

When a lesion is seen in the retroperitoneum, it is important to assess whether it is renal or adrenal in etiology. Cystic renal masses are discussed earlier. The most common solid renal mass *in utero* is a congenital mesoblastic nephroma. The two main considerations for an adrenal lesion are neuroblastoma and adrenal hemorrhage. In addition, a sub- or intradiaphragmatic sequestration can have a solid appearance and masquerade as an adrenal mass in the fetus.

Congenital mesoblastic nephroma is the most common primary renal tumor seen in the first month of life. These are benign tumors with excellent prognosis (45). The masses tend to be large and solid and are well-circumscribed. They are hypervascular leading to polyhydramnios. Congenital mesoblastic nephroma cannot be distinguished from Wilms tumor, on imaging. However, Wilms tumor is exceptionally rare in the fetus. Therefore, when a solid renal neoplasm is seen in the fetus, it is most likely a mesoblastic nephroma (46,47). MR imaging has been found to be better than ultrasound in defining the relationship of the tumor with adjacent structures (Fig. 6.27) (48).

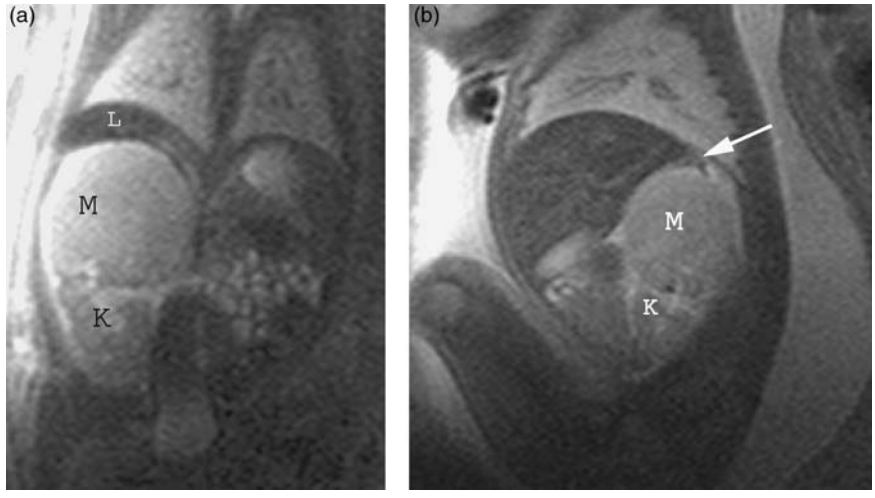

Figure 6.27 Mesoblastic nephroma at 37 weeks gestation. Coronal (a) and sagittal (b) T_2-weighted images depict a well-circumscribed solid mass (M) arising from the upper pole of the kidney, elevating the liver (L). The most common solid renal neoplasm *in utero* is mesoblastic nephroma, which is what this was found to be histologically. K, kidney. [From Levine et al. (20)]

Neuroblastoma is a sarcoma consisting of malignant neuroblasts, typically arising from the adrenal medulla. It is the most common malignant tumor in the neonatal period (49). It may present as a solid, cystic, or mixed solid and cystic suprarenal mass. (Figs. 6.28 and 6.29) (50–53). There are case reports of neuroblastomas with hepatic metastasis identified in fetuses by ultrasound and MR imaging (54). Adrenal hemorrhage on MR imaging has signal characteristics similar to blood products on the various sequences (55).

An extra-pulmonary sequestration (Fig. 6.30) shows high signal intensity on T_2-weighted images. Ultrasound (56) or MR imaging may show a vessel directly off the aorta feeding the mass (Chapter 5, Fig. 5.19).

Abdominopelvic Cysts

When an abdominopelvic cyst is visualized in the fetus, it is important to assess the laterality of the cyst, gender of the fetus, and appearance of adjacent organs. Enteric duplication cysts may occur anywhere along the gastrointestinal tract and are caused by abnormal recanalization of bowel, resulting in two lumen or errors in the embryologic connection between the developing gut and neural tube, as a part of the split notochord syndrome (57). The cyst may indent the adjacent loop of bowel. In a female fetus, a cyst arising from the pelvis may be ovarian in etiology (Fig. 6.31). Right upper quadrant cysts can be choledochal cysts. Duplication

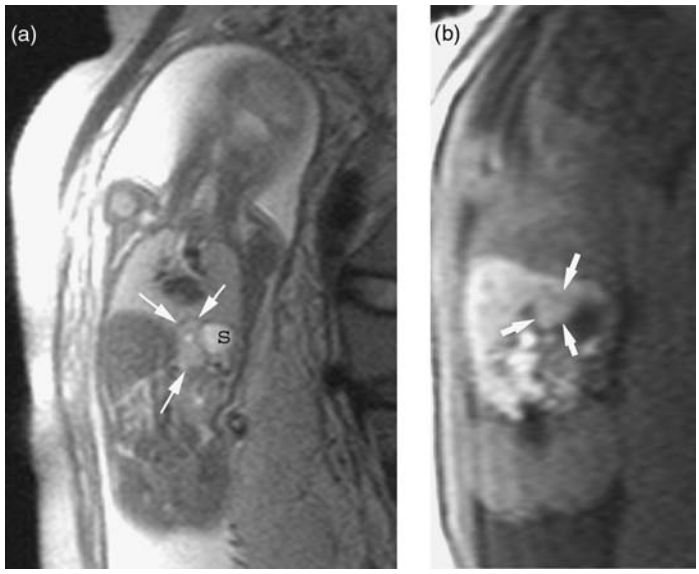

Figure 6.28 Neuroblastoma at 19 weeks gestational age. Coronal images show a left retroperitoneal lesion (arrows) which is of intermediate signal intensity on T_2-weighted image (a) and of increased signal intensity on the T_1-weighted image (b). Note the small cyst seen in the lesion in (a). S, stomach. This is different from the expected signal characteristics of sequestration, which are high on T_2-weighted imaging and low signal intensity on T_1-weighted imaging. Neuroblastoma was confirmed at operation. [From McNamara and Levine (53)]

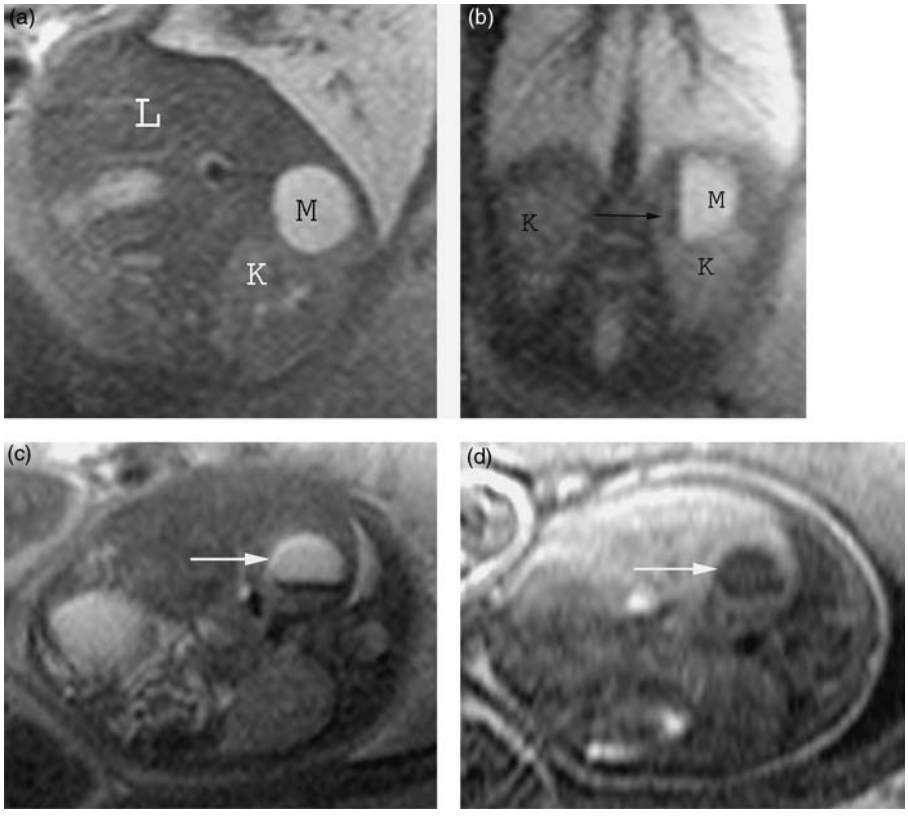

Figure 6.29 Cystic neuroblastoma at 34 weeks gestational age. Sagittal (a) and coronal (b) T_2-weighted images show a well-circumscribed cystic mass (M), compressing the upper pole of the left kidney (K). Axial T_2- (c) and T_1-weighted (d) images (oriented to maternal anatomy to best illustrate the fluid level) show a fluid-fluid level (arrow) within the mass suggesting layering hemorrhage. L, liver. Histology showed a cystic neuroblastoma. [(d) from Trop and Levine (55)]

anomalies of the kidneys can give the appearance of cysts.

When filled with simple fluid, abdominopelvic cysts show high signal intensity on the T_2-weighted images and low signal intensity on T_1-weighted images (Fig. 6.32). However, some duplication cysts can be filled with inspissated secretions and may have signal intensity slightly lower than normal fluid on T_2-weighted images and slightly higher than simple fluid on T_1-weighted images (Fig. 6.33) (58). Hemorrhagic cysts can have variable signal intensity, depending on the age of the hemorrhage.

Abnormalities of the Abdominal Cord Insertion Site

Omphalocele

Omphalocele (Figs. 6.34–6.36) is a congenital ventral wall defect that involves herniation of a portion of the abdominal organs into the base of the umbilical cord. This membrane-covered defect can range in size from small, containing only a portion of the bowel or liver, to large, containing most of the abdominal organs. Small bowel-only omphaloceles (Fig. 6.34) have the highest association with an abnormal karyotype (59–61).

Even when karyotype is normal there is a high incidence of associated abnormalities, up to 88%, including congenital heart disease, genitourinary anomalies, neural tube defects, and intestinal malrotation. In addition, omphalocele may also be associated with several syndromes such as Beckwith–Wiedemann syndrome (Fig. 6.36) (62) or Pentalogy of Cantrell. Prognosis depends largely on the size of the defect and the presence or absence of other anomalies. In the absence of associated abnormalities, omphalocele with liver herniation is associated with a poorer survival rate than those without (63). The utility of MR imaging in the diagnosis of omphalocele is unclear as the diagnosis is readily made by ultrasound, although MR examinations can show the extent of abdominal organ involvement.

Gastroschisis

Gastroschisis occurs when there is an anterior abdominal wall defect just lateral (usually to the right) to the cord insertion site. The diagnosis of gastroschisis is made when an ultrasound evaluation reveals free-floating loops of bowel in the amniotic fluid (Figs. 6.37 and 6.38). Most cases involve the small intestine and a portion of the large intestine. As a consequence of the herniation, the unprotected bowel may not function well. Unlike

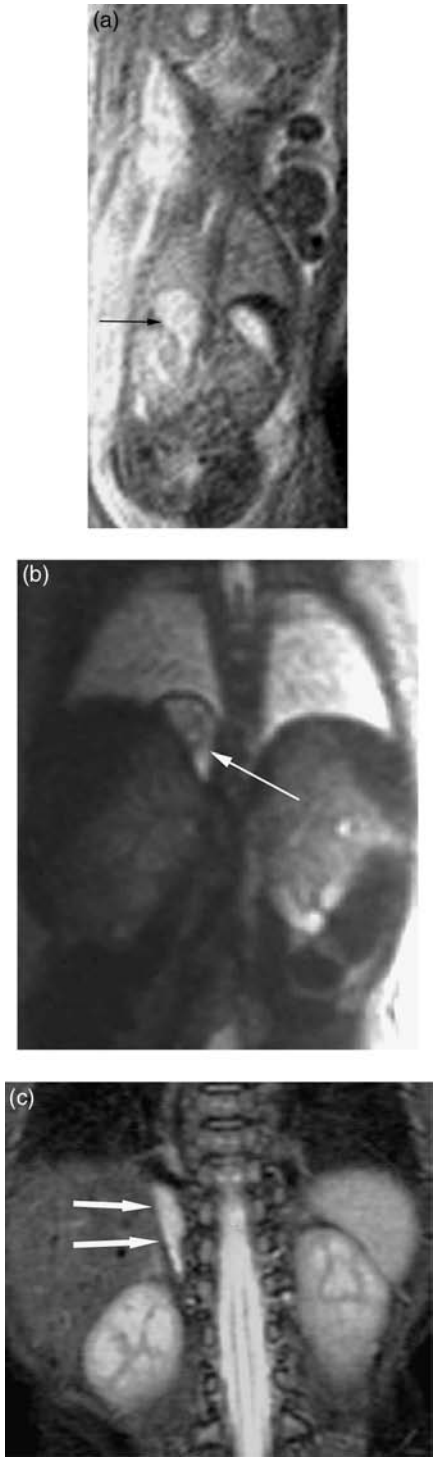

Figure 6.30 Extra-pulmonary sequestration. (a) T_2-weighted image at 19 weeks gestational age shows a high signal lesion in the right upper quadrant (arrows). (b) T_2-weighted image at 38 weeks gestational age shows the lesion lies between the leaves of the diaphragm. (c) Postnatal T_2-weighted image confirms that the lesion is between the leaves of the diaphragm, consistent with an intradiaphragmatic sequestration. [From Levine et al. (20)]

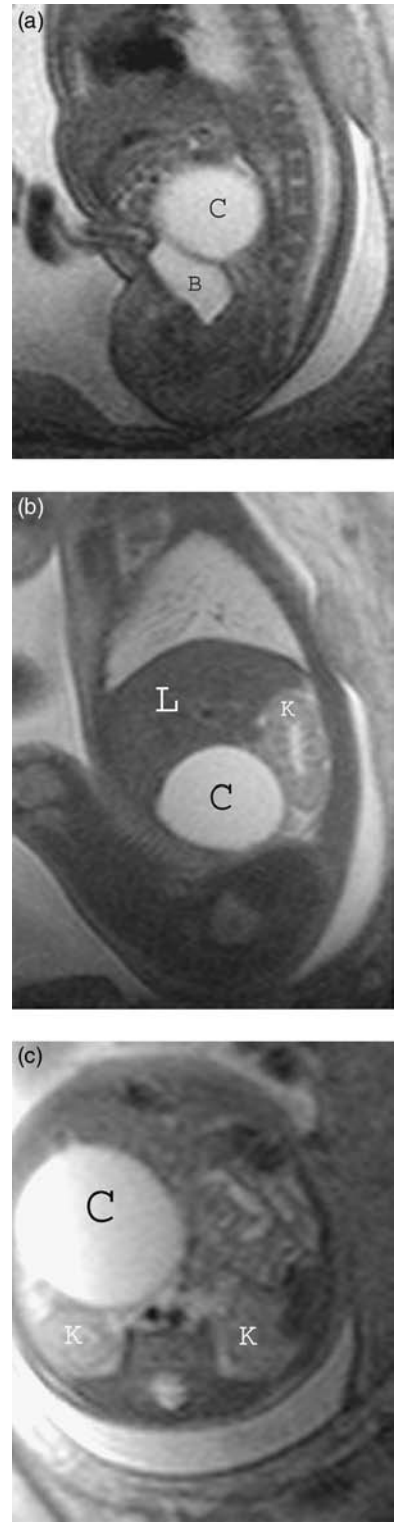

Figure 6.31 Ovarian cyst at 33 weeks gestation in a female fetus. Sagittal (a, b) and axial (c) T_2-weighted images reveal a large cyst (C) separate from the liver (L), right kidney (K), and bladder (B). As the gender was female, this was felt to most likely represent an ovarian cyst. The cyst resolved 3 weeks postnatal. [(a, c) from Levine et al. (20)]

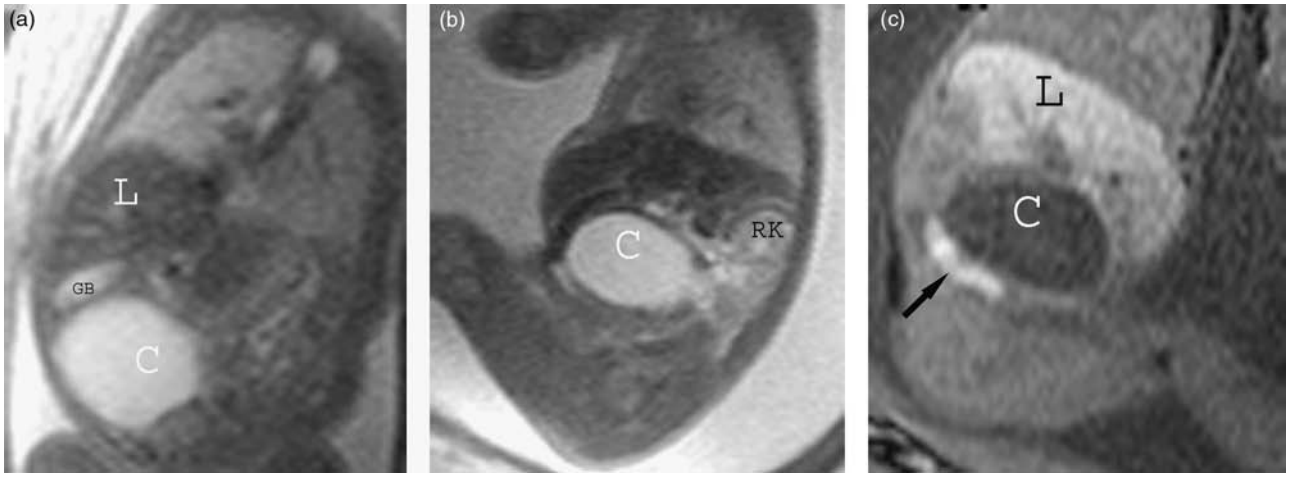

Figure 6.32 Duplication cyst at 26 weeks gestational age. Coronal (a) and sagittal (b) T_2-weighted images and sagittal T_1-weighted image (c) show a well-demarcated right-sided cyst (C) separate from the liver (L), gallbladder (GB), kidney (RK), and colon (arrow). The signal intensity of the cyst follows that of simple fluid. At surgery this was found to be a gastrointestinal duplication cyst.

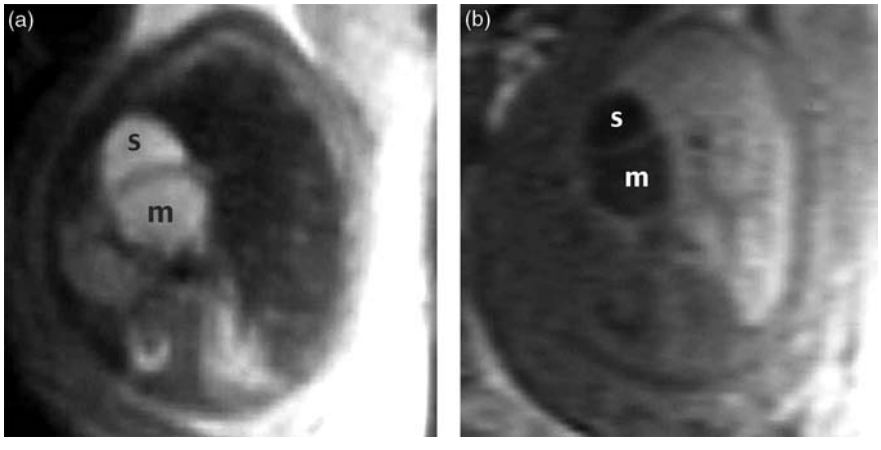

Figure 6.33 Gastric duplication cyst at 24 weeks gestational age. Axial T_2-weighted (a) and T_1-weighted (b) images show a mass (m) adjacent to the stomach (s). Note that the signal intensity of the amniotic fluid in the stomach is slightly different from that of the duplication cyst. [From Levine et al. (58)]

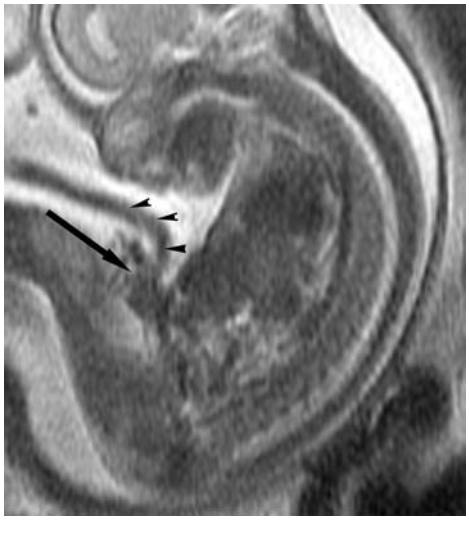

Figure 6.34 Small bowel only omphalocele in trisomy 13 at 21 weeks gestation. Sagittal T_2-weighted image shows a small anterior abdominal wall defect with loops of small bowel (arrow) within it. The small bowel has abnormally low signal intensity. The umbilical cord (arrowheads) is seen inserting into the sac.

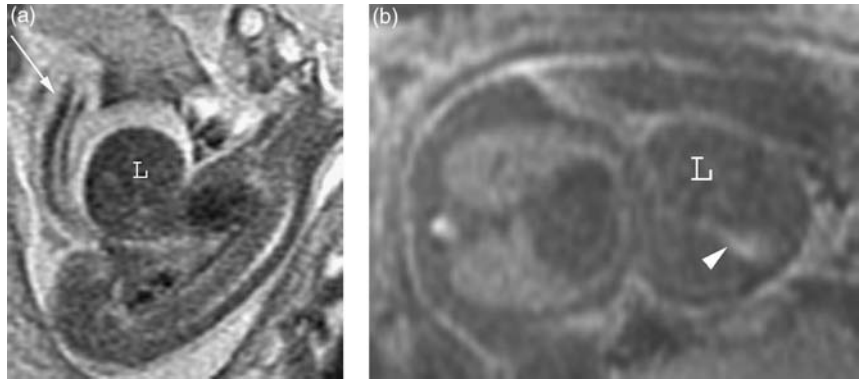

Figure 6.35 Large omphalocele at 21 weeks gestation. Sagittal (a) and axial (b) T_2-weighted images show a large membrane-covered anterior abdominal wall defect containing liver (L) surrounded by fluid. Note gallbladder (arrowhead). On the sagittal view the sac is seen to extend to the region of the xiphoid process. The umbilical cord (arrow) inserts into and then runs along the wall of the sac.

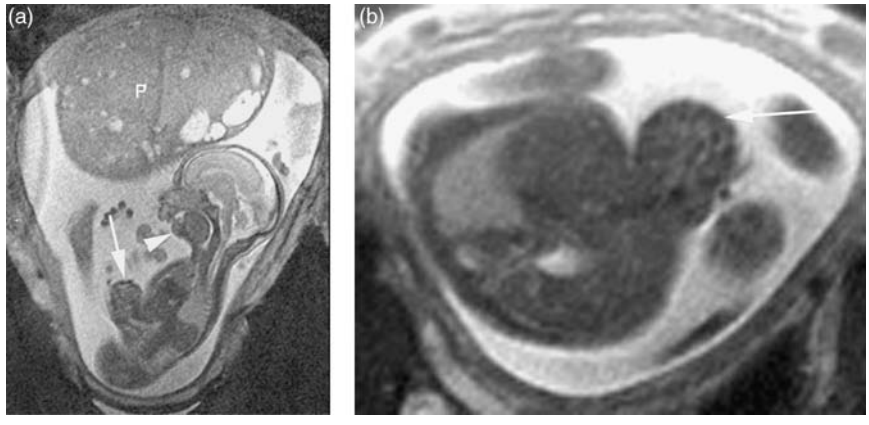

Figure 6.36 Omphalocele in Beckwith–Wiedemann syndrome at 23 weeks gestational age. Sagittal (a) and axial (b) T_2-weighted images show an omphalocele (arrow). Note the large cystic placenta (P), associated with Beckwith–Wiedemann syndrome. An unusual feature of this fetus is micrognathia (arrowhead), which is not a typical finding in this syndrome. [From O'Conner and Levine (62)]

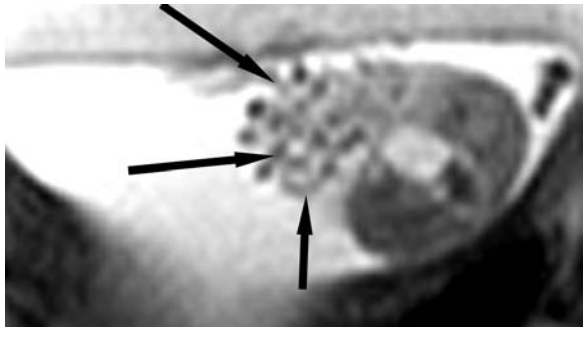

Figure 6.37 Gastroschisis at 20 weeks gestation. Axial T_2-weighted image shows free-floating small bowel loops (arrows). Note the abnormal low signal intensity within the small bowel loops. [From Levine et al. (20)]

other ventral wall defects, gastroschisis is usually not associated with chromosome anomalies (64) or other structural malformations, with the exception of intestinal atresia and malrotation, in which case it may be associated with increased mortality (65,66). In most cases, gastroschisis can be successfully repaired and the long-term prognosis is excellent. The signal intensity of the small bowel is commonly altered in gastroschisis such that the free-floating loops of small bowel have low signal intensity on T_2-weighted images (Fig. 6.37) and/or high signal intensity on T_1-weighted images (Fig. 6.38). It is possible that MR imaging will allow better characterization of the distended loops of bowel to determine whether an early delivery might improve the outcome.

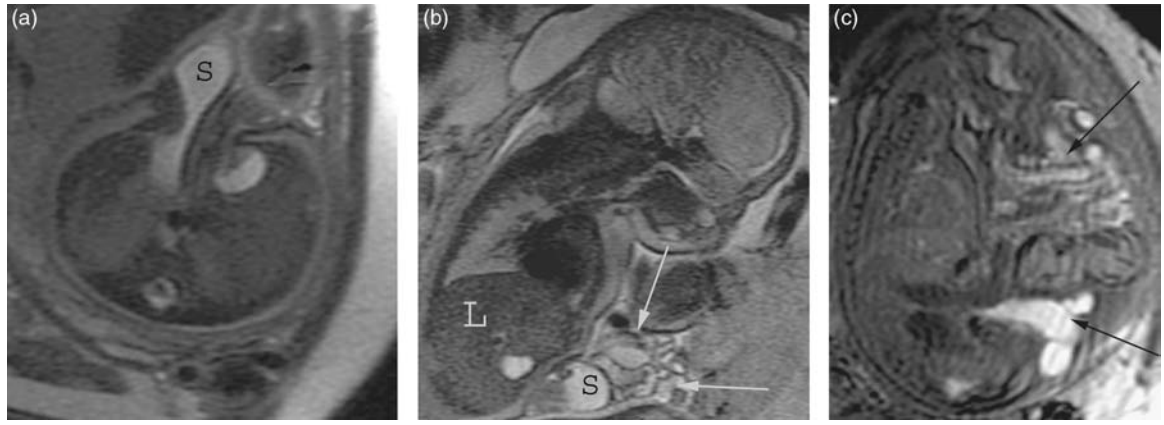

Figure 6.38 Gastroschisis at 34 weeks gestation. Axial (a) and sagittal (b) T_2-weighted images and sagittal T_1-weighted image (c) show an anterior abdominal wall defect with stomach (S), large and small bowel loops (arrows) extending out of the defect. Note that the small bowel signal is abnormal, being bright on both T_1- and T_2-weighted images. L, liver.

Amniotic Band Sequence

Amniotic band sequence occurs when there is either early rupture of the amnion or possibly disruption of the embryonic blood supply with secondary adhesion of the amnion and rupture (67). In some cases there is disruption of the anterior abdominal wall with herniated abdominal contents (Fig. 6.39).

Extrophy

As mentioned earlier, bladder exstrophy (Fig. 6.26) and cloacal exstrophy (Fig. 6.21) present as infraumbilical masses. In both conditions a normal bladder is not visualized. In bladder exstrophy, the anterior abdominal mass appears solid and amniotic fluid is normal. In cloacal exstrophy, amniotic fluid is frequently low and associated anomalies are present.

Liver and Spleen Abnormalities

Hemochromatosis can be diagnosed noninvasively with BOLD (T2*) MR imaging (68–71). The liver and spleen appear of low signal intensity in this condition (Fig. 6.40).

The most common *in utero* hepatic abnormalities are calcifications, which can be due to tumor, infection or vascular insult. These small calcifications are better visualized on sonography than on MR imaging. Liver tumors can be assessed with prenatal MR imaging (Fig. 6.41)

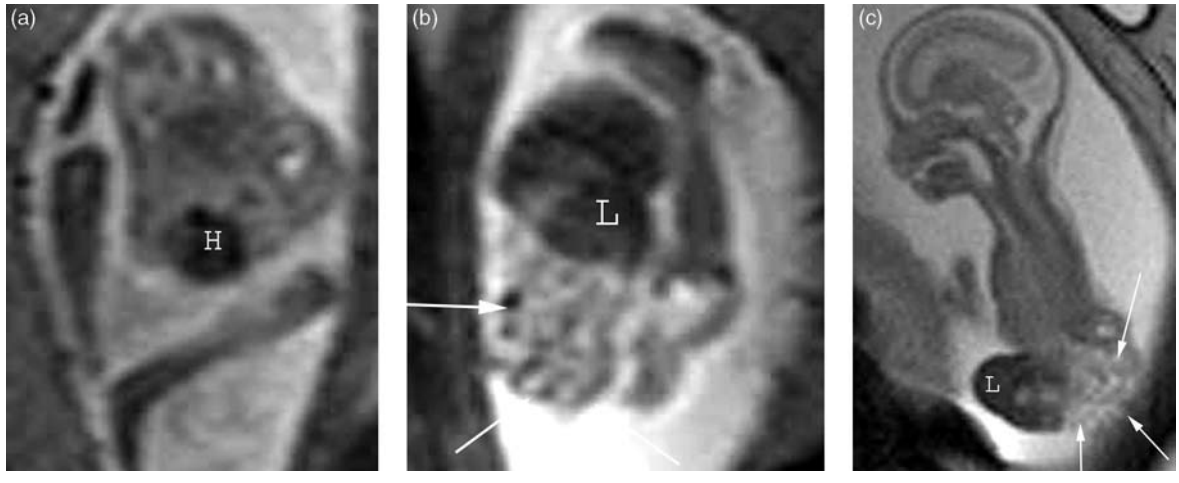

Figure 6.39 Amniotic band syndrome at 17 weeks gestational age. Axial (a, b) and sagittal (c) T_2-weighted images show an anterior abdominal defect with the liver (L) and small bowel loops (arrows) freely protruding into the amniotic fluid. The heart (H) protrudes through the chest wall. This complex assortment of abnormalities suggests amniotic band syndrome. [From Levine et al. (20).] This is the same fetus as shown in Chapter 7, Fig. 7.36.

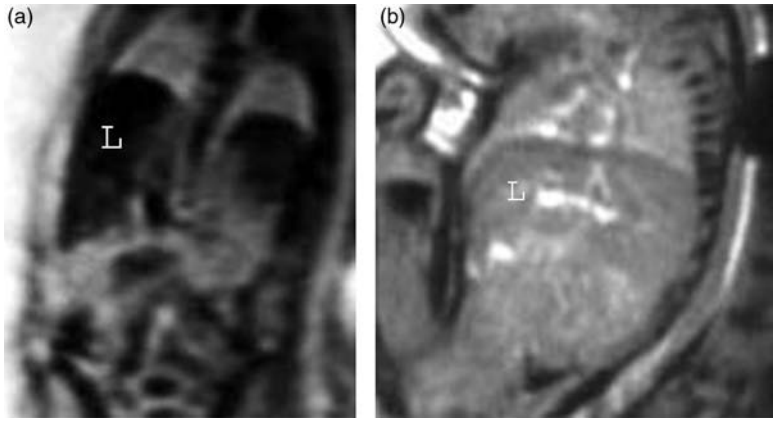

Figure 6.40 Hemochromatosis. Coronal T2*-weighted MR images (130/20, 20° flip angle) in fetuses with (a) and without (b) hemochromotosis. Note the diffusely low T_2 signal consistent with iron deposition in the fetal liver (L) in the affected fetus. (Images courtesy of F. Coakley, San Francisco, CA.)

(72). Magnetic resonance imaging is helpful in visualizing the extent of the tumor and any surrounding lesions. Small liver lesions may be visualized on ultrasound but not on prenatal MR images (21). Fetal splenic abnormalities can be difficult to visualize on ultrasound. Polysplenia, in association with heterotaxy syndrome, can be visualized on prenatal MR (Chapter 5, Fig. 5.35).

Ascites

Fetal ascites may occur in isolation (Chapter 5, Fig. 5.31), in association with hydrops (Fig. 6.42), infection, or tumors, or in gastrointestinal or genitourinary tract perforation. Free-floating loops of bowel are seen in the high signal intensity amniotic fluid on T_2-weighted images (Fig. 6.42).

Genitalia

Genital abnormalities are typically better assessed with sonography than with MR imaging. Hydroceles can be present, visualized as fluid surrounding the testicles. These typically are visualized in association with ascites and hydrops (Fig. 6.42). A scrotal hernia can be assessed with MR imaging (Fig. 6.43) (73).

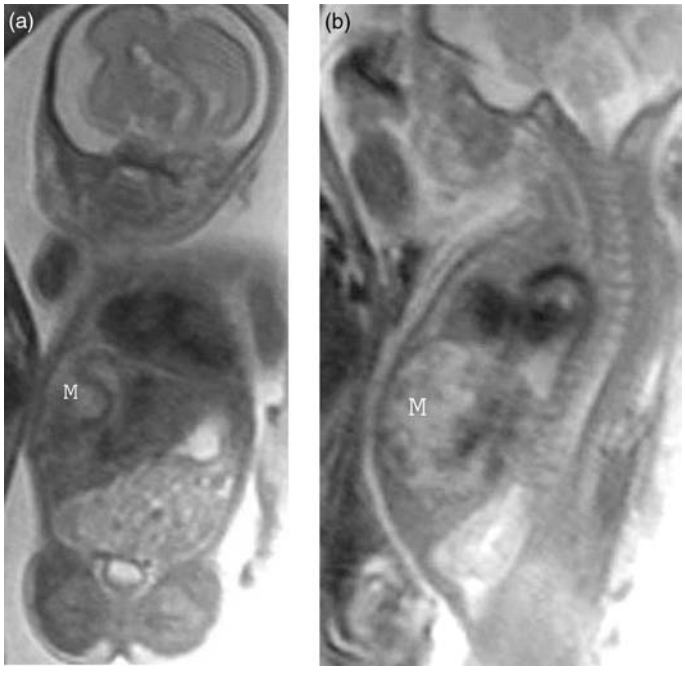

Figure 6.41 Liver tumor at 28 weeks gestational age. Coronal (a) and sagittal (b) T_2-weighted images in a fetus with vascular mass (M) in the liver. This was treated with maternal steroids and the lesion resolved postnatally, consistent with an infantile hemangioma. [(a) from Morris et al. (72)]

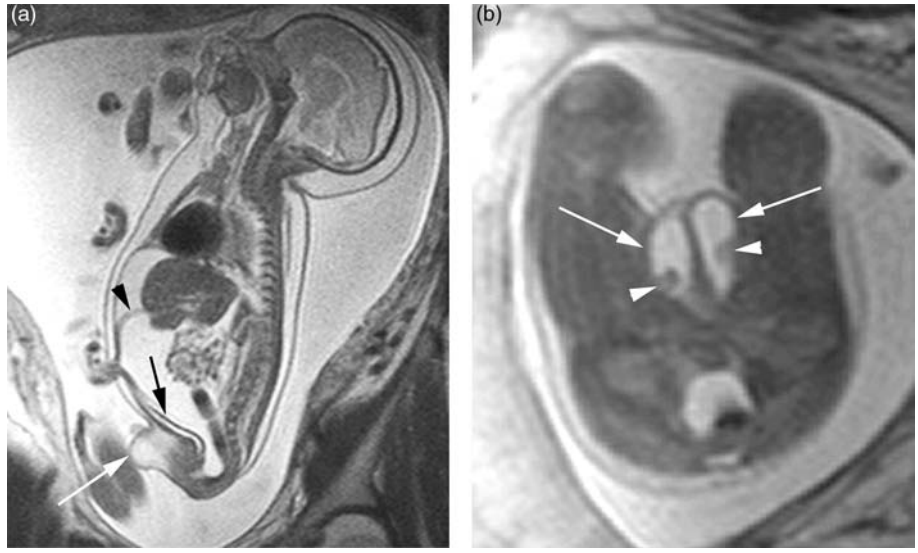

Figure 6.42 Severe ascites in fetus with hydrops at 27 weeks gestational age. (a) Sagittal T_2-weighted image shows a large amount of ascites and skin thickening. There is a small pleural effusion surrounding the lungs. Ascites surrounds the small bowel which is of abnormally low signal intensity. Note the umbilical vein (black arrowhead) and umbilical arteries (black arrows). (b) Axial T_2-weighted image through the lower pelvis shows bilateral hydroceles (white arrows) surrounding the testicles (white arrowheads).

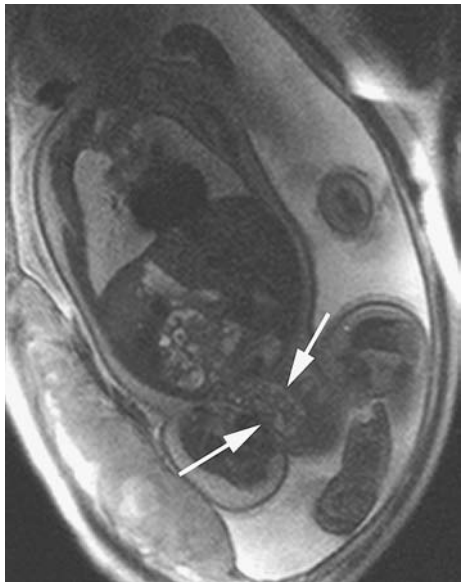

Figure 6.43 Inguinal hernia in a fetus at 36 weeks gestational age. Sonogram (not shown) demonstrated a 4 cm scrotal mass. Coronal MR imaging shows bowel entering into the mass consistent with an inguinal hernia. [From Ji et al. (73)]

CONCLUSION

Ultrasound remains the mainstay in diagnosis of fetal abdominal and pelvic pathology. However, there are certain instances where MR imaging can aid in diagnosis and/or improve characterization of a known anomaly. The exact role of MR imaging in assessing the fetal abdomen remains to be proven.

REFERENCES

1. Hubbard AM. Ultrafast fetal MRI and prenatal diagnosis. Semin Pediatr Surg 2003; 12:143–153.
2. Quinn TM, Hubbard AM, Adzick NS. Prenatal magnetic resonance imaging enhances fetal diagnosis. J Pediatr Surg 1998; 33:553–558.
3. Shinmoto H, Kuribayashi S. MRI of fetal abdominal abnormalities. Abdom Imaging 2003; 28:877–886.
4. Launay S, Cuilleret V, Boyer C et al. Magnetic resonance imaging applications in obstetrics. J Gynecol Obstet Biol Reprod (Paris) 2003; 32:205–220.
5. Dell'Acqua A, Mengozzi E, Rizzo F et al. Ultrafast MR imaging of the foetus: a study of 25 non-central nervous system anomalies. Radiol Med (Torino) 2002; 104:75–86.
6. Bekker MN, van Vugt JM. The role of magnetic resonance imaging in prenatal diagnosis of fetal anomalies. Eur J Obstet Gynecol Reprod Biol 2001; 96:173–178.
7. Shinmoto H, Kashima K, Yuasa Y et al. MR imaging of non-CNS fetal abnormalities: a pictorial essay. Radiographics 2000; 20:1227–1243.
8. Hubbard AM, Harty MP, States LJ. A new tool for prenatal diagnosis: ultrafast fetal MRI. Semin Perinatol 1999; 23:437–447.
9. Vimercati A, Greco P, Vera L et al. The diagnostic role of "*in utero*" magnetic resonance imaging. J Perinat Med 1999; 27:303–308.

10. Amin RS, Nikolaidis P, Kawashima A et al. Normal anatomy of the fetus at MR imaging. Radiographics 1999; 19:S201–S214.
11. Yamashita Y, Namimoto T, Abe Y et al. MR imaging of the fetus by a HASTE sequence. Am J Roentgenol 1997; 168:513–519.
12. Huppert BJ, Brandt KR, Ramin KD et al. Single-shot fast spin-echo MR imaging of the fetus: a pictorial essay. Radiographics 1999; 19:S215–S227.
13. Saguintaah M, Couture A, Veyrac C et al. MRI of the fetal gastrointestinal tract. Pediatr Radiol 2002; 32:395–404.
14. Fradin JM, Regan F, Rodriquez R et al. Hydronephrosis in pregnancy: simultaneous depiction of fetal and maternal hydronephrosis by magnetic resonance urography. Urology 1999; 53:825–827.
15. Pumberger W, Patzak B, Prayer D et al. Fetal liver magnetic resonance imaging in anterior body wall defects: a study of specimens from the museum of pathology. J Pediatr Surg 2003; 38:1147–1151.
16. Pameijer CR, Hubbard AM, Coleman B et al. Combined pure esophageal atresia, duodenal atresia, biliary atresia, and pancreatic ductal atresia: prenatal diagnostic features and review of the literature. J Pediatr Surg 2000; 35:745–747.
17. Tongsong T, Wanapirak C, Sirichotiyakul S et al. Prenatal sonographic markers of trisomy 21. J Med Assoc Thai 2001; 84:274–280.
18. Shyu MK, Shih JC, Lee CN et al. Correlation of prenatal ultrasound and postnatal outcome in meconium peritonitis. Fetal Diagn Ther 2003; 18:255–261.
19. Sergent F, Marret S, Verspyck E et al. Management of meconium peritonitis: a remarkable case of idiopathic meconium peritonitis diagnosed antenatally. J Gynecol Obstet Biol Reprod (Paris) 2003; 32:575–581.
20. Levine D, Stroustrup Smith A, Barbaras L et al. Compendium of Fetal MRI (image). Available from: Beth Israel Deaconess Medical Center Radiology Department website, http://bidmc.harvard.edu/fetalatlas/, 2004.
21. Levine D, Smith AS, McKenzie C. Tips and tricks of fetal MR imaging. Radiol Clin North Am 2003; 41:729–745.
22. Takeuchi K, Moriyama T, Funakoshi T et al. Prenatal diagnosis of fetal urogenital abnormalities with oligohydramnios by magnetic resonance imaging using turbo spin echo technique. J Perinat Med 1998; 26:59–61.
23. Miller OF, Lashley DB, McAleer IM et al. Diagnosis of urethral obstruction with prenatal magnetic resonance imaging. J Urol 2002; 168:1158–1159.
24. Bobrowski RA, Levin RB, Lauria MR et al. *In utero* progression of isolated renal pelvis dilation. Am J Perinatol 1997; 14:423–426.
25. Chitty LS, Altman DG. Charts of fetal size: kidney and renal pelvis measurements. Prenat Diagn 2003; 23:891–897.
26. Poutamo J, Vanninen R, Partanen K et al. Diagnosing fetal urinary tract abnormalities: benefits of MRI compared to ultrasonography. Acta Obstet Gynecol Scand 2000; 79:65–71.
27. Guys JM, Borella F, Monfort G. Ureteropelvic junction obstructions: prenatal diagnosis and neonatal surgery in 47 cases. J Pediatr Surg 1988; 23:156–158.
28. Sozubir S, Lorenzo AJ, Twickler DM et al. Prenatal diagnosis of a prolapsed ureterocele with magnetic resonance imaging. Urology 2003; 62:144.
29. Cassart M, Massez A, Metens T et al. Complementary role of MRI after sonography in assessing bilateral urinary tract anomalies in the fetus. Am J Roentgenol 2004; 182:689–695.
30. Hoffman CK, Filly RA, Callen PW. The "lying down" adrenal sign: a sonographic indicator of renal agenesis or ectopia in fetuses and neonates. J Ultrasound Med 1992; 11:533–536.
31. Ohgiya Y, Gokan T, Hamamizu K et al. Fast MRI in obstetric diagnoses. J Comput Assist Tomogr 2001; 25:190–200.
32. Nishi T. Prenatal diagnosis of urinary tract abnormalities. Acta Obstet Gynecol Scand 1997; 76:409–413.
33. Hutcheson JC, Canning DA, Hubbard AM et al. Magnetic resonance imaging of fetal urinoma. Urology 2002; 60:697.
34. Levine D. Ultrasound versus magnetic resonance imaging in fetal evaluation. Top Magn Reson Imaging 2001; 12:25–38.
35. Nasu K, Yoshimatsu J, Anai T et al. Magnetic resonance imaging of fetal autosomal recessive polycystic kidney disease. J Obstet Gynaecol Res 1998; 24:33–36.
36. Nishi T. Magnetic resonance imaging of autosomal recessive polycystic kidney disease *in utero*. J Obstet Gynaecol 1995; 21:471–474.
37. Nishi T, Iwasaki M, Yamoto M et al. Prenatal diagnosis of autosomal recessive polycystic kidney disease by ultrasonography and magnetic resonance imaging. Acta Obstet Gynecol Scand 1991; 70:615–617.
38. Mine K, Suzuki S, Watanabe S et al. Prenatal diagnosis of autosomal recessive polycystic kidney disease. A case report. Nippon Ika Daigaku Zasshi 1999; 66:188–190.
39. Warne S, Chitty LS, Wilcox DT. Prenatal diagnosis of cloacal anomalies. BJU Int 2002; 89:78–81.
40. Chaubal N, Dighe M, Shah M et al. Calcified meconium: an important sign in the prenatal sonographic diagnosis of cloacal malformation. J Ultrasound Med 2003; 22:727–730.
41. Lee EH, Shim JY. New sonographic finding for the prenatal diagnosis of bladder exstrophy: a case report. Ultrasound Obstet Gynecol 2003; 21:498–500.
42. Langer JC, Brennan B, Lappalainen RE et al. Cloacal exstrophy: prenatal diagnosis before rupture of the cloacal membrane. J Pediatr Surg 1992; 27:1352–1355.
43. Pinette MG, Pan YQ, Pinette SG et al. Prenatal diagnosis of fetal bladder and cloacal exstrophy by ultrasound. A report of three cases. J Reprod Med 1996; 41:132–134.
44. Warf BC, Scott RM, Barnes PD et al. Tethered spinal cord in patients with anorectal and urogenital malformations. Pediatr Neurosurg 1993; 19:25–30.
45. Won HS, Jung E, Lee PR et al. Prenatal detection of mesoblastic nephroma by sonography and magnetic resonance imaging. Ultrasound Obstet Gynecol 2002; 19:197–199.
46. Beckwith JB. Prenatal detection of a Wilms' tumor. Pediatr Radiol 1999; 29:64.
47. Gutjahr P. Congenital Wilms' tumors are mostly (benign) mesoblastic nephromas—significance of prenatally detected solid kidney tumors. Geburtshilfe Frauenheilkd 1991; 51:124–126.

48. Irsutti M, Puget C, Baunin C et al. Mesoblastic nephroma: prenatal ultrasonographic and MRI features. Pediatr Radiol 2000; 30:147–150.
49. Kesrouani A, Duchatel F, Seilanian M et al. Prenatal diagnosis of adrenal neuroblastoma by ultrasound: a report of two cases and review of the literature. Ultrasound Obstet Gynecol 1999; 13:446–449.
50. Anton-Pacheco J, Romeo C, Montero A et al. Fetal cystic neuroblastoma. Cir Pediatr 1994; 7:207–208.
51. Hamada Y, Ikebukuro K, Sato M et al. Prenatally diagnosed cystic neuroblastoma. Pediatr Surg Int 1999; 15:71–74.
52. Sauvat F, Sarnacki S, Brisse H et al. Outcome of suprarenal localized masses diagnosed during the perinatal period: a retrospective multicenter study. Cancer 2002; 94:2474–2480.
53. McNamara A, Levine D. Echogenic masses in the fetal abdomen. Radiographics 2005.
54. Toma P, Lucigrai G, Marzoli A et al. Prenatal diagnosis of metastatic adrenal neuroblastoma with sonography and MR imaging. Am J Roentgenol 1994; 162:1183–1184.
55. Trop I, Levine D. Hemorrhage during pregnancy: sonography and MR imaging. Am J Roentgenol 2001; 176:607–615.
56. Plattner V, Haustein B, Llanas B et al. Extra-lobar pulmonary sequestration with prenatal diagnosis. A report of 5 cases and review of the literature. Eur J Pediatr Surg 1995; 5:235–237.
57. Chou YH, Tiu CM, Pan HB et al. Ultrasonographic demonstration of duplication cyst of the ileum. Zhonghua Yi Xue Za Zhi (Taipei) 1990; 46:237–239.
58. Levine D, Barnes PD, Edelman RR. Obstetric MR imaging. Radiology 1999; 211:609–617.
59. Getachew MM, Goldstein RB, Edge V et al. Correlation between omphalocele contents and karyotypic abnormalities: sonographic study in 37 cases. Am J Roentgenol 1992; 158:133–136.
60. Nyberg DA, Fitzsimmons J, Mack LA et al. Chromosomal abnormalities in fetuses with omphalocele. Significance of omphalocele contents. J Ultrasound Med 1989; 8:299–308.
61. Benacerraf BR, Saltzman DH, Estroff JA et al. Abnormal karyotype of fetuses with omphalocele: prediction based on omphalocele contents. Obstet Gynecol 1990; 75:317–319.
62. O'Connor C, Levine D. Case 49: Beckwith–Wiedemann syndrome. Radiology 2002; 224:375–378.
63. St-Vil D, Shaw KS, Lallier M et al. Chromosomal anomalies in newborns with omphalocele. J Pediatr Surg 1996; 31:831–834.
64. Salihu HM, Boos R, Schmidt W. Omphalocele and gastrochisis. J Obstet Gynaecol 2002; 22:489–492.
65. Prasad TR, Bajpai M. Intestinal atresia. Indian J Pediatr 2000; 67:671–678.
66. Brun M, Grignon A, Guibaud L et al. Gastroschisis: are prenatal ultrasonographic findings useful for assessing the prognosis? Pediatr Radiol 1996; 26:723–726.
67. Bokmand S, Bangsboll S, Ornvold K. Early amnion rupture or amniotic band syndrome. Ugeskr Laeger 1991; 153:1846–1848.
68. Oddone M, Bellini C, Bonacci W et al. Diagnosis of neonatal hemochromatosis with MR imaging and duplex Doppler sonography. Eur Radiol 1999; 9:1882–1885.
69. Hayes AM, Jaramillo D, Levy HL et al. Neonatal hemochromatosis: diagnosis with MR imaging. Am J Roentgenol 1992; 159:623–625.
70. Marti-Bonmati L, Baamonde A, Poyatos CR et al. Prenatal diagnosis of idiopathic neonatal hemochromatosis with MRI. Abdom Imaging 1994; 19:55–56.
71. Coakley FV, Hricak H, Filly RA et al. Complex fetal disorders: effect of MR imaging on management—preliminary clinical experience. Radiology 1999; 213:691–696.
72. Morris J, Abbott J, Burrows P et al. Antenatal diagnosis of fetal hepatic hemangioma treated with maternal corticosteroids. Obstet Gynecol 1999; 94:813–815.
73. Ji EK, Yoon CS, Pretorius DH. Prenatal diagnosis of an inguinoscrotal hernia: sonographic and MRI findings. J Ultrasound Med 2005; 24:239–242.

7

MR Imaging of the Fetal Extremities, Spine, and Spinal Cord

DEBORAH LEVINE, TEJAS MEHTA

INTRODUCTION

The extremities and spine are well evaluated by real-time ultrasonography. The ossified portions of the skeleton exhibit high contrast on ultrasound, allowing for easy visualization throughout gestation (1,2). In contrast, using T_2-weighted magnetic resonance (MR) imaging, the bones are of intermediate signal intensity and can be difficult to visualize distinctly. In addition, fetal motion and off-axis imaging typically limit the utility of MR imaging (Fig. 7.1). However, there are many anomalies for which MR examinations may be performed in which abnormalities of the extremities and spine will be associated findings. Therefore it is important to recognize the normal and abnormal appearance of the fetal musculoskeletal system.

MUSCULOSKELETAL SYSTEM: SCANNING TECHNIQUES AND PITFALLS

Consecutive images are needed to visualize the entire extremity (Fig. 7.2). If the extremity moves out of the plane of imaging, it may not be visualized at all. If the extremity moves in plane on sequential images, portions of the extremity may be visualized more than once (3) or in a different position (Fig. 7.3). Care should be taken to avoid confusing adjacent structures with extremities, for example, a loop of umbilical cord (Figs. 7.3 and 7.4) or a vein in adjacent placenta (Fig. 7.5) (4).

As T_2-weighted imaging is the mainstay of fetal diagnosis, it is typically the type of sequence in which extremities are visualized. However, as small calcifications are difficult to visualize on T_2-weighted images, osseous abnormalities may be missed (Fig. 7.6).

When visualization of an entire extremity is important, a thick-slab ($\geq$20 mm slice thickness) heavily T_2-weighted sequence can be utilized (Fig. 7.7). T_1-weighted imaging can be utilized for visualization and quantification of subcutaneous fat (Fig. 7.8). If visualization of the bones is important, special sequences such as spectral spatial water excitation can be utilized to better assess the bony anatomy (Fig. 7.9, see also Fig. 9.13) (5).

NORMAL ANATOMY

Normal Extremities

Figures 7.10 and 7.11 illustrate the normal appearance of the upper extremities in the second and third trimesters. Figures 7.12–7.14 illustrate the normal appearance of the lower extremities. Visualization of the normal position of the extremities is dependent upon the amount of surrounding amniotic fluid. Late in gestation, the positioning of the feet, in particular, can be difficult to assess. The femoral metaphyses and epiphyses are readily visualized after 18 weeks gestational age. The epiphyses tend to exhibit signal intensity similar to or slightly less than adjacent amniotic fluid (Fig. 7.14).

Normal Spine

The bony anatomy of the spine is well visualized by ultrasound; therefore, MR imaging is unlikely to play a

(*text continued on page 147*)

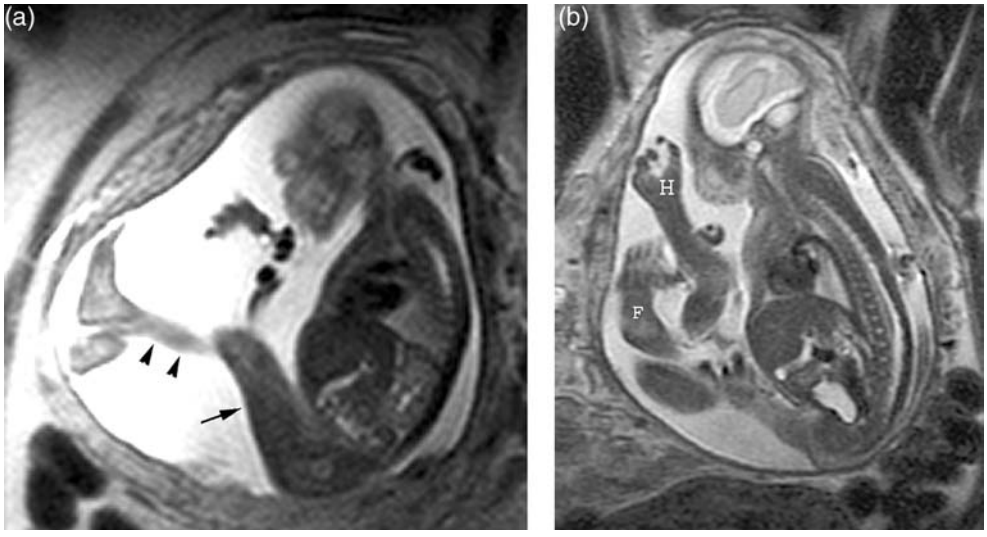

Figure 7.1 Overlapping positions of extremities. T_2-weighted images from fetuses at 24 (a) and 28 (b) weeks gestational age. Note how overlapping positions of the extremities can make evaluation difficult. In (a), the left thigh (black arrow) and right lower leg (black arrowheads) are seen in a single sagittal image. In (b), the extremities appear as a jumble of small parts, as only portions appear on a single image (H, hand; F, foot).

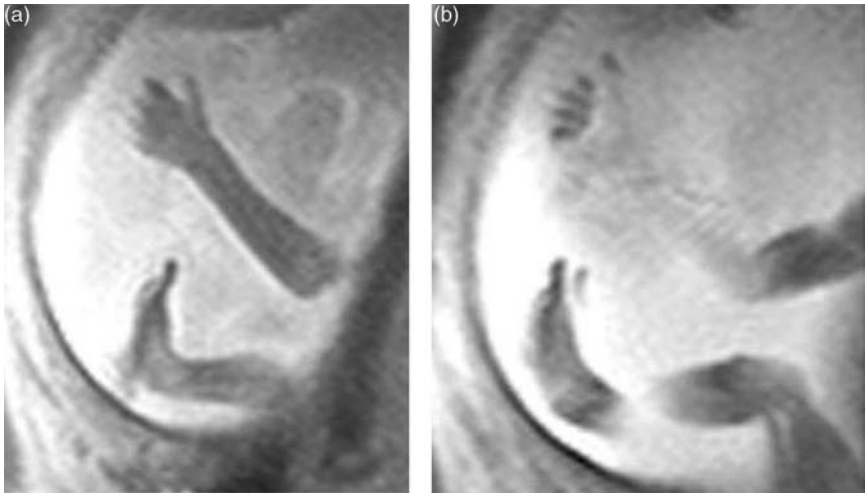

Figure 7.2 Demonstration of consecutive images aiding in assessment of extremities. Two consecutive T_2-weighted images from 20 weeks gestational age fetus show hand and fingers. [From Levine et al. (47)]

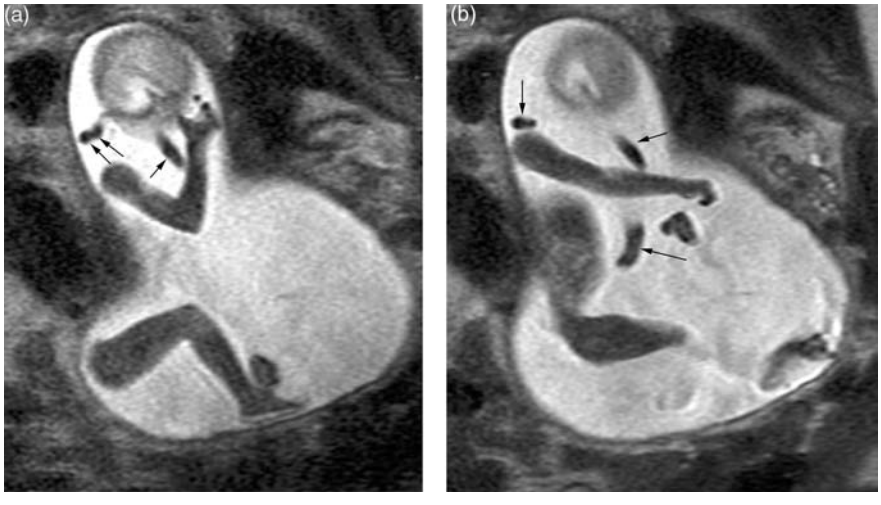

Figure 7.3 Demonstration of motion on visualization of extremities at 21 weeks gestational age. Two sequential T_2-weighted images of the extremities demonstrate motion of the arm that has occurred between image acquisitions. Note also how loops of umbilical cord (arrows) can simulate extremities.

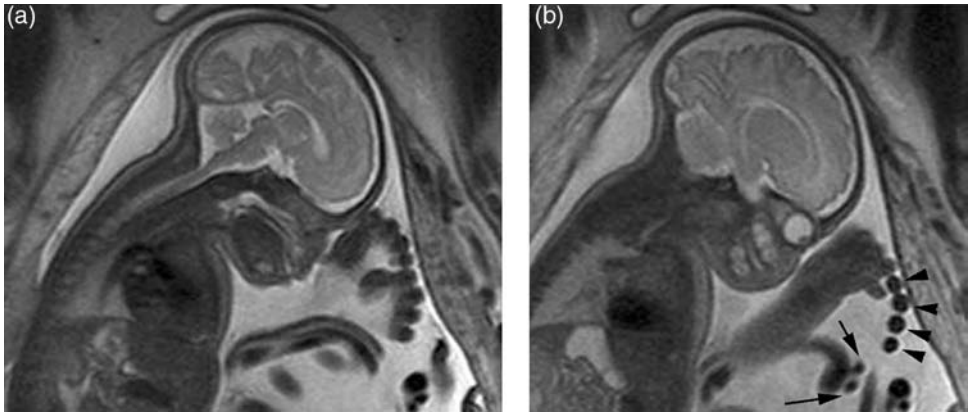

Figure 7.4 Umbilical cord as a pitfall in extremity evaluation at 32 weeks gestational age. Two sequential T_2-weighted images of the hands. Note how the umbilical arteries in cross-section (arrows) can appear similar to the digits (arrowheads). [From Levine et al. (47)]

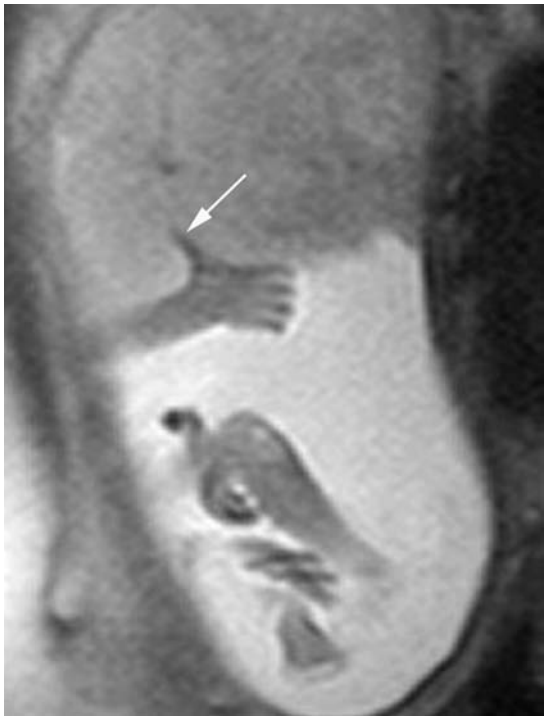

Figure 7.5 Partial volume averaging. T_2-weighted image of partial volume averaging in which a placental vein (arrow) adjacent to the hand appears as a hyperextended thumb. [From Levine et al. (4)]

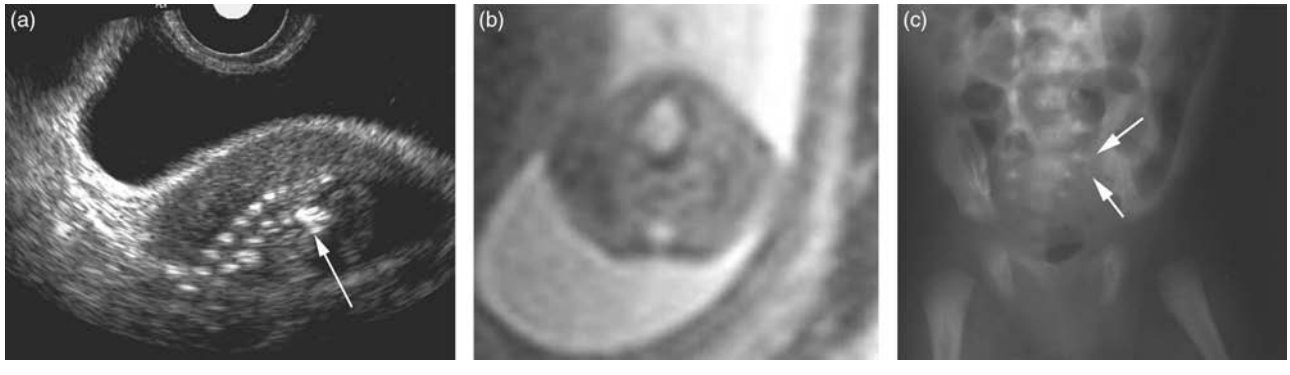

Figure 7.6 Poor visualization of calcifications on T_2-weighted imaging in fetus at 19 weeks gestational age with spondyloepiphyseal dysplasia punctata. (a) Transvaginal sonogram shows calcification (arrow) adjacent to the spine. (b) Axial T_2-weighted image in the same region fails to demonstrate the calcification. The fetus otherwise appears normal. (c) Postnatal radiograph demonstrates the small calcifications adjacent to the spine (arrows).

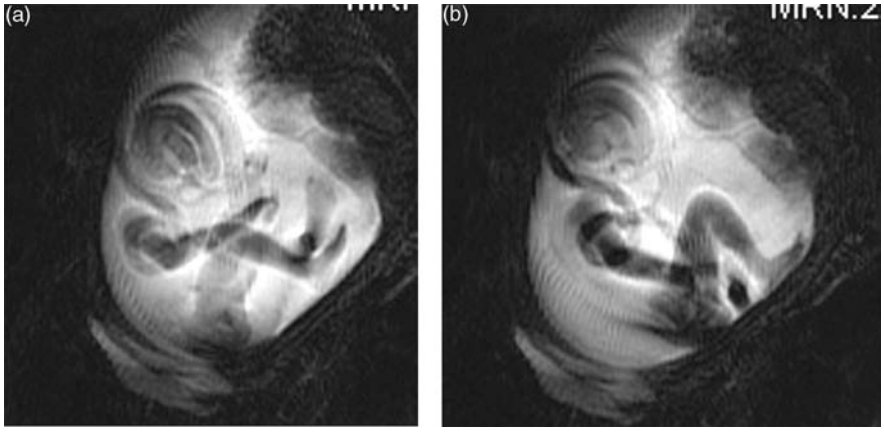

Figure 7.7 Thick-slab imaging of the extremities at 19 weeks gestational age. Thick-slab (slice thickness of 50 mm) heavily T_2-weighted images allow for the majority of an extremity to be visualized in a single image.

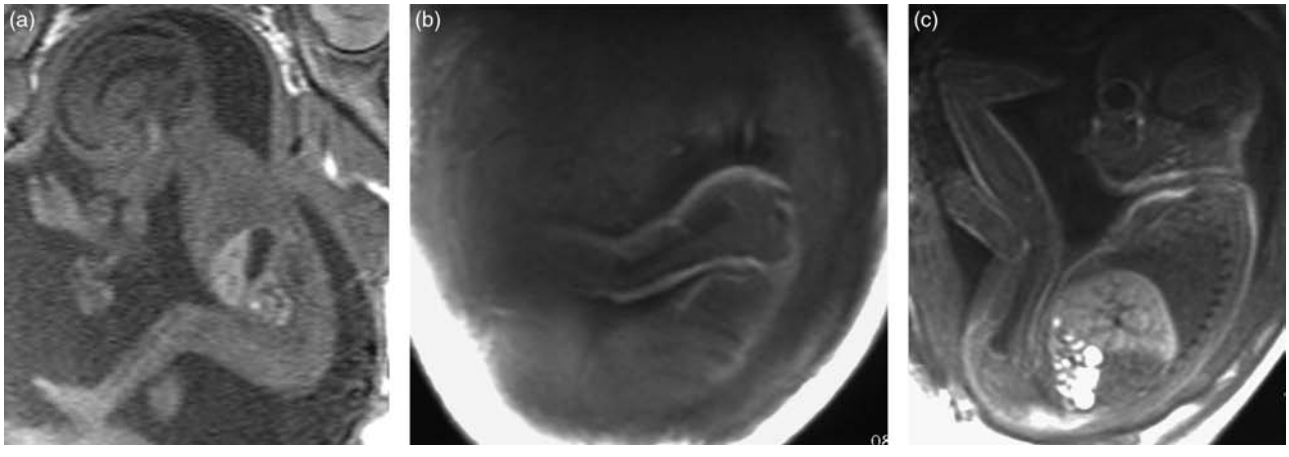

Figure 7.8 T_1-weighted images of the extremities. T_1-weighted images at 24 (a) and 29 (b and c) weeks gestational age. Note the increased signal of the subcutaneous fat in the third trimester.

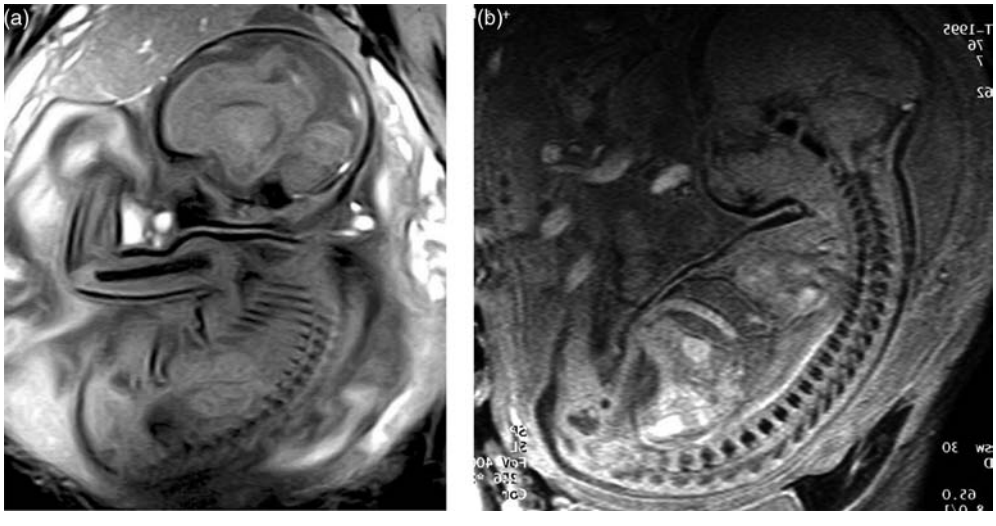

Figure 7.9 Water excitation sequence at 32 weeks gestational age. Note how the bones stand out as black and are better visualized than on the more commonly utilized T_2-weighted sequences. [From Levine et al. (5)]

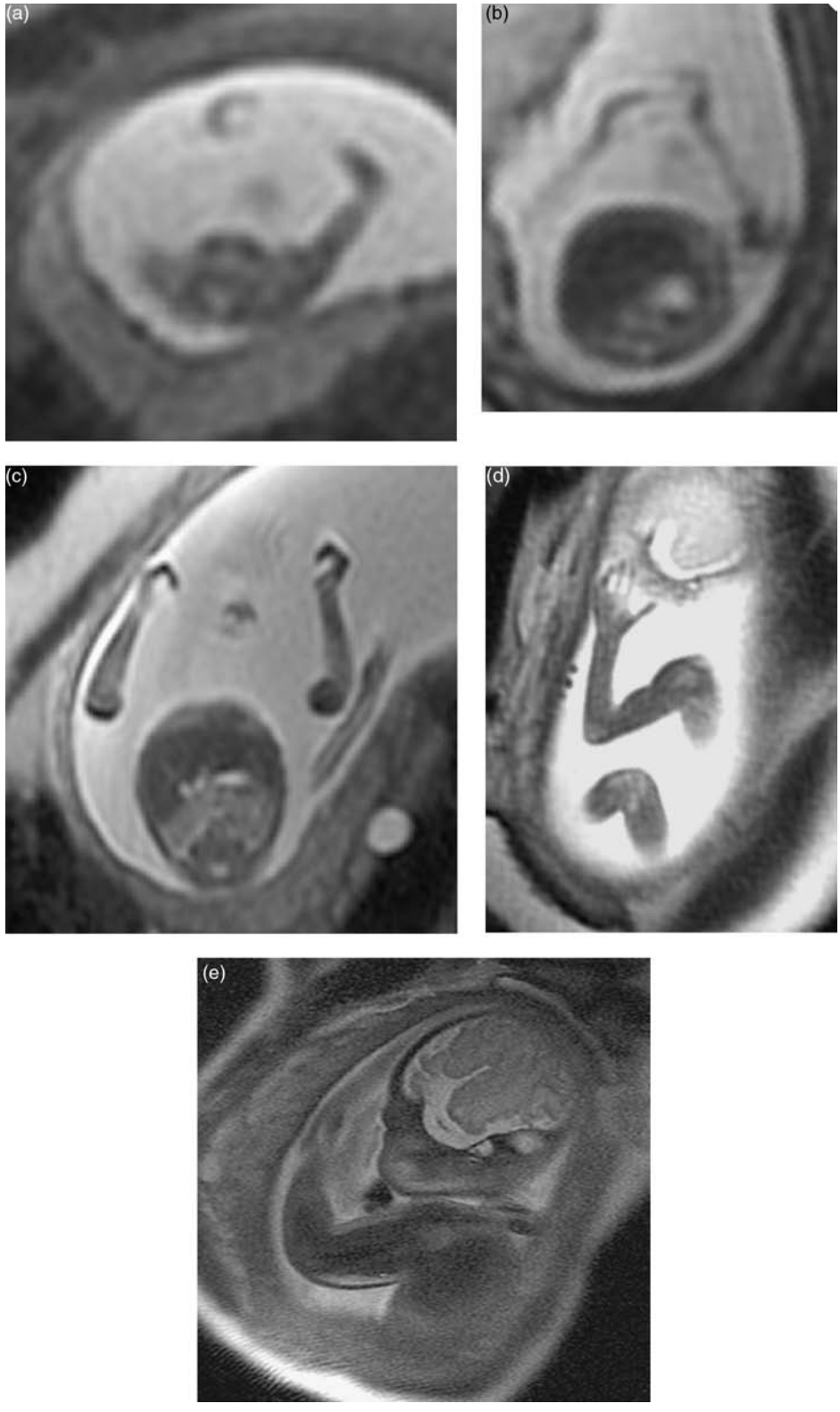

Figure 7.10 Normal arms. T_2-weighted images at 14 (a and b), 18 (c), 19 (d), and 34 (e) weeks gestational age. Note how partial volume averaging with amniotic fluid makes the distal limbs appear attenuated in (b). The normal position of the hands is in a slightly curved "relaxed" position, as in (c), but at times, the fingers extend, as in (d). Note how the musculature of the upper arms becomes more distinct as gestational age progresses.

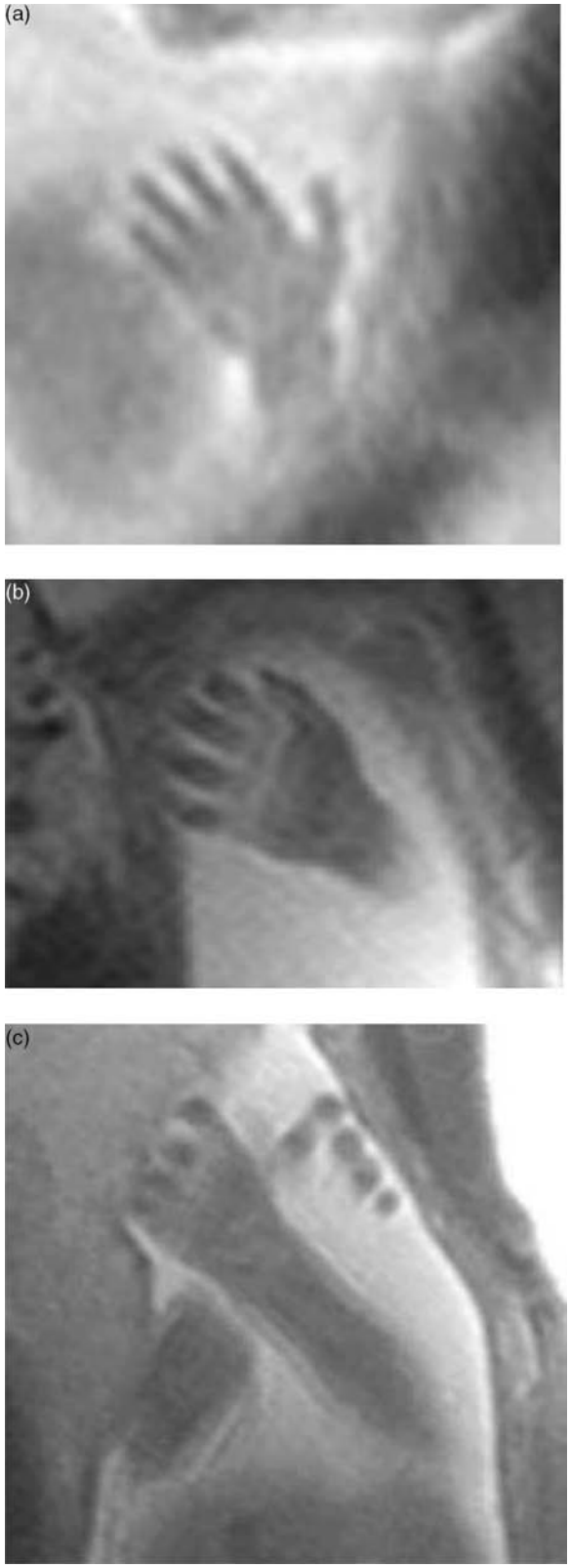

Figure 7.11 Normal hand. T_2-weighted images at 18 (a), 24 (b), and 26 (c) weeks gestational age. Note in (c) that subcutaneous fat is beginning to become apparent.

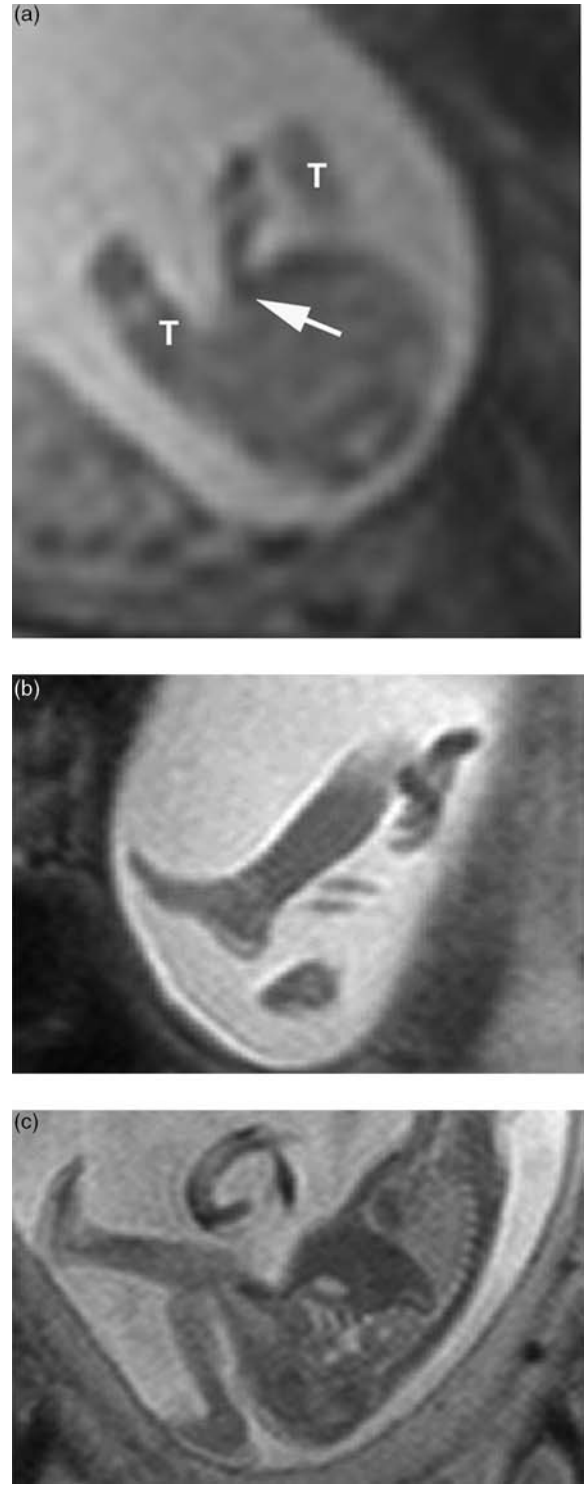

Figure 7.12 Normal lower extremities. T_2-weighted images at 14 (a), 18 (b), and 19 (c) weeks gestational age. Views of the foot position often depend on the amount of surrounding amniotic fluid, allowing for normal positioning of the foot with respect to the ankle. The thighs (T) and cord insertion (arrow) are observed in (a). Notice the relative paucity of subcutaneous fat at these early gestational ages.

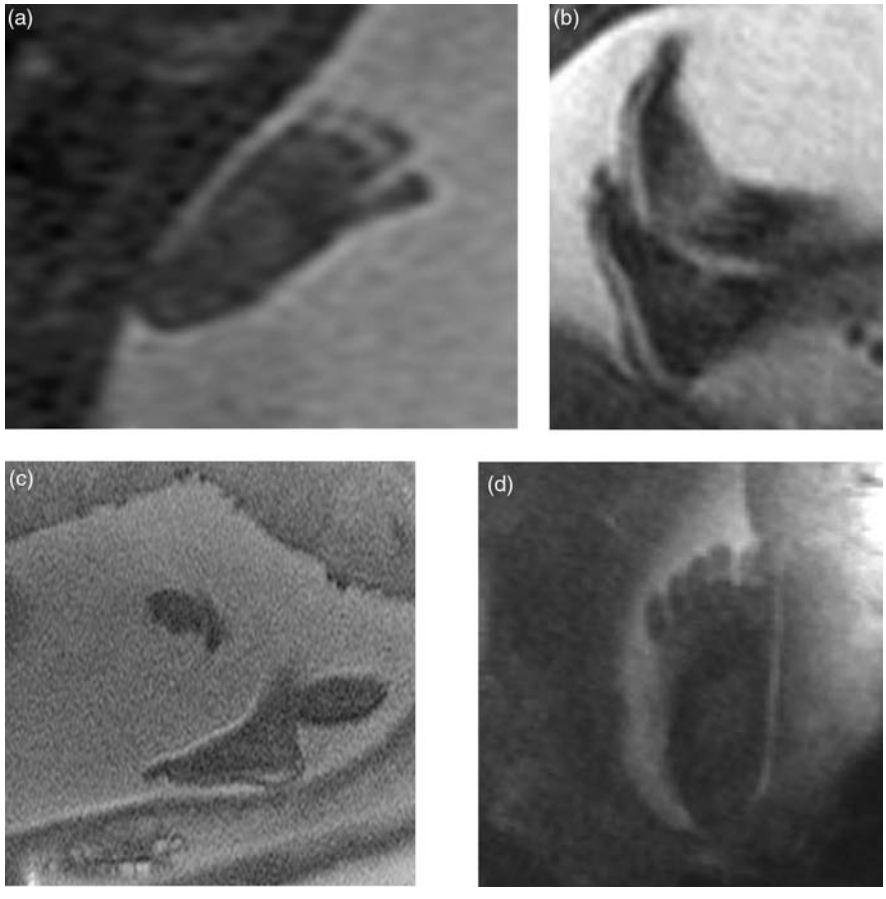

Figure 7.13 Normal feet. T_2-weighted images at 16 (a), 23 (b), 32 (c), and 39 (d) weeks gestational age show the feet and toes.

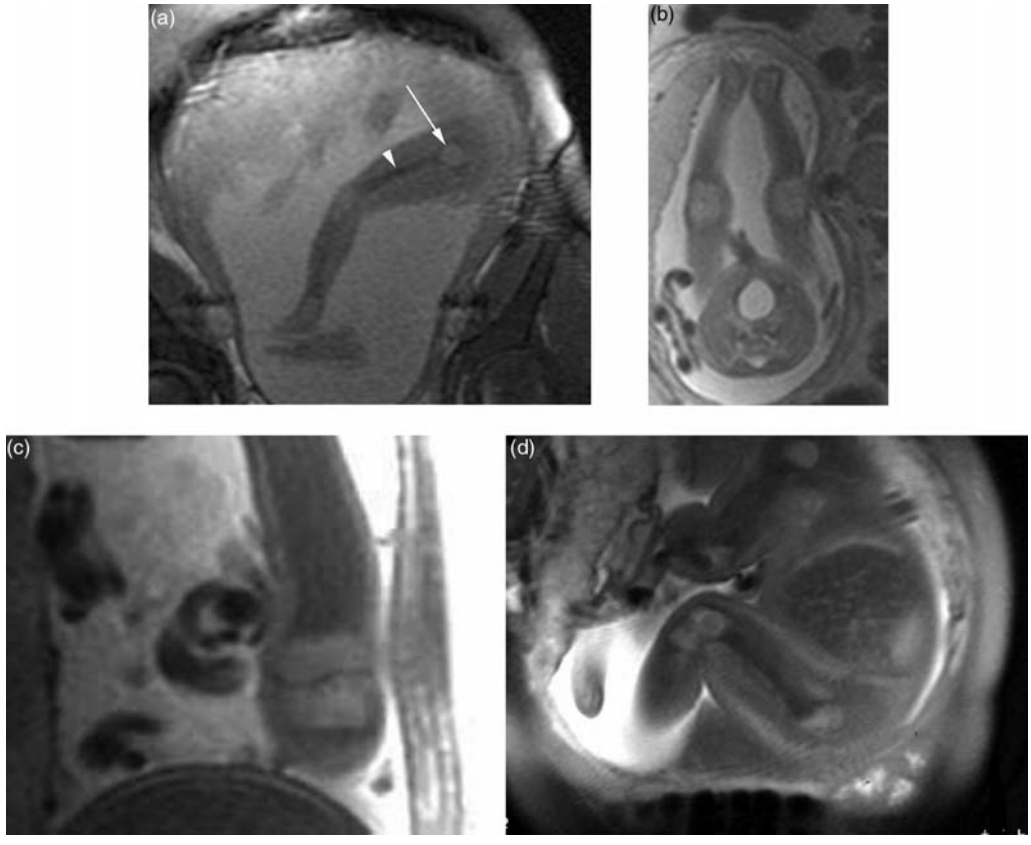

Figure 7.14 Normal femoral and tibial epiphyses. T_2-weighted images at 24 (a), 25 (b), 32 (c), and 35 (d) weeks gestational age. Note the diaphysis (white arrowhead) is of slightly lower signal intensity than adjacent muscle, whereas the epiphysis (white arrow) is of slightly higher signal intensity. In (b), note the "in-curving" of the lower extremities, a normal finding in the fetus.

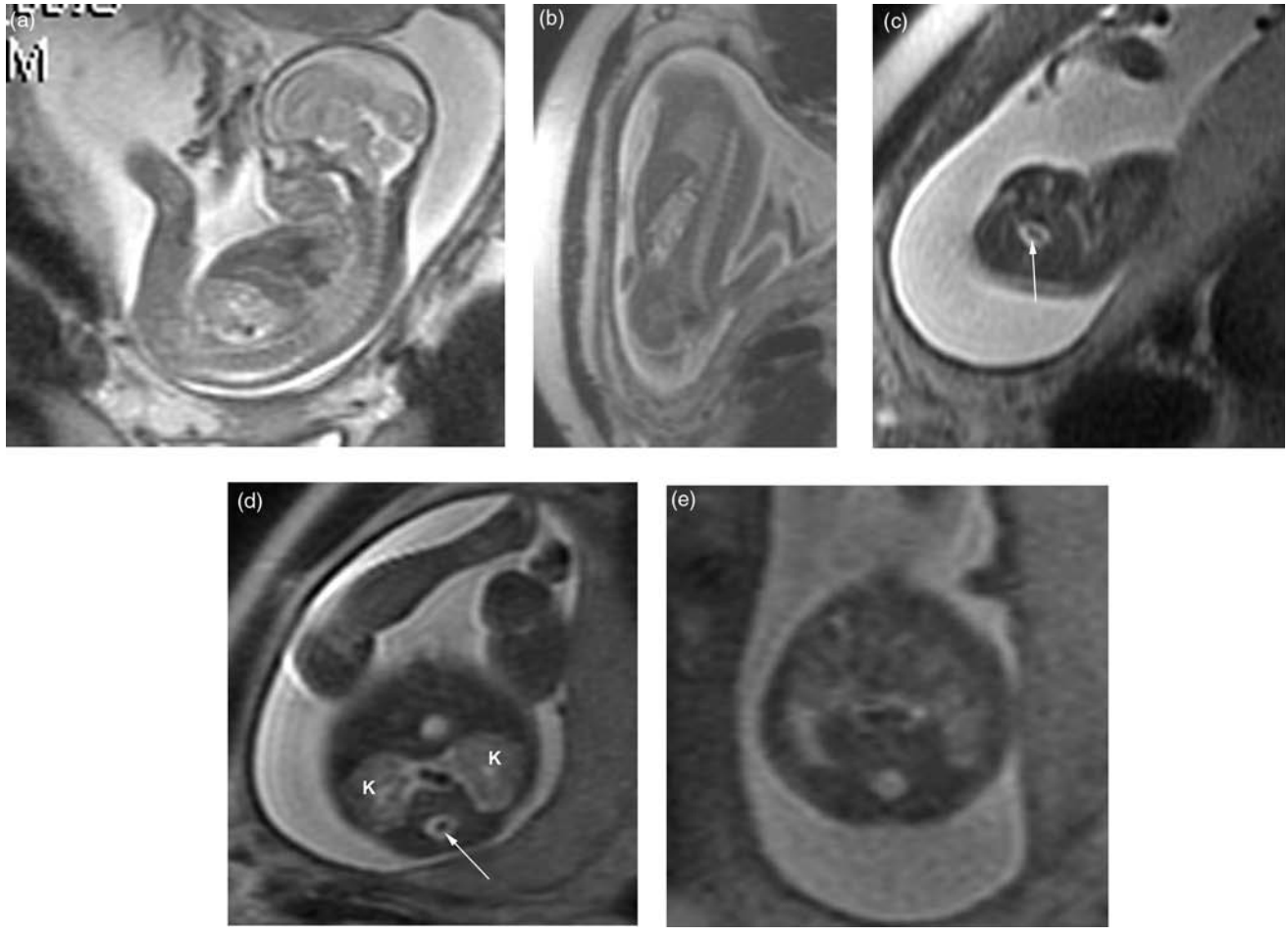

Figure 7.15 Normal spine at 21 weeks gestational age. Sagittal (a) and oblique coronal (b) T_2-weighted images illustrate how the bony anatomy can blend into the musculature. On the axial images at the level of the cervical (c) and lumbar (d and e) regions, the vertebral bodies are better visualized. On images (a–d) the spinal cord (arrow) surrounded by amniotic fluid is well visualized. Note the filum terminale at the level of the kidneys (K).

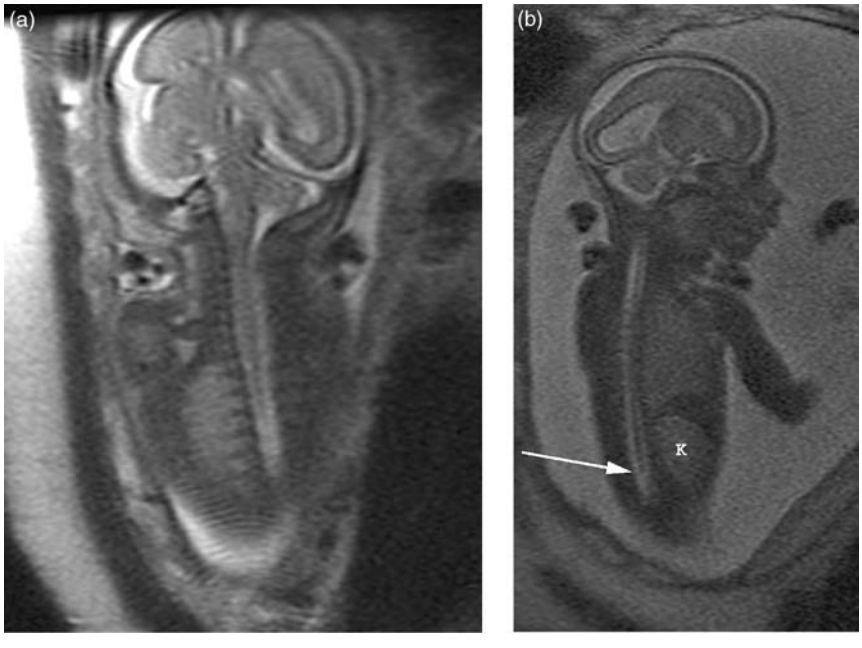

Figure 7.16 Normal spine at 25 weeks gestational age. Two slightly oblique coronal T_2-weighted images. Note that the spinal cord (arrow) terminates at the level of the kidney (K).

role in the primary assessment of spinal abnormalities. However, the spinal cord is typically better visualized by MR imaging than by ultrasound (Figs. 7.15–7.17); therefore, abnormalities of the cord are well assessed by MR examinations. The posterior elements of the spine flare in the upper cervical and lumbar regions and converge in the sacral region. The normal fetal spine has a gentle thoracic kyphosis and lumbar lordosis. Fetal positioning, especially in the third trimester, can make curvature of the spine difficult to assess. Because of these factors, it is difficult to assess the entire spine on a single image. The alignment of the spine is best visualized in the sagittal and coronal planes on MR images. The spinal cord normally terminates at the level of the mid-kidneys (Fig. 7.16).

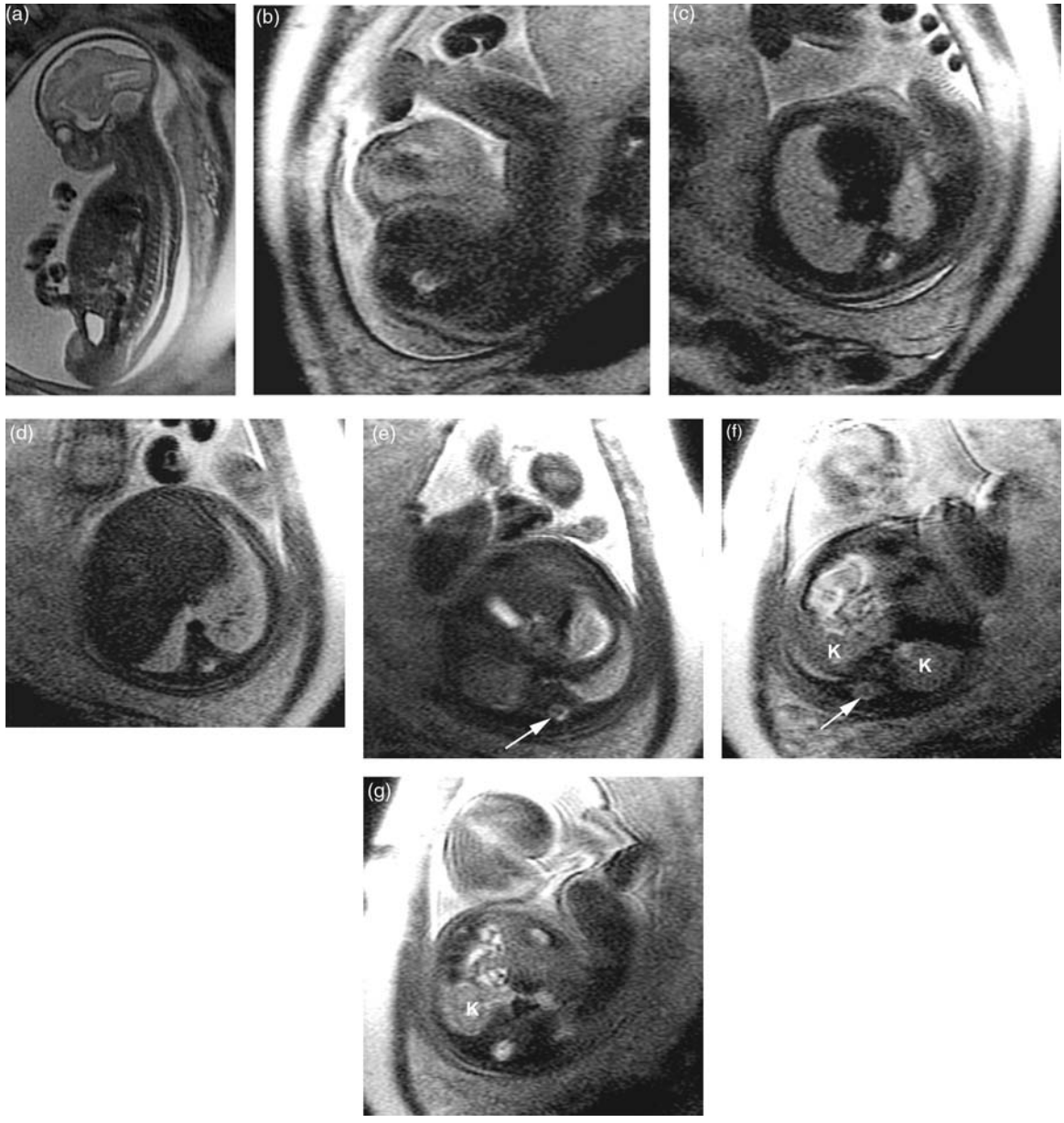

Figure 7.17 Normal images of spine at 31 weeks gestational age. Sagittal (a) and transverse (b–g, from more rostral to more caudal) T_2-weighted images illustrate the changing appearance of the spinal cord (arrow) as it focally enlarges at the conus medullaris at the level of the mid-kidneys (K).

ABNORMAL MUSCULOSKELETAL SYSTEM

Abnormal Extremities

Limb Amputations

Amputated, missing, or malformed limbs are typically isolated findings (Fig. 7.18). These are most easily assessed on sonography. These may be due to anoxia, drugs, hormones, viral infections, irradiation, hyperglycemia, or amniotic band syndrome (6,7). Amniotic band syndrome occurs when constriction bands surround an extremity, resulting in necrosis of a variable amount of bone and soft tissue. These abnormalities are easily missed on MR imaging as it is common for only a portion of an extremity to be visualized. At times, an extremity will be enlarged distal to a constriction band (Fig. 7.19).

Skeletal Dysplasia

It is beyond the scope of this atlas to discuss the wide differential diagnosis of skeletal dysplasia. Skeletal dysplasias are best assessed sonographically, as the long axis of the bone can be obtained with confidence, enabling accurate measurements of long bone length. It is unclear how MR imaging may aid in diagnosis of skeletal dysplasias, although there is a report of MR imaging adding useful information in a case of hypochondrogenesis where MR examination showed ill-defined ossification of the cervical vertebral bodies, a hypoplastic thorax, retarded ossification of the pubic bones, and broad shortened long bones. In this case, ultrasound had shown only the shortened long bones (8). The most common lethal skeletal dysplasia is thanatophoric dysplasia (Fig. 7.20) (9). The most common nonlethal skeletal dysplasia is heterozygous achondroplasia (Fig. 7.21) (9). It is possible that lung volume measurements directly obtained from sequential slices of the lungs will be helpful in cases where lethal pulmonary hypoplasia is of concern (10).

Arthrogryposis

Arthrogryposis results from decreased *in utero* motion from neural, muscular, and connective tissue or infectious etiology. Real-time imaging of the fetus allows for observation of extremity motion. When the extremities are held in fixed position, contractures can occur, and there can be wasting of the fetal soft tissues. Magnetic resonance imaging can be helpful in cases of arthrogryposis to assess central nervous system abnormalities and to illustrate to the patients the position of the fetus (Figs. 7.22 and 7.23).

Abnormal Positioning of the Hands

Clinodactyly refers to the curvature of one or more fingers. If severe, it may be associated with overlapping digits and an overall clenched configuration of the hand. This can be associated with chromosomal abnormalities such as trisomy 18. The classic clenched fist associated with this anomaly is most apparent on ultrasound, but if the fingers cannot be individually visualized throughout the MR examination, this anomaly can be suspected (Fig. 7.24). Abnormal positioning of the hands also can be present with arthrogryposis (Fig. 7.22).

Abnormal Positioning of the Feet

Clubfeet may be an incidental finding or may be associated with neurologic abnormality such as neural tube defect (Fig. 7.25). It also may be due to extrinsic causes such as oligohydramnios. In the third trimester, it can be especially difficult to assess foot position. The diagnosis is made when the relative relationships of the lower leg bones and sole of the foot are not perpendicular (11,12).

Syndactyly

Syndactyly refers to fusion of the digits and may consist of bony or soft tissue fusion. Syndactyly is a difficult diagnosis to make on MR imaging. If suspected on ultrasound, it can be confirmed by viewing the digits without intervening amniotic fluid (Fig. 7.26).

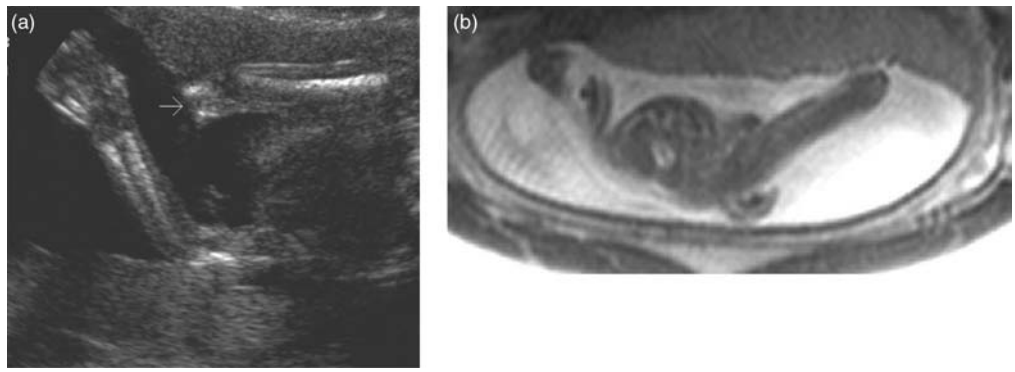

Figure 7.18 Limb amputation at 21 weeks gestational age. Sonogram (a) and T_2-weighted image (b) in fetus with limb amputation. The defect is best visualized on the sonogram (arrow), as it is common to not visualize an entire extremity on MR imaging. [From Levine et al. (47)]

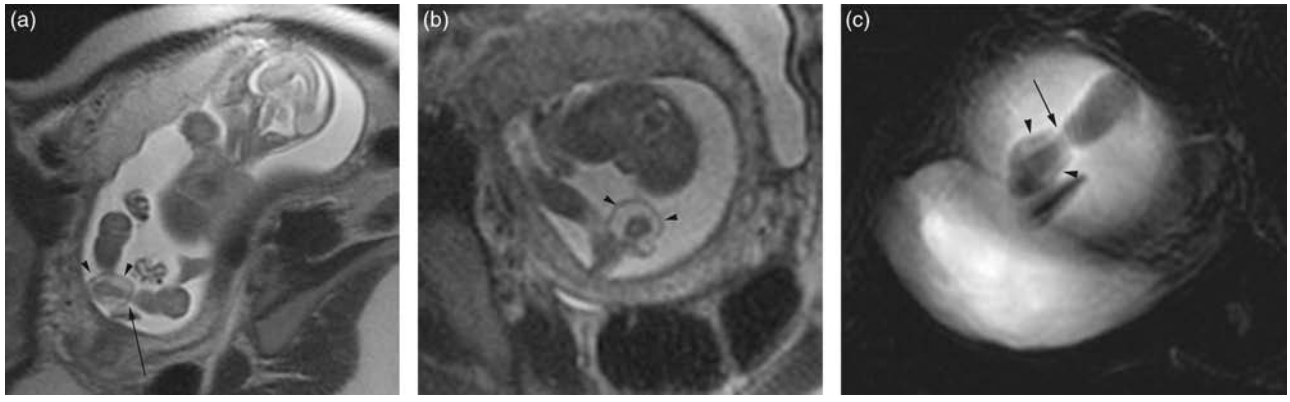

Figure 7.19 Amniotic band syndrome at 20 weeks gestational age. Sagittal (a) and axial (b) thin-slice T_2-weighted images show edematous soft tissues (arrowheads) below a constriction band (arrow). Sagittal T_2-weighted thick-slice (c, 20 mm slice thickness) image further illustrates the constriction band.

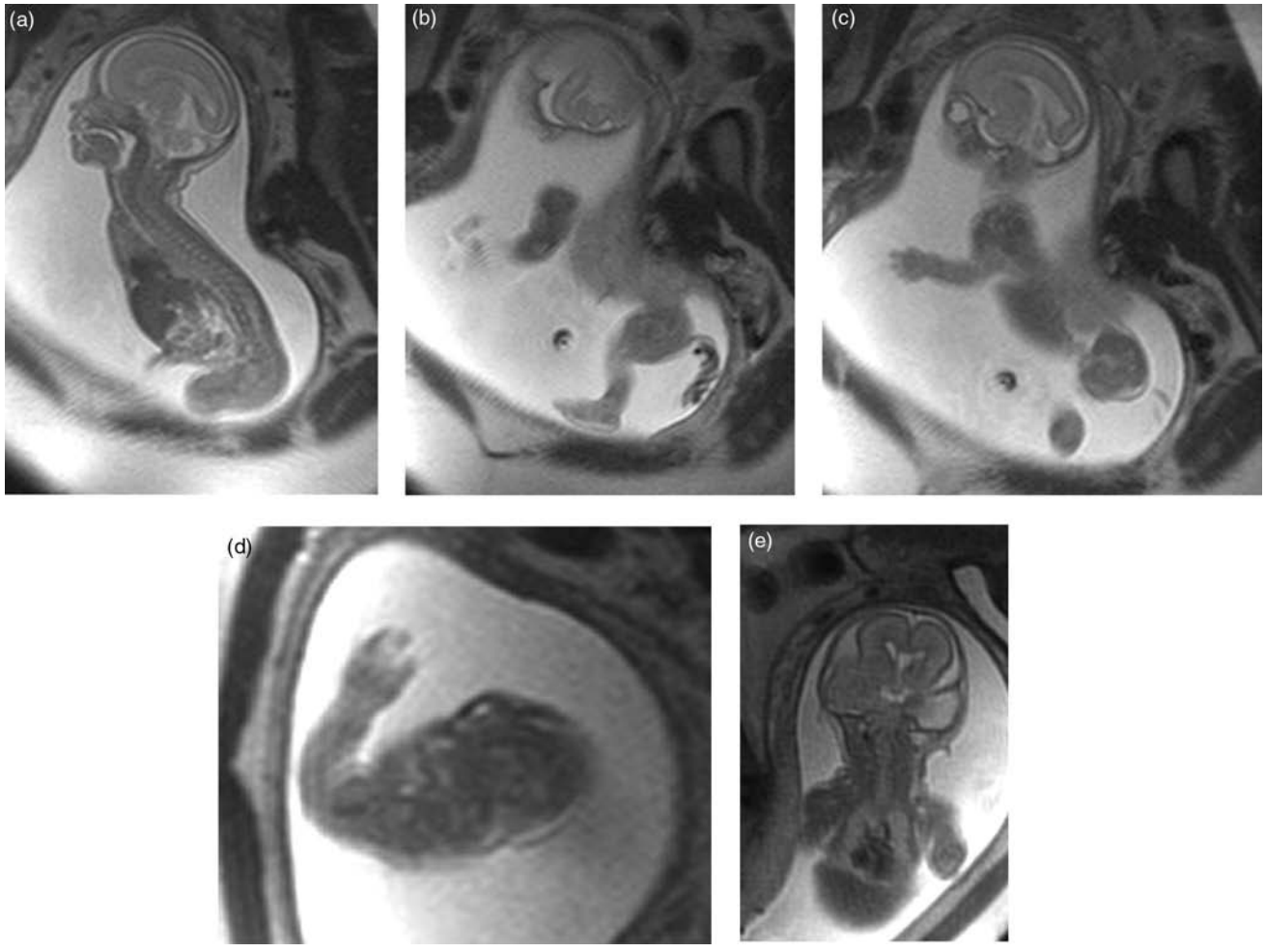

Figure 7.20 Thanatophoric dysplasia at 20 weeks gestational age. Sagittal T_2-weighted images (a–c) demonstrate a small chest, slightly large head with frontal bossing, and severe micromelia. Axial T_2-weighted image of the arm (d) shows the micromelia. Coronal T_2-weighted image of the thorax (e) shows a bell-shaped chest, with the heart occupying the majority of the thoracic diameter.

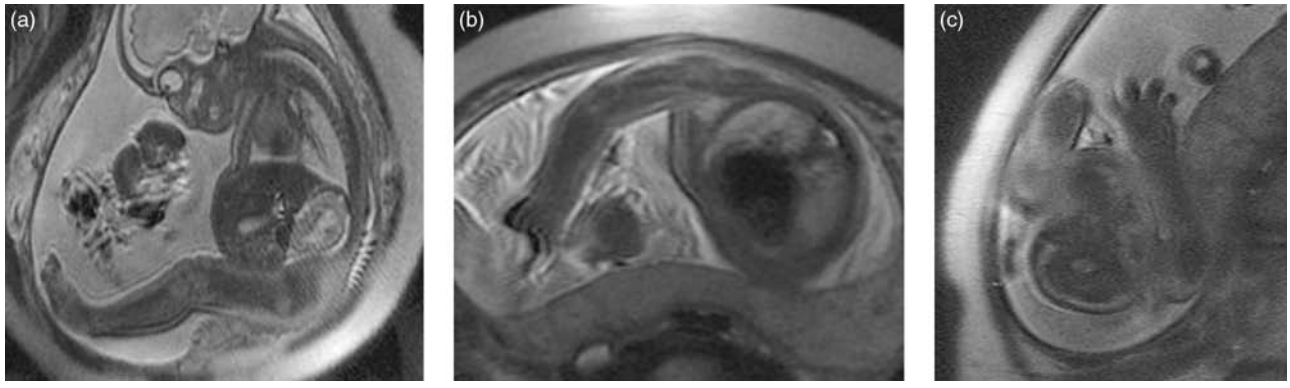

Figure 7.21 Heterozygous achondroplasia at 34 weeks gestational age. Note rhizomelic shortening in (a) and (b). Note the trident fingers in (c).

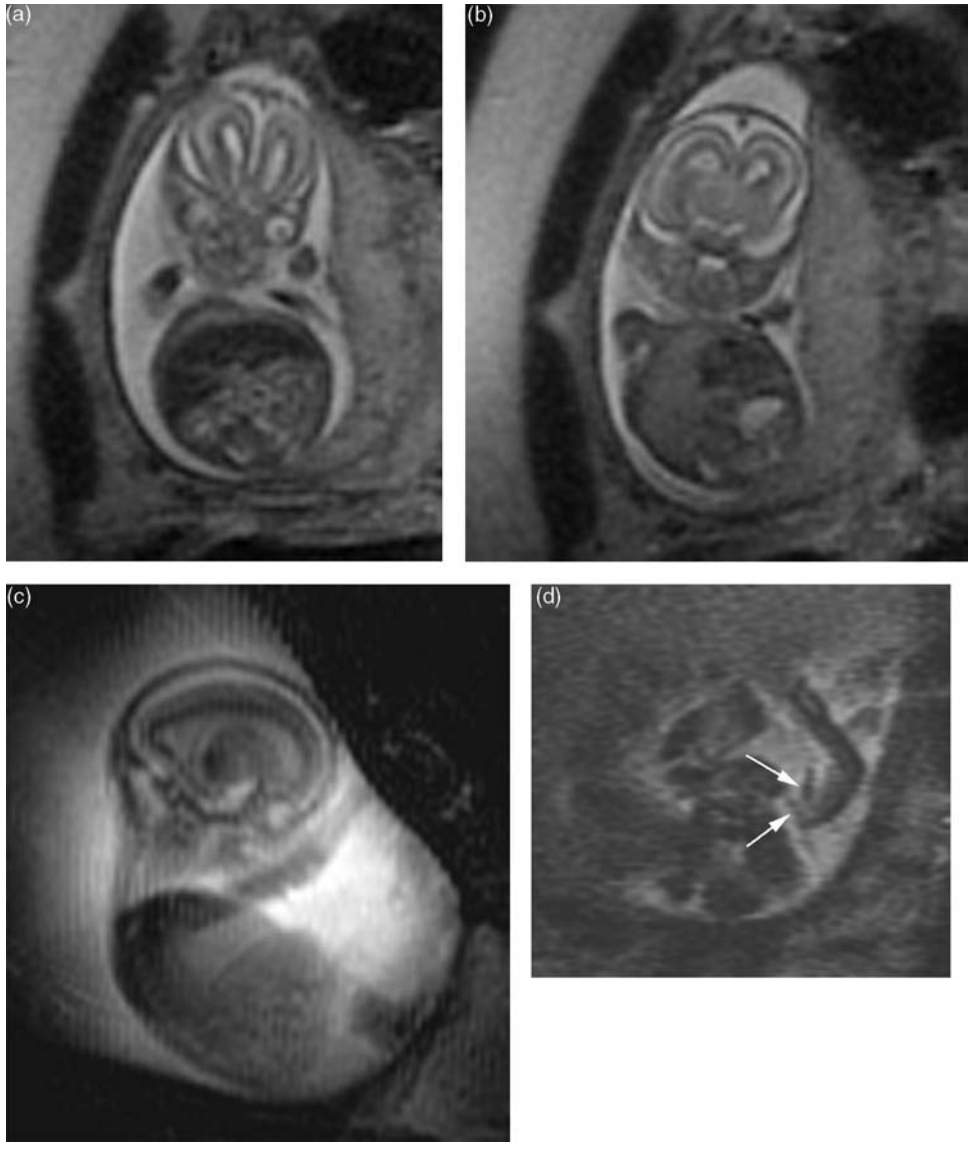

Figure 7.22 Arthrogryposis at 19 weeks gestational age. Coronal views (a and b) show atrophic musculature. Thick-slab (25 mm slice thickness) heavily T_2-weighted image (c) shows the extended position of the arm (which remained constant during the examination). The hand (d) shows the flexion at the wrist and fingers (arrows).

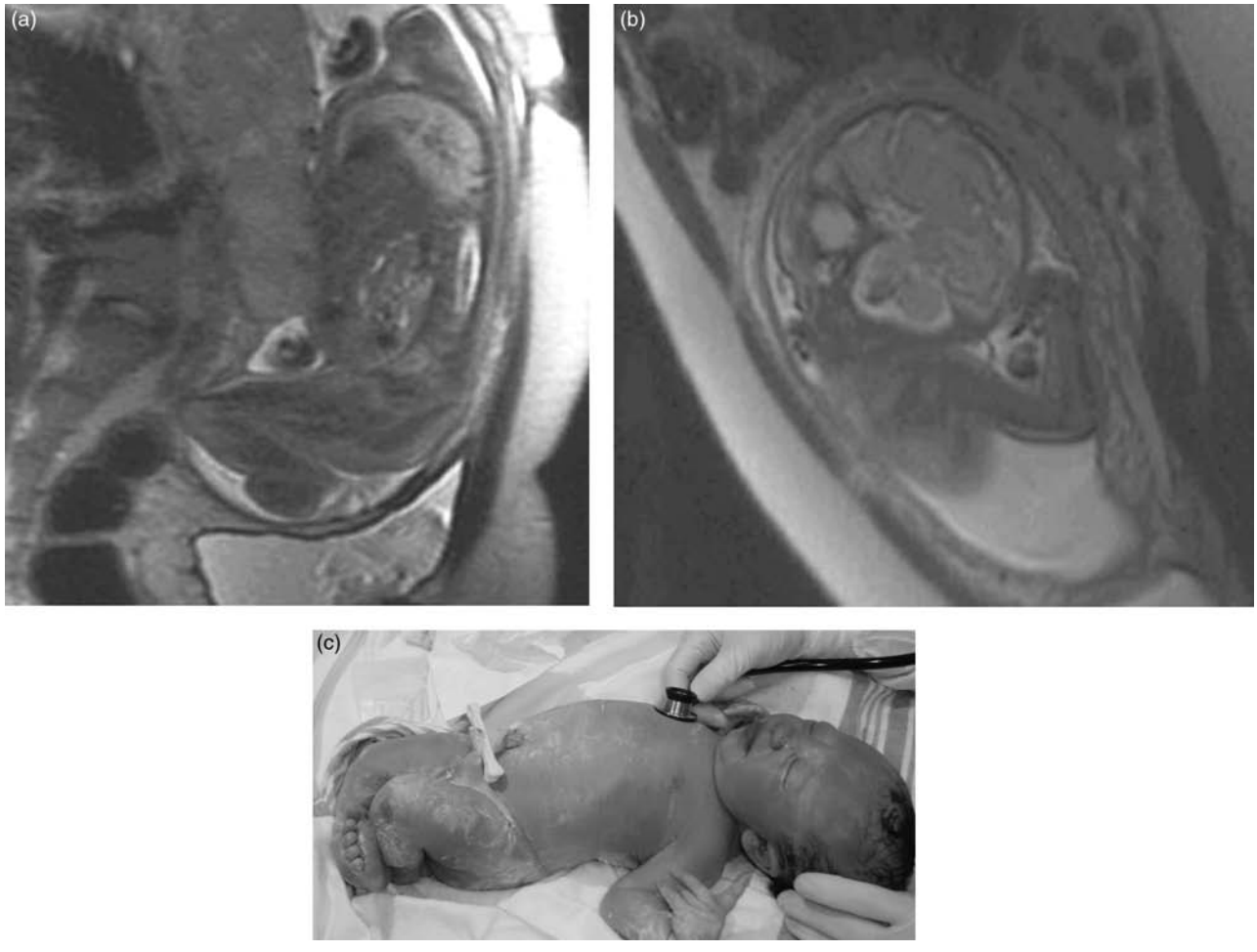

Figure 7.23 Arthrogryposis at 30 weeks gestational age. Sonogram (not shown) revealed clubfeet and fixed position of the extremities. (a) Sagittal T_2-weighted image shows breech position, with leg in flexion and clubfoot. (b) Elbow and wrist are in flexed position. (c) Postnatal photograph shows abnormal positioning of the extremities.

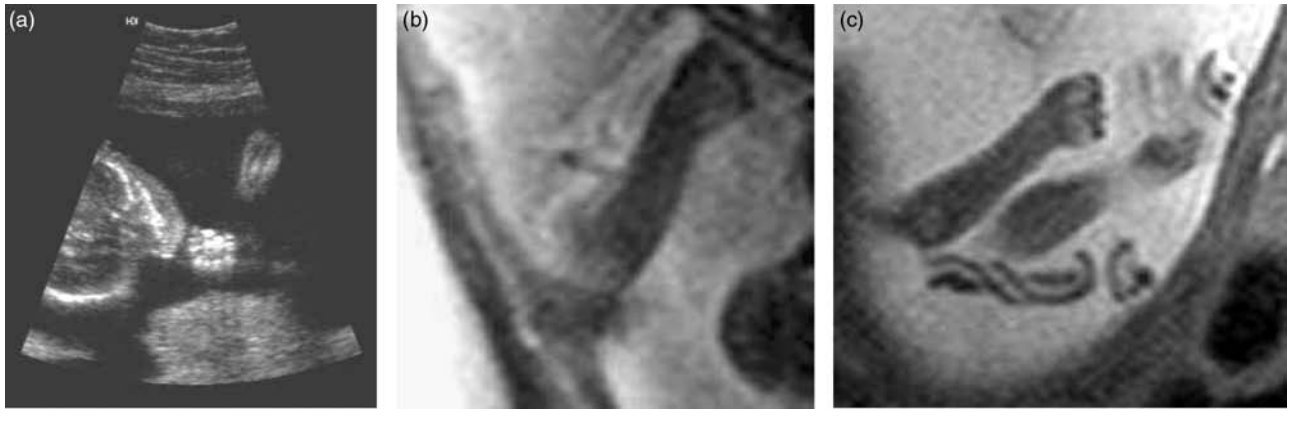

Figure 7.24 Clenched fists in association with trisomy 18 at 22 weeks gestational age. Sonogram (a) and T_2-weighted images (b and c) illustrate the persistent clenched appearance of the hands.

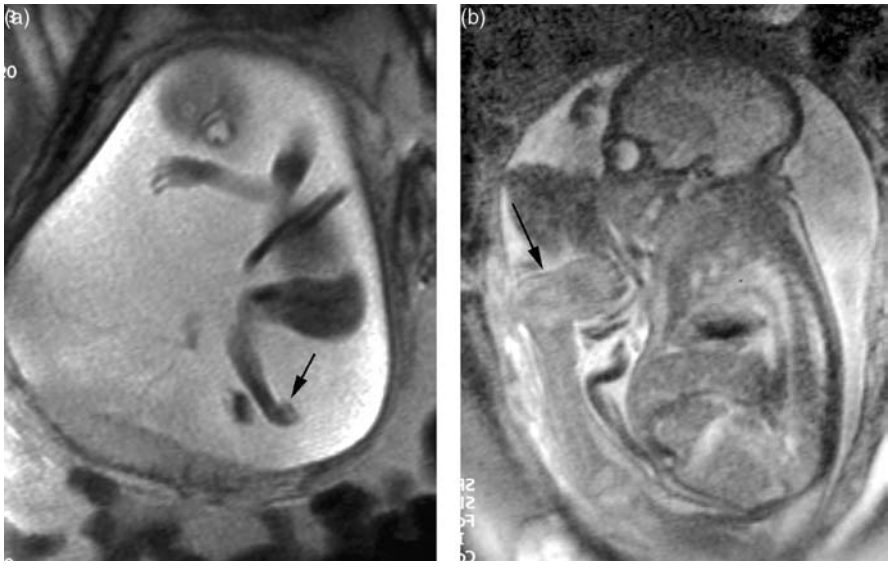

Figure 7.25 Two different fetuses with neural tube defects and clubfeet. Note abnormal position of the foot (arrow) with respect to the leg in fetus at 16 weeks (a) and 34 weeks (b). [(a) from Levine et al. (47); (b) from Levine et al. (5)]

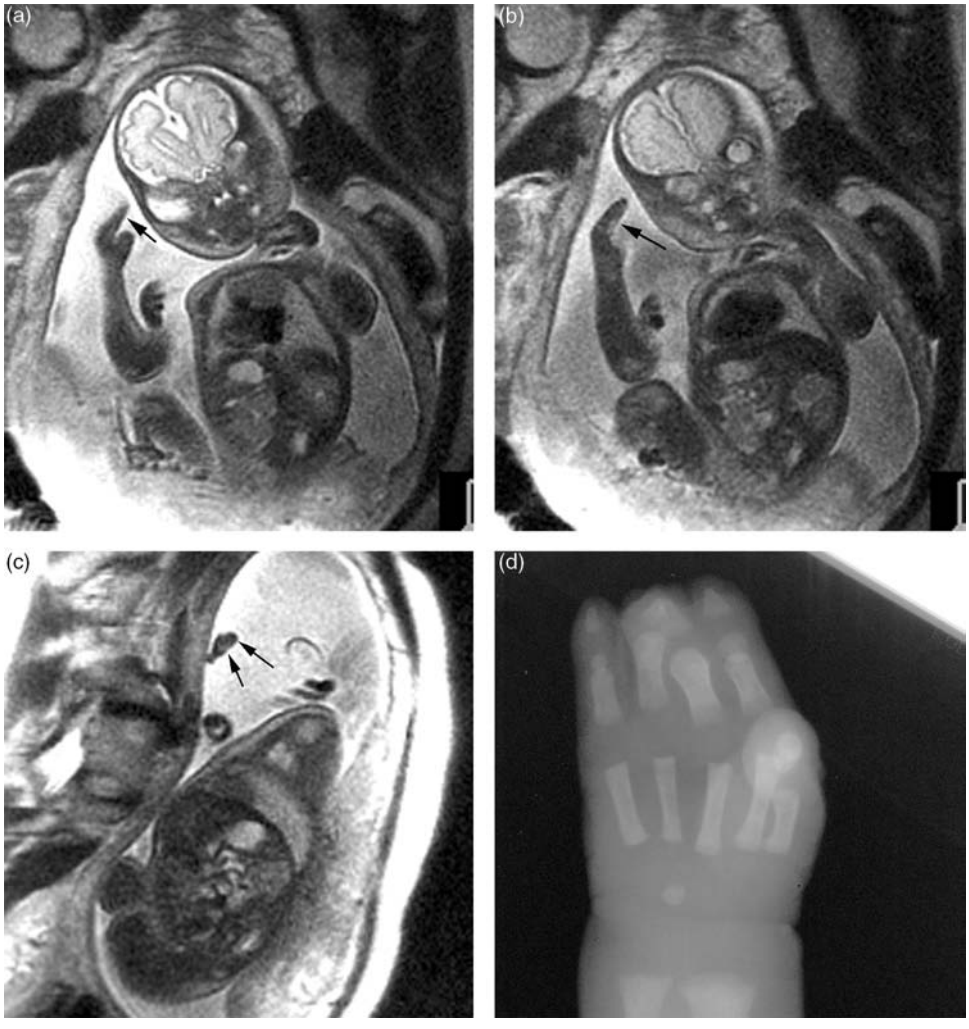

Figure 7.26 Syndactyly in fetus with Aperts syndrome at 32 weeks gestational age. Coronal T_2-weighted image of the brain (a) shows vertical orientation of the frontal horns in this fetus with agenesis of the corpus callosum. In (a), (b), and (c), the hand (arrows) has a mitten-like configuration, and amniotic fluid is never seen separating the digits. Postnatal radiograph (d) demonstrates the syndactyly. This is the same fetus as in Figs. 3.63 and 4.10.

Soft Tissue Tumors

Magnetic resonance imaging can be utilized to illustrate the extent of soft tissue tumors such as hemangiomas and lymphangiomas of the extremities (Fig. 7.27) (13,14).

Abnormal Spine

Secondary neurulation refers to the formation of the caudal neural tube below the notocohord by canalization and retrogressive differentiation. The lower lumbar, sacral, and coccygeal segments are thus formed. This canalization occurs at 4–7 weeks of gestation. Abnormalities associated with defects in secondary neurulation include diastematomyelia, meningocele, lipomeningocele, tethered cord, and caudal regression syndrome.

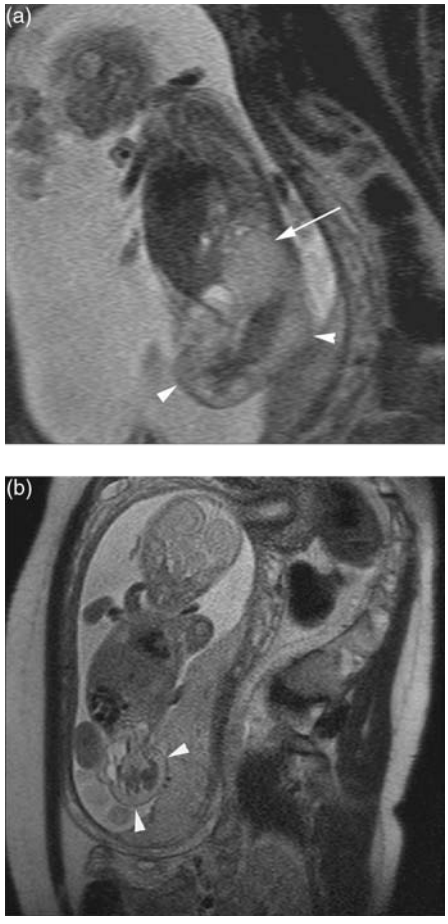

Figure 7.27 Klippel–Trenanay–Weber syndrome with lymphangioma at 20 weeks gestational age. Sagittal (a) and coronal (b) T_2-weighted images show thickened soft tissues of the thigh (arrowheads) with intrapelvic extension (arrow). (Images courtesy of F. Miller, Chicago, IL).

Diastematomyelia

Diastematomyelia involves longitudinal clefting of the spinal cord, which is divided into two hemicords (15). A bony, cartilaginous or fibrous septum is present (Fig. 7.28). The cord is often tethered in an abnormally low position. The hemicords usually each has a distinct arachnoid membrane. On MR examination, a fibrous band may be observed transecting the cord. Alternatively, the split cord and/or thecal sac may be visualized, without visualizing the septum (16).

Meningocele and Myelomeningocele

Spina bifida (i.e., dysraphism) may be subdivided into ventral and dorsal defects. Dorsal defects are most common and are subdivided into open and closed defects. Ventral defects are rare and may have a cyst of neuroenteric origin. In one report, MR imaging better demonstrated this dorsal cyst than did ultrasound (17).

Open neural tube defects have a full-thickness defect of the skin and underlying soft tissues (Figs. 7.29 and 7.30). The vertebral arches are open, with exposure of the spinal canal and neural elements. The defect may be covered by a thin meningeal membrane and contain only spinal fluid (meningocele). When neural tissue is present in the sac, the lesion is defined as a myelomeningocele. Prenatal MR imaging of open neural tube defects shows the thecal sac extending to the skin. When the sac surrounding the defect is thin, it may be better seen on sonography than MR imaging (18). Prenatal MR imaging and ultrasound are equally accurate for the assignment of lesion level in fetuses with myelomenigocele (19). Also, MR imaging can assess the degree of skin-covering, which can be helpful in prognosis (20,21).

Closed neural tube defects have a small defect and are skin covered (Fig. 7.31). In these cases, MR imaging can be helpful, as the position of the spinal cord is better visualized on MR compared with sonographic examinations (Fig. 7.31). Closed spinal dysraphisms with mass include lipomyelocele, lipomyelomeningocele (Fig. 7.32), meningocele (Fig. 7.31), and myelocystocele. The importance of distinguishing between closed and open neural tube defects prenatally is that long-term functional and neurologic prognosis is much better in the group with closed defects. In addition, vaginal delivery is possible with skin-covered defects (22,23).

The most common location for neural tube defects is in the lumbosacral spine. Magnetic resonance imaging often demonstrates a cyst-like lesion located posteriorly, with widening of the neural arches (Fig. 7.29); however, these lesions are typically better demonstrated with ultrasound (24). The reason for this is that the thin membrane of the meningocele or myelomeningocele sac can be obscured by the adjacent spinal fluid on one side and amniotic

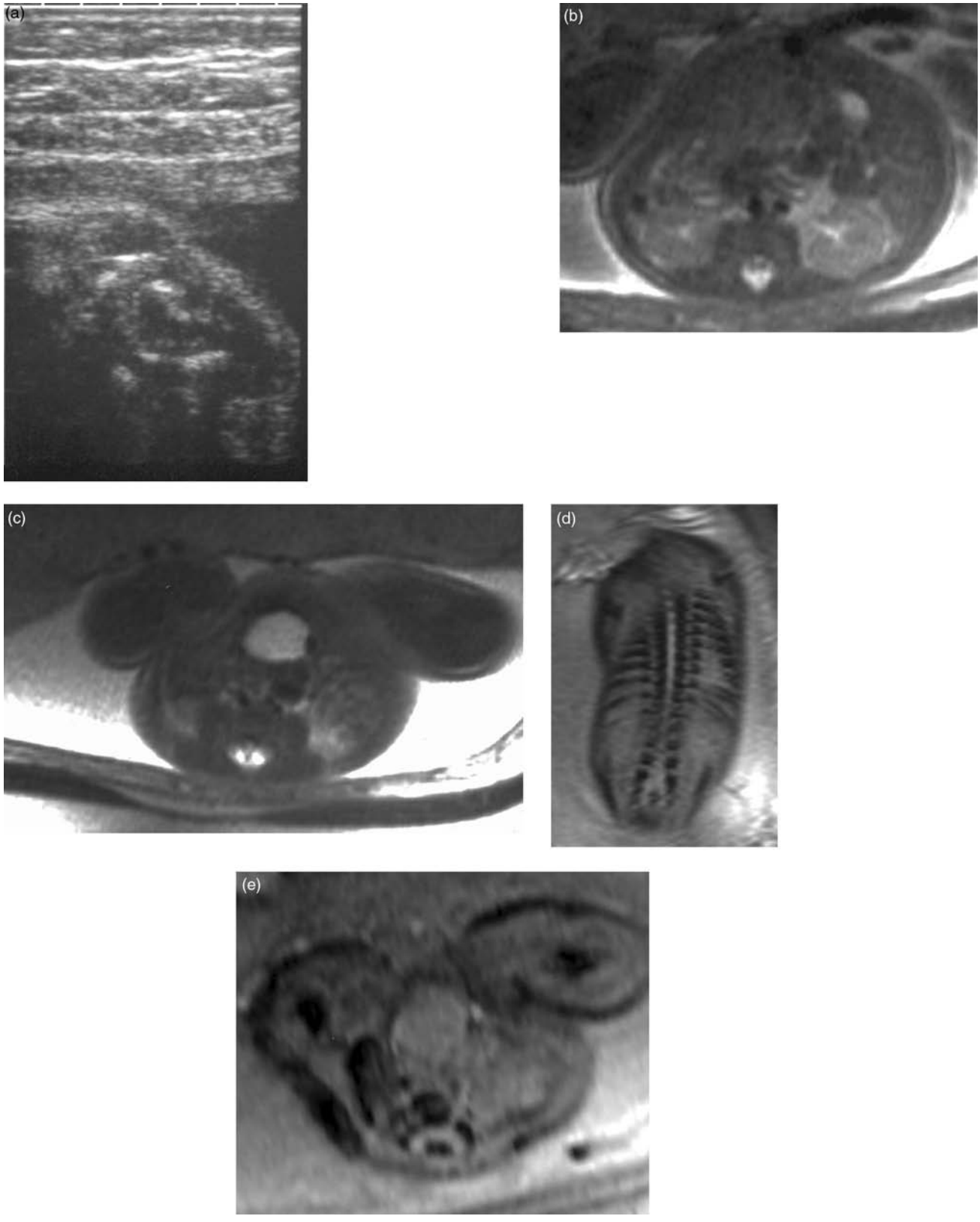

Figure 7.28 Diastematomyelia at 31 weeks gestational age. (a) Sonogram demonstrates a bony or fibrous fragment within the spinal canal. (b) Axial T_2-weighted image at the level of the kidneys shows the split spinal cord. (c) Axial T_2-weighted image at the level of the bladder shows two separate thecal sacs. Coronal (d) and axial (e) spectral spatial water excitation images show the widened thecal sac with the bony/fibrous fragment. [(d and e) from Levine (16)]

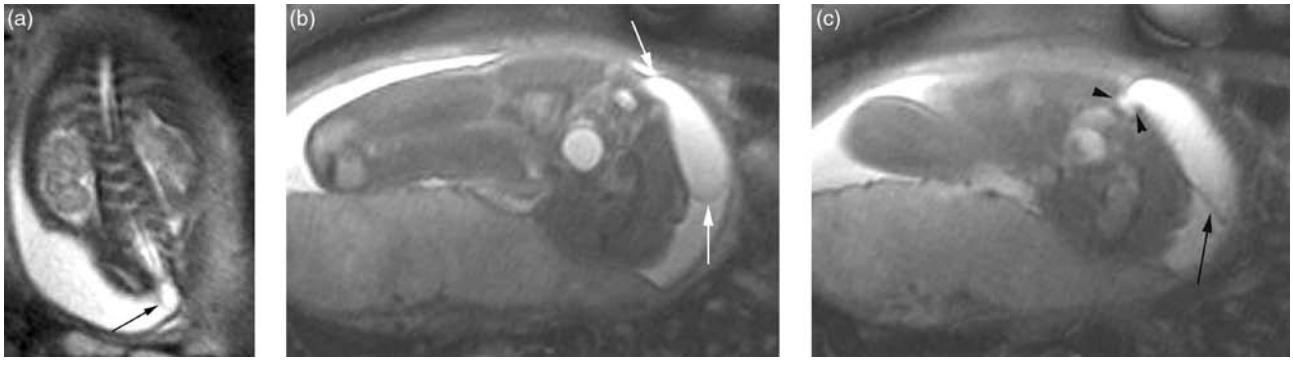

Figure 7.29 Sacral neural tube defect at 33 weeks gestational age. Coronal (a) and axial (b and c) T_2-weighted images of spine show an open neural tube defect (arrowheads). The wall of the sac (arrows) is visualized with cerebrospinal fluid centrally surrounded by amniotic fluid.

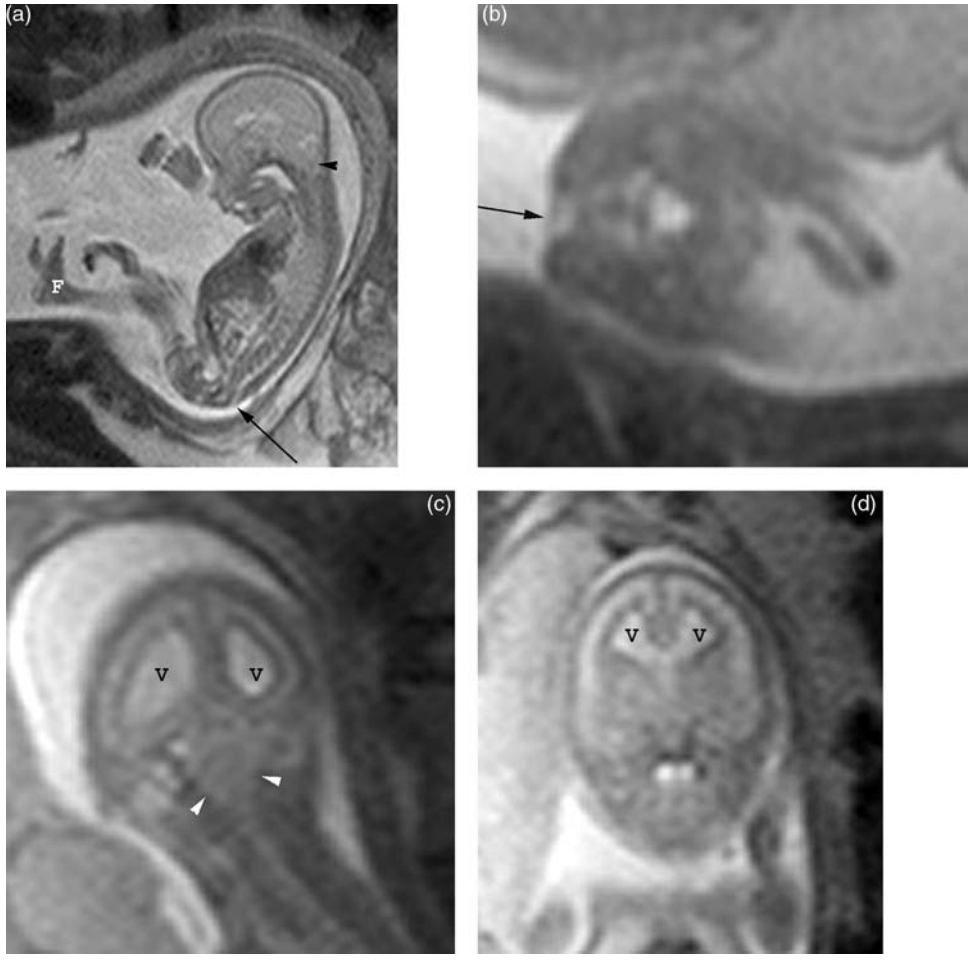

Figure 7.30 Difficult to visualize neural tube defect at 19 weeks gestational age. Sagittal (a) and axial (b) T_2-weighted images show subtle neural tube defect. The thecal sac (arrow) is seen to extend abnormally low and communicate with the amniotic fluid. The thin sac of a meningocele could be missed because of small size and partial volume averaging. The Arnold Chiari malformation is visualized (arrowhead). Coronal views of the brain (c and d) again demonstrate the Arnold Chiari malformation with effacement of the cisterna magna and angular configuration of the ventricles (v), which are the clues to search for the sacral defect. Note the normal position of the foot (F) in (a).

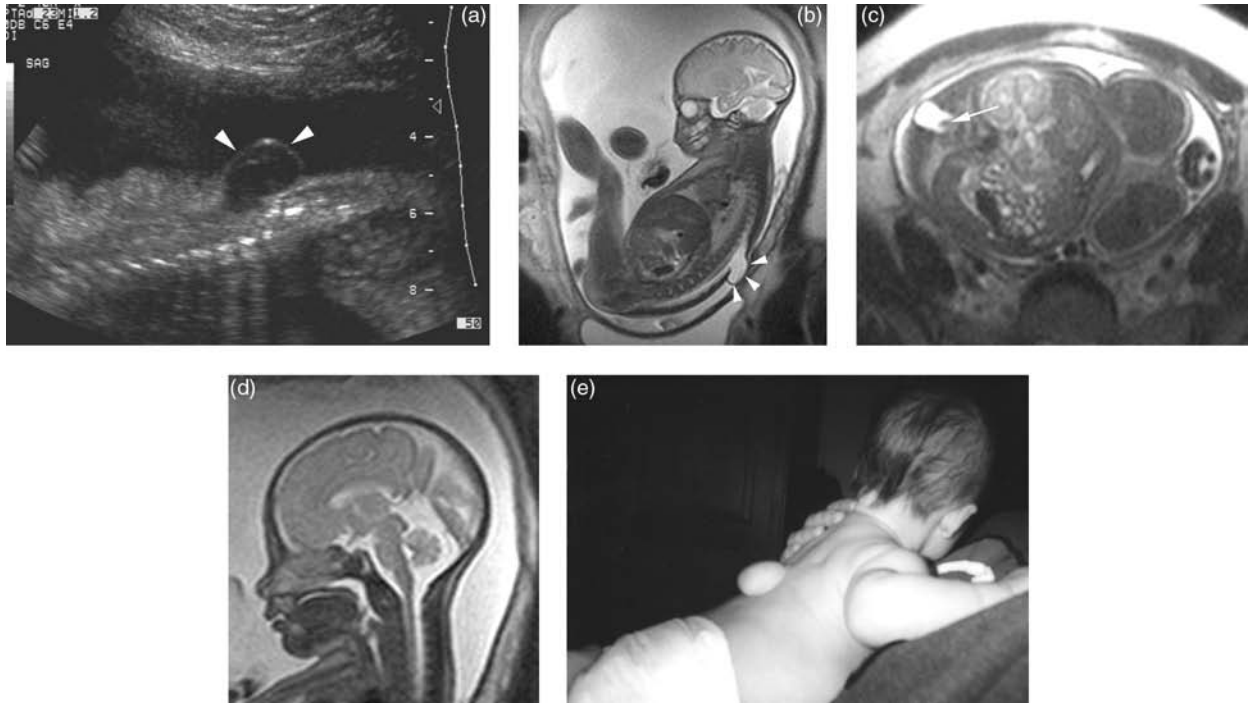

Figure 7.31 Thoracic meningocele at 30 weeks gestational age. Sagittal sonogram (a) demonstrates a thoracic skin-covered neural tube defect (arrowheads). Sagittal (b) T_2-weighted images show the widening of the thecal sac (arrowheads), but no neural elements are visualized within the sac. Axial image (c) shows normal position of the spinal cord (arrow). (d) Sagittal view of the brain demonstrates a normal posterior fossa, reaffirming that this is a closed neural tube defect. Although small neural elements can be missed on MR imaging, the overall appearance is suggestive of a meningocele rather than a meningomyelocele. (e) Postnatal image shows the skin-covered defect. This was repaired and there were no neurologic deficits.

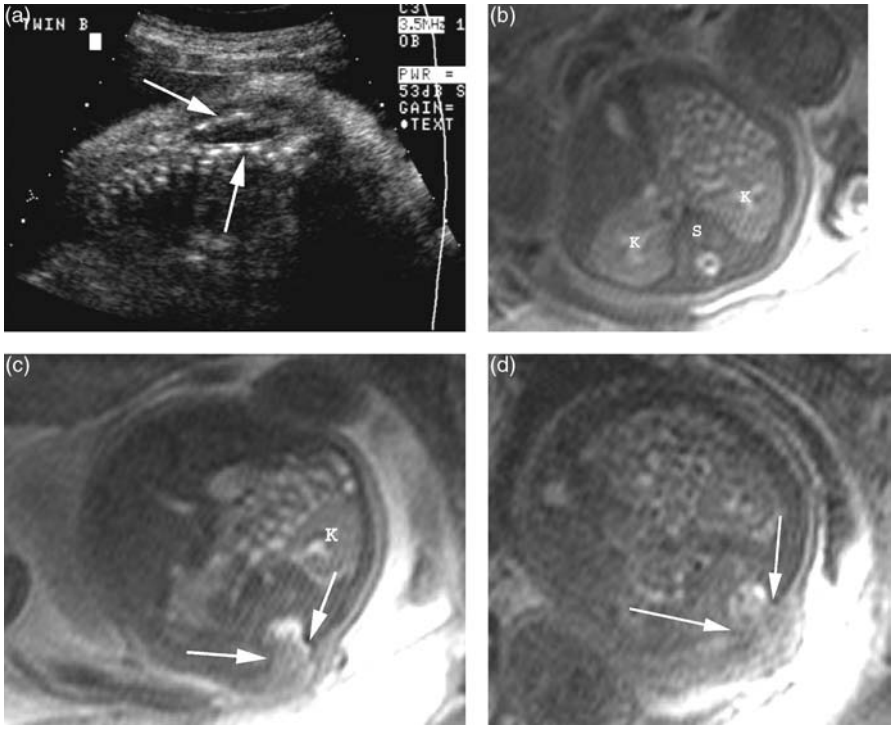

Figure 7.32 Lipomyelomeningocele at 31 weeks gestational age. (a) Coronal sonogram demonstrates widening of the thecal sac (arrows), consistent with a neural tube defect. Axial T_2-weighted images (b–d) show normal spine (S) at the level of the mid-kidneys (K) with opening of the posterior elements just below this region (arrows). There is a large amount of soft tissues with signal intensity similar to subcutaneous fat, consistent with a lipomyelomeningocele. This type of information is important prenatally if fetal surgery is being considered, as lipomyelomeningocele is a contraindication to repair *in utero*. [(c and d) from Levine et al. (47)]

fluid on the other side, due to volume averaging. The cranial findings associated with neural tube defects including the Arnold Chiari malformation (Chiari II) with effacement of the cisterna magna, abnormal configuration of the frontal bones, and ventriculomegaly with angular configuration of the frontal horns are discussed in Chapter 4. When the spinal defect is small and low, the brain findings may be the initial clue to search for the subtle neural tube defect (Fig. 7.30). Other associated findings include clubfeet and hydronephrosis with a neurogenic bladder, the latter being a late finding.

Sacral Dysgenesis

Sacral dysgenesis may be associated with caudal regression syndrome (Fig. 7.33), sirenomelia (vascular steal phenomenon), cloacal exstrophy, or other rare syndromes. Caudal regression syndrome, also known as caudal dysplasia sequence, is characterized by a series of congenital abnormalities including complete or partial agenesis of the sacrum and lumbar vertebrae associated with pelvic deformity. Femoral hypoplasia, clubfeet, and flexion contractures of the lower extremities are also commonly seen. In addition, caudal regression syndrome is often associated with anomalies of the gastrointestinal tract, genitourinary tract, and heart, as well as with neural tube defects. The majority of cases of caudal regression syndrome are sporadic, although it occurs in up to 1% of pregnancies in diabetic women. Up to 14% of cases are associated with diabetes mellitus (25).

Sirenomelia is thought to result from a vascular steal phenomenon that causes severe ischemia of the caudal aspect of the fetus (26). Skeletal abnormalities seen in sirenomelia include sacral agenesis, lumbar agenesis, and dysgenesis of the distal spine. The lower extremities are fused into a single limb or appear as fixed side-by-side

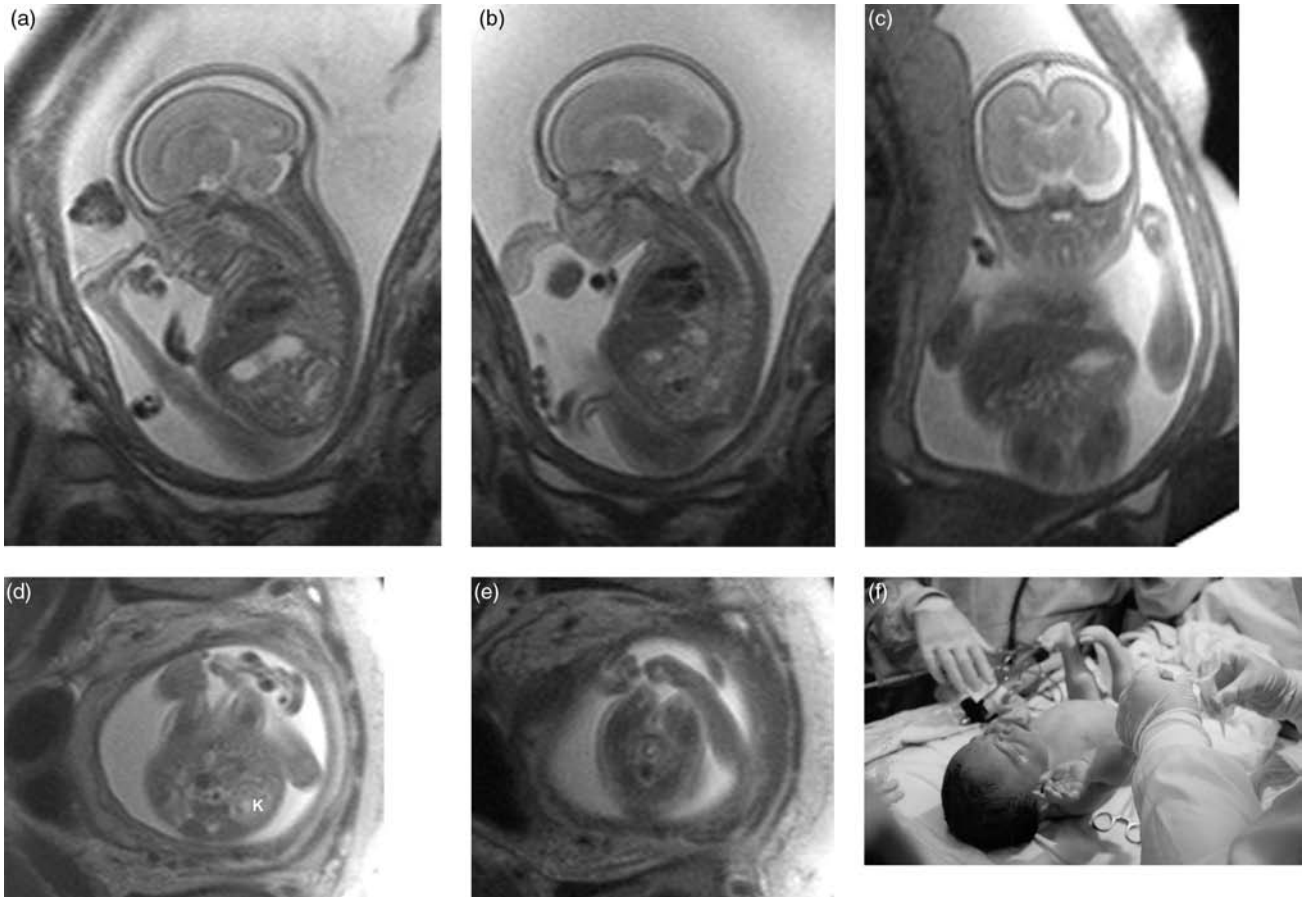

Figure 7.33 Caudal regression syndrome at 23 weeks gestational age. Sagittal (a and b) and coronal (c) T_2-weighted images show the foreshortening of the torso with extended lower extremities with atrophic musculature. Axial T_2-weighted images (d and e) show the presence of a vertebral body at the level of the kidney (K); however, the more caudal image (e) shows no normal bony anatomy and paucity of the soft tissues of the pelvis. (f) Postnatal photograph. [(a) from Stroustrup Smith et al. (27)]

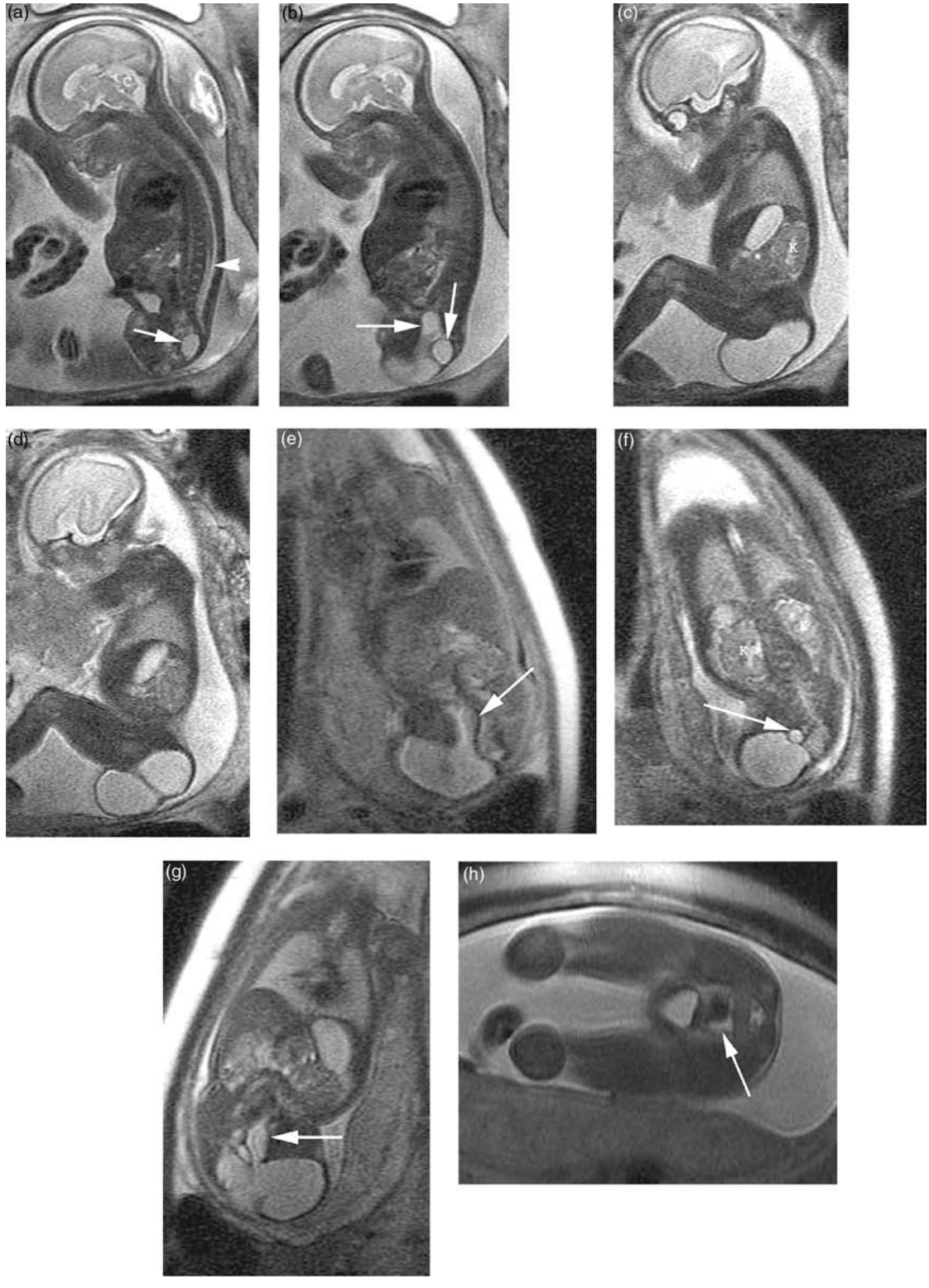

Figure 7.34 Sacrococcygeal teratoma at 32 weeks gestational age. Sagittal (a–d), coronal (e–g), and axial (h) T_2-weighted images show a complex cystic mass off the sacrum. The intrapelvic extent (arrow) is well visualized. This can be differentiated from a neural tube defect by the normal appearance of the cerebellum and cisterna magna as well as the normal ending of the conus (arrowhead) at the level of the kidneys (K). Neural tube defects do not typically have both intra and extrapelvic extent. (Images courtesy of J. Kazan, Sao Paolo, Brazil.)

dysgenic legs. Often, there are fewer leg bones than normal. Sirenomelia is most often fatal due to renal agenesis or severe dysgenesis and accompanying anhydramnios and pulmonary hypoplasia. Magnetic resonance imaging is helpful in demonstrating the normal intracranial anatomy with these conditions (27) and in demonstrating the visceral involvement, especially in cases of sirenomelia where oligohydramnios is present.

Sacrococcygeal Teratoma

Sacrococcygeal teratoma is a germ-cell tumor arising in the presacral area. It is the most common tumor of neonates (28). The tumor is typically extrapelvic, but there may be intrapelvic extension (Fig. 7.34). It is classified according to the degree of extension into the pelvis and abdomen. They may be mature tumors or immature tumors with a risk of malignant degeneration. They may be cystic and/or solid and frequently are highly vascular. At times, the large tumor size, associated hemorrhagic changes, intrapelvic or intraspinal extent, or shadowing from adjacent pelvic bones can make precise diagnosis and description of the tumor difficult (29–32). Sonographic and MR measurements of the tumor have been shown to be similar (29). Magnetic resonance imaging allows for better evaluation of the intrapelvic

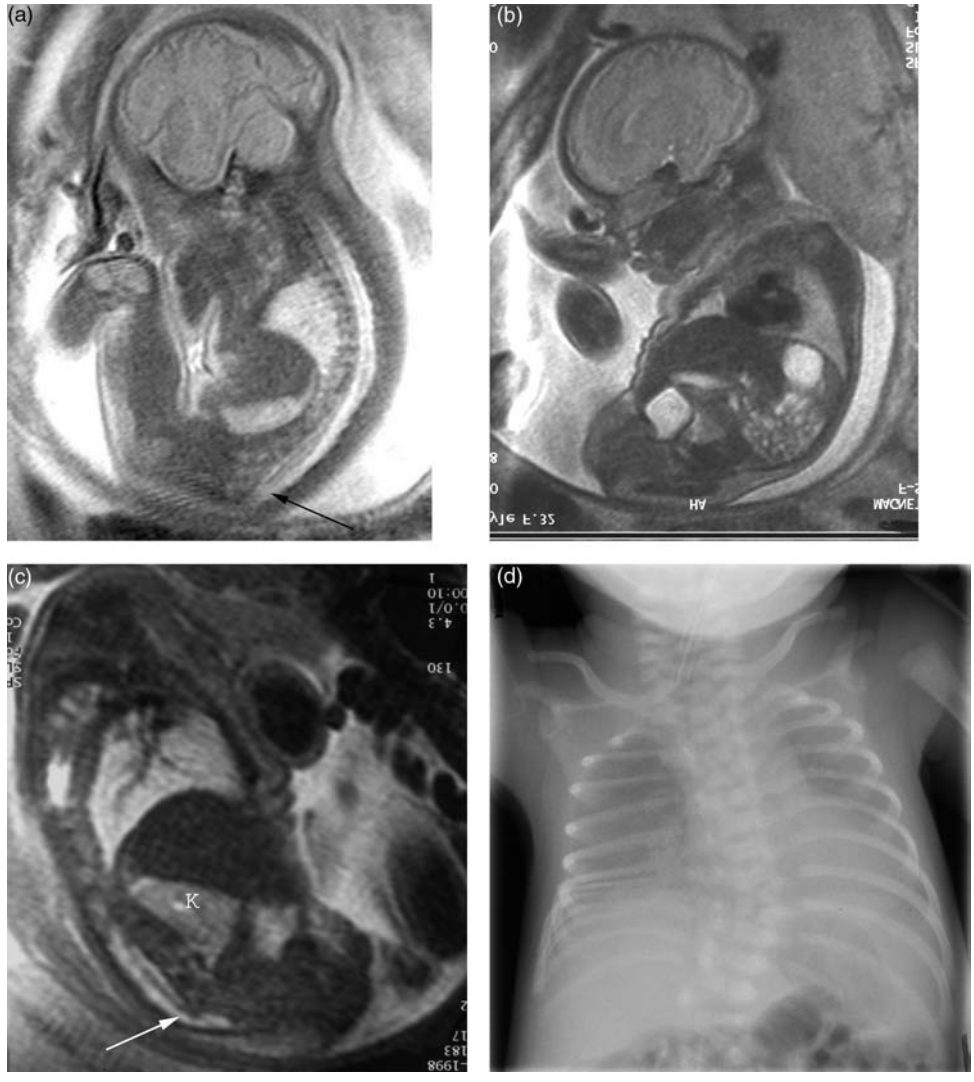

Figure 7.35 Thoracic scoliosis and tethered cord at 34 weeks gestational age. (a and b) T_2-weighted images from the same series show the abdomen in sagittal and coronal planes, due to scoliosis. (c) Sagittal image of the lower abdomen. Note the low position of the spinal cord (arrow) that terminates well below the level of the kidney (K). (d) Postnatal radiograph demonstrates the vertebral abnormality and scoliosis. [(a) From Levine et al. (47)]

extension than does ultrasound (29,33–35). In addition, MR imaging can illustrate intraspinal extent, which may be occult by sonography (29). This information is important, as it will affect the postnatal surgical approach to the lesion (29). Fetal MR imaging has been shown to be useful for planning postpartum surgery (29,33,36,37) and for decision-making regarding the timing and mode of delivery (29).

Scoliosis, Spinal Stenosis, and Tethered Cord

Scoliosis is an abnormal lateral curvature of the spine. Kyphosis is an abnormal curvature of the spine in the anteroposterior direction and may occur in conjunction with scoliosis. Abnormal curvature of the spine is caused by structural anomalies of the vertebral bodies (Fig. 7.35). In the fetus, it is most commonly seen in association with neural tube defects (38). Mild spinal curvature may be an isolated finding (39,40). Other etiologies include vertebral anomalies, arthrogryposis, skeletal dysplasias, and amniotic band syndrome (Fig. 7.36) (41,42). Scoliosis is diagnosed on MR imaging when the normal gentle curvature of the spine is persistently disrupted. Careful observation of consecutive images will illustrate change in body orientation [e.g., fetal torso changing from sagittal to coronal plane on a single sequence without significant fetal motion (Fig. 7.35)]. The diagnosis should be made with caution when there is limited amniotic fluid.

A tethered cord can occur in association with neural tube defect, spinal lipoma, scoliosis (Fig. 7.35) spinal stenosis, or other syndromes such as cloacal exstrophy (Fig. 7.37) (43). The diagnosis is suggested when the cord is seen below the level of the mid-kidneys. Diagnosis

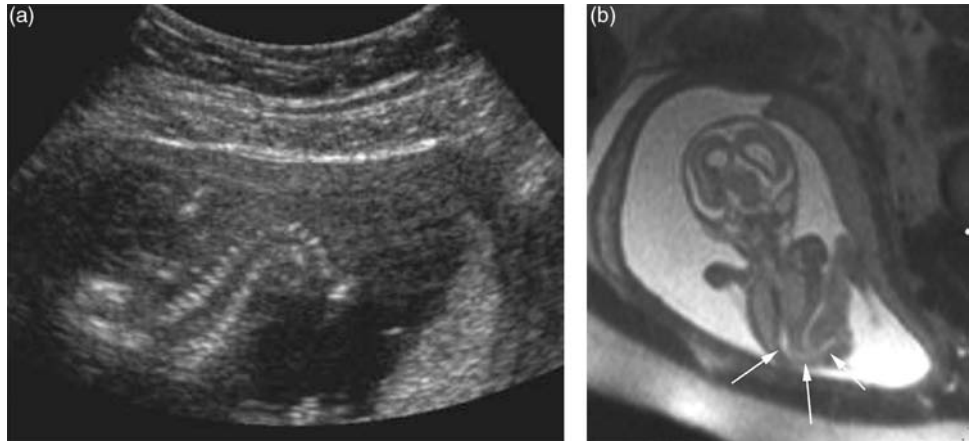

Figure 7.36 Severe scoliosis secondary to amniotic band syndrome at 17 weeks gestational age. Sonogram (a) and coronal T_2-weighted image (b) show marked spinal curvature. In (b), the scoliosis is best appreciated from the deviation of the thecal sac (arrows), which is filled with high signal intensity cerebrospinal fluid. This is the same fetus as in Fig. 6.39. [From Levine et al. (47)]

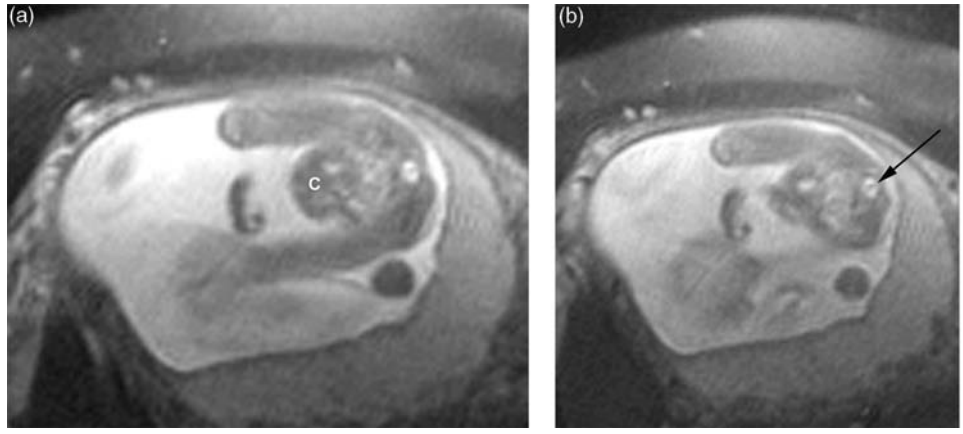

Figure 7.37 Cloacal malformation and tethered cord at 20 weeks gestational age. Axial images show anterior abdominal wall defect low in the pelvis, consistent with cloacal malformation (c). The spinal cord (arrow) extends into the pelvis. This abnormally low position is consistent with a tethered cord, an expected finding in association with cloacal malformation.

of tethered cord is important, as delayed morbidities of weakness, incontinence, and pain can be avoided by early surgery (44–46).

REFERENCES

1. Mahony BS, Filly RA. High-resolution sonographic assessment of the fetal extremities. J Ultrasound Med 1984; 3:489–498.
2. Filly RA, Golbus MS. Ultrasonography of the normal and pathologic fetal skeleton. Radiol Clin North Am 1982; 20:311–323.
3. Levine D, Barnes PD, Sher S et al. Fetal fast MR imaging: reproducibility, technical quality, and conspicuity of anatomy. Radiology 1998; 206:549–554.
4. Levine D, Smith AS, McKenzie C. Tips and tricks of fetal MR imaging. Radiol Clin North Am 2003; 41:729–745.
5. Levine D, Barnes PD, Madsen JR et al. Fetal CNS anomalies revealed on ultrafast MR imaging. Am J Roentgenol 1999; 172:813–818.
6. Swanson AB, Swanson GD, Tada K. A classification for congenital limb malformation. J Hand Surg (Am) 1983; 8:693–702.
7. Bagg HJ. Etiology of certain congenital structural defects. Obstet Gynecol 1924; 8:131.
8. Suzumura H, Kohno T, Nishimura G et al. Prenatal diagnosis of hypochondrogenesis using fetal MRI: a case report. Pediatr Radiol 2002; 32:373–375.
9. Orioli IM, Castilla EE, Barbosa-Neto JG. The birth prevalence rates for the skeletal dysplasias. J Med Genet 1986; 23:328–332.
10. Coakley FV, Lopoo JB, Lu Y et al. Normal and hypoplastic fetal lungs: volumetric assessment with prenatal single-shot rapid acquisition with relaxation enhancement MR imaging. Radiology 2000; 216:107–111.
11. Jeanty P, Romero R, d'Alton M et al. In utero sonographic detection of hand and foot deformities. J Ultrasound Med 1985; 4:595–601.
12. Benacerraf BR, Gelman R, Frigoletto FD Jr. Sonographically estimated fetal weights: accuracy and limitation. Am J Obstet Gynecol 1988; 159:1118–1121.
13. Wagenvoort AM, Bekker MN, Go AT et al. Ultrafast scan magnetic resonance in prenatal diagnosis. Fetal Diagn Ther 2000; 15:364–372.
14. Martin WL, Ismail KM, Brace V et al. Klippel–Trenaunay–Weber (KTW) syndrome: the use of in utero magnetic resonance imaging (MRI) in a prospective diagnosis. Prenat Diagn 2001; 21:311–313.
15. Guthkelch AN. Diastematomyelia with median septum. Brain 1974; 97:729–742.
16. Levine D. Ultrasound versus magnetic resonance imaging in fetal evaluation. Top Magn Reson Imaging 2001; 12:25–38.
17. Gulrajani M, David K, Sy W et al. Prenatal diagnosis of a neurenteric cyst by magnetic resonance imaging. Am J Perinatol 1993; 10:304–306.
18. Levine D, Barnes PD, Madsen JR et al. Central nervous system abnormalities assessed with prenatal magnetic resonance imaging. Obstet Gynecol 1999; 94:1011–1019.
19. Aaronson OS, Hernanz-Schulman M, Bruner JP et al. Myelomeningocele: prenatal evaluation—comparison between transabdominal US and MR imaging. Radiology 2003; 227:839–843.
20. Oya N, Suzuki Y, Tanemura M et al. Detection of skin over cysts with Spina bifida may be useful not only for preventing neurological damage during labor but also for predicting fetal prognosis. Fetal Diagn Ther 2000; 15:156–159.
21. Nakahara T, Uozumi T, Monden S et al. Prenatal diagnosis of open spina bifida by MRI and ultrasonography. Brain Dev 1993; 15:75–78.
22. Seeds JW, Jones FD. Lipomyelomeningocele: prenatal diagnosis and management. Obstet Gynecol 1986; 67:34S–37S.
23. Kim SY, McGahan JP, Boggan JE et al. Prenatal diagnosis of lipomyelomeningocele. J Ultrasound Med 2000; 19:801–805.
24. Mangels KJ, Tulipan N, Tsao LY et al. Fetal MRI in the evaluation of intrauterine myelomeningocele. Pediatr Neurosurg 2000; 32:124–131.
25. Buyse ML. Birth Defects Encyclopedia. Cambridge, MA: Blackwell Science, 1990.
26. Twickler D, Budorick N, Pretorius D et al. Caudal regression versus sirenomelia: sonographic clues. J Ultrasound Med 1993; 12:323–330.
27. Stroustrup Smith A, Grable I, Levine D. Case 66: caudal regression syndrome in the fetus of a diabetic mother. Radiology 2004; 230:229–233.
28. Gross RW, Clatworthy HW Jr, Meeker IA Jr. Sacrococcygeal teratomas in infants and children; a report of 40 cases. Surg Gynecol Obstet 1951; 92:341–354.
29. Avni FE, Guibaud L, Robert Y et al. MR imaging of fetal sacrococcygeal teratoma: diagnosis and assessment. Am J Roentgenol 2002; 178:179–183.
30. Holterman AX, Filiatrault D, Lallier M et al. The natural history of sacrococcygeal teratomas diagnosed through routine obstetric sonogram: a single institution experience. J Pediatr Surg 1998; 33:899–903.
31. Chuileannain FN, Woodrow N, de Crespigny L. Prenatal diagnosis and management of sacrococcygeal teratoma. Aust NZ J Obstet Gynaecol 1999; 39:497–501.
32. Westerburg B, Feldstein VA, Sandberg PL et al. Sonographic prognostic factors in fetuses with sacrococcygeal teratoma. J Pediatr Surg 2000; 35:322–325 (discussion 325–326).
33. Kirkinen P, Partanen K, Merikanto J et al. Ultrasonic and magnetic resonance imaging of fetal sacrococcygeal teratoma. Acta Obstet Gynecol Scand 1997; 76:917–922.
34. Okamura M, Kurauchi O, Itakura A et al. Fetal sacrococcygeal teratoma visualized by ultra-fast T2 weighted magnetic resonance imaging. Int J Gynaecol Obstet 1999; 65:191–193.
35. Hata K, Hata T, Kitao M. Antenatal diagnosis of sacrococcygeal teratoma facilitated by combined use of Doppler sonography and MR imaging. Am J Roentgenol 1991; 156:1115–1116.

36. Shinmoto H, Kashima K, Yuasa Y et al. MR imaging of non-CNS fetal abnormalities: a pictorial essay. Radiographics 2000; 20:1227–1243.
37. Quinn TM, Hubbard AM, Adzick NS. Prenatal magnetic resonance imaging enhances fetal diagnosis. J Pediatr Surg 1998; 33:553–558.
38. Harrison LA, Pretorius DH, Budorick NE. Abnormal spinal curvature in the fetus. J Ultrasound Med 1992; 11:473–479.
39. Benacerraf BR, Greene MF, Barss VA. Prenatal sonographic diagnosis of congenital hemivertebra. J Ultrasound Med 1986; 5:257–259.
40. Abrams SL, Filly RA. Congenital vertebral malformations: prenatal diagnosis using ultrasonography. Radiology 1985; 155:762.
41. Higginbottom MC, Jones KL, Hall BD et al. The amniotic band disruption complex: timing of amniotic rupture and variable spectra of consequent defects. J Pediatr 1979; 95:544–549.
42. Torpin R. Amniochorionic mesoblastic fibrous strings and amnionic bands: associated constricting fetal malformations or fetal death. Am J Obstet Gynecol 1965; 91:65–75.
43. Warf BC, Scott RM, Barnes PD et al. Tethered spinal cord in patients with anorectal and urogenital malformations. Pediatr Neurosurg 1993; 19:25–30.
44. Bruce DA, Schut L. Spinal lipomas in infancy and childhood. Childs Brain 1979; 5:192–203.
45. Hoffman HJ, Taecholarn C, Hendrick EB et al. Management of lipomyelomeningoceles. Experience at the hospital for sick children, Toronto. J Neurosurg 1985; 62:1–8.
46. Kanev PM, Lemire RJ, Loeser JD et al. Management and long-term follow-up review of children with lipomyelomeningocele, 1952–1987. J Neurosurg 1990; 73:48–52.
47. Levine D, Stroustrup Smith A, Barbaras L et al. Compendium of Fetal MRI (image). Available online at Beth Israel Deaconess Medical Center Radiology department website, http://bidmc.harvard.edu/fetalatlas/, 2004.

8

MR Imaging of Multiple Gestations

DEBORAH LEVINE

INTRODUCTION

Fetal magnetic resonance (MR) imaging in multiple gestations is indicated, as in singleton gestations, when there is a fetus with an anomaly not fully characterized by ultrasound. However, there are also indications unique to multiple gestations where MR imaging can be useful. In this chapter, we will discuss twin pregnancies, but the concepts can be applied to higher order multiples as well. When performing MR examinations on twins it is particularly important to pay attention to the location of each gestation. Obtaining and viewing images with a slightly larger field of view than utilized when examining singletons can be helpful in ensuring that each individual fetus is appropriately evaluated.

TWIN MORBIDITY

Twins occur in ~1% of all pregnancies, although this rate is much higher in patients who have undergone hyperstimulation or *in vitro* fertilization. A major complication of twinning is preterm delivery, which occurs in 54% of twins (as opposed to 10% of singletons) (1). Since a short cervix is predictive of preterm delivery (2–4), attention should be paid to the cervix when visualized on MR examination. Even in diamniotic–dichorionic pregnancies, the risk of intrauterine growth restriction (IUGR, Fig. 8.1) and congenital malformations (Fig. 8.2) is higher than that of singletons. It should be recognized that even though monochorionic twins are usually genetically identical, when anomalies are present they may be discordant between the twins (Fig. 8.3).

When twins share a placenta, in addition to the previously mentioned complications, there is the risk of twin–twin transfusion syndrome (TTS). The later the division into twins occurs, the higher the likelihood of congenital anomalies, with monoamniotic twins having the highest anomaly rate. In addition to the above-mentioned morbidities, monoamniotic twins have a likelihood of cord entanglement.

AMNIONICITY AND CHORIONICITY

Dizygotic twins comprise about two-thirds of all twins. The incidence of dizygotic twinning is influenced by maternal age, race, parity, and use of hyperstimulation or *in vitro* fertilization. Monozygotic twins comprise about one-third of all twins. Two-thirds of monozygotic twins are diamniotic monochorionic. About 1% of twins are monoamniotic (and thus, monochorionic).

The determination of chorionicity and amnionicity is typically performed by ultrasound. Two separate placental masses (Fig. 8.4), differing fetal gender, and a thick dividing membrane indicate a dichorionic gestation (5–8). Frequently, dichorionic twin placentas are adjacent to each other in the uterus and appear as a single placental mass (Fig. 8.5). Although termed a "fused placenta," they do not share vasculature. In these cases, the twin peak sign (indicating that the chorion has grown in between the membranes) aids in diagnosis of dichorionic twins (Fig. 8.6) (9). Each of these signs can be assessed with

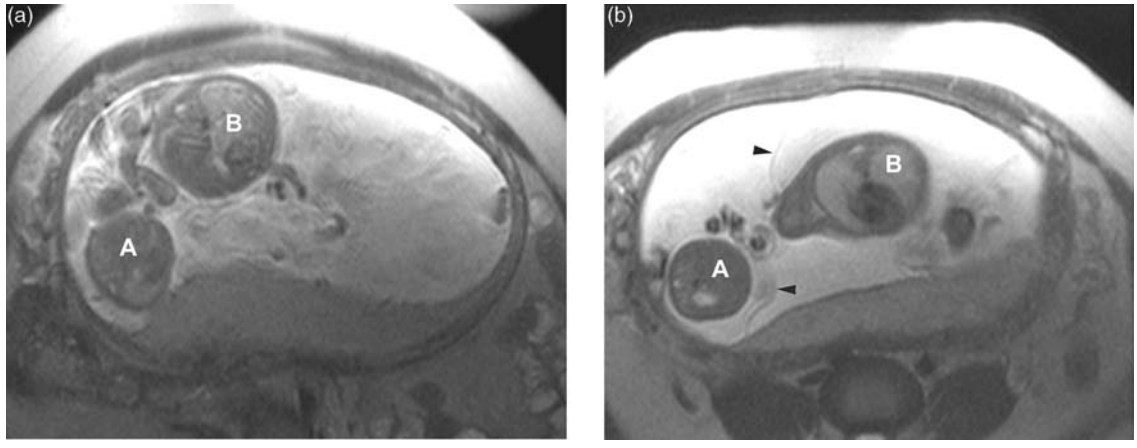

Figure 8.1 Discordant growth of diamniotic dichorionic twins at 23 weeks gestational age. Axial T_2-weighted images of the uterus show twin A being smaller than twin B. Note that although the membrane appears relatively thin (arrows), sonograms earlier in gestation (not shown) had proved these to be dichorionic twins. Note also the relatively large amount of amniotic fluid around twin B indicating mild polyhydramnios.

MR imaging (10). In a review of 20 MR examinations of twins performed between 19 and 32 weeks, in all but one case the inter-twin membrane was visible (10). The one case where it was not identified was a case of twin–twin transfusion with severe oligohydramnios in one sac and polyhydramnios in the other sac; the membrane had not been identified on ultrasound either. As with ultrasound, evaluation of membrane thickness later in gestation is limited by fetal size and progressive thinning of the inter-twin membrane (10). The thin membrane of diamniotic monochorionic twins is frequently difficult to visualize (Fig. 8.7).

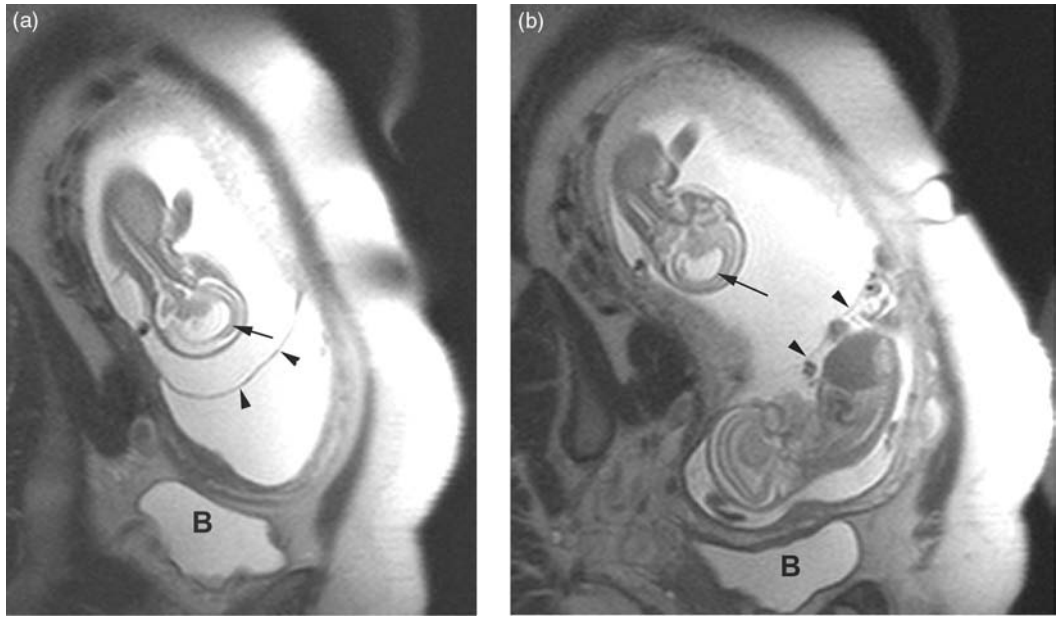

Figure 8.2 Discordant anomalies: diamniotic dichorionic twins at 17 weeks gestational age, one with holoprosencephaly. Sagittal T_2-weighted images of the uterus show twin B with a monoventricle (arrow). Note the thick dividing membrane (arrowheads). B, maternal bladder.

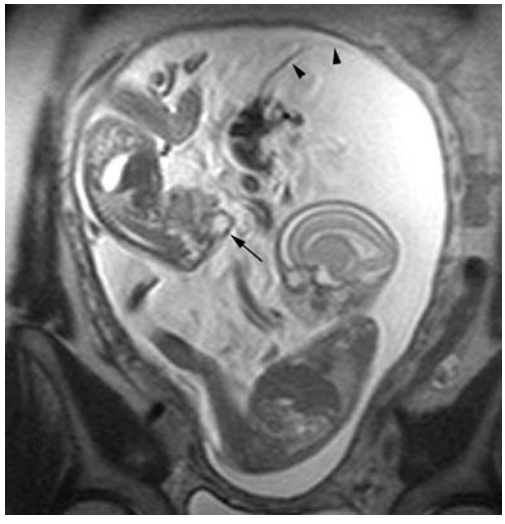

Figure 8.3 Discordant anomaly: diamniotic monochorionic twins at 20 weeks gestational age with one twin with anencephaly. Coronal T_2-weighted image of uterus shows twin B with lack of brain tissue above the orbit (arrow) consistent with anencephaly. Note twin membrane (arrowheads). [From Levine et al. (50)]

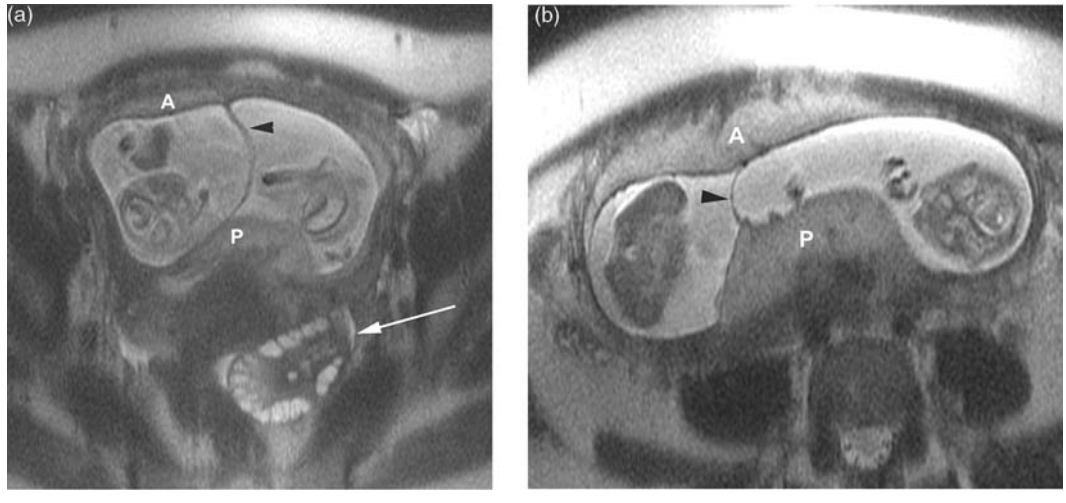

Figure 8.4 Diamniotic dichorionic twins. Axial T_2-weighted images of the pelvis at 14 weeks gestational age (a) and 18 weeks gestational age (b) in two different patients with diamniotic dichorionic twins. Note the anterior placenta (A), posterior placenta (P), and thick dividing membrane (arrowhead). The ovary (in a, arrow) is enlarged due to prior hyperstimulation.

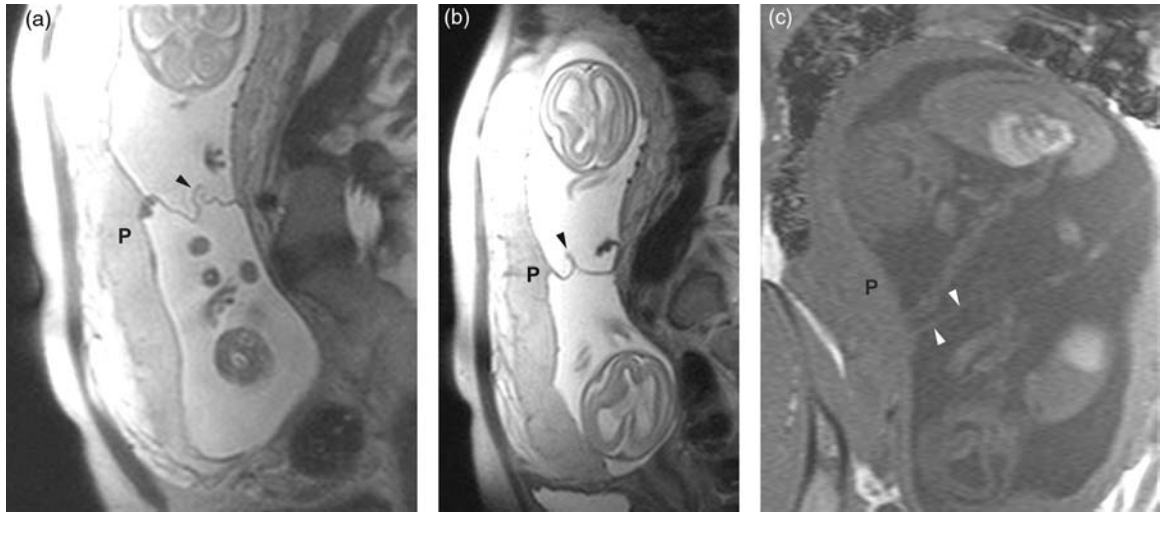

Figure 8.5 "Fused placenta" in diamniotic dichorionic twins at 18 weeks gestational age. Sagittal T_2-weighted images of the uterus (a, b) show an anterior placenta (P) and a thick dividing membrane (arrowheads). Although only a single placental mass is visualized, the thickness of the membrane indicates dichorionic twins. The folding of the membrane in this case is a normal finding. Oblique T_1-weighted image (c) of the uterus shows the soft tissue signal intensity of the membrane.

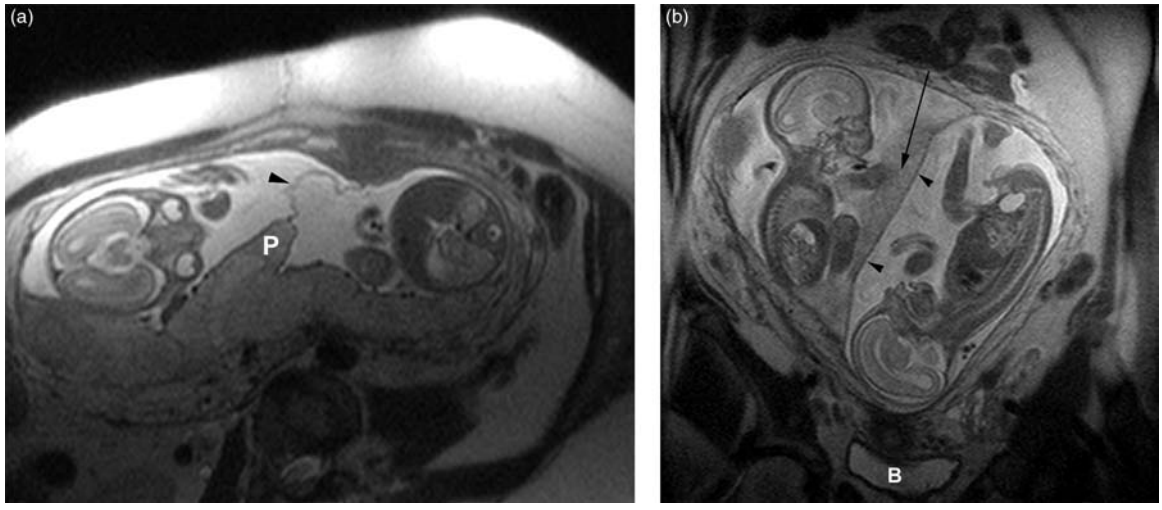

Figure 8.6 Twin peak sign of dichorionic twins at 21 weeks gestational age. Axial (a) and coronal (b) T_2-weighted images of the uterus show the twin peak sign (P). Note the thick dividing membrane (arrowheads). Motion of twin B has caused local decrease in signal intensity (arrow) of the amniotic fluid adjacent to the membrane. B, maternal bladder.

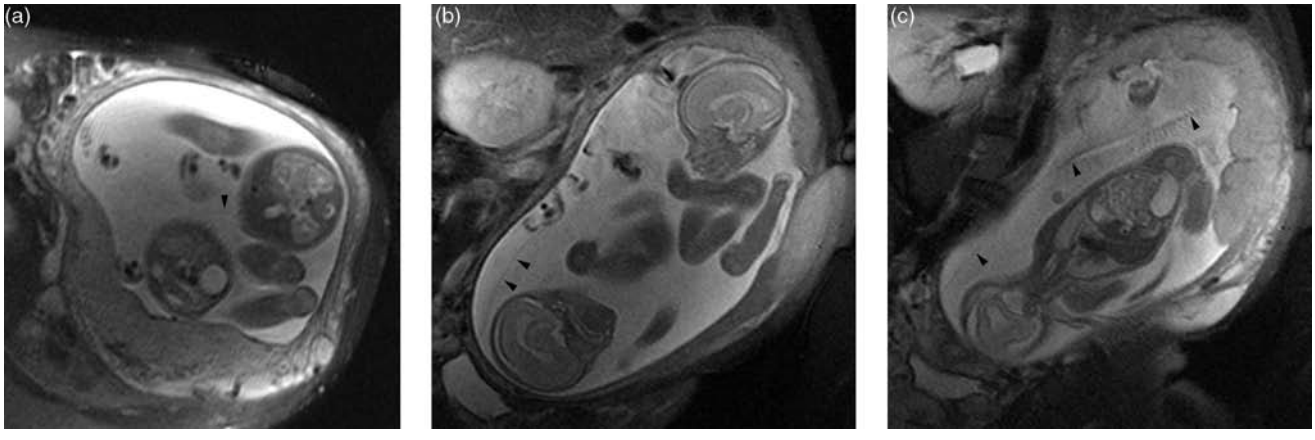

Figure 8.7 Diamniotic monochorionic twins at 24 weeks gestational age. Axial (a) and sagittal (b, c) T_2-weighted image of the uterus. The thin membrane (arrowheads) is poorly visualized in (a), is partially visualized in (b), and seen across the uterus in (c).

TWIN DEMISE

It is common for the demise of a co-twin to occur early in pregnancy. It has been reported that in 21% of first trimester twins verified to be alive with sonography, one of the twins disappeared subsequently (11). If this occurs early in the first trimester, there are generally no consequences to this demise, even in monochorionic twins (12). On MR imaging (as on sonography) an empty sac or a small fetal pole may be identified (Fig. 8.8). Later in gestation, in monochorionic twins, if one dies there is the risk of the so-called "twin embolization" syndrome.

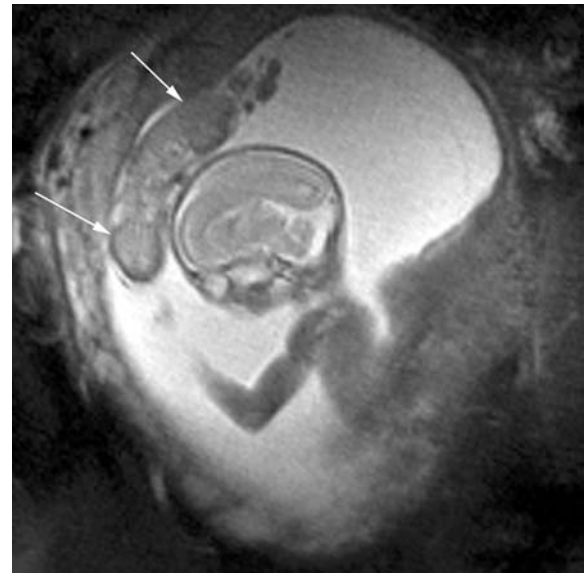

Figure 8.8 Coronal T_2-weighted image of the uterus of a 21-week gestational age fetus status following demise of a diamniotic monochorionic co-twin ~7 weeks earlier. The small demised fetal pole (arrows) is visualized against the uterine wall.

GROWTH DISCORDANCE

Growth discordance can occur in all types of twins. This is diagnosed sonographically when there is a difference in estimated fetal weight (EFW) of >20% (sensitivity 93%, PPV 72%), or an abdominal circumference difference of 20 mm (sensitivity 83%, PPV 83%).

In a retrospective review of 297,155 twins, the smaller twin was at increased risk of stillbirth and malformation-related neonatal death when discordance was ≥10%, and both twins were at risk when discordance was ≥20% (13). Small for gestational age discordant twins are at the highest risk (13). While MR imaging is not yet accepted as a modality to assess fetal weight, gross differences in fetal size can be evident on MR imaging (Fig. 8.1). Similarly, discordance in the amount of subcutaneous fat can be visualized at later stages of pregnancy.

STUCK TWIN

When there is severe oligohydramnios in one twin sac and the co-twin has normal or increased fluid, there may be the appearance of a "stuck twin." While this is most commonly seen in monochorionic twins complicated by TTS (see subsequent sections), it can also occur when one twin (either monochorionic or dichorionic) has bilateral renal anomalies or any complication resulting in severe oligohydramnios. The twin with little or no fluid will be closely apposed to the uterine wall, and will remain in place despite changes in maternal position. The membrane between the twins may be difficult to visualize secondary to being closely adherent to the "stuck twin" (Fig. 8.9).

COMPLICATIONS OF DIAMNIOTIC MONOCHORIONIC TWINS

When twins are monochorionic the vast majority have vascular anastomoses at the placental level. These can be artery-to-artery, vein-to-vein, or artery-to-vein.

Twin–Twin Transfusion Syndrome

Twin–twin transfusion syndrome occurs when there are anastomoses between monochorionic twins that lead to unequal sharing of blood (14,15). These tend to be arterial-to-venous anastomoses (16). The normal configuration of placental surface vessels is for the artery and vein to be paired. When venous-to-venous anastomoses are present, the feeding arterial and the draining venous components are unpaired on the placental surface.

One twin becomes the donor twin (with anemia, IUGR, and oligohydramnios) and the other twin becomes the recipient twin (with polyhydramnios). This occurs in up to 20% of monochorionic twins.

The smaller twin may be growth restricted and develop oligohydramnios, but these findings alone are not sufficient for the diagnosis of TTS. The combination of oligohydramnios in one twin and polyhydramnios in the other twin is more specific for the condition. When oligohydramnios is severe, there can be the appearance of a "stuck twin (Fig. 8.10) (17)." In a 1998 study of 31 cases of TTS, 11 sets of twins had death of one twin *in utero*, and of the 11 surviving twins, 3 subsequently died, 2 were severely handicapped, and 2 had transient changes on head ultrasound after birth (18).

Even without *in utero* demise of a co-twin, monochorionic twins are at risk for cerebral white matter necrosis and associated cerebral palsy. In a study of preterm twins with head sonograms in the first three days of life, white matter necrosis was seen in 12 of 14 (86%) monochorionic infants and in 2 of 61 (3.3%) dichorionic infants (19). Comparing neonates with and without these findings, the authors found that white matter necrosis was associated with monochorionic twins, polyhydramnios, hydrops, placental vascular connections, and intrauterine fetal death of the co-twin (19). Lesions occurred in sets of twins in which both survived, as well in twins where one died *in utero*. Since cavitary lesions appear two or more weeks after the initial insult and brain atrophy develops weeks later (19,20), the etiology of these changes is an intrauterine event. The hypothesis for this finding is that the vascular connections in the placenta of monochorionic pairs allow for ischemia to occur (19,21).

Treatment options for TTS include early delivery (if the syndrome develops late in gestation), serial amniocentesis, amniotomy, and laser ablation of the communicating placental vessels (17,22–31). Endoscopic guided laser ablation procedures are becoming increasingly popular since recent published reports suggest improved survival with lower morbidity after the procedure (27–31). Fetal MR imaging in this situation can be utilized to detect parenchymal brain disease before and/or after intervention. It is also possible that MR mapping of the placental vasculature will aid in treatment planning (Fig. 8.11).

Twin "Embolization" Syndrome

When one of a monochorionic pair dies *in utero*, there is often a sudden change in placental vascular territory perfused by the live twin. The resulting hypotension and anemia can lead to microcephaly, multicystic encephalomalacia, ventriculomegaly, hydranencephaly, limb amputation, intestinal atresia, and aplasia cutis (18,19,32,33). These sequelae were previously felt to be due to microemboli (34–36), but most current theories suggest hypovolemia as the etiology (37–39). Fetal MR imaging can help assess for the presence of brain injury resulting from

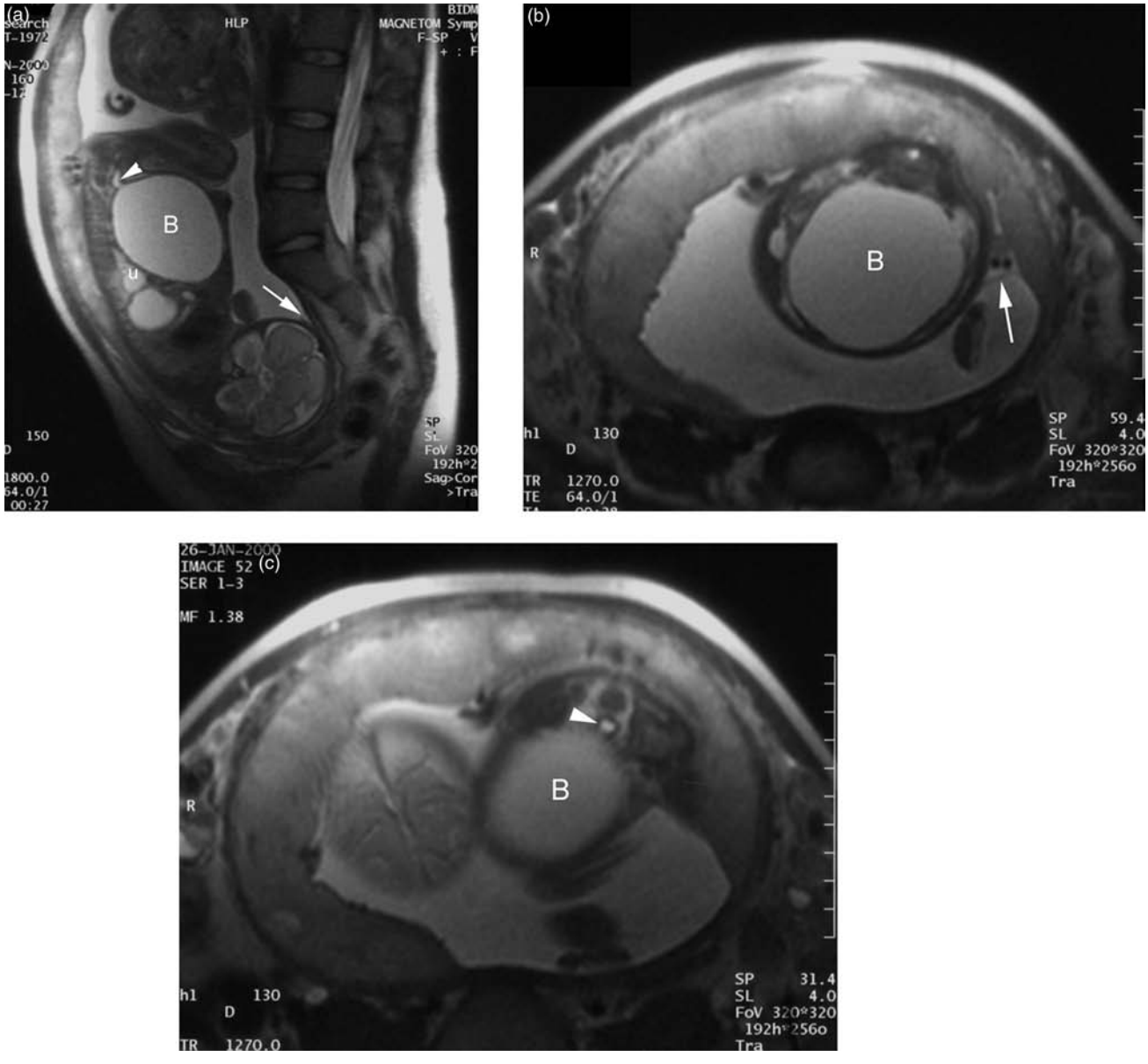

Figure 8.9 Stuck twin secondary to posterior urethral valves in diamniotic dichorionic twin gestation at 28 weeks gestational age. Sagittal (a) and axial (b, c) T_2-weighted images of the uterus with twin B in a "stuck" position with a closely adherent membrane (arrow). Note the enlarged fetal bladder (B), dilated collecting system, dilated ureter (u), and distended posterior urethra (arrowhead). The fluid seen around the twin is actually from the sac of the normal co-twin. Note that the images are displayed with respect to maternal, not fetal anatomy. In all the images, but best visualized on the transverse images, the presenting twin is stuck adjacent to the uterine wall, and in a position not conforming to gravity, whereas in fluid would be visualized around the fetus in a normal gestation.

twin embolization syndrome, which may be occult by ultrasound (Figs. 8.12 and 8.13, see also Fig. 3.71) (40).

However, as mentioned previously, cavitary white matter lesions and cerebral atrophy develop two or more weeks after the acute stage of necrosis in the remaining live twin (19). Therefore MR and ultrasound examinations will be negative until at least 2 weeks after the demise of a twin. The individual ischemic lesions also may be too small to be detected with current imaging methods. Use of prenatal imaging is unlikely to be able to prevent further damage after the acute event of a fetal death, because damage has already occurred by the time imaging findings are present. However, recognition of the severe brain damage seen in this case is important in order to appropriately counsel patients as to the poor prognosis for the fetus, and to plan for appropriate management of delivery (41).

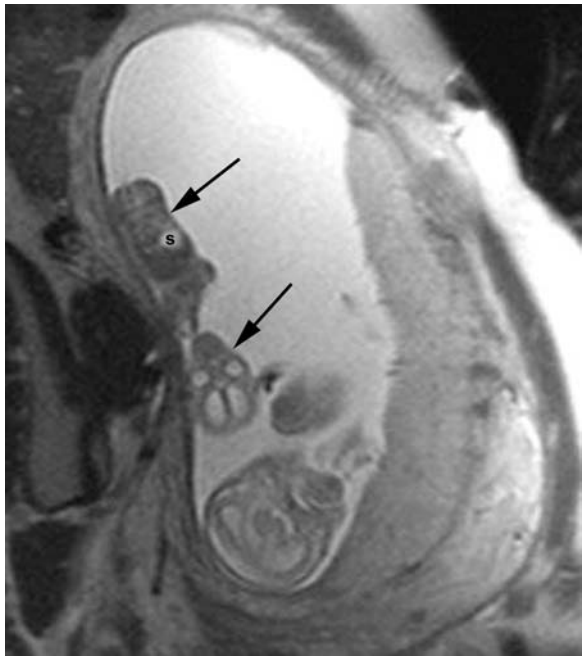

Figure 8.10 Twin–twin transfusion syndrome with "stuck twin." Sagittal T_2-weighted image of the uterus at 19 weeks gestational age in a diamniotic monochorionic twin gestation complicated by TTS. Note the smaller twin (arrows) closely apposed to the uterine wall. The stomach (s) is fluid-filled. The membrane between the twins is not visualized secondary to being closely apposed to the stuck twin.

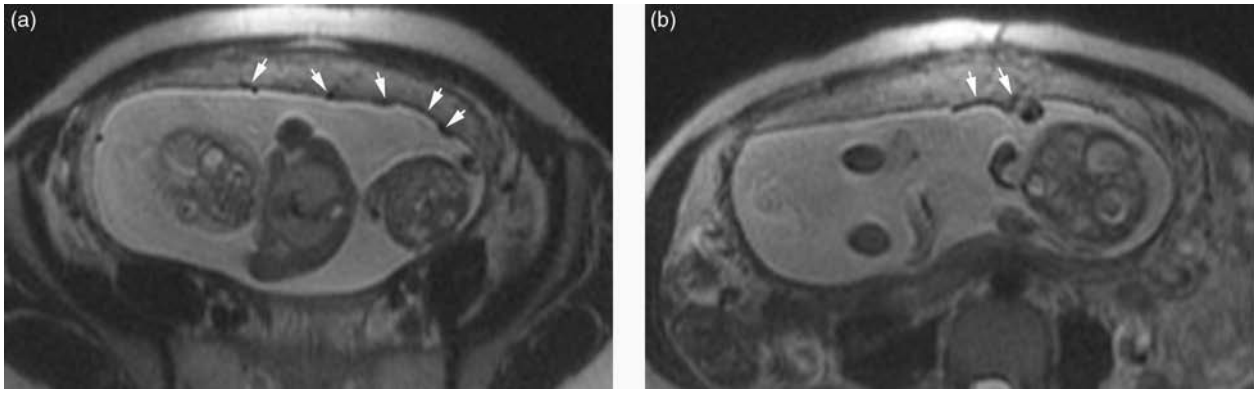

Figure 8.11 Vessel mapping in diamniotic monochorionic twins at 20 weeks gestational age. Axial T_2-weighted images of the uterus show signal voids (arrows) in the surface vessels of the placenta.

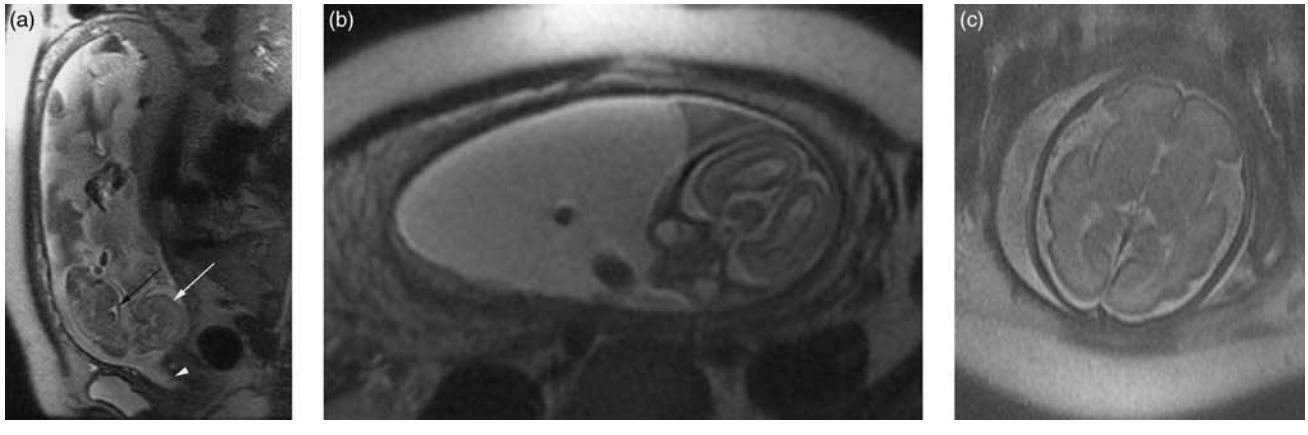

Figure 8.12 Screening for twin embolization syndrome. (a) Sagittal T_2-weighted image of the uterus at 21 weeks gestational age (2 weeks after demise of twin) shows the demised twin with poorly visualized intracranial anatomy (white arrow) and small pleural effusion (black arrow). Note the funneling of the cervix at the internal os (arrowhead). T_2-weighted images of the brain at 21 (b) and 30 (c) weeks gestational age show normal intracranial anatomy. The brain of the surviving twin was normal at birth, but the baby needed surgery for gastrointestinal atresias, presumable secondary to twin embolization syndrome.

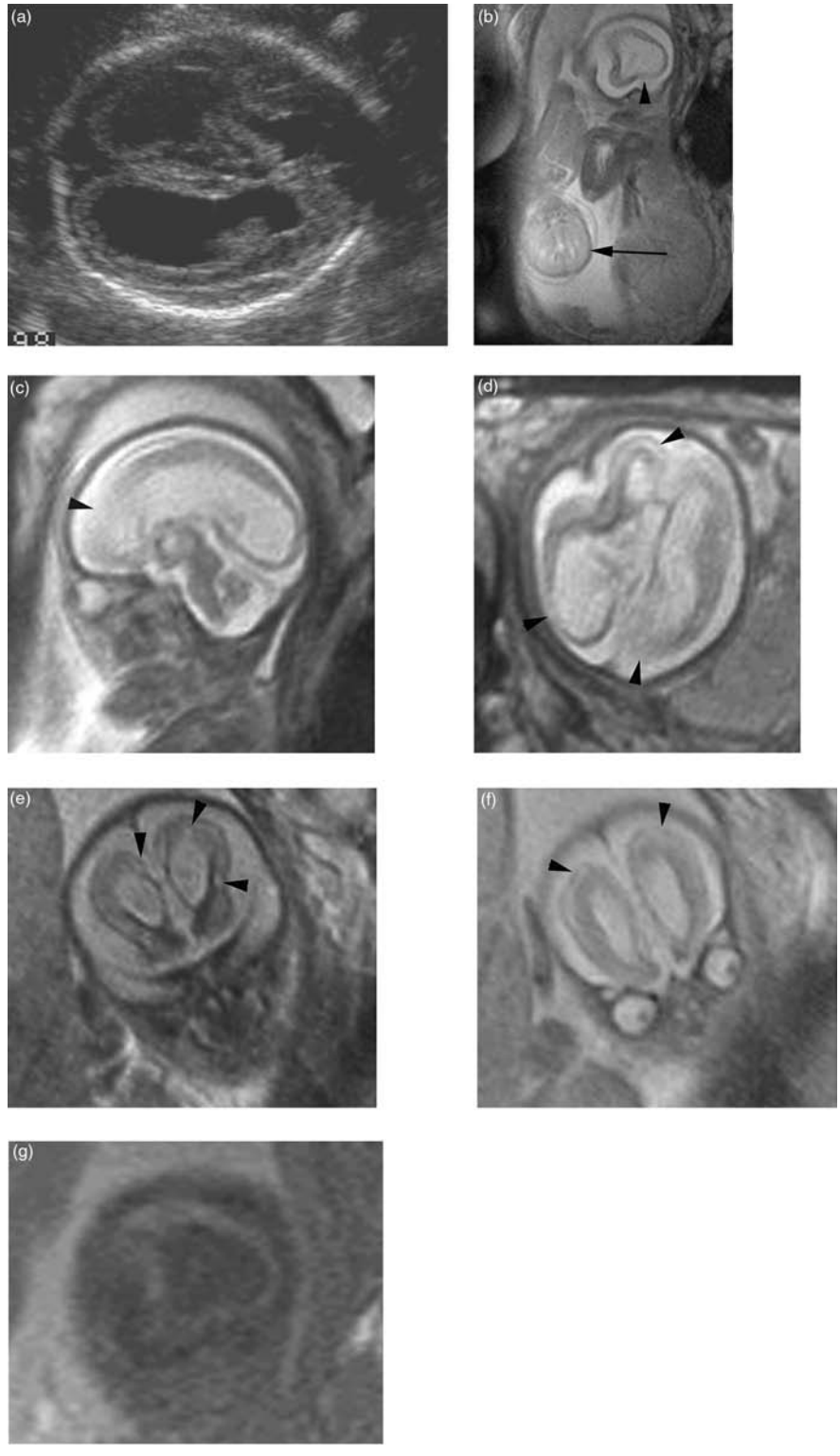

Figure 8.13 Encephalomalacia after demise of monochorionic co-twin. Transabdominal transverse sonogram (a) of the fetal head of the live twin shows enlarged ventricles. The slightly irregular margins of the ventricles suggest encephalomalacia. Coronal T_2-weighted image of the uterus (b) shows two fetal torsos. The smaller fetal body on the right of the image is the demised twin (arrow) with marked skin thickening around the head and pleural effusions. Sagittal (c), axial (d), and coronal (e, f) T_2-weighted images of the head of the live twin show ventriculomegaly with multiple regions of cortical atrophy (arrowheads). Sagittal T_1-weighted image (g) of the fetal head shows areas of increased signal in the parenchyma consistent with either hemorrhage or mineralization.

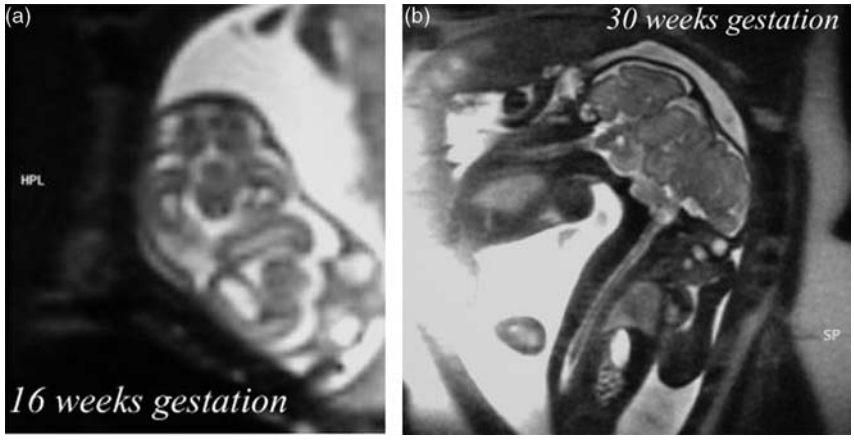

Figure 8.14 Conjoined twins. Two different sets of conjoined twins at 16 weeks (a) and 30 weeks (b) gestational age. The twins are joined at the head in each case. (Images courtesy of S. Sisnott, Melbourne, Australia.)

Acardiac Twin

Acardiac twins occur in 1% of monochorionic twins, with an overall incidence of 1 in 35,000 births (42). While umbilical arterial-to-arterial anastomoses allow the acardiac twin to grow *in utero*, there must be a venous–venous anastomosis to complete the circuit. In the acardiac twin, structures supplied by the distal abdominal aorta and iliac arteries are most well developed. The upper trunk and head are hypo-perfused, and therefore either do not develop or are small. Blood flows retrograde from the normal to the abnormal fetus (43). The diagnosis is made sonographically by the characteristic appearance of the acardiac twin, lack of visualization of a normally pumping heart, and reversed flow in the umbilical vessels supplying the acardiac twin, with the umbilical vein going away from the acardiac twin and the pulsatile arterial flow directed toward the acardiac twin. If untreated, there can be cardiac failure and death of the normal twin in 55% of cases (42). This mortality is due to the additional workload that increases in the third trimester when the size of the acardiac twin becomes larger. Current therapies include radiofrequency ablation of the abdominal vessels in the acardiac twin, or ligation or coagulation of the cord of the acardiac twin (44,45). Since the pump twin is already supplying all the placental circulation, there is no risk of twin embolization syndrome. The role of MR imaging, if any, in these cases has not been established.

COMPLICATIONS OF MONOAMNIOTIC TWINS

Monoamniotic twins can have all the complications of diamniotic monochorionic twins, including TTS. This syndrome will present as growth discordance between the twins, often with polyhydramnios of the shared sac.

For non-conjoined monoamniotic twins, cord entanglement commonly occurs and can lead to *in utero* demise. For this reason, monoamniotic twins are commonly electively delivered at 32 weeks (46).

Conjoined Twins

Conjoined twins occur in about 1 in 50,000 births. This type of twinning occurs when the split occurs after 13 days and before the third week after fertilization. The site and extent of fusion varies. Congenital anomalies are common, and frequently are separate from the region of union. The large field of view on prenatal MR imaging (Fig. 8.14, see also Fig. 10.12) allows for a better understanding of complex anatomy for patients and surgeons (47–49).

SUMMARY

In summary, MR imaging plays a limited role in the diagnosis of most multiple gestations. As with singletons, it can be used to assess anomalies. In cases of TTS, it can assess brain injury that has occurred prior to delivery, especially in cases of demise of a monochorionic co-twin. For conjoined twins, MR is very helpful in surgical planning and patient understanding of the anatomy involved.

REFERENCES

1. Gardner MO, Goldenberg RL, Cliver SP et al. The origin and outcome of preterm twin pregnancies. Obstet Gynecol 1995; 85:553–557.
2. Bergelin I, Valentin L. Cervical changes in twin pregnancies observed by transvaginal ultrasound during the latter half of pregnancy: a longitudinal, observational study. Ultrasound Obstet Gynecol 2003; 21:556–563.

3. Fuchs I, Tsoi E, Henrich W et al. Sonographic measurement of cervical length in twin pregnancies in threatened preterm labor. Ultrasound Obstet Gynecol 2004; 23:42–45.
4. Vayssiere C, Favre R, Audibert F et al. Cervical length and funneling at 22 and 27 weeks to predict spontaneous birth before 32 weeks in twin pregnancies: a French prospective multicenter study. Am J Obstet Gynecol 2002; 187:1596–1604.
5. Stenhouse E, Hardwick C, Maharaj S et al. Chorionicity determination in twin pregnancies: how accurate are we? Ultrasound Obstet Gynecol 2002; 19:350–352.
6. Kurtz AB, Wapner RJ, Mata J et al. Twin pregnancies: accuracy of first-trimester abdominal US in predicting chorionicity and amnionicity. Radiology 1992; 185:759–762.
7. Mahony BS, Filly RA, Callen PW. Amnionicity and chorionicity in twin pregnancies: prediction using ultrasound. Radiology 1985; 155:205–209.
8. Townsend RR, Simpson GF, Filly RA. Membrane thickness in ultrasound prediction of chorionicity of twin gestations. J Ultrasound Med 1988; 7:327–332.
9. Finberg HJ. The "twin peak" sign: reliable evidence of dichorionic twinning. J Ultrasound Med 1992; 11:571–577.
10. Trop I, Levine D. Normal fetal anatomy as visualized with fast magnetic resonance imaging. Top Magn Reson Imaging 2001; 12:3–17.
11. Landy HJ, Weiner S, Corson SL et al. The "vanishing twin": ultrasonographic assessment of fetal disappearance in the first trimester. Am J Obstet Gynecol 1986; 155:14–19.
12. Benson CB, Doubilet PM, David V. Prognosis of first-trimester twin pregnancies: polychotomous logistic regression analysis. Radiology 1994; 192:765–768.
13. Buekens P, Wilcox A. Why do small twins have a lower mortality rate than small singletons? Am J Obstet Gynecol 1993; 168:937–941.
14. Denbow ML, Cox P, Taylor M et al. Placental angioarchitecture in monochorionic twin pregnancies: relationship to fetal growth, fetofetal transfusion syndrome, and pregnancy outcome. Am J Obstet Gynecol 2000; 182:417–426.
15. Machin G, Still K, Lalani T. Correlations of placental vascular anatomy and clinical outcomes in 69 monochorionic twin pregnancies. Am J Med Genet 1996; 61:229–236.
16. Taylor MJ, Farquharson D, Cox PM et al. Identification of arterio-venous anastomoses *in vivo* in monochorionic twin pregnancies: preliminary report. Ultrasound Obstet Gynecol 2000; 16:218–222.
17. Elliott JP, Urig MA, Clewell WH. Aggressive therapeutic amniocentesis for treatment of twin-twin transfusion syndrome. Obstet Gynecol 1991; 77:537–540.
18. van Heteren CF, Nijhuis JG, Semmekrot BA et al. Risk for surviving twin after fetal death of co-twin in twin-twin transfusion syndrome. Obstet Gynecol 1998; 92:215–219.
19. Bejar R, Vigliocco G, Gramajo H et al. Antenatal origin of neurologic damage in newborn infants. II. Multiple gestations. Am J Obstet Gynecol 1990; 162:1230–1236.
20. Banker BQ, Larroche JC. Periventricular leukomalacia of infancy. A form of neonatal anoxic encephalopathy. Arch Neurol 1962; 7:386–410.
21. Hurst RW, Abbitt PL. Fetal intracranial hemorrhage and periventricular leukomalacia: complications of twin-twin transfusion. Am J Neuroradiol 1989; 10:S62–S63.
22. De Lia JE, Kuhlmann RS, Harstad TW et al. Fetoscopic laser ablation of placental vessels in severe previable twin-twin transfusion syndrome. Am J Obstet Gynecol 1995; 172:1202–1208.
23. Dennis LG, Winkler CL. Twin-to-twin transfusion syndrome: aggressive therapeutic amniocentesis. Am J Obstet Gynecol 1997; 177:342–347.
24. Mahony BS, Petty CN, Nyberg DA et al. The "stuck twin" phenomenon: ultrasonographic findings, pregnancy outcome, and management with serial amniocenteses. Am J Obstet Gynecol 1990; 163:1513–1522.
25. Saunders NJ, Snijders RJ, Nicolaides KH. Therapeutic amniocentesis in twin-twin transfusion syndrome appearing in the second trimester of pregnancy. Am J Obstet Gynecol 1992; 166:820–824.
26. Kilby MD, Howe DT, McHugo JM et al. Bladder visualization as a prognostic sign in oligohydramnios-polyhydramnios sequence in twin pregnancies treated using therapeutic amniocentesis. Br J Obstet Gynaecol 1997; 104:939–942.
27. Hecher K, Plath H, Bregenzer T et al. Endoscopic laser surgery versus serial amniocenteses in the treatment of severe twin-twin transfusion syndrome. Am J Obstet Gynecol 1999; 180:717–724.
28. Quintero RA, Bornick PW, Morales WJ et al. Selective photocoagulation of communicating vessels in the treatment of monochorionic twins with selective growth retardation. Am J Obstet Gynecol 2001; 185:689–696.
29. Quintero RA, Comas C, Bornick PW et al. Selective versus non-selective laser photocoagulation of placental vessels in twin-to-twin transfusion syndrome. Ultrasound Obstet Gynecol 2000; 16:230–236.
30. Quintero RA, Morales WJ, Mendoza G et al. Selective photocoagulation of placental vessels in twin-twin transfusion syndrome: evolution of a surgical technique. Obstet Gynecol Surv 1998; 53:S97–S103.
31. Senat MV, Deprest J, Boulvain M et al. Endoscopic laser surgery versus serial amnioreduction for severe twin-to-twin transfusion syndrome. N Engl J Med 2004; 351:136–144.
32. Anderson RL, Golbus MS, Curry CJ et al. Central nervous system damage and other anomalies in surviving fetus following second trimester antenatal death of co-twin. Report of four cases and literature review. Prenat Diagn 1990; 10:513–518.
33. Bernischke K. Twin placenta in prenatal mortality. NY State J Med 1961; 61:1499–1508.
34. Patten RM, Mack LA, Nyberg DA et al. Twin embolization syndrome: prenatal sonographic detection and significance. Radiology 1989; 173:685–689.
35. Szymonowicz W, Preston H, Yu VY. The surviving monozygotic twin. Arch Dis Child 1986; 61:454–458.
36. Larroche JC, Droulle P, Delezoide AL et al. Brain damage in monozygous twins. Biol Neonate 1990; 57:261–278.
37. Okamura K, Murotsuki J, Tanigawara S et al. Funipuncture for evaluation of hematologic and coagulation indices in the

surviving twin following co-twin's death. Obstet Gynecol 1994; 83:975–978.
38. Fusi L, McParland P, Fisk N et al. Acute twin-twin transfusion: a possible mechanism for brain-damaged survivors after intrauterine death of a monochorionic twin. Obstet Gynecol 1991; 78:517–520.
39. Nicolini U, Pisoni MP, Cela E et al. Fetal blood sampling immediately before and within 24 hours of death in monochorionic twin pregnancies complicated by single intrauterine death. Am J Obstet Gynecol 1998; 179:800–803.
40. Levine D, Barnes PD, Madsen JR et al. Central nervous system abnormalities assessed with prenatal magnetic resonance imaging. Obstet Gynecol 1999; 94:1011–1019.
41. Levine D. Case 46: encephalomalacia in surviving twin after death of monochorionic co-twin. Radiology 2002; 223:392–395.
42. Moore TR, Gale S, Benirschke K. Perinatal outcome of forty-nine pregnancies complicated by acardiac twinning. Am J Obstet Gynecol 1990; 163:907–912.
43. Benson CB, Bieber FR, Genest DR et al. Doppler demonstration of reversed umbilical blood flow in an acardiac twin. J Clin Ultrasound 1989; 17:291–295.
44. Rodeck C, Deans A, Jauniaux E. Thermocoagulation for the early treatment of pregnancy with an acardiac twin. N Engl J Med 1998; 339:1293–1295.
45. Tsao K, Feldstein VA, Albanese CT et al. Selective reduction of acardiac twin by radiofrequency ablation. Am J Obstet Gynecol 2002; 187:635–640.
46. Beasley E, Megerian G, Gerson A et al. Monoamniotic twins: case series and proposal for antenatal management. Obstet Gynecol 1999; 93:130–134.
47. Casele HL, Meyer JR. Ultrafast magnetic resonance imaging of cephalopagus conjoined twins. Obstet Gynecol 2000; 95:1015–1017.
48. Spielmann AL, Freed KS, Spritzer CE. MRI of conjoined twins illustrating advances in fetal imaging. J Comput Assist Tomogr 2001; 25:88–90.
49. Turner RJ, Hankins GD, Weinreb JC et al. Magnetic resonance imaging and ultrasonography in the antenatal evaluation of conjoined twins. Am J Obstet Gynecol 1986; 155:645–649.
50. Levine D, Stroustrup Smith A, Barbaras L et al. Compendium of Fetal MRI (image). Available from Beth Israel Deaconess Medical Center Radiology department website, http://bidmc.harvard.edu/fetalatlas/, 2004.

9

Current Techniques and Future Directions for Fetal MR Imaging

CHARLES A. MCKENZIE, DEBORAH LEVINE

INTRODUCTION

Imaging of the fetus is a particularly challenging application for magnetic resonance (MR) imaging as it requires both high spatial resolution and rapid image acquisition. High spatial resolution is necessary to adequately visualize the small anatomic structures of the fetus, whereas rapid image acquisition is needed to obtain images free of artifact induced by fetal and, to a lesser extent, maternal motion (1–10). Because of these two requirements, the signal-to-noise ratio (SNR) is a prime consideration in MR imaging of the fetus as the SNR is reduced as imaging resolution and/or imaging speed is increased. The need to freeze motion has limited most fetal MR imaging to two-dimensional imaging as true high-resolution volumetric imaging requires acquisition times too long to freeze motion. This chapter surveys the current techniques for fetal imaging, illustrates artifacts that can arise, and discusses the emerging strategies for mitigating some of the current limitations.

HARDWARE REQUIREMENTS

Because fetal imaging is challenging in terms of both imaging speed and SNR, high demands are placed on the hardware employed to acquire images. The first consideration is the strength of the imaging unit's main magnetic field. During MR imaging, SNR increases linearly as the strength of the main magnetic field is increased. As fetal MR imaging sequences are invariably SNR starved, imaging at the highest available field strength is very attractive owing to the increased SNR available. However, the only studies examining the safety of MR procedures for fetal imaging have been done at a field strength of $\leq$1.5 T (11–17). For this reason, fetal MR imaging is done at field strengths of $\leq$1.5 T. It may be that in the future, higher field strengths can be utilized safely.

In order to generate an image, the protons in the region of the fetus must be caused to emit a signal. Once the pregnant patient is placed into the main magnetic field, protons align with the field, resulting in a net magnetization pointing in the same direction as the main magnetic field. This net magnetization is known as the longitudinal magnetization. However, the protons generating the longitudinal magnetization do not generate a signal until they are "excited" with a radio-frequency (RF) pulse tuned to the resonant frequency of the protons at the static field strength that is being used for imaging. This excitation causes some fraction of the longitudinal magnetization to be transferred into a plane perpendicular to the longitudinal axis. This plane is often referred to as the transverse plane, and magnetization in this plane is referred to as transverse magnetization. The amount of magnetization transferred from the longitudinal axis to the transverse plane can be visualized as tipping the longitudinal magnetization by an angle. Thus RF pulses are often characterized by the angle of the tip they produce; for example, a 90° or 180° pulse.

The RF pulses used for excitation are nonionizing, so radiation damage is not a concern. However, these pulses can deposit considerable amounts of power (kW), and this power can cause heating of tissues. The amount of heating is quantified as the specific absorption rate

(SAR) and is measured in units of W/kg; thus, SAR is a measure of how much power is delivered to a given mass of tissue.

The SAR produced by a given sequence is a function of a wide variety of parameters. Some factors are easily controlled, for example, SAR increases as pulse repetition time decreases, and flip angle and/or static field strength increase. All clinical magnets have mechanisms to monitor SAR to prevent unsafe levels from being employed. However, in pulse sequences that are RF intensive, some tradeoffs in other sequence parameters may be necessary to keep SAR within safe limits.

Once the longitudinal magnetization has been tipped into the transverse plane, the transverse magnetization begins to precess about the longitudinal axis, and this precessing magnetic field generates an electromagnetic signal that can be received by an antenna, commonly referred to as a coil. In the initial attempts at fetal MR imaging, signal reception was obtained using the body coil built into the structure of the magnet (18–20). Body coils give uniform signal throughout their sensitive volume (which is generally the complete free bore of the magnet), but they have poor overall SNR in that volume. Surface coils, which can be placed directly on the body, give much higher SNR than can be achieved with a body coil, but over a much smaller sensitive volume. This small sensitive volume restricts imaging with single surface coils to organs close to the surface of the body.

The limitations of a single surface coil can be mitigated by using an array of coils. While any single element in an array will still be sensitive to a small volume, the images from each element in the array can be combined. If this is done appropriately (21) it is possible to generate images with large volume coverage and the high SNR of a surface coil.

The last hardware issue that must be considered for fetal imaging is the gradient subsystem of the magnet. As will be discussed in the following section, MR images are encoded by acquiring data while magnetic field gradients are being switched. The maximum gradient strength that can be achieved (measured in mT/m or G/cm) will determine the maximum resolution, and the faster the gradient switching occurs the faster an image can be acquired. The rate at which gradients can be switched has undergone significant growth in recent years, but these increases have now reached a plateau where further increases may cause direct neuromuscular stimulation.

k-SPACE

Unlike most imaging modalities, MR imaging does not produce images directly from the data acquired during the imaging procedure. Instead, the raw data collected are encoded to contain information about the spatial frequencies that represent the object being imaged. These data are often represented by displaying the received signal intensities in spatial frequency space, commonly referred to as *k*-space. Images are formed by invoking a mathematical transform (most commonly the Fourier transform) to convert the spatial frequency data into an image. Understanding *k*-space and how the *k*-space data are collected is key to understand how MR images are formed, so a brief discussion of *k*-space is appropriate before describing specific pulse sequences. For the interested reader, several other reviews (22–25) provide more comprehensive details on *k*-space.

A Cartesian plane is often used to represent *k*-space with the axes being k_x and k_y (Fig. 9.1). This is sufficient to describe two-dimensional imaging. Low spatial frequency data are encoded at the origin of *k*-space (k_x, $k_y = 0$). These data represent the lowest resolution information about the imaged object. The majority of the *k*-space signal resides close to the center and thus

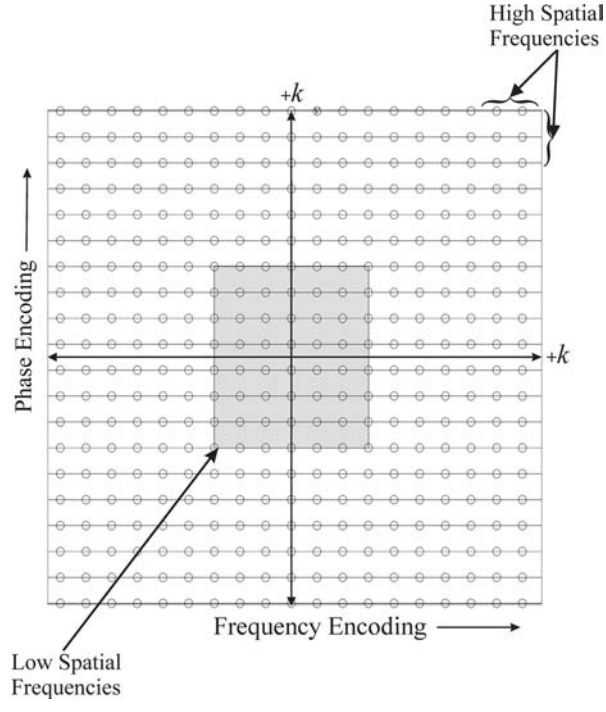

Figure 9.1 Schematic representation of a *k*-space matrix. Frequency encoding occurs in the k_x direction, while phase encoding occurs in the k_y direction. Low spatial frequency information is located at the center of *k*-space. As most of the signal in *k*-space is contained at these low spatial frequencies, this region dominates the contrast of the image. As distance from the center of *k*-space is increased, information about higher spatial frequencies is added and the resolution of the resulting image is increased.

dominates the contrast of the resulting image. The farther the center of *k*-space, the larger the spatial frequency that is being encoded. In general, signal intensity decreases towards the periphery of *k*-space, but these data provide high-resolution information about the imaged object. The maximum distance from the center of *k*-space that is sampled determines the resolution of the resulting image (Fig. 9.2).

The portion of *k*-space sampled during data acquisition is determined by the strength, duration, and direction of the various magnetic field gradients applied during imaging. The timing of the application of these gradients

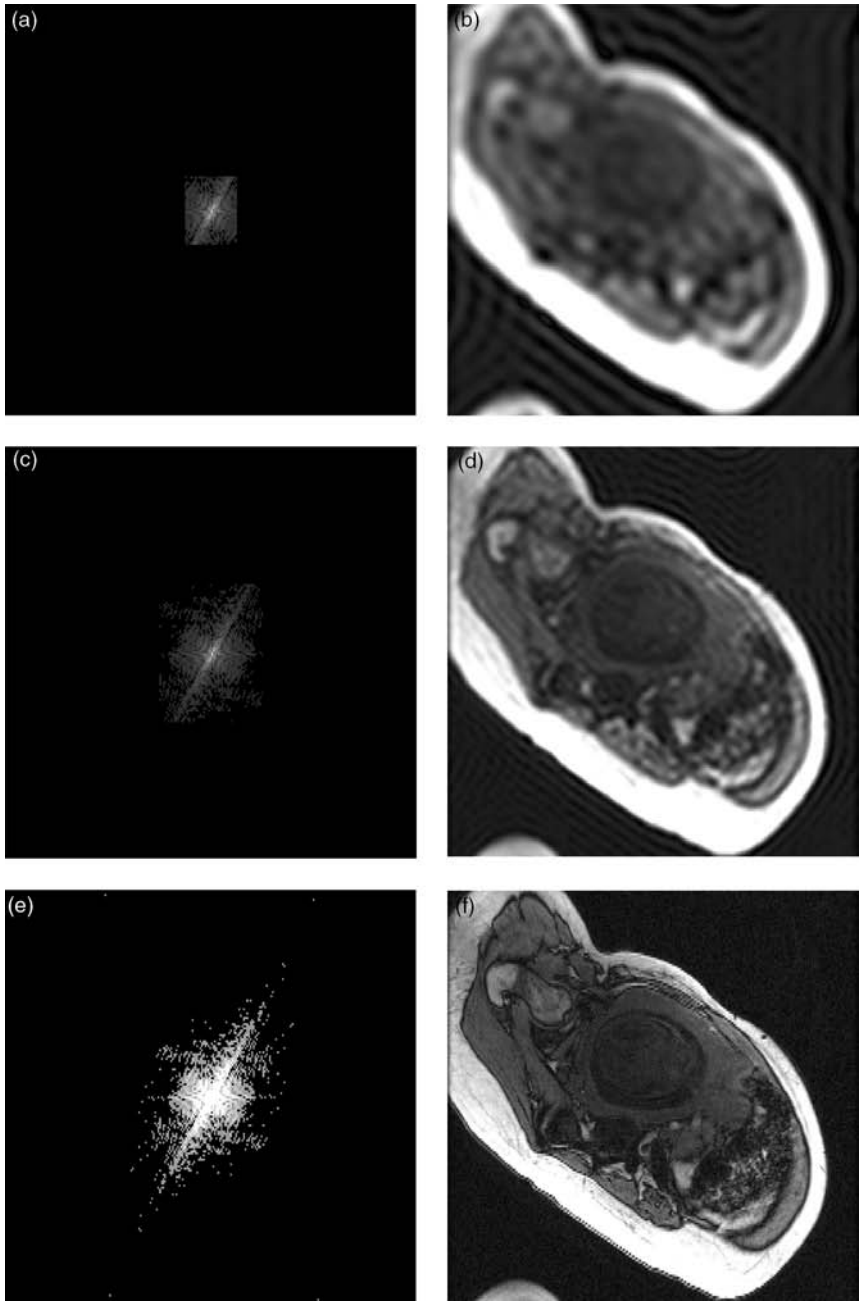

Figure 9.2 Pairs of magnitude images of *k*-space and corresponding anatomic images. (a) Magnitude image of the central portion of *k*-space for fetal imaging. As most of the signal is contained in the center of *k*-space, this region of *k*-space dominates the contrast of the image. However, only the lowest spatial frequencies are present in this *k*-space. Thus, while the contrast of the resulting image (b) is apparent, only the low resolution features are present. (c) Magnitude image of a slightly larger region of *k*-space and resulting anatomic image (d). Note that the resulting image has the same contrast as (b) but with higher resolution. (e) Magnitude image of all the *k*-space data and resulting anatomic image (f). Now the resulting image has all of the high resolution features included.

also determines the trajectory with which *k*-space is sampled. Data are generally collected after a set of gradients have been applied. The area beneath these gradients determines the distance from the origin of *k*-space at which signal is sampled.

In the case of frequency encoding, data are collected while a gradient of constant amplitude is applied. By convention, frequency encoding is done in the k_x direction. As the area under the frequency encode gradient is larger for each consecutive point sampled, each point comes from a single line moving across *k*-space (Fig. 9.3). If no gradients besides the frequency encode have been applied, the region of *k*-space that will be sampled will start at the origin of *k*-space ($k_x = 0$) and extend out in a straight line. To form an image it is generally necessary to sample a region of *k*-space extending in all directions from the origin. In order to do this, other gradients must be applied. In the case of our frequency encode line, applying a gradient of the same strength, but of opposite polarity and half the duration of the frequency encode gradient, will cause data sampling to start at a position $-k_x$ and end at $+k_x$.

Collecting this frequency encode line will resolve the imaged object in the frequency encode direction, but not in the phase encode direction, as the line collected lies along $k_y = 0$ and no data are available from other k_y values. The simplest way to acquire data at other k_y values is to repeat the frequency encoding, but to apply a single gradient along the phase encoding (k_y) direction before applying the frequency encode gradient and collecting data. This phase encode direction will move the frequency encode line up or down in the k_y direction in *k*-space. By repeating this process of applying a phase encode gradient and then turning on a frequency encode gradient and collecting data, a complete two-dimensional region of *k*-space can be sampled. The data from that region can then be Fourier transformed to create a two-dimensional image.

COMMON PULSE SEQUENCES USED FOR FETAL IMAGING

Sequences utilized for fetal imaging must be fast enough to obtain individual images without fetal motion. In general practice this necessitates a scan time of $\leq$1 second per image. For single slice acquisitions, a series of images are obtained in $<$20 seconds, with each individual image being obtained in $\leq$1 second. For T_1-weighted images, gradient echo sequences with very short repetition times (TR) are utilized. When a single slice method is utilized, there is no need for imaging to be performed during a maternal breath-hold. However, when other sequences are utilized, the time for the entire sequence should be $<$20 seconds to allow for imaging during a breath-hold.

T_2-Weighted Imaging

By far the most common sequence currently used for imaging the fetus is a half-Fourier rapid acceleration with relaxation enhancement (RARE) sequence. This sequence has variable names, depending on the manufacturer of the magnet. Examples are single-shot fast spin echo (SSFSE) and half-Fourier acquisition turbo spin echo (HASTE). The popularity of this sequence is because of its highly desirable properties for fetal imaging, which include excellent T_2 contrast, high SNR, and relative insensitivity to susceptibility and motion artifacts (Fig. 9.4) (1,2,4,26,27). With this sequence, each slice is obtained sequentially, and fetal motion, when it occurs, affects the signal in only the slice being obtained at the time of imaging.

In RARE sequences, a 90° pulse is applied to tip all the longitudinal magnetization into the transverse plane. This is followed by a train of RF pulses that generate a series of spin echoes. The flip angle of the train of RF pulses can be as great as 180°, but for fetal imaging 130–150° is preferable in order to decrease energy deposition. However, the use of this lower flip angle decreases the SNR. Gradients are applied during this train of spin echoes so that different phase encode lines are acquired from each echo. The spin echo train is long enough that all the phase encodes necessary to form an image are collected after a single 90° excitation pulse. Because all of the available longitudinal magnetization is used for image formation, RARE images have excellent SNR efficiency.

The time between the RF pulses in the RARE echo train (the inter-echo spacing) can be $\leq$5 ms. This rapid application of pulses prevents dephasing of spins due to susceptibility gradients, making RARE insensitive to imperfections in magnetic field homogeneity. The downside of this is that RARE has a very high rate of RF power deposition and thus a high SAR. In general, the necessity to keep SAR below the safe limit places a lower boundary on the interval between successive RARE acquisitions. As RF power is deposited over all anatomy within the transmission coil, and not just in the slice being imaged, this limit applies equally whether the same slice is being imaged repeatedly or slices in different positions are being acquired.

Because the entire RARE image is acquired in a single echo train, there is significant attenuation of the acquired signal due to T_2 decay during data acquisition. This decay reduces the intensity of the signal in the *k*-space lines acquired at the end of the echo train. As these are the lines that contain the high-resolution information, the reduction of their signal manifests as a blurring of the image in the phase encode direction (Fig. 9.5).

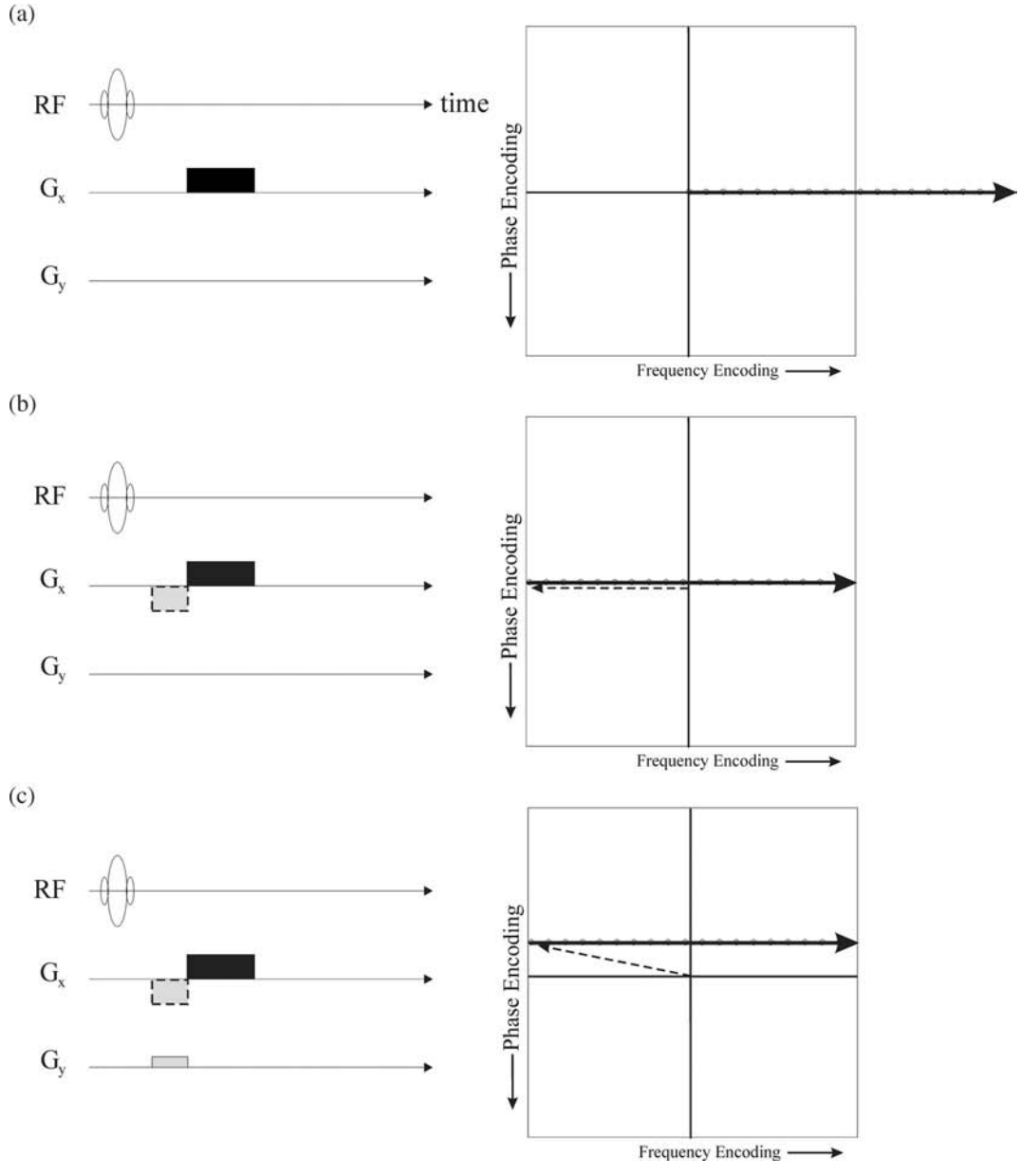

Figure 9.3 *k*-Space trajectories. (a) Diagram showing the *k*-space trajectory when a single gradient (G_x) is turned on in the frequency (k_x) direction: an initial RF pulse tips magnetization into the transverse plane. This RF pulse is followed by application of a gradient. Because this gradient is positive and no other gradients precede this one, the *k*-space trajectory starts at the *k*-space origin and moves in the $+k_x$ direction. The distance traveled from the center of *k*-space is proportional to the area under the gradient. (b) Diagram showing the *k*-space trajectory when a negative gradient (G_x) is turned on in the frequency (k_x) direction, followed by a positive gradient in the same direction: as we usually want to obtain data from the positive and negative sides of *k*-space, it is necessary to preceed our readout gradient with another gradient of opposite polarity to move our starting point from the *k*-space origin to $-k_x$. Note that data are not being read out while this negative gradient is on. The area under this initial gradient is $-1/2$ the area under the readout gradient, so that when the readout gradient is turned on, data will be acquired from $-k_x$ to $+k_x$. (c) Diagram showing the *k*-space trajectory when a gradient (G_y) is turned on in the phase encode (k_y) direction, in addition to the gradients in the frequency direction: the data lines acquired in (a) and (b) both came from the $k_y = 0$ line. This is because no gradients were applied in the phase encode (k_y) direction. In order to form an image, data must be acquired from other k_y values, so another gradient must be generated to move the *k*-space trajectory to a different k_y value. In this example, a phase encode gradient is turned on at the same time as the k_x gradient that moves the acquisition start point to $-k_x$. As the phase encode gradient is on at the same time, the start point also moves to a new position along the k_y direction so a different phase encode line is acquired when data are obtained in the presence of the readout gradient. By repeating this process of acquiring *k*-space lines with different starting k_y values, a complete two-dimensional *k*-space can be formed and transformed into an image.

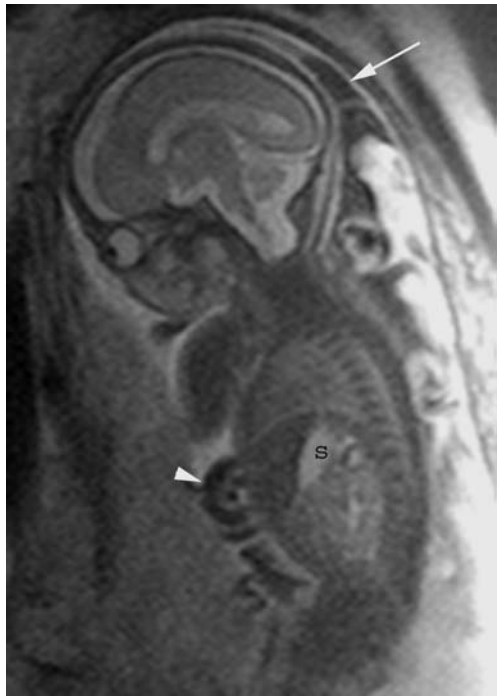

Figure 9.4 Sagittal view of a fetus acquired using SSFSE. TR/TE = 1200/64 ms, matrix 256 × 256, FOV 360 × 280 mm, 130° flip angle, 4 mm thick slice, 832 ms acquisition time. The long TR and TE and large flip angle of this acquisition ensure that the signal intensity of the image is dominated by T_2 effects. Note the relatively high signal in the cerebrospinal fluid, and fluid in the stomach (S). The umbilical cord (arrowhead) has low signal as a result of flowing blood. The amniotic fluid has regions of low signal because of fluid motion (arrow). Notice the bright "layer" around the low signal in the moving amniotic fluid. This brightness is generally because of a lack of motion at the periphery of the fluid space; however, the high signal intensity may also be due to subcutaneous fat (adjacent to the fetus) or fluid in the subamniotic space.

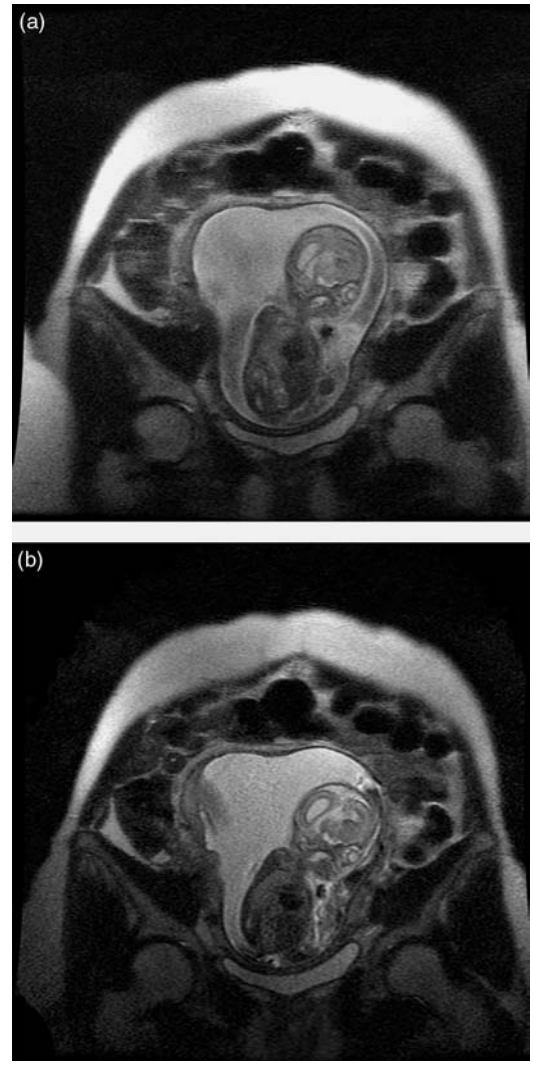

Figure 9.5 Pair of SSFSE images showing the effect of T_2 decay and fetal motion on resolution. These images had a FOV of 360 mm and 256 pixels in the phase encode direction. An echo train of 144 phase encodes was used to acquire (a). Image (b) was identical to (a) except that the echo train was only 80 phase encodes long. Fetal motion has degraded the image, as shown by the loss of signal in the amniotic fluid. However, there is also blurring of signal in the longer echo train length image, as shown by decreased blur in the maternal pelvic bones. Because the echo train for (b) was so much shorter, the high resolution *k*-space data was not affected by T_2 decay as much as the high resolution in (a). This resulted in image (a) exhibiting much more blurring of high resolution structures, despite each image having the same nominal resolution of 1.4 mm/pixel.

The amount of blur depends on the T_2 of the spins being imaged, with shorter T_2 values resulting in increased blurring. This blur is always present and causes the true spatial resolution of a RARE image to be somewhat lower than that indicated by the pixel size determined by dividing the field of view (FOV) by the number of phase encode steps. Note that the blurring worsens as the echo train length increases, implying that doubling the number of phase encode points will not result in a doubling of the spatial resolution.

Setting the time between the 90° excitation pulse and acquisition of the central line of *k*-space controls the T_2-weighting of the resulting image (Fig. 9.6). The interval is commonly called the effective echo time (TE_{eff}), as the contrast of an image is dominated by the center of *k*-space. If *k*-space were acquired in a strictly linear fashion, TE_{eff} would be in excess of 200 ms. Except for some unusual cases, this would be too long to provide useful T_2 contrast. Additionally, the long TE_{eff} would result in low overall SNR as the T_2 of most tissues of interest are $\leq$100 ms.

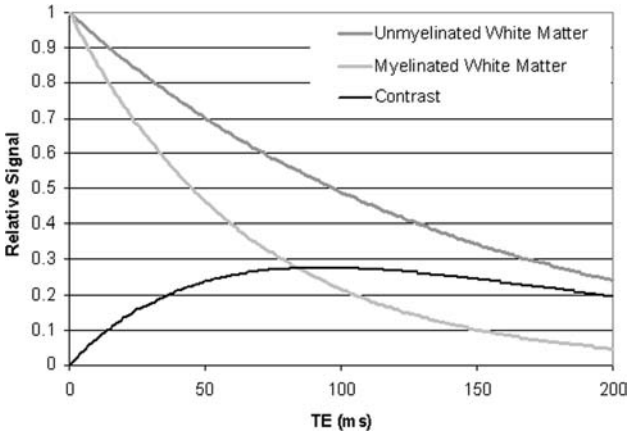

Figure 9.6 Plot of T_2-weighted signal and contrast as a function of TE. In this example, the signals expected from myelinated ($T_2 = 65$ ms) and unmyelinated ($T_2 = 14$ ms) white matter are plotted as a function of the TE of the image acquisition. Both signal curves follow the exponential decay that results from T_2 effects: $S(\mathrm{TE}) = M_0 \exp(-\mathrm{TE}/T_2)$. The solid black line shows the relative contrast between the two tissues (contrast = $S_{\mathrm{unmyelinated}} - S_{\mathrm{myelinated}}$). Note that although both tissues always give more signal at shorter TE values, the contrast between the tissues is maximized at TE of $\sim$100 ms. The precise value of TE that will maximize contrast will vary depending on the tissues of interest, but it can always be estimated if the T_2 values of the two tissues are known.

In order to reduce $\mathrm{TE_{eff}}$ to more reasonable values ($<$100 ms), half-Fourier acquisition techniques are almost always used for RARE acquisition. Half-Fourier imaging relies on the symmetry of *k*-space to reduce imaging time. The phase encode lines in one half of *k*-space are collected with a phase encoding gradient that has positive amplitude, while the lines on the other half are collected with a gradient that has the area, but a negative amplitude. In an ideal case, this means that the data collected at *k*-space position $+k$ is the complex conjugate of the data collected at position $-k$. As it is possible to determine the *k*-space values of one half of *k*-space from the other half, an image can be formed by collecting only one half of *k*-space and calculating the "missing" half of *k*-space from the acquired data.

Unfortunately this ideal situation rarely occurs as there are a number of effects that can distort the symmetry of *k*-space by altering the phase of one half of *k*-space relative to the other half. For this reason, half-Fourier reconstruction requires acquisition of all the phase encodes from one half of *k*-space plus a few lines (generally 8–16) from the other side. The extra lines are used to calculate a phase correction that restores the conjugate symmetry of *k*-space. The missing values can then be determined from the *k*-space symmetry and the resulting full data set can be Fourier transformed normally to produce an image.

Usually the phase encode lines in a half-Fourier RARE acquisition are collected starting on the small "half" of *k*-space and working linearly through the center and out through the "full" half (Fig. 9.7). This results in the center of *k*-space being acquired in as little as 40–80 ms after the 90° excitation pulse, with the correspondingly short $\mathrm{TE_{eff}}$.

Half-Fourier acquisition also reduces the acquisition time by nearly a factor of 2. With an inter-echo spacing (the time between acquisition of consecutive phase encode lines) of 5 ms, a complete image with 256 phase encodes can be acquired in a little over 600 ms. Using 128 phase encodes, an image can be acquired in 300 ms. This rapid acquisition makes half-Fourier RARE highly insensitive to motion, a crucial characteristic when performing fetal imaging. Not only can all but the most rapid fetal motion be effectively frozen, but also the need for maternal breath-holding can be eliminated as breathing motion will be too slow to cause artifacts.

One potential issue with the rapid acquisition is that if the same slice is imaged repeatedly the signal in subsequent acquisitions will be attenuated if the acquisition spacing is too short. This attenuation happens because there has not been sufficient time between acquisitions

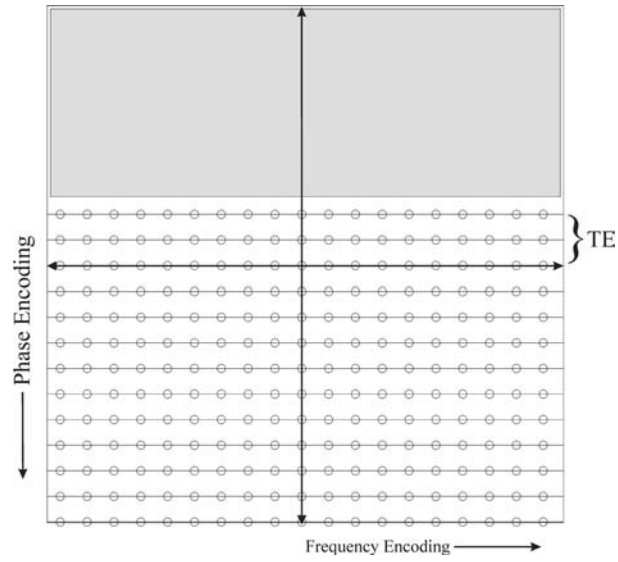

Figure 9.7 Diagram showing the trajectory of a half-Fourier acquisition in *k*-space. Note that a few lines (typically 8–16) are acquired on one half of *k*-space, while all the lines in the other half of *k*-space is acquired. The time elapsed between the excitation pulse and the acquisition of the center line of *k*-space determines how T_2-weighted this acquisition will be. The data in the shaded area are not collected but synthesized after acquisition.

for the longitudinal magnetization to fully recover. Thus when the next 90° excitation pulse is applied, there is less longitudinal magnetization available to tip and the resulting signal is reduced by an equivalent amount. Because the recovery of longitudinal magnetization is governed by T_1 processes, possibly unwanted T_1-weighting will be introduced into the image as a result of the incomplete recovery. In our subjective experience, if repeated imaging is desired in a single fetal slice, a delay of up to 4 seconds, is needed for optimal SNR.

A similar problem can occur when multiple closely spaced slices are being acquired. Because the RF pulses are of finite duration, the slice profiles they excite are not exact, but can extend somewhat outside the desired slice and into adjacent slices. This unwanted excitation of adjacent slices results in attenuated signal in adjacent slices. This can be avoided by acquiring a set of slices in an interleaved fashion; for example, acquiring slices 1, 3, 5, ... and then slices 2, 4, 6, ... This interleaving allows enough time for full recovery of unintentionally disturbed magnetization in adjacent slices.

Echo Planar Imaging

Echo planar imaging (EPI) is another imaging sequence that has been used for fetal imaging (28–31). Like RARE, all of the data needed to reconstruct a single image are acquired in a single echo train. In contrast to RARE, 180° refocusing RF pulses are not applied between acquisitions of each phase encode line. This allows echo spacing to be extremely short (<1 ms) so that the EPI images can be acquired in under 100 ms, making EPI highly insensitive to motion artifacts. The minimal RF excitation necessary for EPI also eliminates any issues related to RF power deposition. EPI images are T_2- (or T_2^*) weighted so they exhibit contrast similar to RARE.

There are a number of downsides that have prevented the widespread use of EPI for fetal imaging. The long, unrefocused gradient echo trains required for data acquisition make EPI exquisitely sensitive to magnetic field inhomogeneity, with off-resonance effects resulting in excessive signal loss and geometric distortion (Fig. 9.8). The lack of RF refocusing also requires very short echo spacing in order for the image to be acquired before the transverse magnetization has decayed to noise owing to T_2^* relaxation. The short echo spacing requires the use of high performance gradient subsystems in order to achieve the necessary high gradient switching rates. These high switching rates in turn can raise safety issues. It is necessary to avoid nerve stimulation, which requires truncation of gradient performance that then limits the speed and/or resolution of EPI acquisitions.

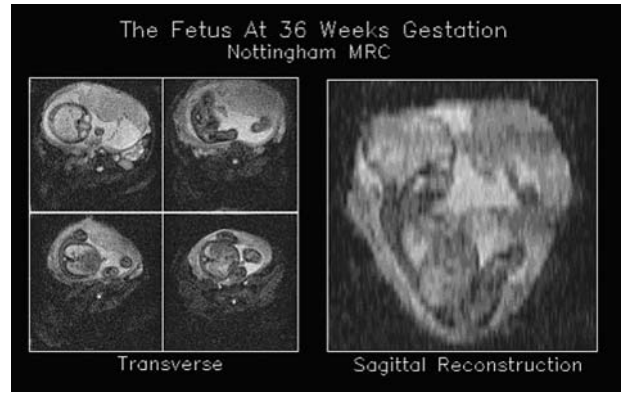

Figure 9.8 T_2-weighted spin-echo EPI image of the fetus. [Image courtesy of K. Duncan, Nottingham, England, (From Chen and Levine (23)]

Because of the fast acquisition time, EPI has been utilized for assessment of fetal volumes (32–37).

T_1-Weighted Imaging

Images with T_1 contrast have been shown to be useful for detecting blood products (38,39), evaluating the liver position in cases of congenital diaphragmatic hernia (40), and evaluating myelination of the brain (41). T_1-weighted images are generally acquired using gradient echo imaging sequences such as gradient refocused acquisition in the steady state (GRASS) or fast low angle shot (FLASH). In order to produce T_1-weighted images, these sequences are typically acquired with short TR (100–200 ms), short TE (2–10 ms), and large flip angles (>60°). Figure 9.9 shows examples of how changing TR and flip angle can affect the signal and contrast of T_1-weighted images.

The short TR and large flip angle allow these images to have reasonable SNR (Fig. 9.10). However, as only a single phase encode is acquired in each TR, the time to acquire any given slice is on the order of 20 seconds. Therefore, these sequences are susceptible to corruption from any motion that occurs within that 20 seconds acquisition window. This motion can be fetal motion, motion from the surrounding maternal bowel peristalsis, or maternal breathing motion. Therefore, the sequence should be obtained during a maternal breath-hold.

The TR is long enough that in multi-slice acquisitions the data from multiple slices can be acquired within a single TR by using slice interleaving (Fig. 9.11), allowing good volume coverage within a maternal breath-hold. An additional advantage of the intermediate-length TR is that acquisition of two gradient echoes per TR is possible, allowing acquisition of images with fat and water both in phase and out of phase, with no penalty to scan

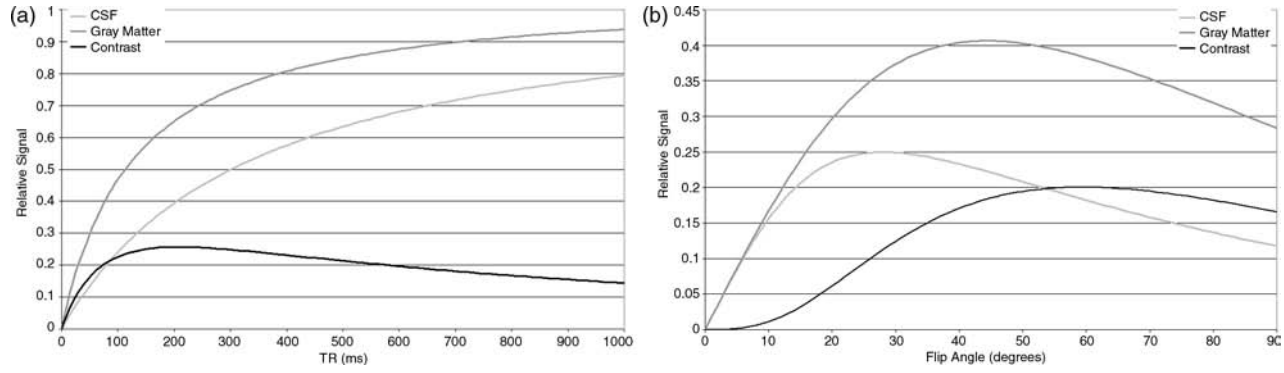

Figure 9.9 Examples of T_1-weighted signal and contrast as a function of TR and flip angle. (a) Plot of T_1-weighted signal and contrast as a function of TR. In this example, the signal expected from cerebrospinal fluid (CSF; $T_1 = 2400$ ms) and gray matter (GM; $T_1 = 900$ ms) are plotted as a function of the TR of the image acquisition. (A flip angle of 30° was assumed for this example.) Both signal curves follow the exponential recovery that results from T_1 effects:

$$S(\mathrm{TR},\ \alpha) = M_0 \frac{1 - \exp(-\mathrm{TR}/T_1)}{1 - \exp(-\mathrm{TR}/T_1)\cos(\alpha)} \sin(\alpha)$$

The solid black line shows the relative contrast between the two tissues (contrast = $S_{GM} - S_{CSF}$). Note that although both tissues always give more signal at longer TR values, the contrast between the tissues is maximized at TE of ~200 ms. The precise value of TR that will maximize contrast will vary depending on the tissues of interest, but it can always be estimated if the T_1 values of the two tissues are known. (b) Plot of T_1-weighted signal and contrast as a function of flip angle. In this example, the signal expected from CSF and GM are plotted as a function of the flip angle of the image acquisition. (A TR of 300 ms was assumed for this example.) Both signal curves follow the same equation as in (a), but with TR held constant. The solid black line shows the relative contrast between the two tissues (contrast = $S_{GM} - S_{CSF}$). Note that increasing flip angle does not always result in increased signal, and that maximal contrast occurs at a flip angle other than the one that maximized signal for either of the two tissues. The precise flip angle that will maximize contrast will vary depending on the tissues of interest, but it can always be estimated if TR and the T_1 values of the two tissues are known.

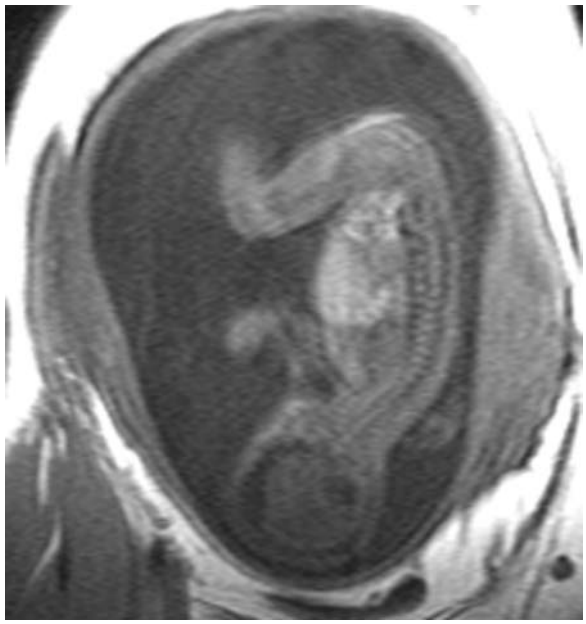

Figure 9.10 Sagittal T_1-weighted image of the fetus. TR/TE/flip angle 90/4.2/60°, matrix 256 × 160, FOV 360 × 240 mm. The acquisition time for this image was 20 s, allowing this image to be acquired during a maternal breath-hold. The short TR and TE and large flip angle of this acquisition ensure that the signal intensity of the image is dominated by T_1 effects.

time. Such images can be useful in evaluating fat distribution (42).

Unlike RARE, the T_1-weighted gradient echo images are acquired under steady-state conditions, so there is minimal change in magnetization during *k*-space acquisition. These sequences, therefore, do not suffer from the T_2-induced blurring in the phase encode direction from which RARE, or any other sequence that uses echo train acquisition, suffers. Practically speaking, this means that for a given FOV and matrix size, echo train-based sequences like RARE will have lower spatial resolution than steady-state sequences.

In the past few years there has been widespread distribution of magnets with gradient systems capable of achieving high gradient strengths (>20 mT/m) and rapid gradient switching rates (<500 μs rise times). This has made an alternative technique [known by names such as Turbo-FLASH or fast gradient recalled echo (FGRE)] for acquiring T_1-weighted images available, which uses very short TR (<5 ms) and TE (<3 ms) to produce an image. The very short TR allows a complete image to be acquired in ≤500 ms (similar to RARE), effectively freezing most fetal and maternal motion. However, in order to preserve the T_1-weighting of the sequence, the very short TR requires very small flip

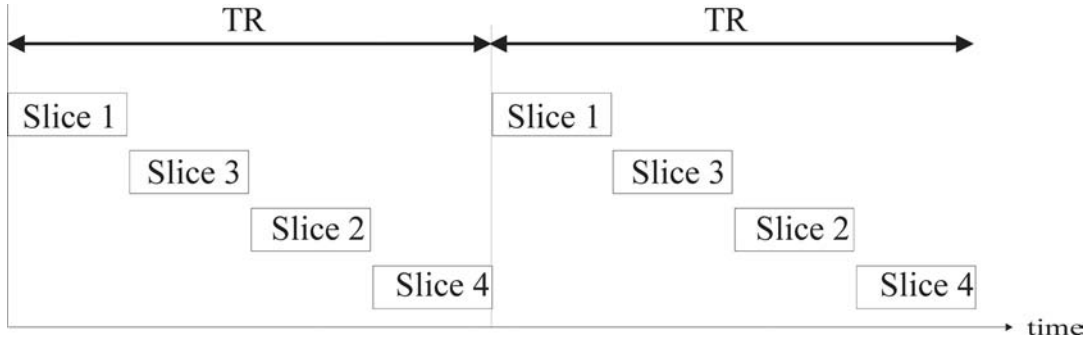

Figure 9.11 Illustration of the relative timing of acquisition of interleaved slices. As the time required to acquire data for a single slice is less than TR, there is considerable "dead time" within a single slice acquisition. Data for other slices can be acquired during this time, as their acquisition will not affect the signal from the first slice. By interleaving data acquisition in this manner the efficiency of the data acquisition can be significantly improved. Note that the acquisition is arranged so adjacent slices are not acquired sequentially, but are separated in time. Excited slice profiles are never perfectly rectangular but extend some distance beyond the nominal slice, with the excitation falling off with distance. If immediately adjacent slices were excited sequentially, the excitation from the first slice could "bleed" into the second slice, affecting the signal in the second slice. By temporally separating the excitation of adjacent slices this crosstalk between slices can be avoided.

angles ($<15^\circ$) to be used, resulting in relatively poor SNR compared with FLASH acquisitions. The very short TR also makes slice interleaving impossible, so Turbo-FLASH images are acquired sequentially. Similarly, dual echo imaging is not possible with very short TR imaging.

Turbo-FLASH sequences are also limited in in-plane resolution both because of their inherently low SNR and because the additional phase encoding required by higher resolution imaging lengthens the acquisition time, thus increasing the motion sensitivity of the sequence.

Steady-State Free Precession

Sequences based on steady-state free precession (SSFP) (43), are becoming increasingly popular. These sequences, which are more commonly known by manufacturer-specific names like TrueFISP (true fast imaging with steady-state precession), FIESTA (fast imaging employing steady-state acquisition), or Balanced FFE (balanced fast field echo), have entered widespread use only recently because of the need for high performance gradient hardware that enable very short TRs in order to avoid off-resonance artifacts (44–46). The derivation of the contrast in SSFP is complicated but is a function of both T_1- and T_2-weighting (43,47,48). The T_2-weighting gives high signal from fluid, while the T_1-weighting gives good contrast in tissue. The high signal of fluid with this sequence makes it an excellent choice for fetal imaging.

Steady state free precession sequences are very similar to gradient echo sequences like FLASH, except that both transverse and longitudinal magnetization (instead of longitudinal magnetization alone) are held in steady state. This allows the use of relatively large flip angles ($45-80^\circ$) and gives SSFP much higher SNR efficiency than gradient echo sequences.

As the TR of SSFP acquisitions are similar to FLASH imaging, they have similar acquisition times and similar advantages with respect to motion artifact. The steady-state nature of the data acquisition also ensures that SSFP does not suffer from the T_2 decay-induced blurring seen in RARE sequences.

In contrast, SSFP is a function of both T_1 and T_2 with the relative amount of T_1- and T_2-weighting being a complicated function of the TR and the flip angle (49); but for moderately large flip angles ($>30^\circ$) the contrast is primarily T_2-weighted (Fig. 9.12). SSFP has been compared with RARE for imaging of the fetal brain and has been shown to produce images at least as good as RARE (50).

Unfortunately, fat is undesirably bright in SSFP images. New techniques for separating fat and water signal in SSFP have been demonstrated but have not (to our knowledge) yet been used for fetal imaging (51–53).

The short TR and large flip angles of SSFP can result in both high RF power deposition and problems with exceeding the neuromuscular stimulation safety limits. In some cases this can limit the acquisition speed or maximum resolution of SSFP imaging. However, these limits are generally less of an issue for SSFP than RARE (for SAR) or EPI (neuromuscular stimulation), so this sequence can represent a good compromise between those two sequences.

Spectral Spatial Water Excitation

It is possible to design slice selective RF pulses that excite only the protons resonating in a narrow frequency band

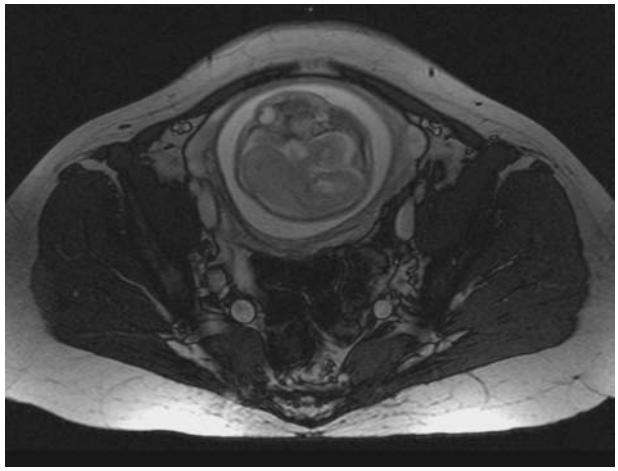

Figure 9.12 TrueFISP image of a fetal head. TR/TE/flip angle 4.8/2.3/70°, matrix 256 × 211, FOV 330 × 330 mm. The acquisition time for this image was 1.01 second, allowing this image to be acquired without a maternal breath-hold.

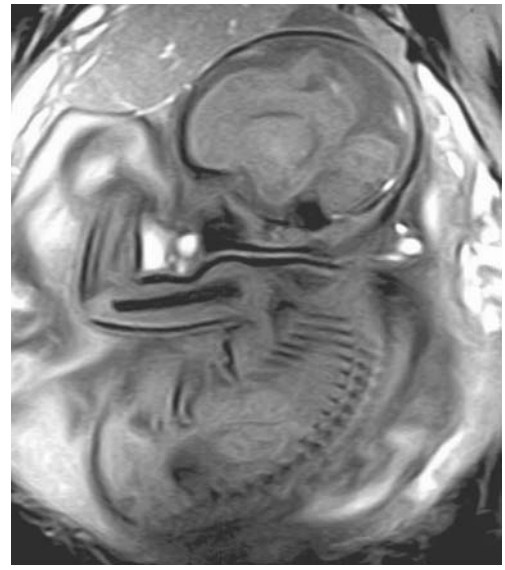

Figure 9.13 Breath-hold T_1-weighted gradient echo with a spectral spatial water excitation prepulse for fat-suppression (TR/TE/flip angle = 40/8/30°, 5 mm slice thickness, 30 × 40 cm FOV, 192 × 256 matrix, two acquisitions, 15 second scan time). Image reveals the bones (humerus, ribs, and vertebral bodies) as dark because of fat suppression. [From Levine et al. (2)]

within the selected slice. These so-called "spectral spatial" pulses can be designed to exploit the frequency difference between water and fat protons by selectively exciting protons in a narrow frequency band around the water resonance. If this spectral band is narrow enough, fat protons will not be excited and thus will not yield any signal. An example of an application for this technique is in the evaluation of fetal bones. Because most of the signal from bones comes from fat, water selective excitation can be used to help view fetal bones late in gestation by making the bones appear black against a bright background (Fig. 9.13).

STANDARD PROTOCOL

At our institution, we perform a three-plane scout, followed by T_2-weighted imaging with half-Fourier RARE in the fetal sagittal, coronal, and axial planes using each sequence as the scout for subsequent imaging. A typical T_2-weighted sequence has echo spacing of 4.2 ms, TE_{eff} = 90 ms, 256 × 256 matrix, 4 mm slice thickness, 26 × 30 cm FOV, and a refocusing flip angle of 150°. The FOV is tailored to be as small as possible such that the maternal structures overlap, but the wrap-around artifact does not obscure the fetus. We typically perform additional sequences with thinner slices or higher in-plane resolution throughout the region of interest.

One T_1-weighted sequence is used in the region of interest. We typically employ a dual echo gradient echo sequence with the following parameters: $TR/TE_1/TE_2$ = 180/2.1/4.2 ms, flip angle = 80°, 5 mm slice thickness, FOV = 30 × 35; matrix = 170 × 256, scan time = 17 seconds (breath-hold).

If a midline central nervous system abnormality is of concern, real-time imaging (see below) is performed in order to obtain a true fetal sagittal midline image. If cleft palate is of concern, repeat images are obtained in the fetal sagittal plane during swallowing in order to outline the soft palate (see Chapter 4).

ARTIFACTS

Common artifacts in fetal MR procedures include motion, aliasing, Gibbs, susceptibility, and partial volume artifacts.

Motion Artifact

Motion artifact is the most common artifact in fetal imaging, resulting from a variety of sources such as maternal breathing or whole body motion, maternal bowel peristalsis and arterial pulsations, and fetal motion. Maternal motion (Fig. 9.14) results in the motion of the entire field of view during data acquisition, and generally results in a blurring of the entire image as well as ghost images in the direction of phase encoding. Movement in a small portion of the imaged area results in blurring and/or ghosting of that small portion of the

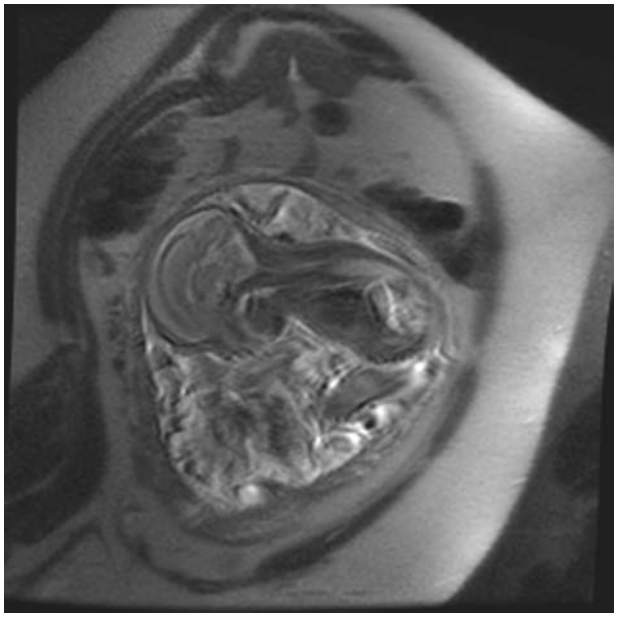

Figure 9.14 Bulk movement. Note the blur of abdominal wall musculature, maternal bowel, and fetus. Heterogeneous signal in the amniotic fluid a result of the fluid motion.

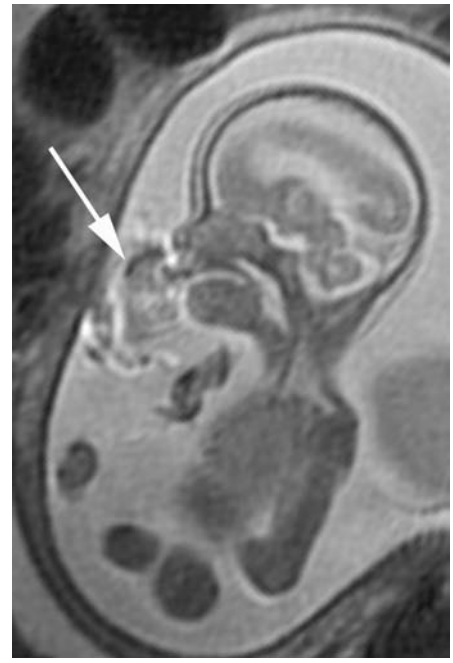

Figure 9.15 Fluid motion. Sagittal view of a fetus at 26 weeks gestation. The fetus was exhaling from the nose during image acquisition causing the fluid immediately anterior to the face to lose signal, imitating a mass.

object across the image. Bulk motion artifact can be distinguished from Gibbs ringing artifact because it extends across the entire FOV, whereas Gibbs ringing diminishes quickly away from the boundary causing the ringing. If bulk motion is present, the patient should be reminded to keep still. Breath-holding is not usually needed during single shot imaging sequences like RARE or EPI, but if the patient is moving during imaging a breath-hold may still be helpful.

Motion in fluid can cause decreased signal. This artifact occurs when spins excited by a slice-selective (RF) pulse change position with respect to the slice and/or spatial encoding gradients before their signal is acquired. Motion artifact can be seen in amniotic fluid (Figs. 9.4, 9.5, 9.14, 9.15) and in other fetal fluid collections such as cerebrospinal fluid and fetal urine (Fig. 9.16). Flowing blood is dark on SSFSE imaging because of this artifact (Fig. 9.5). As fetal imaging is typically performed with single-shot sequences, only the slice that was obtained during the motion is affected. As long as the fetus is not continuously moving, then typically only one or two slices are degraded by motion during a typical sequence acquisition. If the affected slices are not in the region of interest, then the sequence does not have to be repeated. A pitfall in the assumption that dark fluid on RARE imaging is because of motion is shown in Fig. 9.17, where the low signal is a result of blood products.

If the fetus moves during data acquisition and the movement is in plane with imaging, the moving portion of the anatomy may be seen more than once (i.e. a leg or arm appears in two places in the same sequence

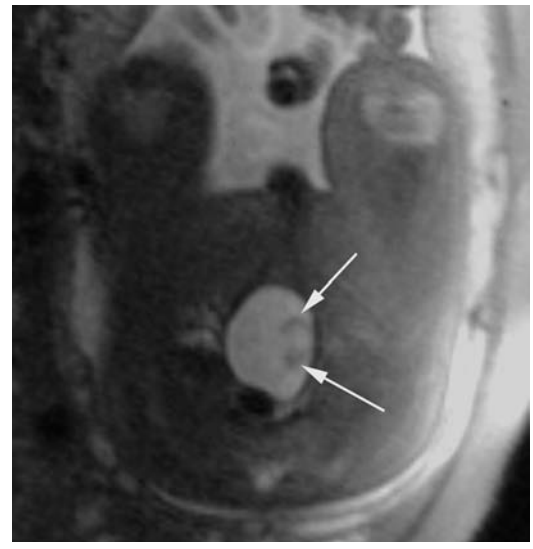

Figure 9.16 Fluid motion in the bladder. Transverse view of the bladder in fetus at 22 weeks gestation. Note the loss of signal (arrow) due to jet of urine entering the bladder from the ureter.

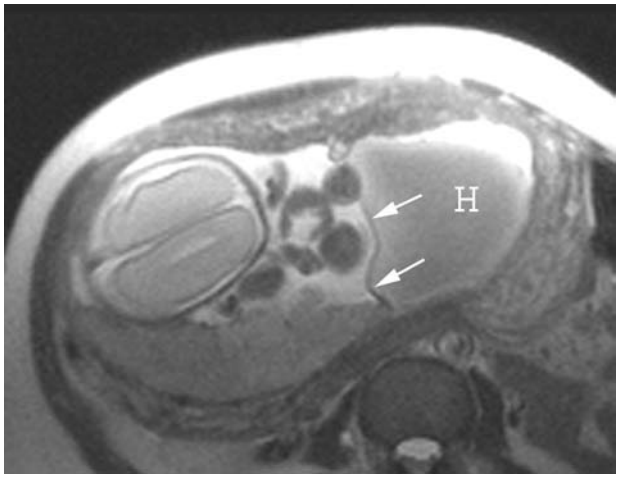

Figure 9.17 Pitfall of fluid motion: dark fluid due to blood products. Transverse T_2-weighted image shows dark fluid in the left aspect of the uterus. The raised chorion (arrows) separates this collection from the amniotic fluid. This is a large hematoma (H) caused by abruption.

(Fig. 9.18) (6,54). More frequently, an extremity will move out of the image plane during sequence acquisition and thus will not be visualized.

Aliasing

Aliasing of the image occurs when the FOV in the phase encode direction is smaller than the anatomy that is being imaged. When this occurs, anatomic structures that extend outside the FOV in the phase encode direction appear to "wrap around" into the opposite side of the image. Depending on the anatomy and the placement of the FOV, the aliased anatomy may overlie and obscure anatomy of interest. This artifact occurs because tissue outside the FOV still gives signal during readout, but it has acquired a phase identical to a position inside the FOV. As spatial position is determined from the phase of the signal emitted by the tissue, all signal with the same phase will be displayed in the same position inside the FOV (55). The simplest way to eliminate aliasing artifact is to increase the FOV so that it contains all the anatomy. The tradeoff is reduced in-plane resolution. For fetal imaging, it is best to use the smallest FOV that permits imaging of the anatomy of interest (Fig. 9.19) so that resolution is maximized.

Susceptibility Artifact

Susceptibility artifact is caused by inhomogeneities in the main magnetic field (B_0), resulting in localized

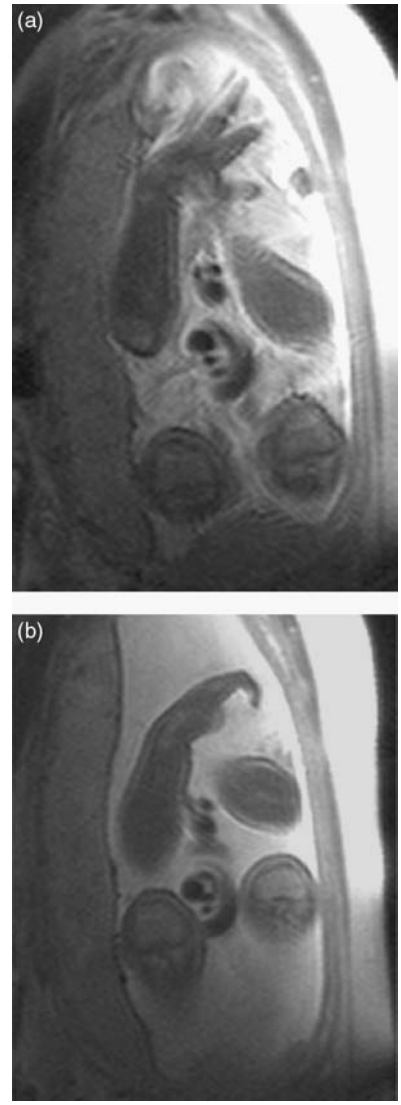

Figure 9.18 Two sequential images of the fetal hand at 32 weeks gestation. Moving extremities can cause either a structure to be visualized twice or not visualized at all. In this case the same hand is seen twice: open with fingers extended in (a) and is in a more relaxed position in (b). [From Levine et al. (54)]

distortions of the geometry or intensity of the image. Spatial distortion results when gradients in B_0 vary over scales that span many voxels. These changes in B_0 cause the spins in different voxels to have slightly different precession frequencies. Spatial position is encoded by the precessional frequency of the spins, so these alterations in frequency can make the signal from spins in one location appear to come from a different position (55). Susceptibility artifact is infrequent with RARE imaging, but it can occur (Fig. 9.20). This artifact can be minimized by shimming to improve the

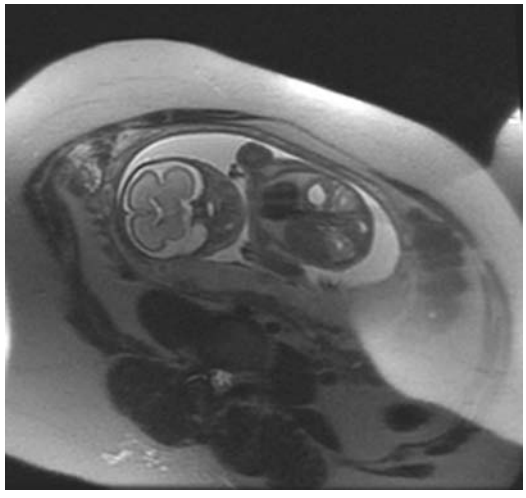

Figure 9.19 Wrap-around artifact. View of fetal head and torso at 22 weeks gestational age. Although the maternal soft tissues wrap around into the gestational sac, they do not overlap the region of the interest, the fetal brain.

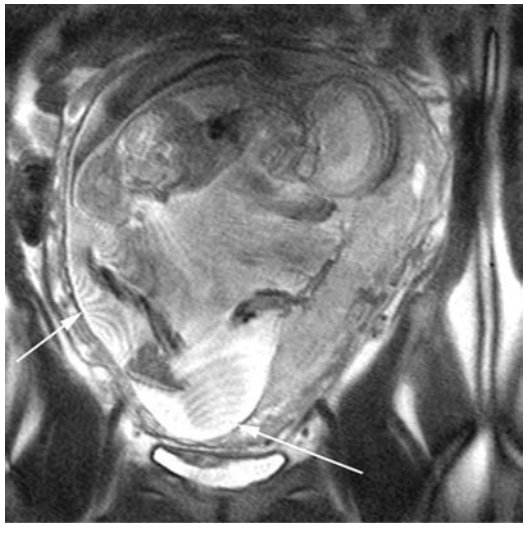

Figure 9.20 Susceptibility artifact. Coronal image through the uterus at 20 weeks gestational age shows multiple geographic areas of increased and decreased signal intensities (arrows) in the amniotic fluid. The pattern of these alternating lines suggests susceptibility artifact. [From Levine et al. (54)]

B_0 homogeneity, increasing readout bandwidth, and/or reducing TE.

Gibbs Artifact

Gibbs ringing (also called truncation) artifact is characterized by alternating bright and dark lines running parallel to a sharp signal interface. These lines diminish quickly away from the boundary causing them (Fig. 9.21).

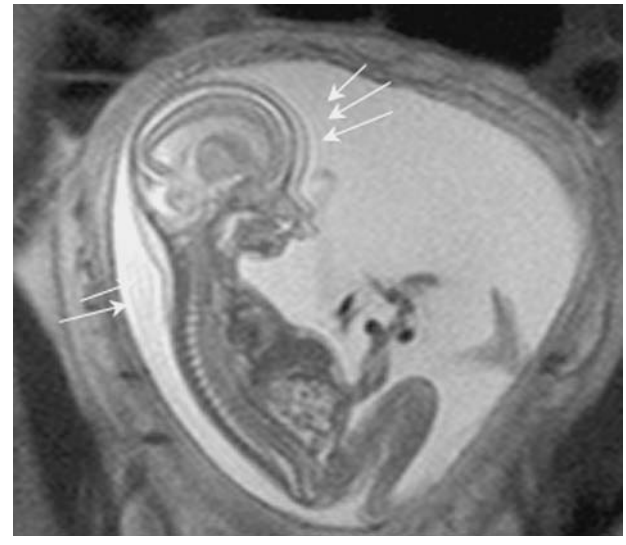

Figure 9.21 Gibbs ringing artifact. A fetus with bilateral cleft lip and palate and a pseudomass in the midline face at 18 weeks gestation. Ripples of high and low signal intensity (arrows) radiating away from the fetal–amniotic fluid interface are a result of Gibbs artifact. [From Levine et al. (54)]

Gibbs ringing occurs when the acquired signal is nonzero at the edges of the acquisition window (55). It is most often observed in low-resolution images where a small acquisition matrix is used. This artifact typically does not limit fetal imaging as long as it is recognized and is not confused with a real structure. Gibbs ringing can be reduced by increasing the resolution of the image or by filtering during image reconstruction. However, increasing resolution will require either longer imaging times or reduced image SNR, while filtering will reduce the resolution of the reconstructed image.

Partial Volume Artifact

Depending on resolution, signal from a single voxel may contain information from multiple anatomic components. The signal of the resulting voxel will be the weighted average of the structures within the voxel which can appear in the image as a loss of resolution because of the averaging of multiple structures. This partial volume effect can be reduced by increasing the resolution of the image, although this comes at the price of increased imaging acquisition time, reduced SNR, or both. In obstetric imaging, this artifact can include structures outside the fetus, for example, in the placenta (Fig. 9.22). Small thin structures surrounded by fluid may not be visualized, such as the wall of an arachnoid cyst surrounded by cerebrospinal fluid or the wall of a myelomeningocele surrounded by amniotic fluid.

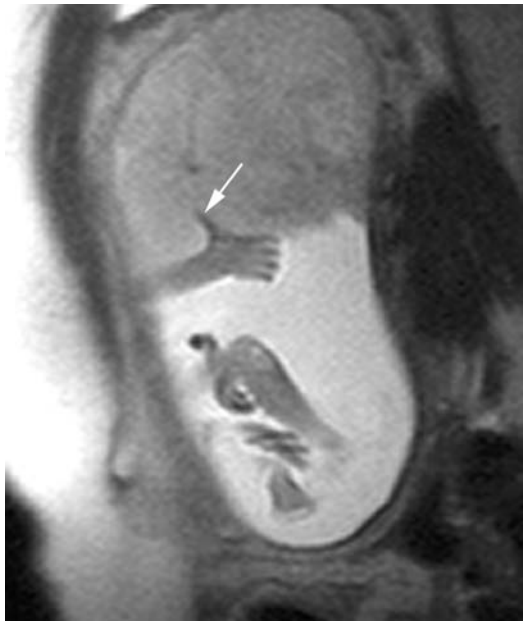

Figure 9.22 Partial volume artifact in a fetus at 19 weeks gestation. This image shows the fetal hand adjacent to the placenta. A prominent vein (arrow) in the placenta looks like a hyperextended thumb. [From Levine et al. (54)]

EMERGING FETAL IMAGING TECHNIQUES

Parallel MR Imaging

Parallel imaging is a recent innovation in MR image reconstruction, in which knowledge of the spatial sensitivity variations of the individual coils in an array is used to perform some of the spatial encoding that would otherwise be done by applying phase encoding gradients. This makes it possible to eliminate some fraction of the phase encodes that would otherwise have to be acquired, thereby reducing the amount of data that need to be acquired before a complete image can be reconstructed. Parallel imaging reconstruction algorithms such as simultaneous acquisition of spatial harmonics (SMASH) (56), sensitivity encoding (SENSE) (57), and others (58–60) are becoming widely available on the most recent generations of commercially available magnets.

The most obvious application of parallel MR imaging is to increase the speed of image acquisition. Parallel MR imaging accelerates data acquisition, making it possible to reduce the motion sensitivity of sequences like T_1-weighted GRE, which must acquire data over timescales long enough to be easily corrupted by motion.

Similarly, application of parallel MR imaging may make it possible to use sequences that would otherwise require too much time to be acquired in a single breath-hold. Three-dimensional imaging sequences require acquisition times $\geq$10 seconds to produce images with useful resolution. While such times are easily achievable within a breath-hold, fetal motion will often corrupt these images (61). If acquisition times for three-dimensional sequences could be reduced by an order of magnitude, robust three-dimensional imaging may become possible. Parallel imaging accelerations of this magnitude have recently been demonstrated for T_1- and T_2-weighted abdominal imaging (62), raising hope that true three-dimensional imaging of the fetus will be possible in the near future.

The trade-off for reduced acquisition times is reduced SNR. In parallel MR imaging the SNR is reduced by at least the square root of the reduction factor. In addition, there is an additional, spatially varying SNR loss (commonly referred to as the *g* factor) that occurs as a function of the direction(s) of the phase encode gradient(s) and the geometry of the coil array used for data acquisition (63,64). The *g*-factor increases super-linearly with the reduction factor, so careful attention must be paid to managing the SNR loss, particularly if large reduction factors are used.

Reductions in acquisition time can be traded off to increase the width of *k*-space that is sampled while acquiring the same number of phase encodes as an unaccelerated acquisition thus increasing the resolution of the final image. It should be noted that the SNR penalties for increasing resolution are more severe than for merely reducing acquisition time, with the SNR falling linearly with the increase in resolution as a result of the reduction in volume of the image voxels.

As fetal imaging tends to be SNR starved, using parallel MR imaging to simply reduce acquisition time or increase resolution is useful only in restricted situations. However, while it is true that accelerating data acquisition results in SNR loss relative to an unaccelerated acquisition, it is possible to use parallel MR imaging to increase the SNR that can be acquired within a given scan time with a given sequence (63). Achieving this increase in SNR efficiency requires judicious tradeoffs between sequence parameters like parallel MR imaging acceleration factor, TR, and flip angle. Where such advantageous tradeoffs can be made, the increased SNR efficiency can be used to help support increases in imaging speed and/or resolution.

There is an additional case where parallel MR imaging may be useful, despite the losses in SNR that it entails. Reductions in the number of phase encodes required to form a given image can result in reductions in certain types of image artifacts, such as those that occur with motion. More subtle improvements can be achieved in sequences like RARE (65,66) or EPI (67,68) that acquire data in trains of echoes. The T_2 decay that occurs during

acquisition of echo trains will cause a widening of the point spread function of the acquired data, and manifest as a blurring of the image in the phase encode direction. This blur increases as the echo train length (ETL) is increased. Using parallel imaging to reduce the length of the echo train used in data acquisition results in a reconstructed image that has higher resolution in the phase encode direction than the equivalent unaccelerated image.

In addition to phase encode blur, EPI acquisitions suffer from geometric distortions caused by phase errors induced by inhomogeneity of the B_0 field. These phase errors increase with ETL with concomitant increases in the magnitude of geometric distortion. By shortening the ETL the phase errors are reduced and the geometric fidelity of the final image will be superior to the unaccelerated image. An example of parallel imaging of the fetus is shown in Fig. 9.23.

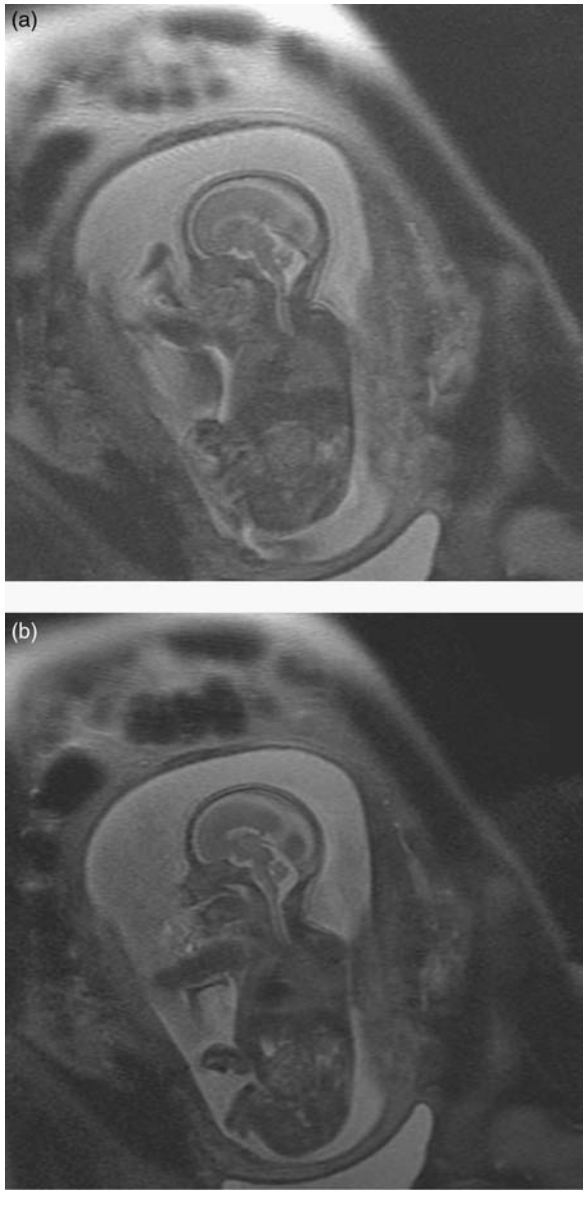

Figure 9.23 Sagittal SSFSE images acquired without and with parallel imaging. Full gradient encoding (a) and twofold acceleration of acquisition using Array Spatial and Sensitivity Encoding Technique (ASSET) (b) sagittal images. In each case the acquisition parameters were single shot TR, TE 90 ms, 360 × 360 mm FOV, 512 × 256 matrix, 4 mm slice thickness. The application of parallel imaging reduced the acquisition time from 20 seconds in (a) to 11 seconds in (b). The image quality of the ASSET accelerated image is comparable to the full encoded image, despite being acquired in roughly half the time.

Real-time Imaging

Real-time imaging techniques that reconstruct and display as quickly as they are acquired are becoming commercially available for both T_1- and T_2-weighted imaging. These techniques are capable of achieving frame rates in excess of one image per second for reasonable (<2 mm/pixel) image resolutions. We have recently started using T_2-weighted real-time imaging based on SSFSE at our institution, and we feel the technique is very promising (Fig. 9.24). While real-time imaging is necessarily limited to displaying a single image at one time, the ability to interactively adjust the scan plane and sequence

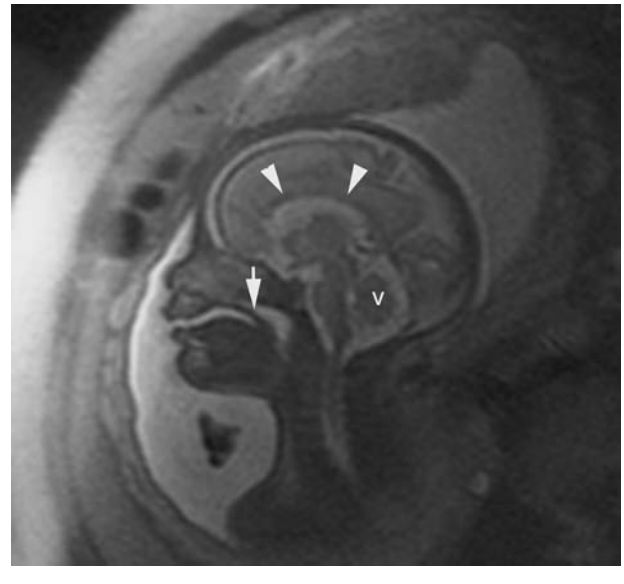

Figure 9.24 Real-time imaging. This sagittal image was obtained using real-time SSFSE (TR 6000 ms, TE 90 ms, 256 × 256 matrix, 360 × 360 mm FOV, 4 mm slice thickness). Real-time SSFSE imaging of the fetus allows for interactive optimization of imaging parameters and slice orientation, and in our experience this results in images of diagnostic quality superior to standard SSFSE imaging. Note the corpus callosum (arrowheads), soft palate (arrow), and vermis of the cerebellum (v).

parameters can be tremendously useful in fetal imaging. With real-time imaging, it is possible to continuously update the scan plane to track motion of the fetus. In addition, the ability to see the effects of adjusting scanning parameters like FOV or TR on image quality in real time makes it possible to precisely tailor the imaging to the particular issue that must be resolved for a particular patient. This has the potential to make fetal MR imaging much more like an interactive ultrasound examination, while taking advantage of the high resolution and contrast that MR imaging provides. With real-time imaging, sequential sagittal images of the fetal head allow for midline views of the corpus callosum, vermis of the cerebellum, and soft palate.

CONCLUSIONS

Fetal MR imaging with current clinically available sequences and hardware has allowed reliable two-dimensional fetal imaging to be performed. Improvements in imaging speed and hardware should make it possible to obtain even higher quality images than currently achievable. Advances such as parallel MR imaging and real-time imaging that are just now becoming available may allow fetal imaging to finally break out of its current paradigm of imaging of limited sets of preselected two-dimensional slices.

REFERENCES

1. Yamashita Y, Namimoto T, Abe Y et al. MR imaging of the fetus by a HASTE sequence. Am J Roentgenol 1997; 168:513–519.
2. Levine D, Hatabu H, Gaa J et al. Fetal anatomy revealed with fast MR sequences. Am J Roentgenol 1996; 167:905–908.
3. Levine D, Edelman RR. Fast MRI and its application in obstetrics. Abdom Imaging 1997; 22:589–596.
4. Tsuchiya K, Katase S, Seki T et al. Short communication: MR imaging of fetal brain abnormalities using a HASTE sequence. Br J Radiol 1996; 69:668–670.
5. Levine D, Barnes PD, Madsen JR et al. Fetal central nervous system anomalies: MR imaging augments sonographic diagnosis. Radiology 1997; 204:635–642.
6. Levine D, Barnes PD, Sher S et al. Fetal fast MR imaging: reproducibility, technical quality, and conspicuity of anatomy. Radiology 1998; 206:549–554.
7. Levine D, Barnes PD, Edelman RR. Obstetric MR imaging. Radiology 1999; 211:609–617.
8. Hubbard AM, Harty MP, States LJ. A new tool for prenatal diagnosis: ultrafast fetal MRI. Semin Perinatol 1999; 23:437–447.
9. Sonigo PC, Rypens FF, Carteret M et al. MR imaging of fetal cerebral anomalies. Pediatr Radiol 1998; 28:212–222.
10. Garel C, Brisse H, Sebag G et al. Magnetic resonance imaging of the fetus. Pediatr Radiol 1998; 28:201–211.
11. Baker PN, Johnson IR, Harvey PR et al. A three-year follow-up of children imaged *in utero* with echo-planar magnetic resonance. Am J Obstet Gynecol 1994; 170:32–33.
12. Chew S, Ahmadi A, Goh PS et al. The effects of 1.5 T magnetic resonance imaging on early murine *in-vitro* embryo development. J Magn Reson Imaging 2001; 13:417–420.
13. Kanal E, Gillen J, Evans JA et al. Survey of reproductive health among female MR workers. Radiology 1993; 187:395–399.
14. Levine D, Zuo C, Faro CB et al. Potential heating effect in the gravid uterus during MR HASTE imaging. J Magn Reson Imaging 2001; 13:856–861.
15. Myers C, Duncan KR, Gowland PA et al. Failure to detect intrauterine growth restriction following in utero exposure to MRI. Br J Radiol 1998; 71:549–551.
16. Wolff S, Crooks LE, Brown P et al. Tests for DNA and chromosomal damage induced by nuclear magnetic resonance imaging. Radiology 1980; 136:707–710.
17. Schwartz JL, Crooks LE. NMR imaging produces no observable mutations or cytotoxicity in mammalian cells. Am J Roentgenol 1982; 139:583–585.
18. Weinreb JC, Lowe T, Cohen JM et al. Human fetal anatomy: MR imaging. Radiology 1985; 157:715–720.
19. Powell MC, Worthington BS, Buckley JM et al. Magnetic resonance imaging (MRI) in obstetrics. II. Fetal anatomy. Br J Obstet Gynaecol 1988; 95:38–46.
20. Smith FW, Adam AH, Phillips WD. NMR imaging in pregnancy. Lancet 1983; 1:61–62.
21. Roemer PB, Edelstein WA, Hayes CE et al. The NMR phased array. Magn Reson Med 1990; 16:192–225.
22. Paschal CB, Morris HD. K-space in the clinic. J Magn Reson Imaging 2004; 19:145–159.
23. Chen Q, Levine D. Fast fetal magnetic resonance imaging techniques. Top Magn Reson Imaging 2001; 12:67–79.
24. Hennig J. *k*-space sampling strategies. Eur Radiol 1999; 9:1020–1031.
25. Duerk JL. Principles of MR image formation and reconstruction. Magn Reson Imaging Clin N Am 1999; 7:629–659.
26. Lan LM, Yamashita Y, Tang Y et al. Normal fetal brain development: MR imaging with a half-Fourier rapid acquisition with relaxation enhancement sequence. Radiology 2000; 215:205–210.
27. Coakley FV, Lopoo JB, Lu Y et al. Normal and hypoplastic fetal lungs: volumetric assessment with prenatal single-shot rapid acquisition with relaxation enhancement MR imaging. Radiology 2000; 216:107–111.
28. Mansfield P, Stehling MK, Ordidge RJ et al. Echo planar imaging of the human fetus in utero at 0.5 T. Br J Radiol 1990; 63:833–841.
29. Johnson IR, Stehling MK, Blamire AM et al. Study of internal structure of the human fetus in utero by echo-planar magnetic resonance imaging. Am J Obstet Gynecol 1990; 163:601–607.
30. Stehling MK, Mansfield P, Ordidge RJ et al. Echo-planar imaging of the human fetus in utero. Magn Reson Med 1990; 13:314–318.
31. Moore RJ, Strachan B, Tyler DJ et al. *In vivo* diffusion measurements as an indication of fetal lung maturation using echo planar imaging at 0.5 T. Magn Reson Med 2001; 45:247–253.

32. Baker PN, Johnson IR, Gowland PA et al. Measurement of fetal liver, brain and placental volumes with echo-planar magnetic resonance imaging. Br J Obstet Gynaecol 1995; 102:35–39.
33. Baker PN, Johnson IR, Gowland PA et al. Estimation of fetal lung volume using echo-planar magnetic resonance imaging. Obstet Gynecol 1994; 83:951–954.
34. Baker PN, Johnson IR, Gowland PA et al. Fetal weight estimation by echo-planar magnetic resonance imaging. Lancet 1994; 343:644–645.
35. Duncan KR, Gowland PA, Moore RJ et al. Assessment of fetal lung growth in utero with echo-planar MR imaging. Radiology 1999; 210:197–200.
36. Duncan KR, Gowland PA, Johnson IR et al. Normal fetal and placental growth defined using echo-planar MRI. J Soc Gynecol Invest 1999; 6:89A.
37. Duncan KR. Fetal and placental volumetric and functional analysis using echo-planar imaging. Top Magn Reson Imaging 2001; 12:52–66.
38. Trop I, Levine D. Hemorrhage during pregnancy: sonography and MR imaging. Am J Roentgenol 2001; 176:607–615.
39. Bradley WG Jr. MR appearance of hemorrhage in the brain. Radiology 1993; 189:15–26.
40. Leung JW, Coakley FV, Hricak H et al. Prenatal MR imaging of congenital diaphragmatic hernia. Am J Roentgenol 2000; 174:1607–1612.
41. Girard N, Raybaud C, Poncet M. *In vivo* MR study of brain maturation in normal fetuses. Am J Neuroradiol 1995; 16:407–413.
42. Dixon WT. Simple proton spectroscopic imaging. Radiology 1984; 153:189–194.
43. Oppelt A, Graumann R, Barfuss H et al. FISP—A new fast MRI sequence. Electromedica 1986; 54:15–18.
44. van der Meulen P, Groen JP, Tinus AM et al. Fast field echo imaging: an overview and contrast calculations. Magn Reson Imaging 1988; 6:355–368.
45. Sekihara K, Kohno H. Image restoration from nonuniform static field influence in modified echo-planar imaging. Med Phys 1987; 14:1087–1089.
46. Duerk JL, Lewin JS, Wendt M et al. Remember true FISP? A high SNR, near 1-second imaging method for T2-like contrast in interventional MRI at 2 T. J Magn Reson Imaging 1998; 8:203–208.
47. Sekihara K. Steady-state magnetizations in rapid NMR imaging using small flip angles and short repetition intervals. IEEE Trans Med Imaging 1987; 6:157–164.
48. Reeder SB, Herzka DA, McVeigh ER. Signal-to-noise ratio behavior of steady-state free precession. Magn Reson Med 2004; 52:123–130.
49. Zur Y, Stokar S, Bendel P. An analysis of fast imaging sequences with steady-state transverse magnetization refocusing. Magn Reson Med 1988; 6:175–193.
50. Chung HW, Chen CY, Zimmerman RA et al. T_2-weighted fast MR imaging with true FISP versus HASTE: comparative efficacy in the evaluation of normal fetal brain maturation. Am J Roentgenol 2000; 175:1375–1380.
51. Foo TK, Sawyer AM, Faulkner WH et al. Inversion in the steady state: contrast optimization and reduced imaging time with fast three-dimensional inversion–recovery–prepared GRE pulse sequences. Radiology 1994; 191:85–90.
52. Reeder SB, McKenzie CA, Shimakawa A et al. Parallel cardiac CINE imaging: application to "Dixon" water–fat separation and steady-state free precession. Proceedings of the International Society for Magnetic Resonance of Medicine, 2004.
53. Huang TY, Chung HW, Wang FN et al. Fat and water separation in balanced steady-state free precession using the Dixon method. Magn Reson Med 2004; 51:243–247.
54. Levine D, Smith AS, McKenzie C. Tips and tricks of fetal MR imaging. Radiol Clin North Am 2003; 41:729–745.
55. Haacke EM, Brown RW, Thompson MR et al. Magnetic Resonance Imaging: Physical Principles and Design. New York: Wiley-Liss, 1999.
56. Sodickson DK, Griswold MA, Edelman RR et al. Simultaneous acquisition of spatial harmonics (SMASH): ultra-fast imaging with RF coil arrays. In: Oudkerk M, Edelman RR, eds. High-power Gradient MR-imaging: Advances in MRI II. Berlin: Blackwell Wissenschafts-Verlag, 1997:381–386.
57. Pruessmann KP, Weiger M, Scheidegger MB et al. SENSE: sensitivity encoding for fast MRI. Magn Reson Med 1999; 42:952–962.
58. Griswold MA, Jakob PM, Heidemann RM et al. Generalized autocalibrating partially parallel acquisitions (GRAPPA). Magn Reson Med 2002; 47:1202–1210.
59. Sodickson DK, McKenzie CA. A generalized approach to parallel magnetic resonance imaging. Med Phys 2001; 28:1629–1643.
60. Bydder M, Larkman DJ, Hajnal JV. Generalized SMASH imaging. Magn Reson Med 2002; 47:160–170.
61. Levine D. Three-dimensional fetal MR imaging: will it fulfill its promise? Radiology 2001; 219:313–315.
62. Zhu Y, Hardy CJ, Sodickson DK et al. Highly parallel volumetric imaging with a 32-element RF coil array. Magn Reson Med 2004; 52:869.
63. Weiger M, Pruessmann KP, Leussler C et al. Specific coil design for SENSE: a six-element cardiac array. Magn Reson Med 2001; 45:495–504.
64. Ohliger MA, Grant AK, Sodickson DK. Ultimate intrinsic signal-to-noise ratio for parallel MRI: electromagnetic field considerations. Magn Reson Med 2003; 50:1018–1030.
65. Griswold MA, Jakob PM, Chen Q et al. Resolution enhancement in single-shot imaging using simultaneous acquisition of spatial harmonics (SMASH). Magn Reson Med 1999; 41:1236–1245.
66. Heidemann RM, Griswold MA, Kiefer B et al. Resolution enhancement in lung 1H imaging using parallel imaging methods. Magn Reson Med 2003; 49:391–394.
67. Preibisch C, Pilatus U, Bunke J et al. Functional MRI using sensitivity-encoded echo planar imaging (SENSE-EPI). Neuroimage 2003; 19:412–421.
68. Bammer R, Keeling SL, Augustin M et al. Improved diffusion-weighted single-shot echo-planar imaging (EPI) in stroke using sensitivity encoding (SENSE). Magn Reson Med 2001; 46:548–554.

10

MR Imaging Before Fetal Surgery: Contribution to Management

BONNIE N. JOE, FERGUS V. COAKLEY

INTRODUCTION

Over the past decades, an increasing number of congenital anomalies have become amenable to prenatal treatment. Pioneering studies conducted on pregnant sheep and monkeys at the University of California Fetal Treatment Center have been critical to the development of fetal surgery (1). Fetal surgery is a new and rapidly evolving specialty that carries considerable maternal risks. Complications of both open and laparoscopic surgeries through the pregnant uterus include preterm labor and amniotic fluid leak. More recently, use of endoscopic techniques has reduced the incidence and severity of preterm labor and amniotic fluid leak, but postprocedural chorioamniotic separation remains an unsolved problem; the umbilical cord or fetal extremities can become entangled in and compromised by frayed and detached membranes (2).

Given the maternal risks involved, fetal surgery was initially reserved for cases in which a life-threatening fetal abnormality could only be reversed by prenatal intervention. The emergence of increasingly safe minimally invasive techniques has raised the question of whether certain selected nonlethal reversible anomalies should also be considered for fetal intervention (3). Currently, common indications for fetal surgery include life-threatening anomalies such as congenital diaphragmatic hernia, cystic adenomatoid malformation, sacrococcygeal teratoma, twin–twin transfusion syndrome, and upper airway obstruction. Myelomeningocele is one of the few current nonlethal indications for fetal intervention, although prenatal surgery for this indication remains controversial.

Ultrasound remains the primary imaging modality for fetal assessment. However, drawbacks such as limited acoustic contrast between soft tissue structures and small field of view can occasionally yield inconclusive results. Particularly in cases where fetal surgery is a consideration, ultrasound alone may be insufficient to guide treatment choices because an extremely high level of diagnostic certainty is required before embarking on such a high-risk procedure. A complementary imaging technique such as magnetic resonance (MR) imaging is desirable. In a study conducted at the University of California, San Francisco, MR findings directly impacted management in 16% of pregnant women with complex fetal abnormalities detected sonographically (Fig. 10.1) (4,5). MR imaging prior to fetal surgery remains a developing application performed in only a small number of academic centers. This chapter focuses on cases in which prenatal MR imaging is useful for fetal surgical planning.

UPPER AIRWAY OBSTRUCTION

Neck Masses

Congenital obstruction of the upper airway is usually due to extrinsic compression by a large neck mass, commonly by a lymphangioma or teratoma (Fig. 10.2). For these cases, prenatal MR imaging is a useful adjunct in treatment planning to evaluate tumor extent, facial involvement, and relationship of the mass to the trachea (Fig. 10.3). Although both lymphangioma and teratoma can appear cystic or solid on imaging, demonstration of a predominantly solid tumor or a cystic tumor with solid nodules favors the diagnosis of teratoma. Intrathoracic extension of tumor favors the diagnosis of lymphangioma (6).

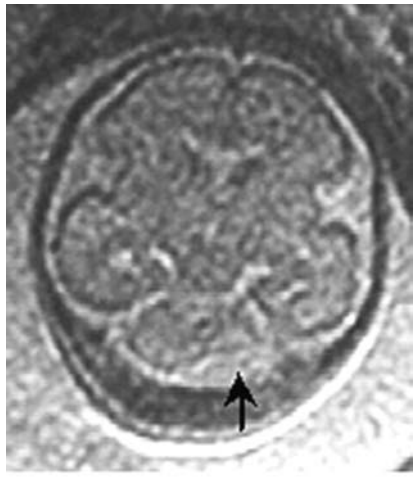

Figure 10.1 Fetus with congenital diaphragmatic hernia diagnosed by prenatal ultrasound being considered for *in utero* surgery. Axial T_2-weighted 4 mm section through the fetal brain obtained at 25 weeks gestation demonstrates unilateral cerebellar deficiency (arrow). The presence of an associated anomaly is a contraindication to fetal surgery for CDH and no intervention was performed. Spontaneous delivery was followed by early demise.

Lymphangiomas are often complicated by hydrops, presumably related to the compression of neck vessels.

Congenital High Airway Obstruction Syndrome

Congenital high airway obstruction syndrome (CHAOS) is a rare intrinsic obstruction of the larynx or upper trachea.

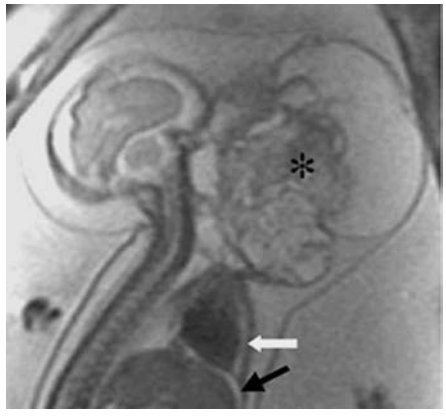

Figure 10.2 Giant cervical teratoma in a fetus at 28 weeks gestational age. Sagittal T_2-weighted 4 mm section of the cervicofacial region demonstrates a large anterior neck mass (asterisk) that obliterated all normal facial structures below the level of the orbits. Note pleural effusion (white arrow), ascites (black arrow), and generalized subcutaneous edema. After parental counseling, pregnancy was electively terminated.

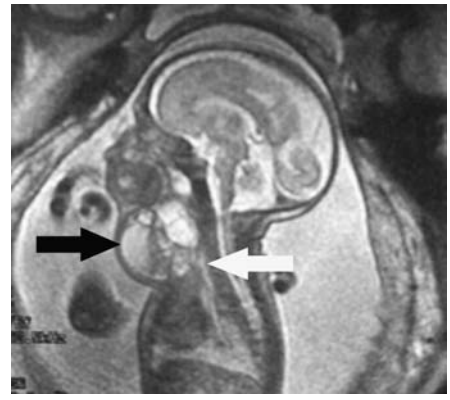

Figure 10.3 Cervical teratoma in a fetus at 26 weeks gestation. Sagittal T_2-weighted 4 mm section of the cervicofacial region demonstrates a large anterior neck mass (black arrow). The airway (white arrow) below the mass is visible, and is not dilated. The fetus was successfully delivered by the EXIT procedure, and the mass was resected postnatally.

With upper airway obstruction, bronchial secretions are retained causing pulmonary distention by the retained fluid. Associated hydrops is felt to be secondary to impaired venous return to the heart from inversion of the diaphragm as the lungs become overdistended with retained fluid. The consequent characteristic constellation of imaging findings includes flattening or inversion of the diaphragm, dilated fluid-filled airways below the level of obstruction and hydrops or ascites. Prenatal MR is useful to confirm the diagnosis of CHAOS prior to surgical treatment (Fig. 10.4).

Ex utero Intrapartum Treatment Procedure

The *ex utero* intrapartum treatment (EXIT) procedure was originally developed as an airway management technique to reverse temporary tracheal occlusion used in fetal surgery procedures for treatment of severe congenital diaphragmatic hernia. It has also proven useful for management of other causes of airway obstruction including large neck masses (Fig. 10.3) and CHAOS (Fig. 10.4) (4,7,8). The EXIT procedure maintains the fetus on maternal uteroplacental support to provide a window of time for surgeons to perform procedures such as tracheotomy or surgical resection of obstructing neck masses in a controlled fashion. Through inhalational agents given to the mother to relax uterine tone and continuous amnioinfusion to maintain stable uterine volume, uteroplacental gas exchange, and blood flow can be maintained for up to an hour, thus converting a crisis situation into a controlled delivery with time for airway management (9).

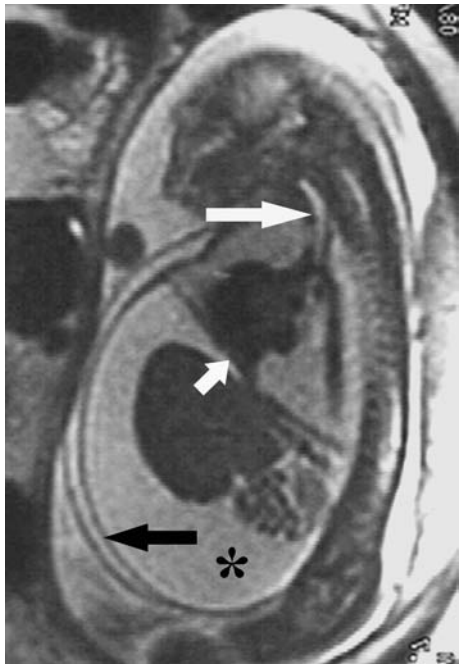

Figure 10.4 Congenital high airway obstruction syndrome in a fetus at 25 weeks gestational age. Congenital high airway obstruction syndrome was suspected at prenatal ultrasound because of large lungs with diaphragmatic inversion and hydrops, although dilated airways were not seen. Oblique longitudinal T_2-weighted 4 mm section of the fetal torso confirms diaphragmatic inversion (short white arrow), with a marked volume of fetal ascites (*), subcutaneous edema (black arrow), and a blind-ending fluid-filled upper airway (long white arrow). These findings are consistent with CHAOS. The fetus subsequently underwent *in utero* tracheostomy and was successfully delivered. Postnatal assessment demonstrated a focal web in the larynx, without laryngeal atresia.

THORACIC ANOMALIES

Congenital Cystic Adenomatoid Malformation

Congenital cystic adenomatoid malformation (CCAM) is composed of a proliferation of terminal bronchioles. The lesion typically derives blood supply from the pulmonary arteries and may communicate with the bronchial tree or gastrointestinal tract. On MR images, CCAMs typically appear as intrapulmonary masses of increased T_2 signal intensity (Fig. 10.5). Discrete cysts of fluid T_2 signal intensity will be seen in macrocystic CCAMs whereas microcystic CCAMs (composed of numerous tiny cysts) are not as bright as fluid but appear brighter than the adjacent lung.

Prenatally detected CCAMs, especially microcystic CCAMs, should be followed closely as they can enlarge to compress the esophagus, vena cava, and lungs resulting in polyhydramnios or hydrops. Development of polyhydramnios or hydrops in an immature fetus is an indication for prenatal resection. MR imaging can provide large field of view images for localizing the CCAM prior to surgery.

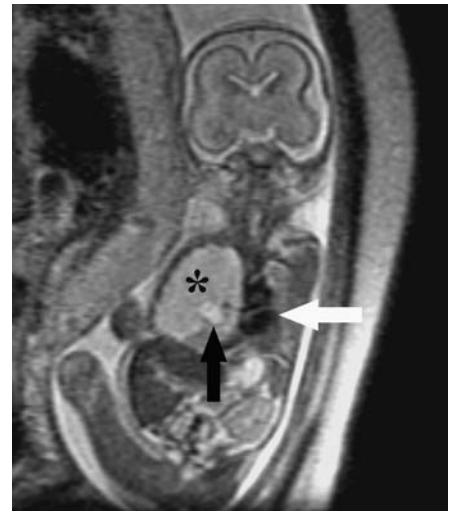

Figure 10.5 Congenital cystic adenomatoid malformation in a fetus at 21 weeks gestational age. T_2-weighted 4 mm oblique coronal section shows a large high signal mass (asterisk) in the right chest causing mediastinal shift of the heart (white arrow) to the left. A 0.8 cm macrocyst (black arrow) can be seen near the right hilum.

Congenital Diaphragmatic Hernia

As the name implies, congenital diaphragmatic hernia (CDH) is a developmental defect in the diaphragm with herniation of abdominal viscera into the thorax. Morbidity and mortality in isolated CDH is due to pulmonary hypoplasia secondary to mechanical compression. Temporary tracheal occlusion, currently performed endoscopically rather than by open fetal surgery, has been shown to be beneficial in selected cases (10). Tracheal occlusion is believed to promote lung growth by the retention of bronchial secretions.

Prenatal MR imaging has multiple roles in the evaluation of CDH. Prenatal MR imaging can be used to confirm the presence of CDH prior to surgery when ultrasound is equivocal. Magnetic resonance imaging can also detect any associated structural abnormalities that would be a contraindication to fetal surgery. The excellent soft tissue contrast of MR imaging allows easier assessment of liver position in left-sided CDH as compared to ultrasound. On ultrasound, lung and liver are of intermediate-to-similar echogenicity. In contrast, lung is of low T_1 and intermediate-to-high T_2 signal intensity whereas liver is of high T_1 and low T_2 signal intensity on MR images (Figs. 10.6 and 10.7). Determination of liver position is important because "liver-up"

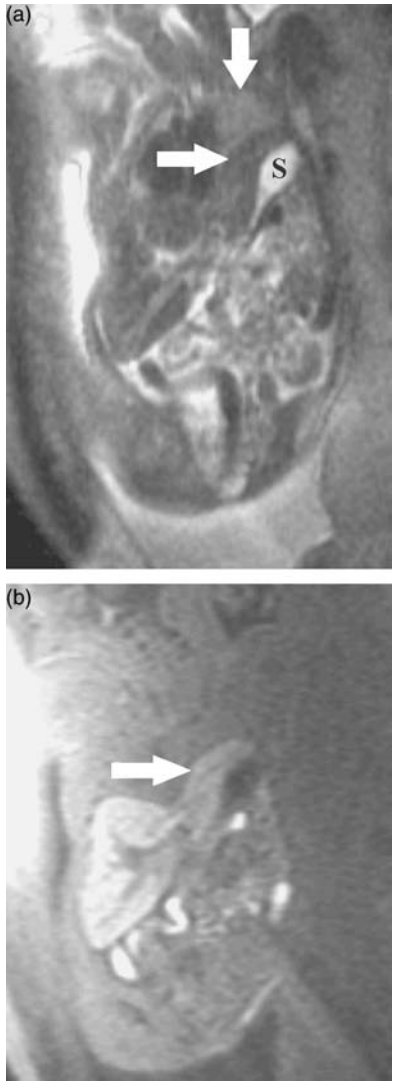

Figure 10.6 Left-sided "liver-up" CDH in a fetus at 24 weeks gestation. (a) Coronal T_2-weighted 4 mm section shows upward herniation of left hepatic lobe (horizontal arrow) superior to the herniated stomach (S). Note the dark T_2 signal of the liver compared with the higher T_2 signal of the lung (vertical arrow). (b) Corresponding coronal T_1-weighted 5 mm section shows upward herniation of left hepatic lobe (arrow). Note the high signal intensity of the liver, which makes it easy to identify on T_1-weighted images.

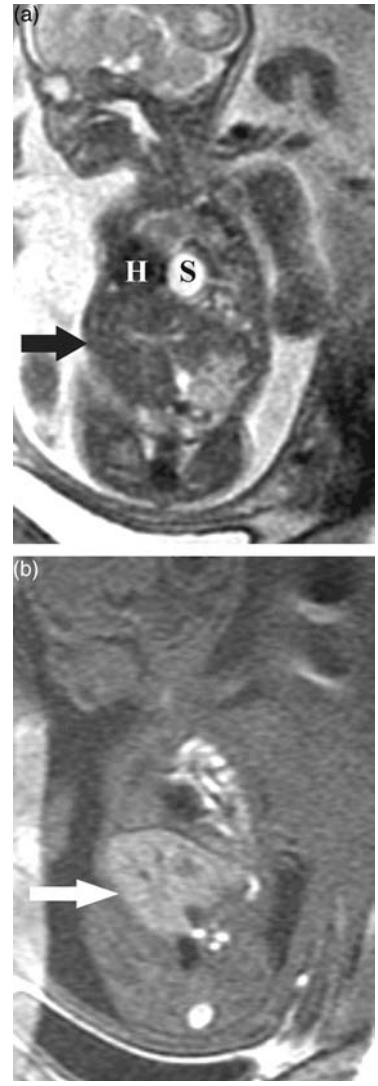

Figure 10.7 Left-sided "liver-down" CDH in a fetus at 21 weeks gestation. (a) Coronal T_2-weighted 4 mm section shows the liver (arrow), which is of low T_2 signal intensity, to be entirely within the abdomen. The heart (H) is shifted to the right by the herniated abdominal contents, including the stomach (S). (b) Corresponding coronal T_1-weighted 5 mm section confirms that liver (arrow), which is of high T_2 signal intensity, is entirely within the abdomen.

or "liver-down" CDHs carry respective mortalities of 57% and 7% (11,12). Given the relatively good prognosis for liver-down CDHs, affected fetuses are not candidates for prenatal surgery. Finally, MR imaging can directly measure lung volume in CDH (Fig. 10.8) as opposed to the indirect measurement of lung-to-head ratio performed with ultrasound (13). Magnetic resonance imaging is also potentially useful for monitoring lung growth after fetal surgery (Fig. 10.9) (13,14).

ABDOMINOPELVIC DISEASE

Sacrococcygeal Teratoma

Sacrococcygeal teratoma is the most common neonatal tumor (15). Although neonatal sacrococcygeal teratomas have a good prognosis, large sacrococcygeal teratomas in the fetus can cause high-output cardiac failure leading to hydrops and fetal demise. Thus, fetal interventions such as amnio reduction, cyst aspiration, and surgical

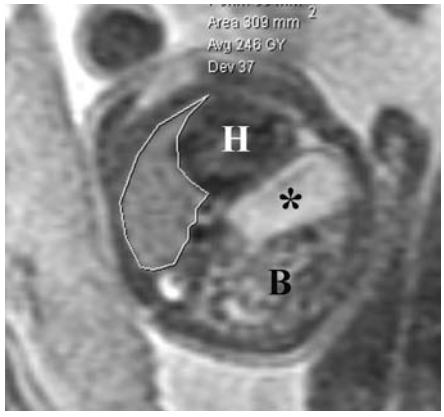

Figure 10.8 Left sided CDH in a fetus at 26 weeks gestational age. Axial T_2-weighted 4 mm section shows the principle of lung volumetry. The right lung has been outlined to calculate the lung cross-sectional area. The heart (H), herniated stomach (*), and herniated bowel (B) are also visible on this section. Lung volume for the section is the area multiplied by slice thickness. Total lung volume is calculated by summing the volumes of all slices on which lung tissue is visible.

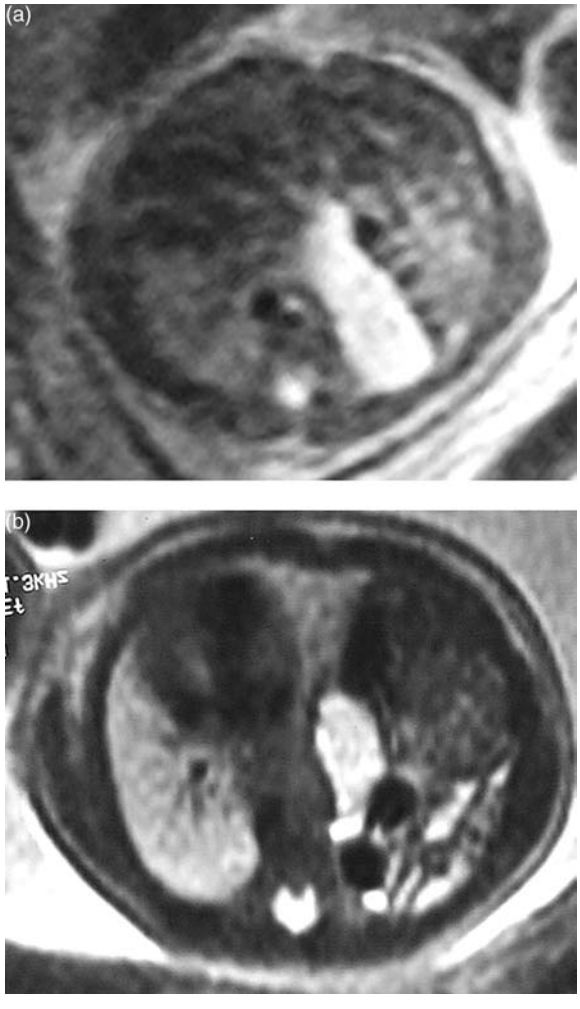

Figure 10.9 Congenital diaphragmatic hernia before and after surgery. (a) Axial T_2-weighted 4 mm section through the chest in a fetus at 23 weeks gestation with congenital diaphragmatic hernia. Total lung volume measured by planimetry was 5.0 cc with a relative lung volume of 20%. (b) After treatment by tracheal occlusion at 26 weeks gestation, axial T_2-weighted 4 mm section obtained at 30 weeks gestation demonstrates increase in lung volume. Total lung volume measured by planimetry was 26.9 cc with a relative lung volume of 43%. This fetus survived postnatally.

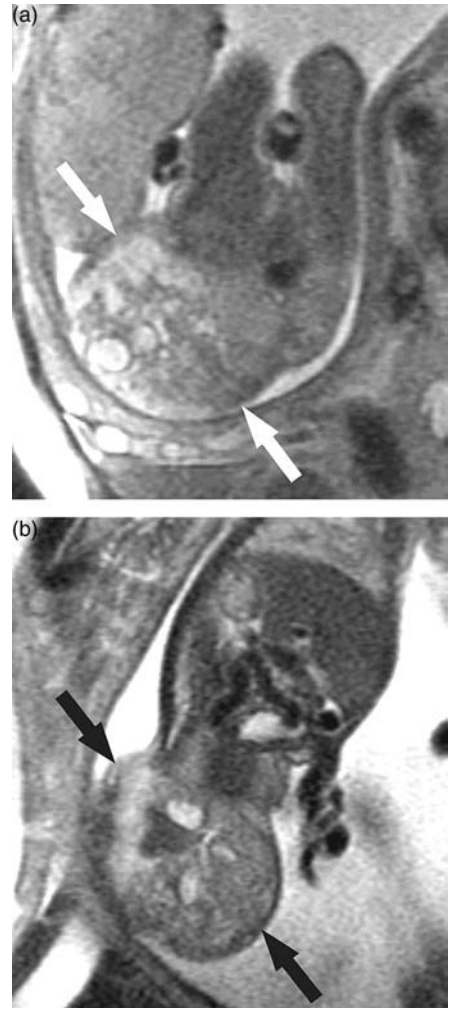

Figure 10.10 Sacrococcygeal teratoma. T_2-weighted 4 mm axial (a) and coronal (b) sections. A large sacrococcygeal solid and cystic tumor is seen extending inferiorly from the pelvis (arrows).

debulking have been attempted in immature fetuses with large sacrococcygeal teratomas who develop hydrops (16). Prenatal MR imaging is useful to demonstrate sacrococcygeal teratomas and to assess intrapelvic extent (Fig. 10.10). With a large intrapelvic component, there is

a greater risk of treatment-related damage to pelvic and perineal structures related to devascularization. MR imaging can also be used to assess tumor volume in response to treatment.

NEUROLOGIC ANOMALIES

Myelomeningocele

Although myelomeningocele is a nonlethal condition, animal studies have suggested that prenatal closure or covering of the myelomeningocele may be therapeutically beneficial (17). In a sheep model, exposure of the spinal cord caused neurological impairment that was ameliorated by placing a musculocutaneous flap over the exposed cord *in utero*, (18,19) suggesting that amniotic fluid or contact with the uterine wall causes damage to the exposed spinal cord. Prenatal closure of myelomeningocele in humans has also been shown to ameliorate hindbrain herniation (20,21). Subsequent work on fetal sheep has suggested that cerebellar herniation in myelomeningocele is the result of altered cerebral spinal fluid hydrodynamics related to the leakage of cerebrospinal fluid through the exposed central canal (22). Prenatal closure of the myelomeningocele also reversed hindbrain herniation in the sheep model. Despite these encouraging results, the appropriateness of fetal surgery for myelomeningocele remains controversial as myelomeningocele is a nonfatal abnormality and controlled clinical trials demonstrating objective evidence of efficacy are not yet available. Nevertheless, myelomeningocele and the associated Chiari malformation are well demonstrated by prenatal MR imaging and can provide a baseline for comparison with the postoperative appearances (Fig. 10.11). Ultrasound remains the technique of choice for assessment of the affected spinal levels because individual vertebrae currently are difficult to distinguish on MR imaging.

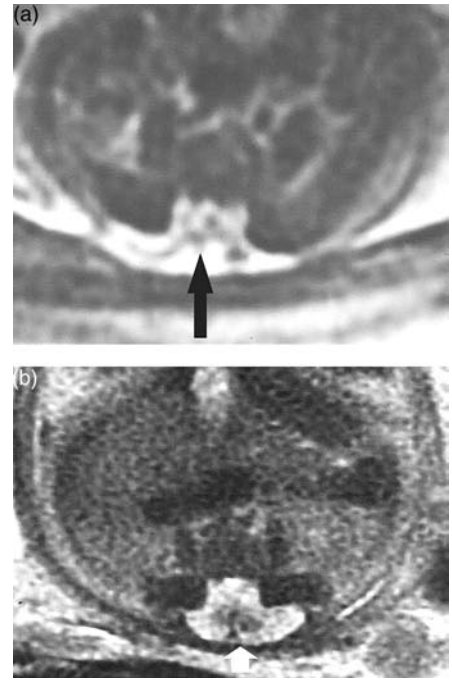

Figure 10.11 Myelomeningocele in a fetus at 23 and 32 weeks gestation. (a) T_2-weighted 4 mm axial section of the spine shows the cord defect and neural placode (arrow). (b). After fetal surgical closure of the myelomeningocele the change in the configuration of the defect secondary to interval surgery is evident (arrow).

COMPLICATED TWIN PREGNANCIES

In general, twin pregnancies carry substantially higher morbidity and mortality compared with singleton pregnancies. Monochorionic twins in particular are subject to several specific complications that may be indications for fetal intervention: twin–twin transfusion syndrome, twin embolization syndrome, acardiac syndrome, and conjoined twinning. These are discussed in more detail in Chapter 8.

Twin–Twin Transfusion Syndrome

In twin–twin transfusion syndrome, abnormal placental vascular communications in the shared placenta results in unequal distribution of blood to the two fetuses. The recipient twin gets too much blood and may die of heart failure whereas the donor twin suffers hypovolemia, oligohydramnios, and intrauterine growth restriction (Fig. 8.10). Progression of the donor to a "stuck twin" with anhydramnios and a recipient twin with hydrops and polyhydramnios carries a dismal prognosis and is an indication for fetal therapy. Aggressive volume reduction amniocentesis of the polyhydramniotic sac is the least invasive treatment with a 37% survival rate reported (23). Riskier therapy is endoscopic guided laser ablation of the abnormal vascular channels. The main role for prenatal MR imaging in this situation is to detect parenchymal brain disease and in particular to establish a baseline prior to intervention.

Conjoined Twins

Conjoined twins result from late and incomplete division of the monozygotic embryo. Prenatal MR imaging may be performed before delivery to assess anatomy for postnatal surgery. After delivery, the twins may be dependent on supportive devices that would interfere with imaging. MR imaging has advantages over ultrasound with a

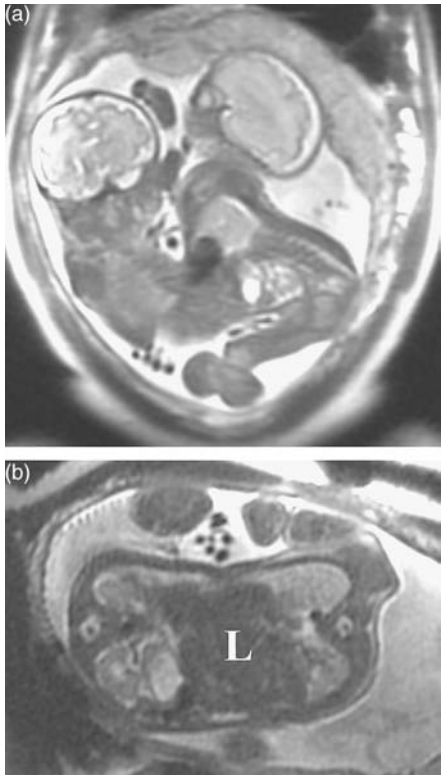

Figure 10.12 Thoraco-omphalopagus conjoined twins at 29 weeks gestation. Sagittal (a) and axial (b) T_2-weighted 6 mm section of the conjoined twins show both twins in the field of view, facilitating understanding of the anatomy by clinicians. Note the conjoined liver (L).

larger field of view capable of depicting both twins simultaneously, and superior tissue contrast to assess visceral organ fusion (Fig. 10.12). Fetal echocardiography is still required for cardiac evaluation; however, individual cardiac chambers typically cannot be resolved and the current temporal resolution of MR does not allow assessment of fetal cardiac function.

CONCLUSION

Fetal surgery remains a risky procedure reserved primarily for the correction of anomalies that would be life-threatening unless reversed prenatally. As such, appropriate selection of patients and careful presurgical planning are critical. With its larger field of view and superior tissue contrast, prenatal MR imaging can be used to further assess anomalies discovered at ultrasound and to exclude other defects that might preclude surgery. Magnetic resonance imaging allows greater accuracy in the demonstration of intracranial abnormalities. Magnetic resonance imaging may also be used to follow response to treatment and to evaluate complications of surgery. Cases presented in this chapter demonstrate the current status of how MR imaging can be a valuable adjunct to prenatal ultrasound for the evaluation of the fetal surgery patient. Prenatal MR imaging and fetal surgery are rapidly evolving fields, often developing in parallel. As a result, guidelines and indications for prenatal MR imaging and fetal surgery are expected to evolve and change over time.

REFERENCES

1. Flake AW, Harrison MR. Fetal surgery. Annu Rev Med 1995; 46:67–78.
2. Wilson RD, Johnson MP, Crombleholme TM et al. Chorioamniotic membrane separation following open fetal surgery: pregnancy outcome. Fetal Diagn Ther 2003; 18:314–320.
3. Albanese CT, Harrison MR. Surgical treatment for fetal disease. The state of the art. Ann NY Acad Sci 1998; 847:74–85.
4. Coakley FV, Hricak H, Filly RA et al. Complex fetal disorders: effect of MR imaging on management—preliminary clinical experience. Radiology 1999; 213:691–696.
5. Coakley FV, Hricak H, Filly RA et al. MR Imaging of fetal abnormalities: relationship between clinical indication and management impact. Radiology 1999; 213(P):446.
6. Hubbard AM, Crombleholme TM, Adzick NS. Prenatal MRI evaluation of giant neck masses in preparation for the fetal exit procedure. Am J Perinatol 1998; 15:253–257.
7. Bouchard S, Johnson MP, Flake AW et al. The EXIT procedure: experience and outcome in 31 cases. J Pediatr Surg 2002; 37:418–426.
8. Hirose S, Farmer DL, Lee H et al. The *ex utero* intrapartum treatment procedure: looking back at the EXIT. J Pediatr Surg 2004; 39:375–380.
9. Liechty KW, Crombleholme TM, Flake AW et al. Intrapartum airway management for giant fetal neck masses: the EXIT (*ex utero* intrapartum treatment) procedure. Am J Obstet Gynecol 1997; 177:870–874.
10. Harrison MR, Mychaliska GB, Albanese CT et al. Correction of congenital diaphragmatic hernia *in utero* IX: fetuses with poor prognosis (liver herniation and low lung-to-head ratio) can be saved by fetoscopic temporary tracheal occlusion. J Pediatr Surg 1998; 33:1017–1022.
11. Adzick NS, Harrison MR, Glick PL et al. Diaphragmatic hernia in the fetus: prenatal diagnosis and outcome in 94 cases. J Pediatr Surg 1985; 20:357–361.
12. Metkus AP, Filly RA, Stringer MD et al. Sonographic predictors of survival in fetal diaphragmatic hernia. J Pediatr Surg 1996; 31:148–151.
13. Coakley FV, Lopoo JB, Lu Y et al. Normal and hypoplastic fetal lungs: volumetric assessment with prenatal single-shot rapid acquisition with relaxation enhancement MR imaging. Radiology 2000; 216:107–111.
14. Paek BW, Coakley FV, Lu Y et al. Congenital diaphragmatic hernia: prenatal evaluation with MR lung

volumetry—preliminary experience. Radiology 2001; 220:63–67.
15. Quinn TM, Adzick NS. Fetal surgery. Obstet Gynecol Clin North Am 1997; 24:143–157.
16. Hedrick HL, Flake AW, Crombleholme TM et al. Sacrococcygeal teratoma: prenatal assessment, fetal intervention, and outcome. J Pediatr Surg 2004; 39:430–438.
17. Olutoye OO, Adzick NS. Fetal surgery for myelomeningocele. Semin Perinatol 1999; 23:462–473.
18. Meuli M, Meuli-Simmen C, Hutchins GM et al. *In utero* surgery rescues neurological function at birth in sheep with spina bifida. Nat Med 1995; 1:342–347.
19. Meuli M, Meuli-Simmen C, Yingling CD et al. *In utero* repair of experimental myelomeningocele saves neurological function at birth. J Pediatr Surg 1996; 31:397–402.
20. Adzick NS, Sutton LN, Crombleholme TM et al. Successful fetal surgery for spina bifida. Lancet 1998; 352:1675–1676.
21. Bruner JP, Tulipan N, Paschall RL et al. Fetal surgery for myelomeningocele and the incidence of shunt-dependent hydrocephalus. JAMA 1999; 282:1819–1825.
22. Bouchard S, Davey MG, Rintoul NE et al. Correction of hindbrain herniation and anatomy of the vermis after *in utero* repair of myelomeningocele in sheep. J Pediatr Surg 2003; 38:451–458.
23. Saunders NJ, Snijders RJ, Nicolaides KH. Therapeutic amniocentesis in twin–twin transfusion syndrome appearing in the second trimester of pregnancy. Am J Obstet Gynecol 1992; 166:820–824.

11

MR Imaging of the Maternal Abdomen and Pelvis in Pregnancy

DEBORAH LEVINE, IVAN PEDROSA

INTRODUCTION

Ultrasound is the method of choice for imaging pregnant patients. However, magnetic resonance (MR) imaging is increasingly being used in patients with complications, in whom the diagnosis is unclear. Although the majority of this atlas is devoted to fetal anatomy and pathology, this chapter is focused on maternal conditions. These include conditions unique to pregnancy that may be evaluated by MR imaging such as pelvimetry, rare cases of ectopic pregnancy, and assessment of the uterus and placenta. MR imaging in the assessment of pelvic tumors is also illustrated. In addition, this chapter discusses the application of MR imaging in the assessment of abdominopelvic pain in pregnancy.

PELVIMETRY

Although pelvimetry is no longer commonly performed, it is beneficial in patients who desire a trial of labor when the fetus is in breech presentation (1–3). It can also be utilized in patients with prior pelvic trauma who desire a vaginal delivery (Fig 11.1). In cases where pelvimetry is requested, MR imaging offers the benefit of assessment of the bony structures and accurate measurements of the pelvis without ionizing radiation.

For MR pelvimetry, fast scan techniques are utilized, and the entire study can take <5 minutes (3,4). A midline sagittal view is obtained for assessment of the fetal presentation and for measurement of the anteroposterior pelvic inlet diameter. The true conjugate measurement is from the sacral promontory to the top of the symphysis pubis, and the obstetric conjugate is from the sacral promontory to the posterosuperior margin of the symphysis pubis (Fig. 11.1). Oblique coronal views (parallel to the anteroposterior pelvic inlet) are obtained for measurement of the pelvic inlet (maximum distance between the arcuate lines of the iliac bones on either side) and bispinous diameter (3).

Using acceptable values of >11.0 cm for the anteroposterior pelvic inlet, >9.5 cm for the transverse midpelvic distance (interspinal distance), and >11.0 cm for the pelvic outlet, van Loon et al. (3) showed that although use of MR pelvimetry in breech presentation at term did not reduce the overall cesarean-section rate, it allowed better selection of the delivery route with a significantly lower rate of emergency cesarean section.

THE CERVIX

The normal cervix in pregnancy is well visualized on a maternal midsagittal image. The non-effaced gravid cervix has an appearance similar to that seen in nonpregnant patients with a high signal intensity endocervical canal, intermediate signal intensity mucosal folds, low signal intensity fibrous stroma, and intermediate signal intensity outer smooth muscle. Studies have shown that a short cervix (<3 cm at 24 weeks) (5) and cervical funneling (6) are predictors of preterm delivery. Although MR is unlikely to be the imaging modality to screen for

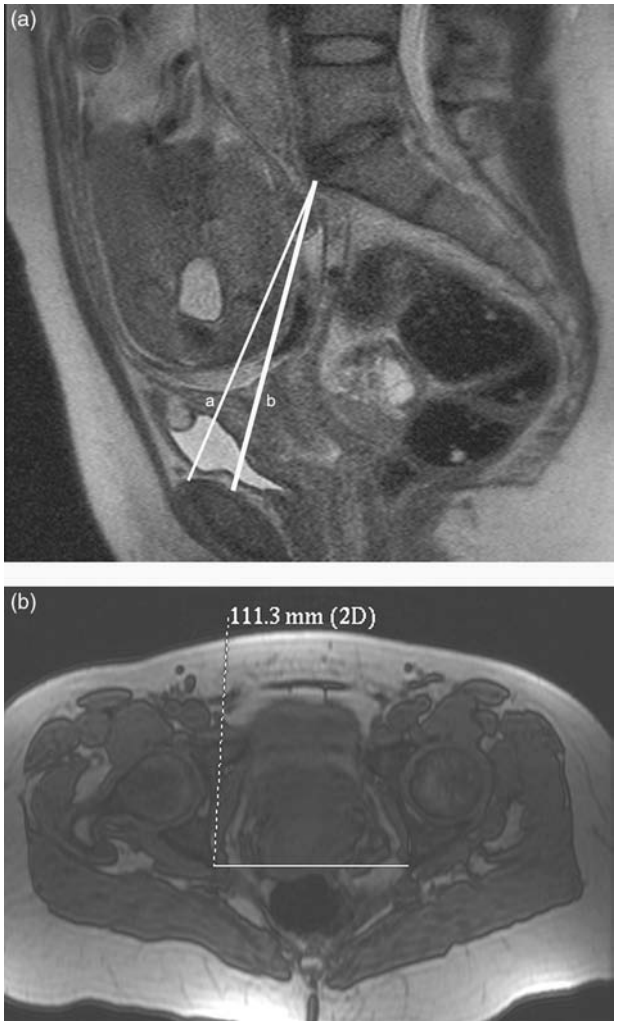

Figure 11.1 Pelvimetry. Sagittal T_2-weighted SSFSE image of the pelvis (a) demonstrates the anteroposterior pelvic inlet diameter measurement. The true conjugate measurement is from the sacral promontory to the top of the symphysis pubis (thin line, a), and the obstetric conjugate is from the sacral promontory to the posterosuperior margin of the symphysis pubis (thick line, b). Axial T_1-weighted opposed-phase gradient echo image of the pelvis (b) in a different patient illustrates the interspinous measurement.

patients with incompetent cervix, it can be useful in select cases (7). Figure 11.2 demonstrates the normal cervix in the first, second, and third trimesters. As shown in Fig. 11.2, the signal intensity of the stroma on T_2-weighted images increases close to term. It may be that analysis of cervical signal intensity will aid in the assessment of incompetent cervix. Examples of a short cervix and cervical funneling are shown in Figs. 11.3 and 11.4, respectively.

Cervical cancer is one of the more common malignancies to occur during pregnancy (8). When diagnosed during pregnancy, MR imaging can be utilized in staging, to help make decisions regarding treatment options (Fig. 11.5). In a study by van der Vange et al. (9) no significant difference was found in patients with early stage disease who were diagnosed in pregnancy compared to age- and stage-matched controls. Cervical cancer is readily seen on T_2-weighted fast spin echo (FSE) images as a mass with intermediate signal intensity that disrupts the hypointense fibromuscular stroma (10). The inherent soft-tissue contrast of MR imaging is particularly suitable for staging cervical carcinoma in pregnant patients because gadolinium contrast agents are not needed to evaluate the extension of the tumor.

THE UTERUS AND PLACENTA

Normal Myometrium and Synnechia

The myometrium should be visualized as a continuous band of soft tissue surrounding the gestational sac (Fig. 11.2). Uterine synnechia (scars) can be seen as thick bands of tissue that stretch across the uterus from one wall to another. They typically have a smooth margin extending into the amniotic fluid. The fetus should be seen to move freely, separate from these bands. These should be described as synnechia and not as "amniotic bands." As illustrated in Chapters 6 and 7, amniotic bands result from early rupture of the amnion and are associated with fetal anomalies. Although the severely scarred uterus can be a cause of infertility, if synnechiae are visualized on MR examination performed for fetal indications, they are likely incidental findings and are unlikely to be of clinical consequence (Fig. 11.6).

Uterine Dehiscence and Rupture

Uterine scar dehiscence and rupture are serious complications that can result in catastrophic outcome. Uterine dehiscence is defined as separation of the uterine musculature without extravasation of intra-amniotic contents and fetal parts into the peritoneal cavity. Uterine rupture implies a defect in the uterine musculature with extravasation of fetal parts and intra-amniotic contents into the peritoneal cavity and is often associated with acute pain and/or blood loss (4). A study by Rozenberg et al. (11) concluded that the risk of uterine rupture was related to the thickness of the lower uterine segment at 37 weeks. Using a cutoff of 3.5 mm, they found that a thin lower uterine segment as visualized on sonography had a sensitivity of 88%, specificity of 73%, positive predictive

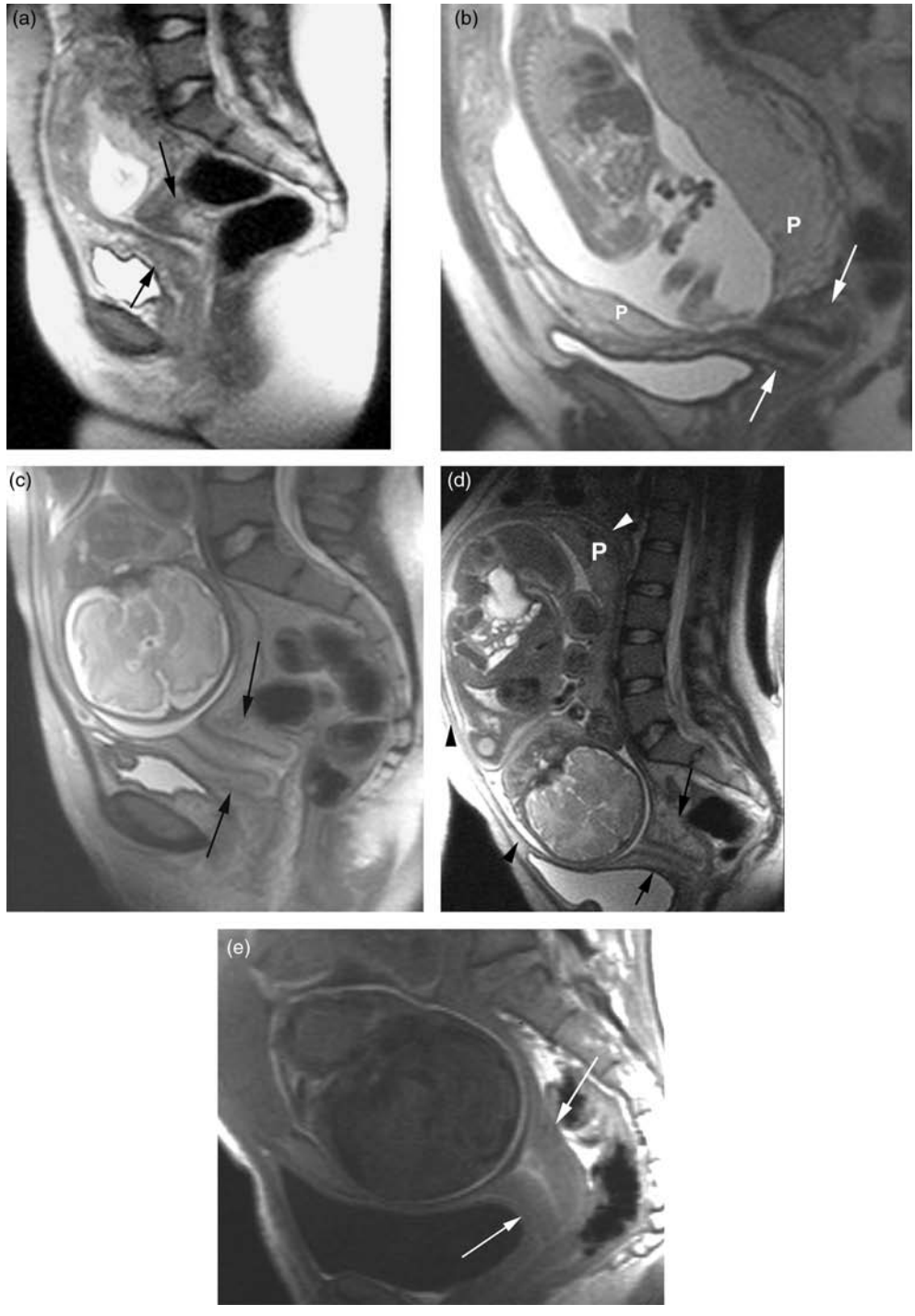

Figure 11.2 Normal cervix. T_2-weighted SSFSE sagittal images at 11 (a), 18 (b), 31 (c), and 37 (d) weeks gestational age and T_1-weighted gradient echo image at 31 weeks gestational age (e) illustrate the normal appearance of the cervix. The normal cervix prior to term has a high signal intensity endocervical canal, intermediate signal intensity mucosal folds, low signal intensity fibrous stroma, and intermediate signal intensity outer smooth muscle. Prior to delivery the signal intensity increases and cervical shortening may be observed. In (b), note that the majority of the placenta (P) is posterior with the tip of the placenta on the posterior lip of the cervix, but not crossing the internal os, and the smaller portion of the placenta is anterior. These two placentae were separate in every imaging plane. This is consistent with a succenturiate lobe. A finding like this puts the patient at risk for vasa previa; however, no vessels were detected crossing the internal os. Note the normal appearance of the myometrium in (d) (arrowheads). The myometrium is of similar signal intensity to the placenta (P). Anteriorly, the bright signal from the subcutaneous fat adjacent to the surface coil makes visualization of the entire anterior myometrium difficult.

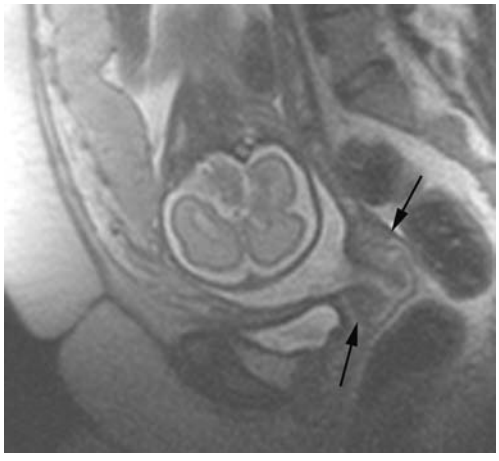

Figure 11.3 Short cervix. Sagittal T_2-weighted image of the uterus at 25 weeks gestational age with a short cervix (arrows) measuring 17 mm.

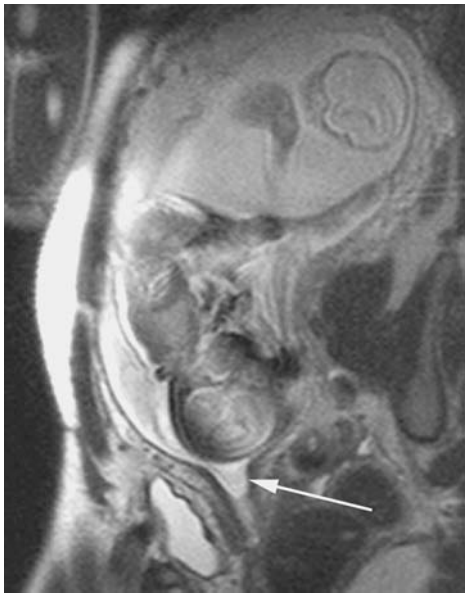

Figure 11.4 Cervical funneling. Sagittal T_2-weighted SSFSE image of the uterus with twins at 19 weeks gestational age. Note the wedge shaped appearance of the internal os (arrow).

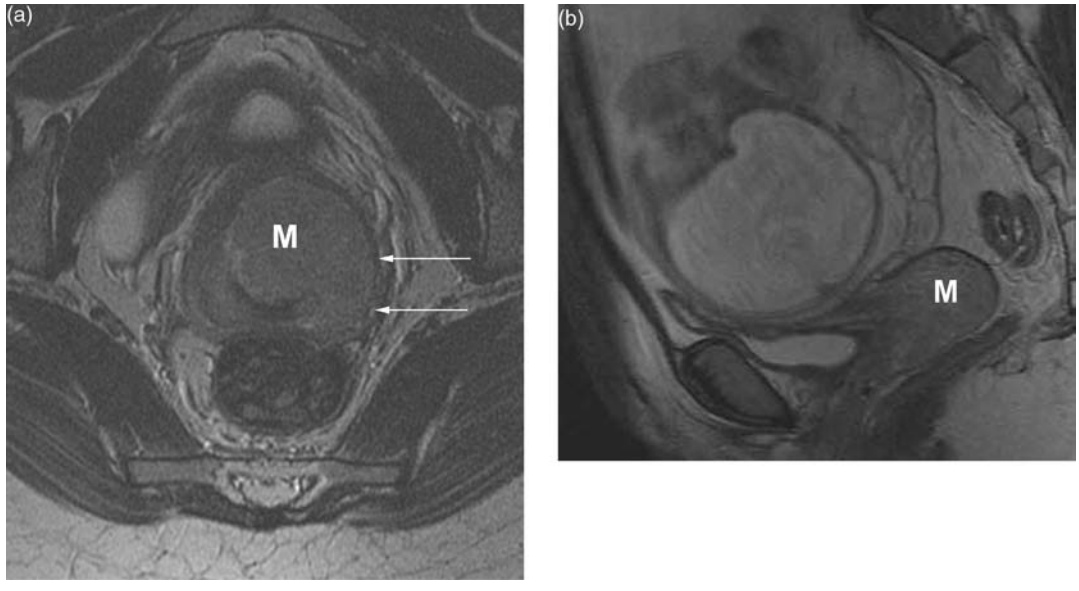

Figure 11.5 Cervical cancer. Axial (a) and sagittal (b) T_2-weighted FSE images show the extent of the intermediate to high signal intensity mass (M). There is disruption of the stromal ring (arrow), but no apparent parametrial invasion, lymphadenopathy, or ascites. On the basis of MR findings, the stage of the cervical cancer is Ib. The patient had a caesarian hysterectomy. Surgical staging was stage Ib. (Courtesy of K. Togashi, Kyoto, Japan.)

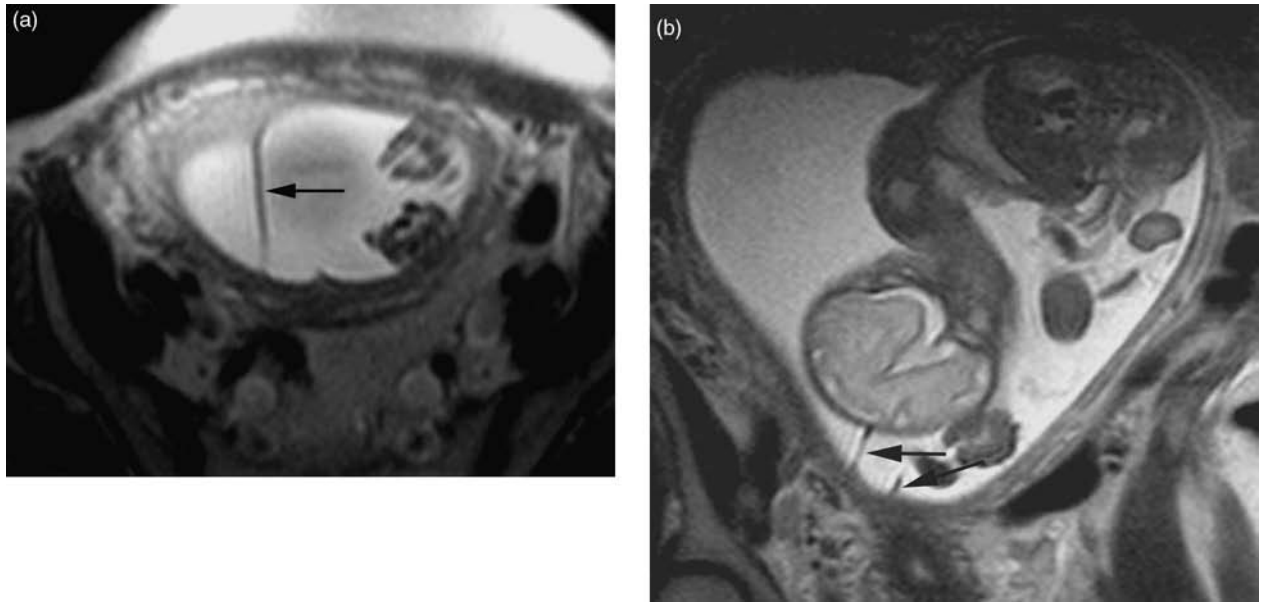

Figure 11.6 Uterine synnechiae in patient being scanned for fetal central nervous system anomaly (26 weeks pregnant). Coronal T_2-weighted SSFSE images of the uterus show two dark bands of soft tissue (arrows). In (a), one of the synnechia extends across the uterus. In (b), one of the bands appears in contiguity with the fetal head. However, on subsequent imaging (not shown), the fetus moved away from the synnechiae.

value of 11.8%, and negative predictive value of 99.3% for prediction of uterine rupture. Given the low positive predictive value, clinicians have not adopted third trimester uterine thickness screening for uterine rupture.

In our experience with assessing the myometrium on MR imaging in patients with prior cesarean section, the myometrium is often extremely thin and is only visualized as a thin low signal intensity line (Fig. 11.7), especially in the third trimester when the head is low in the pelvis. Partial volume averaging makes assessment difficult. The clinical care of the patient is based on a combination of imaging findings and patient symptoms, especially if dehiscence or rupture is suspected preterm (Figs. 11.8 and 11.9) (12,13).

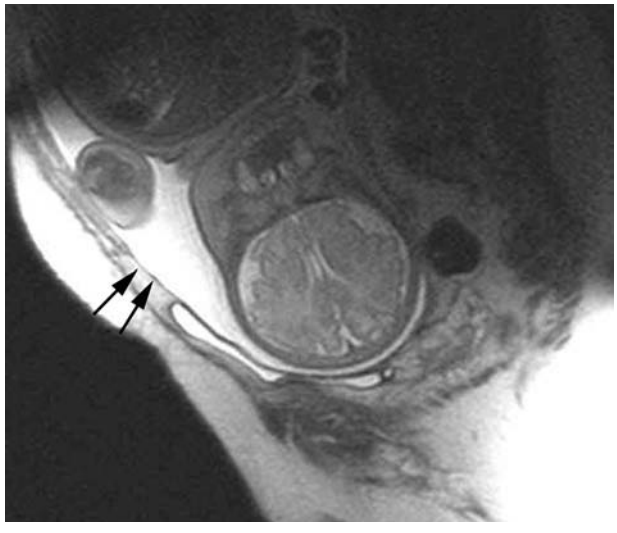

Figure 11.7 Thin myometrium in patient with prior cesarean section (34 weeks pregnant). Sagittal T_2-weighted image shows thin myometrium in the lower uterine segment (arrow). Although the myometrium is thin, the contour of the uterus is normal. This patient had a normal appearance of the lower uterine segment at the time of repeat cesarean section. Because of partial volume averaging, it is very difficult to assess the thin lower uterine segment in pregnancy.

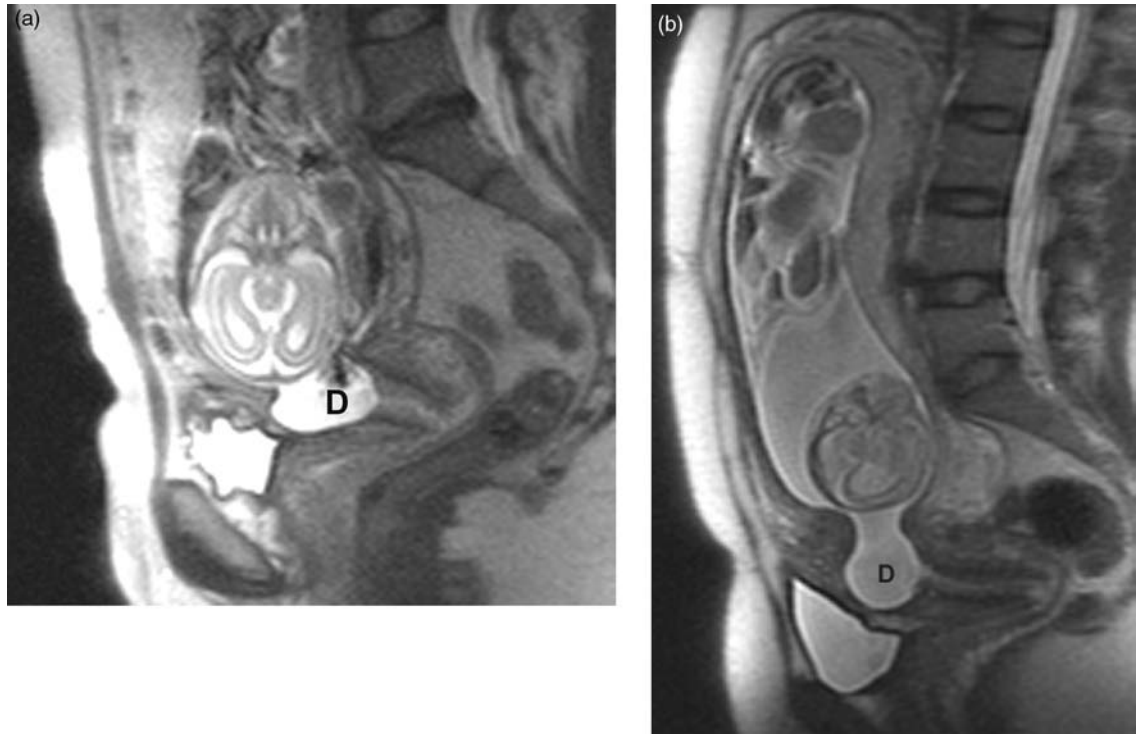

Figure 11.8 Cesarean section defects. Sagittal T_2-weighted SSFSE images in two patients: [(a) a singleton at 20 weeks gestational age and (b) twins at 18 weeks gestational age] with history of prior cesarean section. Note the myometrial defect just above the cervix. The patient in (a) was put on bedrest and was delivered at 31 weeks gestational age, when lower abdominal pain prompted preterm delivery. At the time of cesarean section, there was a 4 cm × 5 cm lower uterine segment dehiscence. The patient in (b) terminated the pregnancy.

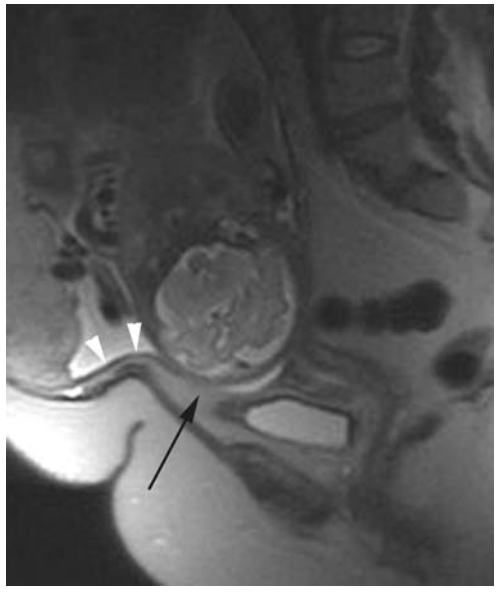

Figure 11.9 Uterine rupture held together by adhesions (28 weeks pregnant). Sagittal T_2-weighted SSFSE image shows normal myometrium (arrow heads) above a region with lack of myometrium (arrow) in the lower uterine segment. The patient was admitted to the hospital for observation and given steroids to help the fetal lungs mature. Delivery was by cesarean section 9 days later, when she had abdominal pain. At the time of delivery, a 4 cm gap was observed in the lower uterine segment, held together by dense adhesions.

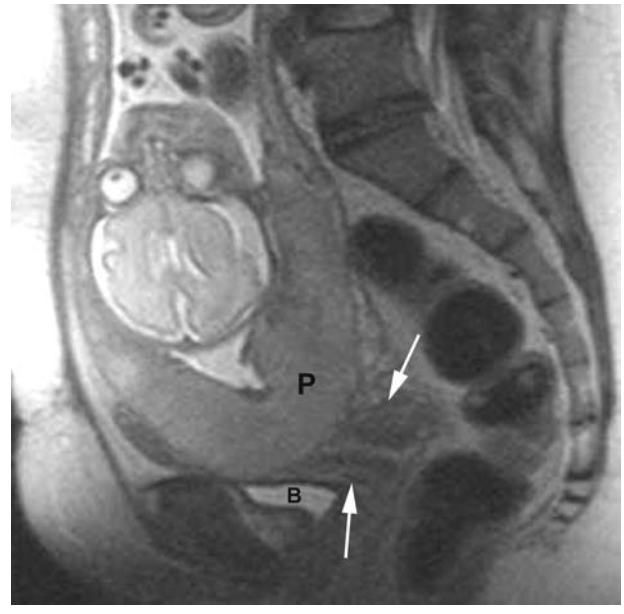

Figure 11.10 Placenta previa at 28 weeks gestation. Sagittal T_2-weighted SSFSE image shows the placenta (P) centered over the internal os consistent with a complete placenta previa. Arrows point to the cervix (B, bladder).

Placenta Previa and Intrauterine Bleeding

In patients with suspected placenta previa, a sagittal MR sequence oriented in the plane of the cervix is used to assess the placental margin (14–16). Given widespread use of endovaginal and translabial ultrasound, this is unlikely to be a common indication for MR examination. However, the placental edge is easily identified with fast scan techniques [Figs. 11.2(b) and 11.10] (17). MR imaging can be utilized to assess placental abnormalities such as placenta previa (Fig. 11.10), succenturiate lobe [Fig. 11.2(b)], vasa previa, and chorioangioma (14–16, 18–20).

Subchorionic hemorrhage is a frequent cause of first and second trimester bleeding. Small amounts of subchorionic blood are commonly noted on obstetric MR examinations and do not necessarily portend a poor prognosis. The appearance of hemorrhage on MR depends on the age of the bleed. Blood may be isointense to myometrium and placenta tissue. When subacute hemorrhage is apparent on fetal MR images, it is typically of low T_2 signal intensity (Figs. 11.11–11.13). Hemorrhage can be visualized on T_1-weighted images as areas of high signal intensity (Fig. 11.11). Hemosiderin, commonly found in chronic stages of hemorrhage, is hypointense on T_1- and T_2-weighted images. Gradient echo images are particularly helpful in screening for hemosiderin because of their increased sensitivity to susceptibility effects. Although most intrauterine hemorrhage is subchorionic, subamniotic hemorrhage can also occur (Fig. 11.13).

The term abruption is typically reserved for cases where there is premature separation of the normally implanted placenta from the uterus, causing hemorrhage that occurs after 20 weeks gestational age. The diagnosis is made when sonography shows retroplacental clot. Clinical signs include pain and vaginal bleeding. In severe cases, there may be hypotension and a tetanic uterus. However, the sonographic findings may be missed (or misinterpreted) on sonographic studies (21). In 50% of cases of abruption, sonography will be negative (22).

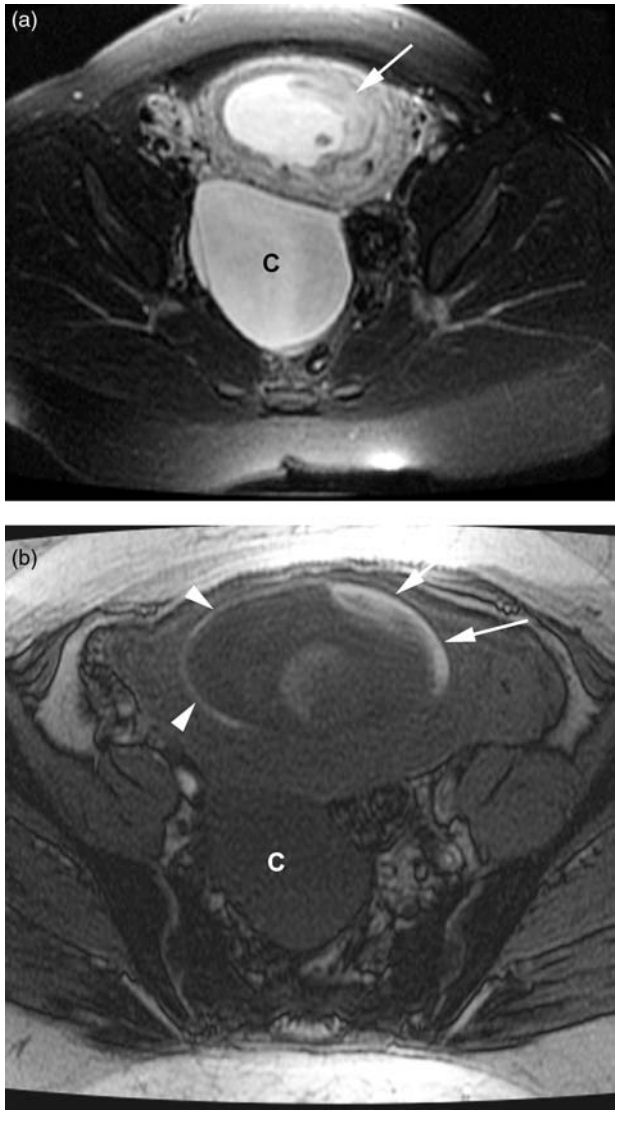

Figure 11.11 Subchorionic hematoma and cystadenoma of ovary (16 weeks pregnant). Axial T_2-weighted fat saturated SFFSE image (a) and T_1-weighted opposed-phase gradient echo image (b) show a thin-walled cyst (C) with signal intensity similar to amniotic fluid, consistent with a serous cystadenoma. The subchorionic hematoma adjacent to the placenta (arrows) is better visualized on the T_1-weighted image as the blood is of similar signal intensity to the placenta and myometrium of the T_2-weighted image. Blood tracking around the chorion (arrowheads) is also better visualized on the T_1-weighted image.

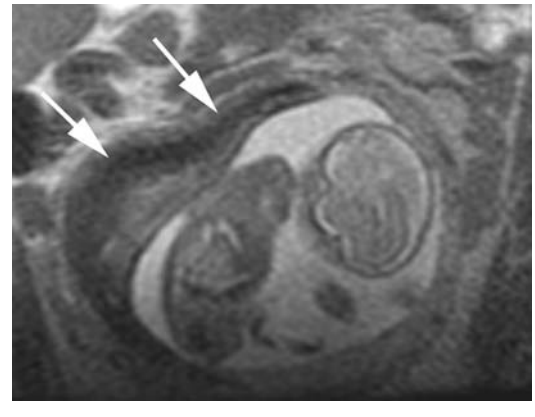

Figure 11.12 Subchorionic hematoma in patient with sickle cell anemia being scanned for acute abdominal pain (16 weeks pregnant). Coronal T_2-weighted SSFSE image shows a moderate amount of blood of low signal intensity. Subsequent sonogram confirmed the subchorionic hematoma, which was the presumed cause of the patient's abdominal pain.

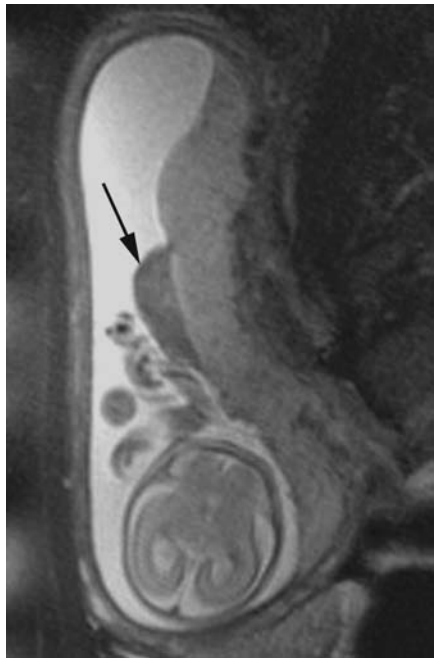

Figure 11.13 Subamniotic hematoma in patient referred for placental mass noted on ultrasound (20 weeks pregnant). Sagittal T_2-weighted SSFSE image shows a low signal intensity collection anterior to the placenta (arrow). This was a presumed subamniotic hematoma. The collection resolved later in pregnancy and at birth the placenta appeared normal.

MR imaging can be utilized to visualize blood products and thus can demonstrate cases of abruption (Figs. 11.14 and 11.15). The clinical utility of MR imaging in suspected cases of sonographically occult abruption has not yet been determined.

Placenta Accreta

Placenta accreta, including its variants increta and percreta, is a disorder that results in significant intrapartum morbidity and mortality. Uncontrollable bleeding frequently leads to hysterectomy. Abnormalities of placental attachment may result in the placenta attaching directly onto the myometrium (placenta accreta), extending more deeply into the myometrium (placenta increta), or invasion through the uterine serosa (placenta percreta). These conditions occur in 5% of patients with placenta previa, in up to 10% of patients after four or more cesarean sections, and in 67% of patients who have both placenta previa and four or more cesarean sections (23). A number of case reports suggest that MR is helpful in the diagnosis of placenta accreta and its variants (24–28). MR findings of placenta accreta or one of its variants include focal exophytic masses and absence of visualized myometrium (Fig. 11.16). At times, MR will demonstrate a focal exophytic mass. Even when accreta is not found at the time of cesarean section, this finding is associated with the need for hysterectomy (Fig. 11.17). A study from our laboratory (29) found that transvaginal ultrasound with a partially full bladder was most beneficial in the evaluation of placenta accreta occurring in the lower uterine segment. However, in one of 17 cases, the placenta accreta was identified only by the MR examination because of a posterior placenta occurring over a region of a previous myomectomy (Fig. 11.18). As the myometrium can be very thin and is of similar signal intensity to placenta, it may be difficult to visualize. We recommend transvaginal ultrasound with a partially full bladder as the method of choice for the evaluation of placenta accreta. However, in cases where the diagnosis is unclear or for patients with a history of myomectomy and posterior or fundal placenta, then MR examination may be considered.

One problem with MR imaging of placenta accreta is that distinction between the myometrium and placenta can be difficult on the types of sequences typically used for obstetric MR imaging. The myometrium is of intermediate signal intensity on T_2-weighted images and may "blend" into the placenta. If compressed by the surface

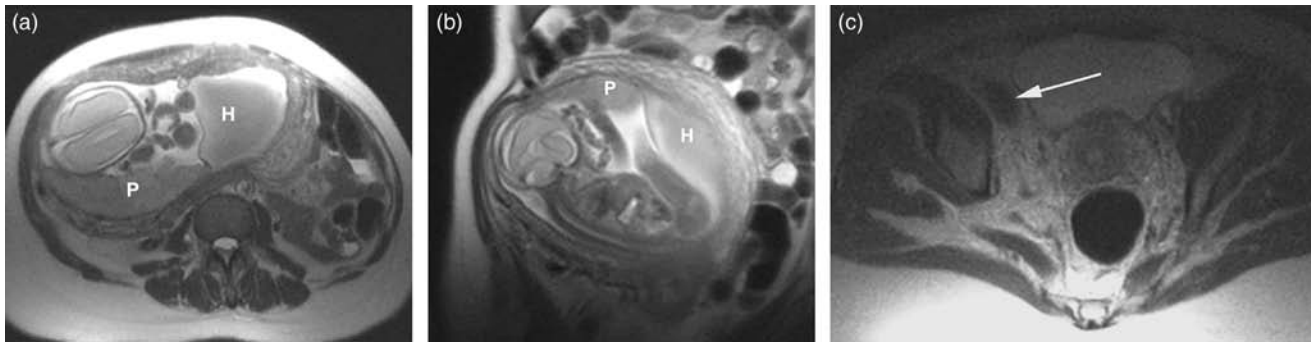

Figure 11.14 Placental abruption in heparinized 52-year-old patient being treated for deep venous thrombosis (20 weeks pregnant). Axial (a) and coronal (b) T_2-weighted SSFSE images of the uterus show a fluid collection of slightly low signal intensity consistent with hematoma (H). The blood extends to the tip of the placenta (P). Note the normal high signal intensity of the amniotic fluid surrounding the fetus. (c) Axial T_2-weighted image low in the pelvis shows the clot in the common iliac vein (arrow).

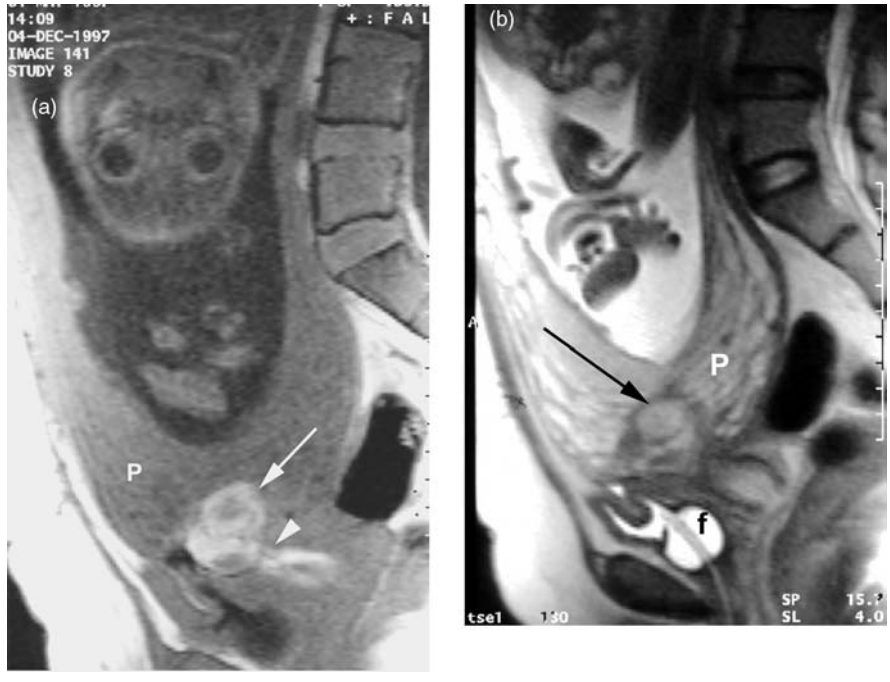

Figure 11.15 Placenta previa in a patient with painful vaginal bleeding (30 weeks pregnant). As placenta previa typically does not cause pain, but abruption does, the clinical question was how much of a retroplacental clot was present. With a large abruption, the plan was to deliver immediately. Sagittal T_1-weighted gradient echo image (a) shows small clot (arrow) above the internal os (arrowheads), with majority of placenta (P) well attached. Sagittal T_2-weighted SSFSE image (b) shows how the blood products are of similar signal intensity to the placenta on this image. Note the foley catheter (f) in the bladder. The finding of only a small amount of retroplacental blood allowed the patient to be managed expectantly with delivery delayed for over 4 weeks. [From Trop and Levine (17)]

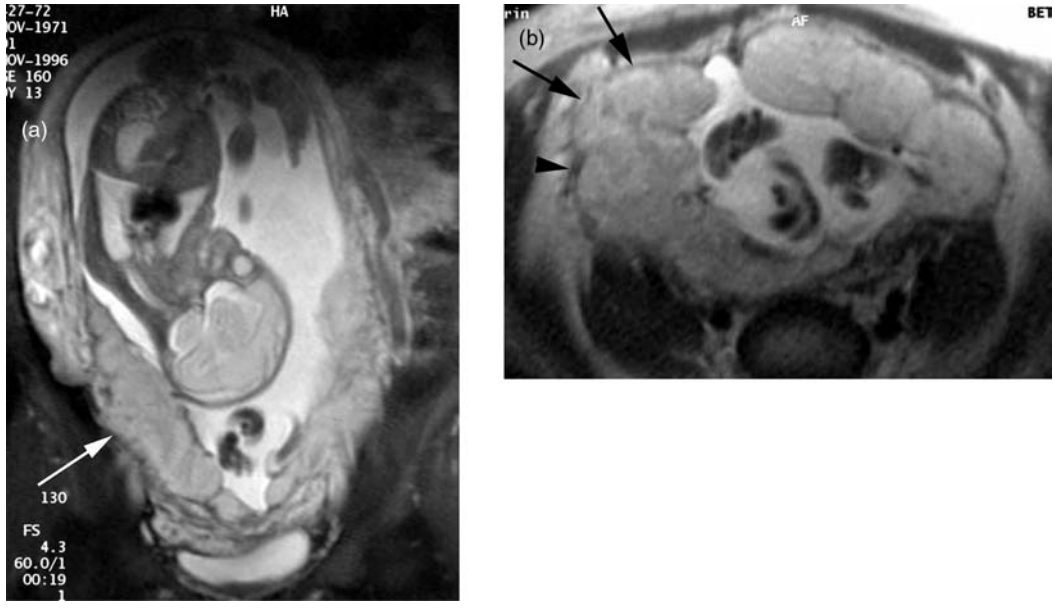

Figure 11.16 Placenta accreta in patient with prior cesarean section and placenta previa (27 weeks pregnant). Coronal (a) and axial (b) T_2-weighted SSFSE images show focal lack of myometrium on the right. Arrows point to the region of placenta without surrounding myometrium. Arrowhead points to some normal myometrium. The finding of a focal area of placenta accreta was confirmed at cesarean section.

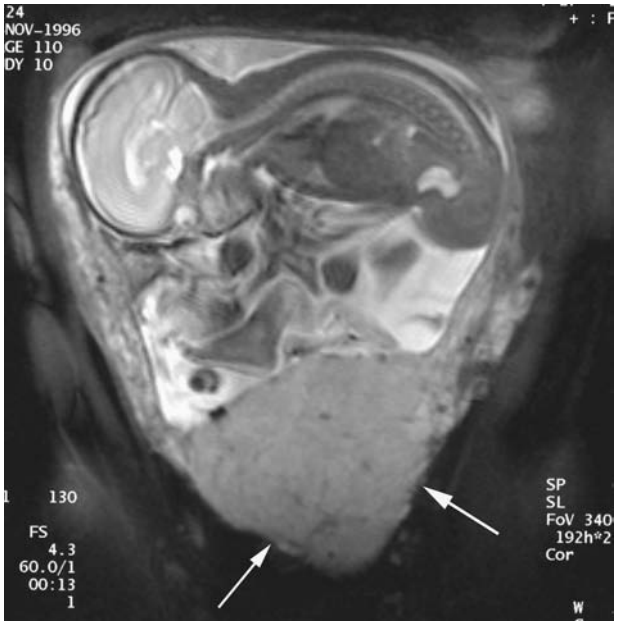

Figure 11.17 Focal exophytic mass in a patient being scanned for possible placenta accreta (26 weeks pregnant). Coronal T_2-weighted SSFSE image shows a focal exophytic mass (arrow) without surrounding myometrium. At the time of delivery, diffuse bleeding necessitated hysterectomy, but at pathology no accreta was found. This illustrates how clinical findings at cesarean section may not correlate with findings at histology. Nonetheless, the MR finding of a focal exophytic mass has been shown to correlate with either a variant of accreta or the need for hysterectomy at the time of delivery.

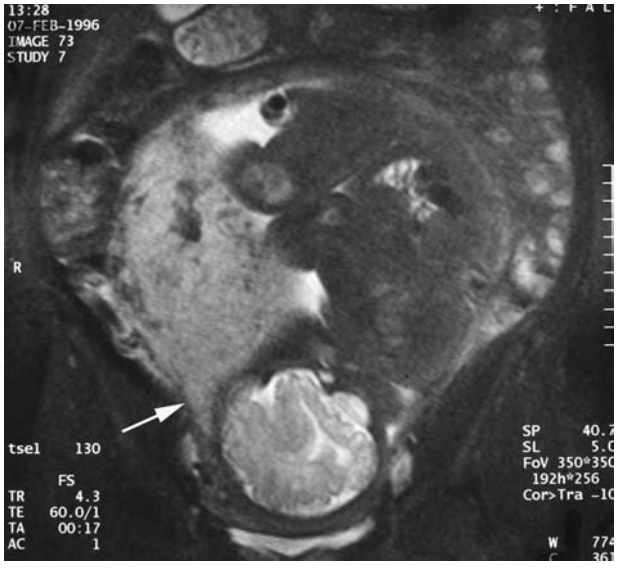

Figure 11.18 Placenta accreta in patient with prior myomectomy and placenta over the region of myomectomy (35 weeks pregnant). Coronal T_2-weighted fat-saturated SSFSE image shows a focal lack of myometrium in the posterolateral right uterus. The finding of a small focal area of accreta was confirmed at cesarean section. [From Levine et al. (29)]

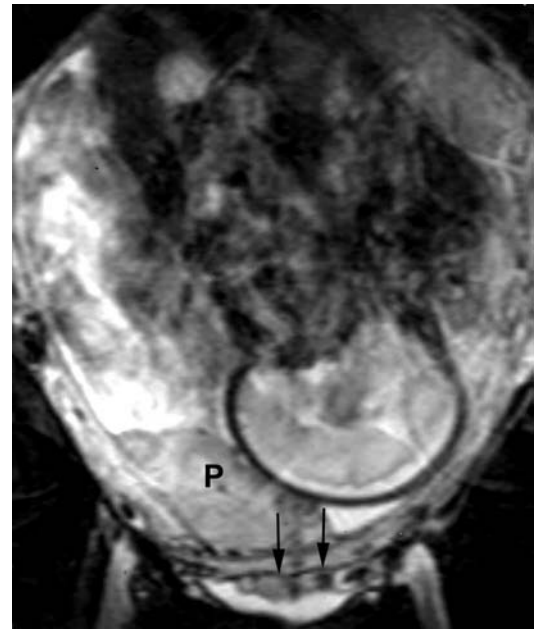

Figure 11.19 Bladder varices. Coronal T_2-weighted FSE image illustrates bladder varices (arrows) clearly separate from the placenta. This is a turbo spin echo image obtained during a 20 second maternal breath-hold, explaining the large amount of motion artifact.

coil, it may not be well visualized. For this reason, some authors have suggested that contrast-enhanced MR imaging can be helpful (30–32). However, gadolinium is considered a pregnancy category C drug (meaning that it should be given only if potential benefit outweighs the risk) because animal studies have revealed adverse effects but no controlled studies have been performed in humans (33,34). This concern is mainly because of the long half-life of the heavy metal contrast agent in the amniotic fluid. If a patient is to be delivered within a day or two of the contrast-enhanced MR examination, and if the results of the MR would affect the mode of delivery, it may be in the future that gadolinium can be utilized in select cases.

An important caveat in the assessment of placenta percreta is to assess the bladder wall. When placenta percreta invades the bladder wall, vessels can be visualized extending from the placenta into the bladder. Bladder varices are common and should not be mistaken for invading placental vasculature (Fig. 11.19).

Fibroids

Because of their prevalence in women of reproductive age, fibroids are often visualized on obstetric MR examinations. Uncomplicated fibroids are of low signal intensity

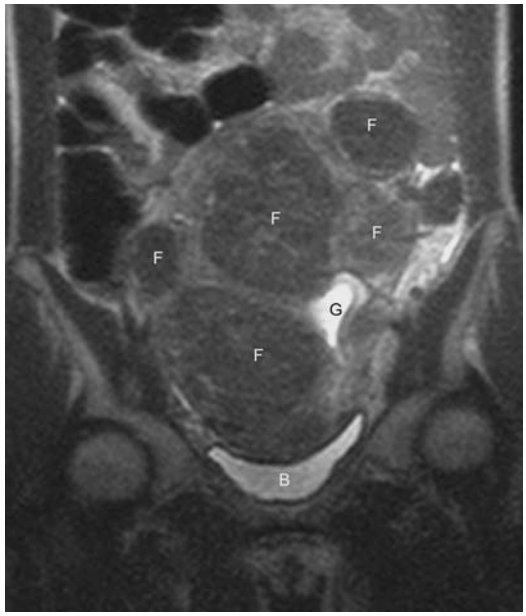

Figure 11.20 Fibroids in a patient with right lower quadrant pain (10 weeks pregnant). Coronal T_2-weighted SSFSE image reveals multiple fibroids (F) distorting the gestational sac (G) (B, bladder).

on T_1- and T_2-weighted imaging (Fig. 11.20). Fibroids tend to enlarge during pregnancy and may decrease in size postpartum. Rapid growth can lead to necrosis and pain. Depending on their number, size, and location, fibroids can cause recurrent miscarriage and malpresentation and can limit the obstetrician's ability to monitor the growth of the fetus because fundal height measurements can be affected by fibroids. When large, fibroids can distort uterine anatomy and make determination of the location of a pregnancy difficult. In these cases, MR imaging can provide an accurate depiction of the location of the gestational sac (Fig. 11.21).

Pain due to fibroids in pregnancy may be because of rapid growth, torsion, or degeneration. Degeneration of fibroids may cause focal pain, tenderness on palpation, low-grade fever, and leukocytosis. Most often, signs and symptoms abate within a few days, but inflammation may stimulate labor. In pregnant patients with abdominal pain secondary to fibroid degeneration, the diagnosis can be made with sonography by demonstrating point tenderness when the probe is over the fibroid. In complicated cases, MR can be helpful in making the diagnosis. Fibroids undergoing hemorrhagic degeneration during pregnancy typically demonstrate diffuse or peripheral high signal intensity on T_1-weighted imaging and variable signal intensity on T_2-weighted imaging (Fig. 11.22) (35). This hyperintense rim on T_1-weighted imaging may correspond to obstructed veins at the periphery of the mass. Edema can cause diffuse increased signal intensity of uterine fibroids on T_2-weighted imaging and may antedate degeneration (Fig. 11.23) (36).

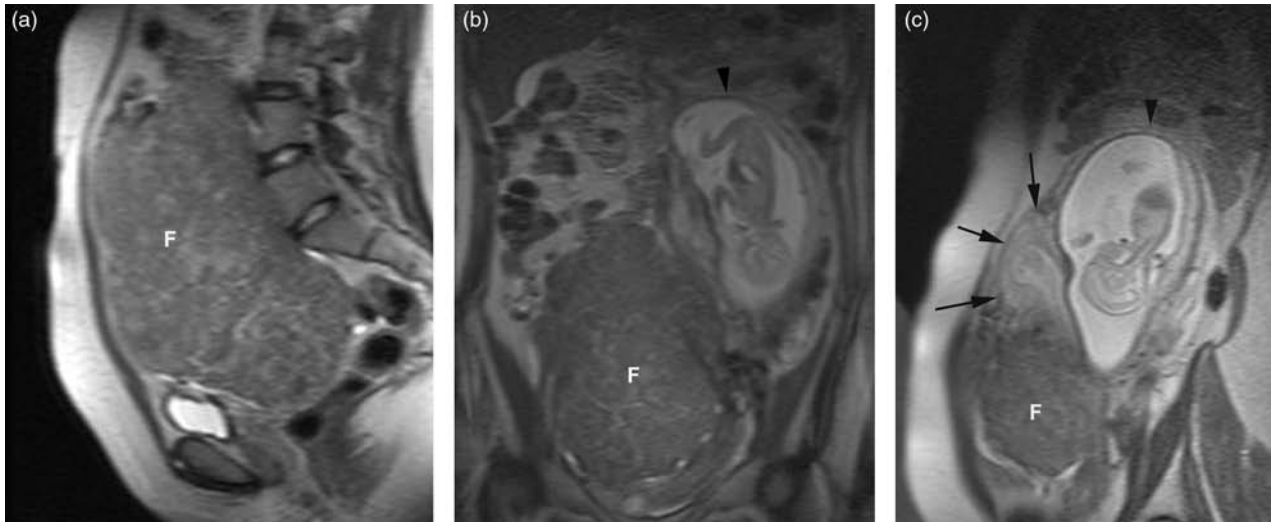

Figure 11.21 Patient referred for question of cornual ectopic pregnancy in bicornuate fibroid uterus at 17 weeks gestational age. (a) Midline sagittal T_2-weighted SSFSE image shows a large fibroid (F). (b) Coronal T_2-weighted image shows the pregnancy, but the relation of the gestational sac to the uterine horns is unclear. (c) Oblique coronal image oriented to the endometrium of the right uterine horn (arrows) shows that the gestational sac is in the left uterine horn. Although the myometrium is thin (arrowhead), it is visualized around the entire gestational sac. This case illustrates the importance of tailoring the examination to the clinical question. Image planes orthogonal to the maternal spine made it difficult to appreciate the pertinent relationships.

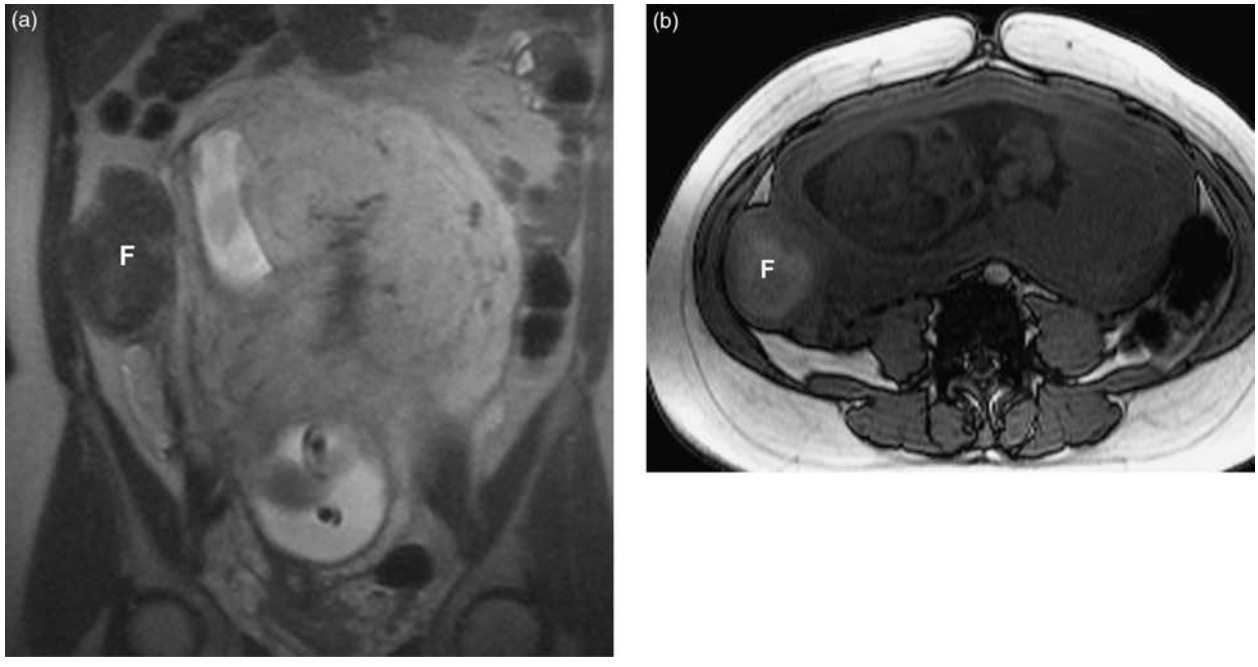

Figure 11.22 Degenerating fibroid in a patient referred for ovarian tumor (14 weeks pregnant). The MR examination was performed without a confirmatory sonogram at our institution. (a) Coronal T_2-weighted SSFSE image shows a slightly exophytic mass of low signal intensity. (b) Axial T_1-weighted opposed-phase gradient echo image shows increased signal intensity in the fibroid consistent with hemorrhagic necrosis. This is a common finding in fibroids in pregnancy. It is possible that this diagnosis could have been made by ultrasound.

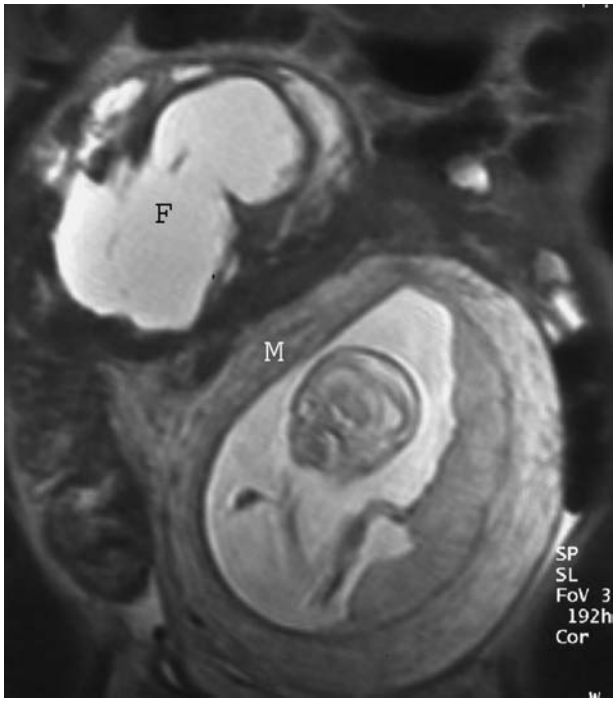

Figure 11.23 Degenerating fibroid in patient with cystic abdominopelvic mass (16 weeks pregnant). The ovaries were visualized separately on ultrasound (not shown), but it was unclear whether the mass was a fibroid or other necrotic tumor. Coronal T_2-weighted SSFSE image demonstrates that the necrotic fibroid (F) clearly arises from the myometrium (M) with a large connection visible to the inferior aspect of the fibroid.

Gestational Trophoblastic Disease

Gestational trophoblastic disease encompasses a broad spectrum of conditions including hydatidiform mole, invasive mole, choriocarcinoma, and placental site trophoblastic tumor. Although sonography is the examination of choice for the initial diagnosis, MR imaging has a role in the detection of gestational trophoblastic disease and the evaluation of the extent of its complications (37,38).

Hydatidiform mole constitutes 80% of cases of gestational trophoblastic disease. These are noninvasive processes that show both proliferation and hydropic swelling of the villi. On T_2-weighted images, a complete mole appears as a heterogeneous mass of high signal intensity that distends the endometrial cavity. Numerous cystic spaces may be present in the mass (39). Because of the high association between molar pregnancy and choriocarcinoma, patients need surveillance after this diagnosis is made. Partial molar pregnancy refers to the combination of a fetus with localized placental molar degeneration. It typically presents on ultrasound as a gestational sac with a fetus and an enlarged placenta with multiple cysts (Fig. 11.24) (40). Approximately 2–6% of patients develop persistent gestational trophoblastic disease after a partial molar pregnancy (41,42). Therefore, these patients require the same post-evacuative surveillance and management as the patient with a complete mole.

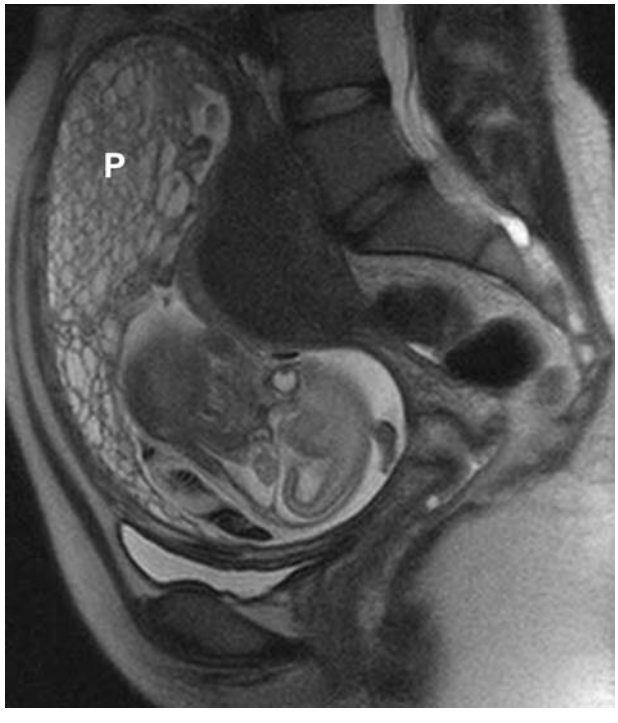

Figure 11.24 Partial molar pregnancy. Sagittal T_2-weighted SSFSE image shows an enlarged cystic placenta (P) and a fetus. This combination suggests a partial molar pregnancy, which was confirmed at pathology. (Courtesy of K. Togashi, Kyoto, Japan.)

THE OVARIES

Normal ovaries in pregnancy have a low signal intensity stroma and small follicles (Fig. 11.25). The corpus luteum cyst can grow to be quite large and when hemorrhagic can have a complex appearance (Figs. 11.26 and 11.27). A thick rim of hyperintense signal intensity on T_1-weighted images and intermediate signal intensity on T_2-weighted images with a very low signal intensity layer in the inner aspect of this rim is characteristic of corpus luteum cyst. The majority of masses <6 cm detected in the first trimester are corpus luteum cysts and resolve spontaneously. If present in the second trimester, 25% of adenexal masses resolve. One in 1300 requires laparotomy. Two to five percent of adnexal masses that are removed during pregnancy are malignant (43). Ovarian masses are typically asymptomatic unless rupture or torsion occurs. Ultrasonography usually facilitates delineation of the size and consistency of adnexal masses. Kier et al. (44) showed that MR correctly identified the origin and nature of the mass to decrease the need for surgery during pregnancy. Although dermoids

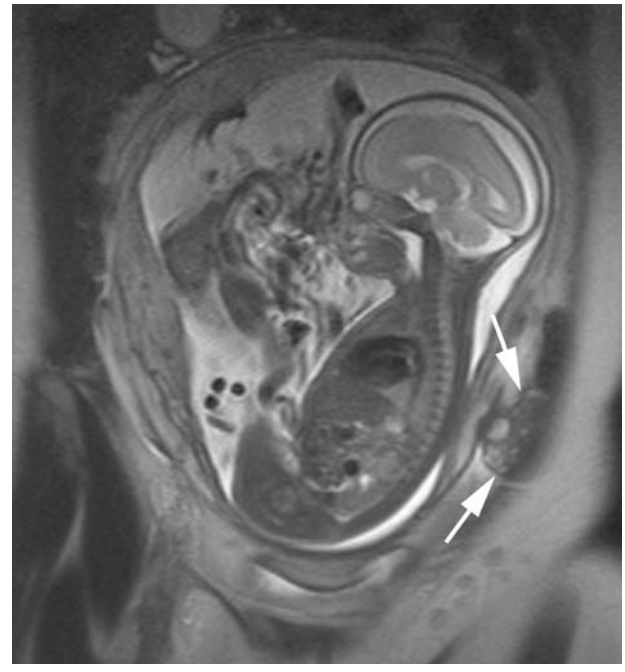

Figure 11.25 Normal left ovary (26 weeks pregnant). Coronal T_2-weighted SSFSE image shows a normal left ovary (arrowhead) with low signal intensity stroma and a few small follicles.

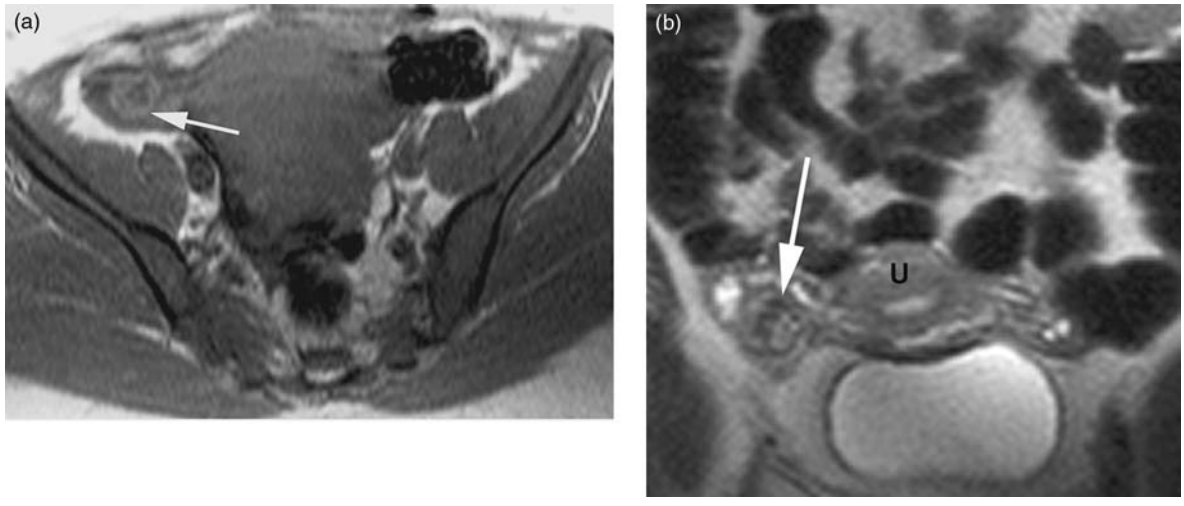

Figure 11.26 Corpus luteum cyst in a patient with severe right lower quadrant pain with human chorionic gonadotropic level of 323 mIU/mL (5 weeks pregnant). Her ultrasound (not shown) demonstrated a right corpus luteum cyst. The MR examination was performed for further evaluation. (a) Axial T_1-weighted image demonstrates a round well-defined lesion in the right adnexa (arrow). Note the hyperintense rim and the central area with low signal intensity characteristic of corpus luteal cysts. (b) Coronal T_2-weighted SSFSE image again shows the corpus luteum cyst (arrow). Note the characteristic hypointense inner layer within the peripheral rim consistent with hemosiderin deposits (arrowhead). Uterus (U). Patient underwent diagnostic laparoscopy to evaluate for a possible ruptured ectopic pregnancy because her hematocrit dropped from 35 to 30%. At surgery, a 1 cm corpus luteum was found in the right ovary. No hemoperitonium or ectopic pregnancy was found at surgery.

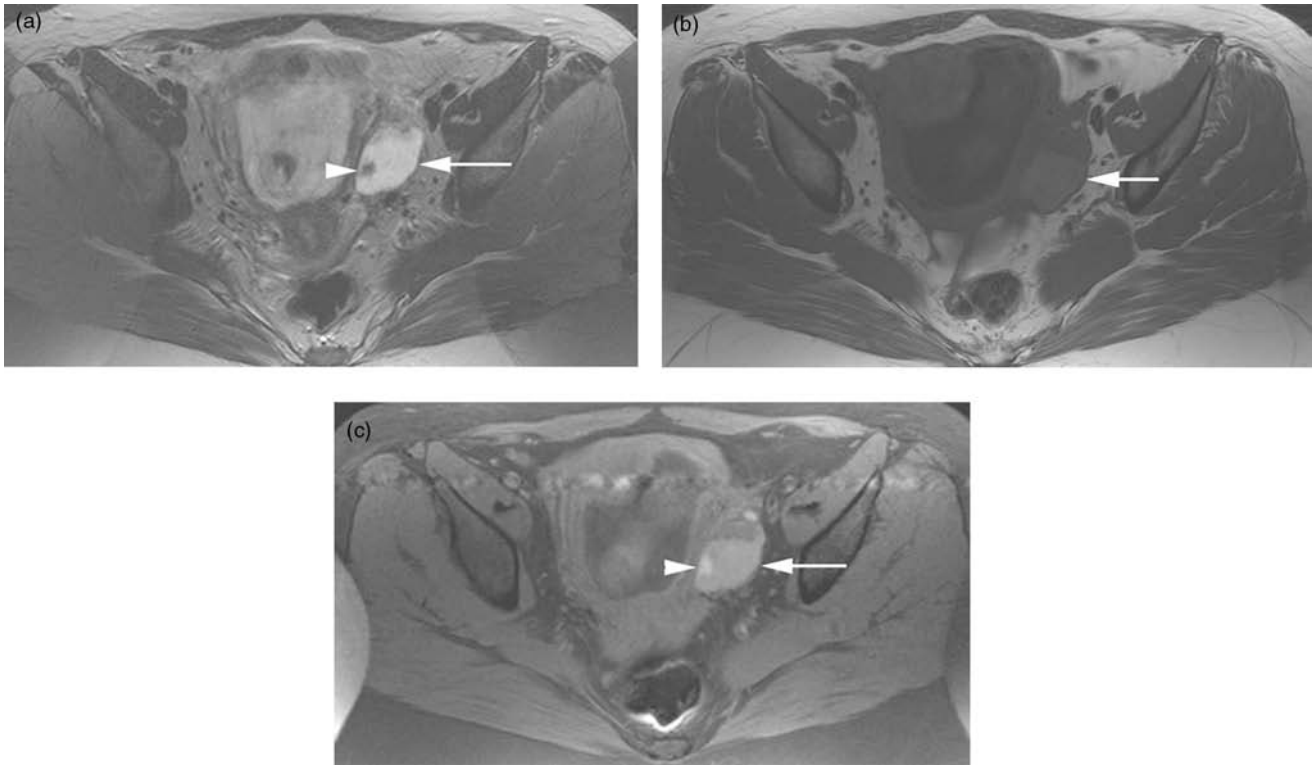

Figure 11.27 Hemorrhagic cyst in 14 weeks pregnant patient. Axial T_2-weighted image (a) shows a 4 cm left cyst with a low signal intensity nodule (arrowhead). T_1-weighted FSE images without (b) and with (c) frequency-selective fat saturation show the cyst to have fluid of slightly high signal intensity and the nodule of very high signal intensity. At surgery, a cyst with focal excrescences along the wall was found and was felt to represent an endometrioma. The final pathology was a hemorrhagic corpus luteum cyst with some areas of decidualization. As gadolinium is not recommended for use in pregnancy, evaluation of tumor nodules in adnexal cysts can be difficult. Both adherent clot and decidual reaction in an endometrioma can mimic a tumor nodule.

are a common cause of ovarian masses in pregnancy, it is important when performing an MR for an adnexal mass to obtain T_1-weighted imaging with frequency-selective fat saturation because the presence of bulk fat is consistent with a benign dermoid (Fig. 11.28). Occasionally, dermoids may contain only small amounts of fat which can be imperceptible on frequency-selective fat-suppressed images but readily detected on T_1-weighted in-phase and opposed-phase imaging. Serous cystadenomas are fluid-filled cysts. The signal intensity of the fluid follows that of fluid seen elsewhere in the body, being of high signal intensity on T_2-weighted images and low signal intensity on T_1-weighted images (Fig. 11.11). Thin septations may be visualized. Lack of solid elements suggests a benign lesion. Mucinous tumors have a stained glass appearance of cysts of differing signal intensity (45). One important aspect of imaging ovarian tumors in pregnancy is to determine whether a solid-appearing portion of a mass is blood clot or vascularized tissue. This can be difficult because gadolinium is not recommended for use in pregnancy. In these cases, ultrasound should be utilized to determine whether a nodule is vascularized, whereas MR imaging can be utilized to evaluate the reminder of the tissue characteristics of the mass (Fig. 11.29).

If pain is localized to an adnexal mass, torsion is of concern. Ultrasonography frequently demonstrates altered blood flow on Doppler studies. MR can demonstrate suggestive features of torsion such as enlarged edematous ovary with diffuse high signal intensity on T_2-weighted images (Figs. 11.30 and 11.31) (46,47).

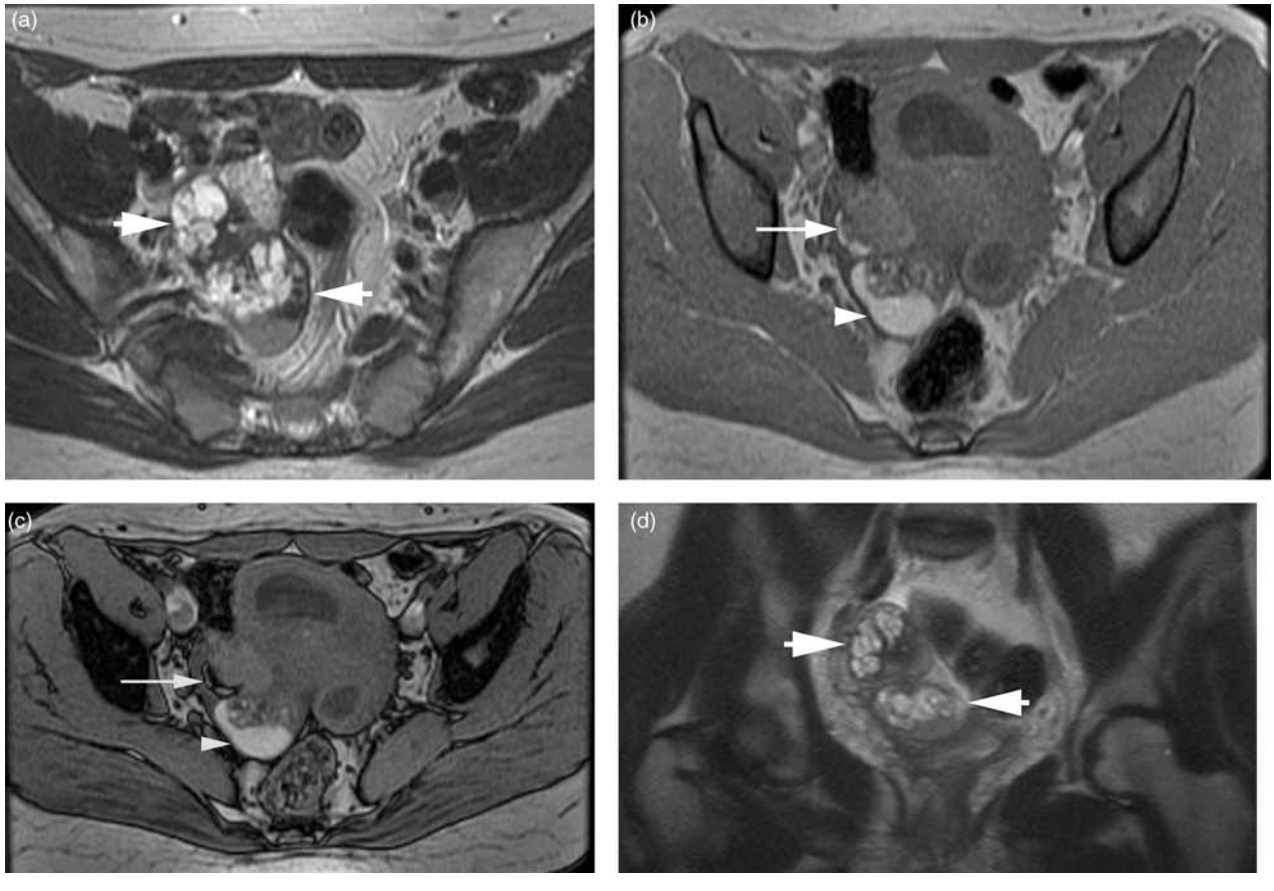

Figure 11.28 Dermoid in pregnancy (a–c) at 7 weeks gestation, and (d) at 30 weeks gestation). (a) Axial T_2-weighted image shows a heterogenous bi-lobed mass (short arrows). T_1-weighted in-phase (b) and opposed-phase (c) gradient echo images show high signal intensity regions. Two hyperintense regions are noted in the right side of the mass and both remain hyperintense on T_1-weighted in- and opposed-phase images. A characteristic India ink effect is noted at the interface between the most anterior area (arrow) and the rest of the mass confirming the presence of fat. The posterior hyperintense area demonstrates no India ink effect, and it is most consistent with blood products or mucinous material. (d) The patient returned at 30 weeks gestation after the sonogram indicated a possible increase in size of the mass. Coronal MR image shows the bi-lobed mass now oriented in the superoinferior direction. The change in orientation of the mass occurred because of the enlarging uterus.

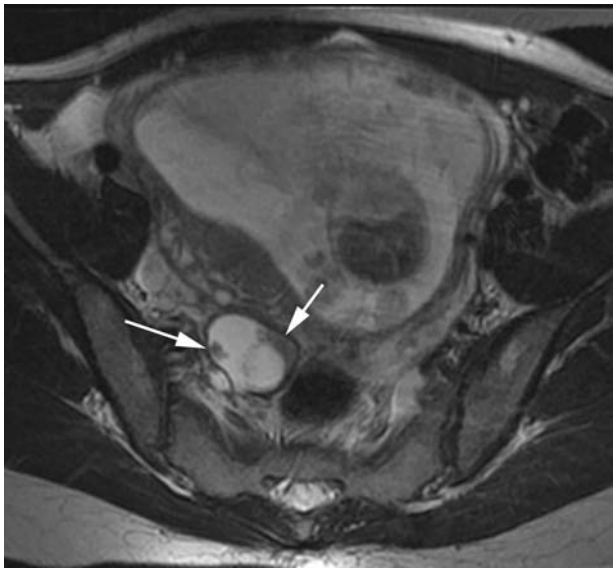

Figure 11.29 Papillary mucinous cystadenocarcinoma in patient being scanned for complex ovarian cyst (16 weeks pregnant). Axial T_2-weighted image shows a complex cyst with low signal intensity nodules. Ultrasound examination (not shown) demonstrated flow in the nodules, proving that these were solid tissue and not blood clot. This was a papillary mucinous cystadenocarcinoma of low malignant potential.

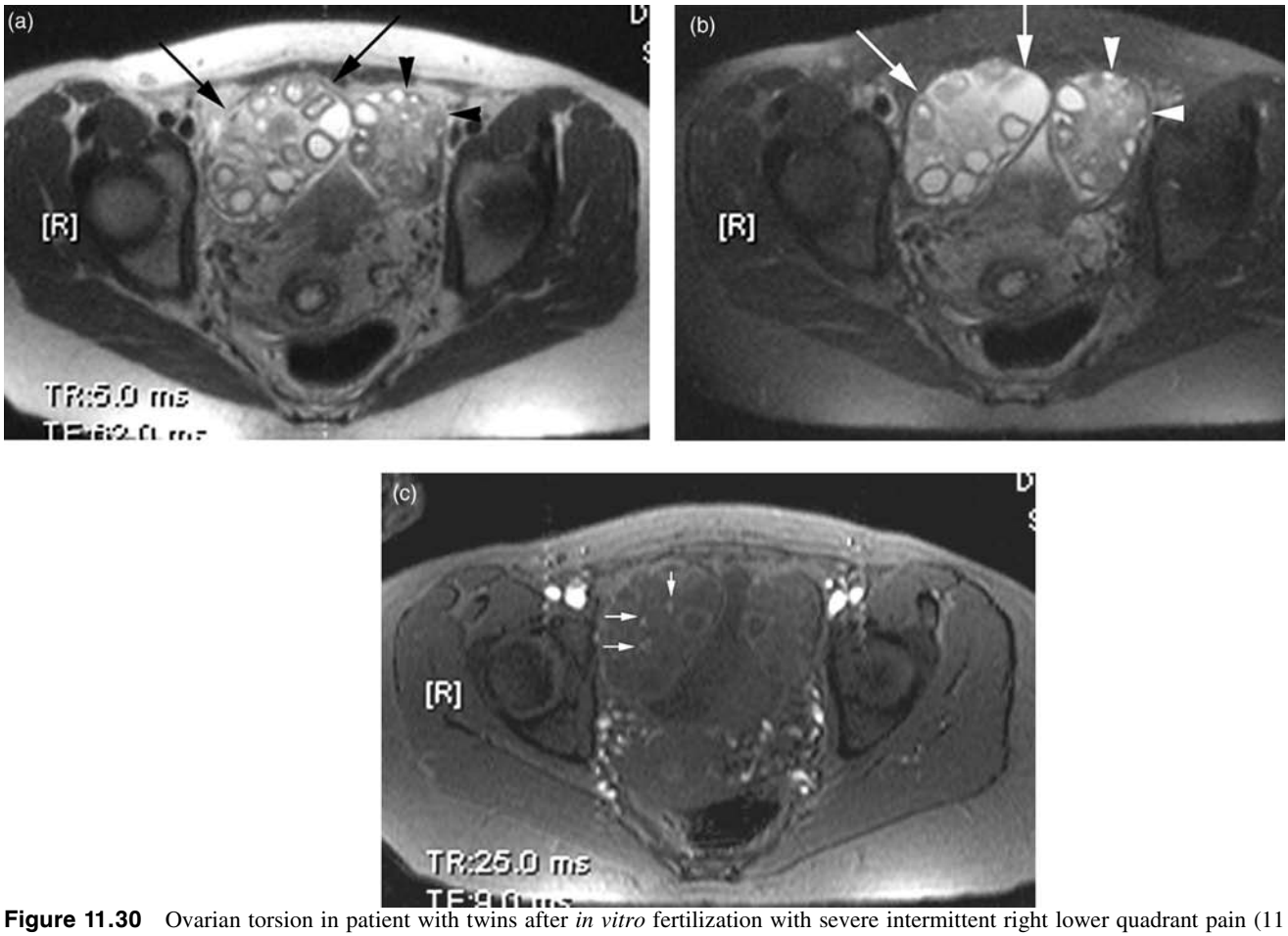

Figure 11.30 Ovarian torsion in patient with twins after *in vitro* fertilization with severe intermittent right lower quadrant pain (11 weeks pregnant). Axial T_2-weighted SSFSE images without (a) and with fat saturation (b) show large ovaries, right (arrows) greater than left (arrowheads), with multiple follicles, consistent with history of hyperstimulation. On the fat saturation image, the edema of the right ovary is more apparent as the stroma is brighter in the right ovary than the left. (c) Axial time-of-flight image confirms the presence of flow with small vessels visible in the middle of the right ovary (arrows). At surgery, the ovary was edematous with 360° of torsion.

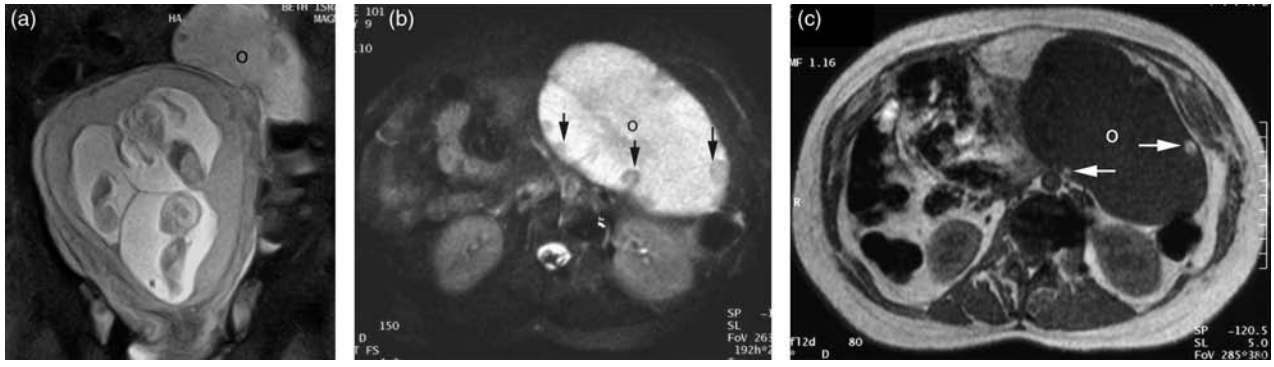

Figure 11.31 Massive ovarian edema in a patient with quadruplets reduced to twins (14 weeks pregnant) with enlarging left ovary after *in vitro* fertilization. Coronal (a) and axial (b) fat saturated T_2-weighted SSFSE images show three of the gestational sacs and the enlarged high signal intensity left ovary (O). Small peripheral follicles (arrows) of low signal intensity are visualized. (c) T_1-weighted gradient echo image shows the small follicles to be of high signal intensity (arrows) likely because of hemorrhage. [(a) from Levine et al. (46)]

MR IMAGING IN THE DIAGNOSIS OF ECTOPIC PREGNANCY

The diagnosis of an ectopic pregnancy is based on the findings of an embryo or fetus in a gestational sac in a location other than the endometrial cavity. MR imaging can define the location of a questionable gestational sac and is used as a problem-solving tool after sonography. The most common location for ectopic pregnancy is in the fallopian tubes. Tubal pregnancies are typically diagnosed sonographically, but at times, the diagnosis is uncertain and MR may be helpful (Fig. 11.32) (20,37,48–52).

MR findings of tubal ectopic pregnancy include an extrauterine mass with heterogeneous signal intensity. At times, there is a dependent low signal intensity component or a rim of low signal intensity due to blood products (53). Kataoka et al. (54) prospectively evaluated suspected cases of ectopic pregnancy with gadolinium-enhanced MR imaging. Tubal wall enhancement and presence of tubal hematoma or gestational sac-like structure were considered diagnostic findings. MR examinations had 12 true positive, three true negative, three false negative, and no false positive results for the diagnosis of tubal pregnancy. The predominant signal intensity of tubal hematoma was an intermediate signal on T_1-weighted imaging and a low signal on T_2-weighted imaging. Ascites showed signal intensity higher than that of urine on T_1-weighted imaging in all cases where free fluid was present.

MR imaging can be helpful when an ectopic location of pregnancy is suspected, but more definition is needed prior to treatment, for example, cervical ectopic (Fig. 11.33) (55), interstitial pregnancy (37), or scar ectopic (Chapter 1, Fig. 1.5) (56). MR imaging can be helpful for depicting the location of a pregnancy in a congenital uterine anomaly (Fig. 11.21) (57) and in surgical management of ovarian ectopics (Fig. 11.34) (58) and heterotopic pregnancy (Fig. 11.34).

Abdominal pregnancies are rare. The pregnancy typically develops in the ligaments of the ovary, usually the broad ligament. It can then obtain blood supply from the omentum and abdominal organs. Sonographically, the pregnancy is seen separate from the uterus, adnexa,

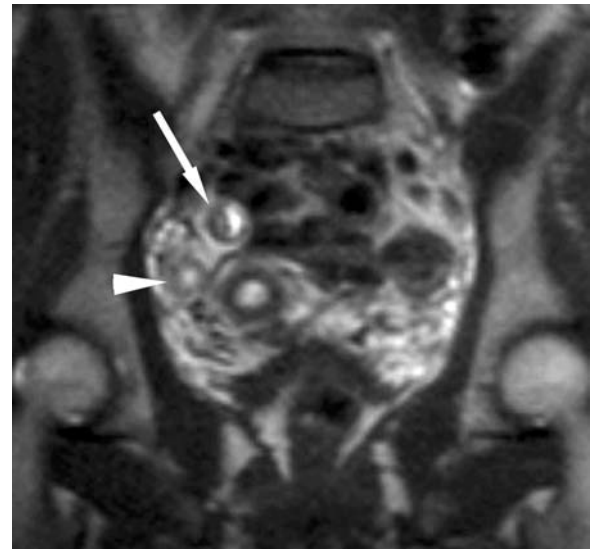

Figure 11.32 Tubal ectopic pregnancy in patient being evaluated for appendicitis (6 weeks pregnant). Sonogram performed 2 days previously had not shown an intrauterine pregnancy. The β-hCG was 1299 mIU/mL. Coronal T_2-weighted image shows the right ovary (arrowhead) with follicles and a corpus luteum with a superomedial mass (arrow) consistent with ectopic pregnancy. An ultrasound (not shown) performed after the MR examination confirmed the diagnosis of ectopic pregnancy. This case illustrates the importance of performing sonograms in pregnant patients prior to MR examinations. If a repeat sonogram had been performed the day of the MR, it is likely that the ectopic pregnancy would have been found, and the MR would not have been needed. [From Dialani and Levine (56)]

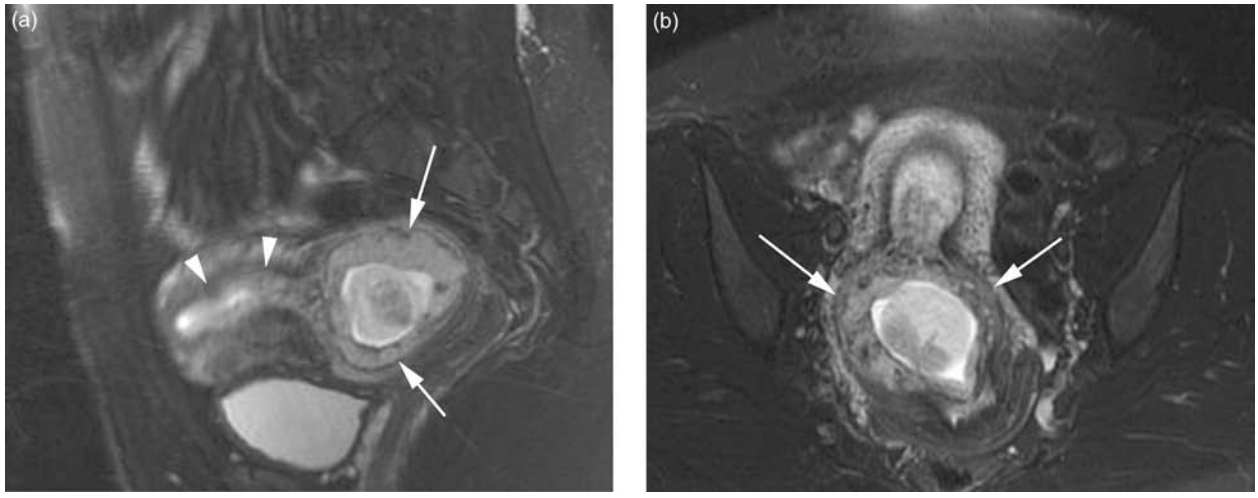

Figure 11.33 Cervical ectopic pregnancy. Sagittal (a) and coronal (b) T_2-weighted fast-saturated FSE show the empty uterine cavity (arrowheads) with the gestational sac in the cervix (arrows). (Courtesy of M. Robbin, Birmingham, Alabama.)

and ovaries (Fig. 11.35). Treatment is by laparotomy or laparoscopy (59). Abdominal pregnancy can result in a life-threatening emergency, and thus are typically operated upon at the time of diagnosis. However, if diagnosed late, a viable pregnancy can result. MR imaging has been shown to be helpful in delineating the extent of peritoneal involvement for preoperative planning and revealing the degree of uterine invasion (60–63). MR angiography can be utilized to show the location and origins of the vasculature supplying the pregnancy (61).

MR DIAGNOSIS OF PELVIC DEEP VENOUS THROMBOSIS

Ultrasound is used in screening for clot in the lower extremities. If pelvic clot is of concern, then MR venography can be performed. A clot will cause local distention of the veins with heterogeneous material on dark blood sequences (e.g., SSFSE, Fig. 11.14). Since gadolinium is typically not administered during pregnancy, un-enhanced MR techniques are utilized. Time-of-flight

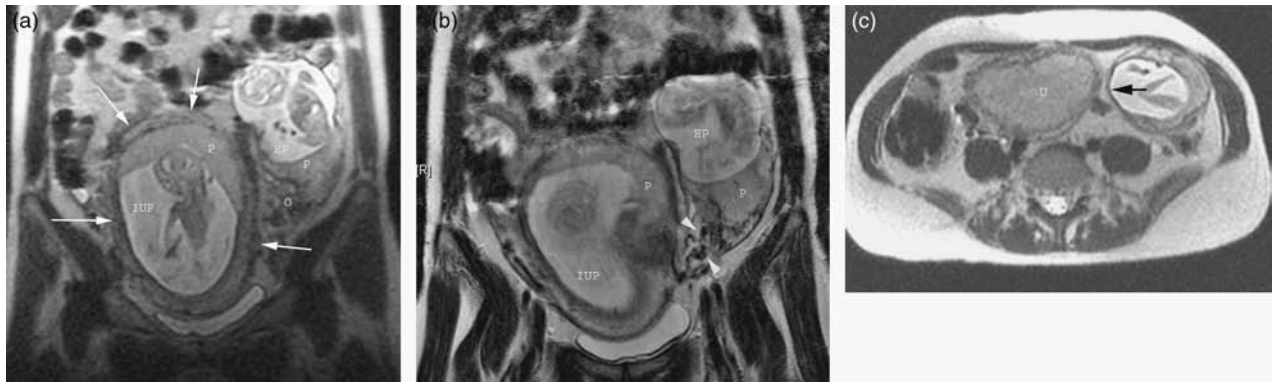

Figure 11.34 Heterotopic pregnancy at 18 weeks gestational age. Coronal T_2-weighted SSFSE (a), FSE (b), and axial T_2-weighted SSFSE (c) images demonstrate an intrauterine pregnancy (IUP) and an ectopic pregnancy arising from the ovary (O). Note that normal appearing placental tissue (P) in each gestational sac. The myometrium (white arrows) surrounds the intrauterine gestation but is not seen around the ectopic. Observe how the slow signal intensity chorion (black arrow in c) can mimic a thin portion of myometrium. The predominant vascular supply was from vessels inferior to the ovary (arrowheads in b). The longer acquisition time of the FSE T_2-weighted image (b) accounts for increased artifacts secondary to motion when compared with the fast scanning techniques in (a) and (c).

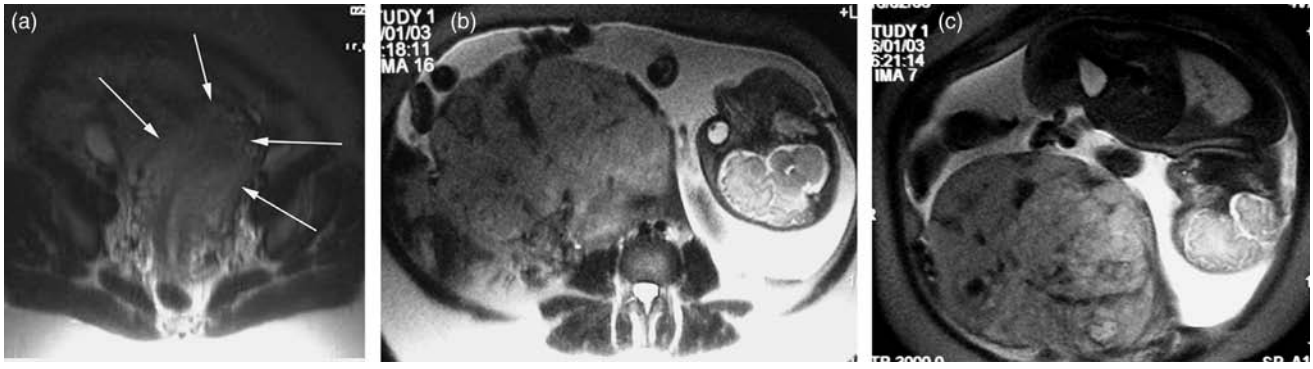

Figure 11.35 Abdominal ectopic pregnancy at term. (a) Axial T_2-weighted SSFSE image in the pelvis shows an empty uterus. Axial (b) and coronal (c) T_2-weighted SSFSE images in the abdomen show the abdominal ectopic pregnancy clearly outside of the uterus surrounded by the chorionic membrane. The delivery was by laparotomy. (Courtesy of S. Ulrich, Perth, Australia.)

images provide bright signal intensity within the blood vessels, on the basis of the differences in excitation history between the static protons in the imaging slice and the flowing protons within the vessels. Time-of-flight images should be obtained perpendicular to the vein of interest to avoid in-plane saturation effects that may mimic intraluminal clot. Compression of the pelvic veins by the gravid uterus may cause turbulent flow which can also be misinterpreted as thrombus on time-of-flight images; cine gradient echo images using cardiac gating can differentiate inconsistent filling defects related to turbulent flow from persistent filling defect secondary to venous thrombus. A targeted sonogram of the venous segment of concern is usually helpful to confirm or exclude the presence of a thrombus.

MR IMAGING OF ABDOMINOPELVIC PAIN IN PREGNANCY

The pregnant patient with abdominal and/or pelvic pain presents a challenge to the clinician. The pain can result from a variety of causes, such as ligamentous laxity or a hemorrhagic corpus luteum cyst, and includes conditions that require surgical intervention, such as ovarian torsion or appendicitis. Appendicitis is a consideration with right-sided pain, even when not localized to the lower quadrant, because the appendix can be displaced during pregnancy.

The imaging modality of choice when a pregnant patient presents with abdominopelvic pain is ultrasound. There are times, however, when ultrasound is not sufficient for a diagnosis, and correlative imaging is needed. MR screening for appendicitis in pregnancy has recently been utilized as MR imaging can provide a systematic cross-sectional view of the anatomic structures and pathologic conditions (64,65).

Technique

Our current MR protocol includes oral preparation with a combination of 300 mL of silicone-coated superparamagnetic iron oxide (Gastromark, Mallinckrodt Medical Inc., St. Louis, MO) and 300 mL of barium sulfate suspension (Readi-cat 2, EZEM Canada Inc., Westbury, NY). This solution is administered 1 hour prior to the examination in order to fill the cecum. This preparation provides negative oral contrast on T_1- and T_2-weighted images without substantial susceptibility effect (65).

Our sequences include T_2-weighted imaging with a nonfat-suppressed half-Fourier single-shot fast spin echo (SSFSE) sequence in the axial, coronal, and sagittal planes using a 4 mm section thickness. The field-of-view is typically 35 cm, and the matrix is 160–192 phase encoding steps and 256 frequency encoding steps. A repeat SSFSE axial acquisition is performed using parameters identical to those described previously, supplemented by fat saturation to improve the visualization of periappendiceal inflammatory changes and to demonstrate early ovarian edema in cases of torsion. Axial 2D time-of-flight images are acquired from the renal veins to the symphysis pubis to screen for venous clot and to differentiate the appendix from the frequently encountered periappendiceal veins. For this sequence, we use the following parameters: TR = 25 ms, TE = minimum with flow compensation, field-of-view = 35 cm, and matrix = 128 × 256. Axial dual echo T_1-weighted images in- and out-of-phases are useful for characterization of hemorrhage or fatty adnexal lesions (65). For patients with suspected choledocholithiasis or ureteral

stone, a heavy T_2-weighted thick slab (typically 20–50 mm thickness) SSFSE sequence is utilized (66).

Obstetric and Gynecologic Causes of Pelvic Pain

As mentioned previously, normal pregnancy with associated ligamentous laxity can be associated with pain. Corpus luteum cysts and miscarriage are common sources of pain in early pregnancy. Abruption, preterm labor, ectopic pregnancy, and uterine dehiscence can be associated with pain. Examples of these have been illustrated previously in this chapter. Ovarian torsion, fibroid degeneration, and fibroid torsion are other causes of pain. These diagnoses can typically be made sonographically when the patient experiences pain when the transducer is over the enlarged torsed ovary or the degenerating fibroid. When an MR examination is performed for abdominopelvic pain, these conditions should be kept in mind, and the ovaries, uterus, and placenta should be carefully assessed.

Renal Causes of Abdominopelvic Pain

Ureteral dilatation is a common finding in pregnancy, because of both hormonal changes that cause smooth muscle relaxation and compressive changes from the enlarging uterus. The right side is typically more dilated than the left. The ureters are dilated above the level of the pelvic brim and smoothly taper below this level (Fig. 11.36). Flank pain may result from hydronephrosis, which may be due to either an obstructing stone or physiologic hydronephrosis of pregnancy (Figs. 11.36–11.38). The right ovarian vein complex, which may greatly dilate during pregnancy, lies obliquely over the right ureter and may contribute to right ureteral dilatation (Fig. 11.39).

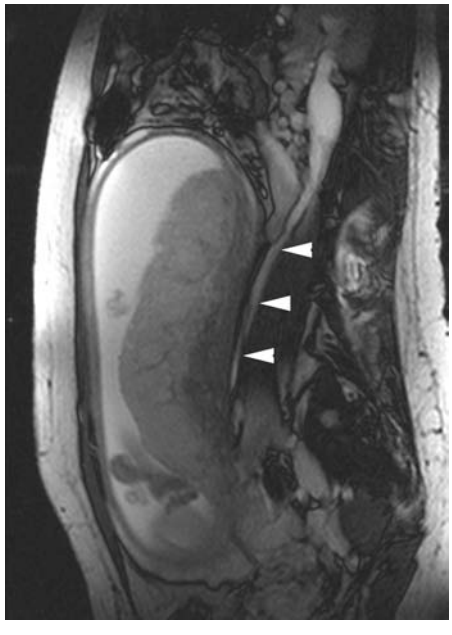

Figure 11.36 Physiologic hydronephrosis of pregnancy in patient with right-sided abdominal pain (24 weeks pregnant). Sagittal true steady state with free precession image depicts a dilated renal pelvis and a dilated ureter that tapers gently (arrowheads) to the pelvic brim.

Nephrolithiasis complicates 1/2000 pregnancies and may lead to premature labor (67). The stones are visualized as hypointense filling defects surrounded by hyperintense urine on T_2-weighted images. Care should be taken to avoid mistaking flow artifact for a stone (Fig. 11.37). The main limitation of MR urography is that resolution tends to be limited and small stones can be missed (Fig. 11.37) (68). If a stone is not visualized, but the level of obstruction is not at the level of the pelvic brim (e.g., at the uteropelvic junction or at the uterovesical junction), then stone disease should still be suspected. If space permits in the magnet bore, it may be helpful to scan the patient in the lateral decubitus position, with the symptomatic side up to relieve the pressure of the uterus from the ureter.

Urinary tract infections are very common during pregnancy, as a consequence of urinary stasis and increased glucose in the urine (Fig. 11.40). *Escherichia coli* is the most common pathogen. Uncomplicated urinary tract infection is usually diagnosed clinically (69). Many women with bacteriuria will develop pyelonephritis during pregnancy. On MR imaging, pyelonephritis is visualized as an enlarged edematous appearing kidney. Focal areas of lower signal intensity on T_2-weighted imaging can be because of focal pyonephrosis.

Hemorrhagic renal masses can present as flank pain in pregnancy (64). Patients with angiomyolipomas may hemorrhage during pregnancy due to rupture of the tumor (Fig. 11.41). Usually, emergency nephrectomy is required, with simultaneous cesarean section in patients at 28 weeks gestation or later (70). However, if patients are stable, close monitoring can be performed and delivery delayed until later in pregnancy (70). Embolization of the renal artery can also be performed during pregnancy, however, that entails radiation dose to the fetus.

Biliary Causes of Abdominal Pain in Pregnancy

Cholecystitis is the second most common surgical condition in pregnancy and occurs in ~1 in 1600 to 1 in 10,000 pregnancies. Cholelithiasis is found in 3.5% of pregnant women undergoing routine obstetric ultrasound examinations (71). This is due to progesterone causing

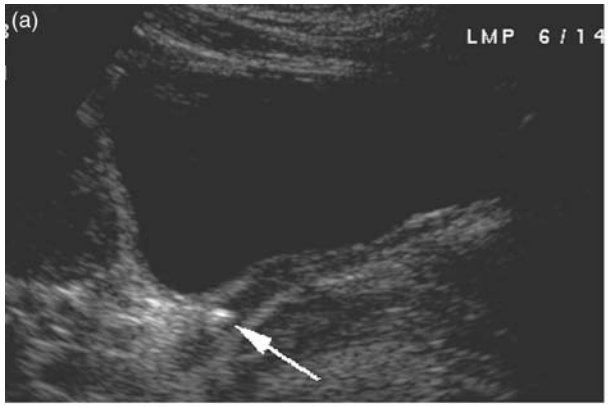

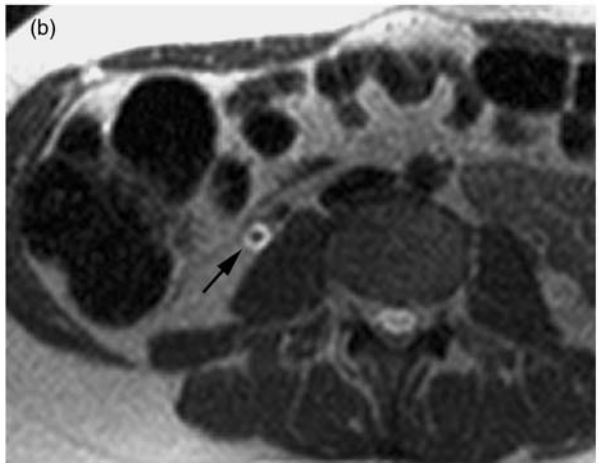

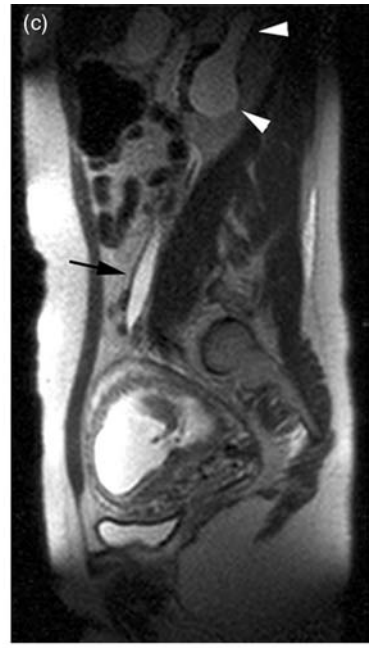

Figure 11.37 Flank pain in pregnancy (14 weeks pregnant). (a) Transabdominal sonogram demonstrates a 5 mm obstructing stone (white arrow) in the distal ureter. Axial (b) and sagittal (c) T_2-weighted SSFSE images (4 days after the sonogram) show a central hypointense filling defect in the mid ureter in (b, black arrow) but no corresponding filling defect within the ureter at the level on the sagittal image (c, black arrow). Moderate hydronephrosis of the right kidney (arrowheads) is apparent. Multiple similar filling defects noted at different levels on the axial images were felt to be due to flow-related artifacts. The patient's symptoms spontaneously resolved, without recurrence. The stone seen on ultrasound was not visualized on MR, possibly because of having been passed prior to the examination. [From Eyvazzadeh et al. (65)]

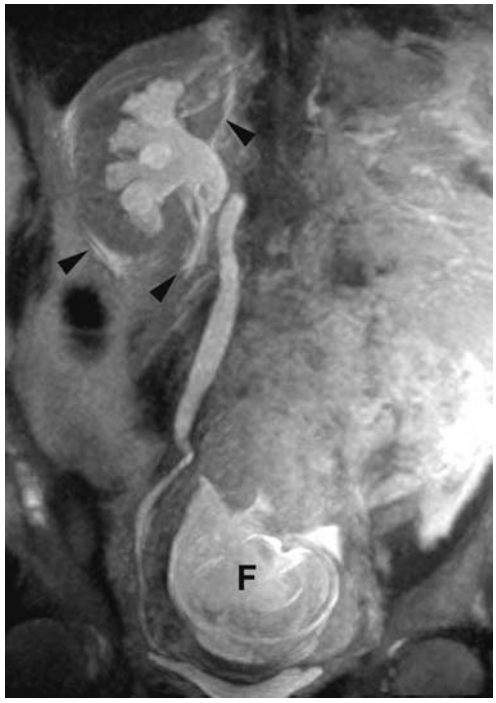

Figure 11.38 Nonvisualized stone in patient with right lower quadrant pain, nausea, vomiting, and elevated white cell count of 24,000 (24 weeks pregnant). Coronal maximal intensity projection T_2-weighted image shows moderate hydronephrosis of the right kidney. Note the perirenal fluid (arrowheads) indicative of acute obstruction, although no stone was detected. The patient passed a stone the day after the MR examination. [From Eyvazzadeh et al. (65)]

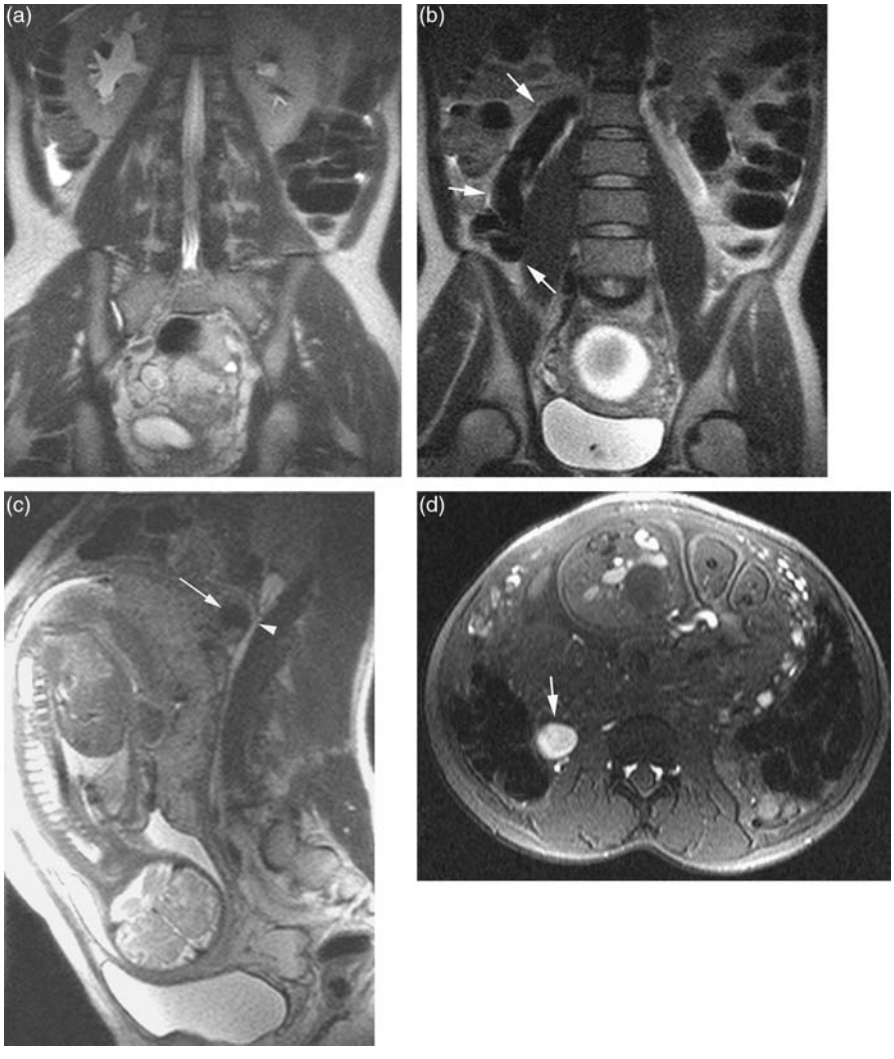

Figure 11.39 Dilated right ovarian vein. Physiologic hydronephrosis of pregnancy and an enlarged right ovarian vein with abdominal pain just superior to and to the right of the umbilicus (36 weeks pregnant). Coronal (a, b) and sagittal (c) T_2-weighted images demonstrate mild right hydronephrosis. The enlarged right gonadal vein (arrows) is well-visualized as a dark tubular structure, due to flowing blood. The tapering ureter (arrowhead) just posterior to the gonadal vein (arrow) is well visualized in image (d). Axial time-of-flight image shows flow in gonadal vein (arrow). Dilatation of the right gonadal vein is common during pregnancy. It may contribute to the renal dilation of pregnancy and may be associated with pelvic pain. [From Eyvazzadeh et al. (65)]

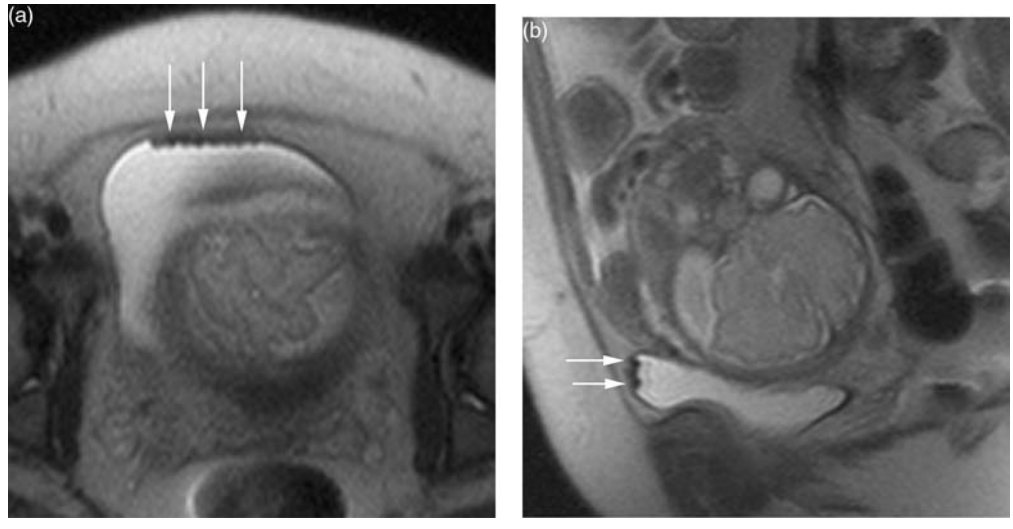

Figure 11.40 Urinary tract infection in patient with lower abdominal pain and elevated white blood cell count (32 weeks pregnant). Previous ultrasound and urine dipstick analysis were normal. Sagittal (a) and axial (b) T_2-weighted SSFSE images show low signal intensity in the nondependent portion of the urinary bladder (arrow) consistent with air. Patient did not have prior instrumentation of the urinary bladder and, therefore, urinary infection was suggested. On the basis of the MR findings, a urine culture was performed which documented $>100{,}000$ *E. coli.* [From Eyvazzadeh et al. (65)]

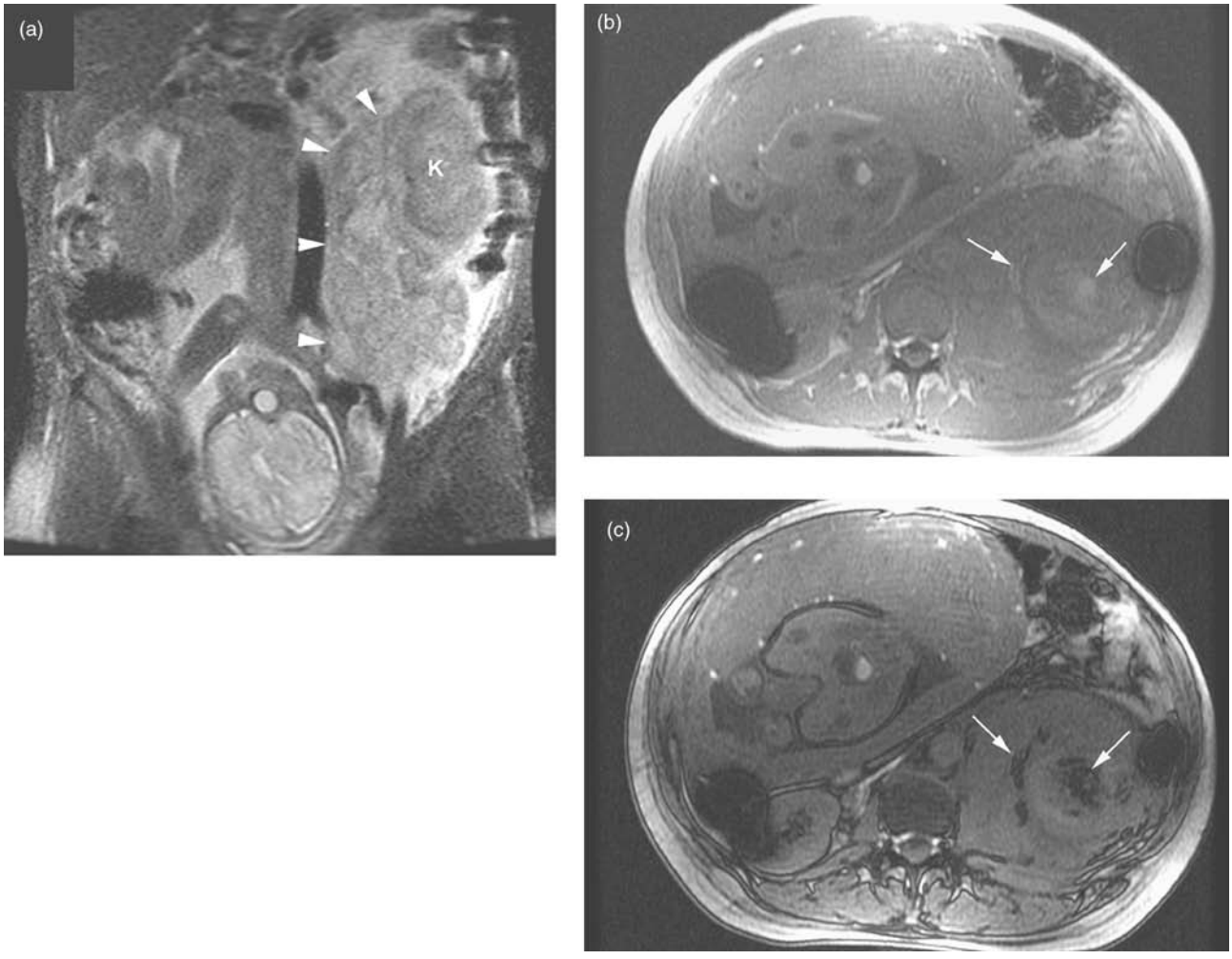

Figure 11.41 Ruptured angiomyolipoma in a patient with a 10 day history of vague abdominal pain and a 1 day history of acute left flank pain (31 weeks pregnant). An outside sonogram (not shown) demonstrated a 7 cm left renal mass. Coronal T_2-weighted fat-saturated SSFSE image (a) shows a heterogenous hyperintense mass extending medially and inferiorly (arrowheads) to the left kidney (K) consistent with a large hematoma. T_1-weighted in-phase gradient echo image (b) shows two areas of hyperintensity within the hematoma. These areas become hypointense (arrows) on the out-of-phase T_1-weighted gradient echo image (c) indicating the intravoxel coexistence of fat and water. T_1-weighted images without and with frequency-selective fat saturation (not shown) confirmed the presence of bulk fat. Although renal angiomyolipoma and renal cell carcinoma are diagnostic considerations when small amounts of lipids are detected on in-phase and opposed-phase imaging, the presence of bulk fat in a renal mass is virtually pathognomonic of angiomyolipoma.

gallbladder atony and increased cholesterol in the bile during pregnancy. The rate of cholelithiasis complicating pregnancy is 3/1000 live births, with the incidence increasing with advancing gestational age. Pregnant patients are at increased risk for gallstones due to the increased levels of progesterone that leads to gallbladder atony. Screening for gallstones is performed with ultrasound. In the cases where ductal stones are of concern, MR cholangiography offers >90% sensitivity for detection of common duct stones (Fig. 11.42) (72–74). In addition, MR cholangiography can be utilized to guide stone extraction and reduce need for fluoroscopy during stone removal in pregnancy (75,76). Stones are visualized as hypointense filling defects with respect to the adjacent hyperintense bile on T_2-weighted imaging. Stones should be documented on more than one sequence to avoid mistaking flow artifact for a stone (77). Endoscopic retrograde pancreatography (with its associated radiation dose) can then be utilized to treat select cases with documented stones in the duct.

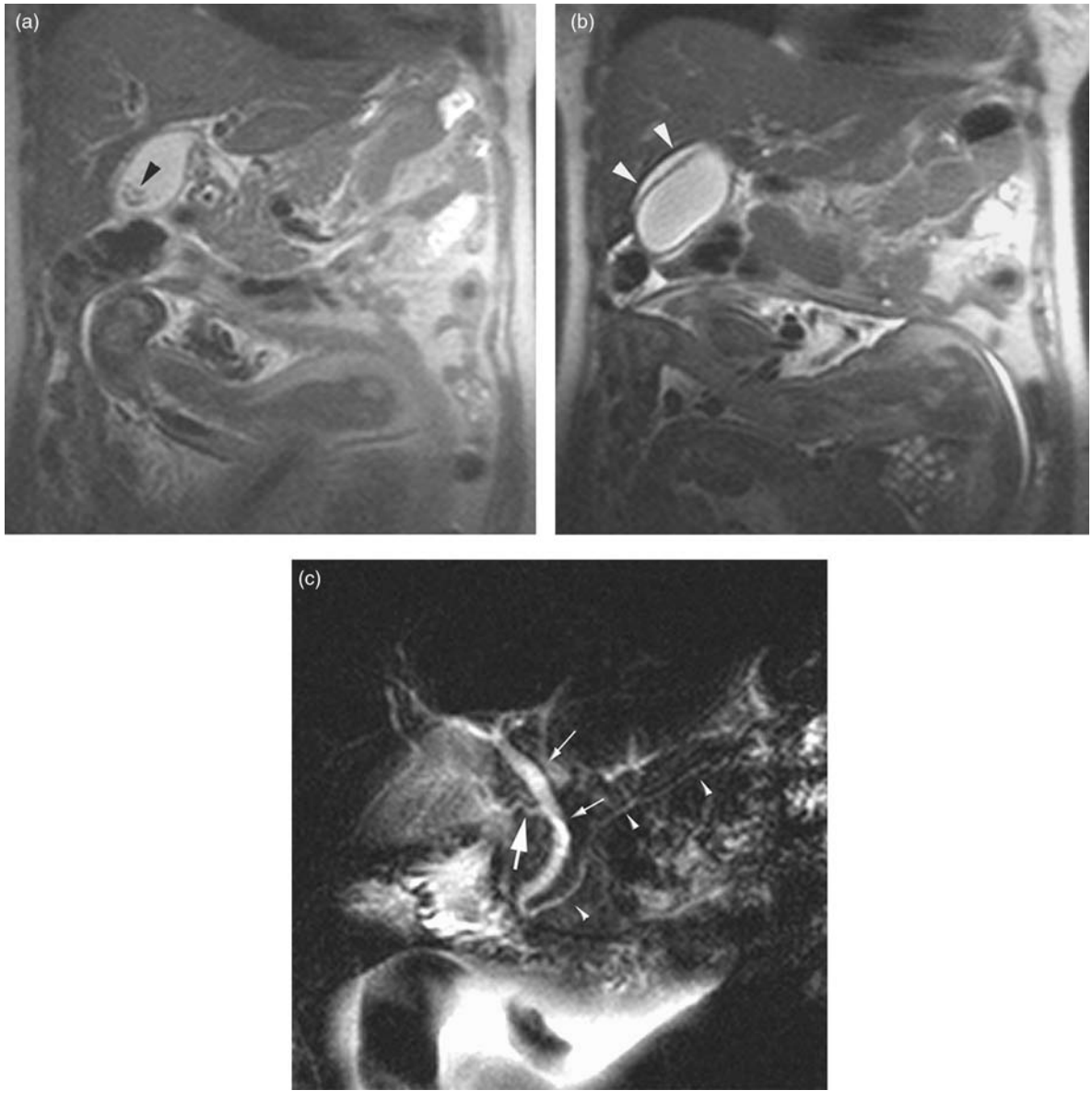

Figure 11.42 Cholelithiasis with pericholecystic fluid in a patient with severe right upper quadrant pain (35 weeks pregnant). Her lipase was elevated at 5342 IU/L. MR examination was performed to assess for obstructing stones and complications of pancreatitis. Axial T_2-weighted SSFSE images (a, b) show diffuse edema in the gallbladder wall (white arrowheads) and gallstones (black arrowhead). Coronal thick slab SSFSE (c, thickness 20 mm) image demonstrates normal intra- and extra-hepatic (small white arrows) bile ducts, cystic duct (large white arrow), and pancreatic duct (small arrowheads). The patient underwent laparoscopic cholecystectomy after delivery. Intraoperative cholangiogram found no stones in the bile ducts. [(c) from Eyvazzadeh et al. (65)]

Gastrointestinal Causes of Abdominopelvic Pain in Pregnancy

Appendicitis

Acute appendicitis is the most common nonobstetrical surgical condition of the abdomen complicating pregnancy. The incidence of appendicitis in pregnancy (0.05–0.07%) is similar to that in the general population, but pregnant patients are more likely to present with perforation (43% vs. 4–19% in the general population) as diagnosis tends to be delayed. Anatomic and physiologic changes that may disguise and delay the diagnosis of acute appendicitis include: 1) cephalad displacement of the appendix from the right lower quadrant by the enlarged uterus (78); 2) increased leukocyte count in pregnancy; and 3) physiologic increase in maternal blood volume

that diminish the woman's ability to demonstrate tachycardia or hypotension.

Radiologic examination is often delayed because of potential hazardous effects of radiation exposure. Ultrasonography with graded compression is valuable for detecting acute appendicitis in pregnant women. In the cases, where a normal appendix is not visualized sonographically, MR imaging can be used to visualize the appendix (64,65).

The normal appendix is seen on MR imaging as a tubular structure of <6 mm diameter. The presence of air or superparamagnetic oral contrast within the lumen of the appendix is visualized as a central hypointense area in the normal appendix. The normal appendix may be located in a variety of locations in the right abdomen, as the enlarging gravid uterus may displace the cecum superiorly (Fig. 11.43). We have found that the use of a cross-referencing function that simultaneously maps position on two or more images in our picture archiving and communications system facilitates localization of the normal appendix (65). A small amount of fluid can be visualized in the pelvis as a normal finding.

MR imaging findings in appendicitis include an enlarged fluid-filled appendix with or without increased signal intensity in the periappendiceal fat on T_2-weighted imaging representing periappendiceal inflammatory changes (Fig. 11.44). A phlegmon or focal fluid collection may be present (Fig. 11.45). In the postappendectomy patient, inflammatory tissue may be noted around the stump (Fig. 11.46) (65).

Bowel Obstruction and Inflammation

Bowel obstruction in pregnancy is an uncommon complication, occurring in 1 in 2500 to 1 in 3500 deliveries. Patients with a history of previous abdominal or pelvic surgery are at increased risk, as the most common cause is adhesions, accounting for 60–70% of cases (71,79).

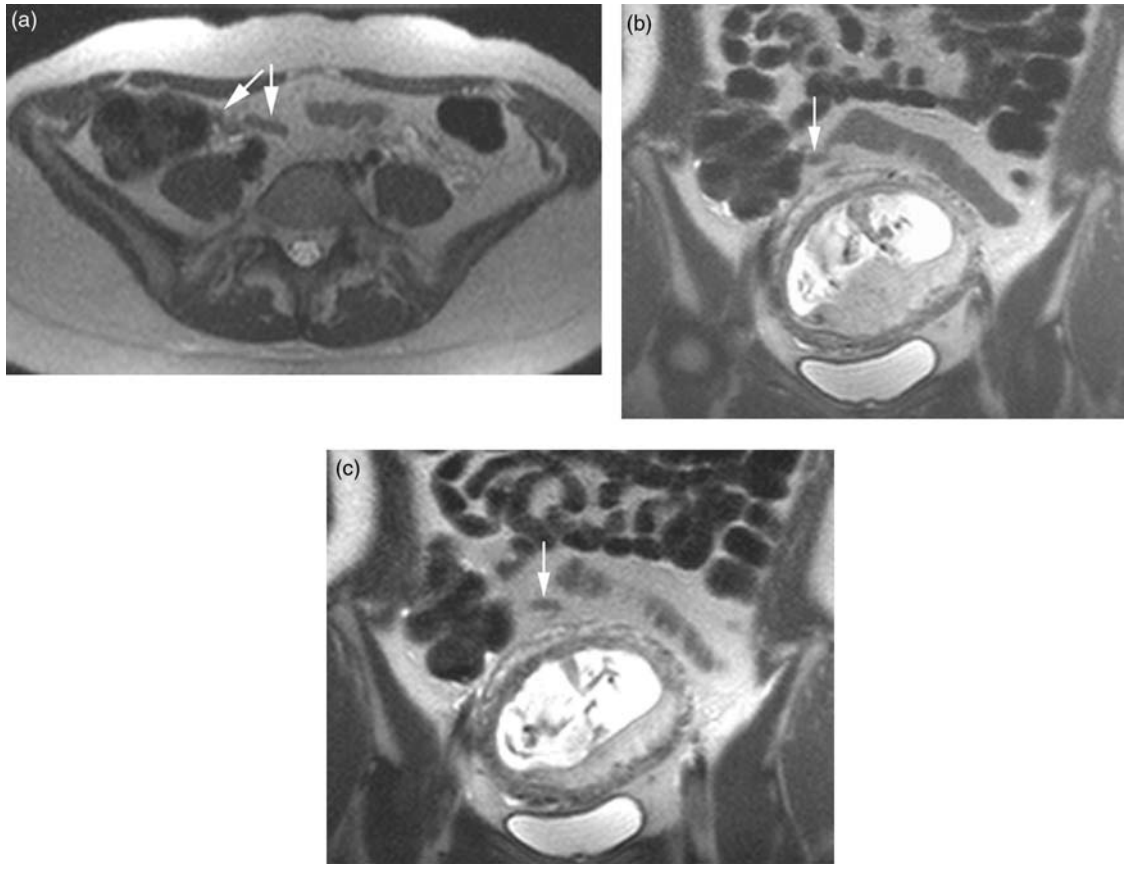

Figure 11.43 Normal appendix in a patient being examined for severe right lower quadrant pain (16 weeks pregnant). Axial (a) and coronal (b, c) T_2-weighted SSFSE images depict the normal appendix (arrows) localized in the right mid abdomen, superiorly displaced by the gravid uterus.

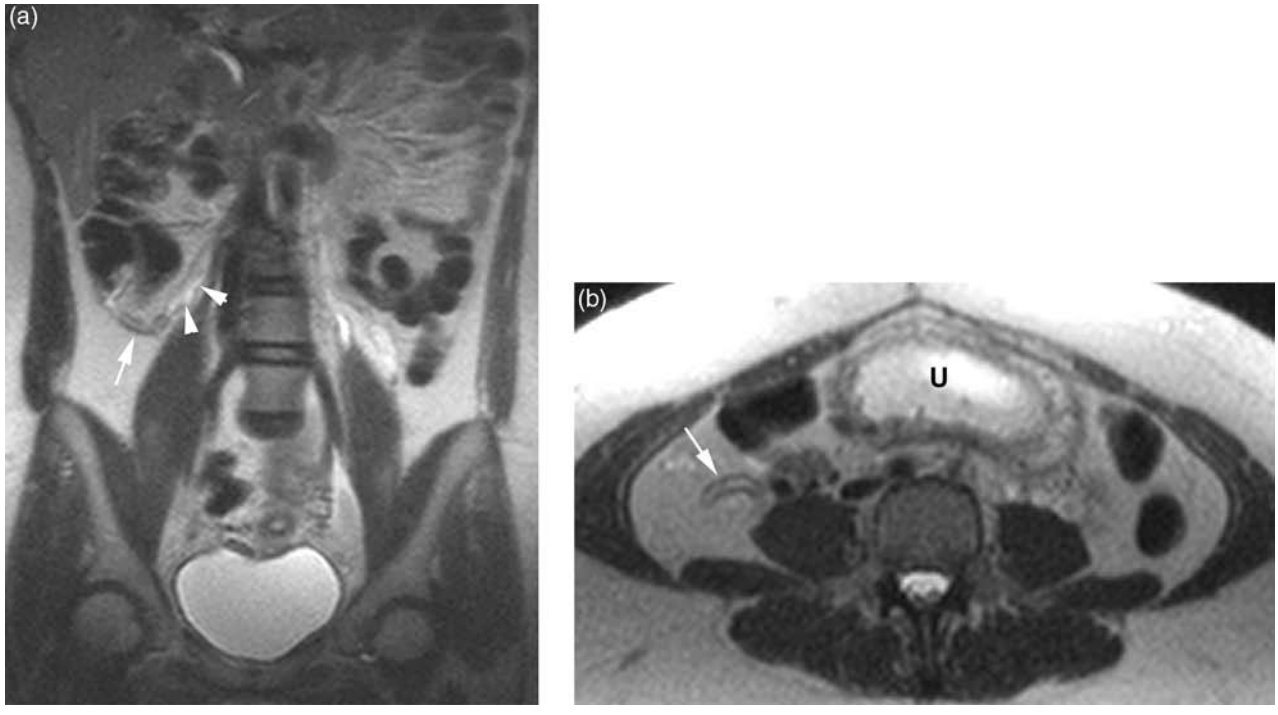

Figure 11.44 Mild acute appendicitis in a patient with severe right lower quadrant pain (13 weeks pregnant). Coronal (a) and axial (b) T_2-weighted images show an enlarged fluid-filled appendix measuring 9 mm in caliber (arrow). Note the increased signal intensity in the mesoappendix consistent with inflammatory changes (arrowheads). Gravid uterus (U). Mild acute appendicitis was confirmed both at surgery and pathology. [From Eyvazzadeh et al. (65)]

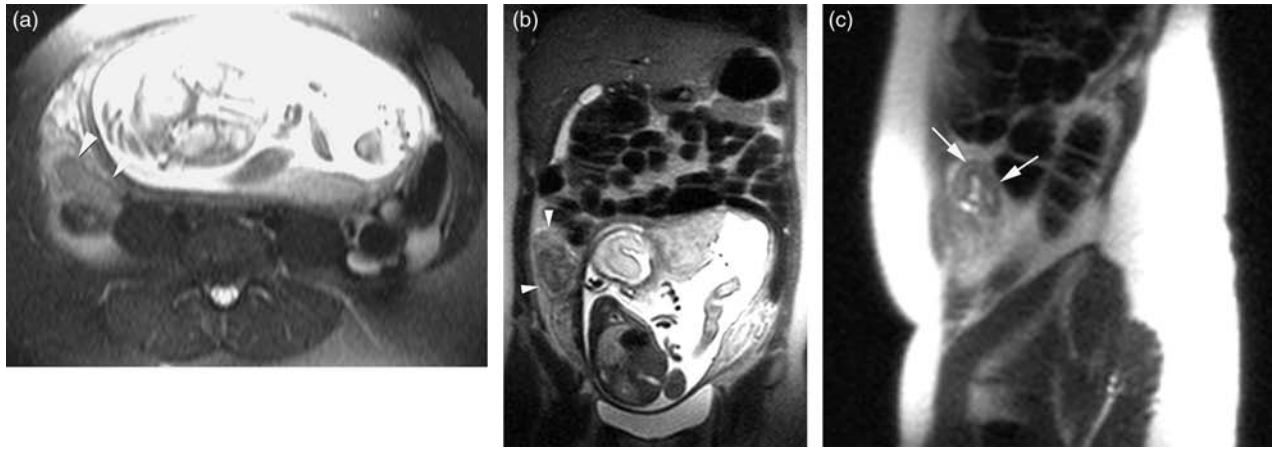

Figure 11.45 Appendicitis with phlegmon in patient with severe right lower quadrant pain (27 weeks pregnant). Sonogram (not shown) demonstrated a right lower quadrant phlegmon. Axial (a) and coronal (b) T_2-weighted SSFSE images show a heterogeneous moderately hyperintense mass in the right lower quadrant consistent with an inflammatory phlegmon with a markedly enlarged appendix measuring 2 cm in diameter (arrowheads). The patient was treated with intravenous antibiotics. (c) After 5 weeks, sagittal T_2-weighted image demonstrates slight decrease in size of the appendix. The patient was delivered at 33 weeks, with appendectomy performed at the time of cesarean section, the latter confirming appendicitis. [(a) from Eyvazzadeh et al. (65)]

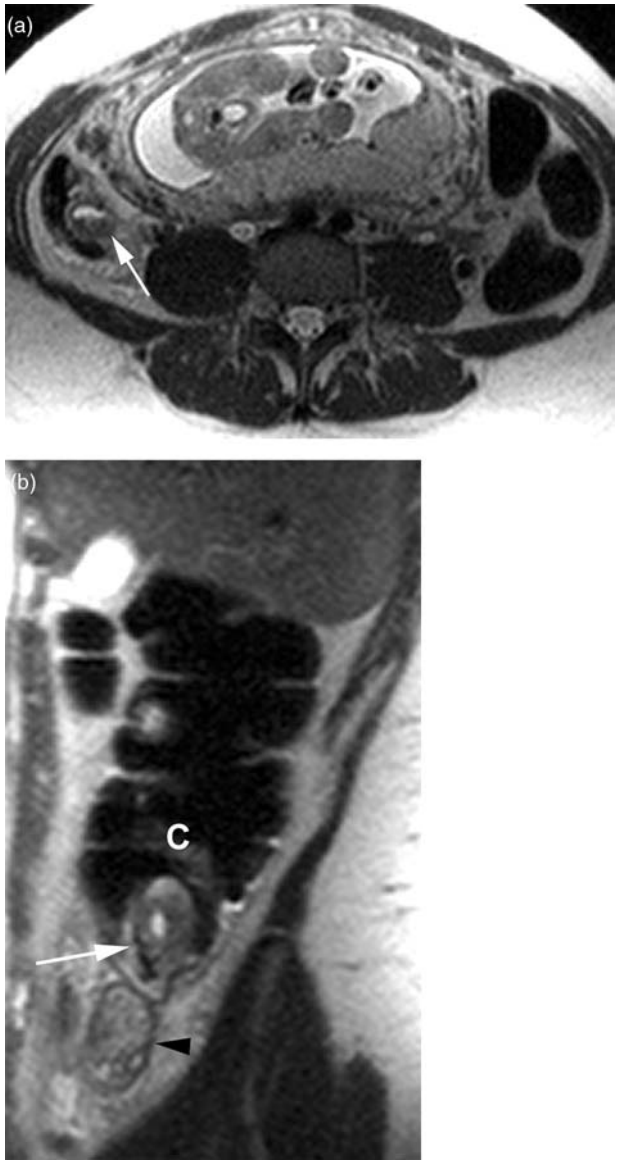

Figure 11.46 Appendiceal stump 13 days after appendectomy in patient with continued right-sided abdominal pain and leukocytosis (21 weeks pregnant). Axial (a) and sagittal (b) T_2-weighted SSFSE images at the level of cecum (c) show a heterogeneously hyperintense mass-like appendiceal stump (arrow) with central high signal intensity due to fluid. Right ovary is seen in (B, arrowhead).

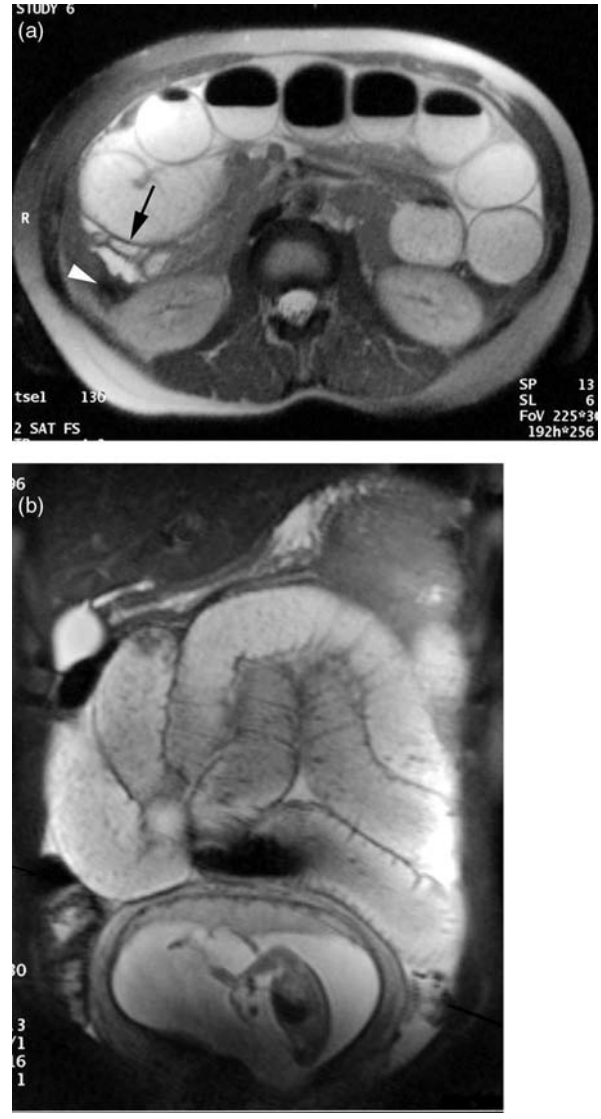

Figure 11.47 Small bowel obstruction due to adhesions in patient with severe abdominal pain and history of prior abdominal surgery (13 weeks pregnant). Axial (a) and coronal (b) T_2-weighted SSFSE images show multiple dilated fluid-filled loops of bowel with air fluid levels. There are some nondilated loops of small bowel in the right lower quadrant, and air in the colon. No obstructing mass was seen. The presumptive diagnosis was obstruction secondary to adhesions. The patient was managed conservatively and did not require surgery during pregnancy. [(b) from Levine et al. (46)]

Obstruction usually occurs at 12–15 weeks as the uterus grows into the abdomen, late in the third trimester as the fetal head descends into the pelvis, or postpartum, when there is rapid change in uterine size. Preterm delivery affects one-third of patients (79). Although experience with MR imaging is limited in evaluating bowel obstruction, it can be helpful in selected patients (Fig. 11.47).

Patients with Crohn's disease and abdominal pain may be particularly difficult to assess during pregnancy because they may require repeated diagnostic examinations and because ileitis may mimic appendicitis. MR can be utilized to assess the bowel in these patients (Fig. 11.48).

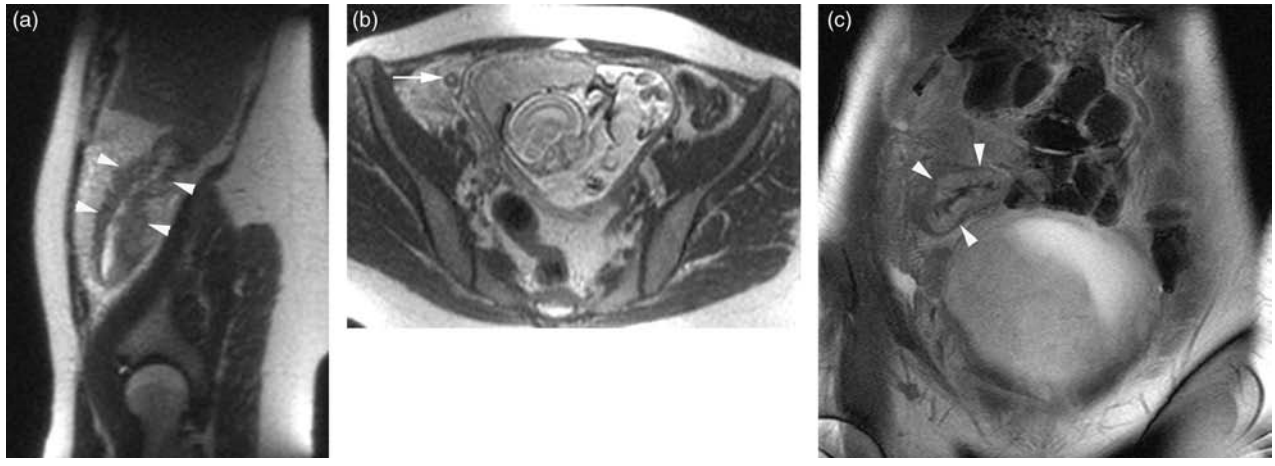

Figure 11.48 Crohns flare in patient with severe right lower quadrant pain (20 weeks pregnant). Sonogram (not shown) demonstrated a thick-walled appendix and thickened terminal ileum. MR examination was performed to assess for appendicitis in addition to Crohns disease. (a) Sagittal T_2-weighted SSFSE image reveals a thickened ascending colon (arrowheads). (b) Axial T_2-weighted image shows a thickened appendix (arrow). However, there is no stranding of the periappendiceal fat to suggest appendicitis. (c) Coronal T_2-weighted image with fat saturation again demonstrates the abnormal ilium with edematous bowel wall. The patient was treated medically for a Crohns flare and discharged from the hospital the following day. A follow-up MR examination 2 weeks after initial study showed significant improvement of the inflammatory changes.

CONCLUSION

MR imaging is increasingly being utilized in pregnant patients as a problem-solving tool. MR pelvimetry is the procedure of choice when pelvic measurements are needed prior to delivery. Assessment of pelvic masses and ectopic pregnancy can be performed with MR imaging. Although pregnant patients with right lower quadrant pain should be initially screened with ultrasound, MR imaging can provide additional valuable information in these patients. It is important for the radiologist to recognize the MR imaging appearance of common causes of right-sided pain in pregnancy, as patients with symptoms may have gastrointestinal, uterine, ovarian, or placental etiologies for their pain during pregnancy.

REFERENCES

1. van Loon AJ, Mantingh A, Thijn CJ et al. Pelvimetry by magnetic resonance imaging in breech presentation. Am J Obstet Gynecol 1990; 163:1256–1260.
2. Stark DD, McCarthy SM, Filly RA et al. Pelvimetry by magnetic resonance imaging. Am J Roentgenol 1985; 144:947–950.
3. van Loon AJ, Mantingh A, Serlier EK et al. Randomized controlled trial of magnetic-resonance pelvimetry in breech presentation at term. Lancet 1997; 350:1799–1804.
4. Wright AR, Cameron HM, Lind T. Magnetic resonance imaging pelvimetry: a useful adjunct in the management of the obese patient. Br J Obstet Gynaecol 1992; 99:852–853.
5. Iams JD, Goldenberg RL, Meis PJ et al. The length of the cervix and the risk of spontaneous premature delivery. National Institute of Child Health and Human Development Maternal Fetal Medicine Unit Network. N Engl J Med 1996; 334:567–572.
6. Berghella V, Kuhlman K, Weiner S et al. Cervical funneling: sonographic criteria predictive of preterm delivery. Ultrasound Obstet Gynecol 1997; 10:161–166.
7. Maldjian C, Adam R, Pelosi M et al. MRI appearance of cervical incompetence in a pregnant patient. Magn Reson Imaging 1999; 17:1399–1402.
8. Oduncu FS, Kimmig R, Hepp H et al. Cancer in pregnancy: maternal-fetal conflict. J Cancer Res Clin Oncol 2003; 129:133–146.
9. van der Vange N, Weverling GJ, Ketting BW et al. The prognosis of cervical cancer associated with pregnancy: a matched cohort study. Obstet Gynecol 1995; 85:1022–1026.
10. Nicolet V, Carignan L, Bourdon F et al. MR imaging of cervical carcinoma: a practical staging approach. Radiographics 2000; 20:1539–1549.
11. Rozenberg P, Goffinet F, Phillippe HJ et al. Ultrasonographic measurement of lower uterine segment to assess risk of defects of scarred uterus. Lancet 1996; 347:281–284.
12. Hamrick-Turner JE, Cranston PE, Lantrip BS. Gravid uterine dehiscence: MR findings. Abdom Imaging 1995; 20:486–488.
13. Hamar BD, Levine D, Katz NL et al. Expectant management of uterine dehiscence in the second trimester of pregnancy. Obstet Gynecol 2003; 102:1139–1142.
14. McCarthy SM, Stark DD, Filly RA et al. Obstetrical magnetic resonance imaging: maternal anatomy. Radiology 1985; 154:421–425.

15. Weinreb JC, Lowe TW, Santos-Ramos R et al. Magnetic resonance imaging in obstetric diagnosis. Radiology 1985; 154:157–161.
16. Powell MC, Buckley J, Price H et al. Magnetic resonance imaging and placenta previa. Am J Obstet Gynecol 1986; 154:565–569.
17. Trop I, Levine D. Hemorrhage during pregnancy: sonography and MR imaging. Am J Roentgenol 2001; 176:607–615.
18. Nimmo MJ, Kinsella D, Andrews HS. MRI in pregnancy: the diagnosis of vasa previa by magnetic resonance imaging. Bristol Med Chir J 1988; 103:12.
19. Mochizuki T, Nishiguchi T, Ito I et al. Case report. Antenatal diagnosis of chorioangioma of the placenta: MR features. J Comput Assist Tomogr 1996; 20:413–416.
20. Angtuaco TL, Shah HR, Mattison DR et al. MR imaging in high-risk obstetric patients: a valuable complement to US. Radiographics 1992; 12:91–109; discussion 110.
21. Nyberg DA, Cyr DR, Mack LA et al. Sonographic spectrum of placental abruption. Am J Roentgenol 1987; 148:161–164.
22. Benedetti TJ. Obstetric hemorrhage. In: Gabbe SG, Niebyl JR, Simpson JL, eds. Obstetrics: Normal and Problem Pregnancies. Philadelphia, PA: Churchill Livingstone, 2002:503–538.
23. Finberg HJ, Williams JW. Placenta accreta: prospective sonographic diagnosis in patients with placenta previa and prior cesarean section. J Ultrasound Med 1992; 11:333–343.
24. Kirkinen P, Helin-Martikainen HL, Vanninen R et al. Placenta accreta: imaging by gray-scale and contrast-enhanced color Doppler sonography and magnetic resonance imaging. J Clin Ultrasound 1998; 26:90–94.
25. Ha TP, Li KC. Placenta accreta: MRI antenatal diagnosis and surgical correlation. J Magn Reson Imaging 1998; 8:748–750.
26. Fejgin MD, Rosen DJ, Ben-Nun I et al. Ultrasonic and magnetic resonance imaging diagnosis of placenta accreta managed conservatively. J Perinat Med 1993; 21:165–168.
27. Thorp JM Jr, Councell RB, Sandridge DA et al. Antepartum diagnosis of placenta previa percreta by magnetic resonance imaging. Obstet Gynecol 1992; 80:506–508.
28. Maldjian C, Adam R, Pelosi M et al. MRI appearance of placenta percreta and placenta accreta. Magn Reson Imaging 1999; 17:965–971.
29. Levine D, Hulka CA, Ludmir J et al. Placenta accreta: evaluation with color Doppler US, power Doppler US, and MR imaging. Radiology 1997; 205:773–776.
30. Tanaka YO, Sohda S, Shigemitsu S et al. High temporal resolution dynamic contrast MRI in a high risk group for placenta accreta. Magn Reson Imaging 2001; 19:635–642.
31. Palacios Jaraquemada JM, Bruno C, Pesaresi M et al. Diagnóstico diferencial de los trastornos adherenciales de la placenta por resonancia magnética nuclear contrastada (acretismo y percretismo placentario). Rev Chil Obstet Ginecol 1999; 64:34–40.
32. Marcos HB, Semelka RC, Worawattanakul S. Normal placenta: gadolinium-enhanced dynamic MR imaging. Radiology 1997; 205:493–496.
33. Product Information, Magnevist, Berlex Laboratories, 2000.
34. Product Information, Omniscan, Amersham Health, 2000.
35. Murase E, Siegelman ES, Outwater EK et al. Uterine leiomyomas: histopathologic features, MR imaging findings, differential diagnosis, and treatment. Radiographics 1999; 19:1179–1197.
36. Ueda H, Togashi K, Konishi I et al. Unusual appearances of uterine leiomyomas: MR imaging findings and their histopathologic backgrounds. Radiographics 1999; 19: S131–S145.
37. Jung SE, Byun JY, Lee JM et al. MR imaging of maternal diseases in pregnancy. Am J Roentgenol 2001; 177:1293–1300.
38. Ha HK, Jung JK, Kang SJ et al. MR imaging in the diagnosis of rare forms of ectopic pregnancy. Am J Roentgenol 1993; 160:1229–1232.
39. Wagner BJ, Woodward PJ, Dickey GE. From the archives of the AFIP. Gestational trophoblastic disease: radiologic-pathologic correlation. Radiographics 1996; 16:131–148.
40. Jauniaux E, Brown R, Rodeck C et al. Prenatal diagnosis of triploidy during the second trimester of pregnancy. Obstet Gynecol 1996; 88:983–989.
41. Goto S, Yamada A, Ishizuka T et al. Development of postmolar trophoblastic disease after partial molar pregnancy. Gynecol Oncol 1993; 48:165–170.
42. Rice LW, Berkowitz RS, Lage JM et al. Persistent gestational trophoblastic tumor after partial hydatidiform mole. Gynecol Oncol 1990; 36:358–362.
43. Hess LW, Peaceman A, O'Brien WF et al. Adnexal mass occurring with intrauterine pregnancy: report of fifty-four patients requiring laparotomy for definitive management. Am J Obstet Gynecol 1988; 158:1029–1034.
44. Kier R, McCarthy SM, Scoutt LM et al. Pelvic masses in pregnancy: MR imaging. Radiology 1990; 176:709–713.
45. Togashi K. MR imaging of the ovaries: normal appearance and benign disease. Radiol Clin North Am 2003; 41:799–811.
46. Levine D, Barnes PD, Edelman RR. Obstetric MR imaging. Radiology 1999; 211:609–617.
47. Ghossain MA, Hachem K, Buy JN et al. Adnexal torsion: magnetic resonance findings in the viable adnexa with emphasis on stromal ovarian appearance. J Magn Reson Imaging 2004; 20:451–462.
48. Nagayama M, Watanabe Y, Okumura A et al. Fast MR imaging in obstetrics. Radiographics 2002; 22:563–580.
49. Nishino M, Hayakawa K, Iwasaku K et al. Magnetic resonance imaging findings in gynecologic emergencies. J Comput Assist Tomogr 2003; 27:564–570.
50. Yoden E, Imajo Y, Yamauchi H et al. Ectopic pregnancy showing interesting findings on MR imaging. Am J Roentgenol 2001; 176:818–819.
51. Kinoshita T, Ishii K, Higashiiwai H. MR appearance of ruptured tubal ectopic pregnancy. Eur J Radiol 1999; 32:144–147.
52. Yamashita Y, Harada M, Torashima M et al. Unruptured interstitial pregnancy: a pitfall of MR imaging. Comput Med Imaging Graph 1995; 19:241–246.

53. Barton JW, McCarthy SM, Kohorn EI et al. Pelvic MR imaging findings in gestational trophoblastic disease, incomplete abortion, and ectopic pregnancy: are they specific? Radiology 1993; 186:163–168.
54. Kataoka ML, Togashi K, Kobayashi H et al. Evaluation of ectopic pregnancy by magnetic resonance imaging. Hum Reprod 1999; 14:2644–2650.
55. Rafal RB, Kosovsky PA, Markisz JA. MR appearance of cervical pregnancy. J Comput Assist Tomogr 1990; 14:482–484.
56. Dialani V, Levine D. Ectopic pregnancy: a review. Ultrasound Q 2004; 20:105–117.
57. Smolders D, Deckers F, Pouillon M et al. Ectopic pregnancy within a rudimentary horn in a case of unicornuate uterus. Eur Radiol 2002; 12:121–124.
58. Stanley JR, Harris AA, Gilbert CF et al. Magnetic resonance imaging in evaluation of a second-trimester ovarian twin pregnancy. Obstet Gynecol 1994; 84:648–652.
59. Siow A, Chern B, Soong Y. Successful laparoscopic treatment of an abdominal pregnancy in the broad ligament. Singapore Med J 2004; 45:88–89.
60. Wagner A, Burchardt AJ. MR imaging in advanced abdominal pregnancy. A case report of fetal death. Acta Radiol 1995; 36:193–195.
61. Malian V, Lee JH. MR imaging and MR angiography of an abdominal pregnancy with placental infarction. Am J Roentgenol 2001; 177:1305–1306.
62. Cohen JM, Weinreb JC, Lowe TW et al. MR imaging of a viable full-term abdominal pregnancy. Am J Roentgenol 1985; 145:407–408.
63. Beddock R, Naepels P, Gondry C et al. Diagnosis and current concepts of management of advanced abdominal pregnancy. Gynecol Obstet Fertil 2004; 32:55–61.
64. Leyendecker JR, Gorengaut V, Brown JJ. MR imaging of maternal diseases of the abdomen and pelvis during pregnancy and the immediate postpartum period. Radiographics 2004; 24:1301–1316.
65. Eyvazzadeh AD, Pedrosa I, Rofsky NM et al. MRI of right-sided abdominal pain in pregnancy. Am J Roentgenol 2004; 183:907–914.
66. Roy C, Saussine C, LeBras Y et al. Assessment of painful ureterohydronephrosis during pregnancy by MR urography. Eur Radiol 1996; 6:334–338.
67. Hendricks SK, Ross SO, Krieger JN. An algorithm for diagnosis and therapy of management and complications of urolithiasis during pregnancy. Surg Gynecol Obstet 1991; 172:49–54.
68. Roy C, Saussine C, Jahn C et al. Fast imaging MR assessment of ureterohydronephrosis during pregnancy. Magn Reson Imaging 1995; 13:767–772.
69. Ovalle A, Levancini M. Urinary tract infections in pregnancy. Curr Opin Urol 2001; 11:55–59.
70. Tanaka M, Kyo S, Inoue M et al. Conservative management and vaginal delivery following ruptured renal angiomyolipoma. Obstet Gynecol 2001; 98:932–933.
71. Sharp HT. The acute abdomen during pregnancy. Clin Obstet Gynecol 2002; 45:405–413.
72. Hochwalk SN, Dobryansky MB, Rofsky NM et al. Magnetic resonance cholangiopancreatography accurately predicts the presence or absence of choledocholithiasis. J Gastrointest Surg 1998; 2:573–579.
73. Boraschi P, Neri E, Braccini G et al. Choledocolithiasis: diagnostic accuracy of MR cholangiopancreatography. Three-year experience. Magn Reson Imaging 1999; 17:1245–1253.
74. Calvo MM, Bujanda L, Calderon A et al. Role of magnetic resonance cholangiopancreatography in patients with suspected choledocholithiasis. Mayo Clin Proc 2002; 77:422–428.
75. Tuech JJ, Binelli C, Aube C et al. Management of choledocholithiasis during pregnancy by magnetic resonance cholangiography and laparoscopic common bile duct stone extraction. Surg Laparosc Endosc Percutan Tech 2000; 10:323–325.
76. Bagci S, Tuzun A, Erdil A et al. Treatment of choledocholithiasis in pregnancy: a case report. Arch Gynecol Obstet 2003; 267:239–241.
77. Irie H, Honda H, Kuroiwa T et al. Pitfalls in MR cholangiopancreatographic interpretation. Radiographics 2001; 21:23–37.
78. Baer JL, Reis RA, Arens RA. Appendicitis in pregnancy with changes in position and axis of normal appendix in pregnancy. J Am Med Assoc 1932; 98:1359.
79. Connolly MM, Unti JA, Nora PF. Bowel obstruction in pregnancy. Surg Clin North Am 1995; 75:101–113.

Index